Refining Lanthanide Luminescence in Metallacrowns by Systematic Alteration of Hydroximate Ligands

by

Jacob C. Lutter

A dissertation submitted in partial fulfillment
of the requirements for the degree of
Doctor of Philosophy
(Chemistry)
in The University of Michigan
2018

Doctoral Committee:

Professor Vincent L. Pecoraro, Chair
Associate Professor Bart M. Bartlett
Dr. Svetlana V. Eliseeva, Habil., Centre National de la Recherche Scientifique
Professor Theodore G. Goodson, III
Professor Stephen C. Rand

Jacob C. Lutter

jclutter@umich.edu

ORCID iD: 0000-0002-0649-3737

Acknowledgements

It is said that it takes a village to raise a child, and the same goes for a PhD. There are many people to thank for various contributions to my growth as a PhD candidate. First and foremost, I want to thank Vince. His steadfast guidance over the past five years has not only helped me grown as a scientist, but also as a person. He encouraged me to take control of my own research, meaning he let me make mistakes, while also setting an example for how to interact with others, even on an international scale. Looking back on who I was during my matriculation, the change Vince has instilled is rather astounding. So with all sincerity, thank you Vince. I look forward to many more years of bugging you for advice.

I would also like to thank my committee. Each of you has had a profound contribution to the direction of my scientific development. Bart, my rotation with you was extremely helpful, and I learned quite a lot about how to think about magnetism beyond the scope of metallacrowns. Ted, my conversations with you were always informative, and also helped me to think about my luminescent complexes from a larger perspective. Steve, you were my favorite committee member at my candidacy. That was an extremely formative time for my career and your genuine interest and zeal for the lanthanide luminescence was a major factor in shaping my dissertation topics of interest. You are an awesome cognate. Lastly, Svetlana, I do not even know where to start. I am simply honored to have had a chance to work with you. You have taught me so much.

I would also like to thank fellow Pecoraro group members past and present, in particular, Evan, David, and Tu. The three of you were critical in my pre candidacy days in the lab and each of you pushed me to be better not only at my science but also in how to think about what each experiment means to my story. Alison and Cathy, thanks for the tough love, especially around candidacy. I feel like the two of you in particular really made me understand what I needed to be doing to prepare not only for the exam, but also for actually working on my dissertation projects. Leela, thank you for the indefatigable encouragement. Thanks to you I never could really hate my science for not working as I intended. Tyler and Karl, you guys are two of my best friends and have always been able to help me redirect my focus in positive ways. April and Bernadette, it's

been fun to be your “Mama Jake” and I have learned a lot from helping both of you get started on your journeys towards your PhD.

There are many others I would like to thank. I would like to thank Jeff Kampf for his help with crystallography. This is by far my favorite technique I have learned while working on my dissertation, and I am very grateful for your continued commitment to the psionics of metallacrowns. Matteo Tegoni, thank you for inviting me to work in Parma and for teaching me more about NMR than I ever thought I would know. Thank you Curt Zaleski for your mentorship while I was still just some punk kid and for the continued mentorship beyond my experiences at Shippensburg University.

Last, but not least, I want to thank my friends and family. Sam, Kyle, Kyle, Jake, Nate, and Molly; each of you have been great friends and I am very glad to know all of you. The board game nights and DnD have been a much needed distraction from the woes of graduate school. And my to my family, my mom, my dad, my brother Andy, thank you for your support as I have worked towards this milestone. You have been my biggest fans, and a much needed reminder that I am not in fact “normal.”

Table of Contents

List of Figures

List of Tables

List of Appendices

Abstract

Metallacrowns (MCs) are highly tunable complexes which have seen a wide range of research application including single-molecule magnets, host-guest studies and Ln-luminescence. The first near-infrared (NIR) emitting MC was a lanthanide-zinc metallacrown ($LnZn_{16}$) which can image human HeLa cells. Recently these MCs have expanded to include systems with gallium. This thesis focuses on the development of new structure types for GaMCs and the systematic modification of existing gallium based metallacrowns via alterations to the hydroximate ligands which act as antenna for lanthanide sensitization.

A new $LnGa_6L_9$ complex is described that has a higher antenna to Ln ratio compared to previously reported GaMCs to explore the relationship between the number of hydroximate ligands and Ln sensitization. This is important since the luminescence intensity (brightness) of the Ln emission is the product of the molar absorption and the quantum yield (QY). The structure contains six Ga(III) with a single Ln(III) encapsulated within a framework that matches a [3.3.1] organic cryptate. This metallacryptate sensitized Pr^{3+}, Nd^{3+}, Sm^{3+}, Tb^{3+}, Ho^{3+}, Er^{3+}, and Yb^{3+} emission, and increased the molar absorbance to $4.5 \cdot 10^4$ $M^{-1} \cdot cm^{-1}$. However, the QYs tended to be lower than previous GaMCs due to the proximity of high energy N-H oscillators, so the brightness of each series was similar. Slow magnetic relaxation was also studied and observed for Nd^{3+}, Dy^{3+} and Yb^{3+}; however, only Dy^{3+} exhibited a real relaxation barrier (U_{eff} = 12.7 K). These complexes could allow preparation of dual addressable “smart materials” which take advantage of both the luminescent and magnetic properties of Ln ions.

New GaMCs prepared with 5-iodosalicylhydroximate and/or 5-iodoisophtalate ligands were investigated for three objectives. First, ring substitution on the hydroximate led to red shifted maximum absorbance from 310 nm to 325 nm π-π* bands. Second, iodide could enhance intersystem crossing (ISC) which might aid lanthanide sensitization. Enhanced sensitization efficiency is observed when iodide is on carboxylate ligands in the case of Er^{3+}, but the cause is not yet known. Third, X-ray attenuation by these heavy atoms could yield bimodal MC based

luminescent/computed tomography (CT) contrast agents. Both monomeric and dimeric gallium 12-MC-4 complexes were made, and diffusion ordered spectroscopy (PGSE-DOSY) showed that only the dimeric complexes were solution stable. So, three combinations were made which had 4, 8, or 12 iodides on the MC. A positive correlation between quantum yield of Ln emission and iodide content was observed in the case of Sm^{3+} and Er^{3+} (up to 3.35% and $1.82 \cdot 10^{-2}$% respectively), suggesting a relationship between enhanced ISC and Ln emission. The brightness of these complexes were similar to a reported analog with no iodides. The ability to attenuate X-rays in DMF solutions was demonstrated, showing that these metallacrowns could be used as bimodal agents.

Successful functionalization of metallacrowns using copper catalyzed alkyne azide cycloaddition (CuAAC) and Sonogashira coupling is also deomonstrated. An ethynyl functionality was added to GaMCs, and the ability to perform CuAAC on these MCs was shown by appending either benzyl azide or biotin functionalized azide. Selective coupling controllably forming either single or multiple functionalization was demonstrated. This synthetic control is important to defray costs for expensive azide coupling partners. This ethynyl functionality was also introduced to the original zinc containing metallacrown scaffold. Finally, two new biaryl hydroximates were synthesized with the goal of red shifting excitation energy and allowing for two photon absorbance in metallacrowns.

Chapter 1

An Introduction to Luminescence, Lanthanide Ions and Metallacrowns

This thesis will demonstrate how the flexible design tenets of metallacrowns may be used to improve a specific property. In particular, the ability of metallacrown complexes to sensitize lanthanide ion emissions will be examined, and three rational design approaches for metallacrown design will be pursued. First, the value of serendipitous discovery of a new scaffold will be demonstrated in chapter 2, via the lanthanides' photophysical and magnetic properties of a new metallacryptate complex. Next, the incorporation of iodides onto known metallacrown scaffolds will be discussed, along with the effects on lanthanide photophysics and potential bimodal imaging potential. Lastly, in chapter 4, the ability to functionalize hydroximates for use in metallacrowns will be discussed, leading to the expansion of the already massive library of possibilities for metallacrown synthetic design. Chapter 5 will discuss the future directions of metallacrowns, based on what is learned from these studies.

1.1 The Phenomenon of Luminescence

Luminescence is the emission of light via the relaxation of electronically excited molecules. This phenomenon known as luminescence was initially reported by Sir John Frederick William Herschel in 1845. Herschel noticed that a solution of quinine in water appears colorless in most cases; however, when exposed to ultraviolet (UV) light the solution has "an extremely vivid and celestial blue color.[1]" This blue color is in fact the fluorescent emission of visible light from quinine excited by UV light. This fascinating phenomenon was then noticed in other aromatic compounds such as fluorescein and rhodamine, and quickly adapted as a method for labeling and monitoring solution state phenomenon. An early example of the use of luminescence was the demonstration of the interconnectivity of the Danube and Rhine via underground aquafers.[2] However, a strong understanding of the phenomenon was not reported

until Alexander Jablonski described the process in 1935 using a prototype of his famous diagram (Figure 1.1).[3]

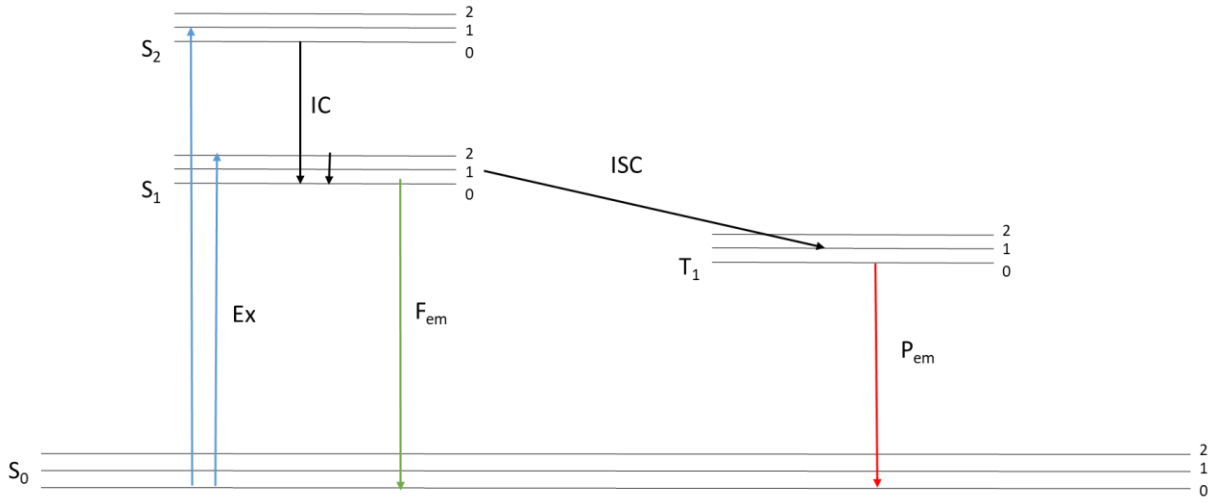

Figure 1.1. A Typical Jablonski Diagram for Luminescence.

A Jablonski diagram is now a staple for the discussion of luminescence since it describes the major pathways of luminescence as fluorescence and phosphorescence. Fluorescence is the process of electronic excitation of a molecule by absorbing a photon from its ground electronic state to an excited state followed by emission of a photon as the molecule relaxes to the ground state. In this case, there is a preservation in spin multiplicity during the transitions, and often involves a singlet to singlet state transition. This process is rapid with lifetimes on the order of nanoseconds since the only intermediary process is an internal conversion of electronic excited states into lower energy vibrational states. Phosphorescence also originates from the absorption of a photon; however, instead of relaxing from the immediately-accessed excited state the molecule undergoes intersystem crossing to another spin multiplicity (i.e. from a singlet to a triplet state). This excited state then relaxes back to the ground singlet state by emitting a photon. Since the process now involves intersystem crossing to and from the alternative multiplicity excited state, the optical transition is forbidden and phosphorescent lifetimes are much slower than fluorescent lifetimes, clocking in on the order of milliseconds to seconds rather than nanoseconds.

Another important aspect of luminescence is the observation that the energy of emission is always less than the energy absorbed. This general rule was first realized by G. G. Stokes in 1852.[4] Stokes used blue stained glass as a filter to isolate light with $\lambda < 400$ nm, which was

allowed to shine on a quinine solution, and was observed through a glass of yellow wine which served as a $\lambda > 400$ nm bandpass filter. This clever experiment demonstrated that higher energy light is absorbed by the solution but light of lower energy is emitted. The reason for this is explained by the Jablonski diagram in Figure 1.1. In the case of fluorescence the photons absorbed usually excite a transition from the $S_{0,0}$ state to an $S_{1,n}$ state. The first loss of energy is the internal conversion of these higher energy vibrational state to the $S_{1,0}$ state. Then as a photon is emitted, the relaxation may land on any $S_{0,n}$ state which again may undergo internal conversion to the $S_{0,0}$ state. These two opportunities for internal conversion of vibrational states are what give rise to the Stokes shift. These same principles are true for phosphorescent emission, with the added energy loss from the intersystem crossing step. This is why phosphorescent emission is not only slower than fluorescent emission but also is even more red-shifted from the energy absorbed.

The final major implication of the Jablonski diagram is the idea that the fluorescent emission band tends to be the mirror image of the absorption band.[2] This observation is supported by the Frank-Condon principle, which states that electronic transitions are much faster than the movement of nuclei so nuclear positions may be assumed as stationary.[2] This also means that if an absorbed photon excites an $S_{0,0} \rightarrow S_{1,1}$ ($0 \rightarrow 1$) as the most likely transition, then the most likely transition for relaxation is the inverse $S_{1,0} \rightarrow S_{0,1}$ ($1 \rightarrow 0$). Also, since ambient temperatures do not provide sufficient energy to populate $S_{0,n}$ states strongly and internal conversion encourages emission from the $S_{1,0}$ state, the energy difference in the absorbance and emission bands tracks with the linear energy difference in vibrational excited states. Of course, the observation of bands rather than lines means that excitation from $S_{0,0}$ and emission from $S_{1,0}$ are not the only pathway, but simply the most common pathway. This mirror image rule will break down for a few reasons.[2] The first is that the S_1 state may be accompanied by required geometric change in the molecule, thus nullifying the Frank-Condon assumption. Second, there may be a reaction between molecules with relatively long lived S_1 states such that excimers may form. Lastly, the excited state may perform energy transfer to a donor instead of emitting a photon, a concept which will become very important in the discussion of lanthanide chromophores in this thesis.

When one discusses luminescence there are two parameters that are always of interest. The first has been mentioned already and is the observed lifetime.[2] These lifetimes are not a

specific time between absorption and emission, but are rather an average of the time spent in an excited state. This value may be calculated by modelling a decay curve of emission intensity as a function of time using a monoexponential function ($I = I_0 e^{-\frac{t}{\tau}}$), where I is intensity, I_0 is the initial intensity, t is the time, and τ is the lifetime. At the point where t equals τ, the expression simplifies to $\frac{I_0}{e}$ allowing for straight-forward experimental determination of the average lifetime. The second parameter is the quantum yield, which is the ratio of the photons emitted to the photons absorbed.[2] There are two methods for determination of quantum yield, direct determination using an integrating sphere, and relative determination using a standard with a known quantum yield.[2,5] In the first case, the number of photons absorbed is determined by measuring the difference in integrated signal observed ($\int_{\lambda_{ex}-n}^{\lambda_{ex}+n} I(\nu)d\nu$) between a blank and the sample (n is the slit width) while the number of photons emitted is determined as the integral of the luminescent emission band ($\int L(\upsilon)d\upsilon$). In principle, these values may be converted into the quantum yield with proper treatment. However, this method requires specialized equipment (integrating spheres) so another method using a standard is also very popular. This method uses solutions of known optical density, typically of 0.1 absorbance units or less to avoid re-absorbance effects. These solutions are measured for emission and integrated just like in the first method. These integrals are then plotted as a linear function of optical density to find a slope, m. These slopes are used to calculate the quantum yield according to equation 1.1

$$\phi = \phi_{std}(\frac{m}{m_{std}})(\frac{n}{n_{std}})^2 \qquad (1.1)$$

Where ϕ is the quantum yield and n is the refractive index of the solvent, and values for the standard are marked with the subscript std. Together these properties express how a lumiphore may be applied, since some application may need the nanosecond lifetimes of fluorescence, while other may need longer lifetimes. The brightness is also important, which is expressed as the product of the absorptivity (or extinction coefficient) and the quantum yield.[6] The scope of this thesis will focus on the luminescence of a specific kind of lumiphore, the lanthanide ions, and explore methods for refining the brightness of these ions in coordination complexes.

1.2 Lanthanide Ions and Their Applications

The lanthanide ions are involved in a wide array of applications including telecommunications, magnetism, luminescence, lasers, and catalysis. In particular, the unique magnetic and optical properties of lanthanide ions will be examined in this thesis. Lanthanides are used in permanent magnetic materials, such as the NdFeB magnets that are common enough to be available to the general public. However, the use of lanthanide (III) ions in molecular magnetism has become desirable due to the large spin-orbit coupling (SOC) inherent in these ions.[5,7] Such SOC properties leads to enhanced single ion anisotropy and access to larger magnetic moments. Both of these properties are thought to be critical for the generation of complexes known as single molecule magnets (SMMs).

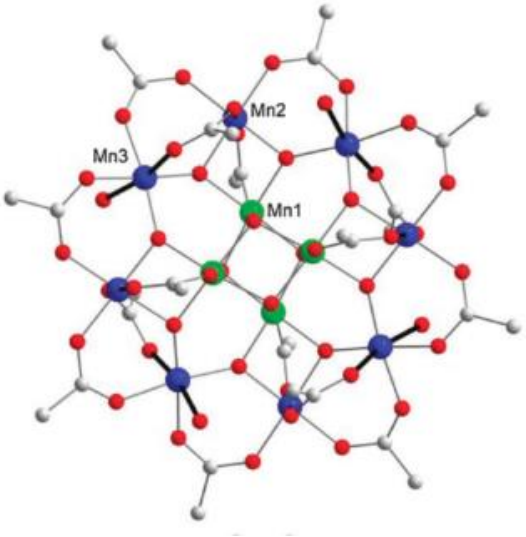

Figure 1.2. Structure of the $Mn_{12}OAc$ complex.[8]

The first of these SMMs was $[Mn_{12}O_{12}(OAc)_{16}(H_2O)_4]\cdot 4H_2O\cdot 2HOAc$ ($Mn_{12}OAc$, Figure 1.2) discovered by Lis in 1980[9] and further characterized by Christou, Hendrickson and Gatteschi in 1993.[10] The basic idea behind SMMs is that a single molecule will have its own barrier to magnetization relaxation, rather than large domains as is observed in magnetite. The height of this energy barrier is dependent on two properties, the total spin (S) and the magnetic anisotropy (D) (Figure 1.3).[11] A larger total spin means that there are more sublevels between Ms = 0 and Ms = max while a larger and negative anisotropy means that these sublevels are spaced further apart, and that the lowest energy level is the maximum value for ±Ms. For an even spin number, this barrier may be expressed as $|D|S^2$ and for odd numbered spins this expression is

|D|(S^2-1/4).[11] This barrier is susceptible to quantum tunneling of magnetization when the ±Ms sublevels have the same energy.[11]

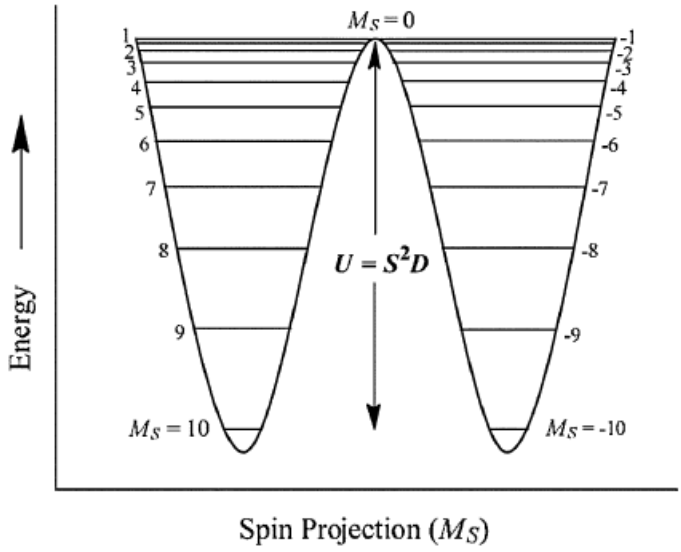

Figure 1.3. Energy diagram for the Mn_{12}OAc complex.[10]

SMMs are characterized by various experiments using a superconducting quantum interference device (SQUID). The first is the observation of an effective barrier to magnetization relaxation. This parameter is observed by characterization of alternating current magnetic susceptibility by varying both the frequency of a small (approx. 3 Oe) drive field and the temperature of the experiment. This experiment expresses the angle of the drive field moment and the sample's moment as χ_m' and χ_m" where χ_m' is the in-phase (also called real) molar susceptibility and χ_m" is the out-of-phase (or imaginary) molar susceptibility (Figure 1.4a). At the maximum value for χ_m" at a given temperature, the frequency of the samples moment reversal matches the drive field, and allows for the calculation of the rate of the reversal. The natural logarithm of this rate versus the inverse of the temperature of the peak maximum gives a linear relation that may be expressed as an Arrhenius relationship. From the Arrhenius plot, the magnitude of the effective barrier may be calculated. Yet, the presence of the χ_m" component is only suggestive of SMM behavior. To demonstrate the SMM as a quantum phenomenon, magnetic hysteresis is used. The application of a strong direct current field will magnetize the sample to match the direction of the applied field. As the field strength increases, the Zeeman Effect will adjust the energies of magnetic sublevels until Ms and Ms-1 are the same energy

(Figure 1.5). This causes a characteristic jump in magnetization in the hysteresis loop and is considered a diagnostic observation for the presence of SMM behavior (Figure 1.4b). From these experiments two other parameters may be extracted, the coercive field (the field strength were the samples moment switches signs) and the blocking temperature (the highest temperature with an open hysteresis loop).

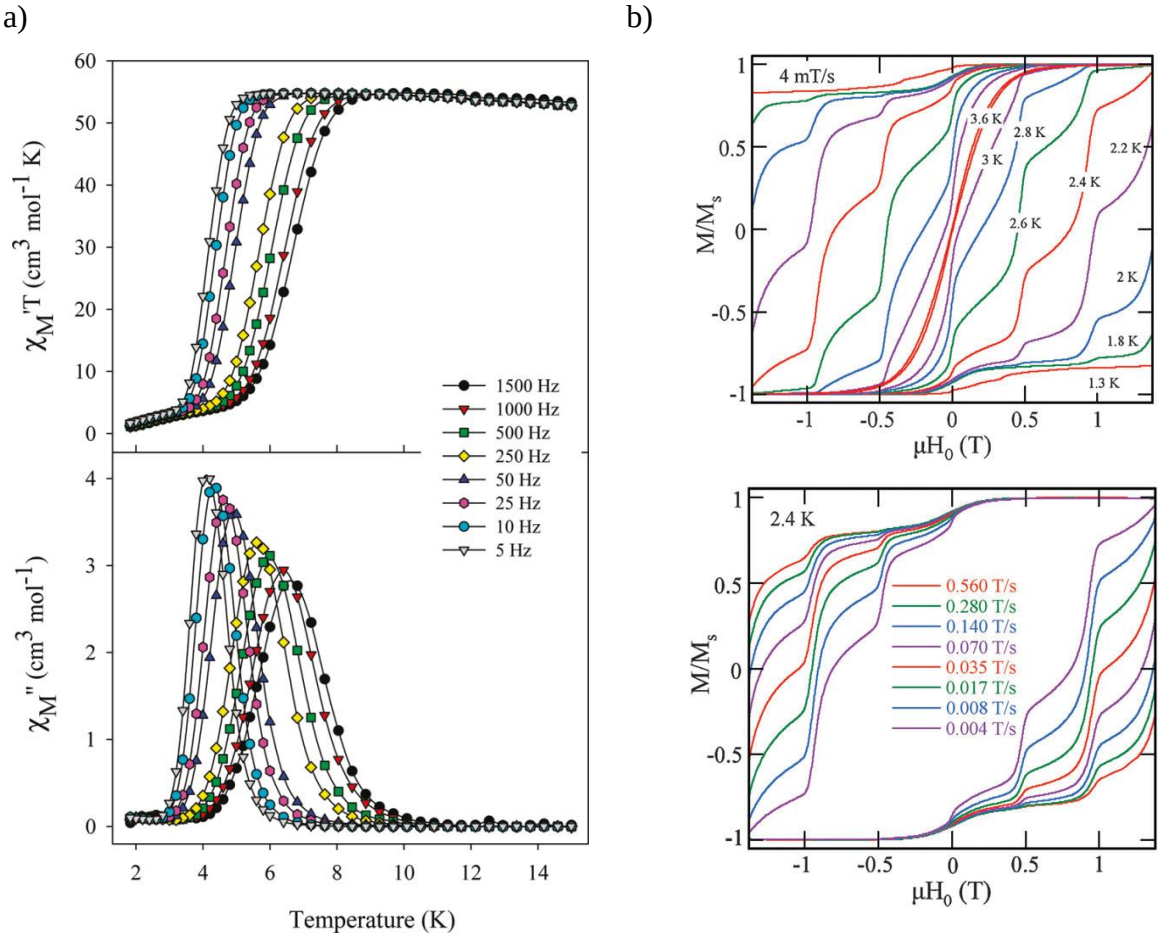

Figure 1.4. a) The AC susceptibility plots for the $Mn_{12}OAc$ where the in-phase component is on top, and the out-of-phase componenet is on the bottom; and b) The magnetic hysteresis of the same, where the temperature is varied on top and the sweep rate is varied on the bottom. Both show the characteristic steps typical of SMMs.[8]

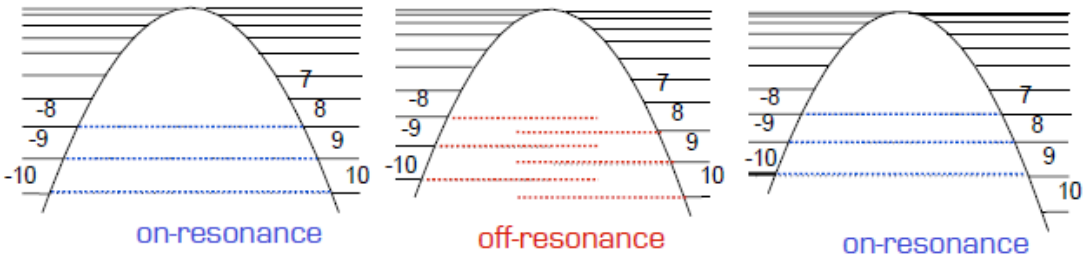

Figure 1.5. The Zeeman effect causes on and off resonance between Ms sublevels.[8]

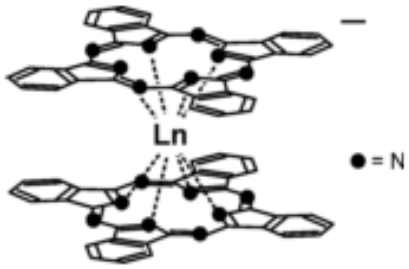

Figure 1.6. Structure of the $Tb(Pc)_2$ complex.[12]

In 2003 Ishikawa and coworkers demonstrated the first observation of a lanthanide only complex with slow magnetic relaxation, the terbium (III) bis(pthalacyanine) complex ($Tb(Pc)_2$, Figure 1.6).[12] This landmark discovery drew attention to the advantages of the lanthanide ions in SMMs, even as the only paramagnetic ion in the complex. Since then, others have worked towards understanding how to control a lanthanide as an SMM. Towards this goal, two groups have been able to generate design principles for the use of SMMs. First, Coronado and coworkers suggested that the coordination geometry of the lanthanide is important. By examining lanthanide complexes between polyoxometallate (POM) structures, he was able to demonstrate that in his POM complexes only Er^{3+} demonstrated true SMM behavior with a measurable barrier.[13] When this is compared to the initial studies by Ishikawa, where only Tb^{3+} behaved as a measureable SMM it is clear that ligand field plays a role.[12] From this knowledge it was postulated that despite the similarity in the coordination environment, the position of the ligands about the lanthanide are very important. For the initial $Tb(Pc)_2$ complex an axial elongation is observed in the square antiprism, while in the POMs an axial compression is observed.[13] This work was expanded by Long and coworkers in 2011, using basic principles to explain how the coordination geometry is important. Long postulated that the inherent anisotropy

from the lanthanide ions goes hand and hand with specific shapes of the electronic cloud from occupied f-oribtals.[7] So as more f-orbitals are populated across the Ln series, the shape changes from oblate to prolate (Ce^{3+} → Sm^{3+} and Tb^{3+} → Yb^{3+}) with the exception of the isotropic ions La^{3+}, Gd^{3+} and Lu^{3+} (Figure 1.7). The design of coordination environments which accommodate this electronic density enforces a ground state with the magnetic moment along the easy axis of magnetization due to minimization of electronic repulsions (Figure 1.8).

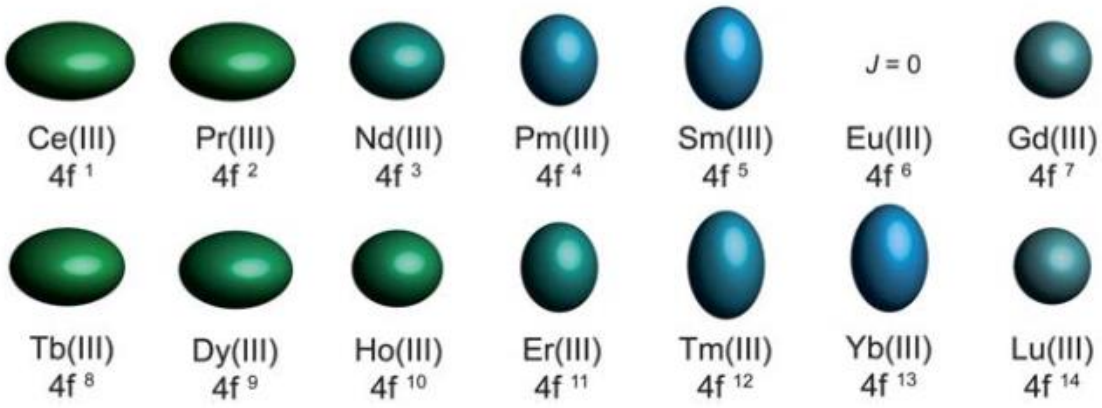

Figure 1.7. The shape of the 4f electronic cloud for each lanthanide.[7]

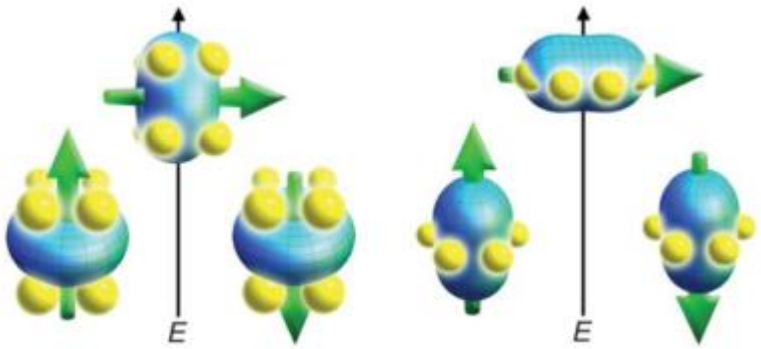

Figure 1.8. Depictions of low and high energy states for oblate (left) and prolate (right) ions shown in blue. The yellow spheres represent the ligand field and the green arrow is the moment of magnetization.[7]

In 2011, Long and coworkers found a way to enforce a pseudoferromagnetic interaction between lanthanide ions by incorporating a small organic radical between the two paramagnetic centers.[14,15] This landmark discovery (with the drawback of requiring air-free conditions) was first demonstrated using a N_2 radical situated between two lanthanides (Gd^{3+}, Tb^{3+}, Dy^{3+},Ho^{3+}, and Er^{3+}, Figure 1.9). The lanthanide moment is able to couple to the diffuse moment from the

unpaired spin on the N_2 radical in an antiferromagnetic manner, making the lanthanide moments appear to be ferromagnetic. Thanks to this pseudoferromagnetic interaction, this compound showed effective barriers and record-setting coercive fields of about 1.5 T and blocking temperatures up to 8.3 K, which was unheard of for a Dy^{3+} complex (Figure 1.10, left). To prove the necessity of the radical species, the radical was allowed to return to a neutral species, and the susceptibility of the species were compared for Gd^{3+} and Dy^{3+}. When the N_2 is a radical, the DC susceptibility shows an increase in moment as the temperature cools, while the moment only decreases in the case of non-radical linker (Figure 1.11). The effective barrier for the Dy^{3+} analog was determined to be 178 K, which is again, impressive for this type of complex.[15] For the Tb^{3+} analog, the results were even better, with a coercive field of about 3.5 T, a blocking temperature of 13.9 K (Figure 1.10, right), and an effective barrier of 326.7 K. Since then, a few other radicals were attempted to try to improve the stability of the radical beyond inert conditions. However, these complexes with bipyrimidine and tetra-2-pyridinylpyrazine linkers showed significantly reduced properties.[16]

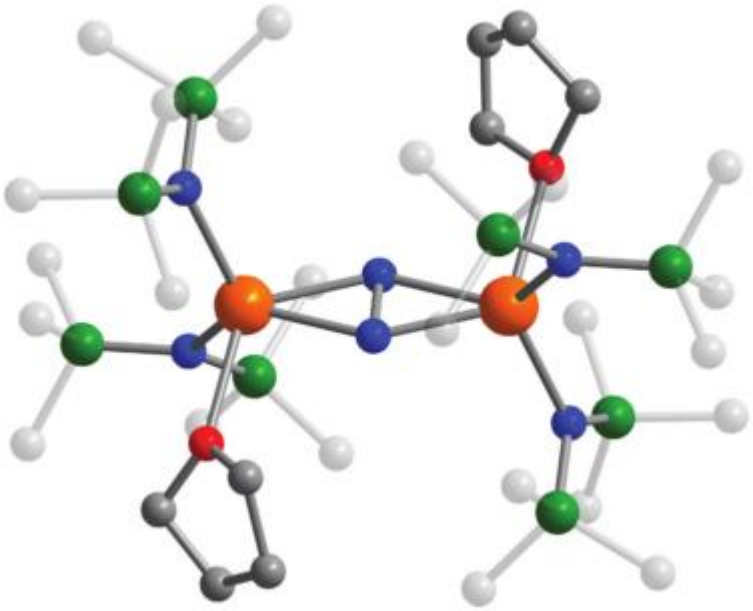

Figure 1.9 Structure of $[\{[(Me_3Si)_2N]_2Gd(THF)]_2(\mu\text{-}\eta^2\text{:}\eta^2\text{-}N_2^-)]$ featuring a bridging radical.[15]

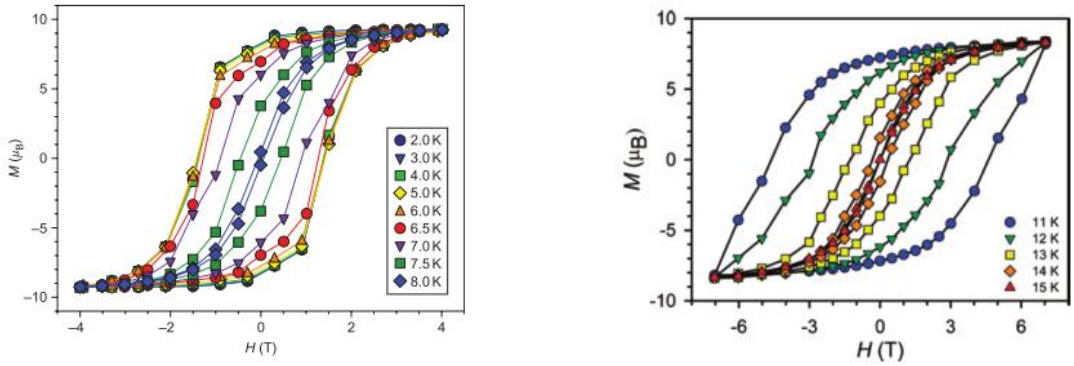

Figure 1.10. Hysteresis loops of the Dy^{3+} (left) and Tb^{3+} (right) analogs of the radical bridged compound.[15,17]

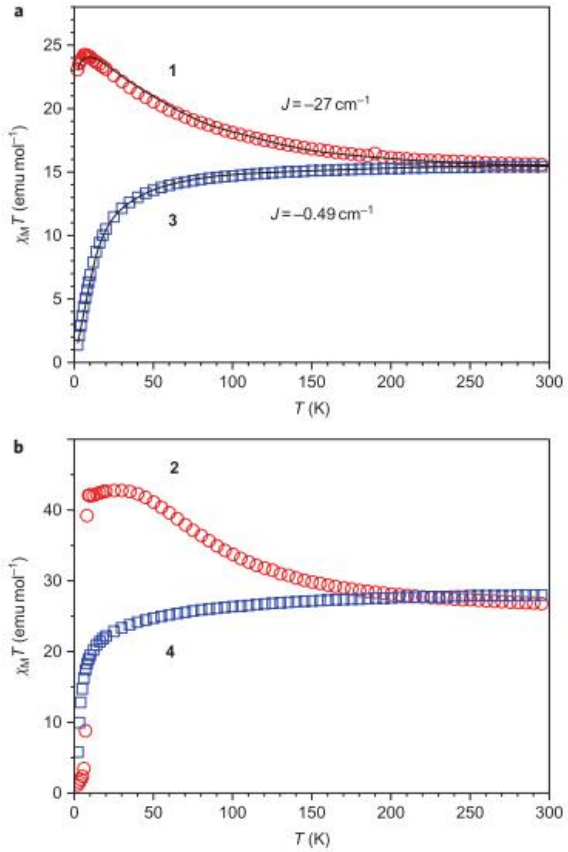

Figure 1.11. DC Susceptibility of a) Gd analogs with the radical (red) and without the radical (blue) and b) DC susceptibility of the Dy analogs of the same.[15,17]

A wide range of optical applications are possible with lanthanides ranging from telecommunications to lasers, thanks to the unique electronics of these ions. Their interesting optical properties were first noticed in the 1880s but were not fully appreciated until van Vleck

discussed them in 1937.[18] In 1979, Soini and Hemmilä began to examine the lanthanide ions as possible probes, even in biological species.[5] Just as in the case of lanthanide magnetic properties demonstrated in the study by Long and coworkers[7], the lack of perturbation of the f-orbitals from the ligand field leads to very unique electronic structure (Figure 1.12), and thus very characteristic transitions with narrow bandwidths.[5,19] However, these f-orbital to f-orbital transitions are also forbidden by the Laporte selection rule which states that an electronic transition may not occur between two states with the same parity. In the context of atomic orbitals, this means that electronic transitions are allowed when moving from an orbital which is gerade (*g*, symmetric about an inversion center) to one that is ungerade (*u*, antisymmetric), but disallowed when moving from *g* to *g* or *u* to *u*. Since the f-orbitals are all *u*, f-f transitions are disallowed by this rule. In the case of other Laporte forbidden transitions such as d-d transitions, vibronic coupling allows for exceptions to this rule. The f-orbitals have infinitesimal, yet nonzero bonding contributions that allow for similar exceptions, but on a much more infrequent scale. This restriction is also applicable to the relaxation of an excited lanthanide ion, which means that the lifetime of a lanthanide emission will be very long compared to many other lumiphores.[5]

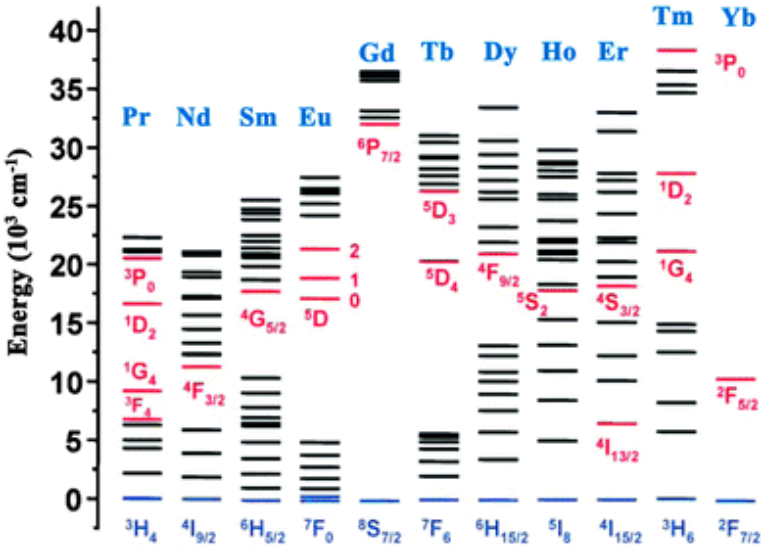

Figure 1.12. An energy diagram for lanthanide electronic energy levels. The possible emissive microstates are shown in pink.[20]

To circumvent the issue of low absorbance, it is possible to use another chromaphore to absorb a photon then transfer this energy to a lanthanide ion.[5,19,21–25] This process, known as the

"antenna effect" is very common, especially in applications using lanthanide probes. The specific pathways of energy transfer are not always fully understood and are likely different on a case by case basis. As shown in Figure 1.14 the energy could be transferred from the singlet, triplet, or charge transfer states. Regardless, the process is known to work quite well when certain design tenets are followed:

1: The ligand should form a stable and coordinatively saturated Ln complex

2: Ln proximity to X-H oscillators (X is carbon, nitrogen or oxygen) should be minimized

3: There is an energy gap of at least 2,500 cm^{-1} between the Ln emissive state and the feeding energy level.

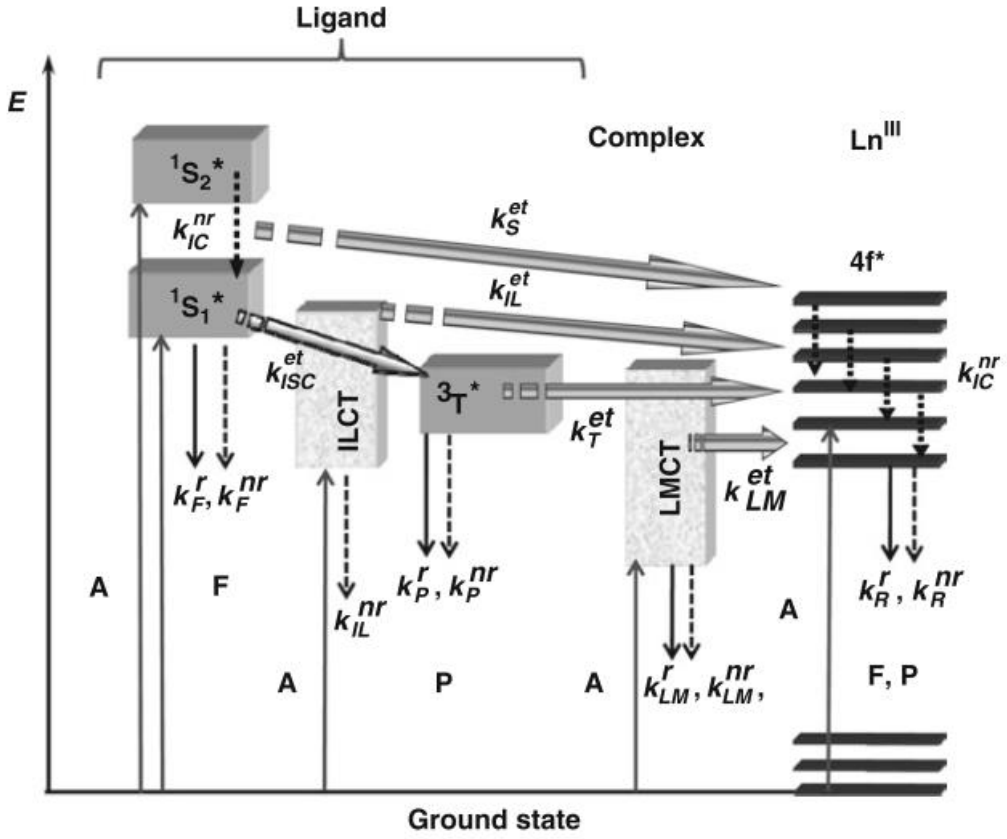

Figure 1.13. Pathways for lanthanide sensitization via the antenna effect. Solid arrows show radiative processes while dotted arrows are non-radiative. A = absorbance, F = fluorescence, P = phosphorescence, IC = internal conversion, ISC = intersystem crossing, k = rate constant, r = radiative, nr = non-radiative, et = energy transfer, ILCT (IL) = intra/inter-ligand charge transfer, LMCT (LM) = ligand to metal charge transfer (usually 5d metal complexes).[5]

The reason for oscillator exclusion is due to the irreversible energy transfer to oscillator overtones from an excited lanthanide ion which will quench the luminescence. Since overtone transitions are forbidden, fewer required overtones to match the Ln energy means more quenching. So the type of oscillator is important, where O-H is the most energetic (and needs the fewest overtones), followed by N-H, then C-H oscillators. This quenching process is also distance dependent, so the design of a ligand may focus on reducing X-H bonds near the lanthanide both from solvent and from the ligand scaffold, selecting for aromatic C-H bonds (the lowest energy of these oscillators) or by using deuterated or fluorinated ligands. Ligand design should exclude higher energy oscillators to longer distances from Ln to avoid the energy transfer, or to use X-H oscillators with a larger number of overtones between the oscillator's ground state and the lanthanide ion's excited state. There have been a large number of successful antenna reported, including Lehn cryptands, DO3A derivatives, and other chelators such as H22IAM, H(2,2)-TIAM, HOPO, and Tsox.[23,26–30,190] In 2011, Pecoraro and coworkers showed that this process is possible using a coordination complex antenna known as metallacrowns.[21] This landmark complex demonstrated excellent sensitization for ytterbium and neodymium as well as oscillator exclusion, and sparked interest in studying these metallacrowns as antennae for lanthanide complexes.

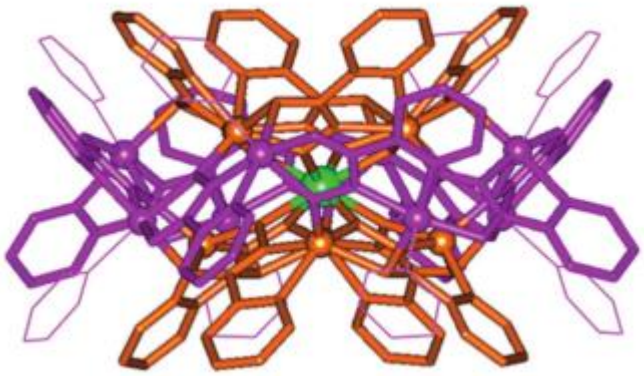

Figure 1.14. The structure of the Ln[12-MC$_{Zn^{II}N(picHA)}$-4]$_2$[24-MC$_{Zn^{II}N(picHA)}$-8](OTf)$_3$ complex.[21]

1.3 Introduction to Metallacrowns

Since their discovery in 1989, metallacrowns (MCs) have found many areas of study and application.[31] These metallamacrocyclic complexes are considered to be an inorganic structural analog of crown ethers, where the $[C\text{-}C\text{-}O]_n$ repeating unit is instead a $[M\text{-}N\text{-}O]_n$ repeating unit and M is typically a 3*d* transition metal (Figure 1.15). The N-O portion typically comes from a hydroximate moiety, which binds two M^{n+} ions as part of a fused chelate ring. Following this analogy, MCs adopt a similar nomenclature to crown ethers, where a classic 12-C-4 may be compared to a 12-MC-4 (Figure 1.15). The scope of sizes of MCs are numerous ranging from 9-MC-3 complexes to 60-MC-20 complexes.[32]

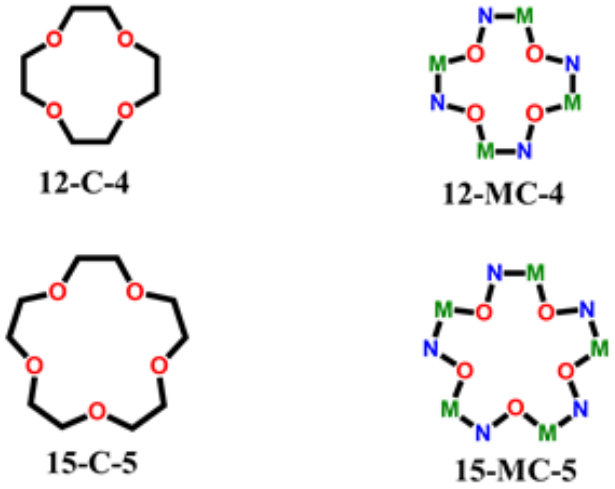

Figure 1.15. Metallacrowns as a structural analog to crown ethers.

As in crown ethers, metallacrowns are capable of binding a wide range of mono-, di- and trivalent cations within the core structure. MCs have also shown tolerance to substitutions of the ring M^{n+} ion and the functionalization of the hydroximate ligand.[21,22,24,32–40] Metallacrown synthesis follows the concepts of supramolecular chemistry, where the rational design of polynuclear complexes can be predicted based on the choice of the metal ion, the MC framework and ancillary ligands. These MCs can also be linked to form higher-ordered structures. Thus, a large library of MC structures are possible. In addition, there are examples of complexes such as metallacryptates and collapsed metallacrowns which still feature the metallacrown M-N-O motif, but do not perfectly align with the crown ether comparison. These molecules are still noteworthy

in the field of molecular magnets or in speciation studies and will also be discussed in this chapter.[39,41–45] Finally, there are azametallacrowns that present nitrogen ligands to the central metal ions and inverted metallacrowns that orient the ring metals toward the center of the metallacycle and subsequently bind anions.[46,47] Given this wide variety of possible metallacrown and metallacrown-like structures, these complexes can be synthesized with specific physical and chemical properties tailored to a particular application.

It turns out that metallacrowns are excellent chelators of lanthanide ions. One study by Pecoraro and coworkers in 2010 showed how a Ca^{2+}[15-$MC_{Cu}{}^{II}{}_{N(L)}$-5], where L is phenylalanine hydroximate or tryptophan hydroximate 15-MC-5 has a preference for binding lanthanides over calcium in the central cavity.[48] By examining spectroscopic changes while titrating in a lanthanide to Ca^{2+}[15-$MC_{Cu}{}^{II}{}_{N(L)}$-5] a log K for the displacement was determined. It was noticed that the later lanthanides (Gd^{3+} to Yb^{3+}) were more selective than the early lanthanides (La^{3+} to Gd^{3+}). The reason for this was assumed to be a better match of the cavity radius to the ionic radius of the lanthanide.[48,49] This kind of selectivity may also be inferred for a manganese(III) salicylhydroximate (shi^{3-}) construct. In the case of only having manganese present, a manganese(II) ion is encapsulated in the central cavity.[31] However, when lanthanides are used the lanthanide is bound to the oxime oxygens instead, even though a stoichiometric excess of manganese is used.[34] In this case it is less about the cavity size and more about the metal preference of the oxime oxygens. Given that lanthanides are hard acids and the oxime oxygens are rather hard bases, this preference makes a fair amount of sense. All of this demonstrates that metallacrowns are excellent binding partners for lanthanides and make for excellent platforms to study lanthanides in a tunable environment.

While metallacrowns have a storied past in host guest binding, molecular magnetism, and lanthanide luminescence; recent literature has shown adaptation of metallacrowns into new extended structures, rational control over magnetic properties, and strong potential in imaging applications. The use of metallacrown complexes as imaging agents in particular will frame the scope of this thesis as the refinement of known luminescent metallacrown structures, but this is only a portion of what is possible with these extraordinary complexes. To appreciate the scope of metallacrown chemistry right now, it is important to summarize these recent studies.

1.4. Extended Structures of Metallacrowns

The formation of coordination polymers composed of metallacrowns has been of growing interest, especially towards development of metal-organic frameworks (MOFs) using MC building blocks.[50] Since MCs have shown interesting properties such as slow magnetic relaxation and lanthanide-based emission and are tolerant to ligand and metal alterations, this push is very logical. After all, the major tenet of MOFs is that a modular design allows substitution of the basic framework with similar nodes or linkers in order to form the same connectivity. Coordination polymers of MCs in one-, two- and three-dimensions have been reported.[51–57] Recent work has focused on 1-D chains of MCs, 2-D networks of MCs that have a stacking structure akin to a MOF, and a 3-D MOF network.

1-D Chains of Metallacrowns

One-dimensional chains of metallacrowns are not a new concept and have come in several different forms including alpha-helical chains.[51,58] These metallacrowns were interesting for many different potential applications such as ion conductivity, catalysis, and single-chain magnets.[16,59–61] Recently Zaleski, *et. al.* had reported the ability of Na_2[12-$MC_{Mn^{III}N(shi)}$-4] MCs, where shi^{3-} is salicylhydroximate, to form 1-D chains using bridging propionate and butyrate ligands to span the MCs.[62] The bridge between the MCs is formed from the binding of the carboxylate group to three metals, a ring manganese(III) and a central cavity sodium ion from one MC, and a ring manganese(III) from an adjacent MC such that the planes of each MC are close to parallel (Figure 1.16).

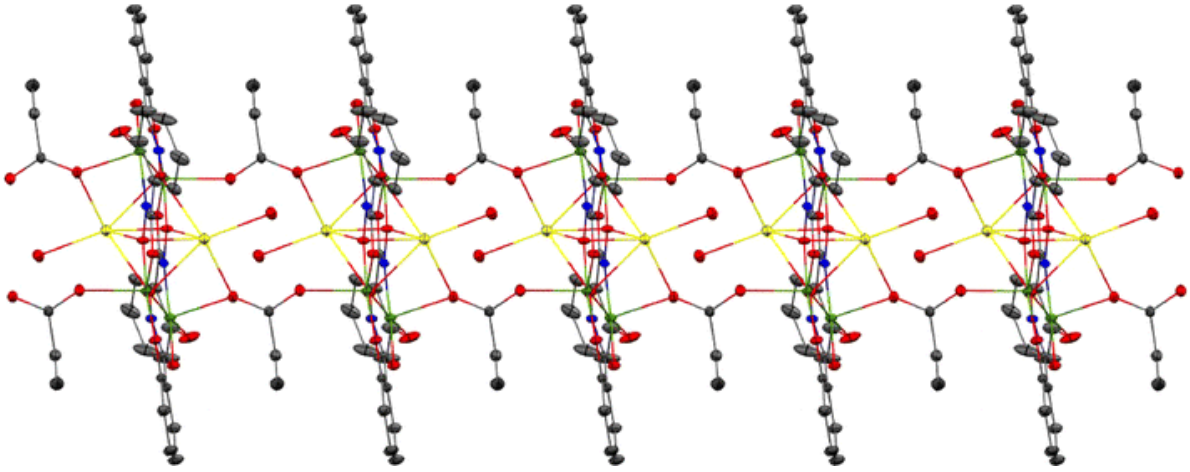

Figure 1.16. One-dimensional chains of Na_2[12-$MC_{Mn^{III}N(shi)}$-4] linked by propionate (top) and butyrate (bottom).[62]

There has also been a report by Croitor, *et. al.* of inverse 9-MC-3 complexes using Cu^{2+} as the ring ion.[63] The MCs were made using pyridine-2-aldoxime, and the MCs formed one-dimensional chains when connected via terephthalate bridging units. At each end of the terephthalate, one oxygen atom of the carboxylate group forms a hydrogen bond with the μ_3-hydroxy group in the center of the inverse MC and the other oxygen atom of the carboxylate group binds to a ring Cu^{2+} ion (Figure 1.17). This connectivity is then repeated to form the one-dimensional chain.

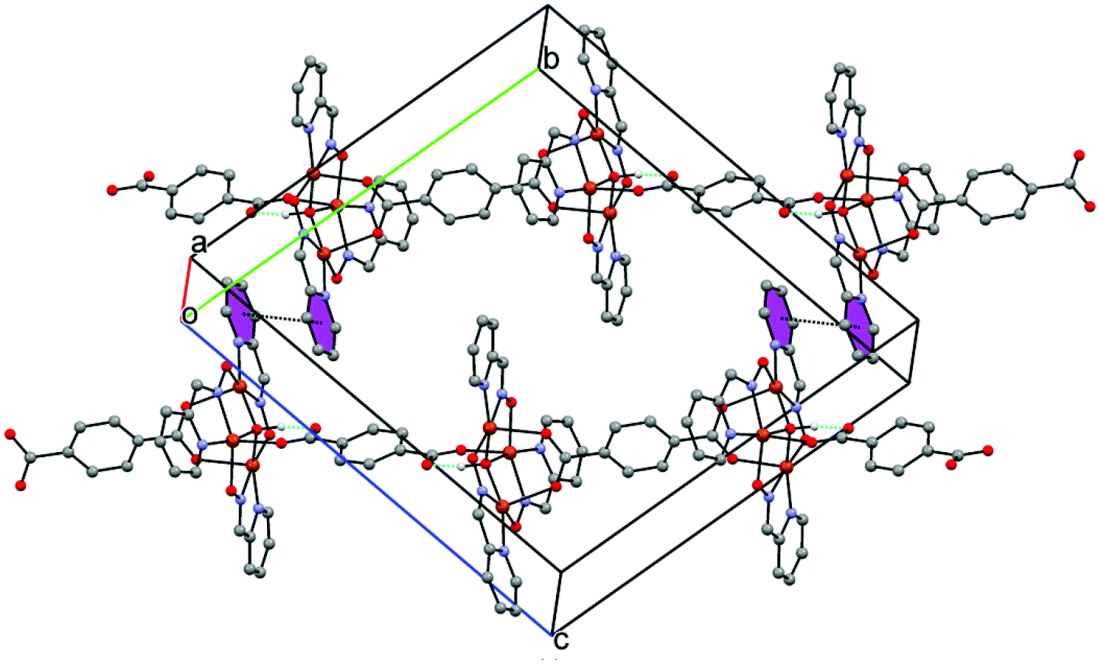

Figure 1.17. One-dimensional chains of inverse copper(II) 9-MC-3s linked by terephthalate anions.[63]

2-D Sheets of Cu^{2+} 12-MC-4 Complexes with Permanent Porosity

Tegoni, Pecoraro, and coworkers demonstrated a set of 2-D networks based on $\{Cu[12\text{-}MC_{Cu^{II}N(hinHA)}\text{-}4]\}^{2-}$ units, where $hinHA^{3-}$ is 3-hydroxyisonicotinic hydroximate.[50] The nitrogen atom in the aromatic ring was the key to forming both networks, with different binding modes to Cu^{2+} ions distinguishing the two solid state structures. The first repetitive motif involved $[(OAc)Cu(Py)]^{+}$, where ^{-}OAc is acetate and Py is pyridine, connectors between the pyridyl nitrogen atoms on $hinHA^{3-}$ ligands from two separate MCs (Figure 1.18). The linking Cu^{2+} ions are in a distorted square planar environment. Each $hinHA^{3-}$ in the MC was able to bind a linker to form a 2-D "checkerboard arrangement." The second MC extended solid did not involve

exogenous Cu^{2+} ions, instead, the pyridyl nitrogen in the $hinHa^{3-}$ ligands bound to ring Cu^{2+} on an adjacent metallacrown, such that rectangular compartments are formed using four MC units (Figure 1.18). The first network was shown to be a permanently porous material, while the second was not porous. However, alterations in metal choice could lead to very interesting coordination polymers utilizing the second network.

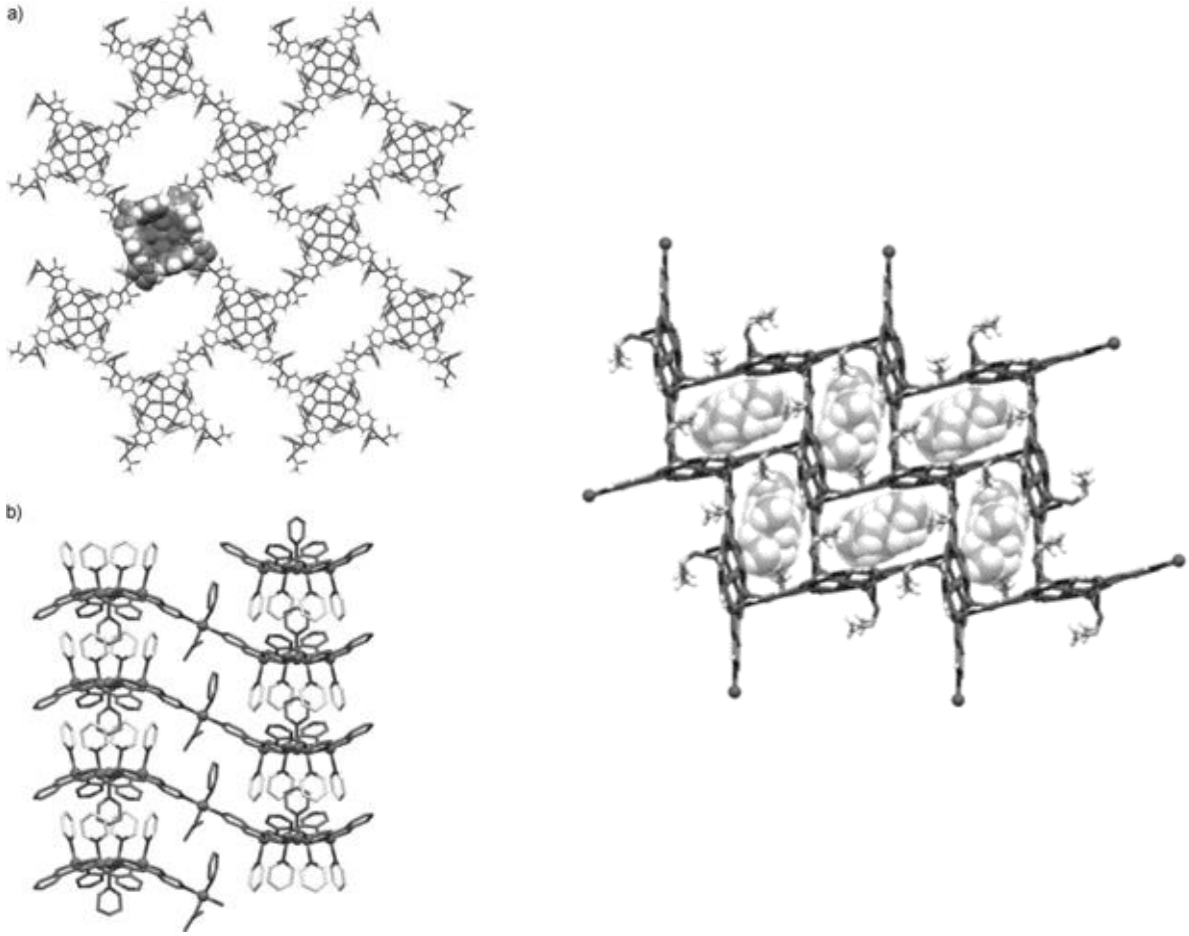

Figure 1.18. A two-dimensional network of Cu[12-$MC_{Cu^{II}N(hinHA)}$-4] complexes linked by $[(OAc)Cu(Py)]^+$ units forms porous channels (left), and a two-dimensional network of Cu[12-$MC_{Cu^{II}N(hinHA)}$-4] complexes, which interact at approx. 90° angles (right).[50]

The permanent porosity and stability of the first network was demonstrated using TGA, PXRD, and isothermal gas adsorption. The TGA analysis shows a two-step decomposition, one close to 60 °C, which was attributed to the loss of solvent molecules in the pores, and another close to 340 °C that is likely the rapid decomposition of the MC within the network. The MC crystallinity was determined to be stable up to temperatures of 225 °C based on variable temperature PXRD experiments. The isothermal gas adsorption experiments were done using N_2

at 77 K, as well as CO_2 at 195 and 273 K. The N_2 adsorption experiment was done to determine the surface area and pore size of the network, which were estimated at 515-568 $m^{2}{\cdot}g^{-1}$ and 0.583 $cm^{3}{\cdot}g^{-1}$, respectively. Isothermal adsorption of CO_2 at 195 K and 273 K showed an uptake of 23.3% and 7.3% (w/w), respectively. These values are comparable to other MOF structures.

A 3-D MOF of 24-MC-6 Metallacrowns

An example of a 3-D MOF was synthesized by Liang and coworkers using 2-hydroxyisophthalic acid (H_3ipO) and Co^{2+}, Mn^{2+}, Cd^{2+}, or Zn^{2+} as the coordinating metals.[64] The four analogs $[M_6(HipO)_6]{\cdot}6H_2O$ were synthesized and characterized by X-ray crystallography, and the compounds were nearly isostructural for all four metals. The MC building blocks of the network consist of 24-MC-6 ring with repeating units of [M-O-C-O] derived from the $HipO^{2-}$ ligands. Each metal has a six coordinate octahedral geometry where five oxygens come from $HipO^{2-}$ carboxylates and the final coordination site is occupied by a phenol oxygen from the $HipO^{2-}$ ligand. The six metal centers are arranged in a chair confirmation around the 24-MC-6 ring, comparable to cyclohexane (Figure 1.19). Each 24-MC-6 is connected to its six nearest 24-MC-6 neighbors by twelve bridging HipO, where the HipO allow for propagation along all three crystallographic axes such that the 24-MC-6 subunits form a cubane like grid with (4,6)-connected pcu topology (Figure 1.20).

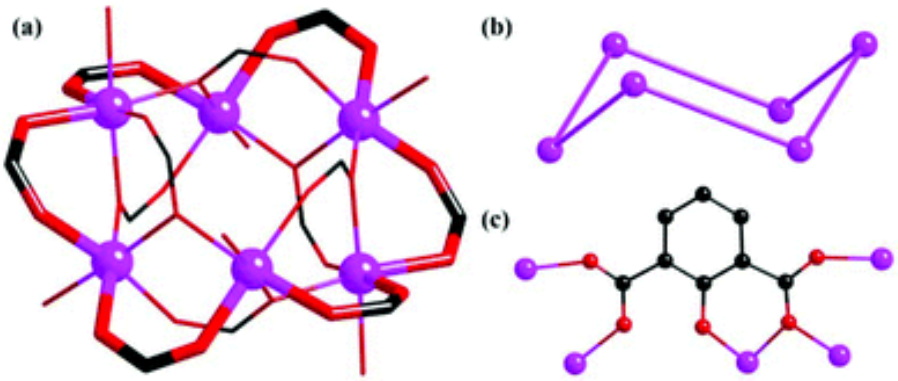

Figure 1.19. 24-MC-6 complexes (left), which arrange its metals in a chair conformation like cyclohexane (top right), form a 3-D MOF. The metal binding scheme for $HipO^{2-}$ is shown in the bottom right.[64]

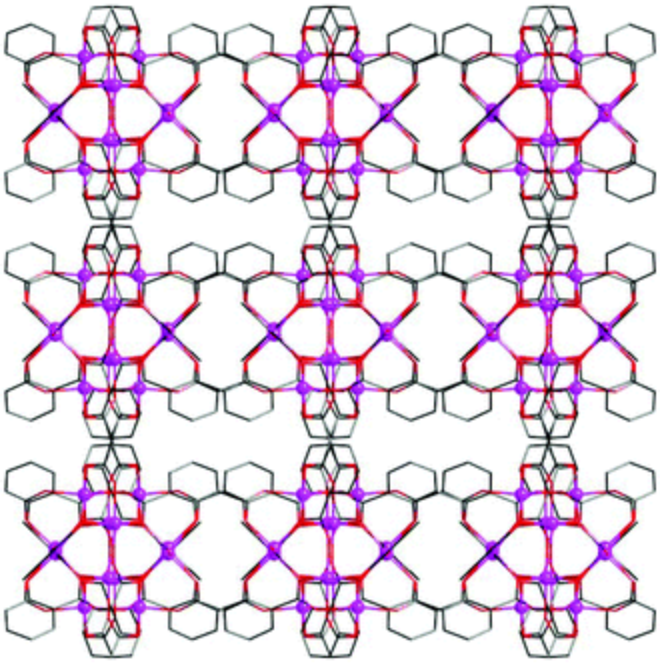

Figure 1.20. Propagation of 24-MC-6 subunits in the 3-D MOF form a cubane-like grid with (4,6)-pcu topology.[64]

The composition of the MOF was further confirmed by TGA and PXRD. The magnetocaloric properties of the Co^{2+} analog will be addressed later in this review, while the Mn^{2+} analog only showed antiferromagnetic interaction between the metal centers. The Cd^{2+} and Zn^{2+} versions were studied for ligand based luminescence properties both of which showed phosphorescence at RT. The complexes were excited at 335 nm and both had emission close to 405 nm. The free ligand was also studied and showed emission at 447 nm upon excitation at 347 nm. There was a blue shift of the luminescence of the MOF which is very interesting and was attributed to the attachment of HipO to the metal centers.

1.5 Metallacrowns as Metal Oxide Precursors

The idea of using "single source" polynuclear precursors along with hydrothermal synthesis for the controlled formation of metal oxides has long been established since these techniques are reliable and lead to materials with high crystallinity.[65] An added benefit is the ability to use multi-walled carbon nanotubes (MWCNTs) to form composite materials that take advantage of both the metal oxide and MWCNTs.[66] However, the use of metallacrowns as precursors for the synthesis of interesting metal oxides is a new application for these metallamacrocycles with only one example reported so far. Kremlev and coworkers prepared a

$Ce(H_2O)_4[15\text{-}MC_{Cu^{II}N(glyHA)}\text{-}5]Cl_3$ complex, which was then subsequently used to prepare Ce/CuO nanocomposites within multiwalled carbon nanotubes (MWCNT) using hydrothermal techniques.[66] The choice of Ce/CuO was made due to the possibilities of using this metal oxide as a catalyst, sensor, and energy storage material.[67–73]

The thermal decomposition of the $Ce(H_2O)_4[15\text{-}MC_{Cu^{II}N(glyHA)}\text{-}5]Cl_3$ MC was explored simultaneously using thermogravimetric analysis (TGA), differential scanning calorimetry (DSC), and mass spectrometry in a helium atmosphere. The crystalline MC lattice appears to have two steps of weight loss, where the first is between 80-150 ºC and is due to the removal of lattice waters. The second step represents the decomposition of the MC into carbon dioxide, water, nitric oxide, formaldehyde, and cyanic acid, which was confirmed by MS of the headspace. The breakdown shows a large mass loss and a spike in the DSC near 240 ºC. The hydrothermal synthesis was optimized near 200 ºC so that the MC would breakdown into the desired Ce/CuO.

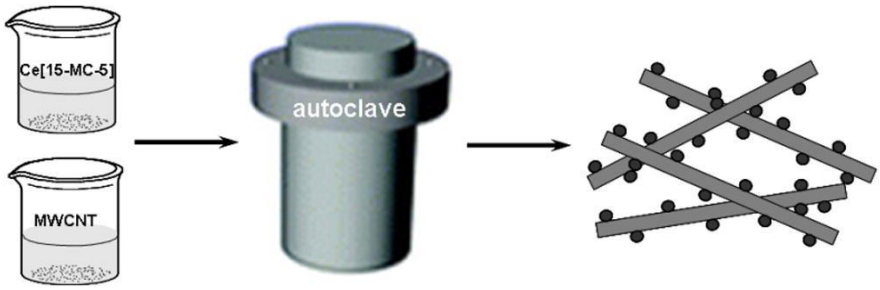

Figure 1.21. Synthetic scheme of the hydrothermal synthesis of the Ce/CuO on MWCNTs.[41]

This procedure involved dissolving the MC in water, which was then mixed with the MWCNTs to form a suspension. This suspension was placed in a modified autoclave and heated at 190 ºC for 20 hours, which yielded the desired Ce/CuO nanoparticles grafted onto the MWCNTs. The loaded MWCNTs were subsequently characterized to confirm the composition of the nanocomposites on the MWCNTs. The powder XRD spectrum (Figure 1.22) demonstrates that the material consists of Cu_2O, CeO_2, and MWCNTs. In addition, high-resolution tunneling electron microscopy confirmed the deposition of Ce/CuO on the walls of the MWCNTs as bowl-like nanostructures (Figure 1.23). This procedure demonstrates a novel, facile, and reliable method to generate these nanobowl structures conveniently placed on MWCNTs. Further

investigation of metallacrowns in this application could prove to yield even more interesting and well controlled metal oxide structures.

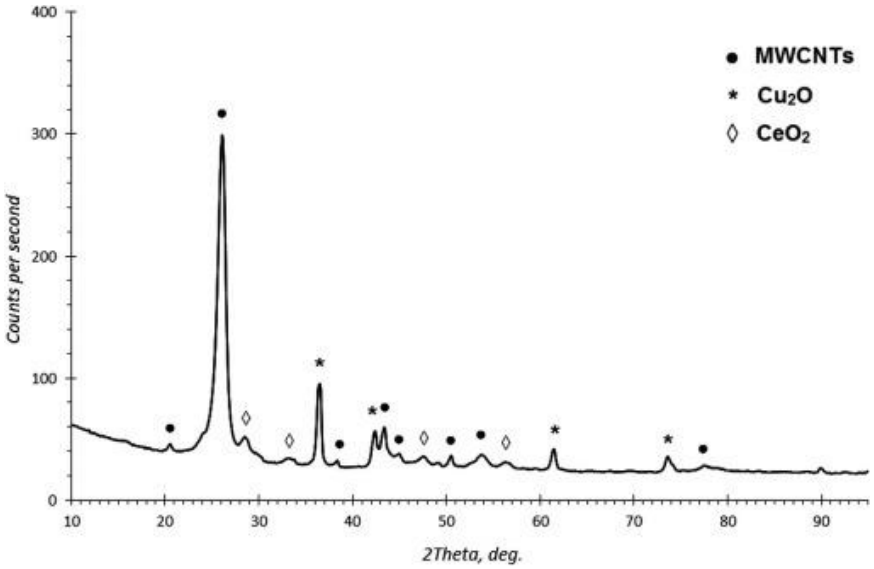

Figure 1.22. PXRD of the resulting Ce/CuO nanostructure on MWCNTs shows signature reflections of each component.[66]

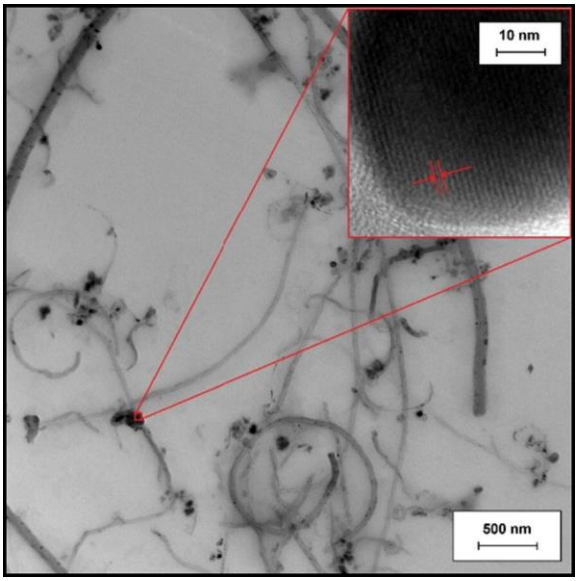

Figure 1.23. High-resolution TEM image shows the nanobowl structures of Ce/CuO on MWCNTs.[66]

1.6 Solution State Examination of Metallacrown Complexes

Solution state studies of metallacrowns are important for elucidation of MC stabilities and possible formation mechanisms. Since some applications such as imaging and host-guest binding rely heavily on the behavior of these MC complexes in solution, such studies are of paramount importance. Within the past three years, work has been done using techniques such as ESI-MS and ^{1}H-NMR to examine MCs in the solution state. There has also been some work on the controllable formation of dimeric MC capsules, which could be selective sequestration or catalytic compounds. Lastly, MC complexes have been used to explore their interactions with DNA and polypeptides.

Insight into Solution-State Speciation of MC complexes and Mechanism for Ln Encapsulation

Previous work using electrospray ionization mass spectroscopy (ESI-MS) examined the speciation of various intermediates or species that are formed in solution during the process of metallacrown assembly.[74–77] Concepts of solvent interaction and geometric matching were able to explain the observations of these studies; however, not all questions have been answered. Tegoni and coworkers extended this work by examining the formation of MCs in water using picoline hydroximate ($picHA^{2-}$) or alanine hydroximate ($alaHA^{2-}$), and nickel, copper and zinc divalent metals.[78–80] The existence of MC species between each metal-ligand combination were compared using potentiometry, and speciation models were proposed. Confirmation of the speciation was confirmed by UV-Vis and ESI-MS measurements. The authors reported that both pK_{a1} and pK_{a2} values of the parent hydroxamic acid ligand mattered with respect to MC speciation. In the case of copper(II), $alaHA^{2-}$ (pK_a H_2ala = 7.33 and 9.15, in 4:1 MeOH:H_2O) 12-MC-4 complexes began to form at higher pH values (4-6), while $picHA^{2-}$ (pK_a H_2picHA = 1.64 and 8.28 in 4:1 MeOH:H_2O) 12-MC-4 complexes began to form at lower pH values (2-6). Through the lens of Lewis acid-base theory of coordination bonds, this observation makes sense, since $picHA^{2-}$ was shown to be the weaker Lewis base when compared to $alaHA^{2-}$. It was also found through potentiometry that the copper(II) and zinc(II) metals tended to favor 12-MC-4s with $picHA^{2-}$ and the nickel preferred a 15-MC-5 structure. For $alaHA^{2-}$ there was no such selectivity with nickel(II), as both 12-MC-4 and 15-MC-5 species were observed, while copper(II) and zinc(II) preferred 12-MC-4 complexes.[79,80] What was most interesting was the comparison of the potentiometric study of the copper(II) complexes with the ESI-MS. In the

ESI-MS spectra, sodium and potassium adducts of 15-MC-5 and 18-MC-6 complexes are observed when picHA^{2-} is used, which were not detected in the potentiometry. The authors postulate that the presence of alkali metals in solution could stabilize these structures and thus account for their presence in MS, but it is also possible that these cations are picked up during the ionization process. Such structures have not been observed for alaHA^{2-}. The observation of 15-MC-5s and 18-MC-6s are an exciting find since this suggests that achieving the synthesis of these larger MCs is possible.[78] Tegoni and coworkers had previously shown evidence for similar 15-MC-5 formation *in situ* by examining the formation of 15-MC-5 complexes when Cu^{2+}/alaHA^{2-} based 12-MC-4 complexes were treated with lanthanum(III).[81] What the study revealed was that the conversion of the 12-MC-4 to the 15-MC-5 was a three-step process. The first step is fast, and was described as the simultaneous shifting of the central Cu^{2+} as the Ln^{3+} binds to form an Ln[12-MC-4]Cu intermediate. This step is independent of concentration of excess alaHA^{2-}. The second, slower step is the binding of another alaHA^{2-} ligand to the copper(II) ion, confirmed by the dependence on alaHA^{2-} concentration and copper(II) EPR. The final step involves the insertion of the Cu-alaHA adduct into the MC ring, transforming the 12-MC-4 into a 15-MC-5. These results are extremely interesting given that this MC conversion has been studied previously concerning the replacement of Ca^{2+} with La^{3+} in a 15-MC$_{Cu^{II}N(typHA)}$-5 structure[48,82–87]. Thus, the elucidation of the mechanism of conversion of a 12-MC-4 to a 15-MC-5 adds significant understanding to the solution dynamics of MCs.

Structural Analysis of Ln(OAc)$_4$[12-MC$_{Mn^{III}N(shi)}$-4]Na Complexes using ^{1}H-NMR

The structural characterization of a series of LnNa(OAc)$_4$[12-MC$_{Mn^{III}N(shi)}$-4](H$_2$O)$_4$ complexes in the solid state was completed by Zaleski, Pecoraro, *et. al.* for all lanthanide analogs ranging from Pr^{3+} to Yb^{3+} (except Pm^{3+}) and Y^{3+} using single crystal X-ray diffraction.[34] However, at the time it was not known if these MCs maintain their structure in solution. To determine the structural integrity of the complexes in soluiton, Tegoni, Zaleski, Di Bari, *et. al.* investigated the ^{1}H-NMR properties of the same series of complexes in *d$_4$*-MeOH. In addition, they were able to assign the proton resonances of the salicylhydroximate (shi^{3-}) and acetate (OAc$^-$) ligands.[88] It is also interesting to point out that proton resonances of the Gd^{3+} analog were able to be observed in the NMR, which is unprecedented for a small Gd^{3+} complex. The

magnetic coupling between the central Gd^{3+} and ring Mn^{3+} ions likely facilitate a shorter electronic relaxation time.

The ^{1}H-NMR spectra revealed that all twelve complexes had a similar pattern; confirming the isostructural nature of the complexes. To assign the proton resonances of the shi^{3-} and OAc^{-} ligands, the chemical shift data were treated with the "all lanthanides" method to determine the pseudo-contract contribution to the Lanthanide Induced Shift (LIS). The authors determined that the LIS of the aromatic protons of the shi^{3-} are opposite in sign with respect to the methyl protons of the acetate bridging ligands. In addition, while the twelve complexes are isostructural with each other in solution, they do differ from the solid state structures. The sodium-23 NMR spectra revealed that the bound Na^{+} ion dissociates from the MC complex in methanol. The dissociation of the Na^{+} ion may allow the Ln^{3+} to move closer to the MC plane in solution than in the solid state. Lastly, this series of complexes served as an example of the limitation of Bleaney's theory with respect to the calculated ligand field splitting parameters (B_{Ln}). For isostructural complexes, the B_0^2 contribution to the ligand field splitting parameters should be fairly similar; however, for this series of 12-MC-4 complexes the B_0^2 values vary greatly (up to 38%) around a mean value of 400 cm^{-1}. The variation is likely due to the inaccuracy in the validity of the Bleaney's constant C_J(Ln) values.

The Selective Binding of Guest Anions in Dimeric Gd[15-MC$_{Cu^{II}(N)pheHA}$-5] Capsules

In the past there has been significant structural analysis of Ln[15-MC$_{CuII(N)pheHA}$-5] structures in the solid state. Some work has shown how inclusion of isonicotinic acid into the hydrophobic cavity of the dimeric structures could lead to non-linear optical properties.[89] Other studies have shown how various dicarboxylates may be sequestered in this hydrophobic cavity, where side chain length of both the amino hydroximate and the dicarboxylate were codependent.[51,52,90–95] Recently Arena, Pecoraro, *et. al.* have looked into how these dimeric capsules (Figure 1.24) could form in solution and what factors are important for dicarboxylate recognition.[96]

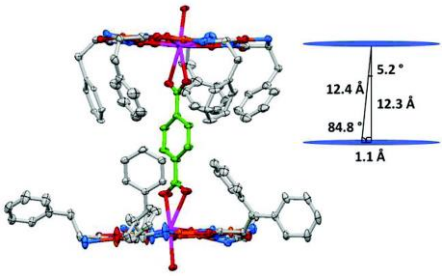

Figure 1.24. Dimers of the Ln[15-MC$_{Cu}^{II}$$_{N(pheHA)}$-5] complexes encapsulate dicarboxylate anions (terephthalate pictured) in solution.[96]

This study utilized isothermal calorimetry to examine the stability of capsules formed from dimers of Gd[15-MC$_{Cu}^{II}$$_{N(pheHA)}$-5], where six different dicarboxylate anions were used to bind to the hydrophobic interior. The carboxylate anions chosen were terephthalate, *trans, trans*-muconate, adipate, fumarate, maleate, and oxylate, which represent a range of sizes and degrees of unsaturation. ESI-MS was used to confirm the accuracy of the assumed species that form in the aqueous solution under the conditions used for isothermal titration calorimetry (ITC). The results of this study showed that four of the six guests (terephthalate, *trans*,*trans*-muconate, andipate, and fumarate) showed a two-step process, where a MC-guest complex formed first followed by the binding of the second metallacrown (Figure 1.25).

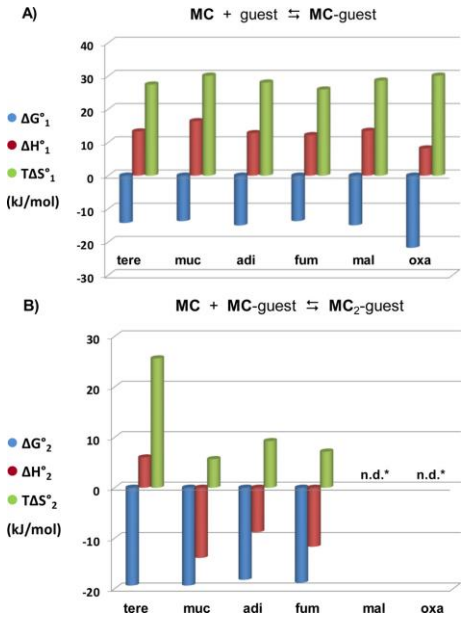

Figure 1.25. Thermodynamic properties of the two-step formation of dimeric Ln[15-MC$_{Cu}^{II}$$_{N(pheHA)}$-5] capsules in aqueous conditions with various dicarboxylate anions, where tere is terephthalate, muc is muconate, adi is adipate, fum is fumarate, mal is maleate, and oxa is oxalate.[96]

However, the oxalate and maleate guest only formed one MC-guest adduct and the second MC binding to the MC-guest adduct was not observed. This is likely due to the smaller length of the maleate and oxalate anions. In contrast to earlier conclusions that suggested that the degree of unsaturation was important for recognition in the MC_2 compartment[52], these studies revealed that in solution molecular discriminate was based on size, but not the degree of guest unsaturation.

Investigation of MC binding to DNA

The ability to target DNA has important implications for the design of drugs which combat cancer and certain viruses; thus, interest lies in the ability to probe and monitor DNA with respect to chemotherapy drugs using metal complexes.[97–99] Using copper as a chemotherapeutic agent is interesting for two reasons. First, copper is already utilized by cells so intrinsically its toxicity should be less than heavy elements. Second, some copper complexes have already shown tumor growth inhibition.[100,101]. Recently, Dou *et. al.* synthesized several Ln[15-MC $_{Cu^{II}N(glyHA)}$-5] complexes, where Ln was La^{3+}, Nd^{3+}, Pr^{3+}, Sm^{3+}, Gd^{3+}, and Tb^{3+}, and elucidated the interaction of DNA with these MC species.[102] To investigate the binding of these MCs to calf thalamus DNA (CT-DNA), a competitive binding assay was developed using ethidium bromide (EB). When EB is intercalated in DNA in aqueous conditions, the EB shows a fluorescence emission centered at 598 nm when excited at 258 nm. These EB-DNA adducts were then exposed to aliquots of Ln[15-MC $_{Cu^{II}N(glyHA)}$-5] complex and the band at 598 was monitored. As more MC complex was added, the EB was displaced resulting in a loss of signal. The fluorescence spectra of the titration of the La^{3+} and Pr^{3+} MC analogs with EB-DNA are shown in Figure 1.26 (left and right, respectively).

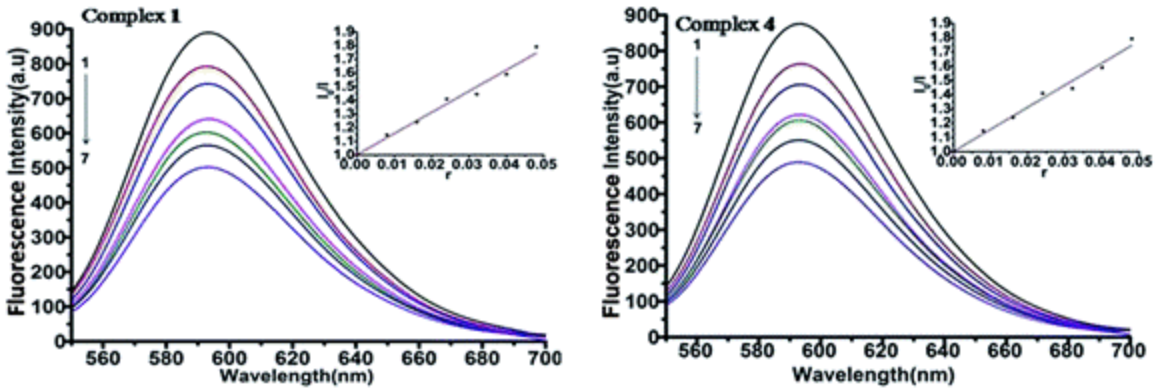

Figure 1.26. Fluorescence intensity of ethidium bromide (EB) decreases as La[15-MC$_{Cu^{II}N(glyHA)}$-5] (left) and Pr[15-MC$_{Cu^{II}N(glyHA)}$-5] (right) equivalents are added to DNA showing intercalation of the MC into DNA.[102]

This data was fit to a Stern-Volmer plot using $I_0/I = 1 + K_{sp} \cdot r$, where I_0 and I are the fluorescent intensities without and with MC added respectively, r is the concentration ratio of MC to DNA, and K_{sp} is the linear Stern-Volmer constant. The K_{sp} values of all analogs except Tb^{3+} (which was 11.20) were approximately 15.5, which implies strong interaction between the DNA and the MC when compared to another copper inverse MC, {(OH)[9-MC$_{Cu^{II}N(PhPyCNO)}$-3} where PhPyCNO is phenyl 2-pyridyl ketoxime.[103] The lower value for the Tb^{3+} complex was rationalized by the smaller size of Tb^{3+} and its ability to sit in the MC plane more so than the other Ln^{3+} analogs, which leads to increased rigidity of the MC and a more pronounced steric hindrance. Circular dichroism (CD) spectra of each MC-DNA analogous structure reveals that the DNA structure is disrupted relative to DNA without the addition of the MC complexes (Figure 1.27). The authors proposed that this data indicates that the MC intercalates into the DNA and likely causes a B-like conformational change. Another possible explanation, that is more consistent with the size and shape of the 15-MC-5s, is that the MC binds non-specifically in an electrostatic manner, disrupting the DNA structure and releasing the EB.

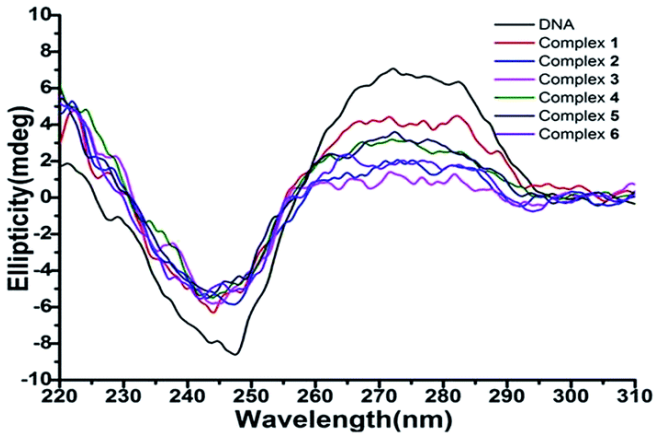

Figure 1.27. CD spectra show a loss of characteristic bands when MCs are added to DNA, showing disruption of DNA structure.[102]

Another study by Juskowiak *et. al.* looked at the interaction of two different analogs of Ln[15-MC$_{Cu^{II}N(pheHA)}$-5], where Ln was Eu^{3+} and Tb^{3+} and pheHA is *S*-phenylalanine hydroximate, with human telomeric G-quadraplex DNA.[104] These G-tetrad DNA sequences are guanine rich, and in the presence of cations such as Na^+, K^+ or Ln^{3+}, adopt parallel or antiparallel four stranded structures (Figure 1.28). These DNA structures are thought to be an excellent target for anticancer agents since the G-quadraplexes inhibit telomerase.

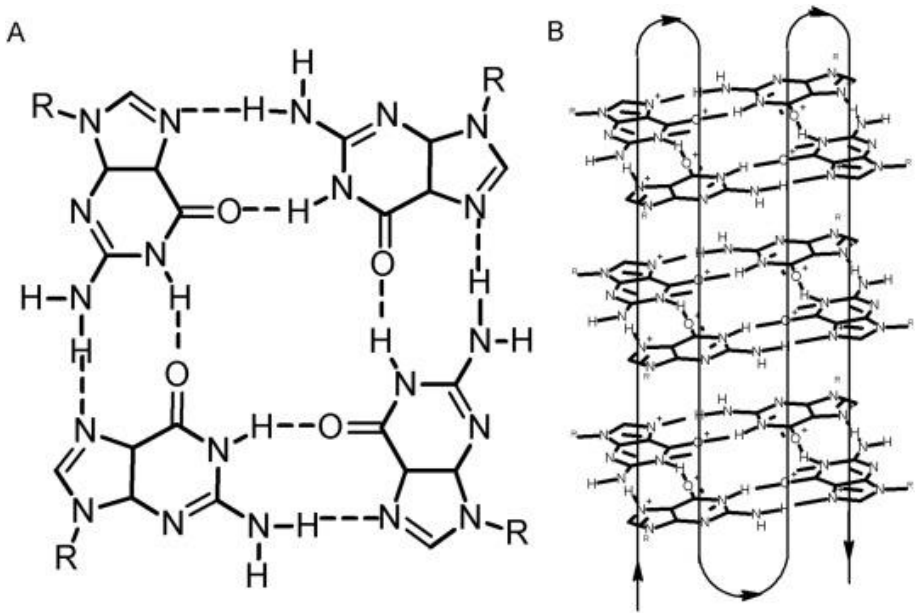

Figure 1.28. Schematic of G-quatraplex DNA structure, showing the planar unit (A) and an antiparallel conformation of the DNA tetramer (B).[104]

This study looked into the ability of the 15-MC-5 complexes to interact with these G-quadraplexes. It should be noted from the outset that the size and shape of 15-MC-5 system is non-commensurate for binding to G-quadruplexes, which are four-fold symmetric. Once again, the high positive charge of the MC is better suited to directly interact with the negatively charged phosphate backbone. Several different approaches were taken to understand this complicated DNA-MC interaction. Since these MCs are chiral with hydrophobic and hydrophilic faces, CD experiments were conducted to understand the interactions between the MCs and the G-quadraplex DNA. CD spectra of the MC revealed a negative band at 220 nm, a negative shoulder at 250 nm, and a broad and positive band at 340 nm (Figure 1.29).The G-quadraplex is known to have a negative band at 260 nm and a positive band at 290. Additional titration of the MCs into a solution of G-quadraplex showed the expected growth of MC-based bands while the tetrad bands simultaneously decreased (Figure 1.30). This suggested that the MC destabilized the DNA structure. To confirm this, melting points (T_m) of the G-quadraplex were determined by UV-Vis absorbance, monitoring a known tetrad peak at 295 nm from 15 to 85 ^oC. The presence of the MCs showed a decrease in the T_m from 58 ^oC (G-quadraplex DNA only) to 42 ^oC and 38 ^oC for the Eu^{3+} and Tb^{3+} analogs, respectively, confirming the destabilizing effect of the MCs.

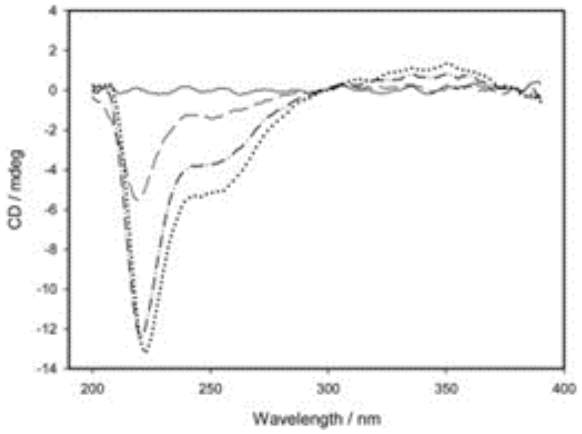

Figure 1.29. CD spectra of additions of Eu[15-$MC_{Cu^{II}N(pheHA)}$-5] in sodium cacodylate buffer.[104]

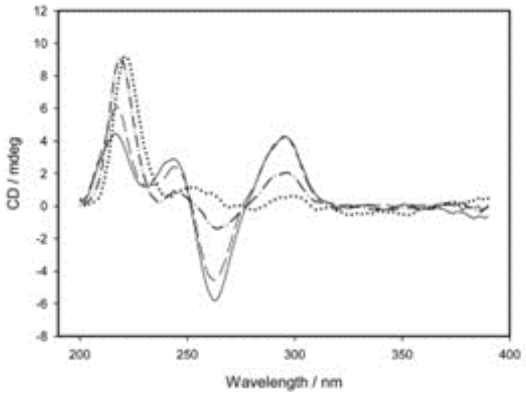

Figure 1.30. CD spectra of Eu[15-$MC_{Cu^{II}N(pheHA)}$-5 added to a solution of G-quadraplex shows decrease in G-quadraplex as MC is added.[104]

To measure the binding of the Ln[15-$MC_{Cu^{II}N(pheHA)}$-5] complexes to the tetrads, two different fluorescent assays were performed with the intent of finding convergent results. One assay is similar to the one used by Meng, *et. al.* where thiazolium orange (TO) was used instead of EB. TO has an intense emission peak at 536 nm when bound to DNA, which was monitored for decreasing intensity as the MC was added. The loss of signal in relation to the addition of MC was assumed to be the replacement of TO with MC for the purposes of the model and binding constants of 1.9×10^5 M^{-1} and 2.5×10^5 M^{-1} were determined for the Eu^{3+} and Tb^{3+} MCs, respectively. The assumption of that the MC replaced the TO was further tested by using a different florescent quenching assay. In this second assay, Tb^{3+} was coordinated inside the G-quadraplex DNA in place of K^+, which allows for observation of intense characteristic Tb^{3+} emissions. As the MC binds to the DNA, the Tb^{3+} emission is quenched (Figure 1.31). A two stage process was postulated based on the results, where the first linear quenching potion of the titration was attributed to the interaction of MC to DNA, and the second portion involved the destabilization of the DNA structure and leaching of Tb^{3+} into water, which will also quench the emission. By focusing on the first linear stage, a Stern-Volmer plot was used to estimate binding constants of 3.9×10^5 M^{-1} and 4.6×10^5 M^{-1} for the Eu^{3+} and Tb^{3+} MCs, respectively. The results were 50% less than the TO assay but on the same order of magnitude, which reasonably confirms the modest destabilizing interaction for the MCs since there are procedural differences in the two assays. Unfortunately, rather than stabilizing the G-quadruplex structure, these 15-MC-5 systems disrupted the teleomer like assembly. Future studies attempting to assess direct base stacking with the tetrads should utilize MC complexes that match the symmetry of the G-quadruplex.

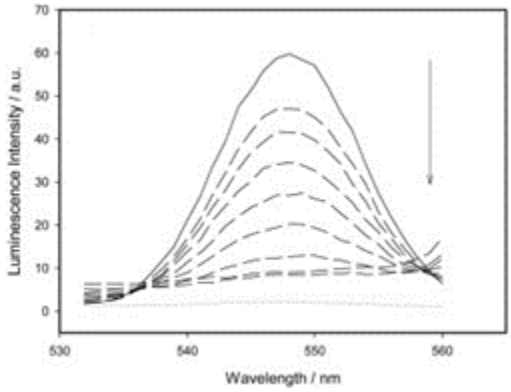

Figure 1.31. Decrease in in characteristic Tb^{3+} emission demonstrates leaching of Tb^{3+} into solution as Eu[15-$MC_{Cu^{II}N(pheHA)}$-5] is added.[104]

Metallacrowns as Scaffolds for Helical Peptide Bundles

Stefanowicz and coworkers have published the only two examples of the use of the metallacrown motif for the self-assembly of helical peptide bundles.[105,106] Metallacrowns offer the ability to act as a rigid template for the formation of alpha-helical bundles and potentially to study protein folding, metal binding, or molecular guest binding in artificial protein systems. In the first example, the metallacrown was composed of five Cu^{2+} ions and four alpha-amino acid peptide chains with either a α-aminohydroximate or a histidine hydroximate group, which form the MC ring, at the C-terminus end of the peptide chain. The peptide chains were acetylated (Ac) at the N-terminus to avoid interactions of N-terminus α-amino groups with the Cu^{2+} ions. The types of peptide chains were short (around 15 amino acids) which did not spontaneously fold into a well-defined secondary conformation, but which had a heptad like repeat that could support α-helical formation when the individual peptides were constrained within a narrow solution volume. Thus, the system represents the TASP (Template Assembled Synthetic Protein) strategy suggested by Mutter (Figure 1.32).[107]

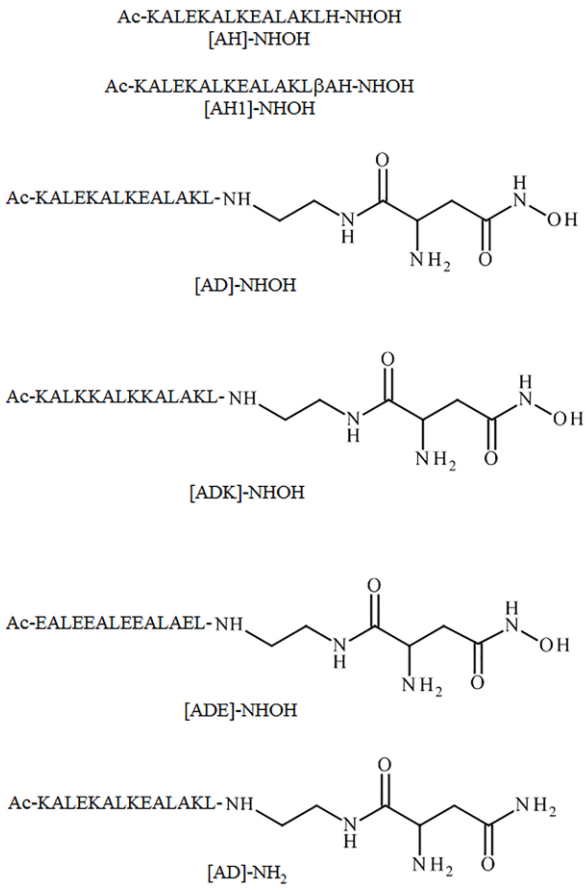

Figure 1.32. Examples of TASP units used in the formation of 12-MC-4 helical bundles.[105]

This assembly leads to the formation of a 12-MC-4 with four Cu^{2+} ions in the MC ring and one central Cu^{2+}, and the MC has an overall square molecular shape with the peptide chains at the corners of the square (Figure 1.33). The formation of the Cu^{II}[12-$MC_{Cu^{II}}$-4]-peptide assemblies for each peptide system were confirmed by ESI-MS spectra with detection of Cu_5[peptide]$_4$ complexes with molecular masses near 7200 Da. In addition, circular dichroism (CD) experiments indicate that the Cu_5[peptide]$_4$ assembly enforces the alpha-helical nature of the peptides. For the [AD]-NHOH 12-MC-4 assembly, the alpha-helical content of the peptide was ~61% when a stoichiometric amount of Cu^{2+} was added to the peptide. In addition, when a mixture of the peptide [AD]-NHOH and Cu^{2+} was treated with the enzyme trypsin, which will hydrolyze peptide chains, the formation of the Cu^{II}[12-$MC_{Cu^{II}}$-4]-peptide assembly protected the peptide chains from hydrolysis. No effort was made to optimize the linkers between the metallacrown templating ligand and the subsequent helical amino acid sequence. It is likely that

modification of the length and the amino acid composition would allow for even more stable, better-folded TASPs.

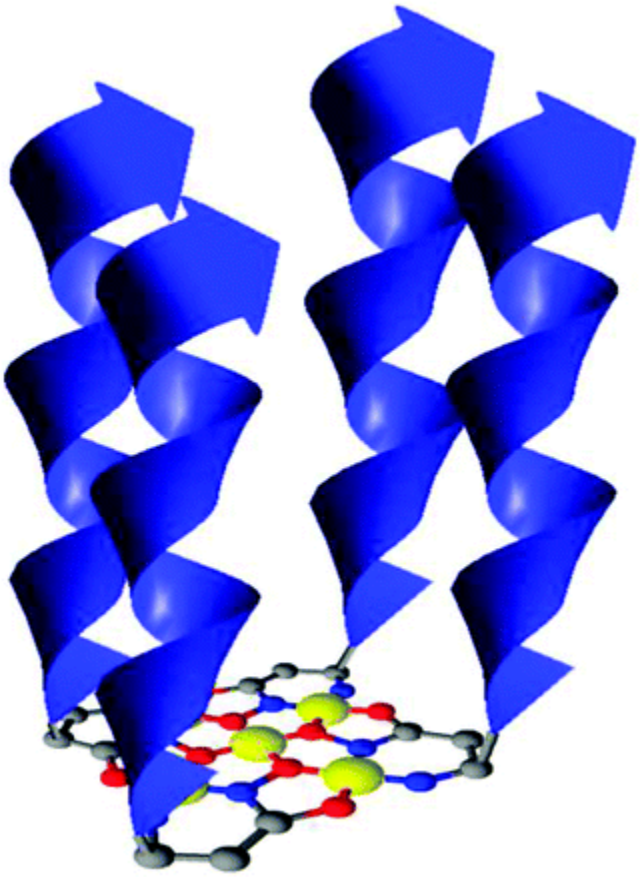

Figure 1.33. Representation of the four-stranded helical bundle possible with the self-association of each strand on a Cu^{II}[12-$MC_{Cu}{}^{II}$-4] complex.[105]

In the second report by Stefanowicz and coworkers, a Cu_5[peptide]$_4$ Cu^{II}[12-$MC_{Cu}{}^{II}$-4]-peptide assembly was again investigated. These assemblies were based on either tripeptides (Ac-KLH-NHOH) or pentadecapeptides ([AH]-NHOH; Figure 1.32) with a histidine hydroximate group at the C-terminus end of the peptide chain. As above, potentiometric studies, ESI-MS, UV-Vis, EPR, and CD data indicate that the Cu^{II}[12-$MC_{Cu}{}^{II}$-4]-peptide assemblies were indeed formed in solution with both peptide systems. In addition, the effect of the peptide chain length on MC stability was determined. Stability constants were measured for the two Cu^{II}[12-$MC_{Cu}{}^{II}$-4]-peptide assembly and compared to that of a Cu^{II}[12-$MC_{Cu}{}^{II}$-4] complex made with the non-peptide ligand N-benzyloxycarbonylhistidine hydroxamic acid (aka *Z*-histidinehydroxamic acid, *Z*-hisHA).[108] The stability constants of the three Cu^{II}[12-$MC_{Cu}{}^{II}$-4] systems with *Z*-hisHA, Ac-

KLH-NHOH, and [AH]-NHOH (Figure 1.32) were 38.50, 36.03, and 34.00, respectively, which indicates that the histidine hydroximate ligand with the shortest substituent forms the most stable MC (Figure 1.34). In other words, as the size of the peptide chain increases, the MC becomes less stable as the steric effects of the peptide chains destabilizes the MC scaffold.

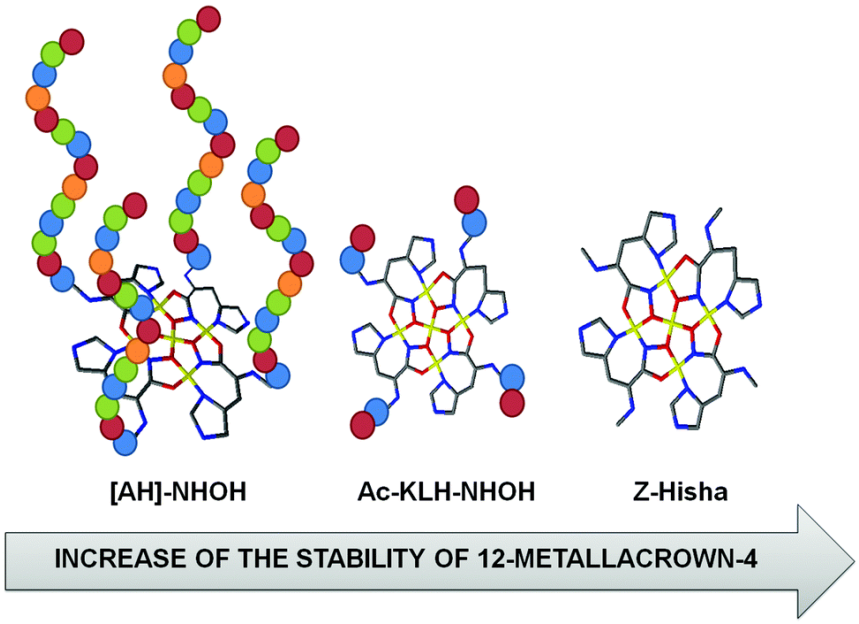

Figure 1.34. For the Cu^{II}[12-$MC_{Cu}{}^{II}$-4] complexes with [AH]-NHOH, Ac-KLH-NHOH, and N-benzyloxycarbonylhistidine hydroxamic (left to right), as the ligand substituent length decreases, the MC stability increases.[106]

This observation suggests that effort may need to be placed into optimizing the interface between the metallacrown ligand and the peptide sequence that will adopt the helical structure. It is well known that achieving the optimal helical twist in designed coiled coil proteins often requires spacers (or loops) to achieve the desired structure.[109] It may be that more stable peptide-MC aggregates will be achieved by sequence and length variations that optimize these parameters. When both Cu_5-$peptide_4$ MC investigations are taken together these assemblies represent a model to design new supramolecular systems. Furthermore, given the alpha-helical nature of the peptide chains and the enzymatic stability of the system, the Cu^{II}[12-$MC_{Cu}{}^{II}$-4]-peptide assembly may represent a model for folded proteins or as an easier method to model parallel two or four-fold symmetric binding sites.

1.7. Single-Molecule Magnets and Magnetorefrigerants

The ability of MCs to place several metal in close proximity in a molecule with a specific arrangement and geometry lends them to interesting magnetic properties that include superparamagnetism and large magnetoentropy changes. In addition, MC molecules are very versatile as the components (MC ring ligands, ancillary ligands, MC ring metals, and central cavity metals) can be easily substituted while at the same time maintain the overall MC framework. In one sense, MCs can be considered modular as specific parts can be easily substituted for other similar components without greatly affecting the structural parameters of the molecule. Thus, magnetic investigations of MCs focus on the variability of the magnetic properties as the identity of the components are changed instead of how the components affect the structure of the MC, which would then alter the magnetic properties. Recently, the study of the magnet properties of metallacrowns has largely focused on the single-molecule magnet (SMM) behavior of 12-MC-4 molecules that contain lanthanide central ions. SMMs have garnered considerable attention as these molecules could be used for memory storage, for quantum processing, or in spintronic devices.[7,60,110,111] This review will mainly give an account regarding the magnetic properties of Ln[12-MC-4] molecules since 2015; however, other relatively new (2015 and later) MCs that behave as single-molecule magnets or possess magnetocaloric effects will also be discussed.

Ln^{III} [12-$MC_{Mn}{}^{III}{}_{(N)shi}$-4] SMMs and the importance of bridging carboxylates and counter ions.

The interest in the lanthanide-containing 12-MC-4 molecules can be traced back to the first reported metallacrown to encapsulate a metal ion in the central cavity, $Mn^{II}(OAc)_2$[12-$MC_{Mn}{}^{III}{}_{N(shi)}$-4](DMF)$_6$, where DMF is *N*,*N*-dimethylformamide (Figure 1.35). This molecule was first reported in 1989 by Lah and Pecoraro, and in 2011 it was shown that this metallacrown displayed single-molecule magnet properties.[31,112]

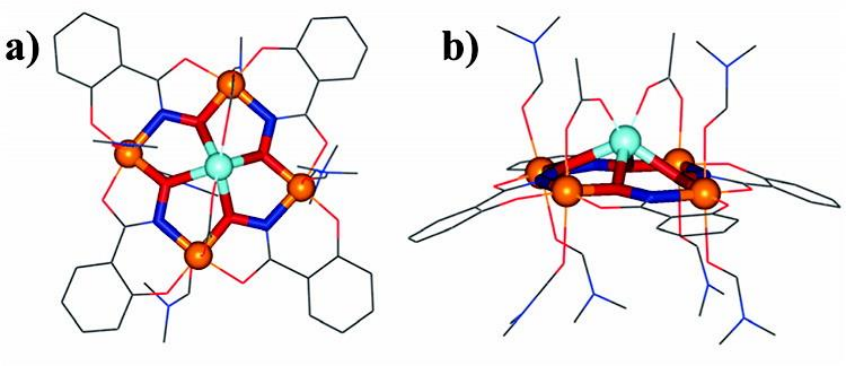

Figure 1.35. X-ray crystal structure of $Mn^{II}(OAc)_2[12\text{-}MC_{Mn}{}^{III}{}_{N(shi)}\text{-}4](DMF)_6$.[112]

This was an extremely surprising observation as molecules with an overall total ground spin state of $S_T = ½$ cannot show magnetic bistability. Instead, it is now realized that due to weak antiferromagnetic coupling between the Mn(III) ring ions themselves and the weak antiferromagnetic exchange between the central Mn(II) and the Mn(III) ring metals, there are low lying excited states (S=3/2 and S=5/2) that can be attained in this system. Even though the total spin is still very small, there was the possibility that the magnetoanisotropy of the molecule was significant due to the shape of the molecule. The idea was that the relatively planar square arrangement of the ring Mn^{III} ions with quasiparallel Jahn-Teller axes could allow each single ion magnetoanisotropy to add constructively, enhancing the overall *molecular* magnetoanisotropy. Thus, even though the total spin of the molecule was minimal, the metallacrown framework might promote the SMM behavior. Further experimentation suggested that it is unlikely that this phenomenon is operative in this case, the concept suggest an alternative process to design molecules with large blocking temperatures. The observation that this MC, with so few atoms and such a low total moment, was capable of showing slow magnetic relaxation has provided a pathway to design other SMMs that relied on the 12-MC-4 framework. One strategy was to replace the central Mn^{II} ion of the $Mn^{II}(OAc)_2[12\text{-}MC_{Mn}{}^{III}{}_{N(shi)}\text{-}4]$ complex with a lanthanide ion as numerous Mn-Ln molecule have shown SMM properties, including some MC and MC-like molecules.[42,113–142] In 2014 we reported the synthesis of the first heterotrimetallic MCs and the first 12-MC-4 molecules to encapsulate a lanthanide ion in the central cavity, $Ln^{III}M^{I}(OAc)_4[12\text{-}MC_{Mn}{}^{III}{}_{N(shi)}\text{-}4](H_2O)_4$, where Ln^{III} is Pr^{III} – Yb^{III} (except Pm^{III}) and Y^{III} and M^{I} is Na^{I} or K^{I} (Figure 1.36).[34]

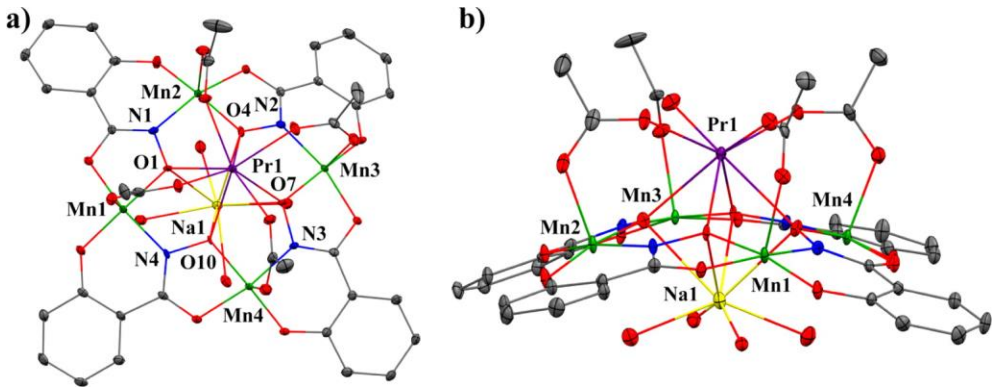

Figure 1.36. X-ray crystal structure of the $Pr^{III}Na(OAc)_4[12\text{-}MC_{Mn}{}^{III}{}_{N(shi)}\text{-}4]$ complex.[34]

The Ln^{III} ion and the alkali metal ion are bound on opposite faces of the MC with the Ln^{III} ion on the convex side of the MC cavity and the alkali metal ion bound to the concave side of the cavity. In 2014 we did not report the magnetic behavior of these molecules; however, in 2016 we demonstrated that the mere presence of a lanthanide ion in the $[12\text{-}MC_{Mn}{}^{III}{}_{N(shi)}\text{-}4]$ framework does not lead to SMM behavior. The identity of ancillary ligands is of vital importance. In the original $Ln^{III}M^{I}(OAc)_4[12\text{-}MC_{Mn}{}^{III}{}_{N(shi)}\text{-}4](H_2O)_4$ molecules four acetate anions serve to tether the lanthanide ion to the $[12\text{-}MC_{Mn}{}^{III}{}_{N(shi)}\text{-}4]$ framework by acting as bridges between the central Ln^{III} and the ring Mn^{III} ions (Figure 1.36). By modifying the MC synthesis, the acetate anions can be replaced with other carboxylate anions.[36,40] For a series of dysprosium-based MCs $Dy^{III}M^{I}(X)_4[12\text{-}MC_{Mn}{}^{III}{}_{N(shi)}\text{-}4]$, where M^{I} is Na^{I} or K^{I} and X^{-} is acetate, benzoate, trimethylacetate, or salicylate, the SMM behavior of the molecules correlated with the identity of the carboxylate (Figure 1.37).[36] Both the Na^{I} and K^{I} versions of $Dy^{III}M^{I}(salicylate)_4[12\text{-}MC_{Mn}{}^{III}{}_{N(shi)}\text{-}4]$ displayed a frequency-dependent out-of-phase ac magnetic susceptibility signal above 2 K in a zero applied dc magnetic field, a hallmark of SMM behavior. However, none of the complexes containing benzoate, acetate, or trimethylacetate (both sodium and potassium versions) displayed an out-of-phase ac magnetic susceptibility signal. The basicity of the ligands may play a part in perturbing the magnetic coupling between the Dy^{III} ions and the Mn^{III} ions.

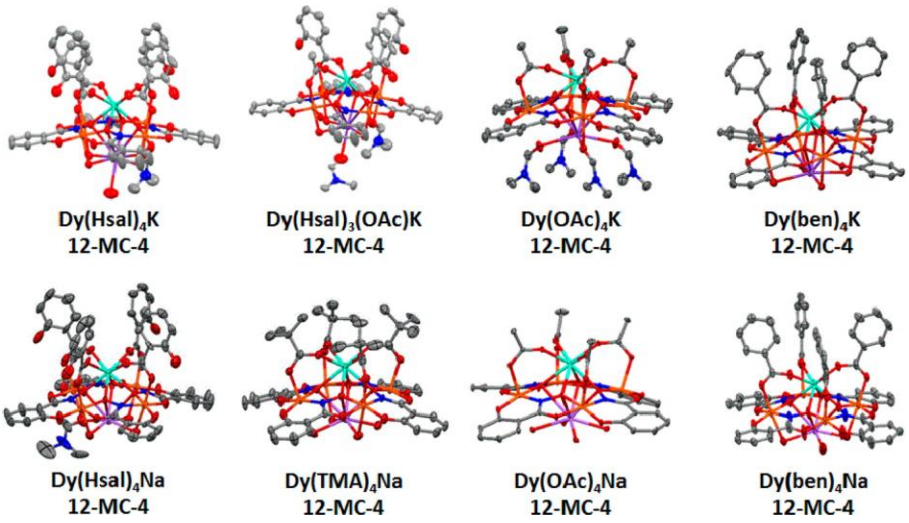

Figure 1.37. For the $Dy^{III}M(X)_4[12\text{-}MC_{Mn}{}^{III}{}_{N(shi)}\text{-}4]$, $M = Na^+$ or K^+ and X^- = acetate (OAc), benzoate (ben), salicylate (Hsal), or trimethylacetate (TMA), variations of carboxylate anion choice showed the importance of ligand basicity on SMM behavior.[36]

Salicylate is the poorest Lewis base of the ligands as judged by the pK_a of the parent salicylic acid (pK_a = 2.93). The better Lewis bases benzoate (benzoic acid pK_a = 4.20), acetate (acetic acid pK_a = 4.77), and trimethylacetate (trimethylacetic acid pK_a = 5.01) do not promote SMM behavior. Thus, the electron-withdrawing ability of the bridging ligand may affect the magnetic coupling between the central Dy^{III} ion and the ring Mn^{III} ions (as well as between the ring Mn^{III} ions themselves) and turn "on" and "off" the SMM behavior of the MCs. In addition, Li and coworkers further demonstrated that the nature of the bridging ligand is important to SMM behavior and the identity of the countercation is not of vital importance.[143] As mentioned above, the presence of either Na^I or K^I did not correlate with the SMM of the $Dy^{III}M^I(X)_4[12\text{-}MC_{Mn}{}^{III}{}_{N(shi)}\text{-}4]$ molecules. Li and coworkers further modified the $Ln^{III}M^I(OAc)_4[12\text{-}MC_{Mn}{}^{III}{}_{N(shi)}\text{-}4]$ molecule by replacing the alkali metal countercation with triethylammonium to produce a heterobimetallic MCs with a vacant concave cavity that is still charge neutral, $[NH(C_2H_5)_3]\{Ln^{III}(OAc)_4[12\text{-}MC_{Mn}{}^{III}{}_{N(shi)}\text{-}4]\}$, where Ln^{III} is Sm^{III}, Gd^{III}, Tb^{III}, and Dy^{III} (Figure 1.38). As in the Na^I and K^I acetate analogues, none of these heterobimetallic $[NH(C_2H_5)_3]\{Ln^{III}(OAc)_4[12\text{-}MC_{Mn}{}^{III}{}_{N(shi)}\text{-}4]\}$ complexes, which contain bridging acetate ions, behave as SMMs.

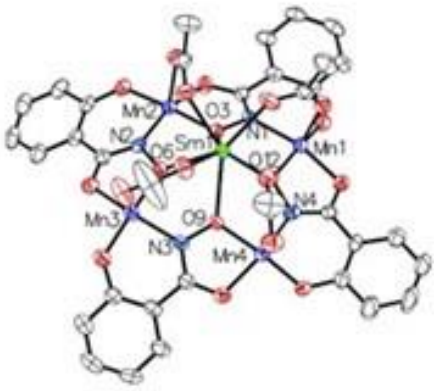

Figure 1.38. X-ray crystal structure of the $Ln(OAc)_4[12\text{-}MC_{Mn^{III}N(shi)}\text{-}4]$ with the countercation triethylammonium (omitted for clarity) instead of an alkali metal.[143]

However, if the magnetic coupling between the ring Mn^{III} ions is changed by the presence of a bound counteranion, then the SMM properties of the $Ln^{III}[12\text{-}MC_{Mn^{III}N(shi)}\text{-}4]$ can be altered. In the original $Mn^{II}(OAc)_2[12\text{-}MC_{Mn^{III}N(shi)}\text{-}4]$ complex and in other similar molecules including the $Dy^{III}M^{I}(X)_4[12\text{-}MC_{Mn^{III}N(shi)}\text{-}4]$, $[NH(C_2H_5)_3]Ln^{III}(OAc)_4[12\text{-}MC_{Mn^{III}(N)shi}\text{-}4]$, and $[N(C_4H_9)_4]\{Y^{III}(OAc)_4[12\text{-}MC_{Mn^{III}N(shi)}\text{-}4]\}$ complexes, the dc magnetic susceptibility signals demonstrate that the ring Mn^{III} ions are antiferromagnetically coupled to each other.[33,36,112,143–146] For the $Mn^{II}(OAc)_2[12\text{-}MC_{Mn^{III}(N)shi}\text{-}4]$ complex, the magnetic coupling between the ring Mn^{III} ions was estimated to be approximately -6.0 cm^{-1}.[112] For three similar MCs with diamagnetic central ions, $Li\{Li(Cl)_2[12\text{-}MC_{Mn^{III}N(shi)}\text{-}4]\}$, $[NH(C_2H_5)_3]_2\{Ca^{II}(benzoate)_4[12\text{-}MC_{Mn^{III}(N)shi}\text{-}4]\}$, and $[N(C_4H_9)_4]\{Y^{III}(OAc)_4[12\text{-}MC_{Mn^{III}N(shi)}\text{-}4]\}$, the ring Mn^{III} ion antiferromagnetic coupling constants are reported to be -4.0 cm^{-1}, -3.39 cm^{-1}, and -2.88 cm^{-1}, respectively.[112,145,146] However, Song, Dou, and coworkers have demonstrated it is possible to change the magnetic coupling between the ring Mn^{III} ions.[146] When a $[W^{V}(CN)_8]^{3-}$ species is bound to the concave side of a $Y^{III}(OAc)_4[12\text{-}MC_{Mn^{III}N(shi)}\text{-}4]$ complex, the ring Mn^{III} ions become ferromagnetically coupled. In the compound $[N(C_4H_9)_4]_5\{Y^{III}(OAc)_4W^{V}(CN)_8[12\text{-}MC_{Mn^{III}N(shi)}\text{-}4]\}(WO_4)_{0.5}$, the central Y^{III} is bound to the MC through 4 acetate bridging anions as in the other $Ln^{III}[12\text{-}MC_{Mn^{III}N(shi)}\text{-}4]$ molecules (Figure 1.39).

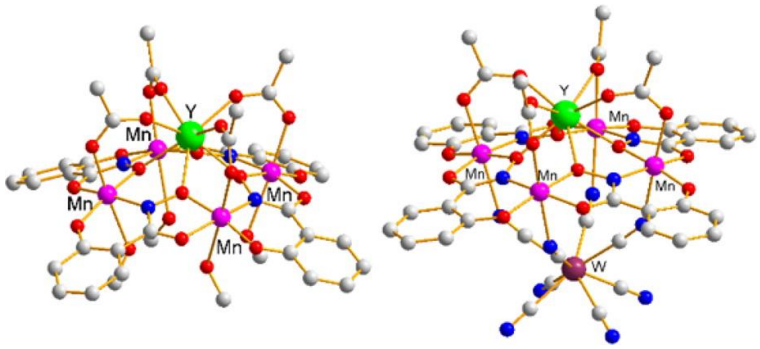

Figure 1.39. X-ray crystal structure of $[N(C_4H_9)_4]\{Y^{III}(OAc)_4[12\text{-}MC_{Mn}{}^{III}{}_{N(shi)}\text{-}4]\}$ (left) and $[N(C_4H_9)_4]_5\{Y^{III}(OAc)_4W^{V}(CN)_8[12\text{-}MC_{Mn}{}^{III}{}_{N(shi)}\text{-}4]\}(WO_4)_{0.5}$(right). The tetrabutylammonium countercation has been omitted for clarity.[146]

However, on the concave side of the MC a W^V ion is coordinated to the MC via four CN^- bridges. The four CN^- anions bridge between the ring Mn^{III} ions and the W^V ion. The coordination sphere of the W^V is completed by four additional terminal CN^- anions. The presence of the paramagnetic W^V and the strong-field CN^- ligands perturbs the magnetic coupling between the ring Mn^{III} ions from the typical antiferromagnetic behavior to ferromagnetic coupling. Strong antiferromagnetic coupling between the Mn^{III} ions and the W^V ion ($J = -21.09\ cm^{-1}$) leads to a spin-frustrated system, and the spin of the Mn_4 MC square is polarized to a ferromagnetic arrangement. Indeed the total ground spin state of the molecule is $S_T = 11/2$ with the Mn_4 MC square possessing a ground spin state of S = 6. The change in the magnetic coupling between the Mn^{III} ions leads to the $[N(C_4H_9)_4]_5\{Y^{III}(OAc)_4W^{V}(CN)_8[12\text{-}MC_{Mn}{}^{III}{}_{N(shi)}\text{-}4]\}(WO_4)_{0.5}$ complex possessing a frequency-dependent out-of-phase ac magnetic susceptibility signal above 2 K in a zero applied dc magnetic field. The energy barrier to magnetization relaxation (U_{eff}) is estimated to be 17.8(1) K. Thus, this is the only lanthanide-like $[12\text{-}MC_{Mn}{}^{III}{}_{(N)shi}\text{-}4]$ with acetate to behave as an SMM.

Yb^{III}-Zn^{II} 12-MC-4 SMMs

A different variation on the 12-MC-4 framework to produce an SMM involves the lanthanide ion Yb^{III}, the ring metal ion Zn^{II}, and the MC ligand quinaldichydroximate ($quinHA^{2-}$).[147] The complexes $\{Yb^{III}(DMF)_4[12\text{-}MC_{Zn}{}^{II}{}_{N(quinHA)}\text{-}4](pyridine)_4\}(CF_3SO_3)_3$ and $\{Yb^{III}(DMF)_4[12\text{-}MC_{Zn}{}^{II}{}_{(N)quinHA}\text{-}4](isoquinoline)_4\}(CF_3SO_3)_3$ possess the overall square arrangement of the 12-MC-4 framework; however, the $[12\text{-}MC_{Zn}{}^{II}{}_{N(quinHA)}\text{-}4]$ framework is considerably more domed than the $[12\text{-}MC_{Mn}{}^{III}{}_{N(shi)}\text{-}4]$ framework (Figure 1.40).

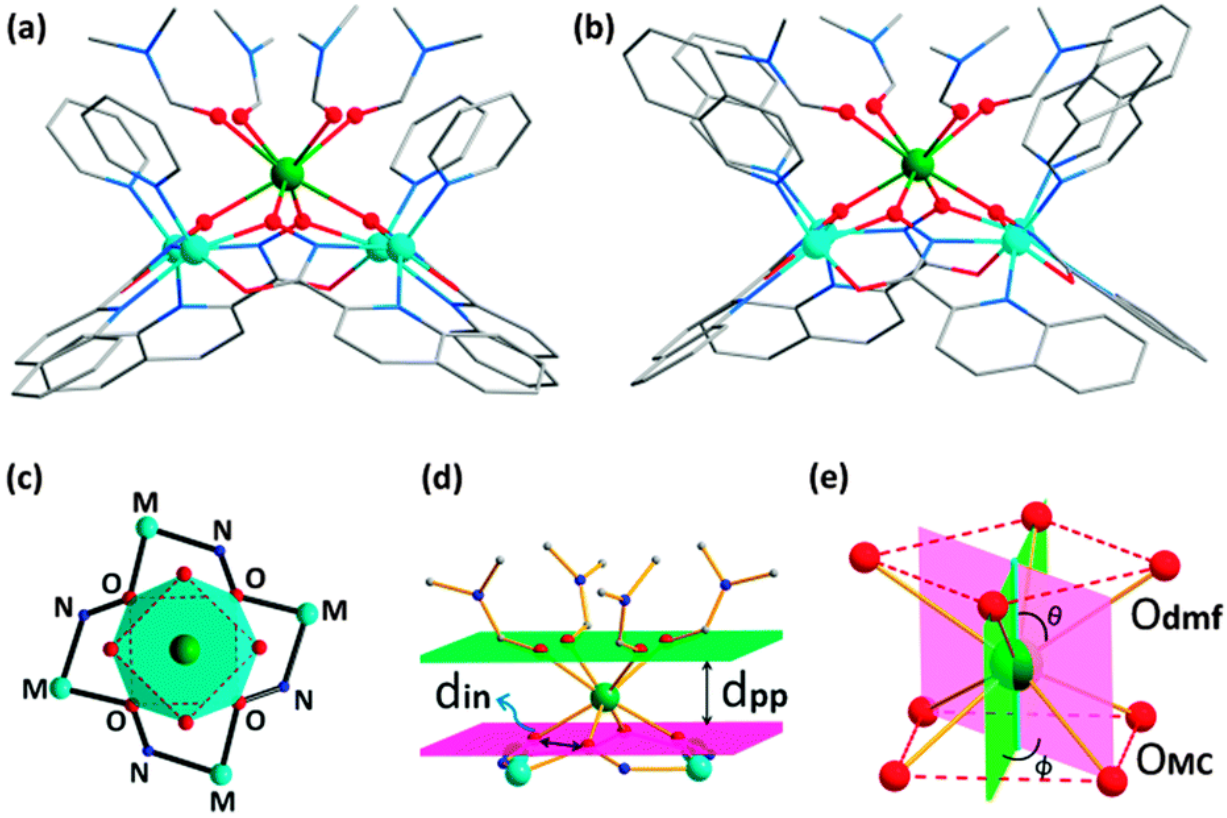

Figure 1.40. The Yb^{3+} ion of the Yb[12-$MC_{Zn}{}^{II}{}_{N(quinHA)}$-4]$(DMF)_4(Py/isoquin)_4$ has a square antiprism geometry (a, b, and e). Schematics related to measurements of the axial compression and skew angles (c and d).[147]

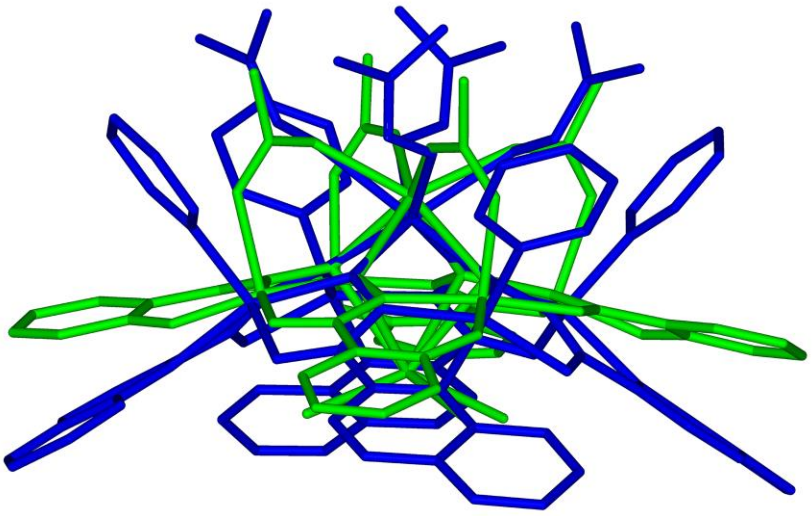

Figure 1.41. Overlay of $Yb^{III}Na^{I}(OAc)_4$[12-$MC_{Mn}{}^{III}{}_{N(shi)}$-4]$(H_2O)_4$ (green) with {$Yb^{III}(DMF)_4$[12-$MC_{Zn}{}^{II}{}_{N(quinHA)}$-4](pyridine)$_4$}$(CF_3SO_3)_3$ (blue) shows a pronounced bowling in the zinc(II)-based structure.

This is likely due to the strain on the fused chelate rings. An overlay of the $\{Yb^{III}(DMF)_4[12\text{-}MC_{Zn^{II}N(quinHA)}\text{-}4](pyridine)_4\}(CF_3SO_3)_3$ structure and the $Yb^{III}Na^{I}(OAc)_4[12\text{-}MC_{Mn^{III}N(shi)}\text{-}4](H_2O)_4$ structure visually demonstrates that the $quin^{2-}$ derivative is significantly more domed than the shi^{3-} version (Figure 1.41). In the traditional $[12\text{-}MC_{Mn^{III}N(shi)}\text{-}4]$ framework, the shi^{3-} ligands place the metal ions at a 90° angle relative to each other due to the 5- and 6-membered fused chelate rings; thus, producing a relatively planar MC (with a slight amount of doming).[148] In the $[12\text{-}MC_{Zn^{II}N(quinHA)}\text{-}4]$ framework, the $quin^{2-}$ place the metal ions at a 108° angle relative to each other due to the 5- and 5-membered fused chelate rings.[149] This arrangement can produce planar pentagonal 15-MC-5 complexes with Cu^{II} and $quinHA^{2-}$ and other ligands that place the metal ions at a 108° angle.[32,148,149] However, with Zn^{II} as the ring metal ion, a 12-MC-4 complex is produced. One other structural difference between the $Yb^{III}[12\text{-}MC_{Zn^{II}N(quinHA)}\text{-}4]$ complexes and the $Ln^{III}(X)_4[12\text{-}MC_{Mn^{III}N(shi)}\text{-}4]$ complexes is that the Yb^{III} ion is not tethered to the MC with carboxylate bridges since the charge balance for the Yb^{III} is maintained by three triflate anions in the lattice. Instead the coordination sphere of the distorted square antiprismatic Yb^{III} is completed by four DMF molecules. In addition, the concave side the MC is vacant. In terms of magnetic properties, the $Yb^{III}(DMF)_4[12\text{-}MC_{Zn^{II}N(quinHA)}\text{-}4]$ complexes present a different magnetic coupling scenario versus the $Ln^{III}(X)_4[12\text{-}MC_{Mn^{III}N(shi)}\text{-}4]$ complexes described in the previous section. The ring metal in the $Yb^{III}(DMF)_4[12\text{-}MC_{Zn^{II}N(quinHA)}\text{-}4]$ complexes is Zn^{II}, which is diamagnetic. Thus, there cannot be any magnetic coupling between the ring metals and the central Ln^{III} ion as in the manganese-based versions of the molecule. The use of diamagnetic Zn^{II} also prevents pathways for relaxation of the magnetization that could lower the effective magnetic barrier. Thus, any out-of-phase ac magnetic susceptibility behavior in the molecule is a result of the Yb^{III} in an MC framework ligand environment. For the $Yb^{III}[12\text{-}MC_{Zn^{II}N(quinHA)}\text{-}4]$ complexes, the quantum tunneling of the magnetization (QTM) is very rapid; thus, no frequency dependent ac magnetic susceptibility signal was observed in a zero applied dc magnetic field. This in contrast to the $Ln^{III}(X)_4[12\text{-}MC_{Mn^{III}N(shi)}\text{-}4]$ complexes, which displayed a frequency-dependent ac magnetic susceptibility signal in a zero applied dc magnetic field. Yet when a small dc magnetic field (600 Oe) was applied to the $Yb^{III}[12\text{-}MC_{Zn^{II}N(quinHA)}\text{-}4]$ complexes to suppress the QTM, a frequency dependent ac magnetic susceptibility was observed above 1.8 K, signifying that the $Yb^{III}[12\text{-}MC_{Zn^{II}(N)quinHA}\text{-}4]$ complexes displays SMM-like behavior. The effective energy barriers to magnetic relaxation were tentatively assigned values of U_{eff}/k_B =

12.6(7) K (9 cm^{-1}) and 22.76(6) K (16 cm^{-1}) for the complexes $\{Yb^{III}(DMF)_4[12\text{-}MC_{Zn}{}^{II}{}_{N(quinHA)}\text{-}4](pyridine)_4\}(CF_3SO_3)_3$ and $\{Yb^{III}(DMF)_4[12\text{-}MC_{Zn}{}^{II}{}_{N(quinHA)}\text{-}4](isoquinoline)_4\}(CF_3SO_3)_3$, respectively. As a note, it is very common to suppress the QTM of a SMM by application of a dc magnetic field (many examples are given below). While in most cases this helps in the characterization of the SMM behavior of the molecule, the application of a dc magnetic field can in some cases cause molecules with an easy plane of magnetization to appear as if they have a slow relaxation of the magnetization.[114,150–153] This can then lead to the misidentification of the molecule as a SMM, when in fact the slow relaxation is simply an artifact of an applied field.

Nontraditional 3d-4f Metallacrown SMMs

The transition metal-lanthanide metal approach to producing metallacrown SMMs can be extended to nontraditional MCs, i.e. complexes without the standard M-N-O repeat unit. One such example is a 15-MC-6 complex with a Cd-O-C-N-O repeat unit that encapsulates either a Ce^{III} or Nd^{III} ion.[154] The $Ln(n\text{-}Bu_3PO)_2I_3[15\text{-}MC_{Cd}{}^{II}{}_{N(quinHA)}\text{-}6]$ complexes, where *n*-Bu_3PO is tributylphosphine oxide and $HquinHA^-$ is the singly deprotonated form of quinaldichydroxamic acid, have a nearly planar MC framework with an eight-coordinate Ln^{III} ion in the central cavity (Figure 1.42).

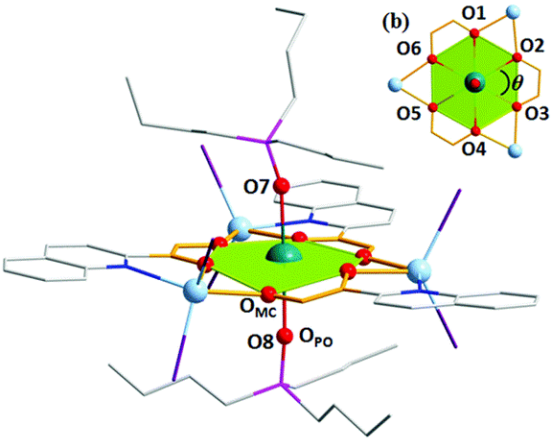

Figure 1.42. X-ray crystal structure of $Ln(n\text{-}Bu_3PO)_2I_3[15\text{-}MC_{Cd}{}^{II}{}_{N(quinHA)}\text{-}6]$ (Ln^{3+} = Ce^{3+} or Nd^{3+}) complexes with a hexagonal bipyramidal coordination geometry.[154]

The Ln^{III} coordination environment is hexagonal bipyramidal and differs from that of the Ln[12-$MC_{Mn}{}^{III}{}_{N(shi)}$-4] and Yb^{III}[12-$MC_{Zn}{}^{II}{}_{N(quinHA)}$-4] complexes, which have the Ln^{III} ion a distorted square antiprism coordination environment. As in the Yb^{III}[12-$MC_{Zn}{}^{II}{}_{N(quinHA)}$-4] complexes, the quantum tunneling of the magnetization (QTM) is very rapid for both the Ce^{III} and Nd^{III} analogues; thus, no frequency dependent ac magnetic susceptibility signal was observed in a zero applied dc magnetic field. When a dc magnetic field (1500 Oe for Ce^{III} and 2500 Oe for Nd^{III}) was applied to suppress the QTM, a frequency dependent ac magnetic susceptibility was observed near 4 K for both complexes, signifying that they may be SMMs. The energy barrier to magnetization relaxation (U_{eff}) values were estimated to be 27 K and 22 K for the Ce^{III} an Nd^{III} derivatives, respectively.

In another example of a MC-like molecule, a $Dy^{III}{}_2Ga^{III}{}_4$ complex made with the common MC ligand salicylhydroxamic acid (H_3shi) also possesses SMM behavior.[43] The complex consists of four peripheral Ga^{III} ions and two Dy^{III} ions in the core (Figure 1.43). Portions of the Ga^{III} coordination are similar to a 12-MC-4 pattern; however, not all of the H_3shi are triply deprotonated as in the 12-MC-4 complexes. However, if one counts the atoms in the M-N-O motif, there are sixteen atoms with six oxygens, thus this may be considered as a 16-MC-6.

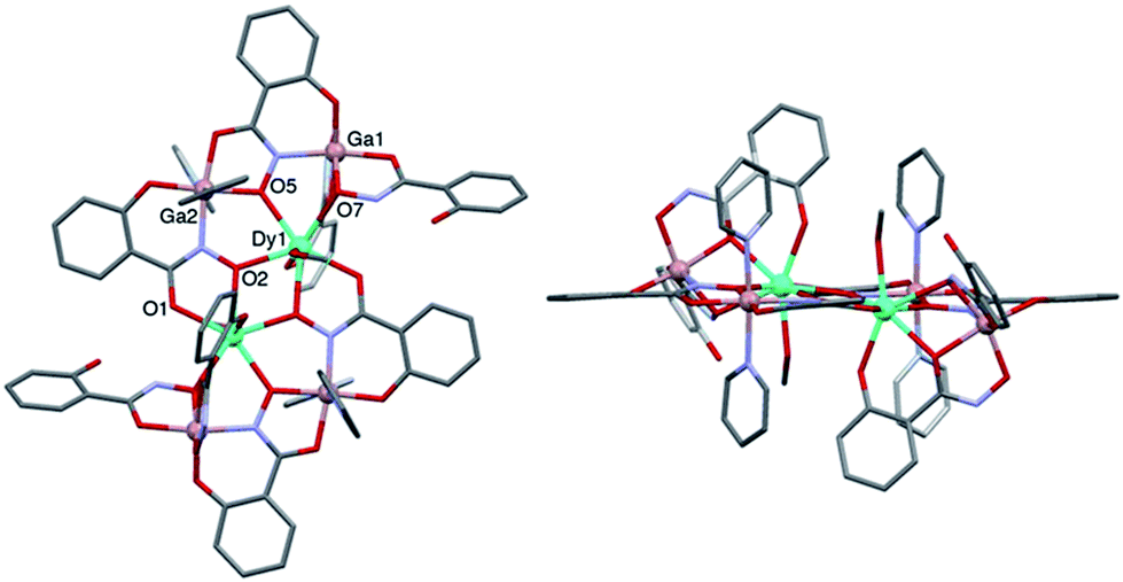

Figure 1.43. X-ray crystal structure of the $Dy^{III}{}_2Ga^{III}{}_4$ 16-MC-6 complex.[43]

The dc magnetic susceptibility data indicate that the Dy^{III} ions are antiferromagnetically coupled with a magnetic coupling of J = -0.29 cm^{-1}. Yet the compound exhibits magnetic hysteresis at

zero field below 1 K and in the ac magnetic susceptibility studies, a frequency-dependent out-of-phase ac magnetic susceptibility signal with maxima above 2 K is observed (Figure 1.44).

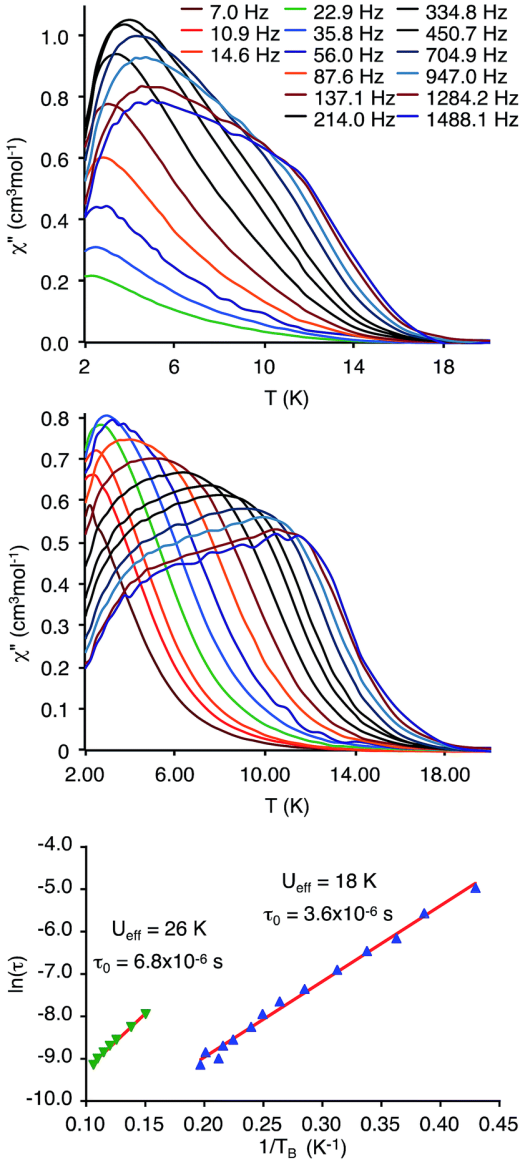

Figure 1.44. The out-of–phase ac magnetic susceptibility behavior of the $Dy^{III}_2Ga^{III}_4$ 16-MC-6 in zero applied dc magnetic field (top), and with a 2000 Oe applied dc magnetic field (middle). Two relaxation pathways were fit to the Arrhenius equation (bottom).[43]

Taken together, both sets of data indicate that the complex is an SMM. The maxima for the out-of-phase ac magnetic susceptibility signals are observed with a zero applied dc magnetic field and with a 2000 Oe applied dc magnetic field. Two slow magnetization relaxation processes are observed for the molecule. The origin of the low temperature relaxation of the magnetization is attributed to a ferromagnetically coupled excited state of the Dy^{III}_2 centers, which lies 4.9 cm^{-1}

above the diamagnetic ground state. The energy barrier to magnetization relaxation (U_{eff}) for the first process is estimated to be 18 K. The high temperature relaxation of the magnetization is attributed to the uncoupled Dy^{III} ions operating independently as the higher temperatures prevent coupling of the magnetic centers. The energy barrier to magnetization relaxation for the second process is estimated to be 26 K. These molecules have an energy separation that is appropriate for being used as Q-bits in quantum computing applications.

Transition Metal-Only Metallacrown SMMs

Though the TM-Ln complexes have proven to be a fruitful area of SMM research, transition metal-only traditional metallacrowns (with a M-N-O repeat unit) can be used to produce SMMs. Rentschler and coworkers have focused on three areas: high-spin ground state Cu^{II}[12-$MC_{Fe^{III}N(shi)}$-4] complexes, using Cu^{II}[12-$MC_{Cu^{II}N(eshi)}$-4] complexes to connect mononuclear Co^{II} SMMs complexes, and Co^{II}[12-$MC_{Co^{III}N(shi)}$-4] SMMs. All of these systems have been extensively reviewed; thus, only a brief overview is provided here.[155,156] In 2014 Happ and Renstschler reported the first 3*d* heterometallic 12-MC-4, $Cu^{II}(DMF)_2Cl_2$[12-$MC_{Fe^{III}N(shi)}$-4](DMF)$_4$ (Figure 1.45).[157]

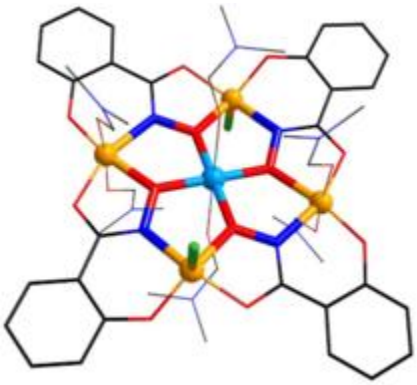

Figure 1.45. X-ray crystal structure of the heterobimetallic $Cu^{II}(DMF)_2Cl_2$[12-$MC_{Fe^{III}N(shi)}$-4](DMF)$_4$.[157]

The synthetic approach of using the monodentate anion Cl^- to achieve charge neutrality instead of a bridging anion as in a carboxylate anion more than likely lead to the formation of the heterometallic MC instead of a homometallic all-iron MC. The antiferromagnetic coupling between the central Cu^{II} ion with the ring Fe^{III} ion (J = -49.2 cm^{-1}) dominates over the Fe^{III}-Fe^{III} antiferromagnetic coupling (-3.8 cm^{-1}) to produce a complex with a high spin ground state of S_T

= 11/2.[157,158] The Cu^{II} ion acts a magnetic director in the system to produce a higher ground spin state than could be achieved if the Fe^{III}-Fe^{III} antiferromagnetic coupling dominated in the complex. Though this molecule does not behave as an SMM, it provides a pathway to develop MCs with large ground spin states. MCs can also be utilized as building blocks to link known SMMs.[156,159] Starting with $(TMA)_2\{Cu^{II}[12\text{-}MC_{Cu^{II}N(eshi)}\text{-}4]\}$, where TMA^+ is tetramethylammonium and $eshi^{3-}$ is 4-ethynylsalicylhydroximate, these MCs (Figure 1.46) can be functionalized on the peripheral $eshi^{3-}$ to have either 1-adamantyl-1H[1,2,3]triazol-4-yl groups or 1-phenyl-1H[1,2,3]triazol-4-yl groups (Figure 1.47).

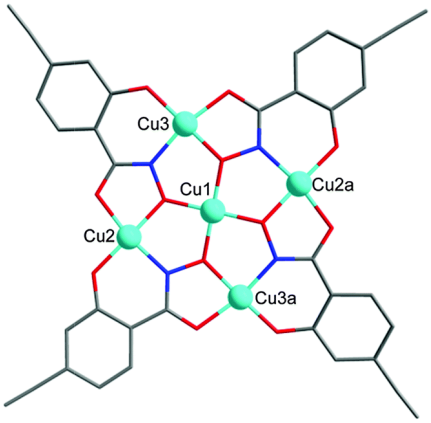

Figure 1.46. X-ray crystal structure of the $Cu[12\text{-}MC_{Cu^{II}N(eshi)}\text{-}4]$ complex.[135]

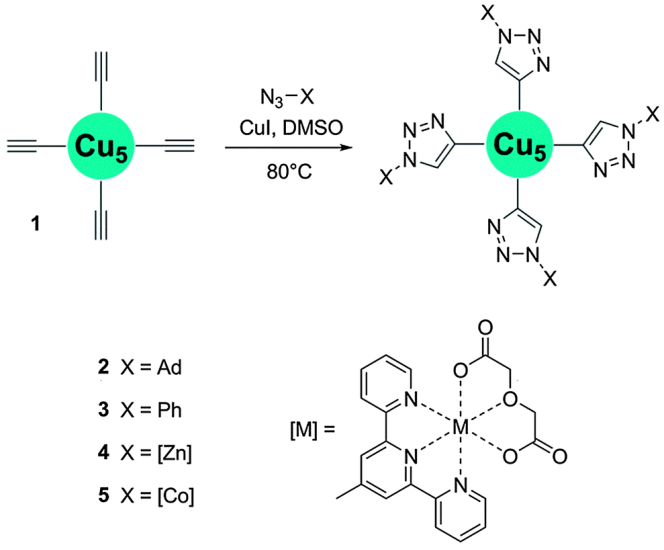

Figure 1.47. Schematic of addition of four Co^{II} SMMs to the $Cu[12\text{-}MC_{Cu^{II}N(eshi)}\text{-}4]$ complex.[135]

These MCs were then reacted with a known mononuclear Co^{II} SMM, [Co(oda)(aterpy)], where oda is oxodiacetate and aterpy = 4′-azido-2,2′:6′,2″-terpyridine.[160] Though the use of these click-enabled molecules, four Co^{II} SMM units were attached to the MC. The Cu^{II}[12-$MC_{Cu^{II}N(eshi)}$-4] now laden with four Co^{II} SMM units did display a frequency-dependent out-of-phase ac magnetic susceptibility signal above 2 K with an applied 0.15 T dc magnetic field. However, the signal is weak and the authors could not rule out the presence of individual mononuclear Co^{II} SMM units. Furthermore, Co^{II}[12-$MC_{Co^{III}N(shi)}$-4] complexes may behave as SMMs.[156] In particular three different compounds have been investigated: (Hpip)(piv)[Li[Co^{II}(μ_2-piv)$_2$(piv)[12-$MC_{Co^{III}N(shi)}$-4](pip)$_5$]]$_2$, Co^{II}(boa)(piv)[12-$MC_{Co^{III}N(shi)}$-4](morph)$_5$(MeOH), and Co^{II}(NO_2)(piv)[12-$MC_{Co^{III}N(shi)}$-4](pic)$_6$, where piv^- is pivalate (aka trimethylacetate), pip is piperidine, boa^- is 2-benzoxazolinonate, morph is morpholine and pic is 3-picoline (Figures 1.48, 1.49, and 1.50).

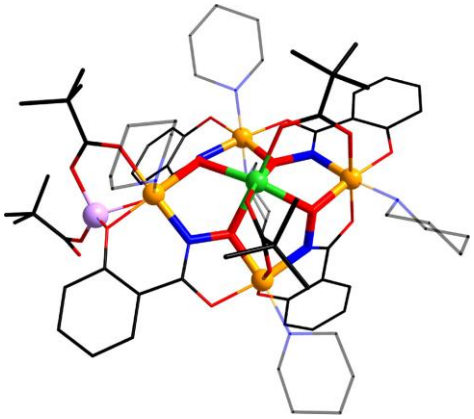

Figure 1.48. X-ray crystal structure of (Hpip)(piv)[Li[Co^{II}(μ_2-piv)$_2$(piv)[12-$MC_{Co^{III}N(shi)}$-4](pip)$_5$]]$_2$.[132]

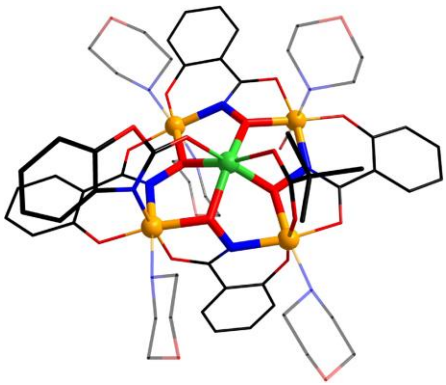

Figure 1.49. X-ray crystal structure of Co^{II}(boa)(piv)[12-$MC_{Co^{III}N(shi)}$-4](morph)$_5$(MeOH).[132]

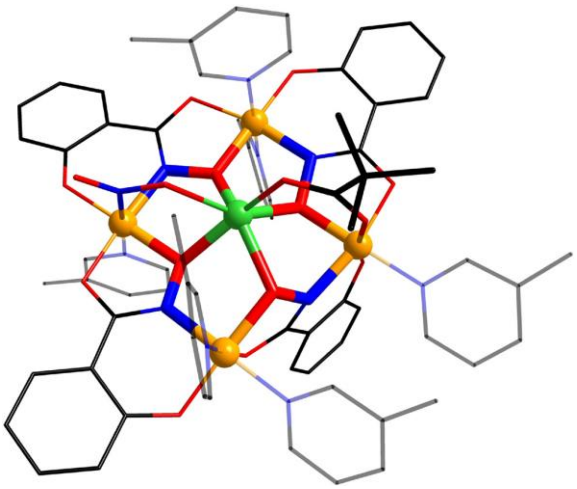

Figure 1.50. X-ray crystal structure of $Co^{II}(NO_2)(piv)[12\text{-}MC_{Co}{}^{III}{}_{N(shi)}\text{-}4](pic)_6$.[132]

In all three structures a Co^{II} ion is bound in the central cavity and Co^{III} serves as the ring metal ion. The Co^{III} ions have an octahedral coordination environment and are diamagnetic with a low-spin d^6 electron configuration. The geometry about Co^{II} varies in the structures. For $(Hpip)(piv)[Li[Co^{II}(\mu_2\text{-}piv)_2(piv)[12\text{-}MC_{Co}{}^{III}{}_{N(shi)}\text{-}4](pip)_5]]_2$ and $Co^{II}(boa)(piv)[12\text{-}MC_{Co}{}^{III}{}_{N(shi)}\text{-}4](morph)_5(MeOH)$, the Co^{II} resides in an octahedral coordination site; however, the authors note that in both molecules the site is strongly distorted and intermediate between that of octahedral and trigonal prism. For the $Co^{II}(NO_2)(piv)[12\text{-}MC_{Co}{}^{III}{}_{N(shi)}\text{-}4](pic)_6$ complex, the Co^{II} resides in a site that is also intermediate between trigonal prism and octahedral; however, the geometry is closer to that of trigonal prism. The dc magnetic susceptibility of each compound reveals that room temperature $\chi_m T$ values (3.15, 3.03, and 3.23 cm^3 K mol^{-1}, respectively) are significantly greater than that expected for a mononuclear high spin Co^{II} complex (S = 3/2, 1.876 cm^3 K mol^{-1}). This result indicates a great deal of magnetoanistropy due to spin-orbit coupling. Indeed for the $Co(NO_2)(piv)[12\text{-}MC_{Co}{}^{III}{}_{N(shi)}\text{-}4](pic)_6$ complex, the axial zero-field splitting parameter D was reported to be -64 cm^{-1}. All three compounds did display a frequency-dependent out-of-phase ac magnetic susceptibility signal with maxima above 2 K with an applied 1500 Oe dc magnetic field. Thus, all three Co^{II}-based MCs display SMM-like behavior. The size of the energy barrier to magnetization relaxation (U_{eff}) was determined to be 14, 35, and 79 K for the three compounds, $(Hpip)(piv)[Li[Co^{II}(\mu_2\text{-}piv)_2(piv)[12\text{-}MC_{Co}{}^{III}{}_{N(shi)}\text{-}4](pip)_5]]_2$, $Co^{II}(boa)(piv)[12\text{-}MC_{Co}{}^{III}{}_{N(shi)}\text{-}4](morph)_5(MeOH)$, and $Co^{II}(NO_2)(piv)[12\text{-}MC_{Co}{}^{III}{}_{N(shi)}\text{-}4](pic)_6$, respectively. The U_{eff} values correspond with the coordination environment of the central Co^{II} ion as it

progressively became less octahedral and more trigonal prismatic, with the $Co^{II}(NO_2)(piv)[12\text{-}MC_{Co}{}^{III}{}_{N(shi)}\text{-}4](pic)_6$ complex having the most trigonal prism Co^{II} ion.

Lastly, inverse Mn^{III}-based MCs have shown SMM behavior.[161] Tangoulis, Psomas, Kessissoglou and coworkers recently reported a $Mn_6(O)_2(dicl)_2(sao)_6(CH_3OH)_6$ complex, where $dicl^-$ is diclofenac and sao^{2-} is salicylaldoximato. The complex consists of two inverse-$[9\text{-}MC_{Mn}{}^{III}{}_{N(sao)}\text{-}3]$ units joined in a stepladder-like fashion (Figure 1.51).

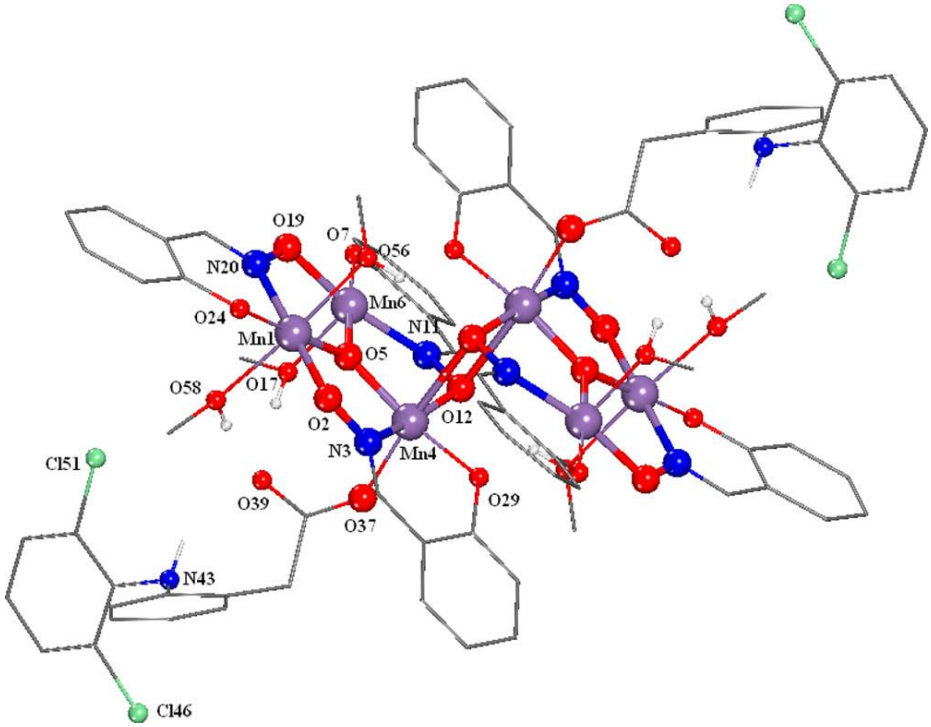

Figure 1.51. X-ray crystal structure of the two inverse-$[9\text{-}MC_{Mn}{}^{III}{}_{N(sao)}\text{-}3]$ units that bind in a stepladder fashion.[161]

The inverse MCs are fused together by two ring oximato oxygen atoms that bind to ring Mn^{III} ions on the opposite MC. In the center of each MC is an μ_3-oxide anion; thus, the inverse nature of the MC. The compound possesses a frequency-dependent out-of-phase ac magnetic susceptibility signal with maxima above 2 K in a zero applied dc magnetic field, again indicating SMM-like behavior (Figure 1.52). For the inverse-$[9\text{-}MC_{Mn}{}^{III}{}_{N(sao)}\text{-}3]_2$ SMM, the size of the energy barrier to magnetization relaxation (U_{eff}) was determined to be 41 K.

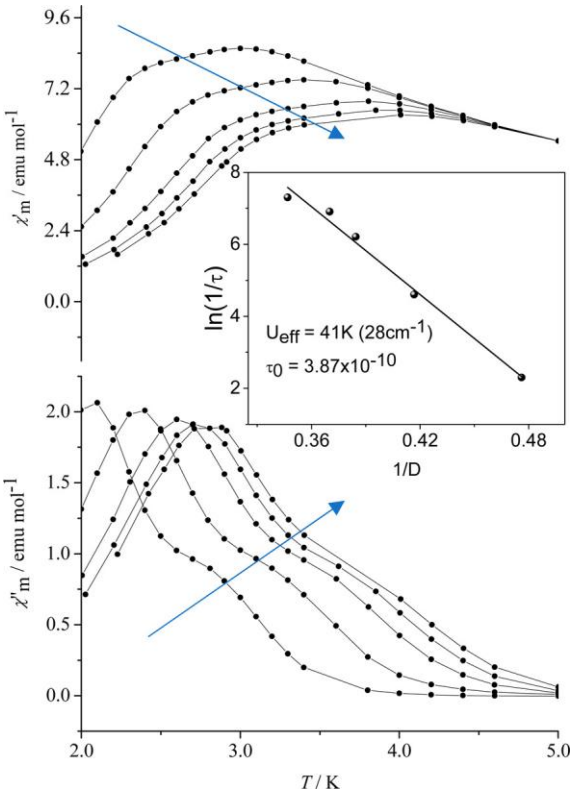

Figure 1.52. The in-phase and out-of-phase ac magnetic susceptibility of the inverse-[9-$MC_{Mn}^{III}{}_{N(sao)}$-3] shows a barrier to relaxation and possibly two unique pathways.[161]

Azametallacrown SMMs

Azametallacrowns, MCs with a M-N-N repeat unit, have also shown the ability to act as SMMs. Recent examples of azaMCs reported by Dou, Song, and coworkers include 3*d*-only azaMCs, a 4*f*-only azaMC, and a mixed 3*d*-4*f* azaMC. Three different Mn-based azaMCs have shown SMM-likebehavior. For the complex $Mn_6(L)_6(OH)_6$, where H_2L is 2-[5-pyridin-2-yl-1-H-pyrazol-3-yl]-phenol, an aza18-MC_{Mn}^{III}-6 structure is formed that has a DMF molecule located in the core (Figure 1.53).[162] The ring Mn^{III} ions are ferromagnetically coupled, and the total ground spin state of the molecule was determined to be $S_T = 11$. The compound possesses a frequency-dependent out-of-phase ac magnetic susceptibility signal above 1.8 K in a 2000 Oe applied dc magnetic field. The energy barrier to magnetization relaxation (U_{eff}) is estimated to be 5.06 K. For the complex $Mn_6O_2(L)_4(OAc)_2(OCH_3)_2(DMSO)_4$, where H_2L is 5-(2-oxyphenyl)-pyrazole-3-carboxylic acid methyl ester and DMSO is dimethylsulfoxide, the structure consists of two inverse-aza[8-$MC_{Mn}^{II}{}_{/Mn}^{III}{}_2$-3] units joined in a stepladder-like fashion (Figure 1.54).[163]

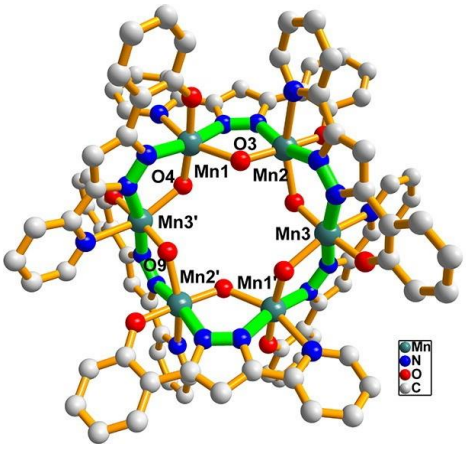

Figure 1.53. X-ray crystal structure of an aza[18-MC_{Mn}^{III}-6] using 2-[5-pyridin-2-yl-1-H-pyrazol-3-yl]-phenol.[162]

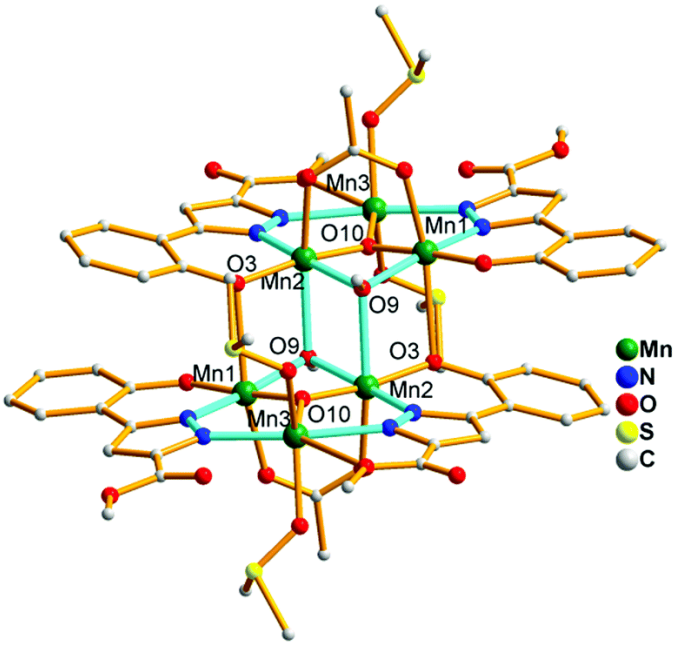

Figure 1.54. X-ray crystal structure of an inverse-aza[8-$MC_{Mn}^{II}{}_{/Mn}^{III}{}_2$-3] dimer using 5-(2-oxyphenyl)-pyrazole-3-carboxylic acid methyl ester, where the MCs are joined in a stepladder fashion.[163]

Each azaMC binds a μ_3-oxide anion in the central cavity. The Mn^{II} ion in each aza[8-$MC_{Mn}^{II}{}_{/Mn}^{III}{}_2$-3] is antiferromagnetically coupled to the two Mn^{III} ions in the azaMC unit (J = -0.96 cm^{-1}), and the Mn^{III} ions in the azaMC unit are also antiferromagnetically coupled to each other (J = -14.38 cm^{-1}). However, the Mn^{III} ions from the adjacent azaMC units are ferromagnetically coupled (J = 4.83 cm^{-1}). This then produces a total ground spin state for the

molecule of S_T = 4. The compound possesses a frequency-dependent out-of-phase ac magnetic susceptibility signal above 1.8 K in a zero applied dc magnetic field. The energy barrier to magnetization relaxation (U_{eff}) is estimated to be 1.24 K. For the complex $Mn_8(\mu_3\text{-}O)_2(\mu_3\text{-}OH)_2(\mu\text{-}OH)_2(L)_6(OAc)_2(OH_2)_4$, where H_2L is 3-(2-hydroxyphenyl)-5-(pyrazin-2-yl)-1,2,4-triazole, the structure consists of an aza[22-$MC_{Mn^{II}_2/Mn^{III}_6}$-8] complex with a –[Mn–O–Mn–N–N–Mn–N–N–Mn–N–N]- connectivity (Figure 1.55).[164]

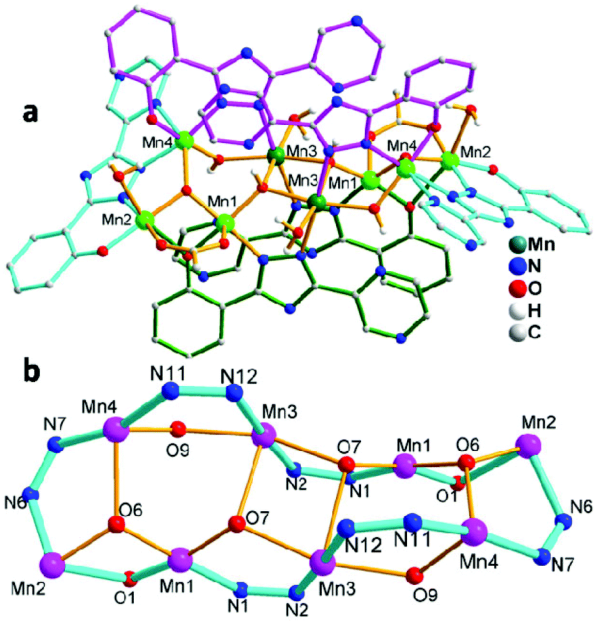

Figure 1.55. X-ray crystal structure of an aza[22-$MC_{Mn^{II}_2/Mn^{III}_6}$-8] complex using 3-(2-hydroxyphenyl)-5-(pyrazin-2-yl)-1,2,4-triazole (top) and the –[Mn–O–Mn–N–N–Mn–N–N–Mn–N–N]- connectivity (bottom).[164]

The dc magnetic susceptibility data reveal that the complex is dominated by antiferromagnetic coupling between the Mn ions; however, the exact nature of the coupling or the total ground spin state for the molecule could not be determined. The compound possesses a frequency-dependent out-of-phase ac magnetic susceptibility signal above 1.8 K in a zero applied dc magnetic field and in a 2000 Oe applied magnetic field. For the 4*f*-only azaMC $Er_4(\mu_3\text{-}OH)_2(ppt)_4(H_2ppt)_2(OAc)_2$, where H_2ppt is 3-(2-hydroxyphenyl)-5-(pyrazin-2-yl)-1,2,4-triazole, the structure consists of an aza[10-$MC_{Er^{III}}$-4] complex with a -[Er^{III}–N–N–Er^{III}–O]- connectivity (Figure 1.56).[165]Two μ_3-OH anions are captured in the azaMC core; thus, this complex could be considered an inverse azaMC. The dc magnetic susceptibility data indicate that the Er^{III} ions are weakly antiferromagnetic coupled; however, the exact nature of the coupling or the total ground spin state for the molecule could not be determined. The compound possesses a frequency-

dependent out-of-phase ac magnetic susceptibility signal above 1.8 K in a zero applied dc magnetic field and in a 2000 Oe applied magnetic field. Lastly, a family of 3*d*-4*f* azaMCs has been reported to be SMMs.[166] For the complexes $Mn^{III}_2Ln^{III}_2(OH)_2(hppt)_4(OAc)2(DMF)_2]$, where Ln^{III} is Dy^{III}, Er^{III}, Yb^{III}, Tb^{III}, and Y^{III} and H_2hppt is 3-(2-oxyphenyl)-5-(pyrazin-2-yl)-1,2,4-triazole, the structure consists of an aza[12-$MC_{Mn^{III}_{2}/Ln^{III}_{2}}$-4] complex with the Mn^{III} and Ln^{III} ions alternating about the azaMC ring (Figure 1.57).The Dy^{III}, Er^{III}, Yb^{III}, Tb^{III} versions of the aza[12-$MC_{Mn^{III}_{2}/Ln^{III}_{2}}$-4] possess a frequency-dependent out-of-phase ac magnetic susceptibility signal above 1.8 K in a zero applied dc magnetic field; however, the Y^{III} analogue did not display an out-of-phase ac magnetic susceptibility signal. Thus, the SMM behavior of these complexes is not merely due to the presence of the Mn^{III} ions. Instead the magnetic interaction between the Mn^{III} ions and the paramagnetic Ln^{III} is of vital importance to inducing SMM behavior in this family of aza[12-$MC_{Mn^{III}_{2}/Ln^{III}_{2}}$-4] molecules.

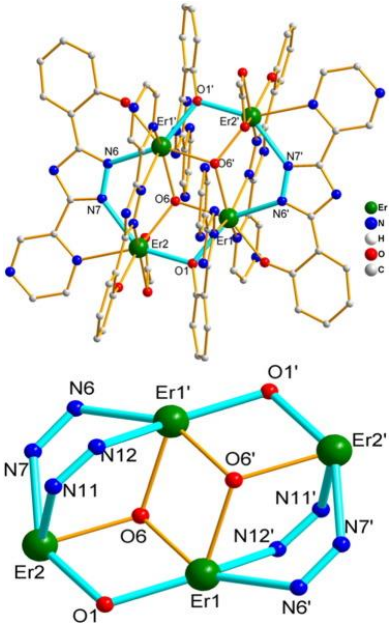

Figure 1.56. X-ray crystal structure of a lanthanide-only aza[10-$MC_{Er^{III}}$-4] using 3-(2-hydroxyphenyl)-5-(pyrazin-2-yl)-1,2,4-triazole.[165]

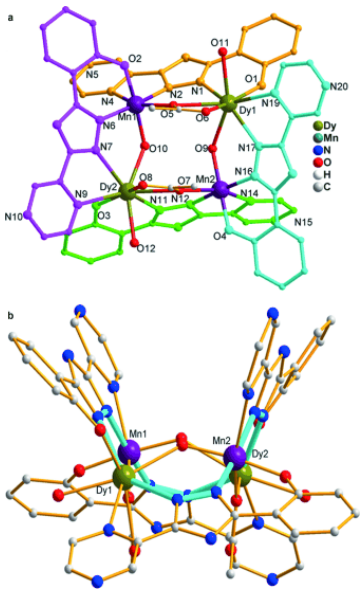

Figure 1.57. X-ray crystal structure of the $Mn^{III}_2Ln^{III}_2(OH)_2(hppt)_4(OAc)_2(DMF)_2]$ complex with an aza[12-$MC_{Mn^{III}_2/Ln^{III}_2}$-4] motif.[166]

Perspective on the Superparamagnetic Behavior of Metallacrowns

Metallacrowns have shown a significant contribution to the field of SMMs and SIMs. Work on inclusion of tungsten(V) in manganese-based MC systems showed the possibility of converting the Mn^{III}-Mn^{III} interaction from antiferromagnetic to ferromagnetic coupling.[116] This implies that there is an opportunity to refine the magnetic properties of these manganese 12-MC-4 heterotrimetallic systems by combining what was learned by Song and Dou and what was shown by Zaleski and Pecoraro, where the bridging carboxylate was shown to have an effect on SMM behavior.[36] Work by Renschler and coworkers demonstrated the ability to reach new heights for the energy barrier to magnetization relaxation using only 3*d* transition metals. From this work it is apparent that the most promising metal ion to work with is likely cobalt(II), where the molecule $Co^{II}(NO_2)(piv)$[12-$MC_{Co^{III}_{N(shi)}}$-4](pic)$_6$ had an energy barrier to magnetization relaxation of 79 K when a field of 1500 Oe is applied to quench the QTM.[155] Perhaps such MCs should be combined with lanthanides as a possible route for improvement. In addition, the ability to link molecules together via click chemistry demonstrated by Renschler and coworkers has rather interesting possibilities for SMM improvement.[160] Lastly, the Ln_2Ga_4 16-MC-6 complex reported by Pecoraro and coworkers demonstrates a rather interesting interaction between adjacent dysprosium(III) ions.[43] There are two processes in the *ac* magnetic susceptibility, where a higher temperature process was attributed to the relaxation of two independent dysprosium(III)

ions while the lower temperature process was from the relaxation of antiferromagentically coupled dysprosium(III) ions. This lower temperature process is exciting for the design of weakly interacting lanthanide ions towards application as qubits. In addition, one analog of this molecule, where the dysprosium(III) is diluted with the substitution of yttrium(III) showed a barrier of 107 K with an applied field of 750 Oe to quench the QTM, which is the current record holder for metallacrown systems.

Metallacrown Magnetorefrigerants

The magnetic properties of MCs have also been exploited for a different area of magnetic research - magnetic refrigeration, which is based on the magnetocaloric effect (MCE). The MCE arises when, under adiabatic conditions, magnetic materials may be heated or cooled upon magnetization or demagnetization of the sample, respectively.[167,168] Typical requirements for a MCE material include a large ground spin state, low magnetoanisotropy, and low-lying excited spin states.[167,168] These criteria are, in part, very different from what is desired for SMMs for which one wants large magnetoanisotropy with significant energy separations between states to minimize relaxation of the oriented moments. Potential applications for magnetic refrigerants include replacing helium-3, for applications that require ultralow temperatures, and in aerospace environments.[167–169] Two recent examples of MCs acting as magnetic refrigerants include a cobalt-based 24-MC-6 metal-organic framework (MOF) and three related iron-based MCs.[64,170] As described above, the 24-MC-6 complex is a composed of six Co^{II} ions, which are linked via twelve carboxylate groups from twelve $Hipo^{2-}$ ligands, where H_3ipo is 2-hydroxyisophthalic acid, and the MC macrocycle has a -[Co-O-C-O]- repeat unit (Figure 1.19).[64] The $Hipo^{2-}$ ligands then serve to connect the MC to neighboring MCs in three dimensions to generate a MOF (Figure 1.21). The dc magnetic susceptibility measurements indicate that above 10 K the Co^{II} ions are antiferromagnetically coupled; however, below 10 K the coupling switches to ferromagnetic. The MCE properties of the Co^{II}-MC MOF were investigated below 10 K and the maximum in the magnetic entropy change ($-\Delta S_m$) was 15.20 J kg^{-1} K^{-1} for an applied field change of ΔH = 50 kG at 6 K. For the iron-based MCs, the structures revolve around one of the first MCs reported, $Fe^{III}(OAc)_3[9\text{-}MC_{Fe^{III}N(shi)}\text{-}3](CH_3OH)_3$ (Figure 1.58).[171]

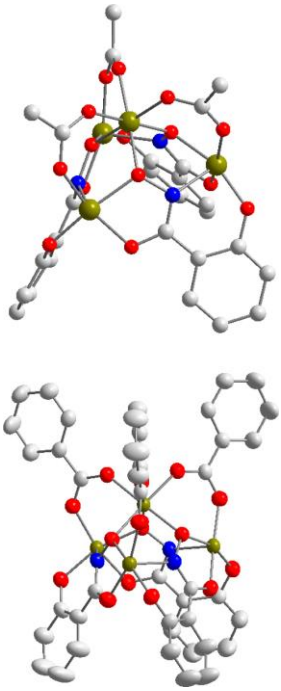

Figure 1.58. X-ray crystal structure of the $Fe^{III}L_3[9\text{-}MC_{Fe^{III}N(shi)}\text{-}3]$ with L = acetate (top) and L = benzoate (bottom).[170]

In this MC a central Fe^{III} ion is connected to the MC cavity via three acetate anions that bridge between the ring and central Fe^{III} ions. This metallacrown can be modified by replacing the acetate anions with benzoate to produce the analogous $Fe^{III}(benzoate)_3[9\text{-}MC_{Fe^{III}N(shi)}\text{-}3](CH_3OH)_3$ (Figure 1.58).[170] Lastly, two $Fe^{III}[9\text{-}MC_{Fe^{III}N(shi)}\text{-}3]$ units may be joined together using the dicarboxylate isophthalate to form the dimeric $Fe^{III}_2(isophthalate)_3[9\text{-}MC_{Fe^{III}N(shi)}\text{-}3]_2(C_2H_5OH)_6$ (Figure 1.59).

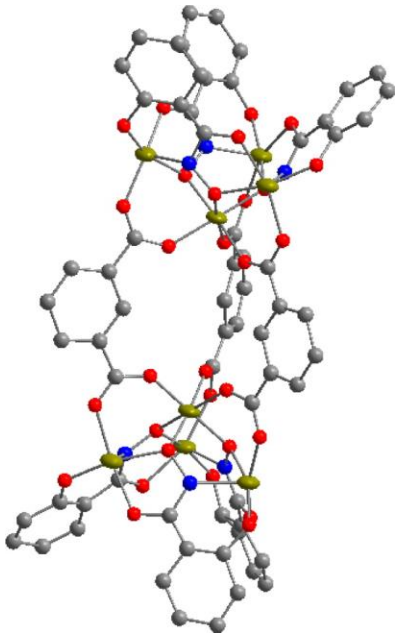

Figure 1.60. X-ray crystal structure of the Fe^{III}[9-$MC_{Fe}{}^{III}{}_{N(shi)}$-3] complex dimerized using isophthalate.[170]

The dimer $Fe^{III}{}_2$(isophthalate)$_3$[9-$MC_{Fe}{}^{III}{}_{N(shi)}$-3]$_2$($C_2H_5OH$)$_6$ molecules pack with a honeycomb arrangement, which leads to large solvent channels in the structure with a diameter of ~15 Å. When these channels lose their solvent, the compound loses its crystallinity. The dc magnetic susceptibility measurements indicate that the Fe^{III} ions in all three compounds are dominated by antiferromagnetic interactions. The ground spin states for the acetate and benzoate derivatives were both determined to be S_T = 5; however, the ground spin state of the dimer could not be determined. It is believed that the Fe_4 MC units in the dimer are antiferromagnetically coupled, which leads to an overall ground spin state of S_T = 0 for the dimer. However, low-lying excited spin states are close in energy to the ground state, and these appreciably affect the magnetocaloric properties of the molecule. The MCE properties of the three Fe^{III}-based 9-MC-3 complexes were investigated and differences where noted between the compounds. For the acetate version of the MC, the maximum in the magnetic entropy change ($-\Delta S_m$) was 15.4 J kg^{-1} K^{-1} for an applied field change of $\mu_o\Delta H$ = 7 T at 3 K. For the benzoate derivative, the maximum in the magnetic entropy change ($-\Delta S_m$) was 7.4 J kg^{-1} K^{-1} for an applied field change of $\mu_o\Delta H$ = 7 T at 7 K. The considerable differences in the MCE values for the structurally analogous compounds likely arises from the intermolecular face-to-face and edge-to-edge π interactions between the benzoate anions of the neighboring Fe^{III}(benzoate)$_3$[9-$MC_{Fe}{}^{III}{}_{N(shi)}$-3] molecules in

the solid state. These π interactions lead to a significant intermolecular antiferromagnetic superexchange ($zJ = -0.69\ cm^{-1}$). These π interactions are lacking in the acetate derivative, and there appears to be no intermolecular magnetic coupling between neighboring molecules. For the solvated dimer the maximum in the magnetic entropy change ($-\Delta S_m$) was 9.9 J kg^{-1} K^{-1} for an applied field change of $\mu_o\Delta H = 7$ T at 5 K. Interestingly, when the compound is nearly desolvated and loses its crystallinity, the maximum in the magnetic entropy change ($-\Delta S_m$) decreases to 5.4 J kg^{-1} K^{-1} for an applied field change of $\mu_o\Delta H = 7$ T at 5 K.

1.8 Lanthanide-based Luminescence and Optical Imaging

The lanthanide(III) ions have been of great interest in the imaging and telecommunication fields as they have sharp, characteristic emission bands. This optical property is due to the fact that the valence 4*f* electrons are shielded by the electrons in the 5*s* and 5*p* orbitals and the 4*f* electrons typically do not participate in bonding.[5-130] Therefore, ligand field effects do not shift the energies of the transitions and vibronic coupling does not broaden the emission.[5,172] However, the *f* to *f* orbital transition is Laporte forbidden and since the *f* orbitals do not participate in bonding, vibrational coupling cannot assist Ln^{3+} absorbance. To overcome the low extinction coefficients (<1 $M^{-1}\cdot cm^{-1}$), organic antenna molecules may be complexed to the Ln^{3+} such that the ion is sensitized by the organic chromophore via the antenna effect.[22] In addition, complexation of Ln^{3+} ions offers the opportunity of exclusion of high energy oscillators such as C-H, N-H and O-H bonds. Overtones of these oscillators may couple to the excited state of the Ln^{3+} and offers a non-radiative decay pathway, but the energy transfer is inversely proportional to distance, meaning that simply moving these oscillators further from the Ln^{3+} drastically lowers the probability of this quenching.[5,21,22]

As previously introduced, a prototypical metallacrown with lanthanide based luminescence was constructed using zinc and picoline hydroximate ($picHA^{2-}$), which encapsulates the lanthanide in between two 12-MC-4s in a square antiprism geometry. This sandwich is also encapsulated in a larger 24-MC-8 which aids in oscillator exclusion and complex stability. Thanks to the tunable nature of metallacrown complexes, this initial structure was easy to tune for a desirable property, such as red-shifting absorbance. In 2014, Pecoraro and coworkers demonstrated the effect of using quinaline hydroximate ($quinHA^{2-}$) instead of $picHA^{2-}$ where the absorbance edge was redshifted to 450 nm from 420 nm.[22] In addition, a third

lanthanide (erbium) was sensitized, and the brightest known ytterbium emission for a molecular complex was also reported.[173]

Since then, work dedicated to the improvement of lanthanide based luminescence in metallacrowns as well as potential applications have been explored. Paramount among these studies has been the development of systems capable of 1) sensitizing multiple lanthanides within the same framework, giving an opportunity to provide multicolor probes; 2) shifting the excitation energy of the antennae to long wavelength in order to obtain deeper tissue penetration (with 650 nm or longer excitation being the primary goal); and 3) obtaining very bright luminescent agents in the Near Infrared (NIR). The latter point is practically very desirable, as emission above 800 nm is not perturbed by autoflouresence of biological samples allowing for quantitative analysis of cell, tissue, and whole animal systems. Discovery of the Ln[12-$MC_{Zn^{II}N(L)}$-4]$_2$[24-$MC_{Zn^{II}N(L)}$-8]$(CF_3SO_3)_3$ was encouraging for the potential application of MCs into optical imaging of biological systems. Towards this end a few goals had to be met: the complex must have acceptable water solubility, absorb at longer wavelengths than 350 nm, and remain stable and emissive in water. The $picHA^{2-}$ and $quinHA^{2-}$ complexes were close to these standards; however, the alteration of these ligands to pyrazine hydroximate ($pyzHA^{2-}$) led to MCs that meet these goals and proved useful for two separate applications (Figure 1.60).[174,175]

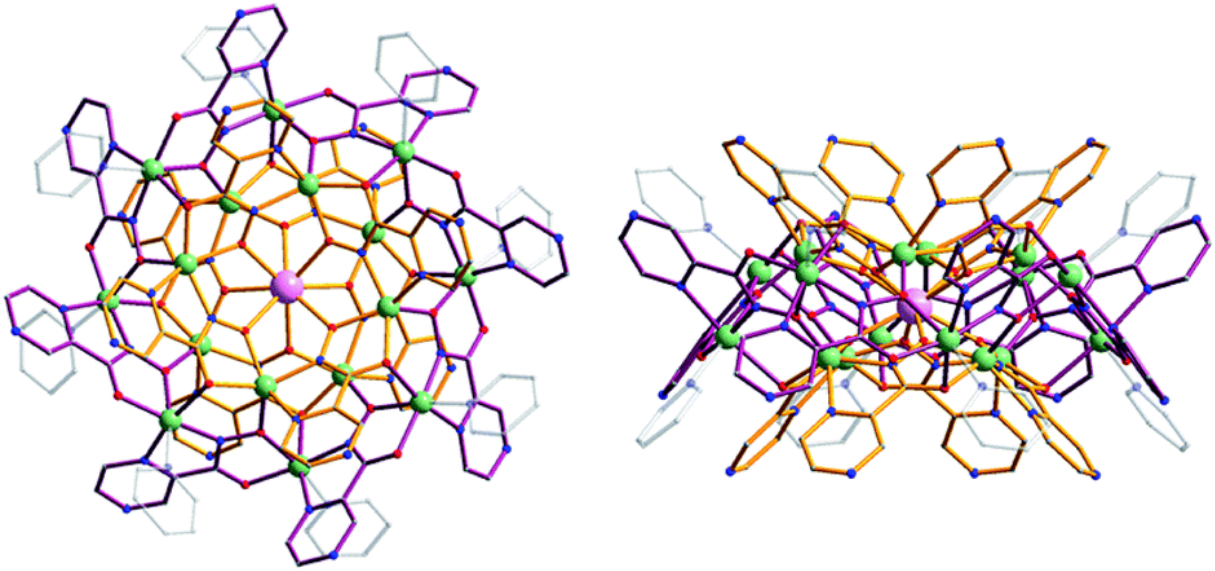

Figure 1.60. Crystal structure of the Yb^{III}[12-$MC_{Zn^{II}N(pyzHA)}$-4]$_2$[24-$MC_{Zn^{II}N(pyzHA)}$-8] complex.[174]

The Ln[12-MC$_{Zn^{II}N(pyzHA)}$-4]$_2$[24-MC$_{Zn^{II}N(pyzHA)}$-8] as a stain and cell fixation agent

Consider the scenario of a biopsy of cancerous cells. To gather the most useful information from cell imaging, the target material must be fixed (a process that preserves the cellular structure in a "lifelike state") and then stained to allow examination of subcellular structures. As standard practice, fixation using paraformaldehyde or alcohol-based precipitating agents are used to prepare the cell structures for imaging .[176] While these techniques are effective, they are not ideal since they often require multiple steps (e.g. fixation and then staining) and each fluorescent stain will require specific optimization for the fixation technique. Furthermore, common organic stains such as propidium iodide will photobleach, thus requiring a second agent to enhance their stability, and only are fluorescent when intercalated within nucleic acids, limiting the range of organelles that may be interrogated. If there was an agent that could simultaneously fix and stain cells, was photostable for long periods, and did not rely on specific binding to cellular components to be emissive, one would obtain a highly valuable staining agent. The elimination of a post fixation optimization saves time, the cost of analysis, and allows for quantitative analysis over long periods throughout the entire cell.

In 2017, Pecoraro, Petoud *et. al.* reported a process which simultaneously fixes and images HeLa (human cervical cancer) cells using Ln[12-MC$_{Zn^{II}N(pyzHA)}$-4]$_2$[24-MC$_{Zn^{II}N(pyzHA)}$-8] (Ln = Nd^{3+} and Yb^{3+}).[174] This process was optimized for both cell fixation and for the simultaneous fixation and counter staining, using the MC itself for optical imaging of the cell. Importantly, the Yb^{3+} MC was able to be observed on typical CCD cameras that are standard for microscopy, which lends credence to the viability of this complex for commercial use. Raman microscopy was used to confirm the ability of the MC to perform cell fixation. The MC method was compared to classical fixation using paraformaldehyde and methanol. The Raman spectra (Figure 1.61) indicted the characteristic loss of the 752 cm^{-1} band from cytochrome C typical of fixed cells.[177]

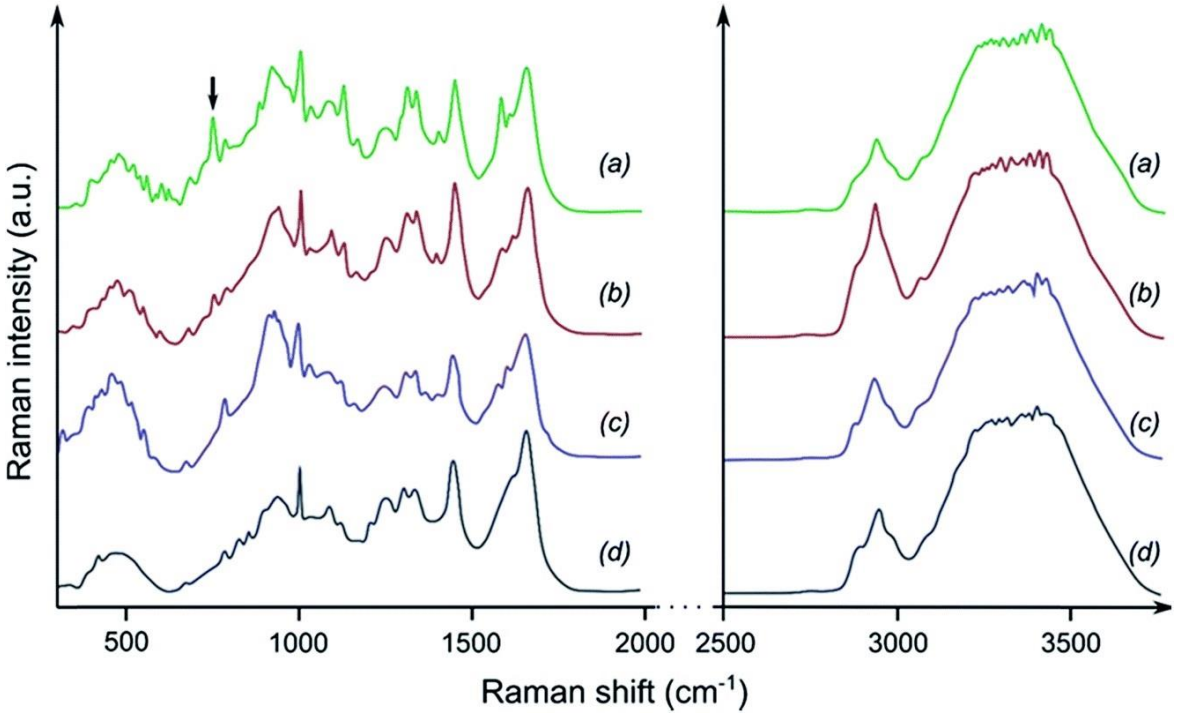

Figure 1.61. Raman spectra of HeLa cells fixed using paraformaldehyde (red), methanol (blue) or the Yb^{III}[12-$MC_{Zn}{}^{II}{}_{N(pyzHA)}$-4]$_2$[24-$MC_{Zn}{}^{II}{}_{N(pyzHA)}$-8] (black) compared to a living cell (green).[174]

In addition, the photophysics of the Yb^{3+} and Nd^{3+} MCs was examined in a variety of environments ranging from simple aqueous solution to HeLa cell suspensions. From these experiments it was found that the Nd^{3+} MC could not be measured well in HeLa cells, while the Yb^{3+} MC was easily detected in all media. Both the Yb^{3+} and Nd^{3+} MCs showed a biexponential decay when the observed lifetimes of the complexes were determined. In both cases the shorter lifetime dominated in water, while the longer lifetime was dominant in the HeLa cells, possibly beacuse the MCs may be interacting with cellular components and biomolecules in such a way that water could be excluded from the Yb^{3+}.

Two other microscopy experiments were performed; epifluorescence of the Yb^{3+} NIR emission in HeLa cells and confocal microscopy of the visible emission from the pyzHA ligand scaffold. In the epifluorescence measurements (Figure 1.62), the cells were treated with Yb^{3+} MCs and UV-A light to fix the cells.

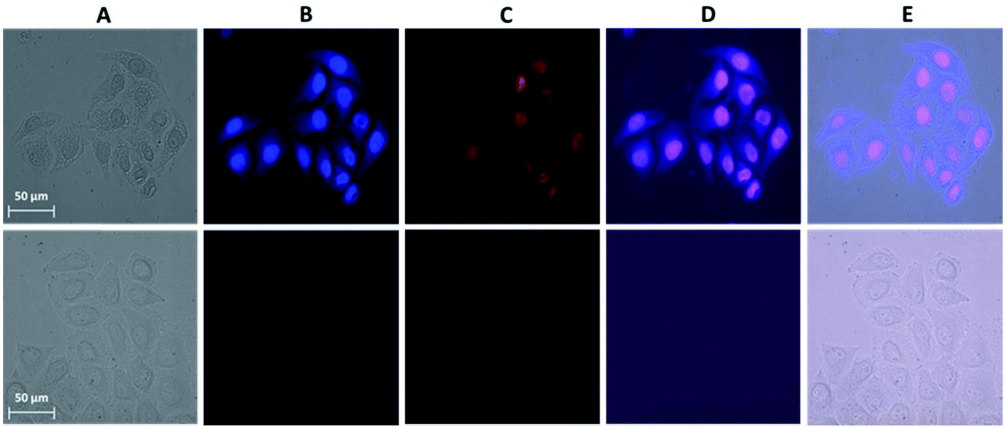

Figure 1.62. The $Yb^{III}[12\text{-}MC_{Zn^{II}N(pyzHA)}\text{-}4]_2[24\text{-}MC_{Zn^{II}N(pyzHA)}\text{-}8]$ (B top) may be used as a stain for fixed HeLa cells which images both the nucleus and cytoplasm, comparison to propidium iodide (C top) proves the cells are fixed and that the MC is not restricted to the nucleus (D top) and that the whole cell is imaged (E top). Controls with no staining (bottom row). λ_{ex} = 447 nm, λ_{em} > 805 nm using a long pass filter for Yb MC; λ_{ex} = 550 nm, λ_{em} =605 nm for PI.[174]

Propidium iodide (PI) was used to stain the nucleus of the cells to confirm cell death and to highlight the nucleus of the cell. The overlay of the MC emission with the PI emission shows that the MC images the nucleus and the cytoplasm of the cell, but appears more intense in the nucleus. However, confocal microscopy (Figure 1.63) showed that the MCs are evenly distributed in the cell, lending credence to the hypothesis that the MCs in the nucleus are brighter likely due to interaction with biomolecules.

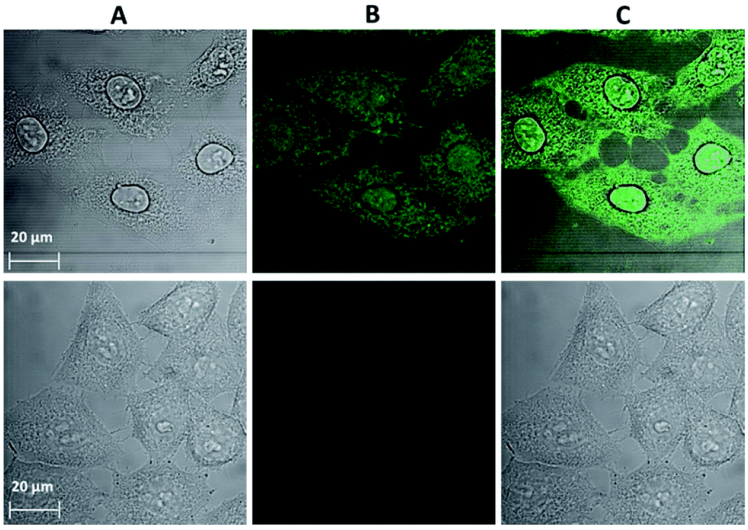

Figure 1.63. Confocal microscopy of $Yb^{III}[12\text{-}MC_{Zn^{II}N(pyzHA)}\text{-}4]_2[24\text{-}MC_{Zn^{II}N(pyzHA)}\text{-}8]$ in HeLa cells (B top) with the corresponding brightfield image (A top) and overlay (C top) compared to a control with no MC (bottom). The MC is confirmed to show visible emission from $pyzHA^{2-}$ evenly throughout the cell. λ_{ex} = 458 nm, λ_{em} = 499-799 nm.[174]

The Ln[12-MC$_{Zn^{II}N(pyzHA)}$-4]$_2$[24-MC$_{Zn^{II}N(pyzHA)}$-8] and imaging of necrotic cells

In addition to demonstrating cell fixation and the possibilities of the MC as a stain, the Ln[12-MC$_{Zn^{II}N(pyzHA)}$-4]$_2$[24-MC$_{Zn^{II}N(pyzHA)}$-8] (Ln = Nd^{3+} and Yb^{3+}) complexes were able to be used to image necrotic cells from living cells selectively.[175] The importance of this discovery by Pecoraro, Petoud, *et. al.* comes from the fact that cell necrosis is often more damaging to surrounding tissue than cell-programmed death (apoptosis). Thus, when evaluating drug candidates, it is important to establish whether cells die apoptotically or necrotically..[178,179] There is a need for compounds that can do such selective imaging rapidly which are photostable and able to be differentiated from biological autofluorescence. Such desires are able to be met by Ln^{3+} containing MCs since photostability and characteristic signal discrimination has been shown in the past.[22] The ability of the Yb^{3+} MC to selectively image necrotic HeLa cells rather than living cells was demonstrated by incubation of the cells in glucose depleted medium with the MC present. First, the concentration of MCs, which allows 90% viability of HeLa cells, was determined so that the cells that survived necrosis inducement would remain living for the course of the study. The Yb^{3+} MC only enters the necrotic cells (confirmed by parallel PI study) leaving the living cells unstained (top; Figure 1.64) compared to a control of only living cells (bottom).

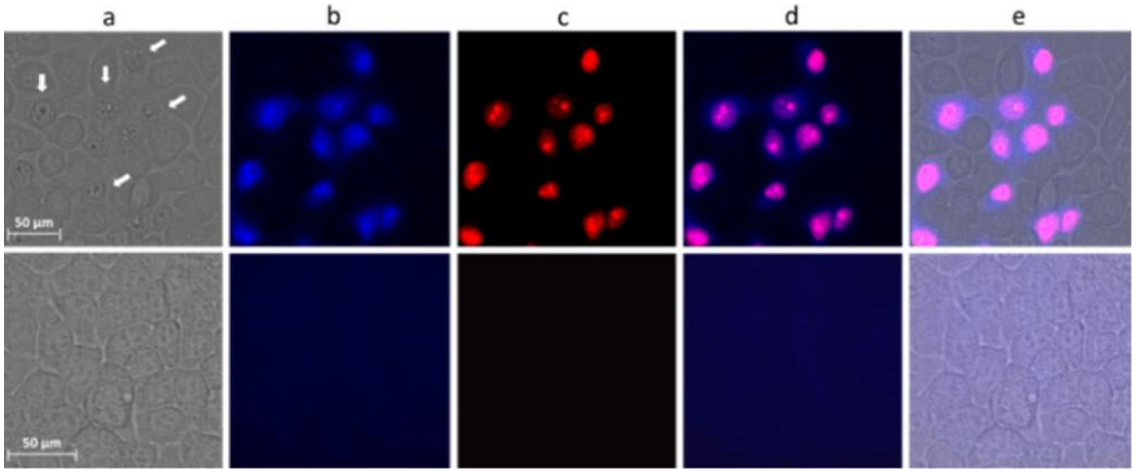

Figure 1.64. Necrotic HeLa cells (confirmed by propodium iodide in red, top C) selectively incorporate the Yb^{III}[12-MC$_{Zn^{II}N(pyzHA)}$-4]$_2$[24-MC$_{Zn^{II}N(pyzHA)}$-8] (top b) into the nucleus and cytoplasm (top d) shown by an overlay of the brightfield image (top a) with MC/PI location (top e). A control with no staining (bottom row). λ_{ex} = 447 nm, λ_{em} > 805 nm using a long pass filter for Yb MC; λ_{ex} = 550 nm, λ_{em} =605 nm for PI.[175]

Co-localization of emission from PI and the Yb^{3+} MC shows that the MC is able to image necrotic cells selectively. In addition, since PI can differentiate late stage apoptotic cells from living cells, the same method was applied to determine if the Yb^{3+} MC could as well. Apoptosis was induced by incubation with etoposide and again, the Yb^{3+} MC co-localized with the PI confirming the Yb^{3+} MC's ability to discriminate these cells from living cells. While organic fluorophores such as PI work well, the MC has advantages of enhanced photostability and NIR emission. The time-lapse comparison of necrotic HeLa cells stained with PI (top; Figure 1.65) and stained with the Yb^{3+} MC (bottom) over the course of 500 seconds demonstrates that the PI emission fades while the Yb^{3+} MC remains constant, a clear indication of the enhanced resistance to photobleaching characteristic of Ln containing MCs. Indeed, this discovery represents a significant contribution to the field thanks to this enhanced photostability.

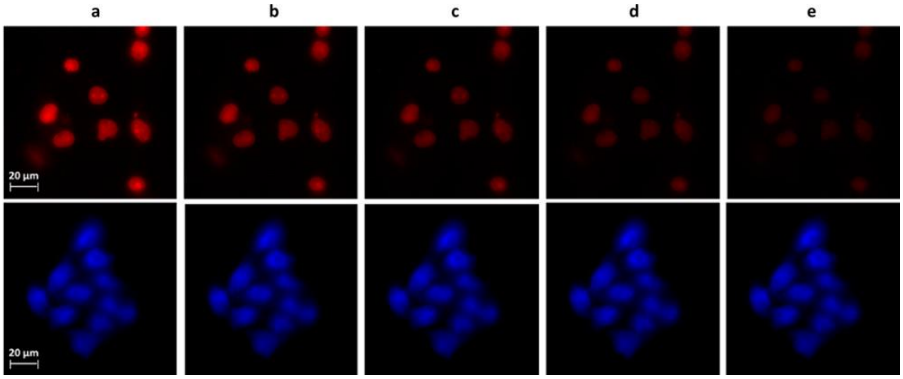

Figure 1.65. Propidium iodide (top row) shows photobleaching over the course of 500 s while the $Yb^{III}[12\text{-}MC_{Zn^{II}N(pyzHA)}\text{-}4]_2[24\text{-}MC_{Zn^{II}N(pyzHA)}\text{-}8]$ (bottom row) does not. λ_{ex} = 447 nm, λ_{em} > 805 nm using a long pass filter for Yb MC; λ_{ex} = 550 nm, λ_{em} =605 nm for PI.[175]

Yb^{3+} Luminescence of a $Yb[12\text{-}MC_{Zn^{II}N(quinHA)}\text{-}4](DMF)_4(OTf)_3$

As outlined in Section 3 the lanthanide ions are interesting not only for their luminescent behavior but also for their magnetic properties.[7] Therefore, a scaffold that allows for simultaneous cross-examination of both properties could yield interesting information on lanthanide electronic structure. One such structure was reported in 2015 by Li and coworkers which consisted of a $[12\text{-}MC_{Zn^{II}N(quinHA)}\text{-}4]$ and four DMF molecules which encapsulated a Yb^{3+} ion.[147] While the magnetic properties of $\{Yb^{III}(DMF)_4[12\text{-}MC_{Zn^{II}N(quinHA)}\text{-}4](pyridine)_4\}(CF_3SO_3)_3$ and $\{Yb^{III}(DMF)_4[12\text{-}MC_{Zn^{II}N(quinHA)}\text{-}4](isoquinoline)_4\}(CF_3SO_3)_3$ were discussed in earlier both of these complexes showed characteristic Yb^{3+} emission bands at low temperatures corresponding to a $^2F_{7/2}$ to $^2F_{5/2}$ transition. The energy difference between the two

ground sublevels was compared to the energy difference of these sublevels calculated from the *dc* and *ac* magnetic susceptibility. The *dc* magnetic susceptibility fitting found a difference of 116 cm^{-1} between the sublevels, which was close to the 169 cm^{-1} difference in sublevels found from analysis of the emission bands. However, the *ac* magnetic susceptibility fittings did not agree well with the emission spectra as the *ac* magnetic data provided a sublevel splitting of 16 cm^{-1} which can be explained by the observation of quantum tunneling of magnetization. This study showed the possibility of agreement between these techniques for determining the energy gap between ground state sublevels of lanthanide ions.

Lanthanide Complexes of Tetrakis-carboxylate and [12-$MC_{Ga}{}^{III}{}_{N(shi)}$-4]

Until recently, only metallacrowns containing Zn^{2+} and $picHA^{2-}$ or derivatives of $picHA^{2-}$ have been synthesized and characterized for lanthanide-based luminescent properties. However, Zn^{2+} is not the only available optically transparent $3d^{10}$ metal that could be used towards such purposes. As an alternative, Ga^{3+} may be employed to match the charge of shi^{3-} and formulate MCs with a new family of hydroximate antenna. Lanthanide-containing 12-MC-4 complexes had been reported with Mn^{3+} as a ring metal and with carboxylate bridges by Pecoraro, Zaleski, *et. al.* in 2014, so the substitution of Ga^{3+} into this structure was straightforward to accomplish.[34] In 2016, Pecoraro, *et. al.* reported this exact complex with benzoate bridges to complete the Ln^{3+} coordination in the [12-$MC_{Ga}{}^{III}{}_{N(shi)}$-4] central cavity (Figure 1.66).[24]

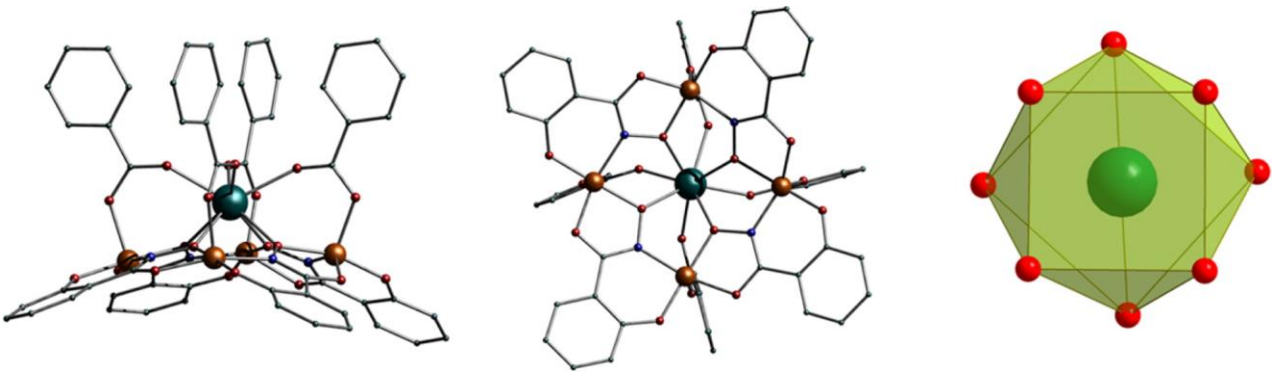

Figure 1.66. X-ray crystal structure of $Dy(OBz)_4$[12-$MC_{Ga}{}^{III}{}_{N(shi)}$-4](HPy): side view (left), top view (center, and the square antiprism coordination environment of the Dy^{III} ion (right).[24]

The structure, solution- and solid-state optical properties, and photophysics were reported for the Sm^{3+}, Eu^{3+}, Gd^{3+}, Tb^{3+}, Dy^{3+}, Ho^{3+}, Er^{3+}, Tm^{3+}, and Yb^{3+} analogs of this molecule (Figure 1.67).

This system thus represented one of the few examples of sensitization of multiple lanthanides and provided the highest quantum yield for a molecular-based complex for the NIR emitting element Yb^{3+}.

The Dy^{3+} analog was crystallized in the space group $P2_1/n$ and used for the structural analysis (Figure 1.66). The Dy^{3+} ion is eight coordinate in a square antiprism geometry. The coordination environment consists of the four oxime oxygen atoms of the 12-MC-4 ring and four oxygen atoms of benzoate ligands. The benzoate anions also serve to span the Ga^{3+} and the Dy^{3+} ions. Each gallium(III) is six coordinate with an octahedral geometry, where two shi^{3-} bind to the Ga^{3+} in the equatorial positions and the axial sites are occupied by the one oxygen atom from a benzoate bridge and an oxygen atom of a MeOH solvent molecule. Indeed this structure is comparable to the previously reported 12-MC-4 structures with Mn^{3+} instead of Ga^{3+}, with the exception of the decreased planarity of the MC ring for the Ga^{3+} MCs.

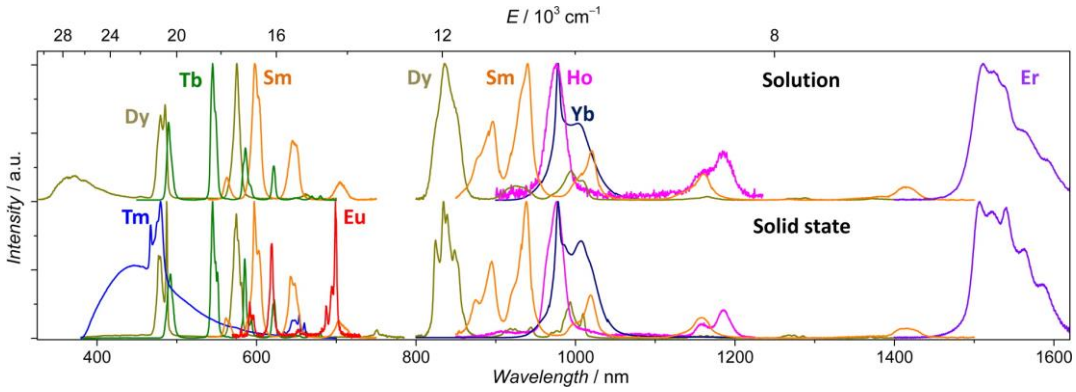

Figure 1.67. Luminescence of the $Ln(OBz)_4[12\text{-}MC_{Ga^{III}N(shi)}\text{-}4](HPy)$ complexes show a large range of lanthanide ions may be sensitized in both the solid state and in solution.[24]

The photophysical properties of this complex were rather interesting and represent a groundbreaking discovery for Ln-based luminescence in MC structures. First and foremost, this scaffold was able to sensitize Ln^{3+} ions ranging in emission from the visible to the near infrared (NIR) (Figure 1.67). This is an impressive feat with few other examples, which is even more impressive given that rarely seen NIR emissions from Tm^{3+} and Ho^{3+} ions plus NIR emissions from Sm^{3+} and Dy^{3+} were observed in this series.[23,180–182] In addition, solid state emission of Eu^{3+} was observed despite the presence of a ligand to metal charge transfer (LMCT) between the shi^{3-} and the Eu^{3+}. Examination of the Gd^{3+} analog allowed for study of the photophysics of the 12-MC-4 scaffold since the emissive state of Gd^{3+} is sufficiently higher that the triplet state of most

organic compounds. This restricts the ability of the ligand scaffold to transfer energy to the Gd^{3+} and simplifies the emissions observed to be only ligand in origin. The energy of the ligand scaffold triplet state was determined to be 22,170 cm^{-1} (451 nm) at 77 K upon excitation with 325 nm light. The absorbance in methanol of the complex was also observed to have an edge near 29,000 cm^{-1} (~345 nm), which means that the lowest singlet excited state and the highest triplet state are 7000 cm^{-1} apart, more than enough for efficient intersystem crossing. This 22,170 cm^{-1} T_1 energy state is important for explaining the remarkable ability of the 12-MC-4 to sensitize a large number of Ln^{3+} ions. First, the T_1 state must be higher in energy than the emissive state, and secondly, an energy difference of 2,500 cm^{-1} is desired to prevent thermally assisted back transfer. This energy gap is met for most of the sensitized Ln^{3+} studied, with the exception of Tm^{3+}, Dy^{3+} and Tb^{3+}. However, observation of these emissions is still possible. The last important observation was comparison of the Yb^{3+} analogs of the Ga^{3+}/shi^{3-} based 12-MC-4 and the Zn^{2+}/$quinHA^{2-}$ complex reported by Pecoraro *et. al*.[22] The observed lifetimes and sensitization efficiency were improved by 1.2 fold and 1.6 fold, respectively, which helps explain the increase in overall quantum yield from 2.44% in the Zn^{2+}/$quinHA^{2-}$ scaffold to 5.88% in the Ga^{3+}/shi^{3-} scaffold. The increase in quantum yield contributes to an increase in brightness of the compound, which is described as the product of the molar absorption cross-section and quantum yield of the same state of matter. In other words, the quantum yield describes the ratio that converts the molar absorption-cross section to the molar emission cross-section. This is an important concept, since brighter compounds are more desirable as imaging agents. Comparing both complexes in MeOH solution shows similar QYs while the Zn^{2+}/$quinHA^{2-}$ scaffold has a higher absorption coefficient, so the Zn^{2+}/$quinHA^{2-}$ is still brighter in solution.

In 2017 this structure was modified to use isopthalate linkers rather than benzoate (Figure 1.68).[25] This resulted in dimerized structures of two gallium metallacrowns, which again was able to sensitize a wide range of lanthanide ions, now including neodymium and praseodymium. When compared on a per lanthanide basis, these new dimerized complexes showed a decrease in quantum yield, but there was also an enhancement in absorbance, sensitization efficiency, and solution state stability demonstrated by ^{1}H-NMR COSY experiments. The loss in overall quantum yield was attributed to the closer proximity of the two lanthanides in the dimerized complex, compared to the distance between two monomeric complexes. These complexes were able to be analyzed for cytotoxicity, where the complex was deemed non cytotoxic to HeLa cells

in concentrations of up to 200 μM. This is indicative of the possible use of these gallium based metallacrowns in biological conditions.

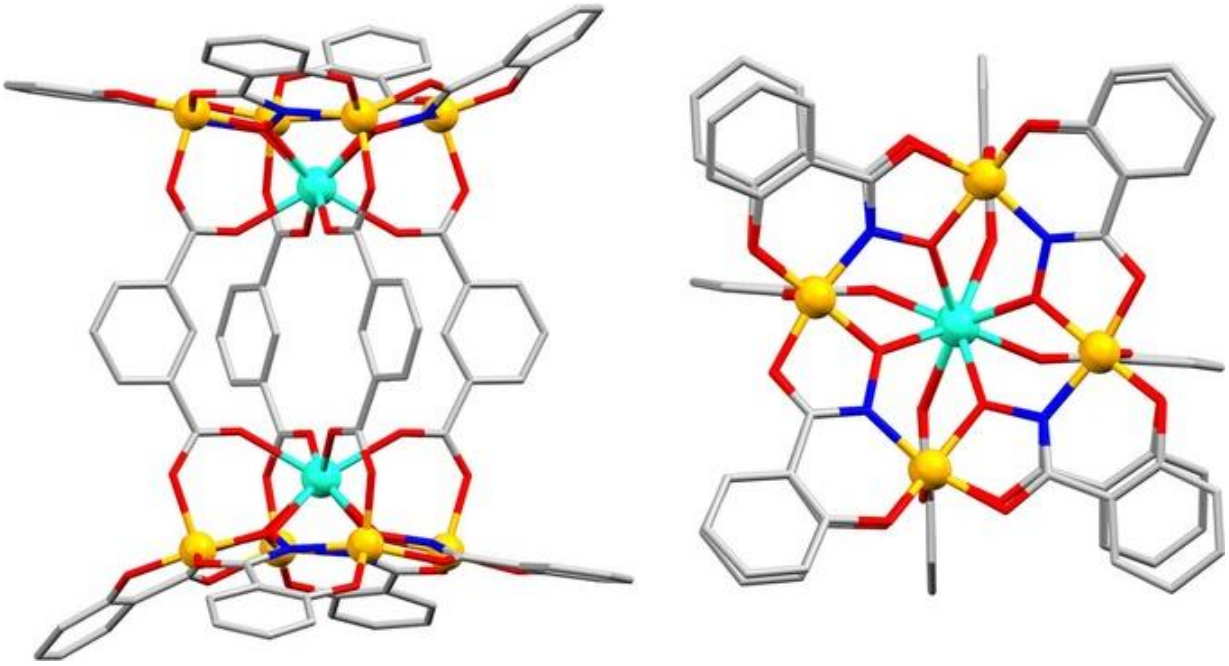

Figure 1.68. X-ray crystal structure of $\{Dy[12\text{-}MC_{Ga}{}^{III}{}_{N(shi)}\text{-}4]\}_2(iph^{2-})_4$ shown from the side (left) and down the fourfold axis (right). Solvent molecules and ammonium countercations are not shown for clarity.[25]

1.9 MCs as Magnetic Resonance Imaging (MRI) Contrast Agents

MRI is a standard medical imaging practice with the ability to image tissues with excellent resolution. Work on contrast agents to differentiate healthy tissue from unhealthy tissue has enhanced the usefulness of this technique, many of which contain Gd^{3+}. Gadolinium(III) is favored due to its high spin of S = 7/2 and long electronic relaxation time.[183] To address concerns of toxicity, the Gd^{3+} ion is often encapsulated in 1,4,7,10-tetraazacyclododecane–N,N',N'',N'''-tetraacetic acid (DOTA) or diethylene-triamine-pentaacetic acid (DTPA), which bind to the ion in eight coordinate geometries. Since Gd^{3+} prefers a nine coordinate environment in this chelate, a solvent water binds to the open site on the Gd^{3+}. Once bound, the paramagnetism of the Gd^{3+} alters the nuclear relaxation rate of the water protons as compared to bulk water allowing for MRI contrast. Currently, there is great interest in compounds designed to operate with higher field magnets, as this equipment is becoming more common thanks to better signal to noise ratios and shorter acquisition times.[184] Among the numerous examples of MCs which contain Gd^{3+},

some of these have been reported as possible MRI contrast agents.[149,185] The Gd[15-$MC_{Cu^{II}N(picHA)}$-5] and Gd[15-$MC_{Cu^{II}N(glyHA)}$-5] MCs were reported to outperform the Gd^{3+} DOTA and DTPA complexes likely due to the coordination of multiple water molecules to the Gd^{3+} in the central cavity of the MC as well as the planar disc shape and high molecular weight of the MC, which alters the solution state rotational correlation time and reorientation rate in a favorable way.[149,184,185] Given these interesting preliminary results, further elaboration on the 15-MC-5 scaffold has been conducted to understand how to improve MCs towards these applications.

A comprehensive structural and relaxometric study was performed by Katkova and co-workers on various forms of Ln[15-$MC_{Cu^{II}N(glyHA)}$-5] metallacrowns, where glyHA is glycinehydroxamic acid and Ln is La^{3+}, Ce^{3+}, Pr^{3+}, Nd^{3+}, Sm^{3+}, Eu^{3+}, Gd^{3+}, Tb^{3+} or Dy^{3+}, with the various counter anions nitrate, acetate, and lactate (Figure 1.69).[186] Four different structure types were observed: two different nitrate bound structures, a structure with bound acetate, and a structure with bound lactate. Both nitrate structures had a planar MC ring; however, the nitrate coordination mode differs in the two structures. In the Nd^{3+} analog, the nitrate is bidentate onto the central Nd^{3+}, while the La^{3+} analog features the nitrate bound as a bridge between the La^{3+} and a Cu^{2+}. The acetate anion analog was crystallized using Y^{3+} as the central metal, which has similar bond distances as mid-series lanthanides such as Eu^{3+} and Gd^{3+} and may be used as a diamagnetic analog. This MC showed the acetate bound to the Y^{3+} in a bidentate fashion with one water on the opposite face of the MC. Also, this structure was bowled such that the water side was in the concavity of the MC. A similar structure was observed with the Gd^{3+} analog of the lactate bound MC, where lactate is bidentate on the Gd^{3+} ion with an opposing water. This MC also showed bowling with a water in the concavity. A relaxometric study was performed on the Gd(lactate)[15-$MC_{Cu^{II}N(glyHA)}$-5] compound and values of 9.1 $s^{-1}{\cdot}mM^{-1}$ and 7.2 $s^{-1}{\cdot}mM^{-1}$ for r_1 and r_2, respectively, in a field of 9.4 T were reported.

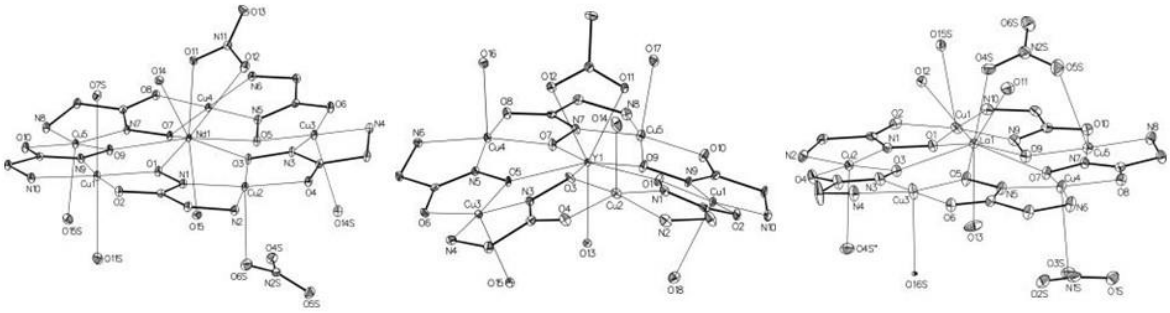

Figure 1.69. X-ray crystal structures of the Ln[15-MC$_{Cu^{II}N(glyHA)}$-5] (Ln^{3+} = Y^{3+}, La^{3+}, or Gd^{3+}) with acetate (left), nitrate (center), and lactate (right).[186]

Recently, Muravyeva and coworkers designed, synthesized, and characterized a new Ln$(H_2O)_4$[15-MC$_{Cu^{II}N(glyHA)}$-5]Cl_3 complex with access for four waters to the Gd^{3+}, and the MC is water soluble (Figure 1.70).[184] The complex was synthesized with lanthanide(III) chloride and copper(II) acetate salts (Ln^{3+} = La^{3+}, Pr^{3+}, Nd^{3+}, Sm^{3+}, Eu^{3+}, Gd^{3+}, Tb^{3+}, Dy^{3+}, Ho^{3+}, Er^{3+}, and Tm^{3+}). The exclusion of the nitrate ion is thought to be important for the access to water in this system, since nitrates are known to bind to the lanthanide in similar 15-MC-5s.[186] Because both Gd^{3+} and Cu^{2+} are paramagnetic and either ion may contribute to the observed proton relaxivity perturbation. To differentiate the effect of waters bound to Cu^{2+} and Ln^{3+}, studies were performed with the diamagnetic La^{3+}. As was expected, only the Gd^{3+} analog showed significant relaxivities in fields of 4.7, 7.0, and 9.4 T of up to 9.5 $s^{-1}{\cdot}mM^{-1}$ and 11.1 $s^{-1}{\cdot}mM^{-1}$ for r_1 and r_2, respectively. When compared to the lactate bound analog, it was noted that the additional three water molecules did not significantly alter the relaxivity values. This observation is difficult to rationalize as more water molecules bound to the Gd^{3+} should lead to higher relaxivity.[187–189] Instead the data suggests that the MC structure is more important to its interesting MRI properties. Nonetheless, this study shows the capability of MC structures to operate as high field contrast agents.

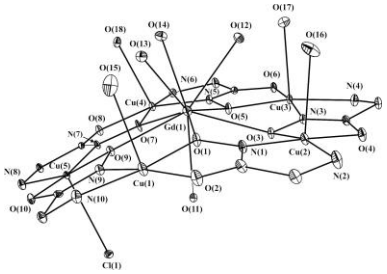

Figure 1.70. X-ray crystal structure of the Gd$(NO_3)_2$[15-MC$_{Cu^{II}N(glyHA)}$-5]$(H_2O)_4$.[184]

1.10. Summary

Over the course of this chapter, a wide range of applications of metallacrown macrocycles has been discussed. Examples of new studies of metallacrowns in the solution state have been explored which answer questions regarding stability and structures compared to the solid state. New uses of metallacrowns have been demonstrated, such as molecular nanocompartments and new approaches to Ce/Cu nanocluster synthesis. Metallacrowns continue to yield interesting magnetic structures and provide the opportunity for significant magnetic investigations. Due to the modular nature of complexes and the ability to easily substitute components in the structures, systematic studies can be conducted to understand the underpinning mechanisms behind the magnetic properties. Thus, metallacrowns have become useful materials for understanding phenomena such as single-molecule magnetism and the magnetocaloric effect. Lastly, metallacrowns and their application in imaging using lanthanide-based luminescence and as MRI-contrast agents have been explored. The optical aspect of zinc "encapsulated sandwich" MCs can be used for cell fixation and staining, as well as for selective imaging of necrotic cells. These $LnZn_{16}$ complexes and the newly developed MC systems using Ga^{3+} hold significant promise for commercialization. The MRI-contrast capabilities of copper and gadolinium 15-MC-5s have shown to outperform current commercial gadolinium complexes, even at high fields. Indeed, metallacrowns continue to reflect a remarkable capability of tailoring metal and ligand choice towards a large number of applications with a list that continues to grow.

References

(1) Herschel, J. F. W. *Philos. Trans. R. Soc. London* **1845**, *135*, 143–145.
(2) Lakowicz, J. R. *Principles of Fluorescence Spectroscopy*, 2nd ed.; Kluwer Academic/Plenum: New York, 1999.
(3) Jabłoński, A. *Zeitschrift für Phys.* **1935**, *94* (1–2), 38–46.
(4) Stokes, G. G. *Philos. Trans. R. Soc. London* **1852**, *142*, 463–562.
(5) Bünzli, J.-C. G.; Eliseeva, S. V. In *Lanthanide Luminescence: Photophysical, Analytical and Biological Aspects*; Hanninen, P., Harma, H., Eds.; Springer: Berlin, 2011; pp 1–45.
(6) Fonin, A. V.; Sulatskaya, A. I.; Kuznetsova, I. M.; Turoverov, K. K. *PLoS One* **2014**, *9* (7), e103878.
(7) Rinehart, J. D.; Long, J. R. *Chem. Sci.* **2011**, *2* (11), 2078.
(8) Bagai, R.; Christou, G. *Chem. Soc. Rev.* **2009**, *38* (4), 1011–1026.
(9) Lis, T. *Acta Crystallogr.* **1980**, *B36*, 2042–2046.
(10) Sessoli, R.; Tsai, H. L.; Schake, A. R.; Wang, S.; Vincent, J. B.; Folting, K.; Gatteschi, D.; Christou, G.; Hendrickson, D. N. *J. Am. Chem. Soc.* **1993**, *115* (5), 1804–1816.
(11) Christou, G.; Gatteschi, D.; Hendrickson, D. N.; Sessoli, R. *MRS Bull.* **2000**, *25*, 66–71.
(12) Ishikawa, N.; Sugita, M.; Ishikawa, T.; Koshihara, S.; Kaizu, Y. *J. Am. Chem. Soc.* **2003**, *125* (29), 8694–8695.
(13) AlDamen, M. A.; Cardona-Serra, S.; Clemente-Juan, J. M.; Coronado, E.; Gaita-Ariño, A.; Martí-Gastaldo, C.; Luis, F.; Montero, O. *Inorg. Chem.* **2009**, *48* (8), 3467–3479.
(14) Rinehart, J. D.; Fang, M.; Evans, W. J.; Long, J. R. *J. Am. Chem. Soc.* **2011**, *133* (36), 14236–14239.
(15) Rinehart, J. D.; Fang, M.; Evans, W. J.; Long, J. R. *Nat. Chem.* **2011**, *3* (7), 538–542.
(16) Demir, S.; Jeon, I.-R.; Long, J. R.; Harris, T. D. *Coord. Chem. Rev.* **2014**, 1–28.
(17) Rinehart, J. D.; Fang, M.; Evans, W. J.; Long, J. R. *J. Am. Chem. Soc.* **2011**, *133* (36), 14236–14239.
(18) Vleck, J. H. V. *J. Phys. Chem.* **1937**, *41* (1), 67–80.
(19) Uh, H.; Petoud, S. *Comptes Rendus Chim.* **2010**, *13* (6–7), 668–680.
(20) Bünzli, J.-C. G.; Piguet, C. *Chem. Soc. Rev.* **2005**, *34* (12), 1048.
(21) Jankolovits, J.; Andolina, C. M.; Kampf, J. W.; Raymond, K. N.; Pecoraro, V. L. *Angew. Chemie Int. Ed.* **2011**, *50* (41), 9660–9664.
(22) Trivedi, E. R.; Eliseeva, S. V.; Jankolovits, J.; Olmstead, M. M.; Petoud, S.; Pecoraro, V. L. *J. Am. Chem. Soc.* **2014**, *136* (4), 1526–1534.
(23) Law, G. L.; Pham, T. A.; Xu, J.; Raymond, K. N. *Angew. Chemie - Int. Ed.* **2012**, *51* (10), 2371–2374.
(24) Chow, C. Y.; Eliseeva, S. V; Trivedi, E. R.; Nguyen, T. N.; Kampf, J. W.; Petoud, S.; Pecoraro, V. L. *J. Am. Chem. Soc.* **2016**, *138* (15), 5100–5109.
(25) Nguyen, T. N.; Chow, C. Y.; Eliseeva, S. V.; Trivedi, E. R.; Kampf, J. W.; Martinić, I.; Petoud, S.; Pecoraro, V. L. *Chem. - A Eur. J.* **2018**, *24* (5), 1031–1035.
(26) Moore, E. G.; Xu, J.; Dodani, S. C.; Jocher, C. J.; D'Aléo, A.; Seitz, M.; Raymond, K. N. *Inorg. Chem.* **2010**, *49* (9), 4156–4166.
(27) Petoud, S.; Muller, G.; Moore, E. G.; Xu, J.; Sokolnicki, J.; Riehl, J. P.; Le, U. N.; Cohen, S. M.; Raymond, K. N. *J. Am. Chem. Soc.* **2007**, *129* (1), 77–83.
(28) Comby, S.; Imbert, D.; Chauvin, A. S.; Bunzli, J. C. G. *Inorg. Chem.* **2006**, *45* (2), 732–743.
(29) Faulkner, S.; Beeby, A.; Carrié, M.-C.; Dadabhoy, A.; Kenwright, A. M.; Sammes, P. G.

Inorg. Chem. Commun. **2001**, *4* (4), 187–190.
(30) Routledge, J. D.; Jones, M. W.; Faulkner, S.; Tropiano, M. *Inorg. Chem.* **2015**, No. Iii, 150309112822003.
(31) Lah, M. S.; Pecoraro, V. L. *J. Am. Chem. Soc.* **1989**, *111*, 7258–7259.
(32) Mezei, G.; Zaleski, C. M.; Pecoraro, V. L. *Chem. Rev.* **2007**, *107* (11), 4933–5003.
(33) Gibney, B. R.; Wang, H.; Kampf, J. W.; Pecoraro, V. L. *Inorg. Chem.* **1996**, *35* (21), 6184–6193.
(34) Azar, M. R.; Boron, T. T.; Lutter, J. C.; Daly, C. I.; Zegalia, K. A.; Nimthong, R.; Ferrence, G. M.; Zeller, M.; Kampf, J. W.; Pecoraro, V. L.; Zaleski, C. M. *Inorg. Chem.* **2014**, *53* (3), 1729–1742.
(35) Lah, M. S.; Kirk, M. L.; Hatfield, W.; Pecoraro, V. L. *J. Chem. Soc. Chem. Commun.* **1989**, No. 21, 1606.
(36) Boron, T. T.; Lutter, J. C.; Daly, C. I.; Chow, C. Y.; Davis, A. H.; Nimthong-Roldán, A.; Zeller, M.; Kampf, J. W.; Zaleski, C. M.; Pecoraro, V. L. *Inorg. Chem.* **2016**, *55* (20), 10597–10607.
(37) Lah, M. S.; Pecoraro, V. L. *J. Am. Chem. Soc.* **1989**, *111* (18), 7258–7259.
(38) Pecoraro, V. L. *Inorganica Chim. Acta* **1989**, *155* (2), 171–173.
(39) Lah, M. S.; Gibney, B. R.; Tierney, D. L.; Penner-Hahn, J. E.; Pecoraro, V. L. *J. Am. Chem. Soc.* **1993**, *115* (13), 5857–5858.
(40) Travis, J. R.; Zeller, M.; Zaleski, C. M. *Polyhedron* **2016**, *114*, 29–36.
(41) Jankolovits, J.; Kampf, J. W.; Pecoraro, V. L. *Inorg. Chem.* **2014**, *53* (14), 7534–7546.
(42) Boron, T. T.; Kampf, J. W.; Pecoraro, V. L. *Inorg. Chem.* **2010**, *49* (20), 9104–9106.
(43) Chow, C. Y.; Bolvin, H.; Campbell, V. E.; Guillot, R.; Kampf, J. W.; Wernsdorfer, W.; Gendron, F.; Autschbach, J.; Pecoraro, V. L.; Mallah, T. *Chem. Sci.* **2015**, *6* (7), 4148–4159.
(44) Psomas, G.; Stemmler, A. J.; Dendrinou-Samara, C.; Bodwin, J. J.; Schneider, M.; Alexiou, M.; Kampf, J. W.; Kessissoglou, D. P.; Pecoraro, V. L. *Inorg. Chem.* **2001**, *40* (7), 1562–1570.
(45) Zaleski, C. M.; Kampf, J. W.; Mallah, T.; Kirk, M. L.; Pecoraro, V. L. *Inorg. Chem.* **2007**, *46* (6), 1954–1956.
(46) Stemmler, A. J.; Kampf, J. W.; Pecoraro, V. L. *Inorg. Chem.* **1995**, *34* (9), 2271–2272.
(47) Lin, S.; Liu, S. X.; Chen, Z.; Lin, B. Z.; Gao, S. *Inorg. Chem.* **2004**, *43* (7), 2222–2224.
(48) Tegoni, M.; Furlotti, M.; Tropiano, M.; Lim, C. S.; Pecoraro, V. L. *Inorg. Chem.* **2010**, *49* (11), 5190–5201.
(49) Zaleski, C. M.; Lim, C.-S.; Cutland-Van Noord, A. D.; Kampf, J. W.; Pecoraro, V. L. *Inorg. Chem.* **2011**, *50* (16), 7707–7717.
(50) Atzeri, C.; Marchiò, L.; Chow, Y. C.; Kampf, J. W.; Vincent, L.; Tegoni, M.; Chow, C. Y.; Kampf, J. W.; Pecoraro, V. L.; Tegoni, M. *Chem. Eur. J.* **2016**, *22* (19), ASAP.
(51) Cutland-Van Noord, A. D.; Kampf, J. W.; Pecoraro, V. L. *Angew. Chemie Int. Ed.* **2002**, *41* (24), 4667–4670.
(52) Jankolovits, J.; Cutland Van-Noord, A. D.; Kampf, J. W.; Pecoraro, V. L. *Dalt. Trans.* **2013**, *42* (27), 9803.
(53) McDonald, C.; Whyte, T.; Taylor, S. M.; Sanz, S.; Brechin, E. K.; Gaynor, D.; Jones, L. F. *CrystEngComm* **2013**, *15* (34), 6672–6681.
(54) Han, L.; Qin, L.; Yan, X.-Z.; Xu, L.-P.; Sun, J.; Yu, L.; Chen, H.-B.; Zou, X. *Cryst. Growth Des.* **2013**, *13* (5), 1807–1811.

(55) Moon, M.; Kim, I.; Lah, M. S. *Inorg. Chem.* **2000**, *39* (13), 2710–2711.
(56) Moon, D.; Lah, M. S. *Inorg. Chem.* **2005**, *44* (6), 1934–1940.
(57) Meng, X.; Song, X.-Z.; Song, S.-Y.; Yang, G.-C.; Zhu, M.; Hao, Z.-M.; Zhao, S.-N.; Zhang, H.-J. *Chem. Commun. (Camb).* **2013**, *49* (76), 8483–8485.
(58) Zaleski, C. M.; Cutland-Van Noord, A. D.; Kampf, J. W.; Pecoraro, V. L. *Cryst. Growth Des.* **2007**, *7* (6), 1098–1105.
(59) Janiak, C. *Dalt. Trans.* **2003**, 2781–2804.
(60) Jeon, I.-R.; Clérac, R. *Dalt. Trans.* **2012**, *41* (32), 9569.
(61) Rach, S. F.; Kühn, F. E. *Chem. Rev.* **2009**, *49* (0), 2061–2080.
(62) Mengle, K. A.; Longenecker, E. J.; Zeller, M.; Zaleski, C. M. *J. Chem. Crystallogr.* **2015**, *45* (1), 36–43.
(63) Croitor, L.; Coropceanu, E. B.; Petuhov, O.; Krämer, K. W.; Baca, S. G.; Liu, S.-X.; Decurtins, S.; Fonari, M. S. *Dalton Trans.* **2015**, *44* (17), 7896–7902.
(64) Wang, K.; Zou, H.-H.; Chen, Z.-L.; Zhang, Z.; Sun, W.-Y.; Liang, F.-P. *Dalt. Trans.* **2014**, *43* (34), 12989.
(65) Hayashi, H.; Hakuta, Y. *Materials (Basel).* **2010**, *3* (7), 3794–3817.
(66) Kremlev, K. V; Samsonov, M. A.; Zabrodina, G. S.; Arapova, A. V; Yunin, P. A.; Tatarsky, D. A.; Plyusnin, P. E.; Katkova, M. A.; Ketkov, S. Y. *Polyhedron* **2016**, *114*, 96–100.
(67) Mariño, F.; Schönbrod, B.; Moreno, M.; Jobbágy, M.; Baronetti, G.; Laborde, M. *Catal. Today* **2008**, *133–135*, 735–742.
(68) Laberty-Robert, C.; Long, J. W.; Lucas, E. M.; Pettigrew, K. A.; Stroud, R. M.; Doescher, M. S.; Rolison, D. R. *Chem. Mater.* **2006**, *18* (1), 50–58.
(69) Li, Z.-X.; Li, L.-L.; Yuan, Q.; Feng, W.; Xu, J.; Sun, L.-D.; Song, W.-G.; Yan, C.-H. *J. Phys. Chem. C* **2008**, *112* (47), 18405–18411.
(70) Avgouropoulos, G.; Ioannides, T.; Matralis, H. *Appl. Catal. B Environ.* **2005**, *56* (1–2), 87–93.
(71) Song, Y.; Wei, W.; Qu, X. *Adv. Mater.* **2011**, *23* (37), 4215–4236.
(72) Hornés, A.; Hungría, A. B.; Bera, P.; Cámara, A. L.; Fernández-García, M.; Martínez-Arias, A.; Barrio, L.; Estrella, M.; Zhou, G.; Fonseca, J. J.; Hanson, J. C.; Rodriguez, J. A. *J. Am. Chem. Soc.* **2010**, *132* (1), 34–35.
(73) Jabłońska, M.; Palkovits, R. *Appl. Catal. B Environ.* **2016**, *181*, 332–351.
(74) Kurzak, B.; Kozłowski, H.; Farkas, E. *Coord. Chem. Rev.* **1992**, *114*, 169–200.
(75) Careri, M.; Dallavalle, F.; Tegoni, M.; Zagoni, I. *J. Ionrg. Biochem* **2003**, *93*, 174–180.
(76) Tegoni, M.; Remelli, M.; Bacco, D.; Marchiò, L.; Dallavalle, F. *Dalt. Trans.* **2008**, 2693–2701.
(77) Tegoni, M.; Remelli, M. *Coord. Chem. Rev.* **2012**, *256*, 289–315.
(78) Marchiò, L.; Marchetti, N.; Atzeri, C.; Borghesani, V.; Remelli, M.; Tegoni, M. *Dalt. Trans.* **2015**, *44* (7), 3237–3250.
(79) Bacco, D.; Bertolasi, V.; Dallavalle, F.; Galliera, L.; Marchetti, N.; Marchiò, L.; Remelli, M.; Tegoni, M. *Dalt. Trans.* **2011**, *40* (11), 2491–2501.
(80) Careri, M.; Dallavalle, F.; Tegoni, M.; Zagnoni, I. *J. Inorg. Biochem.* **2003**, *93*, 174–180.
(81) Beccia, M. R.; García, B.; García-Tojal, J.; Leal, J. M.; Secco, F.; Tegoni, M. *Dalt. Trans.* **2014**, *43* (24), 9271–9282.
(82) Beccia, M. R.; García, B.; García-Tojal, J.; Leal, J. M.; Secco, F.; Tegoni, M. *Dalton Trans.* **2014**, *43* (24), 9271–9282.

(83) Remelli, M.; Bacco, D.; Dallavalle, F.; Lazzari, E.; Marchetti, N.; Tegoni, M. *Dalt. Trans.* **2013**, *42* (22), 8018.
(84) Farkas, E.; Bátka, D.; Csapó, E.; Buglyó, P.; Haase, W.; Sanna, D. *Polyhedron* **2007**, *26* (3), 543–554.
(85) Parac-Vogt, T. N.; Pacco, A.; Görller-Walrand, C.; Binnemans, K. *J. Inorg. Biochem.* **2005**, *99* (2), 497–504.
(86) Dallavalle, F.; Remelli, M.; Sansone, F.; Bacco, D.; Tegoni, M. *Inorg. Chem.* **2010**, *49* (4), 1761–1772.
(87) Pacco, A.; Parac-Vogt, T. N.; Van Besien, E.; Pierloot, K.; Görller-Walrand, C.; Binnemans, K. *Eur. J. Inorg. Chem.* **2005**, No. 16, 3303–3310.
(88) Atzeri, C.; Marzaroli, V.; Quaretti, M.; Travis, J. R.; Di Bari, L.; Zaleski, C. M.; Tegoni, M. *Inorg. Chem.* **2017**, *56* (14), 8257–8269.
(89) Mezei, G.; Kampf, J. W.; Pan, S.; Poeppelmeier, K. R.; Watkins, B.; Pecoraro, V. L. *Chem. Commun.* **2007**, *45* (11), 1148.
(90) Jankolovits, J.; Lim, C.-S.; Mezei, G.; Kampf, J. W.; Pecoraro, V. L. *Inorg. Chem.* **2012**, *51* (8), 4527–4538.
(91) Grant, J. T.; Jankolovits, J.; Pecoraro, V. L. *Inorg. Chem.* **2012**, *51* (15), 8034–8041.
(92) Lim, C.-S.; Jankolovits, J.; Kampf, J. W.; Pecoraro, V. L. *Chem. - An Asian J.* **2010**, *5* (1), 46–49.
(93) Lim, C.-S.; Jankolovits, J.; Zhao, P.; Kampf, J. W.; Pecoraro, V. L. *Inorg. Chem.* **2011**, *50* (11), 4832–4841.
(94) Jankolovits, J.; Lim, C.-S.; Kampf, J. W.; Pecoraro, V. L. *Zeitschrift für Naturforsch. B* **2010**, *65* (3), 263-s314.
(95) Cutland, A. D.; Malkani, R. G.; Kampf, J. W.; Pecoraro, V. L. *Angew. Chemie Int. Ed.* **2000**, *39* (15), 2689–2692.
(96) Sgarlata, C.; Giuffrida, A.; Trivedi, E. R.; Pecoraro, V. L.; Arena, G. *Inorg. Chem.* **2017**, *56* (9), 4771–4774.
(97) Easmon, J.; Pürstinger, G.; Heinisch, G.; Roth, T.; Fiebig, H. H.; Holzer, W.; Jäger, W.; Jenny, M.; Hofmann, J. *J. Med. Chem.* **2001**, *44* (13), 2164–2171.
(98) Trawick, B. N.; Daniher, A. T.; Bashkin, J. K. *Chem. Rev.* **1998**, *98* (3), 939–960.
(99) Koiri, R. K.; Trigun, S. K.; Dubey, S. K.; Singh, S.; Mishra, L. *BioMetals* **2008**, *21* (2), 117–126.
(100) Reddy, P. R.; Shilpa, A.; Raju, N.; Raghavaiah, P. *J. Inorg. Biochem.* **2011**, *105* (12), 1603–1612.
(101) Becco, L.; Rodríguez, A.; Bravo, M. E.; Prieto, M. J.; Ruiz-Azuara, L.; Garat, B.; Moreno, V.; Gambino, D. *J. Inorg. Biochem.* **2012**, *109*, 49–56.
(102) Meng, Y.; Yang, H.; Li, D.; Zeng, S.; Chen, G.; Li, S.; Dou, J. *RSC Adv.* **2016**, *6* (53), 47196–47202.
(103) Afrati, T.; Pantazaki, A. a; Dendrinou-Samara, C.; Raptopoulou, C.; Terzis, A.; Kessissoglou, D. P. *Dalton Trans.* **2010**, *39* (3), 765–775.
(104) Rajczak, E.; Gluszynska, A.; Juskowiak, B. *J. Inorg. Biochem.* **2016**, *155*, 105–114.
(105) Cal, M.; Jaremko, Ł.; Jaremko, M.; Stefanowicz, P. *New J. Chem.* **2013**, *37* (11), 3770.
(106) Cal, M.; Kotynia, A.; Jaremko, Ł.; Jaremko, M.; Lisowski, M.; Cebo, M.; Brasuń, J.; Stefanowicz, P. *Dalt. Trans.* **2015**, *44* (24), 11172–11181.
(107) Grove, A.; Mutter, M.; Rivier, J. E.; Montal, M. *J. Am. Chem. Soc.* **1993**, *115* (14), 5919–5924.

(108) Csapó, E.; Buglyó, P.; Nagy, N. V.; Santos, M. A.; Corona, A.; Farkas, E. *Polyhedron* **2010**, *29* (16), 3137–3145.
(109) Walsh, S. T. R.; Cheng, H.; Bryson, J. W.; Roder, H.; DeGrado, W. F. *Proc. Natl. Acad. Sci.* **1999**, *96* (10), 5486–5491.
(110) Sessoli, R.; Tsai, H.-L.; Schake, A. R.; Wang, S.; Vincent, J. B.; Folting, K.; Gatteschi, D.; Christou, G.; Hendrickson, D. N. *J. Am. Chem. Soc.* **1993**, *115*, 1804–1816.
(111) Craig, G. A.; Murrie, M. *Chem. Soc. Rev.* **2015**, *44* (8), 2135–2147.
(112) Zaleski, C. M.; Tricard, S.; Depperman, E. C.; Wernsdorfer, W.; Mallah, T.; Kirk, M. L.; Pecoraro, V. L. *Inorg. Chem.* **2011**, *50* (22), 11348–11352.
(113) Andruh, M.; Costes, J.; Diaz, C.; Gao, S. *Inorg. Chem.* **2009**, *48* (8), 3342–3359.
(114) Sessoli, R.; Powell, A. K. *Coord. Chem. Rev.* **2009**, *253* (19–20), 2328–2341.
(115) Feltham, H. L. C.; Brooker, S. *Coord. Chem. Rev.* **2014**, *276*, 1–33.
(116) Rosado Piquer, L.; Sañudo, E. C. *Dalt. Trans.* **2015**, *44* (19), 8771–8780.
(117) Liu, K.; Shi, W.; Cheng, P. *Coord. Chem. Rev.* **2015**, *289–290* (1), 74–122.
(118) Mereacre, V.; Prodius, D.; Ako, A. M.; Kaur, N.; Lipkowski, J.; Simmons, C.; Dalal, N.; Geru, I.; Anson, C. E.; Powell, A. K.; Turta, C. *Polyhedron* **2008**, *27* (11), 2459–2463.
(119) Akhtar, M. N.; Zheng, Y.; Lan, Y.; Mereacre, V.; Anson, C. E.; Powell, A. K. *Inorg. Chem.* **2009**, *48* (8), 3502–3504.
(120) Akhtar, M. N.; Lan, Y.; Mereacre, V.; Clérac, R.; Anson, C. E.; Powell, A. K. *Polyhedron* **2009**, *28* (9–10), 1698–1703.
(121) Liu, C.-M.; Zhang, D.-Q.; Zhu, D.-B. *Dalt. Trans.* **2010**, *39*, 11325–11328.
(122) Liu, J.-L.; Guo, F.-S.; Meng, Z.-S.; Zheng, Y.-Z.; Leng, J.-D.; Tong, M.-L.; Ungur, L.; Chibotaru, L. F.; Heroux, K. J.; Hendrickson, D. N. *Chem. Sci.* **2011**, *2* (7), 1268.
(123) Saha, A.; Thompson, M.; Abboud, K. A.; Wernsdorfer, W.; Christou, G. *Inorg. Chem.* **2011**, *50*, 10476–10485.
(124) Ke, H.; Zhao, L.; Guo, Y.; Tang, J. *Dalton Trans.* **2012**, *41* (8), 2314–2319.
(125) Chesman, A. S. R.; Turner, D. R.; Berry, K. J.; Chilton, N. F.; Moubaraki, B.; Murray, K. S.; Deacon, G. B.; Batten, S. R. *Dalt. Trans.* **2012**, *41* (37), 11402–11412.
(126) Alexandropoulos, D. I.; Nguyen, T. N.; Cunha-Silva, L.; Zafiropoulos, T. F.; Escuer, A.; Christou, G.; Stamatatos, T. C. *Inorg. Chem.* **2013**, *52* (3), 1179–1181.
(127) Chandrasekhar, V.; Bag, P.; Speldrich, M.; van Leusen, J.; Kögerler, P. *Inorg. Chem.* **2013**, *52* (9), 5035–5044.
(128) Guedes, G. P.; Mercante, L. a; Speziali, N. L.; Novak, M. a; Andruh, M.; Vaz, M. G. F. *Inorg. Chem.* **2013**, *52*, 8309–8311.
(129) Chen, H.; Ma, C.-B.; Hu, M.-Q.; Wen, H.-M.; Chen, C.-N. *Dalton Trans.* **2014**, *43* (44), 16737–16744.
(130) Liu, J.; Lin, W.; Chen, Y.; Leng, J.; Guo, F.; Tong, M. *Inorg. Chem.* **2013**, *52* (1), 457–463.
(131) Koroteev, P. S.; Efimov, N. N.; Ilyukhin, A. B.; Dobrokhotova, Z. V.; Novotortsev, V. M. *Inorganica Chim. Acta* **2014**, *418*, 157–162.
(132) Bag, P.; Chakraborty, A.; Rogez, G.; Chandrasekhar, V. *Inorg. Chem.* **2013**, *53* (Iii), 6524−6533.
(133) Tziotzi, T. G.; Kalofolias, D. A.; Tzimopoulos, D. I.; Siczek, M.; Lis, T.; Inglis, R.; Milios, C. J. *Dalt. Trans.* **2015**, *44* (13), 6082–6088.
(134) Li, X.-L.; Min, F.-Y.; Wang, C.; Lin, S.-Y.; Liu, Z.; Tang, J. *Dalt. Trans.* **2015**, *44* (7), 3430–3438.

(135) Sun, L.; Chen, H.; Ma, C.; Chen, C. *Dalt. Trans.* **2015**, *44* (48), 20964–20971.
(136) Wang, H.-S.; Yang, F.-J.; Long, Q.-Q.; Huang, Z.-Y.; Chen, W.; Pan, Z.-Q.; Song, Y. *Dalt. Trans.* **2016**, *45* (45), 18221–18228.
(137) Lin, P. H.; Tsui, E. Y.; Habib, F.; Murugesu, M.; Agapie, T. *Inorg. Chem.* **2016**, *55* (12), 6095–6099.
(138) Chen, H.; Ma, C.-B.; Hu, M.-Q.; Wen, H.-M.; Cui, H.-H.; Liu, J.-Y.; Song, X.-W.; Chen, C.-N. *Dalton Trans.* **2013**, *42* (14), 4908–4914.
(139) Zaleski, C. M.; Depperman, E. C.; Kampf, J. W.; Kirk, M. L.; Pecoraro, V. L. *Angew. Chemie Int. Ed.* **2004**, *43* (30), 3912–3914.
(140) Zaleski, C. M.; Kampf, J. W.; Mallah, T.; Kirk, M. L.; Pecoraro, V. L. *Inorg. Chem.* **2007**, *46* (6), 1954–1956.
(141) Cao, F.; Wang, S.; Li, D.; Zeng, S.; Niu, M.; Song, Y.; Dou, J. *Inorg. Chem.* **2013**, *52*, 10747–10755.
(142) Deb, A.; Boron, T. T.; Itou, M.; Sakurai, Y.; Mallah, T.; Pecoraro, V. L.; Penner-Hahn, J. E. *J. Am. Chem. Soc.* **2014**, *136* (13), 4889–4892.
(143) Qin, Y.; Gao, Q.; Chen, Y.; Liu, W.; Lin, F.; Zhang, X.; Dong, Y.; Li, Y. *J. Clust. Sci.* **2017**, *28* (3), 891–903.
(144) Dendrinou-Samara, C.; Papadopoulos, A. N.; Malamatari, D. A.; Tarushi, A.; Raptopoulou, C. P.; Terzis, A.; Samaras, E.; Kessissoglou, D. P. *J. Inorg. Biochem.* **2005**, *99* (3), 864–875.
(145) Koumousi, E. S.; Mukherjee, S.; Beavers, C. M.; Teat, S. J.; Christou, G.; Stamatatos, T. C. *Chem. Commun.* **2011**, *47* (39), 11128–11130.
(146) Cao, F.; Wei, R.-M.; Li, J.; Yang, L.; Han, Y.; Song, Y.; Dou, J.-M. *Inorg. Chem.* **2016**, *55* (12), 5914–5923.
(147) Li, Q.-W.; Liu, J.-L.; Jia, J.-H.; Chen, Y.-C.; Liu, J.; Wang, L.-F.; Tong, M.-L. *Chem. Commun.* **2015**, *51* (51), 10291–10294.
(148) Pecoraro, V. L.; Stemmler, A. J.; Gibney, B. R.; Bodwin, J. J.; Wang, H.; Kampf, J. W.; Barwinski, A. *Metallacrowns: a new class of molecular recognition agents*; John Wiley & Sons, Inc., 1997; Vol. 45.
(149) Stemmler, A. J.; Kampf, J. W.; Kirk, M. L.; Atasi, B. H.; Pecoraro, V. L. *Inorg. Chem.* **1999**, *38* (12), 2807–2817.
(150) Rinehart, J. D.; Meihaus, K. R.; Long, J. R. *J. Am. Chem. Soc.* **2010**, *132* (22), 7572–7573.
(151) Lin, P. H.; Burchell, T. J.; Clérac, R.; Murugesu, M. *Angew. Chemie - Int. Ed.* **2008**, *47* (46), 8848–8851.
(152) Lannes, A.; Luneau, D. *Inorg. Chem.* **2015**, *54* (14), 6736–6743.
(153) Woodruff, D. N.; Winpenny, R. E. P.; Layfield, R. A. *Chem. Rev.* **2013**, *113* (7), 5110–5148.
(154) Li, Q.-W.; Wan, R.-C.; Chen, Y.-C.; Liu, J.-L.; Wang, L.-F.; Jia, J.-H.; Chilton, N. F.; Tong, M.-L. *Chem. Commun.* **2016**, *52*, 13365–13368.
(155) Happ, P.; Plenk, C.; Rentschler, E. *Coord. Chem. Rev.* **2015**, *289–290* (1), 238–260.
(156) Ostrowska, M.; Fritsky, I. O.; Gumienna-Kontecka, E.; Pavlishchuk, A. V. *Coord. Chem. Rev.* **2016**, *327–328*, 304–332.
(157) Happ, P.; Rentschler, E. *Dalt. Trans.* **2014**, *43* (41), 15308–15312.
(158) Happ, P.; Sapozhnik, A.; Klanke, J.; Czaja, P.; Chernenkaya, A.; Medjanik, K.; Schuppler, S.; Nagel, P.; Merz, M.; Rentschler, E.; Elmers, H. J. *Phys. Rev. B* **2016**, *93* (17), 174404.
(159) Plenk, C.; Krause, J.; Beck, M.; Rentschler, E. *Chem. Commun.* **2015**, *51* (30), 6524–

6527.
(160) Plenk, C.; Krause, J.; Rentschler, E. *Eur. J. Inorg. Chem.* **2015**, *2015* (3), 370–374.
(161) Tarushi, A.; Hatzidimitriou, A. G.; Estrader, M.; Kessissoglou, D. P.; Tangoulis, V.; Psomas, G. *Inorg. Chem.* **2017**, *56* (12), 7048–7057.
(162) Yang, W.; Yang, H.; Yao, Q.; Zeng, S.; Li, D.; Dou, J. *Inorg. Chem. Commun.* **2017**, *82*, 16–19.
(163) Yang, H.; Cao, F.; Li, D.; Zeng, S.; Song, Y.; Dou, J. *Dalt. Trans.* **2015**, *44* (14), 6620–6629.
(164) Yang, H.; Yao, Q.-X.; Li, Y.-W.; Li, D.-C.; Dou, J.-M. *Dalt. Trans.* **2014**, *43* (45), 16986–16991.
(165) Yang, H.; Li, D.; Zeng, S.; Dou, J. *Inorg. Chem. Commun.* **2015**, *58*, 84–86.
(166) Yang, H.; Cao, F.; Li, D.; Zeng, S.; Song, Y.; Dou, J. *Chem. - A Eur. J.* **2015**, *21* (41), 14478–14485.
(167) Gschneidner, K. A.; Pecharsky, V. K. *Annu. Rev. Mater. Sci.* **2000**, *30*, 387–429.
(168) Sessoli, R. *Angew. Chemie - Int. Ed.* **2012**, *51* (1), 43–45.
(169) Feder, T. *Phys. Today* **2009**, *62* (10), 21–23.
(170) Chow, C. Y.; Guillot, R.; Riviere, E.; Kampf, J. W.; Mallah, T.; Pecoraro, V. L. *Inorg. Chem.* **2016**, In Press.
(171) Lah, M. S.; Kirk, M. L.; Hatfeild, W.; Pecoraro, V. L. *J. Chem. Soc., Chem. Commun.* **1989**, 1606–1608.
(172) Uh, H.; Petoud, S. *Comptes Rendus Chim.* **2010**, *13* (6), 668–680.
(173) Chow, C. Y.; Trivedi, E. R.; Pecoraro, V.; Zaleski, C. M. *Comments Inorg. Chem.* **2015**, *35* (4), 214–253.
(174) Martinić, I.; Eliseeva, S. V.; Nguyen, T. N.; Foucher, F.; Gosset, D.; Westall, F.; Pecoraro, V. L.; Petoud, S. *Chem. Sci.* **2017**, *8* (9), 6042–6050.
(175) Martinić, I.; Eliseeva, S. V; Nguyen, T. N.; Pecoraro, V. L.; Petoud, S. *J. Am. Chem. Soc.* **2017**, *139* (25), 8388–8391.
(176) Howat, W. J.; Wilson, B. A. *Methods* **2014**, *70* (1), 12–19.
(177) Okada, M.; Smith, N. I.; Palonpon, A. F.; Endo, H.; Kawata, S.; Sodeoka, M.; Fujita, K. *Proc. Natl. Acad. Sci.* **2012**, *109* (1), 28–32.
(178) Liu, W.; Sun, P.; Yang, L.; Wang, J.; Li, L.; Wang, J. *Microfluid. Nanofluidics* **2010**, *9* (4–5), 717–725.
(179) Majno, G.; Joris, I. *Am. J. Pathol.* **1995**, *146* (1), 3–15.
(180) Biju, S.; Gopakumar, N.; Bünzli, J.-C. G.; Scopelliti, R.; Kim, H. K.; Reddy, M. L. P. *Inorg. Chem.* **2013**, *52* (15), 8750–8758.
(181) Wartenberg, N.; Raccurt, O.; Bourgeat-Lami, E.; Imbert, D.; Mazzanti, M. *Chem. - A Eur. J.* **2013**, *19* (10), 3477–3482.
(182) Quici, S.; Cavazzini, M.; Marzanni, G.; Accorsi, G.; Armaroli, N.; Ventura, B.; Barigelletti, F. *Inorg. Chem.* **2005**, *44* (3), 529–537.
(183) Viswanathan, S.; Kovacs, Z.; Green, K. N.; Ratnakar, S. J.; Sherry, A. D. *Chem. Rev.* **2010**, *110* (5), 2960–3018.
(184) Muravyeva, M. S.; Zabrodina, G. S.; Samsonov, M. A.; Kluev, E. A.; Khrapichev, A. A.; Katkova, M. A.; Mukhina, I. V. *Polyhedron* **2016**, *114*, 165–171.
(185) Parac-Vogt, T. N.; Pacco, A.; Nockemann, P.; Laurent, S.; Muller, R. N.; Wickleder, M.; Meyer, G.; Vander Elst, L.; Binnemans, K.; Elst, L. Vander; Binnemans, K. *Chem. - A Eur. J.* **2006**, *12* (1), 204–210.

(186) Katkova, M. A.; Zabrodina, G. S.; Muravyeva, M. S.; Shavyrin, A. S.; Baranov, E. V.; Khrapichev, A. A.; Ketkov, S. Y. *Eur. J. Inorg. Chem.* **2015**, *2015* (31), 5202–5208.
(187) Solomon, I.; Bloembergen, N. *J. Chem. Phys.* **1956**, *25* (2), 261–266.
(188) Bloembergen, N.; Morgan, L. O. *J. Chem. Phys.* **1961**, *34* (3), 842–850.
(189) Bloembergen, N. *J. Chem. Phys.* **1957**, *27* (2), 572–573.
(190) DO3A = 1,4,7,10-tetraazacyclododecane-1,4,7-triacetic acid; H22IAM = N,N,N′,N′-tetrakis-(2-aminoethyl)-ethane-1,2-diamine; H(2,2)-TIAM = N,N,N′,N′-tetrakis-(4-methoxy-N1,N3-dimethyl-5-(2-thioxo-thiazolidine-3-carbonyl)-isophthalamide)-ethane-1,2-diamine; HOPO = 1-methyl-3-hydroxy-pyridin-2-one; Tsox = N-{2-{Bis-[(5-sulfo-8-hydroxyquinoline-7-carboxamido)propyl]-amino}-ethyl}-N'-(5-sulfo-8-hydroxyquinoline-7-carboxamidomethyl)-N-[(5-sulfo-8-hydroxyquinoline-7-carboxamidomethyl)propyl]-propane-1,3-diamine.

Chapter 2

Lanthanide Luminescence and Single Ion Magnetic Properties of Gallium [3.3.1] Metallacryptands

Introduction

To reiterate the significance of lanthanide ions, it is important to note that over the past few decades, significant research interest has been focused on lanthanide(III) metal ions and the compounds formed with them. The inherent nature of the valence 4f electrons leads to very interesting electronic properties, especially in terms of luminescence and magnetism. The 4f electrons are shielded by the 5s and 5p orbitals, inhibiting strongly their participation in the formation of coordination bonds.[1] As a result, the 4f electrons are only weakly affected by their coordination environment, leading to sharp, atom-like emission bands ranging from the visible to the near infrared (NIR).[1] Additionally, the lanthanide(III) ions, as emitters, boast other attractive luminescence properties such as long luminescence lifetimes in comparison to organic fluorophores (microsecond to millisecond), emission as sharp bands the wavelengths of which are not affected by experimental conditions and enhanced resistance to photobleaching.[1,2] Such properties have triggered the search for lanthanide(III)-containing compounds for applications in materials science as well as in biology for optical imaging or bioanalytical assays.[2–8] However, due to the symmetry forbidden nature of f-f transitions, most lanthanide(III) ions have extremely low molar absorption coefficients which will affect negatively the number of corresponding emitted photons.[1] To overcome this major limitation, organic chromophoric ligands have been used for the complexation and sensitization of lanthanide(III) ions by a process called the "antenna effect".[9,10] In addition, another aspect that has to be considered for the design of luminescent lanthanide(III) molecular complexes is the proximity of C-H, O-H, and N-H bonds to the lanthanide(III) ions, as their vibrational overtones may couple to Ln^{3+} excited states and quench emission through a non-radiative pathway.[11] The triplet state energy of the chromophoric ligand should also be taken into account: such considerations have led to the design of families

of ligands which either sensitize lanthanide(III) ions emitting in the visible (for example, Tb^{3+}, Dy^{3+}, Sm^{3+}, Eu^{3+}) or in the NIR (for example, Er^{3+}, Yb^{3+}, Nd^{3+}) more easily.[12,13] Only for a few complexes has one type of antenna successfully sensitized both visible and NIR lanthanide(III) emissions.[14–18]

As single-ion magnets, lanthanide(III) ions have been of interest for applications in magnetic storage, quantum computing,[19] and spintronic devices,[20] thanks to their inherent large spin and magnetic anisotropies.[21,22] These properties are due to the unquenched orbital momentum and the strong spin-orbit coupling occurring in these metal ions. As a result, significant effort has been directed to develop strategies to taking advantage of lanthanide intrinsic magnetic properties. It was shown that the control of the ligand field around lanthanide(III) ions has an important impact on their magnetic behavior. As examples, Tb^{3+} complexes formed with phthalocyanine and lanthanide(III) polyoxometallates demonstrated how the geometry of the ligand field influences the presence or absence of an easy-axis of magnetization.[23,24] Long and coworkers proposed that the ligand field will encourage an easy axis if the shapes of the lanthanide(III) orbitals are accommodated by the ligands, where the lanthanide(III) total orbital shape may be described as spherical (Gd^{3+}), oblate (Dy^{3+}, Tb^{3+}), or prolate (Er^{3+}, Yb^{3+}).[25] Ligand fields that are axially elongated promote an easy-axis for oblate ions, while equatorially expanded ligand fields promote an easy-axis for prolate ions.[25]

While there has been significant interest in lanthanide-based lumiphores, metallacrowns have only entered this exciting field within the last decade. Since their discovery in 1989,[26,27] metallacrowns, inorganic structural analogs to crown ethers, have demonstrated potential in numerous applications, including host-guest binding,[28–30] gas adsorption,[31] molecular magnetism,[32–37] and lanthanide(III)-based luminescence.[9,14,38] Metallacrowns possess a high degree of tunability based on the choice of ligand and metal, which uniquely allows for the predictable design of complexes towards a specific application.[39–43] For example, the use of closed shell cations such as gallium(III) and zinc(II) ions has led to the creation and characterization of lanthanide(III) MCs with record-breaking luminescence properties in molecular materials.[9,14] Metallacrowns have also established a rich history in molecular magnetism, both as 3d-4f bimetallic and as lanthanide complexes. Examination of these systems have provided significant insights into the magnetic properties of 3d transition metals in association with lanthanide(III) ions. While the metallacrown analogy has been a powerful

synthetic paradigm for structure prediction, there are examples where serendipity is involved,[44] leading to unexpected structure types,[45,46] which can demonstrate interesting properties. Within this chapter, a new class of metallacrown-like structures are reported, [$LnGa_6(H_2shi)(Hshi)(shi)_7(C_5H_5N)$] ($LnGa_6C_{68}H_{44}N_{10}O_{27}$, shi = salicylhydroximate; Ln = Pr, Nd, Sm, Eu, Gd, Tb, Dy, Ho, Er, Yb) in which the MC complexes resemble more the structures of cryptands rather than those of crown ethers while maintaining metallacrown-like [Metal-N-O] binding motifs. While this is not the first example of work describing a metallacryptate,[46,47] it is the first example of such achievement with lanthanide(III)-based luminescence and magnetic slow relaxation obtained using the same scaffold. This compound has promise for interesting optical and magnetic properties, thanks to a larger ration of antenna to lanthanide ions compared to other known gallium MCs, and has a nine-coordinate lanthanide coordination geometry which is constant across the Ln series. This work will appear in *Chemistry, A European Journal* in the near future.

Experimental

Synthetic Materials. Gallium(III) nitrate hydrate (Sigma Aldrich, 99%), praseodymium(III) nitrate hexahydrate (Sigma Aldrich, 99.9%), neodymium(III) nitrate hexahydrate (Sigma Aldrich, 99.9%), samarium(III) nitrate hexahydrate (Sigma Aldrich, 99.9%), europium(III) nitrate hexahydrate (Sigma Aldrich, 99.9%), gadolinium(III) nitrate hexahydrate (Alfa, Aesar, 99.9%), terbium(III) nitrate pentahydrate (Sigma Aldrich, 99.9%), dysprosium(III) nitrate pentahydrate (Alfa Aesar, 99.9%), holmium(III) nitrate pentahydrate(Sigma Aldrich, 99.9%), thulium(III) nitrate hydrate (Sigma Aldrich, 99.9%), erbium(III) nitrate pentahydrate (Sigma Aldrich, 99.9%), ytterbium nitrate (Sigma Aldrich, 99.9%), salicylhydroxamic acid (Alfa Aesar, 99%), methanol (Fischer, ACS grade), pyridine (Fisher, ACS grade), and triethylamine (Acros, 99%). All reagents were used as received without further purification.

General synthetic procedure for Ln⊂{[3.3.1] 20-$MC_{Ga^{III}N(shi)}$-7 } complexes. The lanthanide(III) nitrate hydrate (0.167 mmol) and gallium(III) nitrate hydrate (1 mmol) salts were mixed in 10 mL of methanol, resulting in the formation of a clear and colorless solution. Separately, salicylhydroxamic acid (1.5 mmol) and triethylamine (4.5 mmol) were mixed in 10 mL of

methanol, followed by an addition of 10 mL of pyridine, resulting in a clear and colorless solution. The solutions were mixed, resulting in the observation of a white precipitate and colorless gas evolved briefly. After several minutes the solution returns to a clear and colorless state and was stirred for one hour, then filtered. Diffusion of diethyl ether into the filtrate afforded pure powder or needle product in periods of time from one to three weeks. Isolated product was dried under vacuum pressure of approximately 100 mTorr.

[PrGa$_6$(H$_2$shi)(Hshi)(shi)$_7$(HNEt$_3$)$_3$(C$_5$H$_5$N)]·C$_5$H$_5$N·4H$_2$O, **Pr[3.3.1]**. The synthetic yield was 28% based on praseodymium nitrate hexahydrate. Elemental analysis of *PrGa$_6$C$_{91}$H$_{105}$N$_{14}$O$_{31}$* [fw = 2450.15 g/mol] found % (calculated): C, 44.98 (44.61); H, 4.28 (4.32); N, 8.22 (8.00). ESI-MS, calculated *PrGa$_6$C$_{63}$H$_{40}$N$_9$O$_{27}$* $[M+H]^{2-}$: 957.33, found 956.33.

[NdGa$_6$(H$_2$shi)(Hshi)(shi)$_7$(HNEt$_3$)$_3$(C$_5$H$_5$N)]·C$_5$H$_5$N·7H$_2$O, **Nd[3.3.1]**. The synthetic yield was 2% based on neodymium nitrate hexahydrate. Elemental analysis of *NdGa$_6$C$_{91}$H$_{111}$N$_{14}$O$_{34}$* [fw = 2507.53 g/mol] found % (calculated): C, 43.59 (43.59); H, 4.30 (4.46); N, 7.87 (7.82). ESI-MS, calculated *NdGa$_6$C$_{63}$H$_{40}$N$_9$O$_{27}$* $[M+H]^{2-}$: 956.83, found 958.83.

[SmGa$_6$(H$_2$shi)(Hshi)(shi)$_7$(HNEt$_3$)$_3$(C$_5$H$_5$N)]·C$_5$H$_5$N·6H$_2$O, **Sm[3.3.1]**. The synthetic yield was 33% based on samarium nitrate hexahydrate. Elemental analysis of *SmGa$_6$C$_{91}$H$_{109}$N$_{14}$O$_{33}$* [fw = 2495.64 g/mol] found % (calculated): C, 43.81 (43.80); H, 4.32 (4.40); N, 8.00 (7.86). ESI-MS, calculated *SmGa$_6$C$_{63}$H$_{40}$N$_9$O$_{27}$* $[M+H]^{2-}$: 961.84, found 961.84.

[EuGa$_6$(H$_2$shi)(Hshi)(shi)$_7$(HNEt$_3$)$_3$(C$_5$H$_5$N)]·C$_5$H$_5$N·3H$_2$O, **Eu[3.3.1]**. The synthetic yield was 12% based on europium nitrate hexahydrate. Elemental analysis of *EuGa$_6$C$_{91}$H$_{103}$N$_{14}$O$_{30}$* [fw = 2443.19 g/mol] found % (calculated): C, 44.62 (44.74); H, 4.18 (4.25); N, 8.17 (8.03). ESI-MS, calculated *EuGa$_6$C$_{63}$H$_{40}$N$_9$O$_{27}$* $[M+H]^{2-}$: 962.84, found 962.34.

[GdGa$_6$(H$_2$shi)(Hshi)(shi)$_7$(HNEt$_3$)$_3$(C$_5$H$_5$N)]·C$_5$H$_5$N·5H$_2$O, **Gd[3.3.1]**. The synthetic yield was 46% based on gadolinium nitrate hexahydrate. Elemental analysis of *GdGa$_6$C$_{91}$H$_{107}$N$_{14}$O$_{32}$* [fw=2484.51 g/mol] found % (calculated): C, 43.98 (43.91); H, 4.44 (4.39); N, 8.27 (7.89). ESI-MS, calculated *GdGa$_6$C$_{63}$H$_{40}$N$_9$O$_{27}$* $[M+H]^{2-}$: 964.84, found 964.84.

[TbGa$_6$(H$_2$shi)(Hshi)(shi)$_7$(HNEt$_3$)$_3$(C$_5$H$_5$N)]·C$_5$H$_5$N·H$_2$O, **Tb[3.3.1]**. The synthetic yield was 36% based on terbium nitrate pentahydrate. Elemental analysis of *TbGa$_6$C$_{91}$H$_{99}$N$_{14}$O$_{28}$* [fw = 2414.13 g/mol] found % (calculated): C, 45.43 (45.28); H, 4.23 (4.13); N, 8.19 (8.12). ESI-MS, calculated *TbGa$_6$C$_{63}$H$_{40}$N$_9$O$_{27}$* $[M+H]^{2-}$: 966.34, found 966.34.

[DyGa$_6$(H$_2$shi)(Hshi)(shi)$_7$(HNEt$_3$)$_3$(C$_5$H$_5$N)]·6H$_2$O, **Dy[3.3.1]**. The synthetic yield was 24% based on dysprosium nitrate pentahydrate. Elemental analysis of *DyGa$_6$C$_{86}$H$_{104}$N$_{13}$O$_{33}$* [fw = 2428.67 g/mol] found % (calculated): C, 42.48 (42.53); H, 4.21 (4.32); N. 7.60 (7.50). ESI-MS, calculated *DyGa$_6$C$_{63}$H$_{40}$N$_9$O$_{27}$* $[M+H]^{2-}$: 966.84, found 967.85.

[HoGa$_6$(H$_2$shi)(Hshi)(shi)$_7$(HNEt$_3$)$_3$(C$_5$H$_5$N)]·C$_5$H$_5$N·8H$_2$O, **Er[3.3.1]**. The synthetic yield was 12% based on holmium nitrate pentahydrate. Elemental analysis of *HoGa$_6$C$_{91}$H$_{113}$N$_{14}$O$_{35}$* [fw = 2546.24 g/mol] found % (calculated): C, 42.63 (42.93); H, 4.38 (4.47); N, 7.64 (7.70). ESI-MS, calculated *HoGa$_6$C$_{63}$H$_{40}$N$_9$O$_{27}$* $[M+H]^{2-}$: 968.34, found 969.35.

[ErGa$_6$(H$_2$shi)(Hshi)(shi)$_7$(HNEt$_3$)$_3$(C$_5$H$_5$N)]·C$_5$H$_5$N·6H$_2$O, **Er[3.3.1]**. The synthetic yield was 10% based on erbium nitrate pentahydrate. Elemental analysis of *ErGa$_6$C$_{91}$H$_{109}$N$_{14}$O$_{33}$* [fw = 2512.53 g/mol] found % (calculated): C, 43.39 (43.50); H, 4.36 (4.37); N, 7.78 (7.80). ESI-MS, calculated *ErGa$_6$C$_{63}$H$_{40}$N$_9$O$_{27}$* $[M+H]^{2-}$: 969.34., found 969.85.

[TmGa$_6$(H$_2$shi)(Hshi)(shi)$_7$(HNEt$_3$)$_3$(C$_5$H$_5$N)]·C$_5$H$_5$N·4H$_2$O, **Tm[3.3.1]**. The synthetic yield was -36% based on thulium nitrate pentahydrate. Elemental analysis of *TmGa$_6$C$_{91}$H$_{105}$N$_{14}$O$_{31}$* [fw = 2495.64 g/mol] found % (calculated): C, 44.12 (44.10); H, 4.30 (4.27); N, 7.95 (7.91). ESI-MS, calculated *TmGa$_6$C$_{63}$H$_{40}$N$_9$O$_{27}$* $[M+H]^{2-}$: 970.35, found 971.35.

[YbGa$_6$(H$_2$shi)(Hshi)(shi)$_7$(HNEt$_3$)$_3$(C$_5$H$_5$N)]·C$_5$H$_5$N·8H$_2$O, **Yb[3.3.1]**. The synthetic yield was 24% based on ytterbium nitrate hexahydrate. Elemental analysis of *YbGa$_6$C$_{91}$H$_{113}$N$_{14}$O$_{35}$* [fw = 2554.36 g/mol] found % (calculated): C, 42.85 (42.79); H, 4.18 (4.46); N, 7.71 (7.68). ESI-MS, calculated *YbGa$_6$C$_{63}$H$_{40}$N$_9$O$_{27}$* $[M+H]^{2-}$: 972.85, found 972.85.

Physical Methods. ESI-QTOF MS was performed on an Agilent 6520 Accurate-Mass Q-TOF LC/MS quadrupole time of flight mass spectrometer in negative ion mode with a fragmentation voltage of 180 V. Samples were prepared by dissolving approximately 1 mg of compound in 1 mL of methanol, then diluting 20 µL of this first solution into another 1 mL of methanol. Samples were directly injected using a syringe (without the HPLC or autosampler). Data were processed with the Agilent MassHunter Qualitative Analysis software. Elemental analyses were performed on a Carlo Erba 1108 or a PerkinElmer 2400 elemental analyzer by Atlantic Microlabs, Inc.

Powder X-ray Diffraction. Samples were ground using a mortar and pestle and then loaded onto glass plates such that the surface of the sample was as flat as possible. Data were collected using a PANalytical Emyprean Series 2 XRD with a 1.54243 Å Cu anode source and an operational tension of 45 kV and current of 40 mA. The collection range was 3 to 15^{o} in 2θ with step size of 0.016711^{o} and a scan speed of 0.2 seconds per step.

X-ray Crystallography. Single crystal X-ray crystallographic data for **Tb[3.3.1]** were collected at 85(2) K on an AFC10K Saturn 944+ CCD-based X-ray diffractometer equipped with a Micromax007HF Cu-target microfocus rotating anode (λ = 1.54187 Å), operated at 1200 W (40 kV, 30 mA). The data were processed using CrystalClear 2.0[48] and corrected for absorption. The structure was solved and refined using the SHELXTL (v. 6.12) software package.[49] Non-hydrogen atoms were refined anisotropically, hydrogen atoms were isotropic and placed in idealized positions. Highly disordered solvent water and methanol were treated using the SQUEEZE function in PLATON.

Table 2.1 Crystallographic Data for Tb[3.3.1]

Chemical Formula	$TbGa_6C_{93.5}H_{99.5}N_{14.5}O_{27}$
Formula Weight	2435.61 g/mol
Crystal System, Space Group	Triclinic, $P\bar{1}$ (No. 2)
T	85(2) K
a	16.4342(3) Å
b	17.2269(3) Å
c	21.6881(4) Å
α	75.6312(16)°
β	70.7189(18)°
γ	89.4616(14)°
Volume	5596.7(2) $Å^3$
λ	1.54184 Å
ρ_{calc}	1.445 mg/m^3
Z	2
μ	5.254 mm^{-1}
F(000)	2458
θ range	2.235° to 73.947°
Limiting Indicies	$-20 < h < 20$
	$-21 < k < 21$
	$-26 < l < 24$
Reflections collected/unique	179289/22055
Completeness to θ	98.7%
No. of Data/Restraints/Params	22055/636/1493
GooF on F^2	1.051
$^aR_1$	0.0472 [I>2σ(I)]; 0.0485 (all data)
$^bwR_2$	0.1406 [I>2σ(I)]; 0.1426 (all data)
Largest Diff. Peak, Hole	1.422 e/$Å^3$; -1.687 e/$Å^3$

^{a} $R_1 = \Sigma(||F_o|-|F_c||)/\Sigma|F_o|$ ^{b} $wR_2 = [\Sigma[w(F_o^2 - F_c^2)^2]/\Sigma[w(F_o)^2]]^{1/2}$; $w = 1/[\sigma^2(F_o^2) + (mp)^2 + np]$; $p = [\max(F_o^2,0) + 2F_c^2]/3$ (*m* and *n* are constants); $\sigma = [\Sigma[w(F_o^2 - F_c^2)^2/(n-p)]^{1/2}$

Photophysical Measurements. Luminescence data were collected and interpreted on samples in the solid state placed in 2.4 mm i.d. quartz capillaries by Dr. Svetlana Eliseeva at the Centre National de la Recherche Scientifique, Orleans, France. Emission and excitation spectra were measured on a custom-designed Horiba Scientific Fluorolog 3 spectrofluorimeter equipped with either a visible photomultiplier tube (PMT) (220-850 nm, R928P; Hamamatsu), a NIR solid-state InGaAs detector cooled to 77 K (800-1600 nm, DSS-IGA020L; Horiba Scientific), or a NIR PMT (950-1650 nm, H10330-75; Hamamatsu). Excitation and emission spectra were corrected for the instrumental functions. Luminescence lifetimes were determined under excitation at 355 nm provided by a Nd:YAG laser (YG 980; Quantel). Signals were detected in the visible or NIR ranges with the help of a Hamamatsu R928P or H10330-75 PMTs, respectively. The output signals obtained from the detectors were fed into a 500 MHz bandpass digital oscilloscope (TDS 754C; Tektronix), transferred to a PC for data processing with the program Origin 8®. Luminescence lifetimes are averages of at least three independent measurements. Quantum yields were determined with a Fluorolog 3 spectrofluorimeter based on an absolute method with the help of an integration sphere (Model G8, GMP SA, Renens, Switzerland). Each sample was measured several times under comparable experimental conditions, varying the position of the sample. Estimated experimental error for quantum yield determination is ~10 %.

Absorption Spectroscopy. Solution-state UV-vis spectra were collected on samples dissolved in methanol (approx. 300 μM), which was then dilutr using a Cary 100Bio UV-Vis spectrophotometer in absorbance mode. Solid-state spectra were recorded using an Agilent-Cary 5000 spectrophotometer equipped with a Praying Mantis diffuse reflectance attachment in reflectance mode. Samples were milled in $BaSO_4$ (1:9 sample:$BaSO_4$ w/w), and a baseline of 100% $BaSO_4$ was used for correction. Reflectance was converted to absorption using the Kubelka-Munk function.

Magnetic Characterization. AC magnetic susceptibility was collected using a Quantum Design MPMS SQUID magnetometer. Samples were prepared in gel capsules and suspended in eicosane (1:2 sample:eicosane w/w). DC magnetic susceptibility was corrected for the capsule, eicosane and sample holder, as well as for diamagnetic contributions using Pascal's constants. Data were processed using Microsoft Excel and SigmaPlot 10 software packages. The temperature and

frequency dependent AC out of phase susceptibility, Arrhenius plot and Cole-Cole plot were fit using least squares methods with SigmaPlot 10.

Results

Synthesis and Structural Analysis.

The reaction between stoichiometric amounts of H_3shi with lanthanide(III) and gallium(III) nitrate salts in presence of triethylamine results in the formation of complexes possessing the following composition, $[LnGa_6(H_2shi)(Hshi)(shi)_7(C_5H_5N)]$ (shi^{3-} = salicylhydroximate; Ln = Pr, Nd, Sm, Eu, Gd, Tb, Dy, Ho, Er, Yb), **Ln[3.3.1]** (Scheme 2.1). X-ray crystallographic data were obtained on single crystals of the terbium(III) analogue for the purpose of structural analysis (Figure 2.3). Powder X-ray diffraction show that these complexes are isostructural within preferential orientation effects and varying degrees of crystallinity (Figure A1, Appendix A). The central lanthanide(III) ion is nine coordinated, with a geometry around it that most closely resembles a tricapped trigonal prism (Figure 2.1). Four of the gallium(III) ions (Ga2, Ga4, Ga5, and Ga6) are located in distorted octahedral environments with propeller conformations; Ga2 and Ga4 adopts a Λ chirality while Ga5 and Ga6 adopt a Δ chirality (Figure 2.2). This type of alternating absolute stereochemical isomerism has been reported for other metallacrowns.[50–52] The remaining gallium(III) ions (Ga1 and Ga3) are five coordinated, with a geometry closer to a square pyramid (Figure 2.2) based on Addison tau values (τ = 0.2525 and 0.2697, respectively).[53]

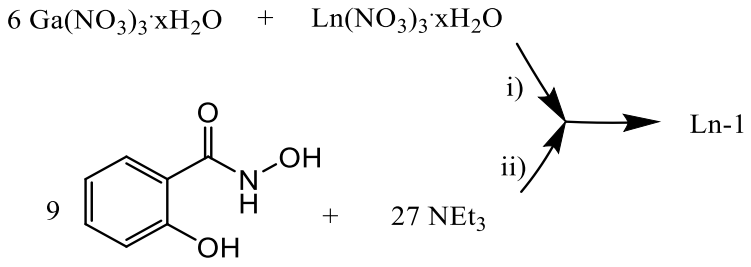

Scheme 2.1 Synthesis of Ln Ga(III) [3.3.1] metallacryptate complexes. i) MeOH ii) MeOH/pyridine.

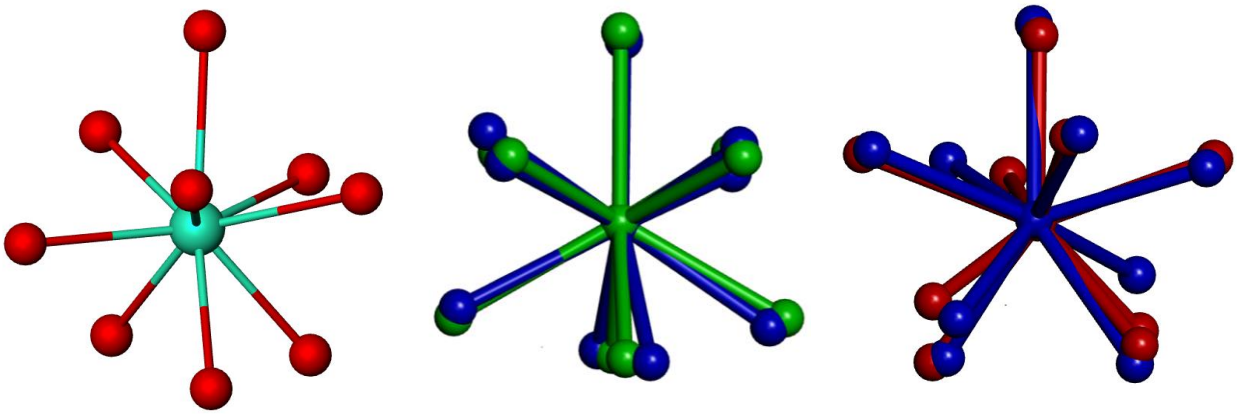

Figure 2.1. First coordination sphere of Tb1 in **Tb[3.3.1]** (left), **Tb[3.3.1]** (blue) overlaid with an ideal tricapped trigonal prism (green) (center), **Tb[3.3.1]** (blue) overlaid with an ideal monocapped square antiprism (red) (right).

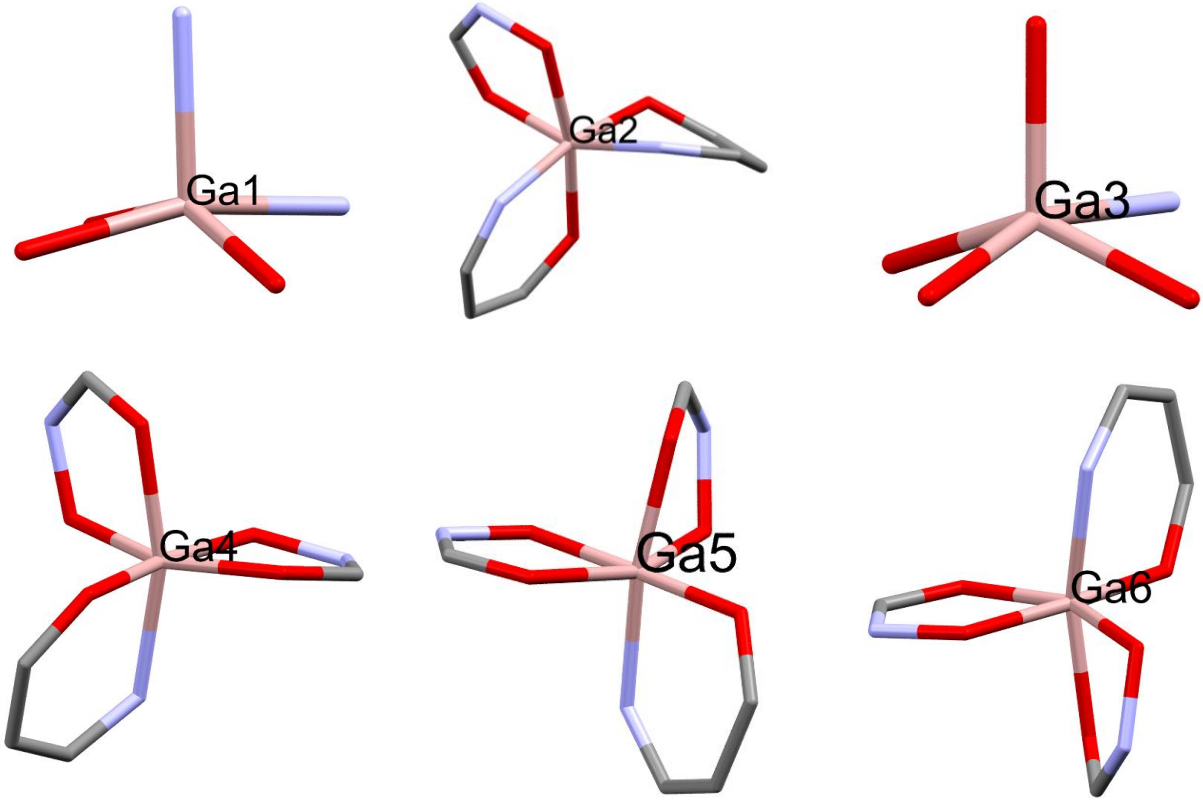

Figure 2.2. Gallium(III) coordination geometries in **Tb[3.3.1]**.

Table 2.3. Structural Parameters for a Tricapped Trigonal Prismatically Coordinated Terbium.					
Atom	Avg. Bond Length	Avg. O-Tb-O capping ligand Angle	Avg. Prism torsion angle	Ln-O_{prism} MP Distance 1	Ln-O_{prism} MP Distance 2
Tb1	2.435	119.96	12.22	1.789	1.670

Table 2.4. Structural Parameters for Square Pyramidally Coordinated Gallium Ions						
Atom	Avg. Bond Length	Avg. Adjacent Basal bond angle	Avg. Apical to Basal Bond Angle	Large Opposite Basal Bond angle	Small Opposite Basal Bond Angle	Addison's Tau Value[37]
Ga1	1.938	87.63	102.39	161.40	146.92	0.2413
Ga3	1.921	87.15	103.74	160.88	143.03	0.2975

Table 2.5. Structural Parameters for Octahedrally Coordinated Gallium Ions						
Atom	Avg Bond length	Avg Equitorial angle	Avg Axial to equatorial angle	Axial bond angle	Avg. Torsion angle on Pseudo-S_6	Chirality
Ga2	1.999	90.64	90.27	170.26	54.60	Λ
Ga4	1.986	90.61	90.35	171.57	60.74	Λ
Ga5	1.975	90.29	90.01	178.33	64.45	Δ
Ga6	1.981	90.47	90.17	175.23	55.70	Δ

Structurally similar to simpler metallacrowns, the described complexes also follow a binding motif which use [M-N-O] repeating units. However, **Ln[3.3.1]** complexes are not analogous to crown ethers but more closely resemble the structure of cryptands; for example, they can be compared to 1,10-diaza-2,5,8,12,15,18,20-heptaoxabicylco[8.8.2]icosane (Figure 2.1d). On the basis of the cryptand nomenclature, the **Ln[3.3.1]** complexes may be described as a Ga(III)[3.3.1]metallacryptand, where Ga2 and Ga5 are considered to be analogous to the nitrogen atoms in a cryptand. With the adaptation of metallacryptand nomenclature defined by Saalfrank, *et. al.*[44] the shorthand is $[Tb\subset\{Ga_6(shi)_7\}(Hshi)(H_2shi)(C_5H_5N)](C_6H_{16}N)_3$. Inclusion of metallacrown style nomenclature gives the name $[Tb\subset\{[3.3.1.]20\text{-}MC_{Ga^{III}N(shi)}$-

7}(Hshi)(H_2shi)(C_5H_5N)]($C_6H_{16}N)_3$. The marriage of these nomenclatures describes the Tb(III) encapsulating Ga(III)[3.3.1]metallacryptand structure very well in shorthand notation, which is useful for future structures of similar composition.

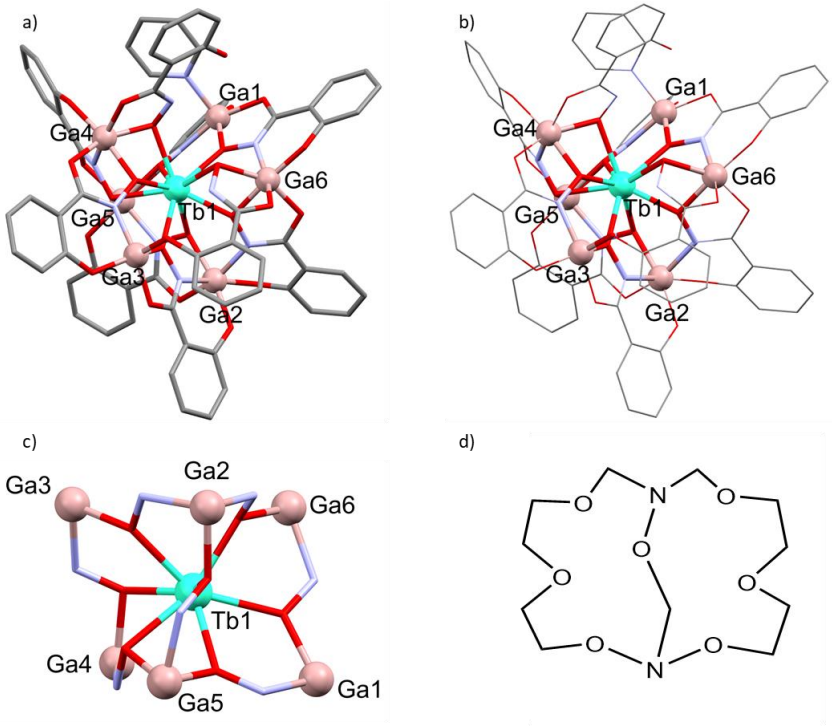

Figure 2.3 a) Representation of the structure of **Tb[3.3.1]** obtained through a crystallographic analysis on single crystals; b) highlight of the Ga-N-O motif; c) the metallacryptate core; d) complementary cryptand as a comparison.

The central metal is the terbium(III) ion, while the six gallium(III) and seven of the shi^{3-} ligands make up the metallacryptand. There are twenty atoms in the [Ga-N-O] motif, seven of which are oxygens that are distributed across three "arms" in a 3:3:1 ratio. The remaining two H_3shi ligands bridge gallium(III) ions to the terbium(III). One H_2shi^- is singly deprotonated and bridges Ga4 to Tb1 in a "standing up" conformation while the other is doubly deprotonated and bridges Ga3 and Ga6 to the Tb1 in a "laying down" conformation (Figure 2.3). There is a coordinated pyridine molecule on Ga1. Three triethylammonium cations provide the charge balance. Elemental analysis results and consistent $[M+H]^{2-}$ peaks observed in ESI-MS spectra

across the compounds prove the stoichiometry and reproducibility of the metallacryptate and confirm that it does not change across the lanthanide series (Appendix 1, Figure A2).

Photophysical Properties

Ligand-centered photophysical properties.

Absorption and diffuse reflectance spectra of the ligand H_3shi and **Ln[3.3.1]** complexes are given in Figure 2.4 below. In methanol solution, the ligand H_3shi exhibit several bands due to $\pi \rightarrow \pi^*$ transitions with the lowest energy one centered at ~300 nm ($\varepsilon = 3.9\times10^3$ M^{-1} cm^{-1}). The formation of **Ln[3.3.1]** metallacryptate leads to a red shift of these absorption bands and to an increase of the molar absorption coefficients which is proportional to the number of H_3shi ligands present in the molecule ($\varepsilon_{\mathbf{Gd\text{-}1}} = 4.5\times10^4$ M^{-1} cm^{-1} at 310 nm). The energy position of the singlet state was estimated from the edge of absorption spectra of **Ln[3.3.1]** complexes and found to be located at energies of 29410 cm^{-1} (340 nm). Diffuse reflectance spectra recorded on solid state samples of **Ln[3.3.1]** exhibit similar broad bands in the range of 200-380 nm except for the **Eu[3.3.1]** metallacryptate where an extension of the band towards lower energies (up to 470 nm) was observed. In addition, in the reflectance spectra of all **Ln[3.3.1]** except for **Eu[3.3.1]** and **Tb[3.3.1]**, narrow bands in the visible and the NIR ranges were observed which correspond to the f-f transitions belonging to the respective lanthanide(III) ions.

To estimate positions of the triplet state energies in **Ln[3.3.1]** complexes, the phosphorescence spectrum of the **Gd[3.3.1]** complex was measured in the solid state at 77 K. Upon excitation at 350 nm with a flash Xenon lamp and application of a 100 µs delay after the excitation flash, **Gd[3.3.1]** revealed the presence of a broad-band emission in the range 430-750 nm (Figure 2.5, black trace). A gaussian deconvolution of the phosphorescence spectrum (Figure 2.3, colored traces) allowed estimation of the position of the triplet state (T_1) as a 0-0 transition, 21600 cm^{-1} (463 nm).

a)

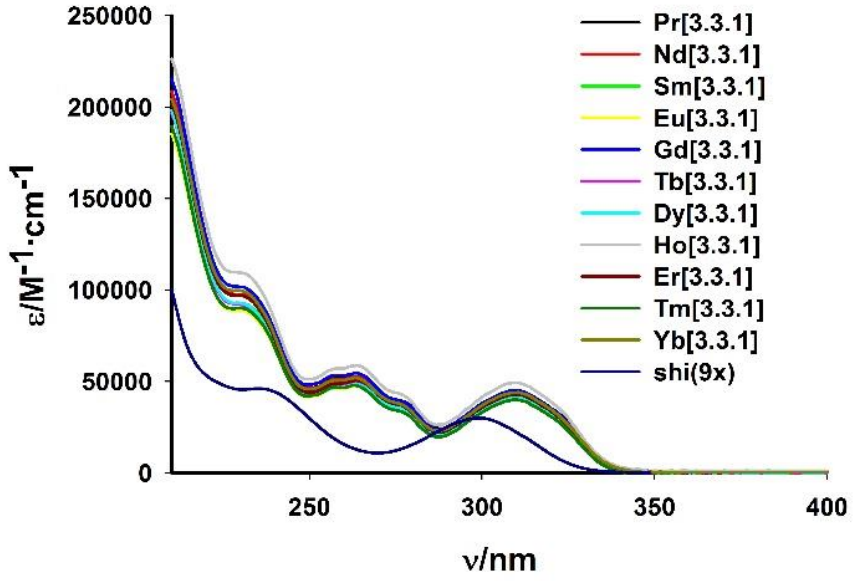

b) c)

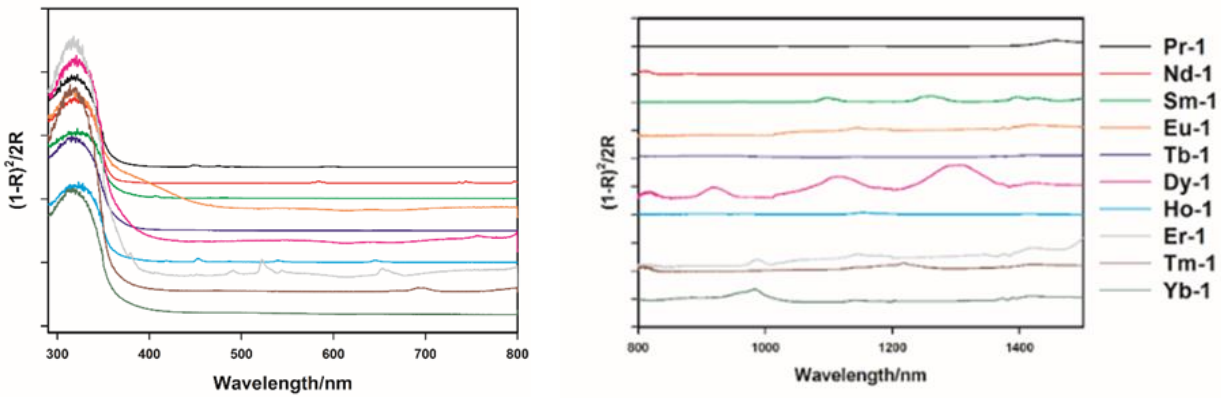

Figure 2.4 a)UV-vis absorption spectra of 1-10 μM **Ln[3.3.1]** metallacryptates and H_3shi ligand (multiplied by 9 to match the number of ligands present in the complex) in methanol solution at room temperature; b) Solid state diffuse reflectance spectra of **Ln[3.3.1]** complexes in the UV-vis region; c) near-infrared region.

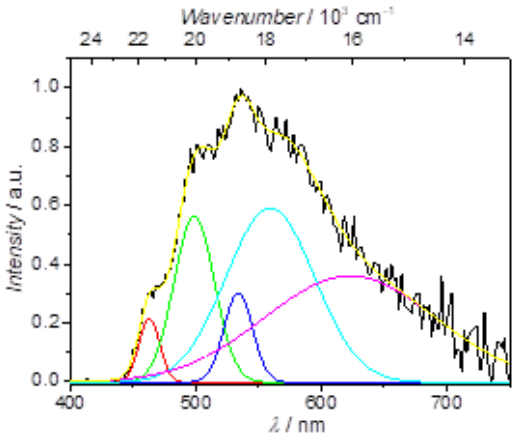

Figure 2.5 Phosphorescence spectrum (black trace) recorded for **Gd[3.3.1]** at 77K in the solid state upon excitation at 350 nm and applying a 100 µs delay after the excitation flash. Colored traces represent the individual Gaussian spectra obtained from the deconvolution of the experimental phosphorescence spectrum.

Lanthanide-centered photophysical properties.

The examination of the photophysical properties of **Ln[3.3.1]** complexes in the solid state at room temperature demonstrated that a wide range of lanthanide(III) ions are sensitized by the gallium(III) [3.3.1] metallacryptate (Figure 2.6). The complexes containing Pr^{3+}, Nd^{3+}, Sm^{3+}, Tb^{3+}, Ho^{3+}, Er^{3+}, and Yb^{3+} all demonstrate characteristic lanthanide(III)-based sharp emission bands upon excitation into the ligand-centered levels in the range 300-350 nm. Excitation spectra of **Ln[3.3.1]** collected upon monitoring the emission of Ln^{3+} at 1025 (Pr^{3+}), 1067 (Nd^{3+}), 600 (Sm^{3+}), 545 (Tb^{3+}), 875 (Ho^{3+}), 1525 (Er^{3+}) and 980 (Yb^{3+}) nm revealed the presence of broad bands in the UV spectral domain (up to 400 nm). The similarity between the shapes of these excitation spectra measured on MCs containing lanthanide cations of different natures and their widths at half size reflects that the energy absorbed is transferred through the electronic structure of the chromophoric ligands, providing an "antenna effect". Several excitation spectra contain additional sharper features corresponding to the energy being loaded directly into the corresponding lanthanide cation in the molecules through f-f transitions (except **Tb[3.3.1]** and **Yb[3.3.1]** metallacryptates, Figure 2.6). Quantitative photophysical parameters, quantum yields upon ligand excitation and luminescence lifetimes of **Ln[3.3.1]** in the solid state are summarized in Table 2.6.

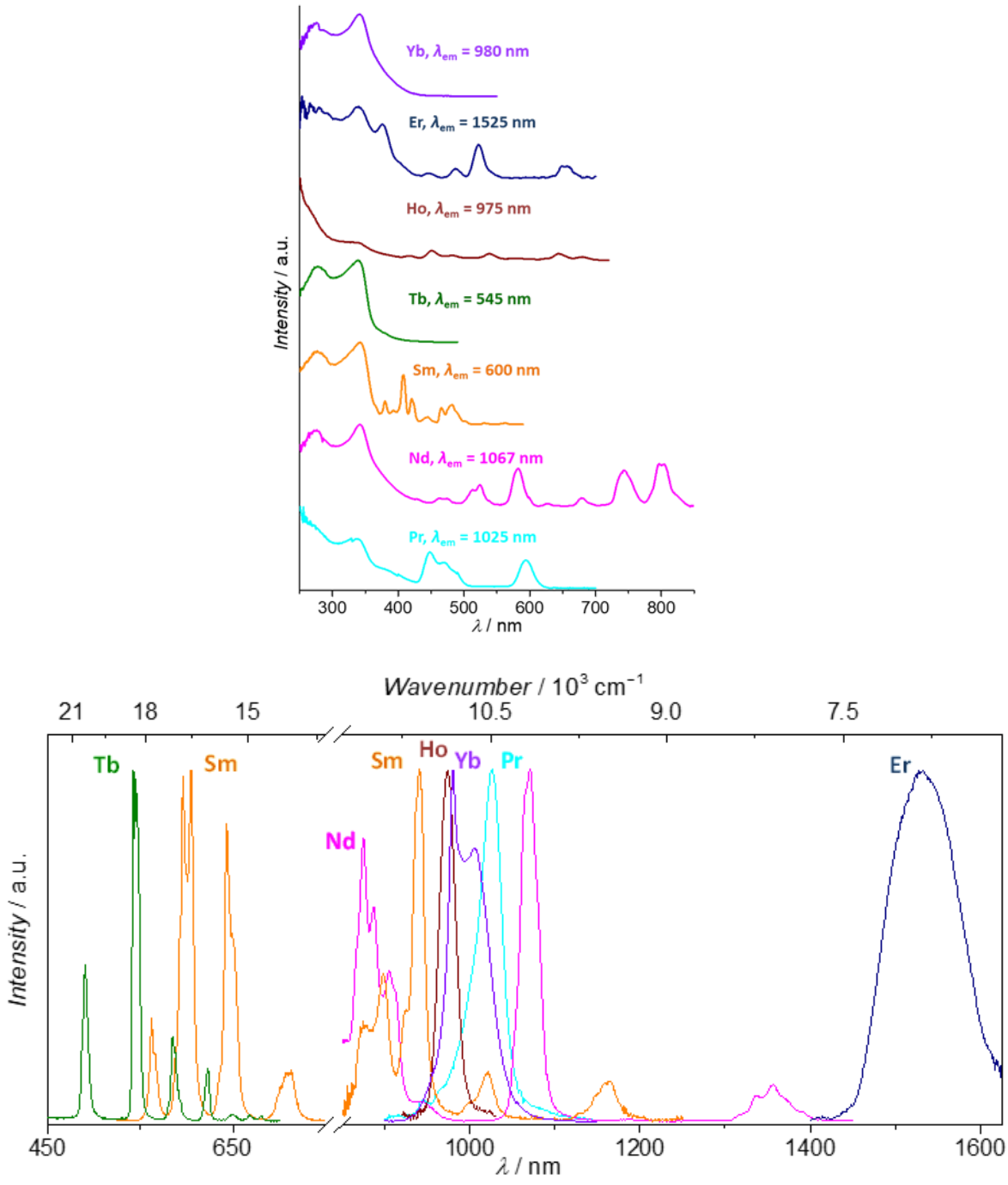

Figure 2.6 (top) Corrected and normalized excitation spectra of **Ln[3.3.1]** complexes in the solid state recorded upon monitoring the main transitions (λ_{em}) of the corresponding Ln(III) ions at room temperature; (bottom) Corrected and normalized emission spectra of **Ln[3.3.1]** complexes measured in the solid state upon excitation at 350 nm at room temperature.

Table 2.6 Photophysical parameters of **Ln[3.3.1]** in the solid state.[a]

Ln[3.3.1][a]	ΔE /cm^{-1} [b]	τ_{obs} / µs [c]	Q^{L}_{Ln} / % [d]
Pr	4760	0.063(1)	$3.7(2)\cdot10^{-3}$
Nd	10140	0.71(1)	0.171(5)
Sm	3700	70(1)	1.70(9)[e]
Tb	1200	20.7(5) : 71% 4.54(6) : 29%	0.189(3)
Ho	6100	0.037(1)	$1.1(2)\cdot10^{-3}$
Er	14900	0.905(8)	$7.1(2)\cdot10^{-3}$
Yb	11300	7.26(2)	0.65(3)

[a] Collected at room temperature, 2σ values are given between parentheses, relative errors: τ_{obs}, ±2%; Q^{L}_{Ln}, ±10%.

[b] $\Delta E(T_1\text{-}E^{Ln})$ is the energy difference between Ln^{3+} emissive state and the ligand-centered triplet state energy T_1 = 21 600 cm^{-1}: $E^{Pr}(^1D_2)$ = 16,840 cm^{-1}, $E^{Nd}(^4F_{3/2})$ = 11,460 cm^{-1}, $E^{Sm}(^4G_{5/2})$ = 17,900 cm^{-1}, $E^{Tb}(^4D_4)$ = 20,400 cm^{-1}, $E^{Ho}(^5F_5)$ = 15,500 cm^{-1}, $E^{Er}(^4I_{13/2})$ = 6,700 cm^{-1}, and $E^{Yb}(^2F_{5/2})$ = 10,300 cm^{-1}.[54,55]

[c] λ_{ex} = 355 nm.

[d]λ_{ex} = 350 nm.

[e]Total quantum yield. Partial Q^{L}_{Ln} in the visible range (500-750 nm) equal to 1.64(9) % and in the NIR range (850-1250 nm) to 0.055(2) %.

Magnetic Behavior.

Magnetic characterization of the Ga(III)[3.3.1]metallacryptate complexes revealed slow relaxation from AC susceptibility experiments for **Nd[3.3.1]**, **Dy[3.3.1]**, and **Yb[3.3.1]**; however, only **Dy[3.3.1]** displays an out of phase susceptibility without the presence of an applied DC field (Figure 2.7). This indicates that only **Dy[3.3.1]** shows enhanced slow relaxation due to a quenching effect of quantum tunneling of magnetization (QTM), and an Orbach relaxation. **Nd[3.3.1]** and **Yb[3.3.1]** show no signs of slow relaxation in absence of an applied field, and do not change the maximum frequency as a function of DC field strength (Figure 2.8). Based on these observations, **Dy[3.3.1]** was characterized more rigorously as a single-ion magnet.

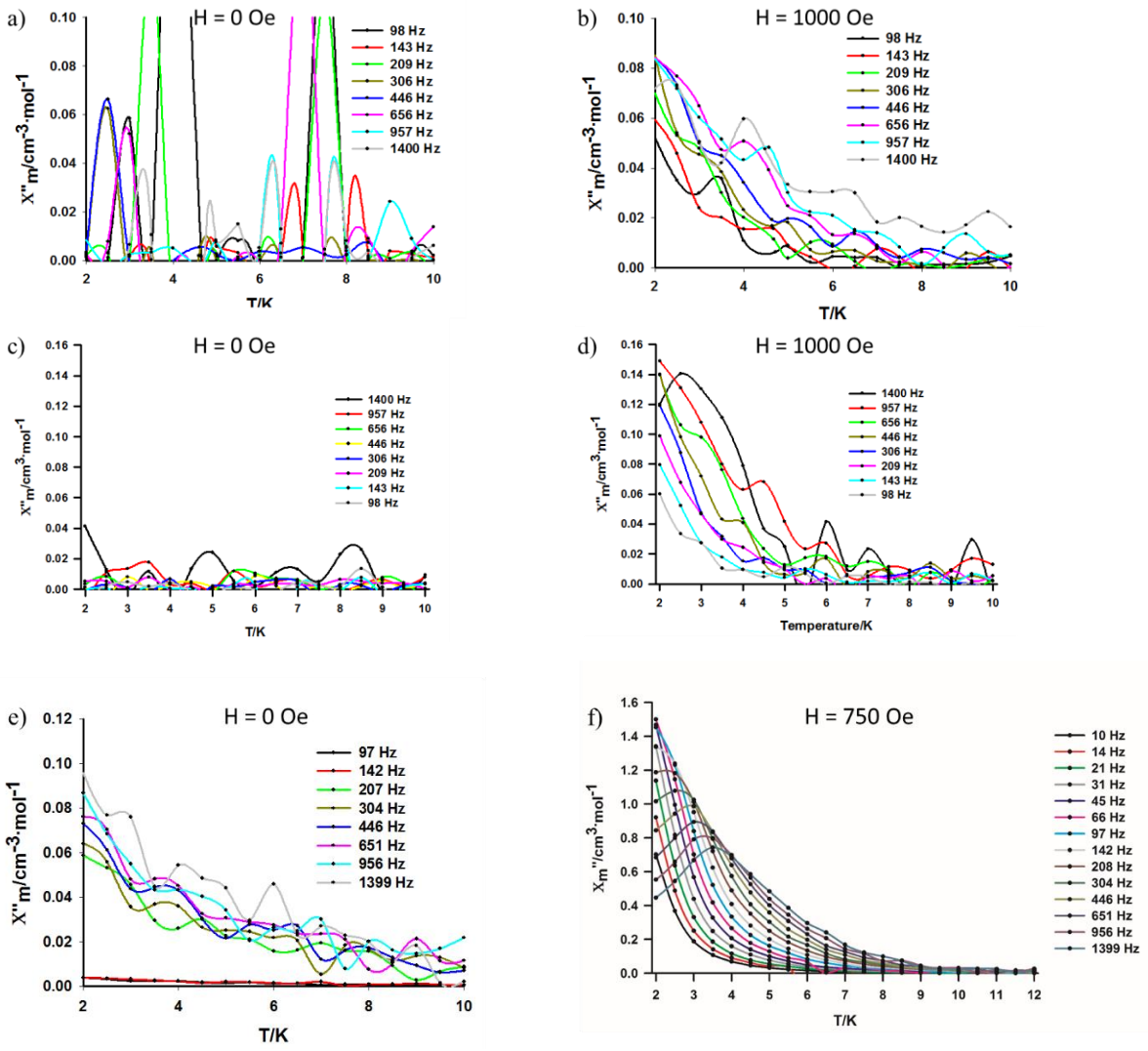

Figure 2.7 AC out of phase susceptibility measurements of **Ln[3.3.1]** using a 3 Oe drive field. a) **Nd[3.3.1]** with zero applied field and b) applied field of 1000 Oe; c) **Yb[3.3.1]** with zero applied field and d) applied field of 1000 Oe; e) **Dy[3.3.1]** with zero applied field and f) applied field of 750 Oe.

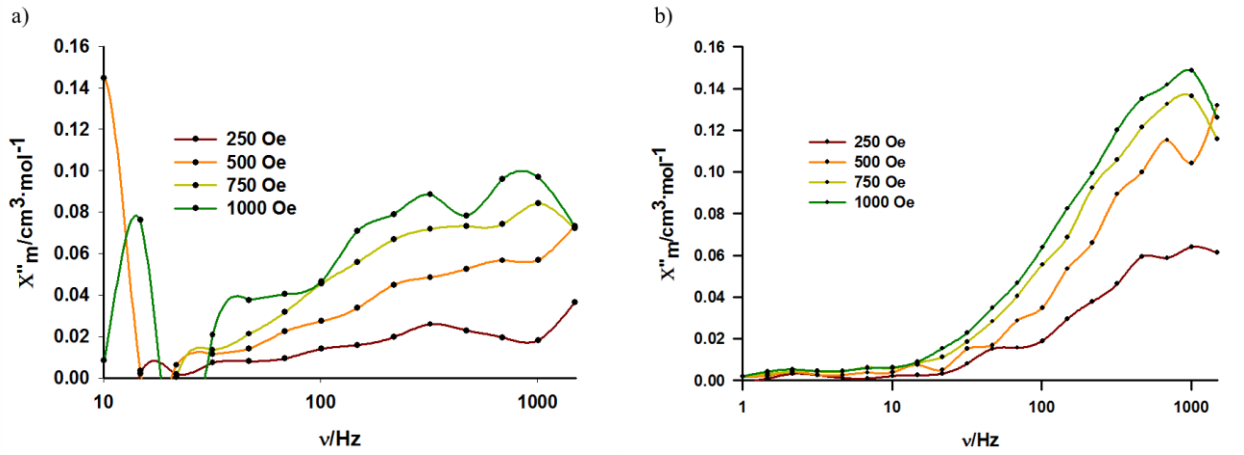

Figure 2.8 Variable frequency AC out of phase behavior of a) **Nd[3.3.1]** and b) **Yb[3.3.1]** in various applied DC fields at 2K.

Temperature dependent DC $\chi_m T$ was measured using a field of 2000 Oe from 2 K to 300 K (Figure 2.9), reaching a value of 13.48 $cm^{3}{\cdot}K{\cdot}mol^{-1}$ at 300 K, which is lower than theoretical values for a single non-interacting Dy^{3+} ion (14.17 $cm^{3}{\cdot}K{\cdot}mol^{-1}$, $^{6}H_{15/2}$, S = 5/2, L = 5, g = 4/3, J = 15/2). This result may be explained by long range antiferromagnetic interaction.[21] The $\chi_m T$ decreases steadily with cooling to a minimal value of 9.18 $cm^{3}{\cdot}K{\cdot}mol^{-1}$ at 2 K, which is likely due to a depopulation of ground J sublevels or to an intermolecular antiferromagnetic interaction.[56–58] Isothermal magnetization at 2 K from 0 T to 7 T (Figure 2.9) increases to a saturation value of 5.55 Nβ, which is lower than theoretical values observed for a single Dy^{3+} ion (10 Nβ), likely due to the presence of low lying excited states and crystal field influence.[59,60]

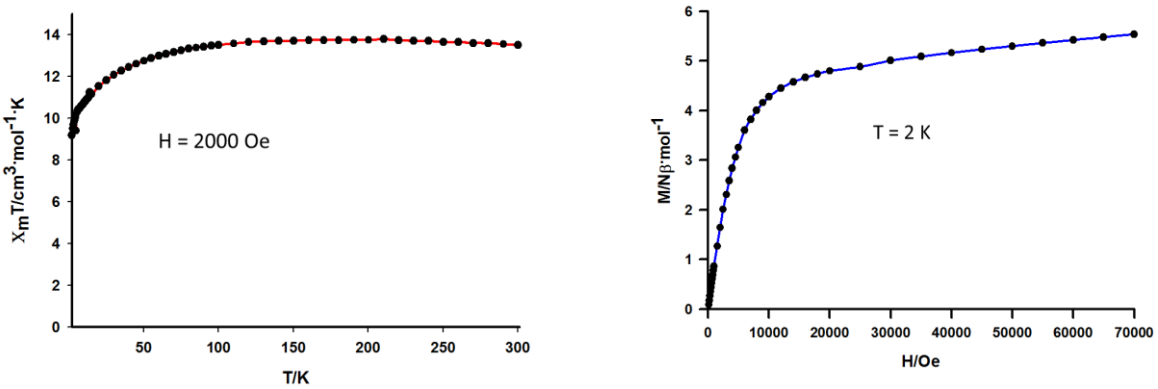

Figure 2.9 DC magnetic susceptibility of **Dy[3.3.1]** in a 2000 Oe applied field, the red line is a guide for the eye (left); Isothermal magnetization of **Dy[3.3.1]** at 2K, the blue line is a guide for the eye (right).

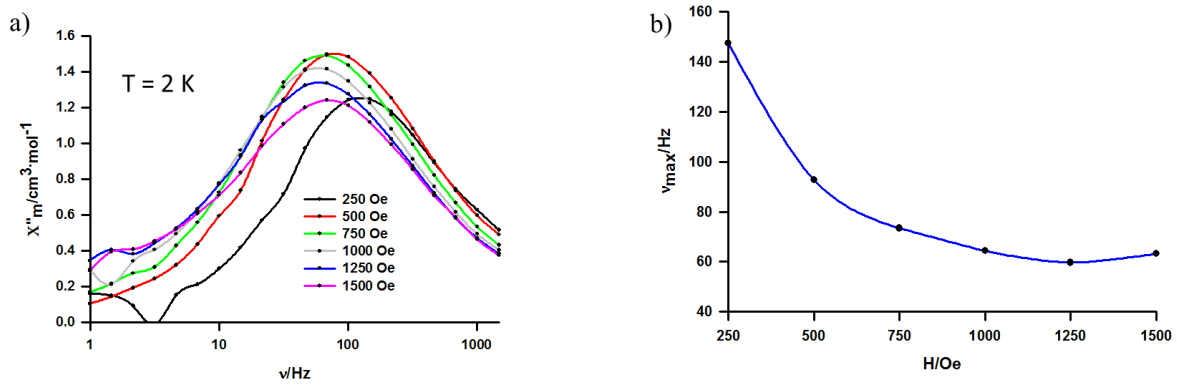

Figure 2.10 a) Variable frequency AC out of phase behavior of **Dy-1** in various applied fields at 2 K; b) plot of ν_{max} minimization as a function of applied field H. ν_{max} was determined from fitting a logarithmic peak function $\chi m\,'' = a \cdot e\text{^}((-0.5 \cdot (ln(\nu/\nu\_max\,)/2)\text{^}2\,)\,)$.

Variable temperature and variable frequency AC susceptibility was collected with an AC field of 3 Oe, and applied DC fields of 0 Oe and 750 Oe to suppress the QTM (Figure 2.7). The small 750 Oe applied field was selected since this field showed the lowest frequency maximum (ν_{max}) while still maintaining higher χ''_m signal (Figure 2.10). Choosing the lowest ν_{max} is desirable since this means that the point at which the signal is most out of phase is also seen with a slower oscillation and thus has a higher barrier. In a 0 Oe applied field, the χ''_m increases slightly at temperatures below 10 K, but no peak maxima are present, a prevalent observation of lanthanide SIMs.[23,58,61–63] However, under the 750 Oe applied field, the χ''_m signal rises significantly between 7-9 K and peak maxima were observable due to the suppression of QTM (Figure 2.11). Fitting the temperature dependent data from 208 Hz to 1399 Hz to a Lorenzian function ($\chi''_m = a/(1 + ((T\text{-}T_0)/b)^2)$) allowed for the generation of an Arrhenius plot (Figure 2.12a), which was fit to the Arrhenius Law ($\ln(1/\tau) = \ln(1/\tau_0) - U_{eff}/k_B T$). This operation resulted in evidence for a pre-exponential term of $\tau_0 = 3.6 \cdot 10^{-6}$ s^{-1} and an effective barrier (U_{eff}) of 12.7 K, confirming field enhanced magnetic slow relaxation.

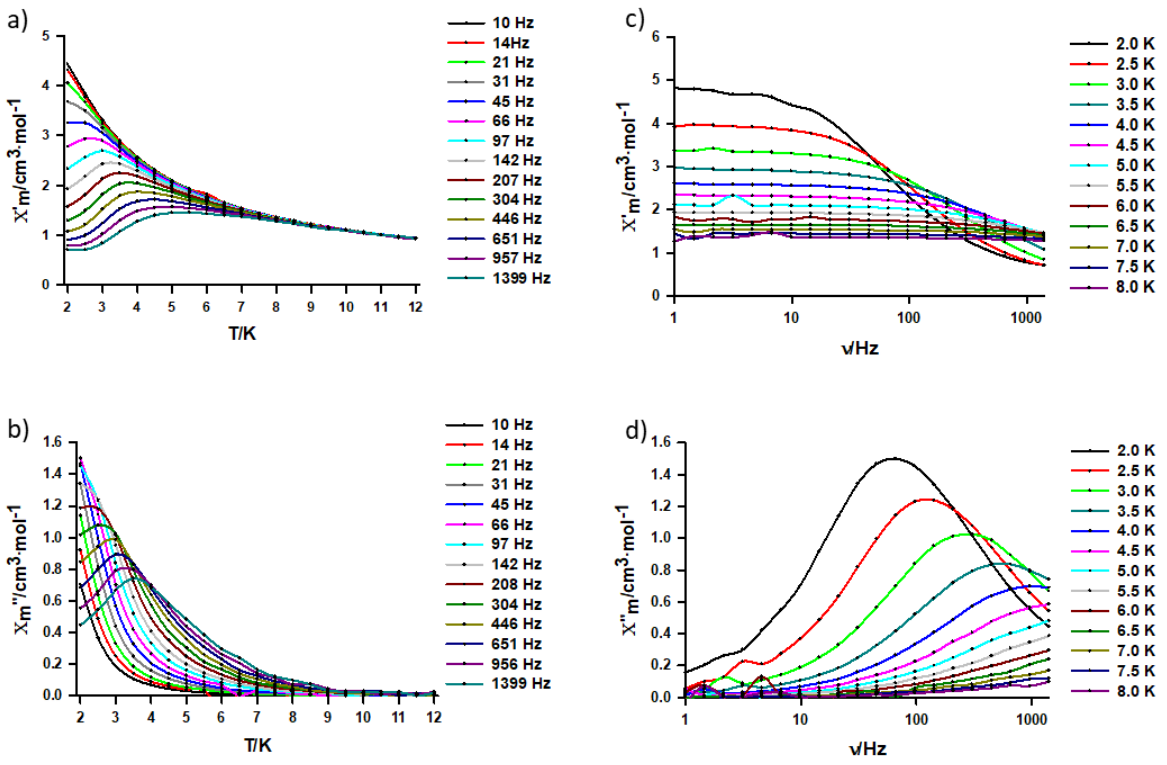

Figure 2.11 AC susceptibility of **Dy[3.3.1]**; a) in phase temperature dependent curves; b) out of phase temperature dependent curves; c) in phase frequency dependent curves; d) out of phase frequency dependent curves, under an applied field of 750 Oe. Solid lines are plotted as a guide for the eye.

To probe the molecular environment of the **Dy[3.3.1]** complex, Cole-Cole plots (Figure 2.12b) from 2 K to 4 K were fitted using equations 2.1 and 2.2.[64]

$$\chi_m'(\omega) = \chi s + \frac{(\chi_T - \chi_S)[1+(\omega\tau)^{(1-\alpha)}\sin\left(\frac{\alpha\pi}{2}\right)]}{1+2(\omega\tau)^{(1-\alpha)}\sin\left(\frac{\alpha\pi}{2}\right)+(\omega\tau)^{2(1-\alpha)}} \quad (2.1)$$

$$\chi_m''(\omega) = \frac{(\chi_T - \chi_S)[(\omega\tau)^{(1-\alpha)}\cos\left(\frac{\alpha\pi}{2}\right)]}{1+2(\omega\tau)^{(1-\alpha)}\sin\left(\frac{\alpha\pi}{2}\right)+(\omega\tau)^{2(1-\alpha)}} \quad (2.2)$$

Where χ_S is the adiabatic susceptibility, χ_T is the isothermal susceptibility, ω is the angular frequency, τ is the magnetic relaxation time, and α is a parameter constrained between 0 and 1 which describes the relative range of distributions. Fits gave a range of α = 0.2041 - 0.2790 (Table 2.7), which suggests that there is a small distribution of molecular environments. The semicircular shape indicates that there is one barrier of relaxation, and the symmetrical shape indicates that only one species is present.

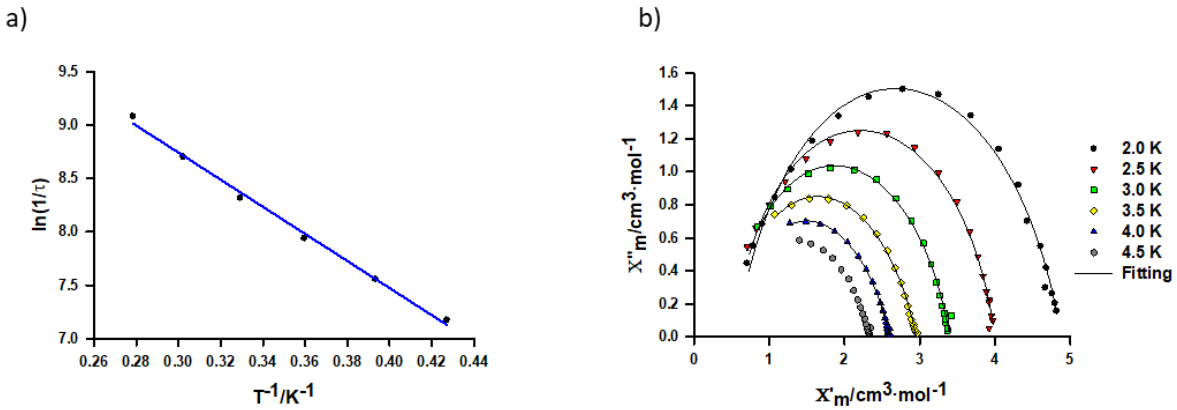

Figure 2.12 a) Arrhenius plot of **Dy[3.3.1]**, derived from temperature dependent χ''_m, the blue line represents the best fit to the Arrhenius law; b) Cole-Cole plot of **Dy[3.3.1]**, black line represents fit using Eqs. 2.1 and 2.2.

Table 2.7 Cole-Cole fitting for the parameter α

T/K	α (X_m')	α (X_m")
2.0	0.2247	0.2375
2.5	0.2041	0.2316
3.0	0.2265	0.2393
3.5	0.2661	0.2634
4.0	0.2790	0.2823

Discussion

Structural Analysis

One of the advantages of metallacrown complexes is the large degree of structural tunability that these species may tolerate. For example, the classic 12-MC-4 structure type has been synthesized using several trivalent metals of different natures, with varying bridging anions and with the ligand shi^{3-} or one of its derivatives.[14,41,65] Because of the nature of the self-assembly process used for the synthesis of MCs many meta-stable intermediates can be isolated upon modifications of the experimental conditions such as changing solvents or varying counter

anions: These new species correspond to alternative, unpredicted structures or superstructures related to the classic MC archetype. Often, once these "serendipitous" molecules have been isolated, they can be prepared in a controlled way as they possess remarkable stability. One of these variants was reported by Lah *et. al.* and described as a "metallacryptate" where three sodium(I) ions were bound to two 12-$MC_{Ga^{III}N(shi)}$-4 in a sandwich-like fashion, four μ_2-hydroxide ions connecting the gallium(III) ions across the MC interface (Figure 2.13).[46] The coordination environments around Ga^{3+} ions are square pyramidal with the hydroximate ligands located in the plane and a bridging μ_2-hydroxide in the apical position. The central sodium ion is eight-coordinated with a square prismatic geometry while the two remaining sodium ions on the structure are seven-coordinated with a monocapped octahedral geometry. While this structure was initially described as a "metallacryptate", in retrospect, it is more reminiscent of an isolated clathrate unit of cubic structure. This system was also the first example of gallium(III) in a metallacrown assembly. However, the combination of gallium(III) and sodium(I) did not offer the opportunity for this complex to demonstrate molecular magnetism or other functional properties. Later, Dendrinou-Samara *et. al.* reported another cage-like molecule that can be described as a metallacryptate based on manganese(II/III) cations, where the core of manganese(III) oxide/methoxide was encapsulated inside of the metallacryptand arms (Figure 2.13).[47] This structure was formed *in situ* by the conversion of 2,2'-dipyridylketonoxime into 2,2'-dipyridylketonediolate ($pdol^{2-}$) where four Mn(II), six Mn(III), 12 $pdol^{2-}$ and six azide ions made up the metallacryptand "arms". This structure can be deconstructed into the 16 Mn core and a 6-armed adamantoid metallacryptate. As shown in Figure 2.13, the topology of this molecule is close to an heteroadamantane. This complex was characterized as a single molecule magnet. Subsequently, the perchlorate salt was isolated, which exhibited a slightly higher level of symmetry enhancing the SMM behavior. Fitting the frequency-dependent out-of-phase magnetic susceptibility to the Arrhenius equation yielded an effective energy barrier to magnetization relaxation, U_{eff}, of 11.5 cm^{-1} for the azide complex and of 25.1 cm^{-1} for the perchlorate complex.[66]

In 2011, Jankolovits, *et. al.* created another interesting type of structure using zinc(II) and picolinic hydroximate ($picHA^{2-}$), which form an "encapsulated sandwich" topology that has similarities with $Na_3[12\text{-}MC_{Ga^{III}N(shi)}\text{-}4]_2(OH)_4^-$ (Figure 2.13).[38,46] Here, two 12-MC-4 units encapsulate a lanthanide(III) cation instead of a sodium(I). The whole complex is stabilized by a

larger 24-MC-8 ring, rather than by four μ_2-hydoxides. The central lanthanide(III) is eight-coordinated in a square antiprism geometry while the zinc atoms are five-coordinated in a square pyramidal geometry in the 12-MC-4s and octahedral within the 24-MC-8. This complex was not only fascinating from a structural point of view of supramolecular complexation, but it was the first example of a metallacrown complex to demonstrate a sensitization of characteristic NIR luminescence of ytterbium(III) and neodymium(III). Moreover, recent work has shown that lanthanide(III)-zinc(II) MCs with an "encapsulated sandwich" topology assembled using pyrazine hydroximate ($pyzHA^{2-}$) are valuable agents for simultaneous cell fixation and staining and for NIR imaging of necrotic cells.[67,68]

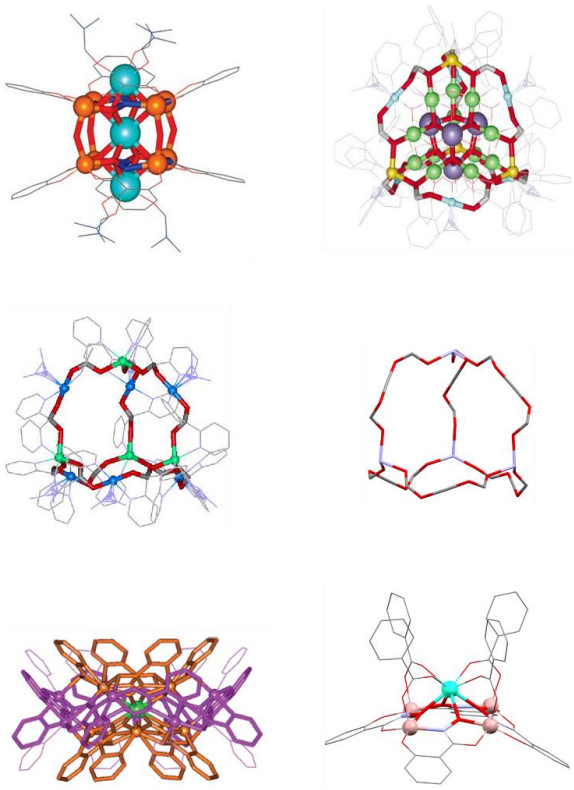

Figure 2.13 Previously described metallacrowns and metallacryptates. Upper left:[46] $Na_3[12\text{-}MC_{Ga^{III}N(shi)}\text{-}4]_2(OH)_4^-$. Upper right,[47] $[Mn^{II}_4Mn^{III}_{22}(pdol)_{12}(\mu_2\text{-}OCH_3)_{12}(\mu_3\text{-}O)_{10}(\mu_4\text{-}O)_6(N_3)_6]^+$. Center left: Representation of the metallacryptand topology with four capping Mn^{II} ions and six linking Mn^{III} cations with the MnO core removed for clarity. Center right: A representation of the metallacryptand is depicted as a hetero adamantane with propeller Mn^{II} as nitrogen, $pdol^{2-}$ oxygens retained as oxygen atoms and all other atoms as carbon. Bottom left:[38] $Tb^{III}[12\text{-}MC\text{-}4]_2[24\text{-}MC\text{-}8]^{3+}$ Bottom right:[14] Crystallagraphic representation of $Dy(benzoate)_4[12\text{-}MC_{Ga^{III}N(shi)}\text{-}4]$.

The new gallium[3.3.1] metallacryptand demonstrates an entirely different type of structure for the class of cage like metallacrowns. The metallacryptand binds a lanthanide(III) in a nine-coordinate tricapped trigonal prism environment (Figure 2.1), utilizing only the shi^{3-} ligands to form the structure. Unlike the previously reported gallium(III) 12-MC-4 structures from Lah *et. al*. and Chow *et. al.*[14,46] (Figure 2.13) this structure utilizes six gallium(III) in four octahedral sites which are in propeller conformations as well as two which are in square pyramidal coordination geometries. If one were to follow the path of Ga5-Ga4-Ga3-Ga2-Ga6-Ga1 through the Ga-N-O motif the geometries observed are Δ-octahedral, Λ-octahedral, square pyramidal, Λ-octahedral, Δ-octahedral, and square pyramidal. This kind of "alternating chirality" has been observed in other metallacrown complexes such as the ruffled manganese 15-MC-5 reported by Kessissoglou *et. al.*[50] This nine-coordinate lanthanide(III) geometry is also rarely observed in metallacrown-type structures, offering a unique opportunity to probe the possibility for single ion magnetism of lanthanide(III) ions in this environment. Because of the inclusion of nine shi^{3-} ligands into the lanthanide(III) coordination environment, the UV-Vis absorption due to the shi^{3-} π-π* transition should be larger than for the previously reported luminescent $Ln^{III}(benzoate)_4[12\text{-}MC_{Ga^{III}N(shi)}\text{-}4]$, that only contains four shi^{3-} chromophores.[14] As the optically silent Ga(III) ion was used in the metallacycle, and shi^{3-} is known to sensitize a large number of lanthanide(III) ions, this compound showed a strong potential for the sensitization of lanthanide(III) ions providing attractive emission properties.[14]

Photophysical Properties

The energy positions of the ligand-centered excited states, in particular singlet (S_1) and triplet (T_1), with respect to the Ln^{3+} resonance accepting levels, are crucial for the design of luminescent lanthanide(III)-based complexes and materials, controlling rates of different energy transfer steps and as a consequence global photophysical parameters. In particular, the triplet state is considered to be one of the major feeding levels for Ln^{3+} while $\Delta E(S_1\text{-}T_1)$ is affecting the efficiency of intersystem crossing. Thus, the energy of the S_1 state in **Ln[3.3.1]** complexes was found to be located at 29,410 cm^{-1}, while that of T_1 at 21,600 cm^{-1} giving an energy difference of 7,810 cm^{-1}. The latter value is greater than 5,000 cm^{-1}, which is regarded as a benchmark for efficient intersystem crossing. In general, the T_1 level is located higher in energy than the main emissive states of Ln^{3+} which range from 21,350 cm^{-1} for Tm^{3+} to 6,700 cm^{-1} for Er^{3+}.[54,55]

Compared to the previously reported Ga^{3+}/Ln^{3+} metallacrowns, the core of which is also assembled from H_3shi ligands, singlet and triplet states in **Ln[3.3.1]** metallacryptates are lower in energy by 440 and 570 cm^{-1}, respectively.[14] This difference is small but can be significantly detrimental to the sensitization of some Ln^{3+}, like Tm^{3+}, Dy^{3+} and Tb^{3+} with emissive energy levels located too close to the T_1 energy level that increases the probability of back energy transfer processes from Ln^{3+} levels to those of the ligands: $^1G_4$ (Tm^{3+}, 21,350 cm^{-1}), $^4F_{9/2}$ (Dy^{3+}, 21,100 cm^{-1}) and $^5D_4$ (Tb^{3+}, 20,400 cm^{-1}).[54,55] Indeed, characteristic Tm^{3+} and Dy^{3+} emissions were not observed in **Ln[3.3.1]** metallacryptates while these were detected in Ga^{3+}/Ln^{3+} metallacrowns.[14] Back energy transfer processes are also likely responsible for the modest luminescence performance of the Tb^{3+} in metallacryptates in which the energy difference $\Delta E(T_1$-$^5D_4)$ is only 1200 cm^{-1}, in comparison with the Ga^{3+}/Tb^{3+} metallacrown (quantum yield values: 0.189(3) *vs*. 34.7(1) %, τ_{obs}: 19.4(5) *vs*. 1080(10) µs; Table 2.8).

Table 2.8 Comparison of photophysical parameters of Gd^{3+}/Ln^{3+} MCs([Ln[12-MC-4])[14] and metallacryptates **Ln[3.3.1]**

Lanthanide Complex	ε/$M^{-1}\cdot cm^{-1}$ [b]	Q_{Ln}^{L}/%	τ_{obs} / µs
Sm[12-MC-4]	21910	2.91(8)[c]	148(1)
Sm[3.3.1]	42184	1.70(9)[c]	70(1)
Tb[12-MC-4]	22517	34.7(1)	1080(10)
Tb[3.3.1]	40733	0.189(3)	20.7(5) : 71% 4.54(6) : 29%
Ho[12-MC-4]	23246	$2.0(2)\cdot10^{-3}$	0.029(1)
Ho[3.3.1]	49267	$1.1(2)\cdot10^{-3}$	0.037(1)
Er[12-MC-4]	20133	0.044(1)	6.75(3)
Er[3.3.1]	42879	$7.1(2)\cdot10^{-3}$	0.905(8)
Yb[12-MC-4]	21934	5.88(2)	55.7(3)
Yb[3.3.1]	43975	0.65(3)	7.26(2)

[a] Taken from Ref.[14]
[b] Molar absorption coefficients are given at 310nm for both Ln[12-MC-4] and Ln[3.3.1].
[c] Total quantum yield of visible and NIR emissions.

Among other studied lanthanide(III) ions, intense characteristic emission in the NIR range resulting from Pr^{3+}, Nd^{3+}, Ho^{3+}, Er^{3+}, and Yb^{3+}, as well as Sm^{3+} in both visible and NIR ranges, could be observed for **Ln[3.3.1]** metallacryptates upon excitation into the ligand-centered levels in the range 300-350 nm demonstrating the presence of the antenna effect. On the other hand, Eu^{3+} emission was not detected in **Eu[3.3.1]** which is most probably caused by a quenching effect induced by the formation of ligand-to-metal charge transfer (LMCT) states. The

presence of a LMCT is reflected by the broadening and the red-shifting of the diffuse reflectance band in **Eu[3.3.1]** complexes compared to these of the other **Ln[3.3.1]** formed with lanthanide cations that cannot be reduced to the 2+ oxidation state (Figure 2.4b,c). In addition, the broad-band character observed on the excitation and absorption/reflectance spectra of **Ln[3.3.1]** complexes (Ln^{3+} = Pr, Nd, Sm, Tb, Ho, Er, Yb) suggests that the electronic structure of the chromophores is used for the conversion of the energy and that the metallacryptate scaffold can act as efficient sensitizer of characteristic Ln^{3+} emission (Figure 2.6 and 2.4b,c). The presence of sharper bands corresponding to the f-f transitions in the excitation spectra of **Ln[3.3.1]** metallacryptates reflects the additional possibility of direct excitation of some of the lanthanide(III) ions (Figure 2.6). Quantitative photophysical parameters (absolute quantum yields (Q_{Ln}^{L}) and luminescence lifetimes (τ_{obs}) (Table 2.6)) are significantly lower for **Ln[3.3.1]** (Ln^{3+} = Nd, Sm, Tb, Ho, Er, Yb) metallacryptates compared to the corresponding Ln^{III}(benzoate)$_4$[12-MC-4]metallacrowns previously reported (Table 2.8). Such behavior can be most probably attributed to the proximity of N-H oscillators (~3.2-3.5 Å) on the protonated H_3shi ligands that bridge Ln^{3+} to the metallacryptate scaffold, vibrational overtones of which may couple with the excited states of the lanthanide(III) ions leading to their depopulation.

Magnetic Slow Relaxation

The magnetic properties of the Ln(III)Ga(III)[3.3.1] metallacryptates demonstrate a slow magnetization relaxation for **Dy[3.3.1]**, **Nd[3.3.1]** and **Yb[3.3.1]**. The **Dy[3.3.1]** analog was distinct in behavior, given that it was the only ion to demonstrate an out-of-phase signal both with and without the presence of an applied field; and the change of maximum when studied under various applied field strengths (Figure 2.7 and 2.10). The **Yb[3.3.1]** and **Nd[3.3.1]** analogs were the only ones able to show an out-of-phase signal when under the effect of an applied field, and maintenance of a constant maximum when the field strength is varied (Figure 2.7 and 2.9). In the work of Lannes and Luneau similar phenomena, i.e. slow magnetization relaxations, have been observed for a nine-coordinate tricapped-trigonal prism dysprosium(III) and ytterbium(III) complexes, [Ln(Tpz)$_2$Bpz]·xCH$_2$Cl$_2$.[62] Based on crystal-field calculations of the pyrazolyl borates it was determined that the relaxation of the Dy(III) in [Dy(Tpz)$_2$Bpz]·xCH$_2$Cl$_2$ was consistent with a thermally driven Orbach process, while the one of the Yb(III) ion was better described by a Raman process, rendering any effective barrier to magnetization relaxation an

artifact of the applied field.[62] In addition, tris-oxydiacetate complexes of dysprosium(III) and erbium(III) were characterized by Coronado and coworkers.[69] In this case both the Dy(III) and Er(III) complexes demonstrated frequency dependent χ" responses both in the presence and absence of an applied 1000 Oe field. However, the Dy(III) analog was not strong enough to show peak maxima above 2 K, while the Er(III) complex was determined to have a barrier of 46 K. Our findings are consistent with Lannes and Luneau's work, where both prolate and oblate lanthanide(III) ions showed slow magnetic relaxation in a nine-coordinate environment. The prolate Yb(III) ion and intermediate Nd(III) ion did display similar behavior, given that the field strength did not change the frequency of the relaxation, suggesting that like the pyrazolyl borate complex, these ions likely follow Raman processes with artificial relaxation barriers from the applied field. The oblate Dy(III) ion, however, does show a true thermal barrier to relaxation, with a value that is roughly half of that observed for the pyrazolyl borates (U_{eff} = 20.3 K vs. 12.7 K), which may be explained by differences in the ligand field. However, the oblate Dy(III) showed a larger barrier to relaxation than the corresponding tris-oxydiacetate. The observation of slow relaxation of Nd(III) ion in single-ion complexes of nine-coordinate geometry is somewhat rare, and has only been observed in one other complex reported by Coronado and coworkers, which was also based on pyrazolyl borates.[70] Unlike the tris-oxydiacetate complexes, Er(III) did not display slow relaxation as the [3.3.1]metallacryptate. The differences in this behavior is likely due to the variation of the ligand field geometry between the metallacryptate and the tris-oxydiacetates where in the former Ln(III) ion is located in a distorted tricapped trigonal prism environment while in the latter the true tricapped trigonal prism with D_3 symmetry has been observed.[24,25]

Conclusions

A new class of coordination compounds were discovered here which, like metallacrowns, contain a [M-N-O] repeating motif resulting from the coordination of gallium metals to salicylhydroximate ligands. This complex is reminiscent of cryptates, and is best described as a lanthanide(III) complex of a gallium [3.3.1] metallacryptand which is able to complex all lanthanide(III) ions between praseodymium and ytterbium, with the possible exception of radioactive promethium which was not studied. Lanthanide(III)-based luminescence was observed in both the visible and NIR ranges in the solid state for praseodymium, neodymium,

samarium, terbium, holmium, erbium, and ytterbium metallacryptates upon excitation into ligand-centered levels. These complexes are comparable in brightness to other metallacrown complexes for NIR emission, though their quantum yields are likely diminished by coupling to vibronic oscillations of a closely located N-H bond of the ligand. Slow magnetization relaxation was observed for neodymium, dysprosium, and ytterbium. Dysprosium demonstrated an Orbach relaxation with an effective barrier of 12.7 K, while neodymium and ytterbium likely follow Raman processes with artificial, field-induced barriers of relaxation. The study of these combined properties could provide a path for deeper understanding of lanthanide electronic structure. In fact, the determination of the spacing of the electronic sublevels from a magnetization barrier alongside luminescence for a Yb^{3+} metallacrown has already been shown to be very informative.[37] However, the idea of studying lanthanide luminescence in a magnetic field could lead to fascinating discoveries. For example, certain bands may grow or shrink in intensity in various applied fields as the relaxation into J states are enhanced by the presence of the magnetic field. To simultaneously study these properties can lend insight into the magnetic structure of the lanthanide as well as enforcing control over which optical transitions dominate. So it could be possible to have a color change related to magnetic field, and thus have an optical storage device. It is clear from this and previous studies that metallacrowns, and now metallacryptates, provide an ideal scaffold that allows for the further study of lanthanide electronic states by this two-pronged strategy of comparing luminescence and magnetic properties.

References

(1) Bünzli, J. G.; Eliseeva, S. V. In *Lanthanide Luminescence: Photophysical, Analytical and Biological Aspects*; Hanninen, P., Harma, H., Eds.; Springer: Berlin, 2011; pp 1–45.
(2) Eliseeva, S. V; Bünzli, J.-C. G. *Chem. Soc. Rev.* **2010**, *39* (1), 189–227.
(3) Bünzli, J. C. G.; Eliseeva, S. V. *J. Rare Earths* **2010**, *28* (6), 824–842.
(4) Amoroso, A. J.; Pope, S. J. A. *Chem. Soc. Rev.* **2015**, *44* (14), 4723–4742.
(5) Martinić, I.; Eliseeva, S. V; Petoud, S. *J. Lumin.* **2017**, *189*, 19–43.
(6) Binnemans, K. *Chem. Rev.* **2009**, *109*, 4283–4374.
(7) Eliseeva, S. V.; Bünzli, J.-C. G. *New J. Chem.* **2011**, *35* (6), 1165–1176.
(8) Sy, M.; Nonat, A.; Hildebrandt, N.; Charbonnière, L. J. *Chem. Commun.* **2016**, *52* (29), 5080–5095.
(9) Trivedi, E. R.; Eliseeva, S. V.; Jankolovits, J.; Olmstead, M. M.; Petoud, S.; Pecoraro, V. L. *J. Am. Chem. Soc.* **2014**, *136* (4), 1526–1534.
(10) Uh, H.; Petoud, S. *Comptes Rendus Chim.* **2010**, *13* (6–7), 668–680.
(11) Comby, S.; Bünzli, J.-C. G. In *Handbook on the Physics and Chemistry of Rare Earths, Vol 37: Optical Spectroscopy;* Gschneidner, K. A., Bünzli, J.-C. G., Pecharsky, V. K., Eds.; Elsevier Science: Amsterdam, 2007.
(12) Petoud, S.; Muller, G.; Moore, E. G.; Xu, J.; Sokolnicki, J.; Riehl, J. P.; Le, U. N.; Cohen, S. M.; Raymond, K. N. *J. Am. Chem. Soc.* **2007**, *129* (1), 77–83.
(13) Zhang, J.; Badger, P. D.; Geib, S. J.; Petoud, S. *Angew. Chemie Int. Ed.* **2005**, *44* (17), 2508–2512.
(14) Chow, C. Y.; Eliseeva, S. V; Trivedi, E. R.; Nguyen, T. N.; Kampf, J. W.; Petoud, S.; Pecoraro, V. L. *J. Am. Chem. Soc.* **2016**, *138* (15), 5100–5109.
(15) Biju, S.; Eom, Y. K.; Bunzli, J.-C. G.; Kim, H. K. *J. Mater. Chem. C* **2013**, *1* (21), 3454–3466.
(16) Law, G. L.; Pham, T. A.; Xu, J.; Raymond, K. N. *Angew. Chemie - Int. Ed.* **2012**, *51* (10), 2371–2374.
(17) Wartenberg, N.; Raccurt, O.; Bourgeat-Lami, E.; Imbert, D.; Mazzanti, M. *Chem. - A Eur. J.* **2013**, *19* (10), 3477–3482.
(18) Quici, S.; Cavazzini, M.; Marzanni, G.; Accorsi, G.; Armaroli, N.; Ventura, B.; Barigelletti, F. *Inorg. Chem.* **2005**, *44* (3), 529–537.
(19) Winpenny, R. E. P. *Angew. Chemie - Int. Ed.* **2008**, *47* (42), 7992–7994.
(20) Bogani, L.; Wernsdorfer, W. *Nat. Mater.* **2008**, *7* (3), 179–186.
(21) Benelli, C.; Gatteschi, D. *Chem. Rev.* **2002**, *102* (6), 2369–2388.
(22) Sorace, L.; Benelli, C.; Gatteschi, D. *Chem. Soc. Rev.* **2011**, *40* (6), 3092.
(23) Ishikawa, N.; Sugita, M.; Ishikawa, T.; Koshihara, S.; Kaizu, Y. *J. Am. Chem. Soc.* **2003**, *125* (29), 8694–8695.
(24) AlDamen, M. A.; Cardona-Serra, S.; Clemente-Juan, J. M.; Coronado, E.; Gaita-Ariño, A.; Martí-Gastaldo, C.; Luis, F.; Montero, O. *Inorg. Chem.* **2009**, *48* (8), 3467–3479.
(25) Rinehart, J. D.; Long, J. R. *Chem. Sci.* **2011**, *2* (11), 2078.
(26) Pecoraro, V. L. *Inorganica Chim. Acta* **1989**, *155* (2), 171–173.
(27) Lah, M. S.; Pecoraro, V. L. *J. Am. Chem. Soc.* **1989**, *111*, 7258–7259.
(28) Grant, J. T.; Jankolovits, J.; Pecoraro, V. L. *Inorg. Chem.* **2012**, *51* (15), 8034–8041.
(29) Jankolovits, J.; Cutland Van-Noord, A. D.; Kampf, J. W.; Pecoraro, V. L. *Dalt. Trans.* **2013**, *42* (27), 9803.
(30) Lim, C.-S.; Tegoni, M.; Jakusch, T.; Kampf, J. W.; Pecoraro, V. L. *Inorg. Chem.* **2012**, *51*

(21), 11533–11540.
(31) Atzeri, C.; Marchiò, L.; Chow, Y. C.; Kampf, J. W.; Vincent, L.; Tegoni, M. *Chem. Eur. J.* **2016**, ASAP.
(32) Zaleski, C. M.; Depperman, E. C.; Kampf, J. W.; Kirk, M. L.; Pecoraro, V. L. *Inorg. Chem.* **2006**, *45* (25), 10022–10024.
(33) Zaleski, C. M.; Tricard, S.; Depperman, E. C.; Wernsdorfer, W.; Mallah, T.; Kirk, M. L.; Pecoraro, V. L. *Inorg. Chem.* **2011**, *50* (22), 11348–11352.
(34) Zaleski, C. M.; Kampf, J. W.; Mallah, T.; Kirk, M. L.; Pecoraro, V. L. *Inorg. Chem.* **2007**, *46* (6), 1954–1956.
(35) Boron, T. T.; Kampf, J. W.; Pecoraro, V. L. *Inorg. Chem.* **2010**, *49* (20), 9104–9106.
(36) Chow, C. Y.; Bolvin, H.; Campbell, V. E.; Guillot, R.; Kampf, J. W.; Wernsdorfer, W.; Gendron, F.; Autschbach, J.; Pecoraro, V. L.; Mallah, T. *Chem. Sci.* **2015**, *6* (7), 4148–4159.
(37) Li, Q.-W.; Liu, J.-L.; Jia, J.-H.; Chen, Y.-C.; Liu, J.; Wang, L.-F.; Tong, M.-L. *Chem. Commun.* **2015**, *51* (51), 10291–10294.
(38) Jankolovits, J.; Andolina, C. M.; Kampf, J. W.; Raymond, K. N.; Pecoraro, V. L. *Angew. Chemie Int. Ed.* **2011**, *50* (41), 9660–9664.
(39) Mezei, G.; Zaleski, C. M.; Pecoraro, V. L. *Chem. Rev.* **2007**, *107* (11), 4933–5003.
(40) Zaleski, C. M.; Lim, C.-S.; Cutland-Van Noord, A. D.; Kampf, J. W.; Pecoraro, V. L. *Inorg. Chem.* **2011**, *50* (16), 7707–7717.
(41) Azar, M. R.; Boron, T. T.; Lutter, J. C.; Daly, C. I.; Zegalia, K. A.; Nimthong, R.; Ferrence, G. M.; Zeller, M.; Kampf, J. W.; Pecoraro, V. L.; Zaleski, C. M. *Inorg. Chem.* **2014**, *53* (3), 1729–1742.
(42) Gibney, B. R.; Stemmler, A. J.; Pilotek, S.; Kampf, J. W.; Pecoraro, V. L. *Inorg. Chem.* **1993**, *32* (26), 6008–6015.
(43) Chow, C. Y.; Trivedi, E. R.; Pecoraro, V.; Zaleski, C. M. *Comments Inorg. Chem.* **2015**, *35* (4), 214–253.
(44) Saalfrank, R. W.; Maid, H.; Scheurer, A. *Angew. Chemie Int. Ed.* **2008**, *47* (46), 8794–8824.
(45) Jankolovits, J.; Kampf, J. W.; Pecoraro, V. L. *Inorg. Chem.* **2014**, *53* (14), 7534–7546.
(46) Lah, M. S.; Gibney, B. R.; Tierney, D. L.; Penner-Hahn, J. E.; Pecoraro, V. L. *J. Am. Chem. Soc.* **1993**, *115* (13), 5857–5858.
(47) Dendrinou-Samara, C.; Alexiou, M.; Zaleski, C. M.; Kampf, J. W.; Kirk, M. L.; Kessissoglou, D. P.; Pecoraro, V. L. *Angew. Chemie Int. Ed.* **2003**, *42* (32), 3763–3766.
(48) CrystalClear Expert 2.0 r16, Rigaku Americas and Rigaku Corporation (2014), Rigaku Americas, 9009, TX, USA 77381-5209, Rigaku Tokyo, 196-8666, Japan.
(49) Sheldrick, G. M. *Acta Crystallogr. Sect. A Found. Crystallogr.* **2007**, *64* (1), 112–122.
(50) Kessissoglou, D. P.; Kampf, J.; Pecoraro, V. L. *Polyhedron* **1994**, *13* (9), 1379–1391.
(51) Afrati, T.; Dendrinou-Samara, C.; Zaleski, C. M.; Kampf, J. W.; Pecoraro, V. L.; Kessissoglou, D. P. *Inorg. Chem. Commun.* **2005**, *8* (12), 1173–1176.
(52) Jin, L.; Yu, H.; Wu, S.; Xiao, F. *Dalt. Trans.* **2009**, No. 1, 197–201.
(53) Addison, A. W.; Rao, T. N.; Reedijk, J.; van Rijn, J.; Verschoor, G. C. *J. Chem. Soc. Dalt. Trans.* **1984**, 1349–1356.
(54) Carnall, W. T.; Fields, P. R.; Rajnak, K. *J. Chem. Phys.* **1968**, *49* (10), 4424–4442.
(55) Carnall, W. T.; Fields, P. R.; Rajnak, K. *J. Chem. Phys.* **1968**, *49* (10), 4447–4449.
(56) Kahn, M. L.; Ballou, R.; Porcher, P.; Kahn, O.; Sutter, J. *Chem. Eur. J.* **2002**, *8* (947),

525–531.
(57) Abbas, G.; Lan, Y.; Kostakis, G. E.; Wernsdorfer, W.; Anson, C. E.; Powell, A. K. *Inorg. Chem.* **2010**, *49* (17), 8067–8072.
(58) Gao, F.; Cui, L.; Song, Y.; Li, Y.-Z.; Zuo, J.-L. *Inorg. Chem.* **2014**, *53* (1), 562–567.
(59) Osa, S.; Kido, T.; Matsumoto, N.; Re, N.; Pochaba, A.; Mrozinski, J. *J. Am. Chem. Soc.* **2004**, *126* (2), 420–421.
(60) Tang, J.; Hewitt, I.; Madhu, N. T.; Chastanet, G.; Wernsdorfer, W.; Anson, C. E.; Benelli, C.; Sessoli, R.; Powell, A. K. *Angew. Chemie - Int. Ed.* **2006**, *45* (11), 1729–1733.
(61) Ishikawa, N.; Sugita, M.; Wernsdorfer, W. *Angew. Chemie - Int. Ed.* **2005**, *44* (19), 2931–2935.
(62) Lannes, A.; Luneau, D. *Inorg. Chem.* **2015**, *54* (14), 6736–6743.
(63) Demir, S.; Jeon, I.-R.; Long, J. R.; Harris, T. D. *Coord. Chem. Rev.* **2014**, 1–28.
(64) Bagai, R.; Christou, G. *Chem. Soc. Rev.* **2009**, *38* (4), 1011–1026.
(65) Lah, M. S.; Pecoraro, V. L. *J. Am. Chem. Soc.* **1989**, *111* (18), 7258–7259.
(66) Zaleski, C. M.; Depperman, E. C.; Dendrinou-Samara, C.; Alexiou, M.; Kampf, J. W.; Kessissoglou, D. P.; Kirk, M. L.; Pecoraro, V. L. *J. Am. Chem. Soc.* **2005**, *127* (37), 12862–12872.
(67) Martinić, I.; Eliseeva, S. V.; Nguyen, T. N.; Foucher, F.; Gosset, D.; Westall, F.; Pecoraro, V. L.; Petoud, S. *Chem. Sci.* **2017**, *8* (9), 6042–6050.
(68) Martinić, I.; Eliseeva, S. V; Nguyen, T. N.; Pecoraro, V. L.; Petoud, S. *J. Am. Chem. Soc.* **2017**, *139* (25), 8388–8391.
(69) Baldoví, J. J.; Duan, Y.; Morales, R.; Gaita-Ariño, A.; Ruiz, E.; Coronado, E. *Chem. - A Eur. J.* **2016**, *22* (38), 13532–13539.
(70) Baldoví, J. J.; Clemente-Juan, J. M.; Coronado, E.; Gaita-Ariño, A. *Polyhedron* **2013**, *66*, 39–42.

Chapter 3

Incorporation of Iodine onto Metallacrown Scaffolds

Introduction

Given the exciting progress of metallacrown complexes as lanthanide based lumiphores, there is strong motivation to improve the brightness of these complexes. In addition, the demonstration of numerous metallacrown species with strong luminescence, even in HeLa cell imaging, offers an opportunity for combining these optical properties with another imaging technique.[1–6] Such complexes, referred to as bimodal imaging agents, are attractive in the field for a few reasons. First, the ability to use two different imaging techniques allows for complementary analysis where the drawbacks of one method are compensated by the other method.[7] Second, each imaging technique could satisfy a different role. For example, one agent could be the workhorse for imaging the tissue, while the other acts as an optical sensor for a specific molecule related to a disease.[8] Lastly, these bimodal agents could be used a "theranostic", where the compound not only allows for diagnostic imaging, but also can act as a therapeutic agent.[7,8] Given the highly tunable nature of metallacrown complexes, a straightforward approach involving the incorporation of halogens onto MCs is described in this chapter as a means to accomplish both of these goals.

Towards the goal of brighter luminescence the incorporation of halogens may take advantage of a phenomenon known as the heavy atom effect. Essentially, relativistic effects of a large atom enhances spin-orbit coupling in a chromophore which leads to enhanced intersystem crossing. Theoretically, the relationship of atomic size to enhanced spin orbit coupling arises from the relationship of the spin-orbit coupling constant and effective nuclear charge (Z_{eff}):[9]

$$\zeta = \frac{R\alpha^2 \left(Z^{eff}\right)^4}{n^3 l(l+\frac{1}{2})(l+1)} \tag{3.1}$$

Where ζ is the spin-orbit coupling constant, n is the principle quantum number, l is the angular momentum quantum number of the electron, R is the Rydberg constant, α is a constant equal to about 1/137. This expression demonstrates a direct proportionality of ζ to $(Z^{eff})^4$, which is related to atomic size and the basis of the heavy atom effect.[9]

This phenomenon was first reported in 1949 when McClure demonstrated the relationship between the spin-orbit coupling constant for heavy atoms and the phosphorescent lifetime within naphthalene derivatives.[10] In addition, later studies by McClure showed that there is not only an increase in the radiative rate of phosphorescence but also notable quenching of fluorescent emission.[11,12] This discovery sparked further investigation, the most notable of which is a study by Ermolaev and Svitashev in 1959.[13] This study examined the systematic change of naphthalene by halogenating the 1 position with fluorine, chlorine, bromine, and iodine.[13] Observation of absolute quantum yields of fluorescence and phosphorescence in conjunction with rates of phosphorescence and intersystem crossing showed that halogen size directly related to the extent of fluorescence quenching, phosphorescence enhancement in emission and rate, and the rate of intersystem crossing.[13] In 1970, Galiazzo and coworkers studied phenanthrene, where the 3 and 9 positions were methylated, chlorinated or brominated.[14] Again, the heavy atom effect was noted but the bromine location appeared to have some impact on the photophysics of the compound. In the nine position, the phosphorescent rate decreased five-fold compared to a bromine in the three position and the rate of intersystem crossing increased drastically beyond a measurable amount with the instrumentation available.[14] However, the heavy atom effect is not exclusive to bound halogens, but is also observed from halogens introduced in co-crystallization or within the solvent.[15–17] Recently, work by Kim and coworkers in 2011 showed that the heavy atom effect can be rationally optimized by the location of the halogen.[18] DFT calculations on 4-bromobenzaldehyde showed that in the triplet state, electron density is localized on the aldehyde carbonyl oxygen.[18] In the solid state, the compound crystallizes such that the bromine is halogen bonded to this oxygen, and demonstrates a marked enhancement in the phosphorescence.[18]

The study of this phenomenon is not limited to organic chromophores, and has been examined for some organometallic complexes. In 1972 Dolphin and coworkers performed an extensive study of group (IV) halide containing porphyrins.[19] What was observed is that the

heavy atom effect is not only relevant for the halogens, but is also observed for group (IV) elements from silicon to tin.[19] Comparison of analogous selenium(IV), germanium (IV) and tin(IV) species showed a decrease in fluorescence yield accompanied by an increase in phosphorescence yield. In addition, the observed lifetime of phosphorescence also decreased in accordance with the heavy atom effect. However, comparison of tin(IV) structures with fluorine, chlorine, bromine, or iodine showed a much stronger trend, which suggests that halogenation of the porphyrin has a stronger effect than the encapsulated metal. More recently Xu and coworkers demonstrated the heavy atom effect on copper (I) chelates in tridentate phosphine halides, proving that this phenomenon could be observed in 3d complexes as well.[20] The sum total of this work raises the question of whether the heavy atom effect may be combined with the antenna effect for lanthanide complexes. If so, then the incorporation of heavy atoms onto metallacrown complexes could lead to better sensitization by enhancing triplet state generation in the antenna.

In addition to the potential benefits of the heavy atom effect, incorporation of iodine onto metallacrown complexes could lead to the opportunity to create complexes which may not only be used for optical imaging but also as computed tomography (CT) contrast agents. The CT imager was built by Hounsfield in 1972 and reported in 1978 by Oldendorf, revolutionizing the scope of imaging using x-ray radiation.[21,22] However, imaging of soft tissues is difficult using x-rays since density and atomic number are proportional to the absorption coefficient, so there is little attenuation compared to denser substances such as bone.[22] To compensate, contrast agents are used which contain large atoms since x-ray attenuation is related to scattering which scales with an atom's structure factor. There are many commercial agents but the current gold standard in CT contrast is 1-N,3-N-bis(1,3-dihydroxypropan-2-yl)-5-[(2S)-2-hydroxypropanamido]-2,4,6-triiodobenzene-1,3-dicarboxamide which is commonly referred to as Iopamidol.[22] While these iodinated compounds do work well as contrast agents, there are a few drawbacks. First, these iodinated complexes have low imaging time since they are rapidly cleared by the kidneys.[23,24] Second, because of the kidney clearance, there is the potential for renal toxicity.[24] To address this, there have been examples of bismuth sulfide, tantalum oxide and gold nanoparticles (NPs) which can be used as CT contrast agents.[25–28] These NPs do not suffer the same drawbacks and gold NPs were shown to give even greater contrast than the iodinated compounds.[29]

However, since lanthanides have a large structure factor, are luminescent, and are the current frontrunner for contrast agents in magnetic resonance imaging (MRI), the use of

lanthanides as multimodal imaging agents across CT, optical imaging and MRI contrast is a logical goal. Multimodal agents are useful for a number of reasons, including reduced time and effort in gathering imaging data as well as complementary advantages accessible using multiple techniques.[7,8] For example, CT imaging is great for its high resolution 3D imaging, but is not sensitive enough to image smaller structures such as single cells.[7,8,29,30] But, optical imaging is sensitive enough to image these smaller structures but does not give high resolution 3D images.[7,8,29,30] By combining these techniques, using the same compound, there is immediate access to both diagnostic tools. In 2012, Shi and coworkers reported the ability to span these imaging techniques using a $NaYbF_4$:Tm^{3+} nanoparticle (approx. 20 nm) which on its own had excellent CT contrast and near infrared emission arising from Tm^{3+} at 800 nm.[30] The Yb^{3+} component was used to absorb 980 nm light and sensitize the Tm^{3+} emission via up-conversion. Another article in 2012 by this same group reported a NaY/GdF_4 nanoparticle using lanthanide dopants such as Er^{3+}, Tm^{3+}, and Yb^{3+} as the core of a PEGylated SiO_2-Au nanoparticle shell with a size of 50 nm.[29] In this case, the gold nanoparticle was the sensitizer via surface plasmon resonance of a near infrared emitting lanthanide while also having the strong presence of Gd^{3+} for MRI contrast via T_1 weighting. Experimentation on mouse models showed that these nanoparticles are able to function as multimodal contrast agents and were not cytotoxic for up to one month. While these nanoparticles represent an amazing demonstration of the flexibly of using lanthanides as imaging agents with the ability to be sensitized using 980 nm light (thus having excellent tissue penetration), there are drawbacks compared to a metallacrown. First, MCs do not blink as NPs are known to do. Second, the metallacrowns have massive absorption cross sections, which means that these molecules tend to have very bright emission even in HeLa cells.[5,6] Like NPs, MCs are also highly functionalizable which will be demonstrated in the next chapter. So the development of a multimodal CT/optical imaging metallacrown scaffold could allow for a quantitative and brighter bimodal agent with straightforward tunability and functionalization potential.

Experimental

Synthetic Materials. Gallium(III) nitrate hydrate (Acros, 99.9998%), praseodymium(III) nitrate hexahydrate (Sigma Aldrich, 99.9%), neodymium(III) nitrate hexahydrate (Sigma Aldrich, 99.9%), samarium(III) nitrate hexahydrate (Sigma Aldrich, 99.9%), europium(III) nitrate hexahydrate (Sigma Aldrich, 99.9%), gadolinium(III) nitrate hexahydrate (Alfa, Aesar, 99.9%), terbium(III) nitrate pentahydrate (Sigma Aldrich, 99.9%), dysprosium(III) nitrate pentahydrate (Alfa Aesar, 99.9%), holmium(III) nitrate pentahydrate (Sigma Aldrich, 99.9%), thulium(III) nitrate hydrate (Sigma Aldrich, 99.9%), erbium(III) nitrate pentahydrate (Sigma Aldrich, 99.9%), ytterbium nitrate pentahydrate (Sigma Aldrich, 99.9%), 5-iodosalicylic acid (Acros, 97%), 5-aminoisophthalic acid hydrate (Chem Impex, 99%), isophthalic acid (Acros, 99%), potassium iodide (Acros, 99%), sodium nitrite (Sigma Aldrich, 97%), sodium hydroxide (Fisher, ACS Grade), potassium hydroxide (Fisher, 85%), hydroxylamine hydrochloride (Sigma Aldrich, 99%), methanol (Fisher, ACS grade), ethanol (Decon Labs, 200 Proof), dichloromethane (Fisher, ACS Grade), ethyl acetate (Fisher, ACS Grade), sulfuric acid (Fisher, ACS Grade), hydrochloric acid (Fisher, 37% w/w), anhydrous sodium sulfate (Fisher, ACS Grade). All materials were used as received without further purification.

Synthetic Procedures

Ethyl 5-iodosalicylate. Ethyl 5-iodo salicylate was synthesized using a standard Fischer esterification.[31] Fifty mmol of 5-iodosaylicylic acid (13.20 g, 1 equiv.) was dissolved in 150 mL of 200 proof ethanol, followed by sodium sulfate such that there was an apparent reaction volume of 200 mL. 40 mmol of sulfuric acid (2.132 mL, 0.8 equiv.) was added and the reaction was warmed to reflux, then stirred for 24 hours. The reaction was removed from heat and quickly vacuumed filtered to remove sodium sulfate. The clear and colorless filtrate was reduced to a volume of 30 mL using a flash evaporator. This concentrate was taken up in 50 mL of distilled water and the pH was adjusted to 8 using saturated aqueous sodium carbonate. A colorless precipitate of ethyl 5-iodosalicylate was observed and vacuum filtered from a clear and colorless filtrate. The synthetic yield was 53%. Elemental analysis for $C_9H_9IO_3$ [292.07 g/mol] % found (calculated): %C 37.03 (37.01); %H 2.95 (3.11); %N 0.00 (0.00). ^{1}H-NMR (400 MHz, d_6-

DMSO): 10.56 ppm (1H, broad s), 8.00 ppm (1H, d), 7.78 ppm (1H, dd), 6.83 ppm (1H, d), 4.34 ppm (2H, q), 1.33 ppm (3H, t).

5-iodosalicylhydroxamic acid (H_3mishi). Fifteen mmol of ethyl 5-iodosalicylate (4.38 g, 1 equiv.) was dissolved in 75 mL of methanol to a clear and colorless solution. Separately, 45 mmol of hydroxylamine hydrochloride (3.13 g, 3 equiv.) and 60 mmol of potassium hydroxide (3.96 g, 4 equiv.) were dissolved in 75 mL of methanol to form clear and colorless solutions. The hydroxylamine hydrochloride and potassium hydroxide solutions were combined and a colorless potassium chloride precipitate was observed. The mixture was let stir for 10 minutes, then the potassium chloride was vacuum filtered from a clear and colorless filtrate. This filtrate was combined with the solution of ethyl 5-iodosalicylate to form a clear and faintly yellow solution. This solution was stirred for 20 hours. Next, another set of hydroxylamine hydrochloride and potassium hydroxide solutions in 75 mL of methanol were prepared, combined and filtered as described previously to obtain another clear and colorless filtrate. This filtrate was combined into the reaction solution and let stir for another 25 hours. The resulting clear and yellow solution was then reduced to 75 mL on a flash evaporator. The concentrate was acidified to pH 1 using aqueous 2 M hydrochloric acid and then mixed into 300 mL of distilled water. An off-white precipitate formed and was vacuum filtered from a clear and yellow filtrate. The precipitate was triturated in 50 mL of dichloromethane for 20 minutes, then vacuum filtered to yield an off-white 5-iodosalicylhydroxamic acid precipitate from a faintly yellow filtrate. The synthetic yield was 89%. Elemental Analysis of $C_7H_3NO_3I$ [fw = 279.03 g/mol] found % (calculated): C, 29.94 (30.13), 2.10 (2.17), 4.96 (5.02). ^{1}H-NMR (400 MHz, d_6-DMSO): 12.17 ppm (1H, s), 11.37 ppm (1H, s), 9.39 ppm (1H, s), 7.98 ppm (1H, d), 7.65 ppm (1H, dd), 6.75 ppm (1H, d).

5-iodoisophthalic acid (H_2iiph). The preparation of 5-iodoisophthalic acid was performed by modifying a previously reported procedure.[32] Twenty-five mmol of 5-aminoisophthalic acid (4.98 g, 1 equiv.) was suspended in a mixture of 50 mL of distilled water and 50 mL of 37% hydrochloric acid to form a cloudy and pink solution. This was cooled in an ice bath and stirred. Next, 26.25 mmol of sodium nitrite (1.8113 g, 1.05 equiv.) was dissolved in 10 mL of distilled water to form a clear and colorless solution which was added to the reaction solution dropwise at a rate of 1 drop every 2 seconds. The solution became cloudy and yellow and was let stir on ice

for another 10 minutes after all of the sodium nitrite was added. Then 81.25 mmol of potassium iodide (13.49 g, 3.25 equiv.) was dissolved in 40 mL of distilled water to form a clear and colorless solution which was added dropwise to the reaction at a rate of 1 drop every second. The reaction solution turned a dark shade of purple and a brown foam formed. Once all of the potassium iodide solution was added the reaction was let warm to room temperature then warmed until a purple haze is observed. The reaction was let stir for 2.5 hours, then let cool in a 4ºC fridge overnight. A gray precipitate was vacuum filtered from a clear and red filtrate. This precipitate was suspended in 50 mL of methanol and warmed to reflux to form a clear and orange solution. The solution was concentrated to 20 mL under a stream of nitrogen, then taken up in 100 mL of distilled water. The cloudy orange mixture was extracted with four 40 mL portions of ethyl acetate, dried over sodium sulfate and then filtered. The filtrate was condensed to an orange powder on a rotovap. This powder was triturated in 60 mL of hexanes for 20 minutes, then vacuum filtered from a purple filtrate and washed with hexanes until the wash was no longer purple. This product was 95% pure by elemental analysis, [0.95 $C_8H_5IO_4$:0.05 $C_8H_7NO_4$]·0.75 H_2O [fw = 300.00 g/mol] % found (calculated): %C 32.19 (32.03); %H 2.23 (2.22); %N 0.24 (0.23). ^{1}H-NMR (400 MHz, d_6-DMSO): 8.42 ppm (3H, s).

General procedure for {Ln[12-MC$_{Ga}{}^{III}{}_{N(L)}$-4]Na}$_2$(L')$_4$. The synthesis of Ln-Ix complexes was modified from a known procedure.[4] First, 0.125 mmol of Ln$(NO_3)_3$·xH_2O (1 equiv., Ln = Pr, Nd, Sm, Eu, Gd, Tb, Dy, Ho, Er, Tm ,Yb, Y, or Lu) and 0.5 mmol of $Ga(NO_3)_3$ (0.1279 g, 4 equiv.) were dissolved in 2.5 mL of N,N-dimethylformamide to form a clear and colorless solution. Separately, 0.5 mmol of L (4 equiv., L = H_3shi, or H_3mishi) and 0.25 mmol of L' (2 equiv, L' = H_2iph or H_2iiph) was dissolved in 7.5 mL of DMF to form a clear and yellow solution. 2.0 mmol of NaOH was added as a saturated aqueous solution (101.4 µL, 16 equiv.) to the L/L' solution which forms a small amount of clear and colorless precipitate. The Ln/Ga solution was immediately added to the L/L' solution and let stir for about one hour. The solution was then gravity filtered, and the filtrate was let crystallize by slow evaporation in a humid environment for 2-4 weeks, which yields crystalline needles or plates.

$Pr_2Ga_8(shi)_8(iiph)_4Na_2(DMF)_{15}(H_2O)_8$, **Pr-I$_4$.** The percent yield was 19% based on praseodymium nitrate hexahydrate. Elemental analysis of *$Pr_2Ga_8Na_2C_{133}H_{165}N_{23}O_{63}I_4$* [fw =

4487.08 g/mol] found % (calculated): C, 35.64 (35.60); H, 4.03 (3.71); N, 7.09 (7.18). ESI-MS, calculated $Pr_2Ga_8C_{88}H_{44}N_8O_{40}I_4$ $[M]^{2-}$: 1599.50, found 1600.51.

$Nd_2Ga_8(shi)_8(iiph)_4Na_2(DMF)_{16}(H_2O)_{10}$, **Nd-I4.** The percent yield was 27% based on neodymium nitrate hexahydrate. Elemental analysis of $Nd_2Ga_8Na_2C_{136}H_{176}N_{24}O_{66}I_4$ [fw = 4602.87 g/mol] found % (calculated): C, 35.48 (35.49); H, 4.04 (3.85); N, 7.30 (7.30). ESI-MS, calculated $Nd_2Ga_8C_{88}H_{44}N_8O_{40}I_4$ $[M]^{2-}$: 1601.50, found 1603.50.

$Sm_2Ga_8(shi)_8(iiph)_4Na_2(DMF)_{11}(H_2O)_4$, **Sm-I4.** The percent yield was 25% based on samarium nitrate hexahydrate. Elemental analysis of $Sm_2Ga_8Na_2C_{121}H_{129}N_{19}O_{55}I_4$ [fw = 4141.54 g/mol] found % (calculated): C, 35.34 (35.09); H, 3.11 (3.14); N, 6.46 (6.43). ESI-MS, calculated $Sm_2Ga_8C_{88}H_{44}N_8O_{40}I_4$ $[M]^{2-}$: 1611.51, found 1609.50. ^{1}H-NMR (500 MHz, d_4-MeOH): 8.92 ppm (1H, s); 8.87 ppm (0.5H, s); 8.54 ppm (0.5H, broad s); 8.15 ppm (1.5H, d); 7.51 ppm (1H, broad s); 7.27 ppm (1.5H, m); 7.05 ppm (1.5H, m); 6.80 ppm (1.5H, m); 5.10 ppm (1H, m).

$Eu_2Ga_8(shi)_8(iiph)_4Na_2(DMF)_{12}(H_2O)$, **Eu-I4.** The percent yield was 28% based on europium nitrate hexahydrate. Elemental analysis of $Eu_2Ga_8Na_2C_{124}H_{130}N_{20}O_{53}I_4$ [fw = 4163.80 g/mol] found % (calculated): C, 35.93 (35.77); H, 3.38 (3.15); N, 6.60 (6.73). ESI-MS, calculated $Eu_2Ga_8C_{88}H_{44}N_8O_{40}I_4$ $[M]^{2-}$: 1610.51, found 1610.51.

$Gd_2Ga_8(shi)_8(iiph)_4Na_2(DMF)_{10}(H_2O)_5$, **Gd-I4.** The percent yield was 22% based on gadolinium nitrate hexahydrate. Elemental analysis of $Gd_2Ga_8Na_2C_{118}H_{124}N_{18}O_{55}I_4$ [fw = 4100.24 g/mol] found % (calculated): C, 34.65 (34.57); H, 3.18 (3.05); N, 6.04 (6.15). ESI-MS, calculated $Gd_2Ga_8C_{88}H_{44}N_8O_{40}I_4$ $[M]^{2-}$: 1617.52, found 1616.51.

$Tb_2Ga_8(shi)_8(iiph)_4Na_2(DMF)_{18}(H_2O)_{10}$, **Tb-I4.** The percent yield was 17% based on terbium nitrate pentahydrate. Elemental analysis of $Tb_2Ga_8Na_2C_{142}H_{190}N_{26}O_{68}I_4$ [fw = 4778.43 g/mol] found % (calculated): C, 35.50 (35.69); H, 4.02 (4.01); N, 7.63 (7.62). ESI-MS, calculated $Tb_2Ga_8C_{88}H_{44}N_8O_{40}I_4$ $[M]^{2-}$: 1617.52, found 1618.51.

$Dy_2Ga_8(shi)_8(iiph)_4Na_2(DMF)_{15}(H_2O)_9$, **Dy-I4.** The percent yield was 21% based on dysprosium nitrate pentahydrate. Elemental analysis of $Dy_2Ga_8Na_2C_{133}H_{167}N_{23}O_{64}I_4$ [fw = 4548.28 g/mol] found % (calculated): C, 35.19 (35.12); H, 3.84 (3.70); N, 7.07 (7.08). ESI-MS, calculated $Dy_2Ga_8C_{88}H_{44}N_8O_{40}I_4$ $[M]^{2-}$: 1621.52, found 1621.51.

$Ho_2Ga_8(shi)_8(iiph)_4Na_2(DMF)_{13}(H_2O)_2$, **Ho-I4.** The percent yield was 23% based on holmium nitrate pentahydrate. Elemental analysis of $Ho_2Ga_8Na_2C_{127}H_{139}N_{21}O_{55}I_4$ [fw = 4280.84 g/mol] found % (calculated): C, 35.75 (35.63); H, 3.49 (3.27); N, 6.88 (6.87). ESI-MS, calculated $Ho_2Ga_8C_{88}H_{44}N_8O_{40}I_4$ $[M]^{2-}$: 1623.52, found 1624.52.

$Er_2Ga_8(shi)_8(iiph)_4Na_2(DMF)_{12}(H_2O)_3$, **Er-I4.** The percent yield was 27% based on erbium nitrate pentahydrate. Elemental analysis of $Er_2Ga_8Na_2C_{124}H_{134}N_{20}O_{55}I_4$ [fw = 4230.42 g/mol] found % (calculated): C, 35.33 (35.21); H, 3.43 (3.19); N, 6.48 (6.62). ESI-MS, calculated $Er_2Ga_8C_{88}H_{44}N_8O_{40}I_4$ $[M]^{2-}$: 1625.52, found 1626.52.

$Tm_2Ga_8(shi)_8(iiph)_4Na_2(DMF)_{12}(H_2O)_7$, **Tm-I4.** The percent yield was 24% based on thulium nitrate pentahydrate. Elemental analysis of $Tm_2Ga_8Na_2C_{124}H_{142}N_{20}O_{59}I_4$ [fw = 4305.83 g/mol] found % (calculated): C, 34.59 (34.59); H, 3.39 (3.32); N, 6.51 (6.51). ESI-MS, calculated $Tm_2Ga_8C_{88}H_{44}N_8O_{40}I_4$ $[M]^{2-}$: 1627.53, found 1627.52.

$Yb_2Ga_8(shi)_8(iiph)_4Na_2(DMF)_{13}(H_2O)_6$, **Yb-I4.** The percent yield was 20% based on ytterbium nitrate pentahydrate. Elemental analysis of $Yb_2Ga_8Na_2C_{127}H_{147}N_{21}O_{59}I_4$ [fw = 4369.15 g/mol] found % (calculated): C, 34.89 (34.91); H, 3.47 (3.39); N, 6.68 (6.73). ESI-MS, calculated $Yb_2Ga_8C_{88}H_{44}N_8O_{40}I_4$ $[M]^{2-}$: 1631.53, found 1632.52.

$Lu_2Ga_8(shi)_8(iiph)_4Na_2(DMF)_{10}$, **Lu-I4.** The percent yield was 23% based on lutetium nitrate pentahydrate. Elemental analysis of $Lu_2Ga_8Na_2C_{118}H_{114}N_{18}O_{50}I_4$ [fw = 4045.60 g/mol] found % (calculated): C, 35.35 (35.03); H, 2.94 (2.84); N, 6.04 (6.23). ESI-MS, calculated $Lu_2Ga_8C_{88}H_{44}N_8O_{40}I_4$ $[M]^{2-}$: 1633.53, found 1634.52. ^{1}H-NMR (500 MHz, d_4-MeOH): 8.99 ppm (1H, d); 8.64 ppm (0.5H, t); 8.54 ppm (1H, d); 8.15 ppm (0.5H, t); 8.09 ppm (2H, t); 7.68 ppm (0.5H, t); 7.26 ppm (1.5H, m); 7.02 ppm (1.5H, dd); 6.79 ppm (1.5H, t).

$Y_2Ga_8(shi)_8(iiph)_4Na_2(DMF)_{12}(H_2O)_3$, **Y-I4.** The percent yield was 28% based on yttrium nitrate hexahydrate. Elemental analysis of $Y_2Ga_8Na_2C_{124}H_{134}N_{20}O_{55}I_4$ [fw = 4073.71 g/mol] found % (calculated): C, 36.66 (36.56); H, 3.38 (3.32); N, 6.53 (6.88). ESI-MS, calculated $Y_2Ga_8C_{88}H_{44}N_8O_{40}I_4$ $[M]^{2-}$: 1547.50, found 1548.49. ^{1}H-NMR (500 MHz, d_4-MeOH): 8.99 ppm (1H, d); 8.58 ppm (0.5H, d); 8.55 ppm (1H, s); 8.51 ppm (0.5H, s); 8.01-8.09 ppm (2H, m); 7.59 ppm (0.5H, t); 7.26 ppm (1.5H, m); 7.01 ppm (1.5H, m); 6.78 ppm (1.5H, t).

$Pr_2Ga_8(mishi)_8(iph)_4Na_2(DMF)_{10}(H_2O)_{10}$, **Pr-I8.** The percent yield was 12% based on praseodymium nitrate hexahydrate. Elemental analysis of $Pr_2Ga_8Na_2C_{118}H_{130}N_{18}O_{60}I_8$ [fw = 4661.22 g/mol] found % (calculated): C, 30.55 (30.41); H, 2.87 (2.81); N, 5.32 (5.41). ESI-MS, calculated $Pr_2Ga_8C_{88}H_{40}N_8O_{40}I_8$ $[M]^{2-}$: 1851.28, found 1852.28.

$Nd_2Ga_8(mishi)_8(iph)_4Na_2(DMF)_{11}(H_2O)_9$, **Nd-I8.** The percent yield was 9% based on neodymium nitrate hexahydrate. Elemental analysis of $Nd_2Ga_8Na_2C_{121}H_{135}N_{19}O_{60}I_8$ [fw = 4722.97 g/mol] found % (calculated): C, 30.77 (30.77); H, 2.98 (2.88); N, 5.62 (5.63). ESI-MS, calculated $Nd_2Ga_8C_{88}H_{40}N_8O_{40}I_8$ $[M]^{2-}$: 1853.30, found 1855.28.

$Sm_2Ga_8(mishi)_8(iph)_4Na_2(DMF)_{14}(H_2O)_4$, **Sm-I8.** The percent yield was 15% based on samarium nitrate hexahydrate. Elemental analysis of $Sm_2Ga_8Na_2C_{130}H_{146}N_{22}O_{58}I_8$ [fw = 4864.41 g/mol] found % (calculated): C, 32.29 (32.10); H, 3.04 (3.03); N, 6.43 (6.33). ESI-MS, calculated $Sm_2Ga_8C_{88}H_{40}N_8O_{40}I_8$ $[M]^{2-}$: 1863.31, found 1862.29. ^{1}H-NMR (500 MHz, d_4-MeOH): 8.69 ppm (2H, d); 8.62 ppm (1H, d); 8.36 ppm (2H, dd); 7.57 ppm (1H, q); 7.50 ppm (2H, d), 6.86 ppm (2H, d).

$Eu_2Ga_8(mishi)_8(iph)_4Na_2(DMF)_{14}(H_2O)_7$, **Eu-I8.** The percent yield was 16% based on europium nitrate hexahydrate. Elemental analysis of $Eu_2Ga_8Na_2C_{130}H_{152}N_{22}O_{61}I_8$ [fw = 4921.67 g/mol] found % (calculated): C, 31.94 (31.73); H, 3.26 (3.11); N, 6.24 (6.26). ESI-MS, calculated $Eu_2Ga_8C_{88}H_{40}N_8O_{40}I_8$ $[M]^{2-}$: 1862.31, found 1863.29.

$Gd_2Ga_8(mishi)_8(iph)_4Na_2(DMF)_8(H_2O)_4$, **Gd-I8.** The percent yield was 9% based on gadolinium nitrate hexahydrate. Elemental analysis of $Gd_2Ga_8Na_2C_{112}H_{104}N_{16}O_{52}I_8$ [fw = 4439.62 g/mol] found % (calculated): C, 30.37 (30.30); H, 2.54 (2.36); N, 5.07 (5.05). ESI-MS, calculated $Gd_2Ga_8C_{88}H_{40}N_8O_{40}I_8$ $[M]^{2-}$: 1869.31, found 1868.30.

$Tb_2Ga_8(mishi)_8(iph)_4Na_2(DMF)_{15}(H_2O)_7$, **Tb-I8.** The percent yield was 16% based on terbium nitrate pentahydrate. Elemental analysis of $Tb_2Ga_8Na_2C_{112}H_{104}N_{16}O_{52}I_8$ [fw = 5008.68 g/mol] found % (calculated): C, 31.97 (31.89); H, 3.26 (3.20); N, 6.46 (6.43). ESI-MS, calculated $Tb_2Ga_8C_{88}H_{40}N_8O_{40}I_8$ $[M]^{2-}$: 1869.31, found 1870.30.

$Dy_2Ga_8(mishi)_8(iph)_4Na_2(DMF)_9(H_2O)_5$, **Dy-I8.** The percent yield was 10% based on dysprosium nitrate pentahydrate. Elemental analysis of $Dy_2Ga_8Na_2C_{112}H_{104}N_{16}O_{52}I_8$ [fw = 4541.23 g/mol] found % (calculated): C, 30.44 (30.42); H, 2.68 (2.51); N, 5.23 (5.24). ESI-MS, calculated $Dy_2Ga_8C_{88}H_{40}N_8O_{40}I_8$ $[M]^{2-}$: 1873.31, found 1873.80.

$Ho_2Ga_8(mishi)_8(iph)_4Na_2(DMF)_8(H_2O)_6$, **Ho-I8.** The percent yield was 24% based on holmium nitrate pentahydrate. Elemental analysis of $Ho_2Ga_8Na_2C_{112}H_{108}N_{16}O_{54}I_8$ [fw = 4491.01 g/mol] found % (calculated): C, 29.77 (29.95); H, 2.36 (2.42); N, 5.10 (4.99). ESI-MS, calculated $Ho_2Ga_8C_{88}H_{40}N_8O_{40}I_8$ $[M]^{2-}$: 1875.32, found 1876.30.

$Er_2Ga_8(mishi)_8(iph)_4Na_2(DMF)_{12}(H_2O)_4$, **Er-I8.** The percent yield was 9% based on erbium nitrate pentahydrate. Elemental analysis of $Er_2Ga_8Na_2C_{124}H_{132}N_{20}O_{56}I_8$ [fw = 4752.02 g/mol] found % (calculated): C, 31.28 (31.34); H, 2.81 (2.80); N, 5.85 (5.90). ESI-MS, calculated $Er_2Ga_8C_{88}H_{40}N_8O_{40}I_8$ $[M]^{2-}$: 1877.32, found 1878.31.

$Tm_2Ga_8(mishi)_8(iph)_4Na_2(DMF)_{15}(H_2O)_7$, **Tm-I8.** The percent yield was 7% based on thulium nitrate pentahydrate. Elemental analysis of $Tm_2Ga_8Na_2C_{133}H_{159}N_{23}O_{62}I_8$ [fw = 5028.70 g/mol] found % (calculated): C, 31.90 (31.77); H, 3.28 (3.19); N, 6.33 (6.41). ESI-MS, calculated $Tm_2Ga_8C_{88}H_{40}N_8O_{40}I_8$ $[M]^{2-}$: 1879.32, found 1879.30.

$Yb_2Ga_8(mishi)_8(iph)_4Na_2(DMF)_{16}(H_2O)_8$, **Yb-I$_8$.** The percent yield was 24% based on ytterbium nitrate pentahydrate. Elemental analysis of $Yb_2Ga_8Na_2C_{136}H_{168}N_{24}O_{64}I_8$ [fw = 5128.05 g/mol] found % (calculated): C, 31.91 (31.85); H, 3.33 (3.30); N, 6.45 (6.56). ESI-MS, calculated $Yb_2Ga_8C_{88}H_{40}N_8O_{40}I_8$ $[M]^{2-}$: 1883.32, found 1884.31.

$Lu_2Ga_8(mishi)_8(iph)_4Na_2(DMF)_8(H_2O)_4$, **Lu-I$_8$.** The percent yield was 3% based on lutetium nitrate pentahydrate. Elemental analysis of $Lu_2Ga_8Na_2C_{112}H_{104}N_{16}O_{52}I_8$ [fw = 4475.06 g/mol] found % (calculated): C, 30.25 (30.06); H, 2.21 (2.34); N, 5.02 (5.01). ESI-MS, calculated $Lu_2Ga_8C_{88}H_{40}N_8O_{40}I_8$ $[M]^{2-}$:1885.33, found 1885.31. 1H-NMR (500 MHz, d_4-MeOH): 9.11 ppm (1H, s); 9.06 ppm (1H, s); 8.32 ppm (2H, m); 8.26 ppm (1H, d); 8.20 ppm (1H, d), 7.48 ppm (2H, m); 7.29 ppm (2H, q); 6.80 ppm (2H, dd).

$Y_2Ga_8(mishi)_8(iph)_4Na_2(DMF)_{12}(H_2O)_4$, **Y-I$_8$.** The percent yield was 24% based on yttrium nitrate hexahydrate. Elemental analysis of $Y_2Ga_8Na_2C_{124}H_{132}N_{20}O_{56}I_8$ [fw = 4595.31 g/mol] found % (calculated): C, 32.36 (32.41); H, 2.89 (2.90); N, 6.04 (6.10). ESI-MS, calculated $Y_2Ga_8C_{88}H_{40}N_8O_{40}I_8$ $[M]^{2-}$: 1799.29, found 1800.28. 1H-NMR (500 mHz, d4-MeOH): 9.07 ppm (1H, d), 8.32 ppm (2H, m), 8.25 ppm (1H, d), 8.20 ppm (1H, d), 7.48 ppm (2H, d), 7.30 ppm (1H, q), 6.80 ppm (2H, d).

$Pr_2Ga_8(mishi)_8(iiph)_4Na_2(DMF)_{14}(H_2O)_4$, **Pr-I$_{12}$.** The percent yield was 29% based on praseodymium nitrate hexahydrate. Elemental analysis of $Pr_2Ga_8Na_2C_{130}H_{142}N_{22}O_{58}I_{12}$ [fw = 5349.09 g/mol] found % (calculated): C, 29.25 (29.19); H, 2.79 (2.68); N, 5.77 (5.76). ESI-MS, calculated $Pr_2Ga_8C_{88}H_{36}N_8O_{40}I_{12}$ $[M]^{2-}$: 2103.09, found 2104.08.

$Nd_2Ga_8(mishi)_8(iiph)_4Na_2(DMF)_{14}(H_2O)_5$, **Nd-I$_{12}$.** The percent yield was 32% based on neodymium nitrate hexahydrate. Elemental analysis of $Nd_2Ga_8Na_2C_{130}H_{144}N_{22}O_{59}I_{12}$ [fw = 5373.78 g/mol] found % (calculated): C, 29.15 (29.06); H, 2.89 (2.70); N, 5.78 (5.73). ESI-MS, calculated $Nd_2Ga_8C_{88}H_{36}N_8O_{40}I_{12}$ $[M]^{2-}$: 2105.09, found 2107.08.

$Sm_2Ga_8(mishi)_8(iiph)_4Na_2(DMF)_{12}(H_2O)_2$, **Sm-I$_{12}$.** The percent yield was 32% based on samarium nitrate hexahydrate. Elemental analysis of $Sm_2Ga_8Na_2C_{124}H_{124}N_{20}O_{54}I_{12}$ [fw = 5185.78

g/mol] found % (calculated): C, 28.76 (28.72); H, 2.46 (2.41); N, 5.36 (5.40). ESI-MS, calculated $Sm_2Ga_8C_{88}H_{36}N_8O_{40}I_{12}$ $[M]^{2-}$: 2115.10, found 2114.08. ^{1}H-NMR (500 MHz, d_6-DMSO): 8.51 ppm (1H, d); 8.42 ppm (1H, s); 8.12 ppm (2 H, m); 7.46 ppm (2H, d), 6.78 ppm (2H, d), 5.41 ppm (1H, d).

$Eu_2Ga_8(mishi)_8(iiph)_4Na_2(DMF)_{10}(H_2O)_7$, **Eu-I$_{12}$.** The percent yield was 28% based on europium nitrate hexahydrate. Elemental analysis of $Eu_2Ga_8Na_2C_{118}H_{120}N_{18}O_{57}I_{12}$ [fw = 5132.87 g/mol] found % (calculated): C, 27.76 (27.61); H, 2.58 (2.36); N, 4.75 (4.91). ESI-MS, calculated $Eu_2Ga_8C_{88}H_{36}N_8O_{40}I_{12}$ $[M]^{2-}$: 2114.10, found 2114.09.

$Gd_2Ga_8(mishi)_8(iiph)_4Na_2(DMF)_{16}(H_2O)_5$, **Gd-I$_{12}$.** The percent yield was 34% based on gadolinium nitrate hexahydrate. Elemental analysis of $Gd_2Ga_8Na_2C_{136}H_{158}N_{24}O_{61}I_{12}$ [fw = 5545.98 g/mol] found % (calculated): C, 29.44 (29.45); H, 2.91 (2.87); N, 5.96 (6.06). ESI-MS, calculated $Gd_2Ga_8C_{88}H_{36}N_8O_{40}I_{12}$ $[M]^{2-}$: 2121.11, found 2120.09.

$Tb_2Ga_8(mishi)_8(iiph)_4Na_2(DMF)_{13}(H_2O)_5$, **Tb-I$_{12}$.** The percent yield was 33% based on terbium nitrate pentahydrate. Elemental analysis of $Tb_2Ga_8Na_2C_{127}H_{137}N_{21}O_{58}I_{12}$ [fw = 5330.05 g/mol] found % (calculated): C, 28.64 (28.62); H, 2.61 (2.59); N, 5.44 (5.52). ESI-MS, calculated $Tb_2Ga_8C_{88}H_{36}N_8O_{40}I_{12}$ $[M]^{2-}$: 2121.11, found 2122.09.

$Dy_2Ga_8(mishi)_8(iiph)_4Na_2(DMF)_{14}(H_2O)_4$, **Dy-I$_{12}$.** The percent yield was 35% based on dysprosium nitrate pentahydrate. Elemental analysis of $Dy_2Ga_8Na_2C_{130}H_{142}N_{22}O_{58}I_{12}$ [fw = 5392.28 g/mol] found % (calculated): C, 29.02 (28.96); H, 2.61 (2.65); N, 5.65 (5.71). ESI-MS, calculated $Dy_2Ga_8C_{88}H_{36}N_8O_{40}I_{12}$ $[M]^{2-}$: 2125.11, found 2125.09.

$Ho_2Ga_8(mishi)_8(iiph)_4Na_2(DMF)_{14}(H_2O)_5$, **Ho-I$_{12}$.** The percent yield was 30% based on holmium nitrate pentahydrate. Elemental analysis of $Ho_2Ga_8Na_2C_{130}H_{144}N_{22}O_{59}I_{12}$ [fw = 5415.15 g/mol] found % (calculated): C, 28.89 (28.83); H, 2.71 (2.68); N, 5.60 (5.69). ESI-MS, calculated $Ho_2Ga_8C_{88}H_{36}N_8O_{40}I_{12}$ $[M]^{2-}$: 2127.11, found 2128.09.

$Er_2Ga_8(mishi)_8(iiph)_4Na_2(DMF)_{14}(H_2O)_7$, **Er-I$_{12}$.** The percent yield was 33% based on erbium nitrate pentahydrate. Elemental analysis of *$Er_2Ga_8Na_2C_{130}H_{148}N_{22}O_{61}I_{12}$* [fw = 5455.84 g/mol] found % (calculated): C, 28.66 (28.62); H, 2.71 (2.73); N, 5.55 (5.65). ESI-MS, calculated *$Er_2Ga_8C_{88}H_{36}N_8O_{40}I_{12}$* $[M]^{2-}$: 2129.11, found 2130.09.

$Tm_2Ga_8(mishi)_8(iiph)_4Na_2(DMF)_{14}(H_2O)_5$, **Tm-I$_{12}$.** The percent yield was 30% based on thulium nitrate pentahydrate. Elemental analysis of *$Tm_2Ga_8Na_2C_{130}H_{144}N_{22}O_{59}I_{12}$* [fw = 5423.16 g/mol] found % (calculated): C, 29.00 (28.79); H, 2.81 (2.68); N, 5.68 (5.68). ESI-MS, calculated *$Tm_2Ga_8C_{88}H_{36}N_8O_{40}I_{12}$* $[M]^{2-}$: 2131.11, found 2132.09.

$Yb_2Ga_8(mishi)_8(iiph)_4Na_2(DMF)_{14}(H_2O)_4$, **Yb-I$_{12}$.** The percent yield was 35% based on ytterbium nitrate pentahydrate. Elemental analysis of *$Yb_2Ga_8Na_2C_{130}H_{142}N_{22}O_{58}I_{12}$* [fw = 5413.39 g/mol] found % (calculated): C, 28.86 (28.84); H, 2.59 (2.64); N, 5.59 (5.69). ESI-MS, calculated *$Yb_2Ga_8C_{88}H_{36}N_8O_{40}I_{12}$* $[M]^{2-}$: 2135.12, found 2136.10.

$Lu_2Ga_8(mishi)_8(iiph)_4Na_2(DMF)_8(H_2O)_4$, **Lu-I$_{12}$.** The percent yield was 4% based on lutetium nitrate pentahydrate. Elemental analysis of *$Lu_2Ga_8Na_2C_{112}H_{100}N_{16}O_{52}I_{12}$* [fw = 4978.64 g/mol] found % (calculated): C, 26.93 (27.02); H, 1.93 (2.02); N, 4.41 (4.50). ESI-MS, calculated *$Lu_2Ga_8C_{88}H_{36}N_8O_{40}I_{12}$* $[M]^{2-}$: 2137.12, found 2137.11. ^{1}H-NMR (500MHz, *d_6*-DMSO): 8.68 ppm (1H, d), 8.05-8.20 ppm (4H, m); 7.42 ppm (2H, d), 6.72 ppm (2H, t).

$Y_2Ga_8(mishi)_8(iiph)_4Na_2(DMF)_{15}(H_2O)_5$, **Y-I$_{12}$.** The percent yield was 33% based on yttrium nitrate pentahydrate. Elemental analysis of *$Y_2Ga_8Na_2C_{133}H_{151}N_{23}O_{60}I_{12}$* [fw = 5336.20 g/mol] found % (calculated): C, 30.05 (29.94); H, 2.86 (2.85); N, 5.89 (6.04). ESI-MS, calculated *$Y_2Ga_8C_{88}H_{36}N_8O_{40}I_{12}$* $[M]^{2-}$: 2051.09, found 2052.08. ^{1}H-NMR (500 MHz, *d_6*-DMSO): 8.69 ppm (1H, d); 8.05-8.20 ppm (4H, m), 7.41 ppm (2H, d), 6.72 ppm (2H, t).

$Sm(OBz)_4[12\text{-}MC_{Ga^{III}N(mishi)}\text{-}4]Na$. First, 0.25 mmol of $Sm(NO_3)_3{\cdot}6H_2O$ (0.1111 g, 1 equiv.) and 0.5 mmol of $Ga(NO_3)_3$ (0.1279 g, 2 equivs.) was dissolved in 5 mL of methanol to form a clear and colorless solution. Separately, 0.5 mmol of H_3mishi (0.1395 g, 2 equivs.) and 2.0 mmol of sodium benzoate (0.2442 g, 8 equivs.) were dissolved in 15 mL of methanol to form a clear and

faintly yellow solution. The solutions were combined and let stir for approximately one hour, and then gravity filtered. The filtrate was allowed to slowly evaporate with an aluminum foil cover that had one hole poked on top. The following day the filtrate was gravity filtered to remove a fine colorless precipitate and the filtrate was allowed to continue to slowly evaporate with the aluminum cover. Faintly yellow crystalline needles or plates were observed after 1 week and collected by vacuum filtration.

Sm(mishi)$_4$(OBz)$_{3.75}$(NO$_3$)$_{0.25}$Na(H$_2$O), **SmGa$_4$-I$_4$**. The percent yield was 18% based on 5-iodosalicylhydroxamic acid. Elemental analysis of SmGa$_4$C$_{54.25}$H$_{32}$N$_{4.25}$O$_{21.25}$I$_4$Na [fw = 2043.22 g.mol] found % (calculated): %C 31.91 (31.87); %H 1.57 (1.72); %N 3.13 (2.92). ESI-MS, calculated *SmGa$_4$C$_{56}$H$_{32}$N$_4$O$_{20}$I$_4$* [M]$^-$: 2107.40, found 2109.41. 1H NMR (400 MHz, d4-MeOH): 8.40 ppm (1H, broad s), 7.81 ppm (2H, broad s), 8.52 ppm (1H, d), 7.43 ppm (1H, s), 7.26 ppm (2H, broad s), 6.86 ppm (1H, d).

General procedure for Ln(OBz)$_4$[12-MC$_{Ga}{}^{III}{}_{N(mishi)}$-4]Na, Ln = Gd, Yb, or Y. First, 0.125 mmol of Ln(NO$_3$)$_3$·xH$_2$O (1 equiv.) and 0.5 mmol of Ga(NO$_3$)$_3$ (0.1279 g, 4 equiv.) was dissolved in 5 mL of methanol to form a clear and colorless solution. Separately, 0.5 mmol of H$_3$mishi (0.1395 g, 4 equiv.) and 2.0 mmol of sodium benzoate (0.2442 g 16 equiv.) were dissolved in 15 mmol of methanol to form a clear and faintly yellow solution. The two solutions were combined and let stir for one hour. Then the reaction was gravity filtered and the filtrate was allowed to slowly evaporate with aluminum foil covers with one hole poked on top. Crystalline needles or plates were observed after approximately one week, and collected by vacuum filtration.

Gd(mishi)$_4$(OBz)$_4$Na(MeOH)$_2$, **GdGa$_4$-I$_4$**. The percent yield was 16% based on gadolinium nitrate hexahydrate. Elemental analysis of GdGa$_4$C$_{58}$H$_{40}$N$_4$O$_{22}$I$_4$Na [fw = 2111.71 g/mol] found % (calculated): %C 32.96 (32.99); %H 1.98 (1.91); %N 2.58 (2.65). ESI-MS, calculated *GdGa$_4$C$_{56}$H$_{32}$N$_4$O$_{20}$I$_4$* [M]$^-$: 2023.40, found 2023.41.

Yb(mishi)$_4$(OBz)$_3$(NO$_3$)Na, **YbGa$_4$-I$_4$**. The percent yield was 65% based on ytterbium nitrate pentahydrate. Elemental analysis of *YbGa$_4$C$_{49}$H$_{27}$N$_5$O$_{21}$I$_4$Na* [fw = 2004.32 g/mol] found %

(calculated):%C 29.68 (29.36); %H 1.43 (1.36): %N 3.88 (3.49). ESI-MS, calculated $YbGa_4C_{56}H_{32}N_4O_{20}I_4$ $[M]^-$: 2041.42, found 2039.43.

Y(mishi)$_4$(OBz)$_4$Na(MeOH)(H$_2$O)$_2$, **YGa$_4$-I$_4$**. The percent yield was 22% based on yttrium nitrate hexahydrate. Elemental analysis of $YGa_4C_{56}H_{36}N_4O_{22}I_4Na$ [fw = 2015.32 g/mol] found % (calculated): %C 33.20 (33.38); %H 1.57 (1.80); %N 2.86 (2.78). ESI-MS, calculated $YGa_4C_{56}H_{32}N_4O_{20}I_4$ $[M]^-$: 1954.39, found 1956.39. 1H-NMR (400 MHz, d4-MeOH): 8.36 ppm (1H, d), 8.01 ppm (2H, broad s), 7.51 ppm (1H, dd), 7.46 ppm (1H, broad s), 7.32 ppm (1H, broad s), 6.83 ppm (1H, d).

Physical Methods. ESI-QTOF MS was performed on an Agilent 6520 Accurate-Mass Q-TOF LC/MS quadrupole time of flight mass spectrometer in negative ion mode with a fragmentation voltage of 250 V. Samples were prepared by dissolving approximately 1 mg of compound in 1 mL of methanol, then diluting 20 µL of the solution into another 1 mL of methanol. Samples were directly injected using a syringe (without the HPLC or autosampler). Data were processed with Agilent MassHunter Qualitative Analysis software. Elemental analysis was performed on a Carlo Erba 1108 elemental analyzer and a PerkinElmer 2400 elemental analyzer by Atlantic Microlabs, Inc.

Proton Nuclear Magnetic Resonance. ^{1}H NMR spectra were collected using a 400 MHz Varian MR400 spectrometer. Solutions were prepared in d_6-DMSO or d_4-MeOH and collected using a standard pulse sequence for 45^o excitation. Spectra were processed using MestraNOVA 6.0 software.

Pulsed Gradient Spin Echo Diffusion Ordered Spectroscopy (PGSE-DOSY). Diffusion coefficients were determined on a 500 MHz Varian vnmrs 500 spectrometer in solutions of d_4-MeOH. A double pulsed field gradient stimulated echo sequence was used which included convection compensation[33], a relaxation delay of 1.5 seconds, a gradient pulse of 1.1 or 1.5 ms, diffusion delay of 120 ms, and an array of 16 gradient strengths from 1.5 T/m to 1000 T/m in approximately 66.6 T/m increments. Spectra and diffusion coefficients were processed using Varian VnmrJ$_4$ software and hydrodynamic radii were determined using Stokes-Einstein

equations in Excel with the assistance of Prof. Matteo Tegoni (Appendix B, Scheme B1). Tetrakis(trimethylsilyl)silane (TMSS) was used as a standard for hydrodynamic radii determination.

X-ray Crystallography. Single crystal X-ray crystallographic data for **Sm-I$_4$**, **Sm-I$_8$**, **GdGa$_4$-I$_4$**, and **SmGa$_4$-I$_4$**, were collected at 85(2) K on an AFC10K Saturn 944+ CCD-based X-ray diffractometer equipped with a Micromax007HF Cu-target microfocus rotating anode (λ = 1.54187 Å), operated at 1200 W (40 kV, 30 mA). The data were processed using CrystalClear 2.0[34] and corrected for absorption. The structure was solved and refined using the SHELXTL (v. 6.12) software package.[35] Non-hydrogen atoms were refined anisotropically, hydrogen atoms were isotropic and placed in idealized positions.

Table 3.1 Crystallographic Data for Halogenated Metallacrowns

Metallacrown	**Sm-I$_4$**	**Sm-I$_8$**	**SmGa$_4$-I$_4$**	**GdGa$_4$-I$_4$**
Chemical Formula	$Sm_2Ga_8C_{91}H_{75}N_9O_{51}I_4Na_2$	$Sm_2Ga_8C_{86}H_{44}N_{10}O_{42}I_8Na_2$	$SmGa_4C_{61}H_{38}N_4O_{20}I_4Na$	GdGa4C56H40N4O24I4Na
Formula Weight	3522.81 g/mol	3808.95 g/mol	2106.86 g/mol	2119.72 g/mol
Crystal System, Space Group	Tetragonal, I4/m (No.87)	Triclinic, $P\bar{1}$ (No. 2)	Monoclinic, $P2_1/n$ (No.14)	Monoclinic, C2/c (No.15)
T	85(2) K	85(2) K	85(2) K	85(2) K
a	17.6823(1) Å	16.5646(2)	15.1006(1)	29.4982(6) Å
b	17.6823(1) Å	22.6005(3)	19.8977(1)	28.8988(4) Å
c	31.331(2) Å	26.6734(3)	27.7320(1)	24.0103(7) Å
α	90.00°	85.5920(10)	90.00°	90.00°
β	90.00°	72.7190(10)	103.554(1)°	109.699(3)°
γ	90.00°	84.4050(10)	90.00°	90.00°
Volume	9796.07(10) Å^3	9477.43 Å^3	8100.49 Å^3	19270.0(7) Å^3
λ	1.54184 Å	1.54184 Å	1.54184 Å	1.54184 Å
ρ_{calc}	1.194 g/cm^3	1.335 g/cm^3	1.727 g/cm^3	1.461 g/cm^3
Z	2	2	4	8
μ	21.855 mm^{-1}	33.075 mm^{-1}	19.414 mm^{-1}	32.341 mm^{-1}
F(000)	5884	7136	4032	14960
θ range	2.82° to 69.35°	1.74 to 69.88°	2.76 to 69.45°	2.57 to 69.60°
Limiting Indicies	-21 < h < 20	-20<h<20	-17<h<16	-35<h<35
	-21 < k < 21	-26<k<27	-23<k<24	-34<k<34
	-37 < l < 38	-31<l<32	-33<l<33	-28<l<28
Reflections collected/unique	76333/4675	144867/34384	122843/14910	145933/17906
Completeness to θ	99.7%	95.8%	98.1%	98.7%
No. of Data/Restraints/Params	4675/0/217	34384/16/2125	14910/0/858	17906/0/427
GooF on F^2	3.967	1.541	1.878	2.280
[a]R_1	0.1360 [I>2σ(I)]; 0.1361 [all data]	0.0624 [I>2σ(I)]; 0.0651 [all data]	0.0815 [I>2σ(I)]; 0.0819 [all data]	0.1310 [I>2σ(I)]; 0.1375 [all data]
[b]wR_2	0.4007 [I>2σ(I)]; 0.4011 [all data]	0.1947 [I>2σ(I)]; 0.2005 [all data]	0.2141 [I>2σ(I)], 0.2143 [all data]	0.3545 [I>2σ(I)]; 0.3625 [all data]
Largest Diff. Peak, Hole	9.202 e/Å^3; --2.691 e/Å^3	3.248 and -3.714 e/Å^3	3.944 and -1.184 e/Å^3	4.011 and -2.870 e/Å^3

[a] $R_1 = \Sigma(||F_o|-|F_c||)/\Sigma|F_o|$ [b] $wR_2 = [\Sigma[w(F_o^2 - F_c^2)^2]/\Sigma[w(F_o)^2]]^{1/2}$; $w = 1/[\sigma^2(F_o^2) + (mp)^2 + np]$; $p = [\max(F_o^2,0) + 2F_c^2]/3$ (m and n are constants); $\sigma = [\Sigma[w(F_o^2 - F_c^2)^2/(n-p)]^{1/2}$

Solid State Photophysical Measurements. Luminescence data were collected by Dr. Svetlana Eliseeva (unless otherwise stated) on samples in the solid state placed in 2.4 mm i.d. quartz capillaries. Emission and excitation spectra were measured on a custom-designed Horiba Scientific Fluorolog 3 spectrofluorimeter equipped with either a visible photomultiplier tube (PMT) (220-850 nm, R928P; Hamamatsu), a NIR solid-state InGaAs detector cooled to 77 K (800-1600 nm, DSS-IGA020L; Horiba Scientific), or a NIR PMT (950-1650 nm, H10330-75; Hamamatsu). Excitation and emission spectra were corrected for the instrumental functions. Luminescence lifetimes were determined under excitation at 355 nm provided by a Nd:YAG laser (YG 980; Quantel). Signals were detected in the visible or NIR ranges with the help of a Hamamatsu R928P or H10330-75 PMTs, respectively. The output signals from the detectors were fed into a 500 MHz bandpass digital oscilloscope (TDS 754C; Tektronix), transferred to a PC for data processing with the program Origin 8®. Luminescence lifetimes are averages of at least three independent measurements. Quantum yields were determined with the Fluorolog 3 spectrofluorimeter based on an absolute method with the use of an integration sphere (Model G8, GMP SA, Renens, Switzerland). Each sample was measured several times under comparable experimental conditions, varying the position of samples. Estimated experimental error for quantum yield determination is ~10 %.

Absorption Spectroscopy. Solution-state UV-vis spectra were collected on samples dissolved in methanol (approx. 100 μM) using a Cary 100Bio UV-Vis spectrophotometer in absorbance mode. Extinction coefficients were determined using the Beer-Lambert law by measuring five serial additions of the 100 mM stock to 3 mL of methanol.

X-ray Attenuation Measurements. *In vitro* measurements of X-ray attenuation were performed and analyzed by Dr. Ivana Martinic at CNRS-Orleans using a Bruker Skyscan 1278 CT. Metallacrown samples were ground and dissolved in 20 mM solutions of DMF. Scans were acquired using a source voltage of 45 kV, a source current of 996 μA, an exposure time of 25 ms, a step size of 0.5^{o} using a 360^{o} rotation. Image reconstruction was performed using Nrecon 1.6.10.6 software, including a ring artefact correction and a beam hardening correction of 35%.

Results and Discussion

Synthesis and Structure. Stoichiometric amounts of metals and ligands yielded the desired metallacrown complexes in a straightforward manner. X-ray quality crystals were obtained for **Sm-I$_4$** and **Sm-I$_8$**; however, crystals of sufficient quality could not be obtained for any **Ln-I$_{12}$**. The **Sm-I$_4$** crystallized in I_4/m with two Ln[12-MC$_{Ga}{}^{III}{}_{N(L)}$-4] motifs bridged by 5-iodoisophthalate such that each samarium is eight coordinate with a square antiprism shape (Figure 3.1c). The gallium ions are all six-coordinate and octahedral with hydroximate ligands in equatorial positions, as well as a carboxylate oxygen and solvent in the axial positions. Sodium countercations are bound to the MC in an eight-coordinate square antiprism geometry on the opposite face of the MC from the Sm^{3+}. In addition, there is a whole molecule disorder arising from diasteriomers formed from combinations of clockwise (cMC) and anticlockwise (aMC) MC enantiomers paired across the 5-iodoisophthalate bridges. This combination of diasteromers are the reason for a high R_1 value in **Sm-I$_4$**. For **GdGa$_4$-I$_4$**, the higher R_1 value is due to a large unit cell size that is likely two times larger than required.

Serendipitously, this disorder was not observed in the **Sm-I$_8$** structure which crystallized in $P\bar{1}$. It is interesting to note that the **Sm-I$_8$** structure showed two crystallographically distinct MCs where the sodium counteraction binds in two different sites (Figure 3.1a and b). The first is the eight-coordinate square antiprism motif seen in **Sm-I$_4$** and the previously reported manganese MCs, whereas the second has the sodium bound to the side of the metallacrown in a six coordinate octahedral environment. Three atoms come from solvent molecules, while the other three are the phenolic and carbonyl oxygens of the $mishi^{3-}$ in addition to a carboxylate of the iph^{2-}. ^{1}H-NMR/PGSE, ESI-MS and elemental analysis confirm that all analogs are of consistent composition in each series and differ only in number of extraneous solvent.

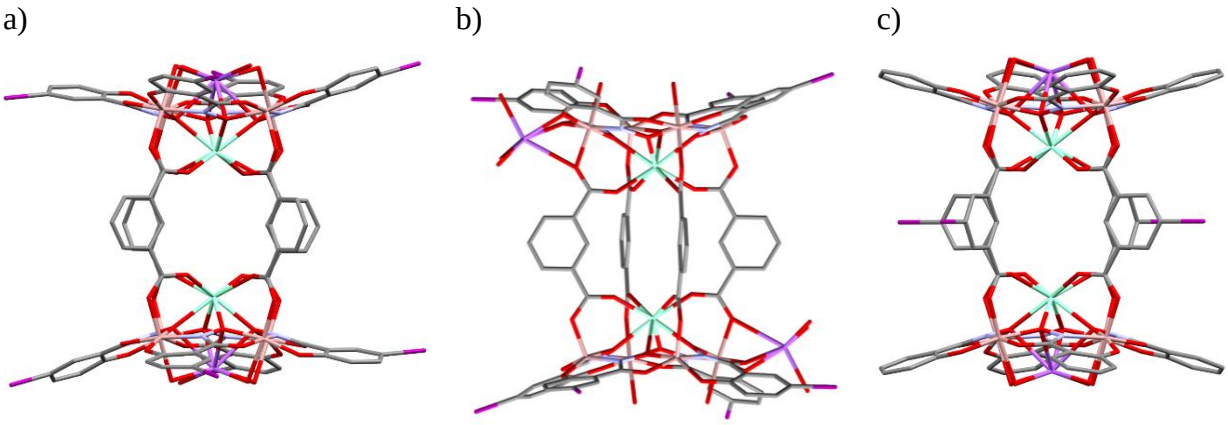

Figure 3.1 Crystal Structures of **Sm-I$_8$** with a) sodium bound below b) and to the side. c) Crystal Structure of **Sm-I$_4$**.

For the **LnGa$_4$-I$_4$**, complexes crystallographic data were obtained for **GdGa$_4$-I$_4$**, and **SmGa$_4$-I$_4$**. **GdGa$_4$-I$_4$** crystallized in C2/c with the gadolinium in an eight coordinate distorted square antiprism geometry (Figure 3.2), where the Gd is not quite in the center between the oxygen mean planes. Two gallium are six coordinate in an octahedral geometry with the equatorial positions filled by the hydroximates, and the axial positions have a carboxylate oxygen from benzoate on the same side as the lanthanide while the opposite axial site is filled by a solvent molecule. The other two are five coordinate square pyramidal. The sodium countercation is below the metallacrown ring in an eight coordinate square antiprism. This configuration is reminiscent of other 12-MC-4 complexes formed with manganese(III) reported by Zaleski and Pecoraro in 2014.[36]

The **SmGa$_4$-I$_4$** metallacrown crystallized in $P\bar{1}$ and also shows the samarium to be in an eight coordinate distorted square antiprismatic geometry (Figure 3.2), with the same kind of distortion. However, there are two distinct structural differences between **GdGa$_4$-I$_4$** and **SmGa$_4$-I$_4$**. The first is that the gallium in **SmGa$_4$-I$_4$** are all five coordinate square pyramidal where the basal ligands are the hydroximates and the apical position is filled by an oxygen from the benzoate. The second is a different binding mode for the sodium ion. In this case, the sodium is six coordinate in an octahedral environment where the phenolic oxygen of one mishi^{3-} and the carbonyl oxygen of an adjacent mishi^{3-} of one metallacrown bind to the ion, while another two equivalent oxygens from another metallacrown bind in a propeller type fashion. The final two

coordination sites are filled in by solvent molecules. The overall result is a dimerized structure in the solid state where two metallacrowns are connected by two sodium ions (Figure 3.4b).

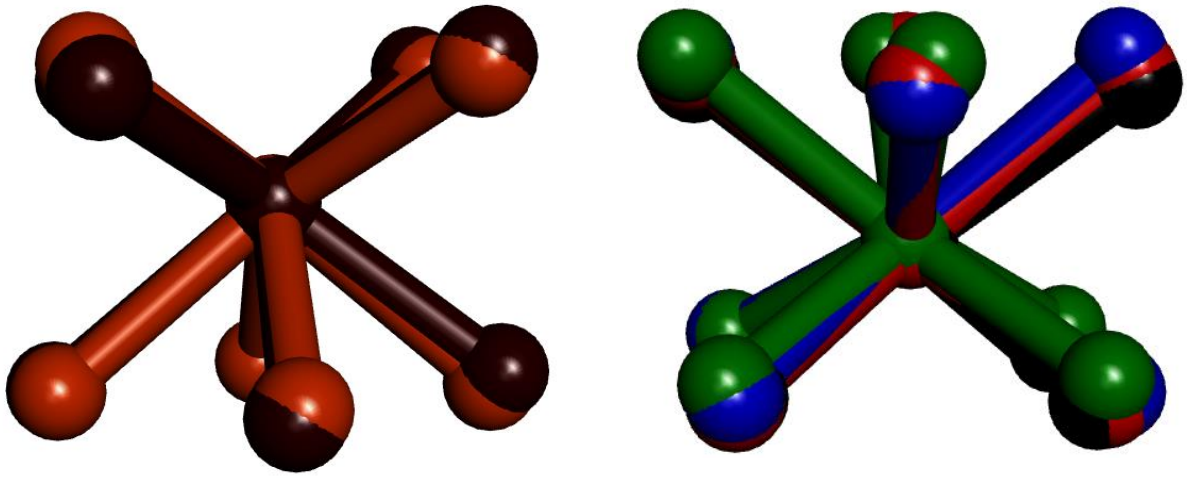

Figure 3.2. Lanthanide 1st coordination spheres of a) **GdGa$_4$-I$_4$** (orange) and **Sm-Ga$_4$-I$_4$** (brown); b) **Dy-I$_0$** (black), **Sm-I$_4$** (red), **Sm-I$_8$a** (green), **Sm-I$_8$b** (blue).

Table 3.2. Structural Parameters for Square Antiprismatically Coordinated Lanthanides.

Atom	Avg. Bond Length	Avg. O_{ox}-Ln-O_{ox} Angle	Avg. O_{cb}-Ln-O_{cb} Angle	Avg Torsion Angle	Ln-O_{ox} MP Distance	Ln-O_{cb} MP Distance	Average O-O Distance	Compression Factor[a]
Gd1 GdGa$_4$-I$_4$	2.359	100.14	125.29	43.55	1.526	1.075	2.759	0.942
Sm1 SmGa$_4$-I$_4$	2.384	102.36	127.00	49.67	1.495	1.063	2.822	0.906
Sm1 Sm-I4	2.382	103.07	126.27	47.96	1.490	1.070	2.820	0.908
Sm1 Sm-I8a	2.388	100.87	129.81	41.74	1.535	1.008	2.825	0.900
Sm2 Sm-I8b	2.383	103.78	125.91	40.27	1.470	1.087	2.833	0.903

[a] The compression factor is the sum of the Ln-O MP distances divided by the average O-O distance, which approximates a ratio between the height of the square antiprism and the average edge length.

Table 3.3. Structural Parameters for Square Pyramidally Coordinated Gallium Ions

Atom	Avg. Bond Length	Avg. Adjacent Basal bond angle	Avg. Apical to Basal Bond Angle	Large Opposite Basal Bond angle	Small Opposite Basal Bond Angle	Addison's Tau Value[37]
Ga2 $GdGa_4$-I_4	1.932	87.99	100.89	158.38	156.46	0.0320
Ga4 $GdGa_4$-I_4	1.933	89.07	97.45	164.77	162.34	0.0405
Ga1 $SmGa_4$-I_4	1.920	86.56	104.25	151.54	150.55	0.0165
Ga2 $SmGa_4$-I_4	1.925	86.68	103.90	153.74	149.30	0.0740
Ga3 $SmGa_4$-I_4	1.923	87.61	101.94	159.98	150.88	0.1517
Ga4 $SmGa_4$-I_4	1.910	86.85	103.74	156.54	147.58	0.1493
Ga6 Sm-I8b	1.925	86.89	103.62	156.02	148.38	0.1273
Ga7 Sm-I8b	1.922	87.88	101.32	161.58	151.84	0.1623

Table 3.4. Structural Parameters for Octahedrally Coordinated Gallium Ions

Atom	Avg Bond length	Avg Equitorial angle	Avg Axial to equatorial angle	Axial bond angle	Avg. Torsion angle on Pseudo-S_6	M-O_{cb} distance	M-O_{solv} Distance
Ga1 $GdGa_4$-I_4	2.020	89.31	89.96	177.68	59.93	1.964	2.405
Ga3 $GdGa_4$-I_4	1.994	89.49	90.01	178.92	59.18	1.964	2.230
Ga1 Sm-I4	2.000	89.66	89.91	175.03	60.32	1.987	2.315
Ga1	1.988	89.54	89.92	175.97	60.01	1.975	2.246

Sm-I8a							
Ga2 Sm-I8a	2.009	89.24	89.91	175.10	60.00	1.965	2.366
Ga3 SmI8a	1.991	89.74	90.06	176.55	60.73	2.000	2.207
Ga4 Sm-I8a	1.987	89.66	89.96	178.00	59.60	1.971	2.220
Ga5 Sm-I8b	1.991	89.97	89.99	177.43	61.87	2.012	2.124
Ga8 Sm-I8b	1.980	89.95	89.91	172.53	61.32	2.006	2.143

Table 3.5. Coordination Environment of Sodium Ions

Atom	Avg. Bond Length	Avg Equitorial angle	Avg Axial to equatorial angle	Axial bond angle	Avg. Torsion angle on Pseudo-S_6	Shape
Na1 $SmGa_4$-I_4	2.414	93.08	89.72	170.62	59.89	Octahedral
Na2 Sm-I_8b	2.461	88.46	89.14	163.70	59.95	Octahedral

Atom	Avg. Bond Length	Avg. O_{ox}-Na-O_{ox} Angle	Avg. O_{solv}-Na-O_{solv} Angle	Avg Torsion Angle	Na-O_{ox} MP Distance	Na-O_{solv} MP Distance	Average O-O Distance	Compression Factor	Shape
Na1 $GdGa_4$ -I_4	2.624	86.51	154.57	61.06	1.941	0.571	3.073	0.817	Square antiprism
Na1 Sm-I_4	2.589	88.26	151.56	62.33	1.933	0.608	3.022	0.841	Mono-capped square antiprism
Na1 Sm-I_8a	2.546	89.60	150.00	62.12	1.871	0.635	2.991	0.838	Square antiprism

The new MC variants of the {Ln[12-MC$_{Ga}^{III}{}_{N(L)}$-4]Na}L'$_4$ are essentially isostructural not only to each other, but also to the parent structure previously reported by Pecoraro and coworkers (hereafter referred to as **Ln-I$_0$**).[4] **Ln-I$_0$** differs only by absence of iodine on the ligands and the use of an ammonium countercation rather than a sodium countercation. An overlay of **Dy-I$_0$**, **Sm-I$_4$**, and **Sm-I$_8$a/b** confirms there is little structural change (Figure 3.3). Therefore, **Ln-I$_0$** will be used as a part of the analysis of the effects of increasing iodine content on optics, photophysical parameters, and as potential X-ray attenuating contrast agents in computed tomography.

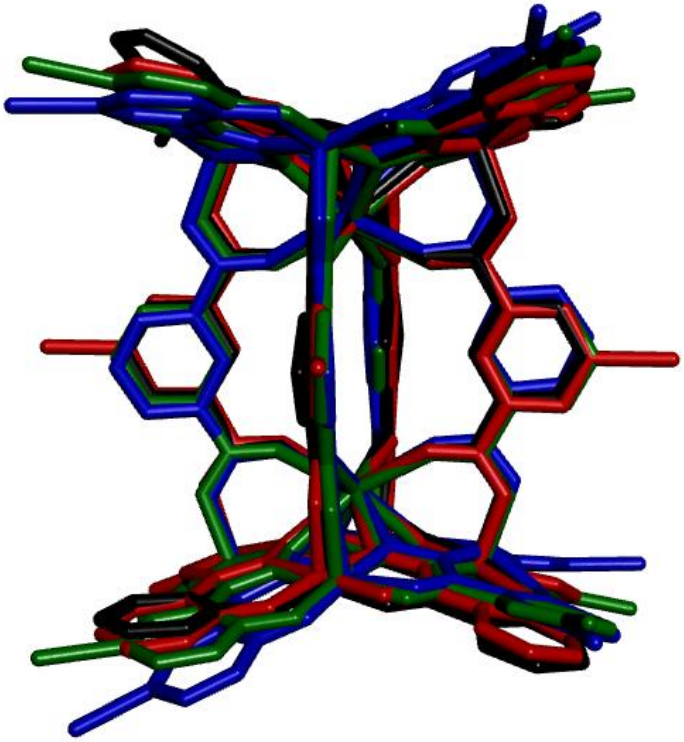

Figure 3.3. Structural overlay of **Dy-I$_0$** (black), **Sm-I$_4$** (red), **Sm-I$_8$a** (green), and **Sm-I$_8$b** (blue) shows little change to the overall structure.

The synthesis of each series ranging from I_0 to I_{12} species also speaks to the capability of rational modification on the {Ln[12-MC$_{Ga}^{III}{}_{N(L)}$-4]Na}L'$_4$ structure, a concept commonly displayed by metallacrowns. The 12-MC-4 with benzoate shows more flexibility with respect to sodium binding and overall bowling of the MC. The reason for this change in binding is likely related to lanthanide size within the central metallacrown cavity. An overlay of both **GdGa$_4$-I$_4$** and **SmGa$_4$-I$_4$** structures (Figure 3.4c) shows that there is significantly more bowling in the **SmGa$_4$-**

I_4 structure due to the increase in Sm-O bonds compared to Gd-O bonds. This bowling pulls the oxime oxygens more towards the convex side of the bowled metallacrown and thus less accessible for sodium binding. Therefore, the sodium binds on the side of the metallacrown instead. If one thinks back to the **Sm-I_8** structure the sodium countercation binds in two different ways, which results in two crystallographically distinct metallacrowns. An overlay of **Sm-I_8** (where Na is below the MC) and **SmGa_4-I_4** does not show a marked difference in the extent of bowling, however, these structures have one key difference. In **SmGa_4-I_4**, the gallium are five coordinate, while **Sm-I_8** has gallium that are six coordinate. To understand these structures a closer analysis is required.

To assess the extent of bowling mathematically a few different criteria were considered. In the past for Mn^{3+} structures the metallacrown planarity was described as the difference between the oxime oxygen (O_{ox}) mean plane (MP) and the manganese MP. In these cases, this was a fair measurement since the Mn^{3+} were all octahedral with an axial Jahn-Teller distortion. However, in Ga^{3+} metallacrowns, the gallium is not always the same coordination number, so comparing a five coordinate to a six coordinate gallium will not appropriately describe the deviation from planarity of the metallacrown since five coordinate gallium will be slightly above the basal plane of the square pyramidal shape, while a six coordinate octahedral gallium will be in this plane. Therefore, I proposed two other parameters as better metrics. These are the **average angle of deviation** from the O_{ox} MP for the hydroximate ligand and the **distance between the O_{ox} and carbonyl oxygen (O_{cb}) MPs** of the hydroximate. The angle of deviation is calculated by measuring the angle between the O_{ox}, O_{cb} and pseudo-C_4 axis. The MP distance is straightforward to calculate and may be done so just as the distance between O_{ox} MP and Mn^{3+} MP were in work reported by Zaleksi and Pecoraro. Table 3.6 summarizes these values for all four structures given in this chapter. The bond to a solvent molecule in the six coordinate gallium(III) is longer than the bond to the carboxylate oxygen, likely to compromise between the binding to both gallium(III) and sodium (I) in the structure.

Based on these calculations, the binding of sodium may be explained for each structure type. To start, structural comparison of **SmGa_4-I_4** and **Sm-I_8a** (Na below) reveals that there is less bowling in **Sm-I_8a**. This is also the case when comparing **Sm-I_4** to **SmGa_4-I_4**. This slight change may be just enough to discourage sodium binding below the MC in the case of **SmGa_4-I_4**. Finally, when comparing **GdGa_4-I_4** to **SmGa_4-I_4**, there is also less bowling in the case of Gd

compared to Sm. So it seems that the extent of bowling in the structure effects the availability of the oxime oxygens to bind a sodium and in the case of **SmGa$_4$-I$_4$** and **Sm-I$_8$b** it is no longer possible to bond an Na(I) below the ring.

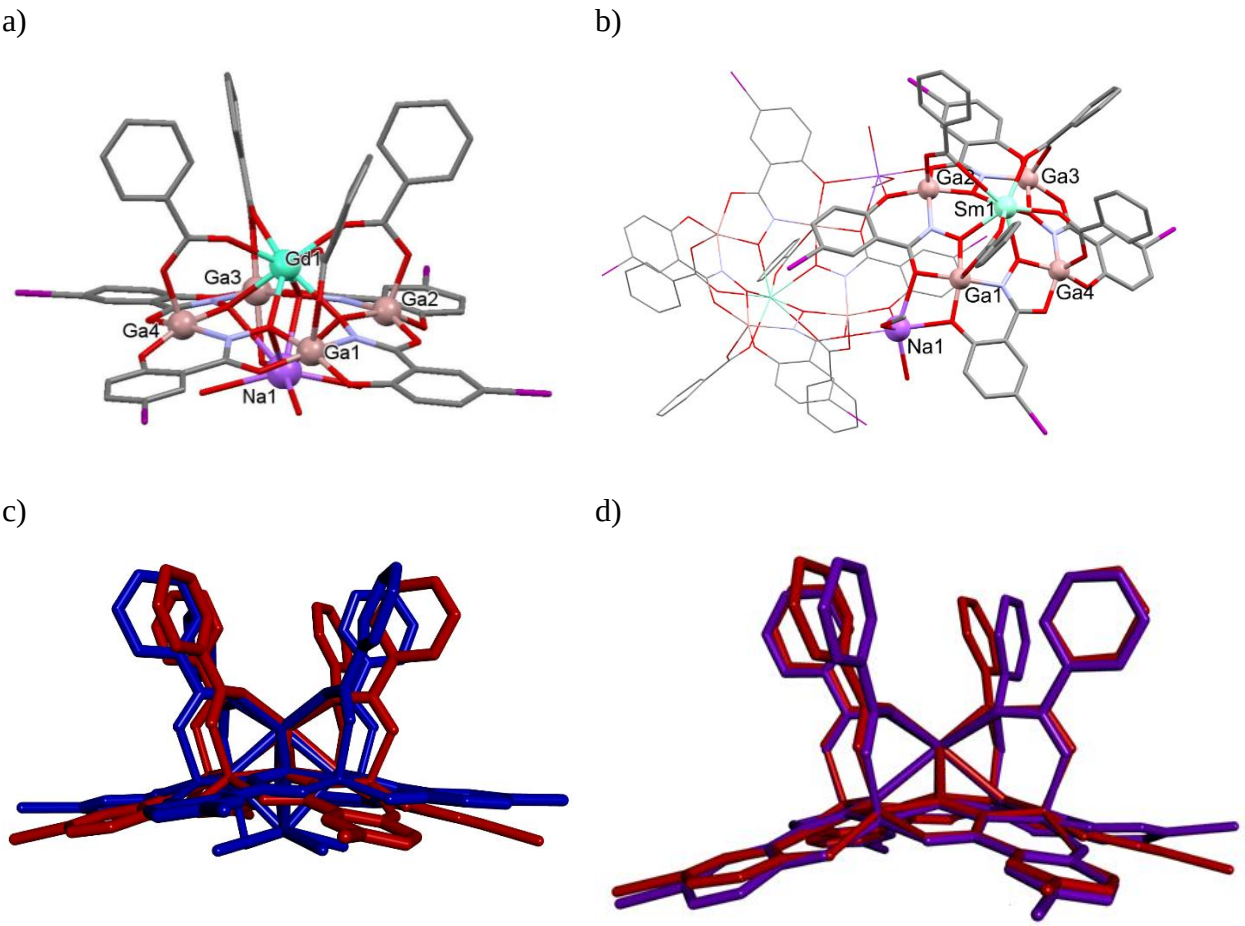

Figure 3.4 Crystal Structures of a) **GdGa$_4$-I$_4$**, b) **SmGa$_4$-I$_4$**, c) overlay of **GdGa$_4$-I$_4$** (blue) and **Sm-Ga$_4$-I$_4$** (red), d) overlay of **SmGa$_4$-I$_4$** (red) and **Sm-I$_8$** (purple). Only one MC of **Sm-I$_8$** and comparable atoms of iph^{2-} were included to allow clarity.

Table 3.6. Measurements for the Extent of Bowling in Iodinated Metallacrowns

Metallacrown	O_{ox} to O_{cb} MP distance/Å	Avg Angle of Deviation
Sm-I$_4$	0.736	17.28^o
Sm-I$_8$a	0.781	18.22^o
Sm-I$_8$b	0.882	19.22^o
SmGa$_4$-I$_4$	0.938	22.33^o
GdGa$_4$-I$_4$	0.646	15.08^o

^{1}H-NMR and pulsed gradient spin echo diffusion ordered spectroscopy (PGSE-DOSY) experiments were performed on **Ln-I$_4$**, **Ln-I$_8$**, **Ln-I$_{12}$**, and **LnGa$_4$-I$_4$** (Ln = Y, Sm, Lu). The ^{1}H-NMR of each species in d$_4$-MeOH, (Appendix B, Figs. B5 through B16) shows the expected signals for pseudofour-fold symmetry. In the case of the **Ln-I$_4$**, **Ln-I$_8$** and **Ln-I$_{12}$**, the presence of the diastereomers seen in crystallography is observable in **Ln-I$_4$** and **Ln-I$_8$** species as roughly equivalent concentrations using ^{1}H-NMR via peak doubling. PGSE-DOSY experiments (Table 3.7) on different Ln sizes in **Ln-I$_x$** with little to no paramagnetic contributions (Sm, Y, and Lu) were performed to access MC stability in methanol. This technique is used to determine the hydrodynamic radius (r_H) of a molecule by relating the diffusion of the compound of interest to a standard such as tetrakis(trimethylsilyl)silane. This technique may be used to analyze small molecule binding, coordination complexes, and even proteins such as myoglobin.[38–41] Overlapping peak signals were not integrated to be sure that only signal from one ligand was examined in each r_H calculation. Since this experiment is intended to assess solution state stability of the metallacrowns, this precaution allows one to compare the diffusion of a carboxylate proton to a hydroximate proton. If these two protons from different ligands give the same diffusion coefficient and thus the same r_H, then the complex may be considered thermodynamically stable since all protons are diffusing together. If there is disagreement, then the complex is not stable since there is a population of the ligand that is not bound to the metallacrown, usually observed as an artificially small r_H. Since there are consistent hydrodynamic radii values for all **Y-I$_x$** MC protons (Figure 3.6, Table 3.7) in each system it appears that these compounds are stable in methanol. However, for **LnGa$_4$-I$_4$**, the PGSE-DOSY shows an apparently smaller hydrodynamic radius for benzoate protons (Figure 3. 5, Table 3.7), which suggests that there is dissociation of the benzoate bridges in methanol. Upon addition of excess benzoate (see Appendix B, Figure B16), the peaks sharpen and also give an even larger disparity in r_H, which suggests that this instability is due to a thermodynamic equilibrium of bound and free benzoate. Therefore, the **Ln-I$_x$** metallacrowns were chosen for more comprehensive study thanks to greater solution state stability.

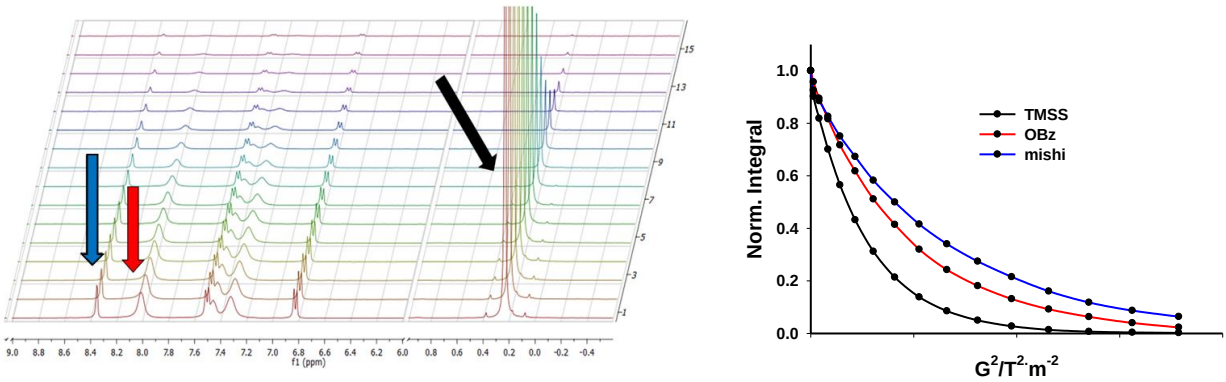

Figure 3.5. PGSE-DOSY on **YGa$_4$-I$_4$** shows a significant difference in diffusion of OBz$^-$ protons (red) compared to mishi^{3-} protons (blue). TMSS is indicated in black.

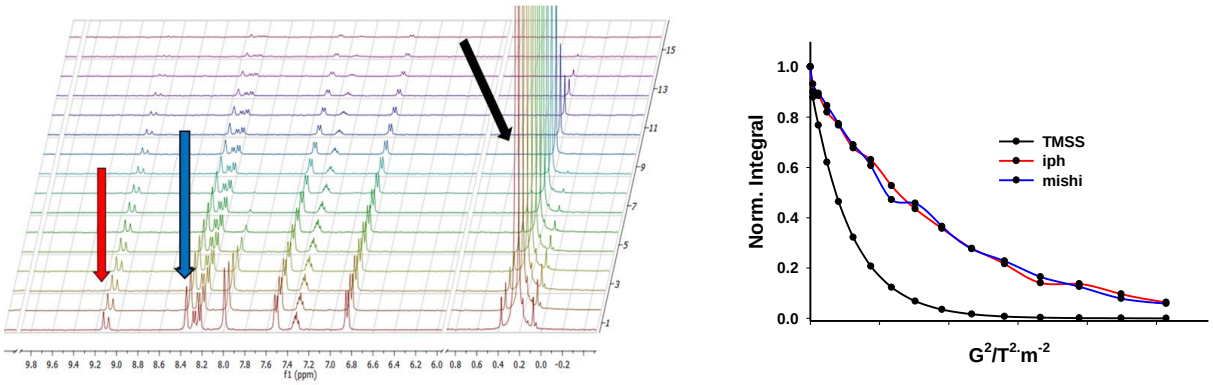

Figure 3.6. PGSE-DOSY on **Y-I$_8$** shows little difference in diffusion when comparing iph^{2-} protons (red) to mishi^{3-} protons (blue). TMSS is indicated in black.

Table 3.7. Calculated Hydrodynamic Radii of Halogenated Metallacrowns. Hydroximate Protons are Marked with an H and Carboxylate Protons are Marked with a C.

Metallacrown	**Peak positions/ppm**	**Diffusion Coefficient/ 10^{-10} $m^2 \cdot s^{-1}$**	**r_H/Å[a]**
Sm-I$_4$	C-8.93	3.27(10)	11.09(106)
	C-8.88	3.58(21)	10.18(178)
	H-8.13	3.43(9)	10.59(87)
	H-7.28	3.42(12)	10.63(117)
	H-7.06	3.34(9)	10.86(92)
	H-6.81	3.35(8)	10.83(83)
	C-5.12	3.16(27)	11.43(294)
Y-I$_4$	C-8.98	3.44(31)	10.65(286)
	C-8.56	4.19(20)	8.86(123)
	H-8.09	3.32(19)	10.99(188)
	H-7.26	3.34(16)	10.94(152)

	H-7.01 H-6.78	3.33(16) 3.32(10)	10.93(163) 11.05(102)
Lu-I_4	C-9.02 C-8.97 C-8.56 C-8.51 H-8.09 H-7.27 H-7.02 H-6.79	3.39(15) 3.46(11) 3.24(4) 3.40(6) 3.28(3) 3.18(2) 3.26(3) 3.22(3)	10.18(103) 9.97(95) 10.63(41) 10.13(53) 10.48(25) 10.78(20) 10.56(28) 10.67(25)
Sm-I_8	C-8.71 C-8.61 H-8.36 H-7.59 C-7.48 H-6.86	3.12(3) 3.36(4) 3.14(2) 3.17(4) 3.14(2) 3.08(2)	10.96(58) 9.62(55) 10.56(51) 10.81(53) 10.70(28) 10.97(43)
Y-I_8	C-9.10 C-9.06 C-8.33 H-8.26 H-8.21 H-7.49 C-7.31 H-6.82	3.37(4) 3.39(4) 3.21(1) 3.29(3) 3.42(3) 3.30(2) 3.37(4) 3.22(2)	10.37(34) 10.32(35) 10.86(21) 10.62(32) 10.22(27) 10.58(22) 10.38(35) 10.81(26)
Lu-I_8	C-8.32 H-8.26 H-8.20 H-7.49 C-7.29 H-6.81	3.07(10) 3.54(23) 3.54(24) 3.21(11) 3.44(29) 3.14(11)	10.62(106) 9.29(173) 9.29(179) 10.17(104) 9.54(224) 10.39(105)
Sm-I_{12}[b]	C-8.42 H-8.13 H-7.45 H-6.78	0.84(5) 1.00(4) 0.76(5) 0.93(6)	12.52(135) 10.67(85) 13.70(152) 11.47(119)
Y-I_{12}[b]	C-8.72 C-8.66 C/H-8.11 H-7.42 H-6.72	0.76(8) 0.92(15) 0.98(3) 1.00(5) 0.91(6)	15.22(338) 12.66(378) 11.98(131) 11.71(145) 12.82(190)
$SmGa_4$-I_4	H-8.38 C-7.29 H-6.83	4.52(15) 6.23(23) 4.32(8)	7.80(79) 5.90(62) 8.10(57)
YGa_4-I_4	H-8.33 C-8.00 C-7.30 H-6.80	4.40(4) 5.97(4) 5.80(8) 4.34(2)	8.36(25) 6.38(13) 6.53(25) 8.45(14)

	H-8.33	4.31(3)	8.02(26)
	C-7.95	7.41(4)	5.06(14)
YGa_4-I_4	H-7.49	4.49(7)	7.73(40)
Ex. NaOBz	C-7.40	7.13(10)	5.22(22)
	C-7.30	7.32(15)	5.11(28)
	H-6.80	4.03(3)	8.49(30)

[a] Hydrodynamic radii were calculated with the assistance of Prof. Matteo Tegoni using Stokes Einstein equations and r_H(MeOH) = 2.48 Å and r_H(TMSS) = 4.24 Å.[41] For details see Appendix D.

[b] Due to solubility restrictions Ln-I_{12} MCs were examined in DMSO (r_H = 2.72), which changes the r_H of TMSS to 4.28 Å.[41] The **Lu-I_{12}** could not give a strong enough signal for PGSE-DOSY.

Absorption Spectroscopy of Iodinated Metallacrowns

Solution state UV-Vis spectroscopy shows how the incorporation of iodine alters the optical properties of each series. Each **Ln-I_x** series show a consistent spectral profile across their lanthanide analogs (Figures 3.7, 8, and 9); however, comparison of optical properties spanning **Sm-I_0** to **Sm-I_{12}** demonstrates the effects of the incorporation of iodine onto each of the ligands (Figure 3.12). The UV-Vis spectra of **Sm-I_0** and **Sm-I_4** are essentially identical, where these structures only differ by inclusion of iodine onto the iph^{2-}. However, if **Sm-I_0** and **Sm-I_8** are compared, which differ by inclusion of iodine onto shi^{3-}, there is a shift in the π- π^* transition λ_{max} from 310 nm (32,258 cm^{-1}) to 325 nm (30,769 cm^{-1}). In addition, the extinction coefficient decreases slightly from about 40,000 $M^{-1}\cdot cm^{-1}$ to approximately 35,000 $M^{-1}\cdot cm^{-1}$. This suggests that the incorporation of iodine onto the scaffold only significantly red shifts the lowest energy band absorbance if the shi^{3-} ligand is substituted. The spectrum of **Sm-I_{12}** confirms this hypothesis, since the profile is essentially identical to **Sm-I_8**, demonstrating that the inclusion of iodine onto the iph^{2-} in addition to the shi^{3-} does not alter the optics any further.

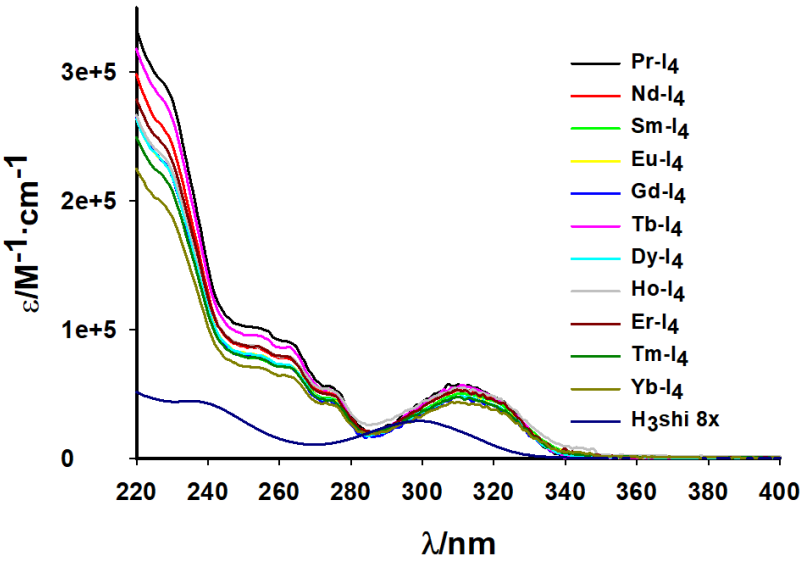

Figure 3.7. UV-Vis spectra of **Ln-I₄** MCs in MeOH at RT at concentrations of 1-10 µM.

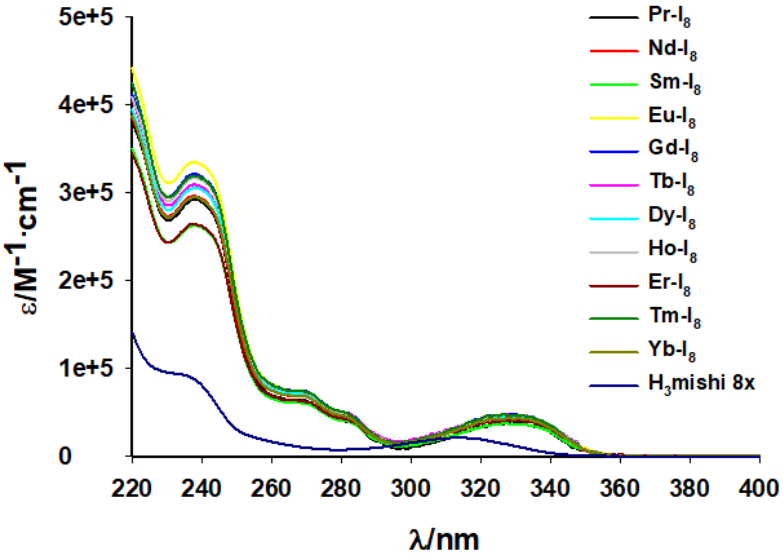

Figure 3.8. UV-Vis spectra of **Ln-I₈** MCs in MeOH at RT at concentrations of 1-10 µM.

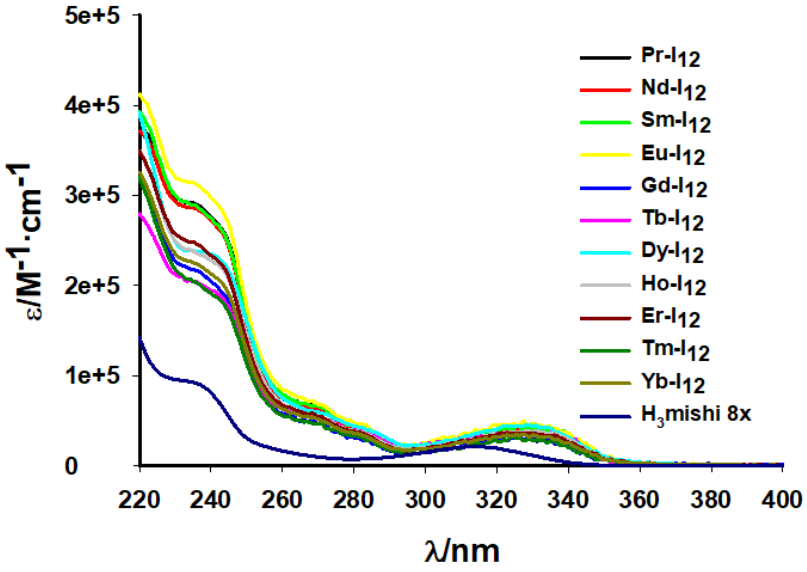

Figure 3.9. UV-Vis spectra of **Ln-I$_{12}$** MCs in MeOH at RT at concentrations of 1-10 µM.

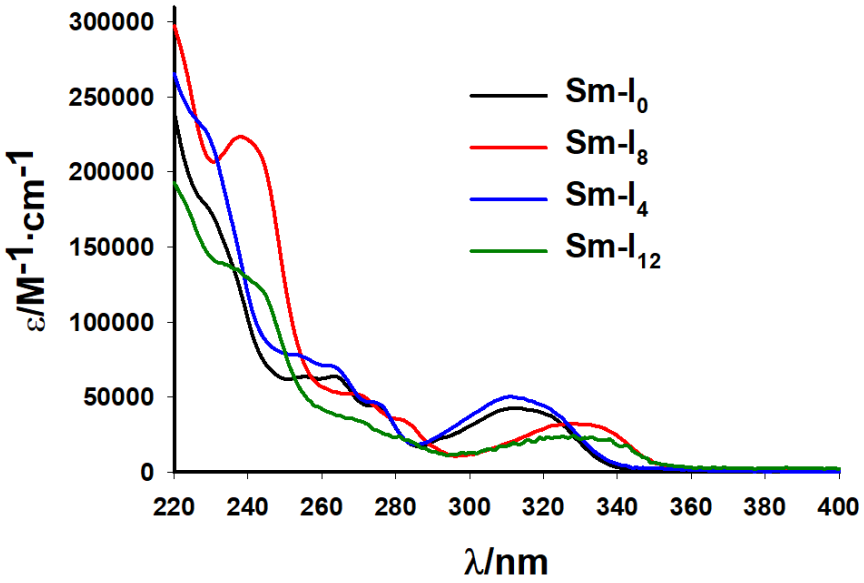

Figure 3.10 Comparison of UV-Vis spectra of **Sm-I$_X$** (X = 0 (black), 4 (blue), 8 (red), and 12 (green)) in MeOH at RT.

Photophysical Measurements of Iodinated Metallacrowns

The solid state excitation and emission spectra for luminescent Ln-Ix species were collected and analyzed by Dr. Eliseeva. Of the lanthanides, sensitization was shown for Pr^{3+}, Nd^{3+}, Sm^{3+}, Tb^{3+}, Dy^{3+}, Ho^{3+}, Er^{3+}, and Yb^{3+}. Figure 3.11 shows the characteristic emission spectra of the **Ln-I$_4$**, **Ln-I$_8$**, and **Ln-I$_{12}$** series. The excitation spectra show excitation due to the antenna effect (as a smooth broad band) out to 355 nm (28,169 cm^{-1}) for the **Ln-I$_4$** metallacrowns. The **Ln-I$_8$** and **Ln-I$_{12}$** metallacrowns extend further with antenna effect excitation out to about 380 nm (26,316 cm^{-1}). This red shift tracks with the redshift in absorption from the mishi^{3-} ligand.

Solid state spectra of **Ln-I$_x$** complexes shows that the iodine on the isophthalate is not innocent in terms of lanthanide sensitization. Comparison of excitation spectra spanning **Sm-I$_0$** to **Sm-I$_{12}$** reveals the effect of iodine on emission as a result of the antenna effect is extended to 370 nm from 355 nm whien iodide is on the hydroximate ligand. This matches what is observed in the solution state absorbance. The triplet energies differ depending on the iodination of the hydroximate, where a T_1 = 445 nm (22470 cm^{-1}) for **Gd-I$_4$**, and a T_1 = 460 nm (21740 cm^{-1}) for Gd-I_8 and Gd-I_{12} (Figure 3.13).

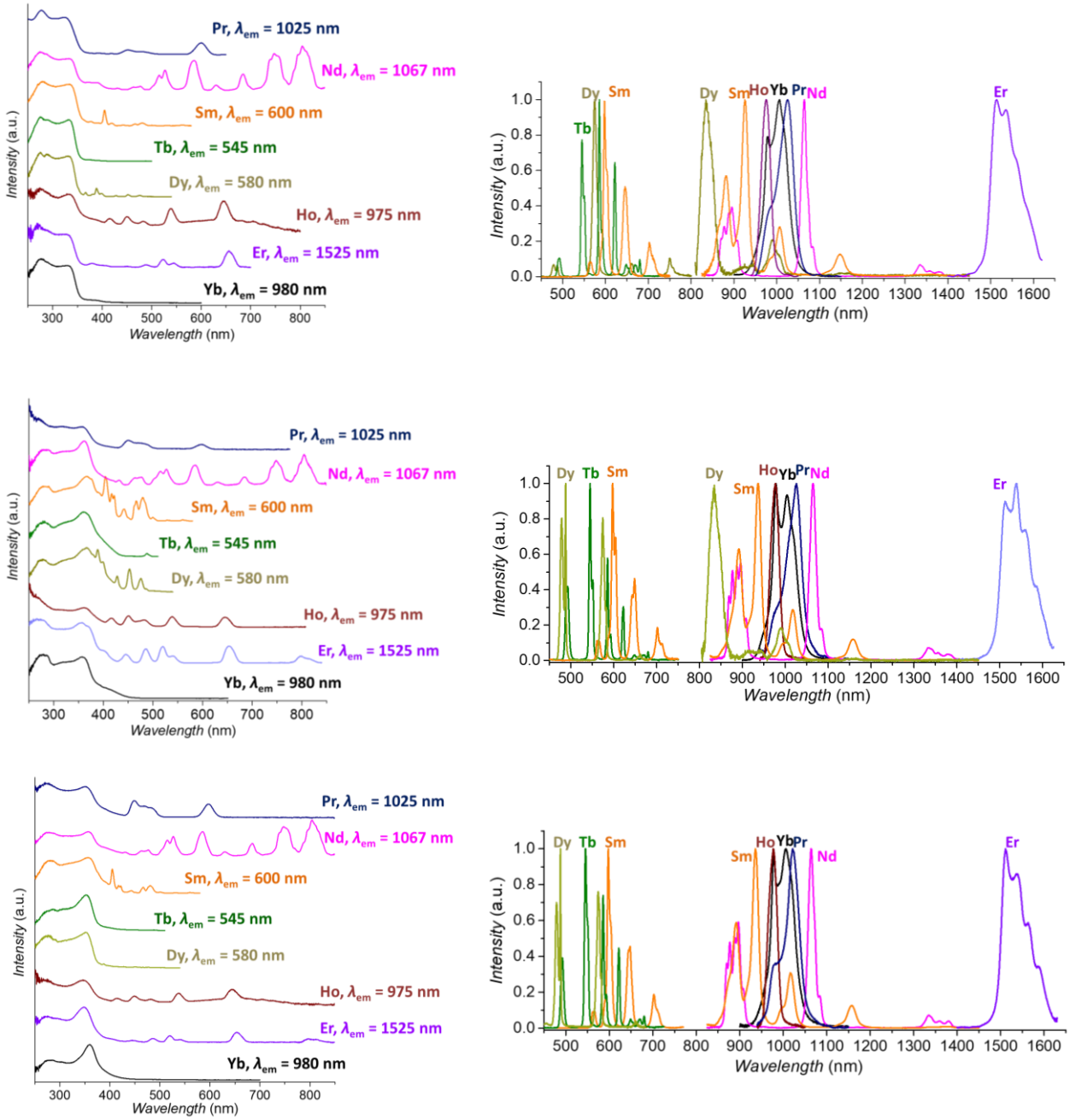

Figure 3.11. Solid state excitation (left) and emission spectra (right) of **Ln-I$_4$** (top), **Ln-I$_8$** (middle), and **Ln-I$_{12}$** (bottom). Emission spectra were taken using an excitation wavelength of 330 nm for **Ln-I$_4$** and 350 nm for **Ln-I$_8$** and **Ln-I$_{12}$**.

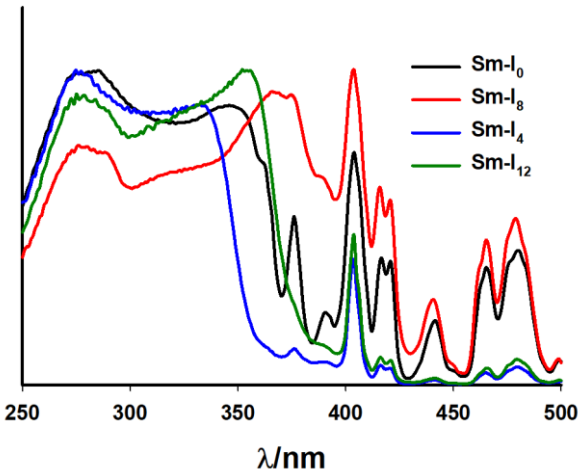

Figure 3.12 Overlay of solid state excitation spectra of **Sm-Ix** complexes (λem =595 nm) (X = 0 (black),4 (blue),8 (red), and 12(green)) which are normalized. Spectra were collected by Jacob Lutter with the assistance of Prof. Evan Trivedi at Oakland University.

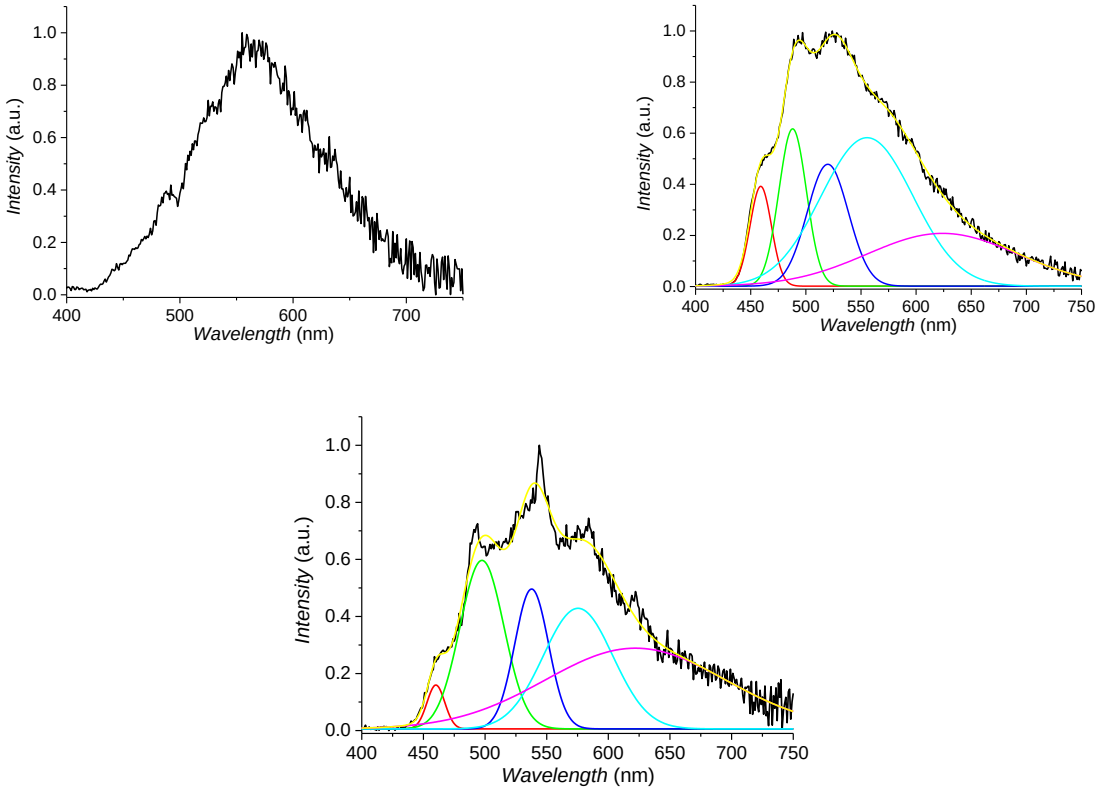

Figure 3.13 Triplet energies of **Gd-I4** (top left), **Gd-I8** (top right), and **Gd-I12** (bottom) at 77 K with a 100 µs delay. The colored traces represent a Gaussian decomposition.

Comparison of lifetimes and quantum yields shows some rather interesting phenomenon. First, as more iodine is included into the system the lifetimes of Ln^{3+} emission decreases or has little change (Table 3.8). The reason for this may have to do with the heavy atom effect, however, slight structural variations and crystal packing differences can also play a role. Since the heavy atom effect relies upon the enhancement of intersystem crossing, and the antenna effect is thought to operate via the ligand triplet state, a faster rate of ISC may explain the decrease in overall lifetime since the scaffold could be relaxing via ligand based phosphorescence rather than via Ln sensitization. This could also explain the general trend of decreased quantum yield (Figure 3.14), where the rate of phosphorescence of the ligand scaffold outcompetes the energy transfer rate to the lanthanide to a greater degree. However, there are outliers for this trend in quantum yield, namely Sm^{3+} and Er^{3+}. The reason for these outliers is not yet understood.

The sensitization efficiency (η_{sens}) of the Nd^{3+} and Er^{3+} analogs were compared to gain some insight on this topic. The η_{sens} value was calculated by dividing the overall quantum yield (Q_{Ln}^{L}) by the quantum yield of a direct f-f excitation (Q_{Ln}^{Ln}). What is observed is that the η_{sens} of the Nd^{3+} analog is static as the amount of iodine increases, but for Er^{3+} the η_{sens} increases (Table 3.9). The radiative lifetime (the theoretical lifetime of emission without non-radiative processes) of both ions decreases alongside the overall observed lifetimes (Table 3.10). This data only suggests that the rates of each process are altered with iodine, but does not describe how this occurs. Still it appears that having iodide in the structure, particularly when there is iodide on the isophthalate, has an effect on the photoluminescence.

Table 3.8. Photophysical properties of **Ln-I$_x$** complexes per lanthanide in the solid state.

Ln-I$_x$	τ_{obs} / µs [a]	Q_{Ln}^{L} (vis)/ % [b]	Q_{Ln}^{L} (NIR)/ % [b]
Pr-I_0	0.901(6)	----	$9.3(1)\cdot10^{-3}$
Pr-I_4	0.0767(9)	----	$2.29(8)\cdot10^{-3}$
Pr-I_8	0.0694(3)	----	$4.1(1)\cdot10^{-3}$
Pr-I_{12}	0.064(1)	----	$4.34(5)\cdot10^{-3}$
Nd-I_0	2.46(1)	----	0.99(2)
Nd-I_4	1.53(1)	----	0.49(1)
Nd-I_8	1.48(2)	----	0.57(2)

Nd-I_{12}	1.42(2)	----	0.542(7)
Sm-I_0	117(1)	2.09(5)	0.269(3)
Sm-I_4	98.8(6)	2.01(4)	0.14(1)
Sm-I_8	93.8(2)	2.48(4)	0.238(4)
Sm-I_{12}	106(1)	3.35(4)	0.22(2)
Tb-I_0	1410(1)	31.2(2)	----
Tb-I_4	560(10): 81.6(1)%	3.6(2)	----
	121(4): 18.4(1)%		
Tb-I_8	136(2): 76.9(2)%	1.9(1)	----
	34.7(2): 23.1(2)%		
Tb-I_{12}	74(2): 75.7(1)%	0.70(3)	----
	19.8(1): 24.3(1)%		
Dy-I_0	15.0(1)	0.85(1)	$7.5(1)\cdot10^{-2}$
Dy-I_4	26.7(2): 77.3(1)%	0.30(4)	$3.11(6)\cdot10^{-2}$
	6.0(2): 23.7(1)%		
Dy-I_8	4.7(2): 76.7(2)%	0.19(1)	$1.57(4)\cdot10^{-2}$
	0.94(5): 23.3(2)%		
Dy-I_{12}	1.17(2): 61.5(2)%	$1.6(1)\cdot10^{-2}$	----
	0.266(6): 38.5(2)%		
Ho-I_0	0.032(1)	----	$3.3(1)\cdot10^{-3}$
Ho-I_4	0.031(1)	----	$1.8(5)\cdot10^{-3}$
Ho-I_8	0.028(1)	----	$1.75(1)\cdot10^{-3}$
Ho-I_{12}	0.029(1)	----	$1.59(4)\cdot10^{-3}$
Er-I_0	5.23(2)	----	$5.7(1)\cdot10^{-3}$
Er-I_4	2.67(6)	----	$1.7(1)\cdot10^{-2}$
Er-I_8	3.02(3)	----	$2.06(5)\cdot10^{-2}$
Er-I_{12}	2.53(3)	----	$1.82(9)\cdot10^{-2}$
Yb-I_0	30.5(1)	----	2.43(6)
Yb-I_4	22.4(1)	----	1.45(5)
Yb-I_8	22.4(5)	----	1.17(1)
Yb-I_{12}	13.6(1)	----	0.78(2)

[a] λ_{ex} = 355 nm

[b] λ_{ex} = 330 nm for **Ln-I_4**, 350 nm for **Ln-I_8** and **Ln-I_{12}**

[c] **Ln-I_0** data were used from Ref 4.

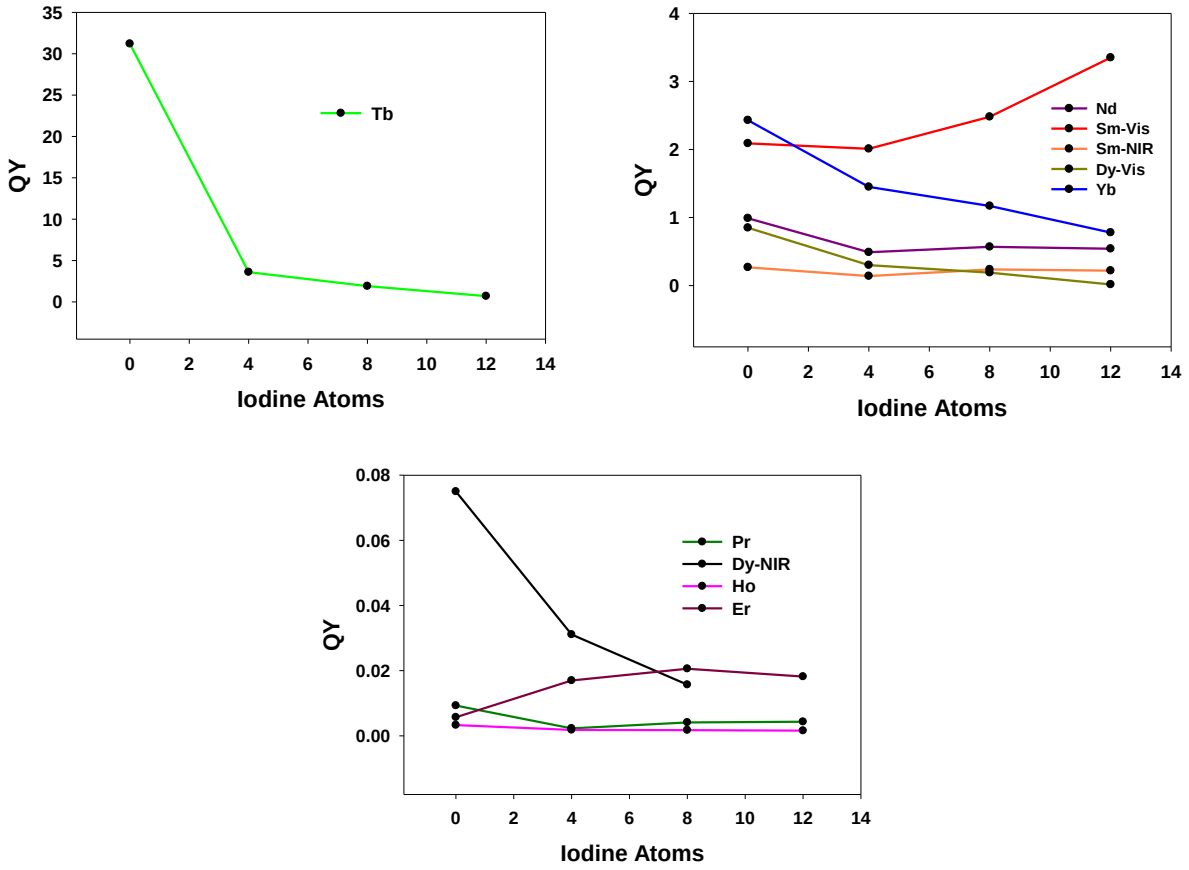

Figure 3.14 Comparison of quantum yields of each Ln analog from I_0 to I_{12}. Solid lines are a guide for the eye.

Table 3.9. Sensitization Efficiencies of Iodinated Metallacrowns				
Ln	I_0	I_4	I_8	I_{12}
Nd	1.2	1.0	1.0	0.9
Er	0.2	0.6	0.6	0.9

Table 3.10. Radiative lifetimes of Iodinated MCs in ms.				
Ln	I_0	I_4	I_8	I_{12}
Nd	0.30	0.31	0.26	0.24
Er	21	9.0	8.0	13

X-ray Attenuation of Iodinatinated Metallacrowns in an in vitro Micro-CT Experiment

CT scans on *in vitro* samples of **Yb-I$_0$**, **Yb-I$_4$**, **Yb-I$_8$** and **Yb-I$_{12}$** were performed in 20 mM solutions of metallacrown in DMF (Figure 3.15) by Dr. Ivana Martinic in CNRS Orleans. The Eppendorf on the far right shows the attenuation of the DMF solvent only, and has minimal X-ray attenuation. The second tube from the right contains the **Yb-I$_0$** complex, which shows that the heavy atoms in the original structure (ytterbium and gallium) do have a significant capability for X-ray attenuation. On the far left is the tube containing the **Yb-I$_4$** complex, which appears to be an even brighter white and thus a slightly better attenuator. The tube second from the left is the **Yb-I$_8$** metallacrown, which is even brighter/ better attenuating than **Yb-I$_4$**. Lastly, in the center is **Yb-I$_{12}$** which was not fully soluble at a concentration of 20 mM. However, the solution and the pellet at the bottom still are a very bright white color and again show that this complex is an excellent attenuator for X-rays. These *in vitro* experiments in combination with the promising Yb^{3+} luminescent properties suggest that these complexes could be developed into a bimodal imaging agent.

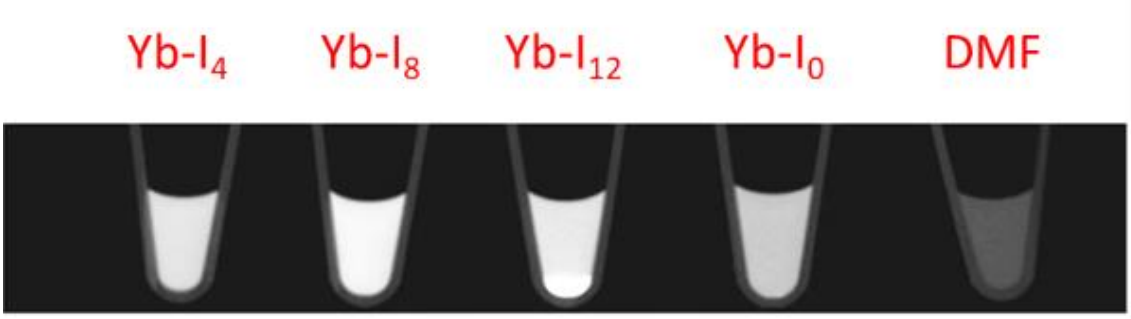

Figure 3.15 CT images of **Ln-I$_x$** complexes in 20 mM solutions of DMF.

Conclusions

New species of gallium(III) metallacrown species were synthesized which incorporate iodine onto the metallacrown scaffold. Both monomeric and dimeric gallium metallacrowns were synthesized, but the solution state instability of the monomeric metallacrowns lead to favoring the dimeric species for further study. The motivation for iodination was two–fold; to explore the possibility of enhancing the antenna effect in these lanthanide sensitizing scaffolds, and to explore the possibility of a multimodal imaging agent based on metallacrowns. Both of these goals were met with limited success. Towards antenna effect enhancement, samarium(III) and

erbium(III) showed an increase in overall quantum yield as a function of attached iodides, while most others had a decrease in quantum yield. The η_{sens} of neodymium(III) and erbium(III) were calculated and there is a clear enhancement in sensitization of the erbium(III) ion which tracks with the number of attached iodides. What is interesting is that the η_{sens} increase is significant when the iodine is added onto the iph^{2-} but not the shi^{3-}. This suggests that the carboxylate may have a significant role in the sensitization. This evidence, in combination with an overall decrease in lifetimes as more iodine is included, shows that the heavy atom is influencing the lanthanide photophysics, but the mechanism is not yet confirmed. Lastly, initial in vitro studies of the X-ray attenuation of these iodinated metallacrowns shows an apparent increase in attenuation which tracks with the amount of iodine incorporated onto the metallacrown. These initial results suggest that these complexes could be used as a bimodal CT contrast/optical imaging agent which shifts the optical absorption range and enhances the X-ray contrast compared to parent non-iodinated metallacrown.

References

(1) Jankolovits, J.; Andolina, C. M.; Kampf, J. W.; Raymond, K. N.; Pecoraro, V. L. *Angew. Chemie Int. Ed.* **2011**, *50* (41), 9660–9664.
(2) Trivedi, E. R.; Eliseeva, S. V.; Jankolovits, J.; Olmstead, M. M.; Petoud, S.; Pecoraro, V. L. *J. Am. Chem. Soc.* **2014**, *136* (4), 1526–1534.
(3) Chow, C. Y.; Eliseeva, S. V; Trivedi, E. R.; Nguyen, T. N.; Kampf, J. W.; Petoud, S.; Pecoraro, V. L. *J. Am. Chem. Soc.* **2016**, *138* (15), 5100–5109.
(4) Nguyen, T. N.; Chow, C. Y.; Eliseeva, S. V.; Trivedi, E. R.; Kampf, J. W.; Martinić, I.; Petoud, S.; Pecoraro, V. L. *Chem. - A Eur. J.* **2018**, *24* (5), 1031–1035.
(5) Martinić, I.; Eliseeva, S. V; Nguyen, T. N.; Pecoraro, V. L.; Petoud, S. *J. Am. Chem. Soc.* **2017**, *139* (25), 8388–8391.
(6) Martinić, I.; Eliseeva, S. V.; Nguyen, T. N.; Foucher, F.; Gosset, D.; Westall, F.; Pecoraro, V. L.; Petoud, S. *Chem. Sci.* **2017**, *8* (9), 6042–6050.
(7) Deigner, H.-P. *Atherosclerosis* **2016**, *254*, 307–308.
(8) Bonnet, C. S.; Tóth, É. *Comptes Rendus Chim.* **2010**, *13* (6–7), 700–714.
(9) Solov'ev, K. N.; Borisevich, E. A. *Uspekhi Fiz. Nauk* **2005**, *175* (3), 247.
(10) McClure, D. S. *J. Chem. Phys.* **1949**, *17* (10), 905–913.
(11) Gilmore, E. H.; Gibson, G. E.; McClure, D. S. *J. Chem. Phys.* **1952**, *20* (5), 829–836.
(12) Gilmore, E. H.; Gibson, G. E.; McClure, D. S. *J. Chem. Phys.* **1952**, *23* (5), 399–399.
(13) Ermolaev, V. L.; Svitashev, K. K. *Opt. Spektrosk* **1959**, *7*, 664.
(14) Masetti, F.; Mazzucato, U.; Galiazzo, G. *J. Lumin.* **1971**, *4* (1), 8–12.
(15) Pang, X.; Jin, W. J. 2014; pp 115–146.
(16) White, W.; Seybold, P. G. *J. Phys. Chem.* **1977**, *81* (21), 2035–2040.
(17) Dvornikov, S. S.; Solov'ev, K. N.; Tsvirko, M. P.; Gradyushko, A. T. *J. Appl. Spectrosc.* **1976**, *25* (6), 1522–1526.
(18) Bolton, O.; Lee, K.; Kim, H.-J.; Lin, K. Y.; Kim, J. *Nat. Chem.* **2011**, *3* (3), 205–210.
(19) Gouterman, M.; Schwarz, F. P.; Smith, P. D.; Dolphin, D. *J. Chem. Phys.* **1973**, *59* (2), 676–690.
(20) Zhang, J.; Duan, C.; Han, C.; Yang, H.; Wei, Y.; Xu, H. *Adv. Mater.* **2016**, *28* (28), 5975–5979.
(21) Oldendorf, W. H. *Neurology* **1978**, *28* (6), 517–517.
(22) Lusic, H.; Grinstaff, M. W. *Chem. Rev.* **2013**, *113* (3), 1641–1666.
(23) Bourin, M.; Jolliet, P.; Ballereau, F. *Clin. Pharmacokinet.* **1997**, *32* (3), 180–193.
(24) Haller, C.; Hizoh, I. *Invest. Radiol.* **2004**, *39* (3), 149–154.
(25) Oh, M. H.; Lee, N.; Kim, H.; Park, S. P.; Piao, Y.; Lee, J.; Jun, S. W.; Moon, W. K.; Choi, S. H.; Hyeon, T. *J. Am. Chem. Soc.* **2011**, *133* (14), 5508–5515.
(26) Wang, H.; Zheng, L.; Peng, C.; Guo, R.; Shen, M.; Shi, X.; Zhang, G. *Biomaterials* **2011**, *32* (11), 2979–2988.
(27) Geso, M. *Br. J. Radiol.* **2007**, *80* (949), 64–65.
(28) Rabin, O.; Manuel Perez, J.; Grimm, J.; Wojtkiewicz, G.; Weissleder, R. *Nat. Mater.* **2006**, *5* (2), 118–122.
(29) Xing, H.; Bu, W.; Zhang, S.; Zheng, X.; Li, M.; Chen, F.; He, Q.; Zhou, L.; Peng, W.; Hua, Y.; Shi, J. *Biomaterials* **2012**, *33* (4), 1079–1089.
(30) Xing, H.; Bu, W.; Ren, Q.; Zheng, X.; Li, M.; Zhang, S.; Qu, H.; Wang, Z.; Hua, Y.; Zhao, K.; Zhou, L.; Peng, W.; Shi, J. *Biomaterials* **2012**, *33* (21), 5384–5393.
(31) Fischer, E.; Speier, A. *Berichte der Dtsch. Chem. Gesellschaft* **1895**, *28* (3), 3252–3258.

(32) Bazaga-García, M.; Colodrero, R. M. P.; Papadaki, M.; Garczarek, P.; Zoń, J.; Olivera-Pastor, P.; Losilla, E. R.; León-Reina, L.; Aranda, M. A. G.; Choquesillo-Lazarte, D.; Demadis, K. D.; Cabeza, A. *J. Am. Chem. Soc.* **2014**, *136* (15), 5731–5739.
(33) Nilsson, M.; Gil, A. M.; Delgadillo, I.; Morris, G. A. *Anal. Chem.* **2004**, *76* (18), 5418–5422.
(34) CrystalClear Expert 2.0 r16, Rigaku Americas and Rigaku Corporation (2014), Rigaku Americas, 9009, TX, USA 77381-5209, Rigaku Tokyo, 196-8666, Japan.
(35) Sheldrick, G. M. *Acta Crystallogr. Sect. A Found. Crystallogr.* **2007**, *64* (1), 112–122.
(36) Azar, M. R.; Boron, T. T.; Lutter, J. C.; Daly, C. I.; Zegalia, K. A.; Nimthong, R.; Ferrence, G. M.; Zeller, M.; Kampf, J. W.; Pecoraro, V. L.; Zaleski, C. M. *Inorg. Chem.* **2014**, *53* (3), 1729–1742.
(37) Addison, A. W.; Rao, T. N.; Reedijk, J.; van Rijn, J.; Verschoor, G. C. *J. Chem. Soc. Dalt. Trans.* **1984**, 1349–1356.
(38) Lin, P.-C.; Kreutzer, U.; Jue, T. *Biophys. J.* **2007**, *92* (7), 2608–2620.
(39) Price, W. S.; Elwinger, F.; Vigouroux, C.; Stilbs, P. *Magn. Reson. Chem.* **2002**, *40* (6), 391–395.
(40) Cohen, Y.; Avram, L.; Frish, L. *Angew. Chemie - Int. Ed.* **2005**, *44* (4), 520–554.
(41) Zuccaccia, D.; Macchioni, A. *Organometallics* **2005**, *24* (14), 3476–3486.

Chapter 4

Functionalization of Luminescent Metallacrowns

Introduction

The previously reported metallacrown complexes with lanthanide based luminescence have significant capabilities; the gallium and shi^{3-} MCs show a remarkable range of lanthanide sensitization options while the zinc and pyzHA^{2-} MCs show use in cell fixation and selectivity for imaging cells that have undergone non-programmed cell death (necrosis). Chapter 3 of this thesis explored one method for increasing brightness and prototypical examples of multi-modal imaging possibilities of metallacrown complexes. However, there are many other possibilities for rational redesign. Another route for improvement of the properties of these complexes could be integrating reliable reactive functionalities directly onto the scaffold. This chapter will explore two coupling reactions that can be used to make predictable functionalization and rational design of new antenna, namely copper-catalyzed alkyne azide cycloaddition (CuAAC) and Sonogashira coupling.

The concept of "click" chemistry was introduced by K. Barry Sharpless in 2001.[1] Formally, he defined a "click" reaction as a C-X-C bond (X is a heteroatom) forming reaction with a large driving force (> 20 kcal/mol). The reaction should also have a wide scope for coupling partners, and have easily isolable products in benign solvents such as water. The scope of reactions that falls under "click" chemistry include cycloaddition reactions, nucleophilic ring opening reactions, carbonyl chemistry towards formation of stable products such as ureas or amides, and addition to carbon-carbon multiple bonds (such as a Micheal addition). Common examples of such reactions are provided in Scheme 4.1.

Formation of a thioether: A "click" Micheal addition

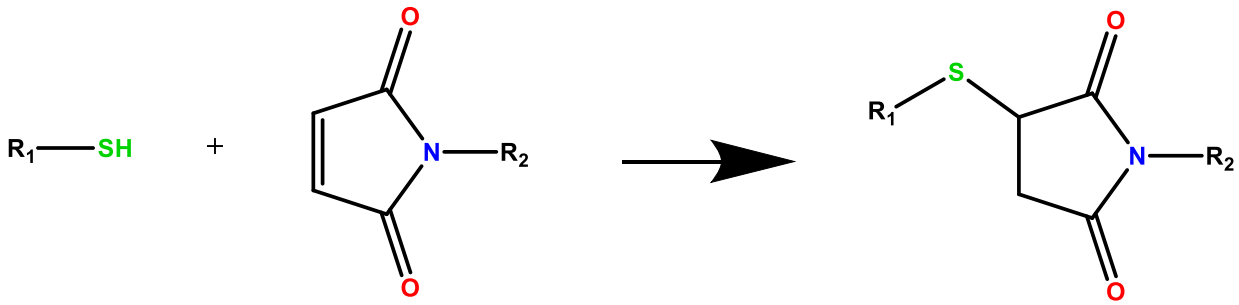

Formation of a thiourea: A "click" reaction with carbonyls

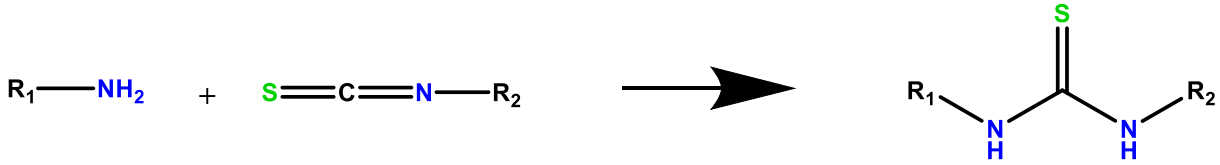

Formation of a 1,4-triazol: A "click" cycloaddition

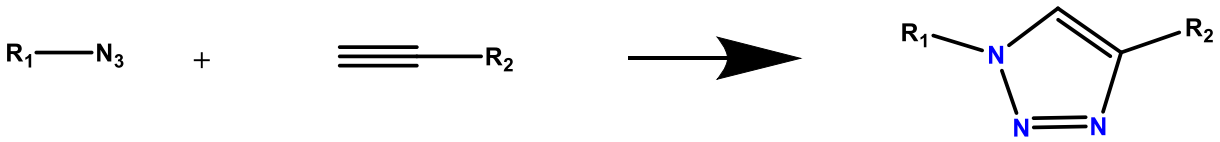

Scheme 4.1. Examples of various "click" chemistry reactions.[1]

The particular "click" reaction of interest for this chapter is the copper-catalyzed alkyne azide [3+2] cycloaddition (CuAAC). Originally called the Huisgen coupling reaction, this reaction combines an alkyne and an azide to form a 1,4 substituted triazole, but was limited as it required energy input in the form of heat.[2] In 2001, Meldal and Sharpless independently discovered that the addition of copper(I) to this system greatly catalyzes the cycloaddition and allows one to work at ambient temperatures.[1,3] In addition, the inclusion of copper (I) chelators such as tris[(benzyl-1,2,3-triazolyl)methyl]amine (TBTA) can also improve the yield and rate of the reaction and opened up the possibility of its use in bioconjugation.[4] The mechanism for the copper catalyzed cycloaddition is not fully understood, but based on kinetic studies the reaction appears to be second order in both the copper catalyst and alkyne, which suggests that the intermediate species has a ratio of 2 copper(I) to 2 alkyne to one azide.[3] The most likely mechanism which includes this ratio was proposed by Meldal in 2008 (Figure 4.1). Despite the

complexity of this reaction, the results are rather straightforward and the CuAAC has found use across the pharmaceutical and biochemical communities.

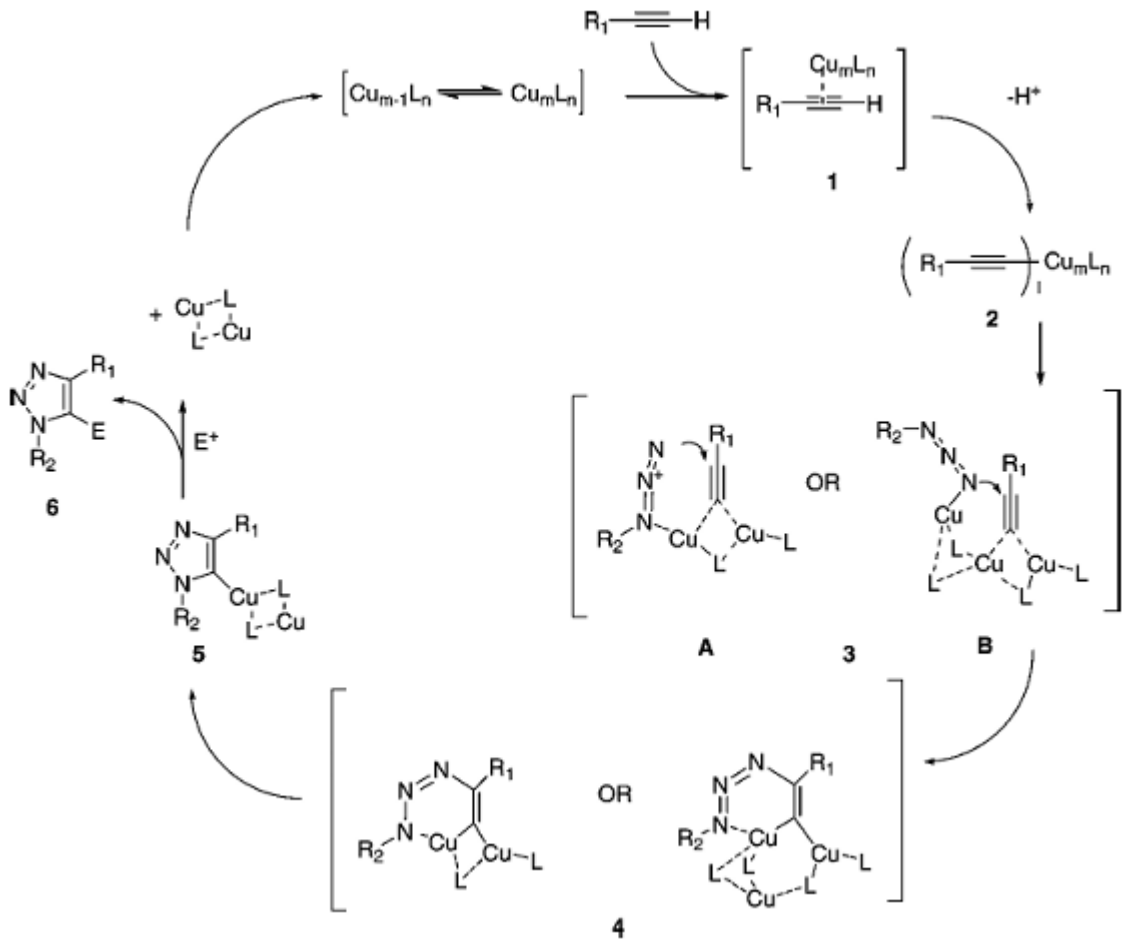

Figure 4.1. Proposed mechanism for CuAAC from Meldal and coworkers.[3]

To incorporate the use of CuAAC onto the metallacrown archetype, a hydroxamic acid with either an alkyne or an azide must be developed. Rentschler and coworkers reported a fascinating salicylhydroxamic acid derivative (H_3eshi) in 2015 which does feature an ethyne in the four position.[5] While her work was focused on coupling azides of interest for magnetic study of copper 12-MC-4s, this same ligand could be of use with gallium metallacrowns which have lanthanide based luminescence, such as the metallacrowns reported by Pecoraro and coworkers in 2016 and 2017.[6,7] These metallacrowns not only feature excellent lanthanide photophysics, but also demonstrate a wide range of lanthanide emission. This feature could be useful towards the development of color coding biological assays. In addition, the inclusion of this ethyne on to a picHA would lead to the use of CuAAC on zinc metallacrowns with the architecture of those

reported by Pecoraro and coworkers in 2011, 2014, and 2017.[8–11] This molecule is of great interest since it has been shown to have use in staining and fixing HeLa cells.[10,11]

The synthesis of the H_3eshi ligand uses Sonogashira coupling, which is a reliable method for combining an sp_2C-halide (usually an iodide) with a terminal alkyne. The reaction was discovered in 1975 by Sonogashira and coworkers by coupling an alkyne with bromoalkenes, iodoarenes and bromopyridines.[12] This reaction utilizes a bimetallic catalytic cycle (Figure 4.2), and is catalyzed by both palladium(II) and copper (I).[13] The palladium cycle begins with an L-Pd(0)-L complex, which undergoes oxidative addition by inserting into an aryl halide bond. Simultaneously, the copper(I) forms an organocuprate with the alkyne by replacing the proton on the terminal carbon. This alkynylcuprate then undergoes transmetallation onto the palladium complex ultimately by replacing the halide. After rearrangement into a cis-confirmation for the aryl and alkynyl groups these reductively eliminate, regenerating the L-Pd(0)-L catalyst and forming the desired aryl-alkyne.

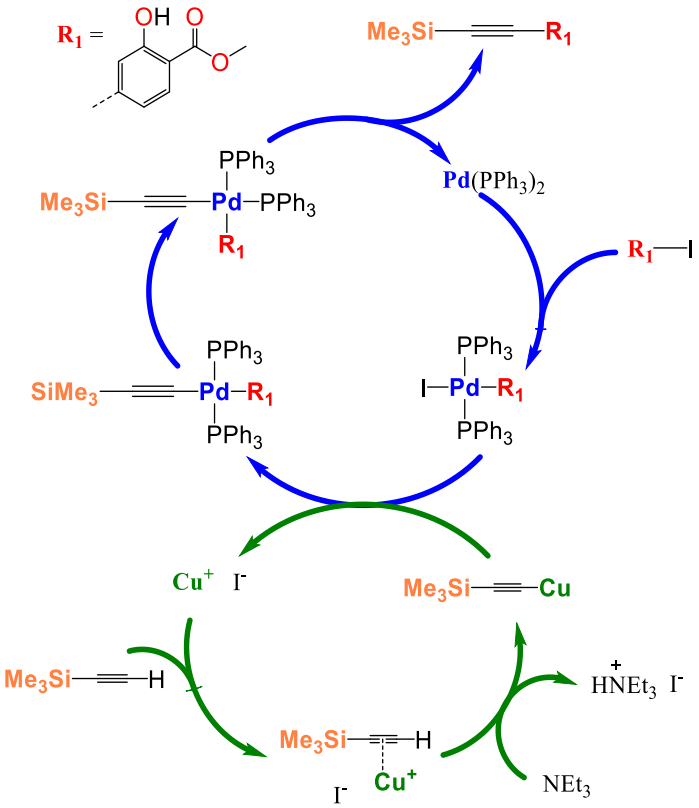

Figure 4.2. The Sonogashira bimetallic catalytic cycle using a precursor for H_3eshi.[13]

Like CuAAC, the scope of this reaction is very broad, and allows for the coupling of an aryl halide to nearly any alkyne. This chapter will demonstrate how to take advantage of the

Sonogashira coupling not only to generate H_3eshi for functionalized luminescent Ga_4 and Ga_8 metallacrowns, but also to prepare an ethynyl picolinehydroxamic acid that can be used to adorn the $LnZn_{16}$ metallacrowns. Finally, more complex biaryl hydroxamic acids are described that represent a first entry for making alternative organic antenna that may be appended to MCs.

Experimental

Synthetic Materials. Gallium(III) nitrate hydrate (Acros, 99.9998%), praseodymium(III) nitrate hexahydrate (Sigma Aldrich, 99.9%), neodymium(III) nitrate hexahydrate (Sigma Aldrich, 99.9%), samarium(III) nitrate hexahydrate (Sigma Aldrich, 99.9%), europium(III) nitrate hexahydrate (Sigma Aldrich, 99.9%), gadolinium(III) nitrate hexahydrate (Alfa, Aesar, 99.9%), terbium(III) nitrate pentahydrate (Sigma Aldrich, 99.9%), dysprosium(III) nitrate pentahydrate (Alfa Aesar, 99.9%), holmium(III) nitrate pentahydrate (Sigma Aldrich, 99.9%), thulium(III) nitrate hydrate (Sigma Aldrich, 99.9%), erbium(III) nitrate pentahydrate (Sigma Aldrich, 99.9%), ytterbium nitrate pentahydrate (Sigma Aldrich, 99.9%), yttrium(III) nitrate hexahydrate (Acros, 99.9%), methyl 4-iodosalicylate (Alfa Aesar, 98%), 4-iodopicolinic acid (Ark Pharm, 98%), isophthalic acid (Acros, 99%), sodium pivolate hydrate (Accela, 99%), sodium benzoate (Aldrich, 99%), 4-iodobenzoic acid (Oakwood Chemical, 99%), palladium(II) bis(triphenylphosphine)dichloride (Ark Pharm, 98%), copper(I) iodide (Aldrich, 99.999%), trimethylsilylacetylene (Matrix Scientific, 98%), 1 M tetrabutylammonium in tetrahydrofuran (Acros, 5% water w/w), dimethylethylenediamine (Oakwood Chemical, 99%), 3-bromopropylamine hydrobromide (Alfa Aesar, 98%), sodium azide (Aldrich, 99%), tripropargylamine (Alfa Aesar, 97%), benzyl azide (Alfa Aesar, 94%), copper(II) sulfate pentahydrate (Mallinckrodt, 99.8%), sodium L-ascorbate (Acros, 99%), D(+)-Biotin (Ark Pharm, 98%), N,N-dicylclohexylcarbodiimide (Sigma Aldrich 99%), sodium hydroxide (Fisher, ACS Grade), potassium hydroxide (Fisher, 85%), hydroxylamine hydrochloride (Sigma Aldrich, 99%), methanol (Fisher, ACS grade), ethanol (Decon Labs, 200 Proof), dichloromethane (Fisher, ACS Grade), ethyl acetate (Fisher, ACS Grade), sulfuric acid (Fisher, ACS Grade), hydrochloric acid (Fisher, 37% w/w), anhydrous sodium sulfate (Fisher, ACS Grade), silica gel 230-400 mesh (Alfa Aesar, 99.5%). All materials were used as received without further purification.

Synthetic Procedures.

Methyl 4-ethynylsalicylate. Methyl 4-ethynylsalicylate was synthesized by modifying a literature procedure.[5] Thirty-six mmol (10.01 g, 1 equiv.) of methyl 4-iodosalicylate was dissolved in 180 mL of triethylamine to form a clear and brown solution. Then, 43.2 mmol (6.15 mL, 1.2 equiv.) of trimethylsilylacetylene was added and stirred. Next, 1.8 mmol (1.2763 g, 0.05 equiv.) of palladium(II) bis(triphenylphosphine)dichloride and 3.6 mmol (0.6855 g, 0.1 equiv.) of copper(I) iodide was added and let stir to form a cloudy brown-green solution which was allowed to stir for 24 hours. The reaction was quenched with 145 mL of 1M aqueous ammonium chloride and let stir for about a half hour. This solution was extracted using two 100 mL portions of ethyl acetate, then another three 50 mL portions which were dried over sodium sulfate and gravity filtered. The filtrate was evaporated on a flash evaporator to a brown-red oil. The residue was dissolved in 10 mL of dichloromethane and purified using a silica gel column with an increasing gradient of dichloromethane in hexanes to yield a yellow oil. The purified intermediate was dissolved in 45 mL of tetrahydrofuran, and treated with 45 mL of 1 M tetrabutylammonium fluoride in tetrahydrofuran for two hours. The resulting honey-colored mixture was acidified to pH 1 using 1M aqueous hydrochloric acid, then mixed with 50 mL of distilled water. The mixture was extracted with four portions of ethyl acetate, dried over sodium sulfate and gravity filtered. The filtrate was evaporated on a flash evaporator to yield methyl 4-ethynylsalicylate as a yellow powder. The synthetic yield was 87%. Elemental analysis of $C_{10}H_8O_3$ [fw = 176.17 g/mol] % found (calculated): %C 67.92 (68.18); %H 4.59 (4.58); %N 0.00 (0.00). ^{1}H-NMR (400 MHz, d_6-DMSO): 10.54 ppm (1H, s), 7.75 ppm (1H, d), 7.07 (ppm, d), 7.02 ppm (1H, dd), 4.45 ppm (1H, s), 3.88 ppm (3H, s).

4-ethynylsalicylhydroxamic acid (H_3eshi). H_3eshi was synthesized by modifying a literature procedure.[5] First, 31.22 mmol of methyl 4-ethynylsalicylate (5.50 g, 1 equiv.) was suspended in 150 mL of methanol. Separately, 93.66 mmol of hydroxylamine hydrochloride (6.51 g, 3 equiv.) and 124.88 mmol of potassium hydroxide (8.24 g, 4 equiv.) were dissolved in 150 mL of methanol to form clear and colorless solutions. The hydroxylamine hydrochloride and potassium hydroxide solutions were combined and a colorless potassium chloride precipitate was observed. The mixture was left to stir for 10 minutes, then the potassium chloride was vacuum filtered from a clear and colorless filtrate. This filtrate was combined with the suspension of methyl 4-

ethynylsalicylate to form a clear and orange solution. This solution was stirred for 24 hours. Next, another set of hydroxylamine hydrochloride and potassium hydroxide solutions in 150 mL of methanol were prepared, combined and filtered as described previously to obtain another clear and colorless filtrate. This filtrate was combined into the reaction solution and let stir for another 24 hours. The solution was evaporated down to approximately 100 mL using a flash evaporator and acidified to a pH of one using 1M hydrochloric acid. Then 500 mL of distilled water was added and 200 mL of brine. This solution was extracted with ten portions of ethyl acetate, dried over sodium sulfate and gravity filtered. The filtrate was evaporated using a flash evaporator to a yellow powder, which was triturated for 20 minutes in 75 mL of dichloromethane. The cloudy mixture was vacuum filtered to yield 4-ethynylsalicylhydroxamic acid as a yellow powder. The synthetic yield was 85%. Elemental analysis for $C_9H_7NO_3 \cdot 0.15H_2O$ [179.86 g/mol] % found (calculated): %C 60.22 (60.10); %H 4.16 (4.09); %N 7.81 (7.79). ^{1}H-NMR (400 MHz, d_6-DMSO): 12.25 ppm (1H, s), 11.42 ppm (1H, s), 9.39 ppm (1H, s), 7.66 ppm (1H, d), 6.98 ppm, (1H, s), 6.96 ppm (1H, d), 4.35 ppm (1H, s).

Tris(benzyltriazolylmethyl)amine, **TBTA**. **TBTA** was synthesized by modifying literature procedure for CuAAC in H_2O/t-butanol.[14] One mmol of tripropargylamine (142 µL, 1 equiv.) and 3 mmol of benzyl azide (375 µL, 3 equiv.) were dissolved in 12 mL of a 1:1 H_2O:*t*-butanol mixture. Next, 0.03 mmol of sodium L-ascorbate was added as a 1M solution in H_2O (300 µL, 0.03 equiv.), followed by 0.03 mmol of copper(II) sulfate as a 3M solution in H_2O (100 µL, 0.03 equiv.). This mixture was allowed to react for 3 days, then was dissolved in 50 mL of cold H_2O. This mixture was then extracted with five portions of 25 mL of ethyl acetate. The organic layers were combined, dried over sodium sulfate, then gravity filtered. The filtrate was evaporated using a flash evaporator, then redissolved in 5 mL of DMF. The solution was evaporated using a flash evaporator to give TBTA as a brown powder. The synthetic yield was 88%. Elemental analysis for $C_{30}H_{30}N_{10} \cdot 1.25\ C_4H_{10}O$ [fw = 623.04 g/mol] % found (calculated): %C 67.45 (67.47). %H 6.49 (6.84), %N 22.49 (22.48). ^{1}H-NMR (400MHz, d_6-DMSO): 8.09 ppm (3H, s), 7.32 ppm (15 H, m), 5.59 (6H, s), 3.61 (6H, s).

4-(benzyltriazolyl)salicylhydroxamic acid. One mmol of H_3eshi (0.1772 g, 1 equiv.) and 1 mmol of benzyl azide (125 µL, 1 equiv.) were suspended in 4 mL of a 1:1 solution of distilled water

and *tert*-butanol. Sodium L-ascorbate (0.03 mmol) was added as a 1 M solution in distilled water (30 µL, 0.03 equiv.) and 0.015 mmol of $[Cu_2(TBTA)](SO_4)$ as a 0.214 M solution in 1:1 distilled water and *tert*-butanol (70 µL, 0.015 equiv.) were added. The solution was left stir for 24 hours, then vacuum filtered to isolate 4-(benzyltriazolyl)salicylhydroxamic acid as a yellow powder. The synthetic yield was 87 %. Elemental analysis of $C_{16}H_{14}N_4O_3 \cdot 0.25\ C_4H_9O$ [fw = 328.59 g/mol] % found (calculated): %C 62.28 (62.14), %H 4.92 (4.98), %N 16.93 (17.05). ^{1}H-NMR (400 MHz, d_6-DMSO): 12.39 ppm (1H, s), 11.44 ppm (1H, s), 9.34 ppm (1H, s), 8.73 ppm (1H, s), 7.74 ppm (1H, d), 7.37 ppm (7H, m), 5.65 ppm (2H, s).

3-azidopropylamine. 3-azidopropylamine was synthesized according to a literature procedure.[15] Fifteen mmol of 3-bromopropylamine hydrobromide (3.28 g, 1 equiv.) was dissolved in 10 mL of distilled water. Separately, 50 mmol of sodium azide (3.25 g, 4/3 equiv.) was dissolved in 15 mL of distilled water. These solutions were combined and then warmed to 95 ^{o}C and stirred for 18 hours. Then, 60 mmol of potassium hydroxide (3.96 g, 4 equiv.) was suspended in 50 mL of diethyl ether and the reaction solution was introduced dropwise once it was cooled back to ambient temperature. The biphasic mixture was separated and the aqueous layer was extracted with two more portions of diethyl ether. The organic layers were combined and dried over sodium sulfate, then gravity filtered. The filtrate was evaporated on the flash evaporator to yield 3-azidopropylamine as a faintly yellow oil. The synthetic yield was 79%. ^{1}H-NMR (400 MHz, d_6-DMSO): 3.37 ppm (2H, t), 2.58 ppm (2H, t), 2.04 ppm, (2H, broad s), 1.59 ppm (2H, p). **Safety note:** This compound is a small organic azide and must be stored at -20 ^{o}C in the dark, and it is strongly advised to avoid storing it for long periods of time. Elemental analysis was not obtained due to restrictions of shipping a possible explosive.

N-oxysuccinamidyl biotinate (Biotin-NHS). **Biotin-NHS** was synthesized according to a literature procedure.[16] First, 4.09 mmol of biotin (1.00 g, 1 equiv.) and 4.09 mmol of N-hydroxysuccinamide (0.47 g, 1 equiv.) were combined in 30 mL of dry dichloromethane and warmed to 60 ^{o}C. Then 5.32 mmol of dicylclohexylcarbimide (1.10 g, 1.3 equiv.) was added and the reaction was allowed to cool to RT and stir for 24 hours. Next, a white precipitate was removed by vacuum filtration leaving a clear and faintly brown filtrate. This filtrate was evaporated using a flash evaporator to a white powder. This powder was triturated in 20 mL of

diethyl ether, then vacuum filtered and washed with isopropanol to yield Biotin-NHS as a white powder. The synthetic yield was 94%. Elemental analysis gives 90% purity with 10% starting material: 0.9 $C_{14}H_{19}N_3O_5S$ · 0.1 $C_{13}H_{24}N_2O$ (dicyclohexyl urea) [fw = 329.68 g/mol] % found (calculated): %C 50.71 (50.64), %H 5.84 (5.96), %N 12.54 (12.32). ^{1}H-NMR (400MHz, d_6-DMSO): 6.38 ppm (2H, d), 4.30 ppm (1H, m), 4.15 ppm (1H, m), 3.10 (1H, M), 2.54-2.87 ppm (8H, multiplets), 1.34-1.70 (6H, multiplets).

3-azidopropane biotinamide, (Biotin-N_3). **Biotin-N_3** was synthesized by modifying a literature procedure.[15] First, 3.84 mmol (1.3092 g, 1 equiv.) of Biotin-NHS was suspended in 50 mL of methanol. Then 4.22 mmol (0.4225 g, 1.5 equiv.) of 3-aziodopropylamine and 8.44 mmol (1.470 mL, 3 equiv.) of diisopropylethylamine were added and the solution was let stir for 20 hours. Then the reaction was evaporated using a flash evaporator to a white powder, which was triturated in ethyl acetate, then vacuum filtered and washed with ethyl acetate and dichloromethane. This white powder was then recrystallized in methanol and isolated by vacuum filtration as a white powder. The synthetic yield was 22%. Elemental analysis show 90% purity with 10% starting material: 0.9 $C_{14}H_{22}N_6O_2S$· 0.1 $C_{14}H_{19}N_3O_5S$ 0.25 C_4H_9O · 0.25 H_2O [fw = 332.42 g/mol] % found (calculated): %C 47.38 (47.33), %H 6.74 (6.73), %N 23.94 (24.02). ^{1}H-NMR (400MHz, d_6-DMSO): 7.82 ppm (1H, t), 6.38 ppm (2H, d), 4.29 ppm (1H, m), 4.11 ppm (1H, m), 3.32 ppm (2H, m), 3.02 ppm (3H, m), 2.79 ppm (1H, dd), 2.48 ppm (1H, d), 2.03 ppm (2H, m), 1.01-1.65 ppm (8H, multiplets).

4-(3-triazolylpropyl biotinamide)salicylhydroxamic acid. 0.5 mmol of H_3eshi (0.0886, 1 equiv.) and 0.5 mmol of 3-aziodpropylbiotinamide (0.1632 g, 1 equiv.) were suspended in 2 mL a 1:1 solution of distilled water and *tert*-butanol. 0.015 mmol of sodium L-ascorbate was added as a 1 M solution in distilled water (15 µL, 0.03 equiv.) and 0.0075 mmol of [Cu_2(TBTA)](SO_4) as a 0.214 M solution in 1:1 distilled water and *tert*-butanol (35 µL, 0.015 equiv.) were added. After two hours 0.5 mL of DMF were added to aid in solubility. The solution was let stir for 20 hours, then diluted in 200 mL of distilled water. The mixture was vacuum filtered to isolate 4-(3-triazolylbiotinamide)salicylhydroxamic acid as a yellow powder. The synthetic yield was 64 %. Elemental analysis of $C_{22}H_{29}N_7O_5S$· 0.25 C_4H_9O · 0.5 H_2O [fw = 530.86 g/mol] % found (calculated): %C 52.03 (52.04), %H 5.99 (6.12), %N 18.28 (18.47). ^{1}H-NMR (400 MHz, d_6-

DMSO): 12.43 ppm (1H, s), 11.47 ppm (1H, s), 9.38 ppm (1H, s), 8.68 ppm (1H, s), 7.79 ppm (1H, t), 7.40 ppm, (1H, s), 7.37 ppm (1H, d), 6.41 ppm (2H, d), 4.32 ppm (1H, t), 4.15 ppm (1H, t), 3.46 ppm (2H, t), 3.13 ppm (3H, t), 2.84 ppm (1H, dd), 2.61 ppm (1H, d), 2.08 ppm (2H, t), 1.06-1.53 ppm (8H, multiplets).

Ethyl 5-(p-ethynyl-N,N-dimethylanisolyl)salicylate. Five mmol of ethyl 5-iodosalicylate (1.4604 g, 1 equiv.) and 5.5 mmol of p-ethynyl-N,N-dimethylaniline (0.7986 g, 1.1 equiv.) were dissolved in 25 mL of triethylamine to form a clear and faintly yellow solution. Then 0.25 mmol of palladium(II) bis(triphenylphospoine)dichloride (0.1755 g, 0.05 equiv.) and 0.5 mmol of copper(I) iodide (0.0952 g, 0.1 equiv.) were added and let stir as a cloudy and dark yellow solution for 24 hours. The reaction was quenched with 25 mL of 1 M aqueous ammonium chloride and stirred for twenty minutes. 5 mL of ethyl acetate was added and the mixture was vacuum filtered to give a yellow precipitate and a red/blue biphasic filtrate. The filtrate was extracted with four portions of ethyl acetate. The yellow precipitate was triturated in 10 mL of ethyl acetate for ten minutes, then vacuum filtered and washed with ethyl acetate until the wash is colorless. Both ethyl acetate solutions were combined and dried over sodium sulfate, then gravity filtered. The filtrate was evaporated using a flash evaporator to a brown powder. This powder was dissolved in 10 mL of ethyl acetate and mixed with 1 g of silica gel. The mixture was evaporated on the flash evaporator to a brown powder. The powder was dry loaded on a silica gel column and then saturated with hexanes. The mixture was purified on a silica gel column using a mobile phase of 9:1 hexanes and ethyl acetate. Evaporation of pure fractions gave ethyl 5-(p-ethynyl-N,N-dimethylanilinyl)salicylate as a tan powder. The synthetic yield was 89%. Elemental analysis of $C_{19}H_{19}NO_3$ [fw = 309.37 g/mol] % found (calculated): %C 73.57 (73.77), %H 6.09 (6.19), %N 4.43 (4.53). ^{1}H-NMR (400 MHz, d_6-DMSO): 10.69 ppm (1H, s), 7.83 ppm (1H, s), 7.59 ppm (1H, d), 7.34 ppm (2H, d), 7.00 ppm (1H, d), 6.70 ppm (2H, d), 4.35 ppm (2H, q), 2.93 (6H, s), 1.34 (3H, t).

5-(p-ethynyl-N,N-dimethylanilinyl)salicylhydroxamic acid (H_3meanshi). Four mmol of 5-(p-ethynyl-N,N-dimethylanilinyl)salicylate (1.2375 g, 1 equiv.) was dissolved in 20 mL of methanol. Separately, 12 mmol of hydroxylamine hydrochloride (0.8340 g, 3 equiv.) and 16 mmol of potassium hydroxide (1.0562 g, 4 equiv.) were dissolved in 20 mL of methanol to form

clear and colorless solutions. The hydroxylamine hydrochloride and potassium hydroxide solutions were combined and a colorless potassium chloride precipitate was observed. The mixture was let stir for 10 minutes, then the potassium chloride was vacuum filtered from a clear and colorless filtrate. This filtrate was combined with the suspension of ethyl 4-ethynylpicolinate to form a clear and orange solution. This solution was stirred for 24 hours. Next, another set of hydroxylamine hydrochloride and potassium hydroxide solutions in 20 mL of methanol were prepared, combined and filtered as described previously to obtain another clear and colorless filtrate. This filtrate was combined into the reaction solution and let stir for another 20 hours. The solution was evaporated to a fifth of its original volume using a flash evaporator, then mixed with 50 mL of distilled water. The orange solution was acidified to a pH of one using 2M hydrochloric acid, causing a blue color to develop. This mixture was adjusted to a pH of 5 using saturated aqueous sodium bicarbonate, then vacuum filtered. The blue precipitate was triturated in 20 mL of dichloromethane for twenty minutes, then vacuum filtered to yield 5-(p-ethynyl-N,N-dimethylanilinyl)salicylhydroxamic acid as a blue powder. The synthetic yield was 33%. Elemental analysis shows that the resulting solid is 80% H_3meanshi with 20% impurity of the respective carboxylic acid, with a half mole of hydrochloride salt: 0.8 $C_{17}H_{16}N_2O_3$ · 0.2 $C_{17}H_{15}NO_3$ · 0.5 HCl [fw = 311.55 g/mol] % found (calculated): %C 65.70 (65.54), %H 5.10 (5.27), %N 8.03 (8.09). ^{1}H-NMR (400 MHz, d_6-DMSO): 12.42 ppm (1H, s), 11.44 ppm (1H, s), 9.39 ppm (1H, s), 7.84 ppm (1H, m), 7.48 ppm (1H, d), 7.32 ppm (2H, d), 6.91 ppm (1H, d), 6.71 ppm (2H, d), 2.94 ppm (6H, s).

Pyrazine hydroxamic acid. Pyrazine hydroxamic acid was synthesized according to a literature procedure.[11] First, 40.29 mmol of 2-pyrazine carboxylic acid (5.00 g, 1 equiv.) was dissolved in dichloromethane under inert atmosphere. Next, 48.35 mmol of N-methylmorpholine (5.32 mL, 1.2 equiv.) was added, then the solution was cooled to 4 ºC while stirring. Afterwards, 48.35 mmol of ethyl chloroformate (4.60 mL, 1.2 equiv.) was added slowly, resulting in a cloudy and yellow solution. After ten minutes, the reaction was let warm to room temperature and stirred for 45 minutes, then vacuum filtered to remove some colorless precipitate. Separately, 60.44 mmol of hydroxylamine hydrochloride (4.20 g, 1.5 equiv.) and 60.44 mmol potassium chloride (3.99 g, 1.5 equiv.) were dissolved in 75 mL of methanol to form clear and colorless solutions. These solutions were combined and let stir for ten minutes. Next, the mixture was vacuum filtered to

remove a potassium chloride precipitate from a clear and colorless filtrate. Both filtrates were combined and let stir for 2 hours, then evaporated on a flash evaporator to a yellow powder. This was taken up in 125 mL of boiling distilled water, then let cool in a 4 ^{o}C fridge overnight. The mixture was vacuum filtered to isolate pyrazine hydroxamic acid as colorless needles. The synthetic yield was 79%. Elemental analysis of $C_5H_5N_3O_2 \cdot H_2O$ [fw = 157.13 g/mol] % found (calculated): %C 38.47 (38.22), %H 4.27 (4.49), %N 26.71 (26.74). ^{1}H-NMR (400 MHz, d_6-DMSO): 11.65 ppm (1H, s), 9.28 ppm (1H, s), 9.11 ppm (1H, s), 8.84 ppm (1H, d), 8.68 ppm (1H, d).

Ethyl 4-iodopicolinate. Ethyl 4-iodopicolinate was synthesized using a Fischer esterification.[17] Forty mmol of 4-iodopicolinc acid (9.96 g, 1 equiv.) was suspended in 80 mL of 200 proof ethanol to form a cloudy and brown solution. Sodium sulfate was added until no more clumping was observed, then 4 mmol of sulfuric acid (213 µL, 0.1 equiv.) was added. The solution was warmed to 90 ^{o}C and let stir for 21 hours. The reaction was vacuum filtered to remove sodium sulfate, and the filtrate was evaporated to a fifth of the original volume using a flash evaporator. The pH was adjusted to 8 using 1M aqueous sodium bicarbonate, then 100 mL of distilled water was added. The mixture was vacuum filtered to isolate ethyl 4-iodopicolinate as a tan powder. The synthetic yield was 66%. Elemental analysis of $C_8H_8NO_2I \cdot 0.25\ H_2O$ [fw = 281.57 g/mol] % found (calculated): %C 34.09 (34.13), %H 2.76 (3.04), %N 4.85 (4.97). ^{1}H-NMR (400 MHz, d_6-DMSO): 8.41 ppm (1H, d), 8.36 ppm (1H, s), 8.10 (1H, dd), 4.35 ppm 92H, q), 1.32 ppm (3H, t).

Ethyl 4-ethynylpicolinate. Ten mmol of ethyl 4-iodopicolinate (2.77 g, 1 equiv.) was dissolved in a 50 mL solution of 1:1 triethylamine and tetrahydrofuran to form a clear and yellow solution. Next 12 mmol of trimethylsilylacetylene (1.708 mL, 1.2 equivs.) was added and stirred. Then 1 mmol of palladium(II) bis(triphenylphosphine)dichloride (0.7019 g, 0.1 equiv.) and 2 mmol of copper(I) iodide (0.3809 g, 0.2 equiv.) were added to form a cloudy black solution. Next, 2 mmol of dimethylethylenediamine (215 µL, 0.2 equiv.) was added, forming a tan precipitate. The reaction was warmed to 50 ^{o}C and let stir for 43.5 hours. The reaction was removed from heat and quenched using 50 mL of 1M aqueous ammonium chloride, and stirred for twenty minutes. Next, 50 mL of brine was added, and the solution was extracted using six portions of ethyl acetate. The extraction was dried over sodium sulfate, then gravity filtered. The filtrate was

evaporated on a flash evaporator to give a red oil. This oil was taken up in 5 mL of ethyl acetate and purified on a silica gel column using a mobile phase of 7:3 hexanes and ethyl acetate. The purified oil was taken up in 7.5 mL of tetrahydrofuran and treated with 7.5 mL of 1M tetrabutylammoinum in tetrahydrofuran for one hour. Next, 10 mL of distilled water was added and the solution was adjusted to a pH of four using 2 M hydrochloric acid. 2 mL of brine was added and the solution was extracted with five portions of ethyl acetate. The extraction was dried over sodium sulfate and gravity filtered. The filtrate was evaporated using a flash evaporator to a brown powder. The powder was triturated in 25 mL of distilled water for twenty minutes and vacuum filtered to yield ethyl 4-ethynylpicolinate as a tan powder. The synthetic yield was 39%. Elemental analysis of $C_{10}H_9NO_2$ [fw = 175.19 g/mol] % found (calculated): %C 68.30 (68.56), %H 5.09 (5.18), %N 7.89 (8.00). ^{1}H-NMR (400 MHz, d_6-DMSO): 8.74 ppm (1H, d), 8.01 ppm (1H, s), 7.72 ppm (1H, dd), 4.77 ppm (1H, s), 4.35 ppm (2H, q), 1.31 ppm (3H, t).

4-ethynylpicoline hydroxamic acid (H_2epic). First, 4.6 mmol of ethyl 4-ethynylpicolinate (0.8063g, 1 equiv.) was dissolved in 20 mL of methanol to form a clear and brown solution. Separately, 13.8 mmol of hydroxylamine hydrochloride (0.9597 g, 3 equiv.) and 18.4 mmol of potassium hydroxide (1.2154 g, 4 equiv.) were dissolved in 20 mL of methanol to form clear and colorless solutions. The hydroxylamine hydrochloride and potassium hydroxide solutions were combined and a colorless potassium chloride precipitate was observed. The mixture was let stir for 10 minutes, then the potassium chloride was vacuum filtered from a clear and colorless filtrate. This filtrate was combined with the suspension of ethyl 4-ethynylpicolinate to form a clear and orange solution. This solution was stirred for 20 hours. Next, another set of hydroxylamine hydrochloride and potassium hydroxide solutions in 20 mL of methanol were prepared, combined and filtered as described previously to obtain another clear and colorless filtrate. This filtrate was combined into the reaction solution and let stir for another 29 hours. The solution was evaporated to an eighth of the original volume using a flash evaporator, then combined with 10 mL of distilled water. The pH was adjusted to 2 using 2M hydrochloric acid, then 50 mL of distilled water was added to form a yellow-orange precipitate. The mixture was vacuum filtered and the precipitate was triturated in 20 mL of dichloromethane for twenty minutes. This mixture was vacuum filtered to yield 4-ethynylpicoline hydroxamic acid as a yellow powder. The synthetic yield was 68%. Elemental analysis for $C_8H_6N_2O_2 \cdot 0.2\ H_2O$ [fw =

165.75 g/mol] % found (calculated): %C 57.99 (57.97), %H 3.89 (3.89), %N 16.63 (16.90). ^{1}H-NMR (400 MHz, d_6-DMSO): 11.52 ppm (1H, s), 9.22 ppm (1H, s), 8.62 ppm (1H, d), 7.91 ppm (1H, s), 7.64 ppm (1H, dd), 4.73 (1H, s).

Ethyl 4-(p-ethynylanisolyl)picolinate. First, 8.71 mmol of ethyl 4-iodopicolinate (2.4126 g, 1 equiv.) was dissolved in 50 mL of a 1:1 solution of triethylamine and tetrahydrofuran to form a cloudy off-white suspension. Next, 9.56 mmol of p-ethynylanisole (1.243 mL, 1.1 equiv.) was added and stirred. The 0.871 mmol of palladium(II) bis(triphenylphosphine)dichloride (0.6112 g, 0.1 equiv.) and 1.74 mmol of copper(I) iodide (0.3317 g, 0.2 equiv.) was added, after which a brown color develops. The mixture was warmed to 60 ^{o}C and let stir for 72 hours. The reaction was quenched with 25 mL of 1M aqueous ammonium chloride and let stir for 20 minutes. Then 25 mL of ethyl acetate was added and the biphasic mixture was acidified so that the aqueous layer had a pH of one using 2M hydrochloric acid. The mixture was vacuum filtered to obtain a brown precipitate and a biphasic dark brown/red filtrate. This mixture was separated, then the red aqueous layer was combined with another 25 mL of ethyl acetate, and its pH was adjusted to 6 using saturated aqueous sodium bicarbonate. Again, the biphasic mixture was separated and the aqueous layer was extracted with two more 30 mL portions of ethyl acetate. All ethyl acetate solutions were combined and dried over sodium sulfate, then gravity filtered. The filtrate was evaporated using a flash evaporator to a red oil. The oil was then dissolved in 15 ml of ethyl acetate and combined with the first brown precipitate. This mixture was purified on a silica gel column using a gradient of ethyl acetate in hexanes. The purified fractions were condensed to give ethyl 4-(p-ethynylanisolyl)picolinate as a yellow powder. The synthetic yield was 80%. Elemental analysis of $C_{17}H_{15}NO_3$ [fw = 281.31 g/mol] % found (calculated): %C 72.34 (72.58), %H 5.43 (5.37), %N 4.93 (4.98). ^{1}H-NMR (400 MHz, d_6-DMSO): 8.73 ppm (1H, d), 8.06 ppm (1H, s), 7.73, ppm (1H, d), 7.60 ppm (2H, d), 7.03 (2H, d), 4.36 ppm (2H, q), 1.34 ppm (3H, t).

4-(p-ethynylanisolyl)picoline hydroxamic acid (H_2maepic). First, 6.69 mmol of ethyl 4-(p-ethynylanisolyl)picolinate (1.8822 g, 1 equiv.) was dissolved in 25 mL of methanol to form a clear and orange solution. Separately, 20.07 mmol of hydroxylamine hydrochloride (1.3951 g, 3 equiv.) and 26.76 mmol of potassium hydroxide (1.7667 g, 4 equiv.) were dissolved in 25 mL of methanol to form clear and colorless solutions. The hydroxylamine hydrochloride and potassium

hydroxide solutions were combined and a colorless potassium chloride precipitate was observed. The mixture was let stir for 10 minutes, then the potassium chloride was vacuum filtered from a clear and colorless filtrate. This filtrate was combined with the suspension of ethyl 4-ethynylpicolinate to form a clear and orange solution. This solution was stirred for 22 hours. Next, another set of hydroxylamine hydrochloride and potassium hydroxide solutions in 25 mL of methanol were prepared, combined and filtered as described previously to obtain another clear and colorless filtrate. This filtrate was combined into the reaction solution and let stir for another 24 hours. The solution was reduced to a fifth of its original volume using a flash evaporator, then acidified to a pH of 1 using 2 M hydrochloric acid. Next, 200 mL of distilled water was added which formed a yellow precipitate. This mixture was vacuum filtered and the precipitate was triturated in 20 mL of dichloromethane for 20 minutes. This was vacuum filtered to yield 4-(p-ethynylanisolyl)picoline hydroxamic acid as a yellow powder. The synthetic yield was 76%. Elemental analysis of $C_{15}H_{12}N_2O_3$ [fw = 268.27 g/mol] % found (calculated): %C 66.96 (67.16), %H 4.58 (4.51), %N 10.45 (10.44). ^{1}H-NMR (400MHz, d_6-DMSO): 11.52 ppm (1H, s), 9.18 ppm (1H, s), 8.61 (1H, dd), 7.99 ppm (1H, s), 7.65 ppm (1H, dd), 7.60 ppm (2H, d), 7.03 ppm (2H, d), 3.81 ppm (3H, s).

$SmGa_4(eshi)_4(OPv)_4Na\cdot(H_2O)_6$, **Sm-e4**. 0.125 mmol of $Sm(NO_3)_3\cdot 6H_2O$ (0.0556g, 1 equiv.) and 0.25 mmol of $Ga(NO_3)_3$ (0.0639 g, 2 equiv.) were dissolved in 2.5 mL of methanol. Separately, 0.25 mmol of H_3eshi (0.0443 g, 2 equiv.) and 1.025 mmol of sodium pivolate hydrate (NaOPv, 0.1457 g, 8.2 equiv.) were dissolved in 7.5 mmol of methanol to form a clear and yellow solution. The two solutions were combined and let stir for approximately one hour. The solution was gravity filtered and let slowly evaporate in a humid environment, yielding fine yellow-brown needles in one week, isolated by vacuum filtration and washing with cold methanol. The synthetic yield was 25% based on samarium nitrate hexahydrate. Elemental analysis for $SmGa_4C_{56}H_{52}N_4O_{22}Na$ [fw = 1589.31 g/mol] % found (calculated): %C 42.24 (42.32); %H 3.53 (3.55); %N 3.58 (3.53). ESI-MS for $SmGa_4C_{56}H_{52}N_4O_{20}$ $[M]^-$, found (calculated): 1531.92 (1529.94). ^{1}H-NMR (500 MHz, d_4-MeOH): 8.11 ppm (1H, d), 7.14 ppm (1H, s), 6.92 ppm (1H, d), 3.51 ppm (1H, s), 1.03 ppm (9H, s).

General synthesis for Ln[12-MC$_{Ga}^{III}{}_{N(eshi)}$-4](L)$_4$Na (Ln = Gd, Tb, Dy, Ho, Er, Tm, Yb, Lu, or Y; L = OPv, OBz). 0.0625 mmol of Ln(NO$_3$)$_3$·xH$_2$O (Ln = Gd, Tb, Dy, Ho, Er, Tm, Yb, Lu, or Y, 1 equiv.) and 0.25 mmol of Ga(NO$_3$)$_3$ (0.0639 g, 4 equiv.) were dissolved in 2.5 mL of methanol. Separately, 0.25 mmol of H$_3$eshi (0.0443 g, 4 equiv.) and 1.025 mmol of L (L = sodium pivolate hydrate (NaOPv), or sodium benzoate (NaOBz), 16.4 equiv.) were dissolved in 7.5 mmol of methanol to form a clear and yellow solution. The two solutions were combined and let stir for approximately one hour. The solution was gravity filtered and let slowly evaporate in a humid environment, yielding fine yellow-brown needles or plates in one week, isolated by vacuum filtration and washing with cold methanol.

GdGa$_4$(eshi)$_4$(OPv)$_4$Na(H$_2$O)$_6$, **Gd-e4**. The synthetic yield was 21% based on gadolinium nitrate hexahydrate. Elemental analysis for *GdGa$_4$C$_{56}$H$_{56}$N$_4$O$_{22}$Na* [fw = 1596.20 g/mol] % found (calculated): %C 42.07 (42.14); %H 3.50 (3.54); %N 3.57 (3.51). ESI-MS for *GdGa$_4$C$_{56}$H$_{52}$N$_4$O$_{20}$* [M]$^-$, found (calculated): 1537.92 (1537.18).

TbGa$_4$(eshi)$_4$(OPv)$_4$Na(H$_2$O)$_2$, **Tb-e4**. The synthetic yield was 49% based on terbium nitrate pentahydrate. Elemental analysis for *TbGa$_4$C$_{56}$H$_{56}$N$_4$O$_{22}$Na* [fw = 1597.88 g/mol] % found (calculated): %C 41.86 (42.09); %H 3.62 (3.53); %N 3.54 (3.91). ESI-MS for *TbGa$_4$C$_{56}$H$_{52}$N$_4$O$_{20}$* [M]$^-$, found (calculated): 1538.92 (1536.94).

YbGa$_4$(eshi)$_4$(OPv)$_4$Na(H$_2$O)$_2$, **Yb-e4**. The synthetic yield was 28% based on ytterbium nitrate pentahydrate. Elemental analysis for *YbGa$_4$C$_{56}$H$_{56}$N$_4$O$_{22}$Na* [fw = 1612.01 g/mol] % found (calculated): %C 41.93 (41.73); %H 3.48 (3.50); %N 3.48 (3.64). ESI-MS for *YbGa$_4$C$_{56}$H$_{52}$N$_4$O$_{20}$* [M]$^-$, found (calculated): 1551.94 (1551.96).

YGa$_4$(eshi)$_4$(OPv)$_4$Na(H$_2$O)$_2$, **Y-e4**. The synthetic yield was 27% based on yttrium nitrate hexahydrate. Elemental analysis for *YGa$_4$C$_{56}$H$_{56}$N$_4$O$_{22}$Na* [fw = 1527.86 g/mol] % found (calculated): %C 43.87 (44.02); %H 3.48 (3.69); %N 3.78 (3.67). ESI-MS for *YGa$_4$C$_{56}$H$_{52}$N$_4$O$_{20}$* [M]$^-$, found (calculated): 1468.91 (1466.93).^{1}H-NMR (500 MHz, *d$_4$*-MeOH): 7.99 ppm (1H, d), 7.05 ppm (1H, s), 6.86 ppm (1H, d), 3.49 ppm (1H, s), 1.13 ppm (9H, s).

$YGa_4(eshi)_4(OBz)_4Na(MeOH)$, **Y-e4OBz**. The synthetic yield was 48% based on yttrium nitrate hexahydrate. Elemental analysis for *$YGa_4C_{65}H_{40}N_4O_{21}Na$* [fw = 1603.83 g/mol] % found (calculated): %C 48.78 (48.68); %H 2.80 (2.51); %N 3.73 (3.49). ESI-MS for *$YGa_4C_{64}H_{36}N_4O_{20}$* $[M]^-$, found (calculated): 1548.78 (1546.80).^{1}H-NMR (500 MHz, *d_4*-MeOH): 8.03 ppm (3H, m), 7.44 ppm (2H, broad s), 7.28 ppm (1H, broad s), 7.09 ppm (1H, s), 6.87 ppm (1H, d), 3.50 ppm (1H, s).

$YGa_4(eshi)_4(piOBz)Na(H_2O)_4$, **Y-e4piOBz**. 0.0625 mmol of $Y(NO_3)_3{\cdot}6H_2O$ (0.0239 g, 1 equiv.) and 0.25 mmol of $Ga(NO_3)_3$ (0.0639 g, 4 equiv.) were dissolved in 2.5 mL of methanol. Separately, 0.25 mmol of H_3eshi (0.0443 g, 4 equiv.) and 1.025 mmol of 4-iodopbenzoic acid (HpiOBz, 0.2542 g, 16.4 equiv.) and 1.775 mmol concentrated aqueous sodium hydroxide (90 µL, 28.4 equiv.) were dissolved in 7.5 mmol of methanol to form a clear and yellow solution. The two solutions were combined and let stir for approximately one hour. The solution was gravity filtered and let slowly evaporate in a humid environment, yielding fine needles in one week, isolated by vacuum filtration and washing with cold methanol. The synthetic yield was 19% based on yttrium nitrate hexahydrate. Elemental analysis for *$YGa_4C_{64}H_{40}N_4O_{24}NaI_4$* [fw = 2147.43 g/mol] % found (calculated): %C 35.69 (35.80); %H 1.83 (1.88), %N 2.70 (2.61). ESI-MS for *$YGa_4C_{64}H_{32}N_4O_{20}I_4$* [M]-, found 2052.37 (calculated): (2050.39).^{1}H-NMR (500 MHz, *d_4*-MeOH): 8.01 ppm (1H, d), 7.68 ppm (4H, broad s), 7.07 ppm (1H, s), 6.86 ppm (1H, d).

General synthesis for {Ln[12-$MC_{Ga}{}^{III}{}_{N(eshi)}$-4]Na}$_2(iph)_4$, **Ln-e8. Ln-e8** were synthesized by modifying a literature procedure.[7] 0.125 mmol of $Ln(NO_3)_3.xH_2O$ (Ln = Pr, Nd, Sm, Eu, Gd, Tb, Dy, Ho, Er, Tm, Yb, or Y, 1 equiv.) and 0.6 mmol of $Ga(NO_3)_3$ (0.1535 g, 4.8 equiv.) were dissolved in 5 mL of DMF. Separately, 0.6 mmol of H_3eshi (0.1063 g, 4.8 equiv.), 0.3 mmol of isophthalic acid (0.0498 g, 2.4 equiv.), and 2.4 mmol of saturated aqueous sodium hydroxide (119.4 µL, 19.2 equiv.) were dissolved in 15 mL of DMF for form a clear and yellow solution. The solutions were combined and let stir for at least one hour, then gravity filtered. The filtrate was let slowly evaporate over 2-4 weeks yielding yellow-brown crystalline plates, isolated by vacuum filtration and washing with cold DMF.

$Pr_2Ga_8(eshi)_8(iph)_4Na_2(DMF)_{10}(H_2O)_7$, **Pr-e8**. The synthetic yield was 34% based on praseodymium nitrate hexahydrate. Elemental analysis for $Pr_2Ga_8C_{134}H_{132}N_{18}O_{57}Na_2$ [fw = 3791.00 g/mol] % found (calculated): %C 42.38 (42.44); %H 3.44 (3.51); %N 6.68 (6.65). ESI-MS for $Pr_2Ga_8C_{104}H_{48}N_8O_{40}$ $[M]^{2-}$, found (calculated): 1444.60 (1444.21).

$Nd_2Ga_8(eshi)_8(iph)_4Na_2(DMF)_{14}(H_2O)_{12}$, **Nd-e8**. The synthetic yield was 28% based on neodymium nitrate hexahydrate. Elemental analysis for $Nd_2Ga_8C_{146}H_{170}N_{22}O_{66}Na_2$ [fw = 4181.30 g/mol] % found (calculated): %C 41.87 (41.94); %H 3.87 (4.10); %N 7.44 (7.37). ESI-MS for $Nd_2Ga_8C_{104}H_{48}N_8O_{40}$ $[M]^{2-}$, found (calculated): 1447.60 (1446.21).

$Sm_2Ga_8(eshi)_8(iph)_4Na_2(DMF)_{15}(H_2O)_8$, **Sm-e8**. The synthetic yield was 10% based on samarium nitrate hexahydrate. Elemental analysis for $Sm_2Ga_8C_{149}H_{169}N_{23}O_{63}Na_2$ [fw = 4194.57 g/mol] % found (calculated): %C 42.73 (42.67); %H 4.00 (4.06); %N 7.87 (7.68). ESI-MS for $Sm_2Ga_8C_{104}H_{48}N_8O_{40}$ $[M]^{2-}$, found (calculated): 1454.19 (1456.22). ^{1}H-NMR (500 MHz, d_4-MeOH): 8.66 ppm (3H, s), 8.08 ppm (2H, d), 7.56 ppm (1H, t), 7.13 ppm (2H, s), 6.88 ppm (2H, d), 3.49 ppm (2H, s).

$Eu_2Ga_8(eshi)_8(iph)_4Na_2(DMF)_{12}(H_2O)_7$, **Eu-e8**. The synthetic yield was 6% based on europium nitrate hexahydrate. Elemental analysis for $Eu_2Ga_8C_{140}H_{146}N_{20}O_{59}Na_2$ [fw = 3960.48 g/mol] % found (calculated): %C 42.53 (42.46); %H 3.76 (3.72); %N 7.01 (7.07). ESI-MS for $Eu_2Ga_8C_{104}H_{48}N_8O_{40}$ $[M]^{2-}$, found (calculated): 1455.70 (1455.22).

$Gd_2Ga_8(eshi)_8(iph)_4Na_2(DMF)_{12}(H_2O)_7$, **Gd-e8**. The synthetic yield was 12% based on gadolinium nitrate hexahydrate. Elemental analysis for $Gd_2Ga_8C_{140}H_{146}N_{20}O_{59}Na_2$ [fw = 3971.05 g/mol] % found (calculated): %C 42.32 (42.34); %H 3.74 (3.71); %N 6.99 (7.05). ESI-MS for $Gd_2Ga_8C_{104}H_{48}N_8O_{40}$ $[M]^{2-}$, found (calculated): 1460.71 (1462.23).

$Tb_2Ga_8(eshi)_8(iph)_4Na_2(DMF)_{12}(H_2O)_5$, **Tb-e8**. The synthetic yield was 23% based on terbium nitrate pentahydrate. Elemental analysis for $Tb_2Ga_8C_{149}H_{169}N_{23}O_{63}Na_2$ [fw = 3938.37 g/mol] % found (calculated): %C 42.78 (42.70); %H 3.67 (3.63); %N 7.11 (7.11). ESI-MS for $Tb_2Ga_8C_{104}H_{48}N_8O_{40}$ $[M]^{2-}$, found (calculated): 1462.71 (1462.23).

$Dy_2Ga_8(eshi)_8(iph)_4Na_2(DMF)_{12}(H_2O)_9$, **Dy-e8**. The synthetic yield was 2% based on dysprosium nitrate pentahydrate. Elemental analysis for $Dy_2Ga_8C_{140}H_{150}N_{20}O_{61}Na_2$ [fw = 4017.17 g/mol] % found (calculated): %C 41.91 (41.85); %H 3.73 (3.76); %N 7.02 (6.97). ESI-MS for $Dy_2Ga_8C_{104}H_{48}N_8O_{40}$ $[M]^{2-}$, found (calculated): 1466.21 (1466.23).

$Ho_2Ga_8(eshi)_8(iph)_4Na_2(DMF)_{13}(H_2O)_9$, **Ho-e8**. The synthetic yield was 11% based on holium nitrate pentahydrate. Elemental analysis for $Ho_2Ga_8C_{143}H_{157}N_{21}O_{62}Na_2$ [fw = 4095.54 g/mol] % found (calculated): %C 42.73 (42.67); %H 4.00 (4.06); %N 7.87 (7.68). ESI-MS for $Ho_2Ga_8C_{104}H_{48}N_8O_{40}$ $[M]^{2-}$, found (calculated): 1498.71 (1468.23).

$Er_2Ga_8(eshi)_8(iph)_4Na_2(DMF)_{12}(H_2O)_6$, **Er-e8**. The synthetic yield was 12% based on erbium nitrate pentahydrate. Elemental analysis for $Er_2Ga_8C_{140}H_{144}N_{20}O_{58}Na_2$ [fw = 3971.14 g/mol] % found (calculated): %C 42.73 (42.67); %H 4.00 (4.06); %N 7.87 (7.68). ESI-MS for $Er_2Ga_8C_{104}H_{48}N_8O_{40}$ $[M]^{2-}$, found (calculated): 1470.71 (1470.23).

$Tm_2Ga_8(eshi)_8(iph)_4Na_2(DMF)_8(H_2O)_6$, **Tm-e8**. The synthetic yield was 12% based on thulium nitrate pentahydrate. Elemental analysis for $Tm_2Ga_8C_{128}H_{116}N_{16}O_{54}Na_2$ [fw = 3684.03 g/mol] % found (calculated): %C 41.72 (41.73); %H 3.19 (3.17); %N 6.05 (6.08). ESI-MS for $Tm_2Ga_8C_{104}H_{48}N_8O_{40}$ $[M]^{2-}$, found (calculated): 1472.71 (1472.24).

$Yb_2Ga_8(eshi)_8(iph)_4Na_2(DMF)_{12}(H_2O)_6$, **Yb-e8**. The synthetic yield was 22% based on ytterbium nitrate pentahydrate. Elemental analysis for $Yb_2Ga_8C_{140}H_{144}N_{20}O_{58}Na_2$ [fw = 3984.65 g/mol] % found (calculated): %C 42.26 (42.20); %H 3.69 (3.64); %N 7.07 (7.03). ESI-MS for $Yb_2Ga_8C_{104}H_{48}N_8O_{40}$ $[M]^{2-}$, found (calculated): 1476.21 (1476.24).

$Y_2Ga_8(eshi)_8(iph)_4Na_2(DMF)_{16}(H_2O)_{12}$, **Y-e8**. The synthetic yield was 11% based on yttrium nitrate hexahydrate. Elemental analysis for $Y_2Ga_8C_{152}H_{184}N_{24}O_{68}Na_2$ [fw = 4216.82 g/mol] % found (calculated): %C 41.72 (41.73); %H 3.19 (3.17); %N 6.05 (6.08). ESI-MS for $Y_2Ga_8C_{104}H_{48}N_8O_{40}$ $[M]^{2-}$, found (calculated): 1395.58 (1392.11). ^{1}H-NMR (500 MHz, d_4-

MeOH): 9.07 ppm (1H, s), 8.23 ppm (2H, d), 8.03 ppm, (2H, d), 7.30 ppm (1H, t), 7.09 ppm (2H, s), 6.85 ppm (2H, d), 3.47 ppm (2H, s).

*CuAAC on **Sm-e8** metallacrowns*

Full functionalization of Sm-e8. To obtain a **Sm-e8** with all eight functionalities reacted with an azide, a modified literature procedure was used.[5] First, 12.7 µmol of Sm-e8 and 13.3 µmol of CuI were dissolved in 1 mL of DMSO. Next, 114 µmol of benzyl azide was added and the reaction was warmed to 75 ^{o}C and stirred for 24 hrs. The solution was allowed to slowly evaporate in a humid environment until a gray powder formed. This powder was isolated via vacuum filtration and washing with cold water.

Partial functionalization on Sm-e8. To partially functionalize **Sm-e8**, 12.7 µmol of Sm-e8, 114 µmol of either benzyl azide or biotin azide, 1.5 µmol of TBTA, 3.0 µmol of CuI and 3.0 µmol of sodium ascorbate were combined in 2 mL of DMF. The reaction was stirred at RT for 48 hrs, then let slowly evaporate in a humid environment. The products were isolated as a yellow powder using vacuum filtration.

Synthesis of the mixed epic/pyzHA YZn_{16} MC. First, 0.24 mmol of H_2pyzHA and 0.08 mmol of H_2epic were mixed in a solution of 10 mL of water and 1 mL of pyridine. Then 0.32 mmol of zinc(II) triflate, followed by 0.04 mmol of yttrium(III) triflate were added. The solution was warmed to 50 ^{o}C and strirred for about one hour. This warm solution was vacuum filtered to yield the mixed ligand metallacrown as a dark yellow precipitate.

CuAAC on the mixed ligand YZn_{16} MC. First, 0.48 µmol of CuI, 0.48 µmol of TBTA, and 0.96 µmol of sodium ascorbate were dissolved in 1 mL of DMF. Next, 10 µmol of biotin azide followed by 2 µmol of mixed ligand MC were added. The solution was stirred for 2 days, then allowed to slowly evaporate until a dark yellow precipitate was observed, which was isolated via vacuum filtration.

Results and Discussion

Solid and Solution State Structure of the Ethynyl Metallacrowns

The **Ln-e4** and **Ln-e8** metallacrown series were synthesized and characterized using elemental analysis and electrospray ionization mass spectrometry. The results confirm consistent composition of each complex. In addition, ^{1}H-NMR of Sm^{3+} and Y^{3+} analogs shows consistent spectra with pseudofourfold symmetry regardless of lanthanide size, which suggests that each of these complexes have the same structure. X-ray crystallographic data were collected on **Gd-e4** and **Sm-e8**.

Table 4.1 Crystallographic Data for Ethynyl Metallacrowns

Compound	**Gd-e4**	**Sm-e8**
Chemical Formula	$GdGa_4C_{61.25}H_{67.75}N_4O_{25.25}Na$	$Sm_2Ga_8C_{149}H_{24}N_{23}O_{69}Na_2$
Formula Weight	1723.2 g/mol	2635.96 g/mol
Crystal System, Space Group	Monoclinic, C2/c (No. 15)	Monoclinic, $P2_1/n$ (No.14)
T	85(2) K	85(2) K
a	24.6616(2) Å	20.0038(2) Å
b	23.0260 (2) Å	24.1645(1) Å
c	25.2986(2) Å	21.5306(1) Å
α	90.00°	90.00°
β	92.37°	108.66°
γ	90.00°	90.00°
Volume	14353.7 $Å^3$	9860.36 $Å^3$
λ	1.54178 Å	1.54178 Å
ρ_{calc}	1.595 g/cm^3	1.775 g/cm^3
Z	8	4
μ	16.433 mm^{-1}	11.836
F(000)	12768	4452
θ range	2.63 to 69.83°	2.63 to 69.55°
Limiting Indices	-27<h<24	-24<h<23
	-27<k<27	-29<k<29
	-30<l<30	-26<l<25
Reflections collected/unique	110499/13198	151379/18273
Completeness to θ	97.2%	98.5%
No. of Data/Restraints/Params	13198/31/881	18273/48/1369
GooF on F^2	1.228	1.758
$^{a}R_1$	0.0421 [I>2σ(I)], 0.0427 [all data]	0.0622 [I>2σ(I)], 0.0635 [all data]
$^{b}wR_2$	0.1370 [I>2σ(I)], 0.1388 [all data]	0.1972 [I>2σ(I)], 0.1990 [all data]
Largest Diff. Peak, Hole	1.986 and -0.796 e/$Å^3$	2.111 and -0.994 e/$Å^3$

^{a} $R_1 = \Sigma(||F_o|-|F_c||)/\Sigma|F_o|$ ^{b} $wR_2 = [\Sigma[w(F_o^2 - F_c^2)^2]/\Sigma[w(F_o)^2]]^{1/2}$; $w = 1/[\sigma^2(F_o^2) + (mp)^2 + np]$; $p = [\max(F_o^2,0) + 2F_c^2]/3$ (m and n are constants); $\sigma = [\Sigma[w(F_o^2 - F_c^2)^2/(n - p)]^{1/2}$

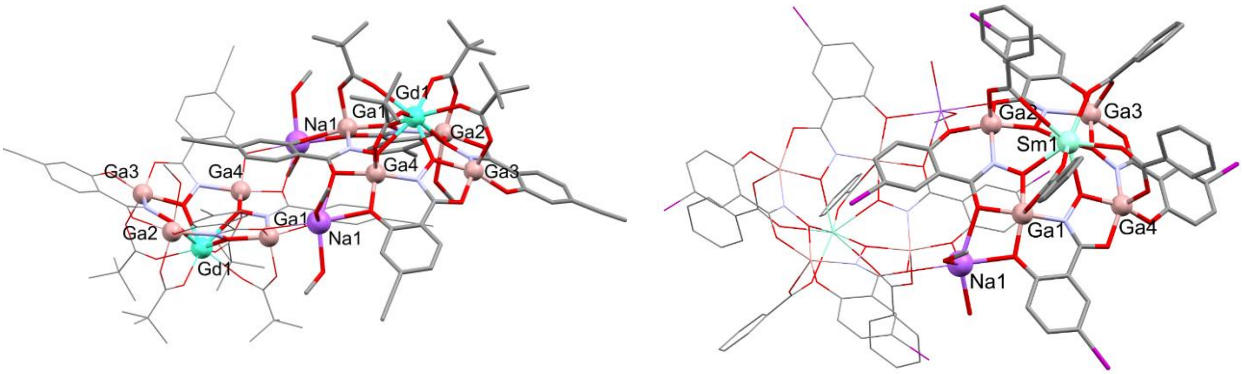

Figure 4.3. X-ray crystal structures of **Gd-e4** (left) and **SmGa$_4$-I$_4$** (right).

Gd-e4 crystallized in the space group C2/c as a dimerized structure similar to **SmGa$_4$-I$_4$** reported in the previous chapter (Figure 4.3). The gadolinium is eight coordinate in a distorted square antiprism comprised of the four oxime oxygens of eshi ligands and an oxygen from pivolate ligands. The compression factor for the distorted square antiprism is 0.892. The gadolinium is closer to the carboxylate oxygen mean plane rather than the oxime oxygen mean plane, and since the bond lengths are nearly equivalent, this must be due to steric restrictions from oxime to oxime distances compared to the required distance of a Gd-O bond. Three gallium ions are five coordinate square pyramidal (τ = 0.4363, 0.3625, 0.3557) and remaining gallium ion is a six coordinate octahedral geometry. The square pyramidal gallium have two eshi ligands that bind bidentate in the basal positions and a pivolate oxygen in the apical position. The octahedral gallium has the same five binding partners as the other three Ga ions but also has an elongated axial bond to a solvent molecule of 2.2 to 2.3 Å compared to the average 1.97 Å bond to the carboxylate oxygen. The sodium countercation is in a six coordinate, distorted octahedral geometry, where two metallacrowns bind bidentate to the sodium in a propeller fashion with the other coordination sites occupied by solvent molecules. Comparison of the gadolinium analogs of the ethynyl (**Gd-e4**) and iodo (**Gd-Ga$_4$I$_4$**) structures shows more bowling in the **Gd-e4** structure with an increase in the oxime mean plane to gallium mean plane distance from 0.221 Å to 0.300 Å, as well as an increase in cavity radius from 0.56 Å to 0.59 Å. An increase in both of these parameters indicates that the metallacrown is more bowled. This is also very noticeable when both structures are overlaid (Figure 4.4).

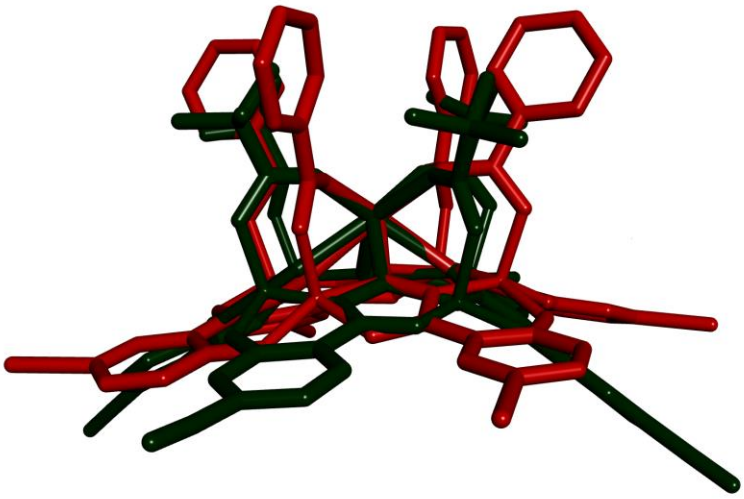

Figure 4.4. Overlay of **Gd-Ga$_4$I$_4$** (red) and **Gd-e4** (green).

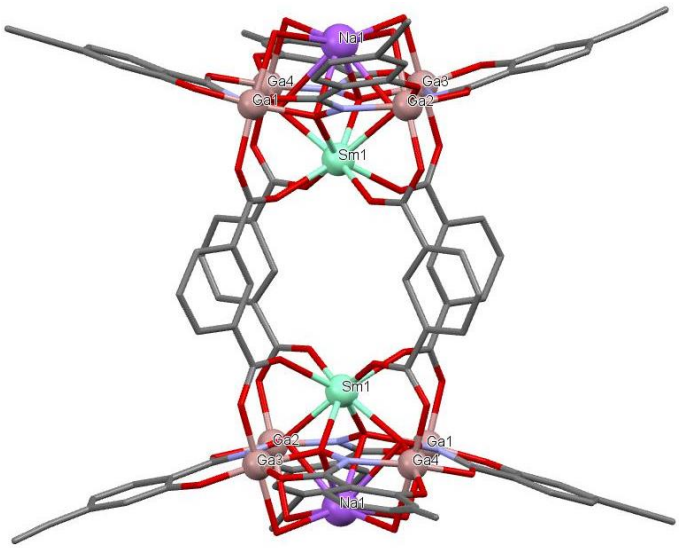

Figure 4.5. X-ray crystal structure of **Sm-e8**. Solvent molecules and hydrogen atoms are removed for clarity.

The **Sm-e8** crystallized in the space group $P2_1/n$ and also features an eight coordinate, distorted square antiprism geometry for the samarium ion (Figure 4.5). The compression factor is 0.915 for this complex, and the samarium is closer to the mean plane of the isophthalate oxygens rather than the oxime oxygens. The slight difference between the **Gd-e4** and **Sm-e4** Ln coordination sites is due to the change in lanthanide. A Sm-O bond should be very slightly longer than a Gd-O bond, which will cause two changes in the coordination site. First, the oxygen mean planes should be further apart for Sm^{3+} than Gd^{3+}, which is observed. Second, the longer Sm-O bond

will push the Sm further from the MC since the oxime oxygens have little flexibility. This forces a more acute O-Sm-O angle between opposite oxime oxygens and a more obtuse O-Sm-O angle between opposing carboxylate oxygens, which is observed. All four of the gallium ions are in six coordinate octahedral environments, with two eshi ligands in the equatorial positions, and isophthalate oxygen in one axial position, and an elongated axial bond to a solvent molecule. The sodium countercation was bound to the metallacrown oxime oxygens and five solvent molecules as a distorted monocapped square antiprism. Four of the five solvent molecules were refined with 100% occupancy while the fifth (the apical cap of the monocapped square antiprism) was only refined with 50% occupancy. This structure is very similar to the **Sm-I$_8$** where the sodium is beneath the metallacrown, demonstrated nicely by an overlay of the structures (Figure 4.6). There is also evidence of the formation of diasteriomers based on combinations of clockwise and anticlockwise metallacrowns in this structure, as seen in **Sm-I$_4$** in the previous chapter.

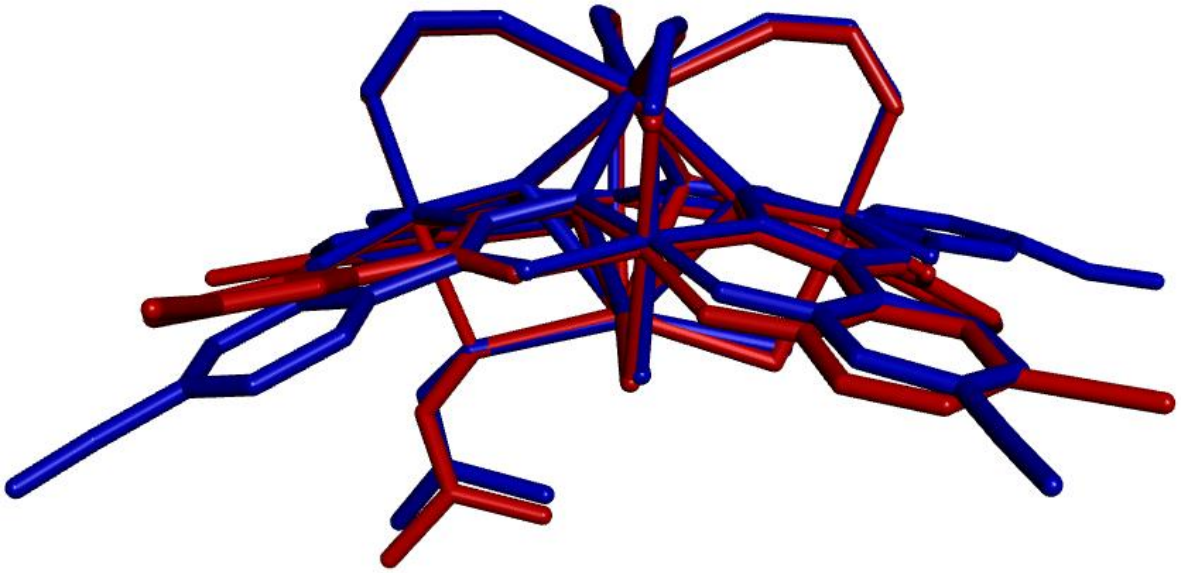

Figure 4.6. Overlay of **Sm-I$_8$** (red) and **Sm-e8** (blue). For simplicity only one of the two metallacrowns are shown with minimal atoms from the isophthalate bridge.

Table 4.2. Structural Parameters for Square Antiprismatically Coordinated Lanthanides.

Atom	Avg. Bond Length	Avg. Oox-Ln-Oox Angle	Avg. Ocb-Ln-Ocb Angle	Avg Torsion Angle	Ln-Oox MP Distance	Ln-Ocb MP Distance	Average O-O Distance	Compression Factor[a]

Sm1 (Sm-e8)	2.383 Å	101.42°	127.11°	48.18°	1.522 Å	1.051 Å	2.811 Å	0.915
Gd 1 (Gd-e4)	2.369 Å	105.12°	125.73°	40.21°	1.440 Å	1.079 Å	2.825 Å	0.892

[a] The compression factor is the sum of the Ln-O MP distances divided by the average O-O distance, which approximates a ratio between the height of the square antiprism and the average edge length.

Table 4.3. Structural Parameters for Octahedrally Coordinated Gallium Ions

Atom	Avg Bond length	Avg Equitorial angle	Avg Axial to equatorial angle	Axial bond angle	Avg. Torsion angle on Pseudo-S_6	M-Ocb distance	M-Osolv Distance
Ga2 (Gd-e4)	1.991 Å	89.34 °	90.00 °	173.38 °	59.14 °	1.932 Å	2.283 Å
Ga1 (Sm-e8)	1.988 Å	89.77 °	89.93 °	176.00 °	59.20 °	1.988 Å	2.244 Å
Ga2 (Sm-e8)	2.003 Å	89.38 °	89.93 °	175.83 °	60.66 °	1.971 Å	2.322 Å
Ga3 (Sm-e8)	1.986 Å	89.82 °	90.03 °	174.74 °	58.42 °	1.981 Å	2.170 Å
Ga4 (Sm-e8)	1.987 Å	89.68 °	90.08 °	177.61 °	61.30 °	1.991 Å	2.216 Å

Table 4.4. Structural Parameters for Square Pyramidally Coordinated Gallium Ions

Atom	Avg. Bond Length	Avg. Adjacent Basal bond angle	Avg. Apical to Basal Bond Anlge	Large Opposite Basal Bond angle	Small Opposite Basal Bond Angle	Addison's Tau Value[18]
Ga1 (Gd-e4)	1.919 Å	87.65 °	103.55 °	165.59 °	139.41 °	0.4363
Ga3 (Gd-e4)	1.920 Å	87.09 °	104.19 °	161.91 °	140.18 °	0.3625
Ga4 (Gd-e4)	1.919 Å	86.94 °	104.43 °	161.09 °	139.13 °	0.3557

Table 4.5. Coordination Environment of Sodium Ions

Atom	Avg. Bond Length	Avg Equitorial angle	Avg Axial to equatorial angle	Axial bond angle	Avg. Torsion angle on Pseudo-S_6	Shape
Na1 (Gd-e4)	2.429 Å	91.52 °	89.63 °	172.72 °	65.11 °	Octahedral

Atom	Avg. Bond Length	Avg. O_{ox}-Na-O_{ox} Angle	Avg. O_{solv}-Na-O_{solv} Angle	Avg Torsion Angle	Na-O_{ox} MP Distance	Na-O_{solv} MP Distance	Average O-O Distance	Compression Factor	Shape
Na1 (Sm-e8)	2.624 Å	86.31 º	157.05 º	27.72 º	1.985 Å	0.505 Å	3.0735 Å	0.810	Monocapped square antiprism

The solution state stabilities of these complexes were examined in methanol using ^{1}H-PGSE-DOSY in the same fashion as was described in chapter 3. The results of the PGSE-DOSY experiments are summarized in Table 4.6. In the case of **Ln-e4**, the carboxylate bridges (the red cells are the carboxylate protons) do not have the same diffusion coefficient as the other protons in the MC structure. This suggests that much like the iodinated 12-$MC_{Ga^{III}N(mishi)}$-4 complexes discussed in the previous chapter, the bridges are not always on the MC complex (Figure 4.7). Three different bridging carboxylates were examined: pivolate, benzoate, and 4-iodobenzoate. In all three cases, ligand dissociation was observed; however, the best agreement in hydrodynamic radii was seen for the pivolate metallacrowns. Still, given the desire to prepare stable luminescent agents for cell imaging, it was decided to perform CuAAC on the **Ln-e8** scaffolds rather than use the **Ln-e4** complexes. This decision is supported for the **Ln-e8** scaffold as they exhibit excellent stability in methanol solution both in the DOSY experiments (Figure 4.8). All MC protons have the same diffusion coefficient and hydrodynamic radius within error and ESI-MS spectra only show one peak corresponding to the desired metallacrown. Therefore, these complexes were used for the CuAAC experiments described below.

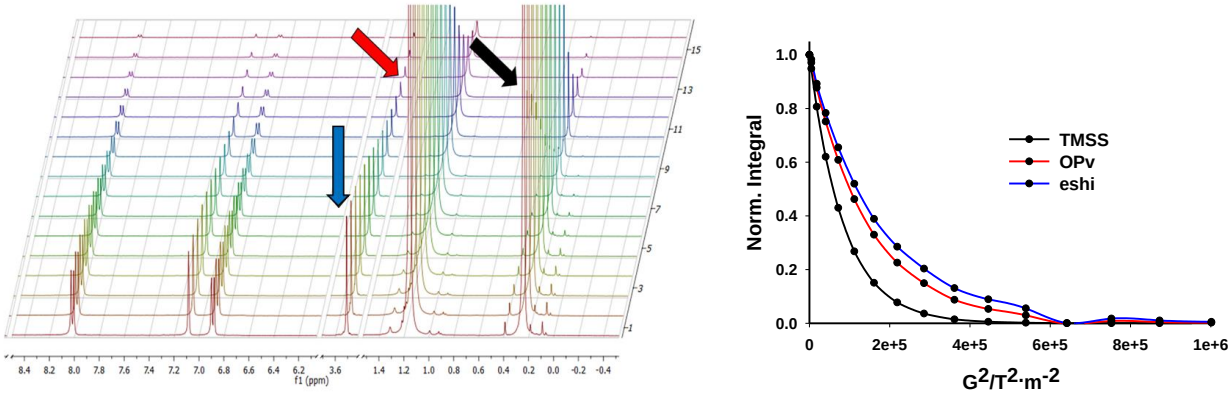

Figure 4.7. PGSE-DOSY on **Y-e4** shows a slight difference in the diffusion of OPv^{-} protons (red) compared to $eshi^{3-}$ (blue). TMSS is indicated in black.

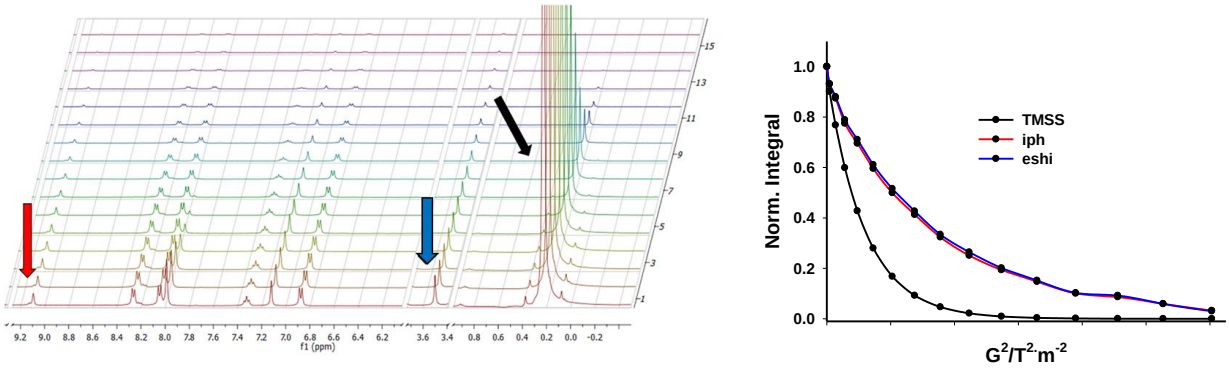

Figure 4.8. PGSE-DOSY on **Y-e8** shows an agreement in the diffusion of iph^{2-} (red) compared to $eshi^{3-}$ (blue). TMSS is indicated in black.

Table 4.6. Diffusion coefficients and hydrodynamic radii of ethynyl metallacrowns in d_4-MeOH. Hydroximate protons are marked as H and carboxylate are marked as C.

Metallacrown	**Peak position/ppm**	**Diffusion Coefficient/ 10^{-10} $m^2 \cdot s^{-1}$**	**r_H/Å[a]**
Sm-e4	H-8.11	4.29	8.44 ± 0.10
	H-7.15	4.21	8.58 ± 0.18
	H-6.91	4.26	8.48 ± 0.09
	H-3.49	4.29	8.43 ± 0.14
	C-1.05	5.62	6.64 ± 0.03
Y-e4	H-7.99	4.23	8.36 ± 0.15
	H-7.05	4.14	8.53 ± 0.14
	H-6.85	4.18	8.45 ± 0.12
	H-3.48	4.30	8.23 ± 0.15
	C-1.14	5.37	6.76 ± 0.05
Y-e4OBz	C-7.37	6.75	5.78 ± 0.19

	H-7.09	4.15	8.84 ± 0.26
	H-6.86	4.08	8.99 ± 0.19
	H-3.51	4.10	8.94 ± 0.22
Y-e4piOBz	H-8.00	4.40	8.37 ± 0.62
	C-7.68	5.52	6.84 ± 0.23
	H-7.07	4.06	9.01 ± 0.47
	H-6.86	3.90	9.35 ± 0.28
	H-3.49	3.93	9.28 ± 0.33
Sm-e8	C/H-8.65	3.07	11.43 ± 0.50
	H-8.09	3.06	11.43 ± 0.49
	C-7.56	3.20	10.99 ± 0.63
	H-7.13	3.08	11.38 ± 0.43
	H-6.89	3.08	11.38 ± 0.46
	H-3.50	3.44	10.29 ± 0.86
Y-e8	C-9.08	3.26	10.86 ± 2.04
	C-8.23	3.11	11.31 ± 0.56
	H-8.04	3.16	11.17 ± 0.35
	C-7.31	3.19	11.09 ± 0.90
	H-7.08	3.08	11.43 ± 0.81
	H-6.86	3.06	11.55 ± 0.34
	H-3.47	3.36	10.54 ± 0.70

[a] Hydrodynamic radii were calculated with the assistance of Prof. Matteo Tegoni using Stokes Einstein equations and r_H(MeOH) = 2.48 Å and r_H(TMSS) = 4.24 Å.[19] For details see Appendix D.

Optical Properties of Ethynyl Metallacrowns

UV-Vis spectra of **Ln-e4** complexes in methanol are shown in Figure 4.9. Each Ln analog has the same profile with a λ_{max} for the π-π* transition close to 335 nm. Comparison of the **Sm-e4** analog to the reported Sm[12-MC$_{Ga}{}^{III}{}_{N(shi)}$-4](OBz)$_4$ complex[6] shows a number of differences (Figure 4.10). First, the extinction coefficients increase for **Sm-e4** compared to the shi^{3-} complex from $\varepsilon_{shi} = 2.2{\cdot}10^4$ $M^{-1}{\cdot}cm^{-1}$ (at 311 nm) to $\varepsilon_{Sm\text{-}e4} = 2.8{\cdot}10^4$ $M^{-1}{\cdot}cm^{-1}$ (at 334 nm). The absorption edge, which is equivalent to the S_1 energy shifts from about 340 nm (29,412 cm^{-1}) for the shi metallacrown to about 370 nm (27,027 cm^{-1}) in Sm-e4. The triplet energy of each scaffold is 22,170 cm^{-1} for the reported shi^{3-} metallacrown and is 20,674 cm^{-1} (Figure 4.14) for **Gd-e4**. Both of these scaffold have a S_1 to T_1 difference exceeding the benchmark value of 5,000 cm^{-1} for efficient intersystem crossing.[20] This difference is slightly greater in the case of the reported shi^{3-} metallacrown by 900 cm^{-1}.

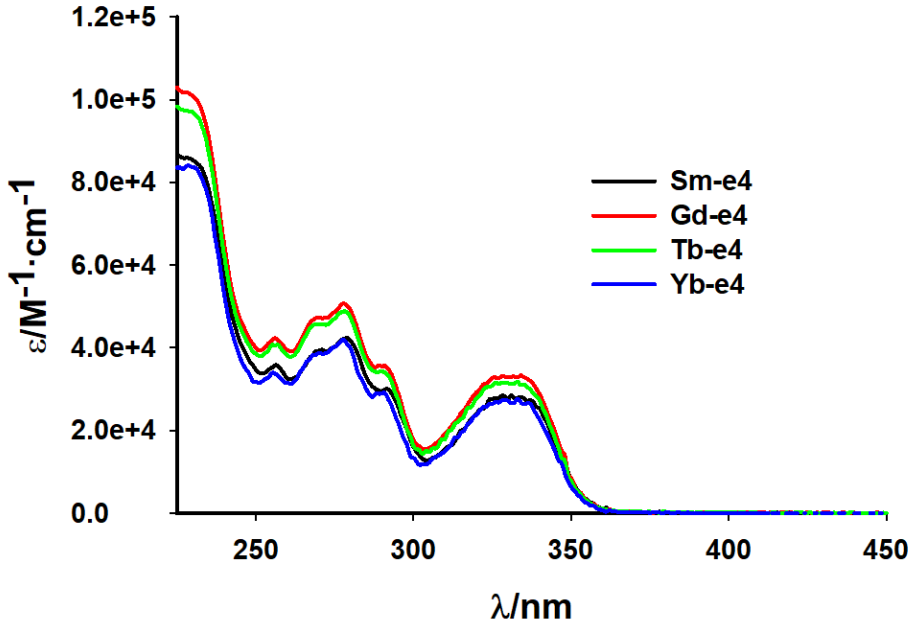

Figure 4.9. UV-Vis absorbance of **Ln-e4** MCs in MeOH at RT in 1-10 µM concentrations.

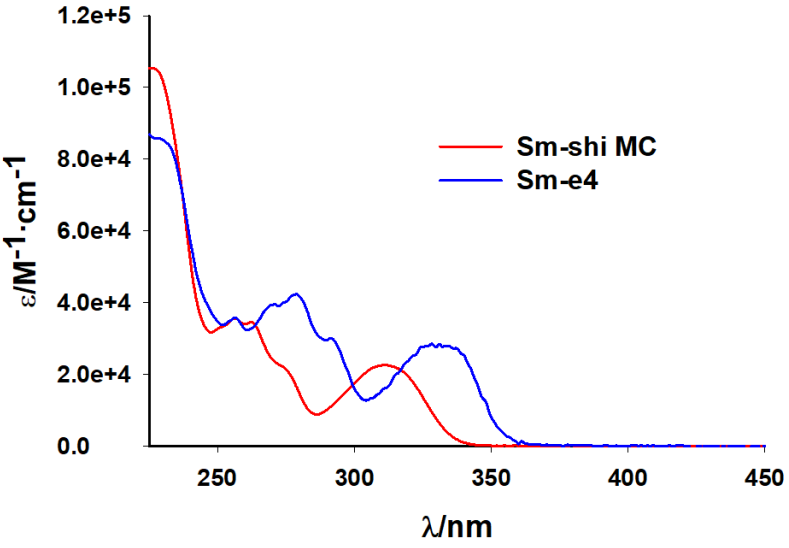

Figure 4.10. Comparison of UV-Vis spectra **Sm-e4** to the Sm[12-MC$_{Ga}{}^{III}{}_{N(shi)}$-4](OBz)$_4$ metallacrown in methanol at RT.

The UV-Vis absorption spectra of the **Ln-e8** derivatives in methanol are shown in Figure 4.11, and tells a very similar story with respect to **Ln-e4**. Each of the lanthanide derivatives have the same spectral profile, with a λ_{max} for the π-π* transition at about 335 nm. Once again,

comparing the Sm^{3+} analog of the reported dimerized $\{Ln[12\text{-}MC_{Ga}{}^{III}{}_{N(shi)}\text{-}4]\}_2(iph)_4$ complex[7] to **Sm-e8** shows some interesting differences. The extinction coefficients increase between the complexes where $\varepsilon_{shi} = 4.5 \cdot 10^4\ M^{-1} \cdot cm^{-1}$ (at 311 nm) and $\varepsilon_{Sm\text{-}e8} = 7.6 \cdot 10^4\ M^{-1} \cdot cm^{-1}$ (at 333nm). The absorption edge shifts from about 340 nm (29,412 cm^{-1}) in the analogous shi dimer complex to approximately 370 nm (27,027 cm^{-1}) when both Sm analogs are compared (Figure 4.12). This edge represents the S_1 energy of the metallacrown. The triplet energy of the reported complex is 455 nm (21,980 cm^{-1}) and the **Gd-e8** complex was determined to be 497 nm (Figure 4.16, 20,100 cm^{-1}). The difference in the S_1 to T_1 is greater than the benchmark 5,000 cm^{-1} for efficient intersystem crossing in both cases.[20] However, this difference is slightly larger for the shi^{3-} complex by approximately 500 cm^{-1}. Comparing **Ln-e4** to **Ln-e8** shows an expected increase in extinction coefficient of approximately two fold, and the S_1 to T_1 difference is 400 cm^{-1} larger for the **Ln-e8** complexes.

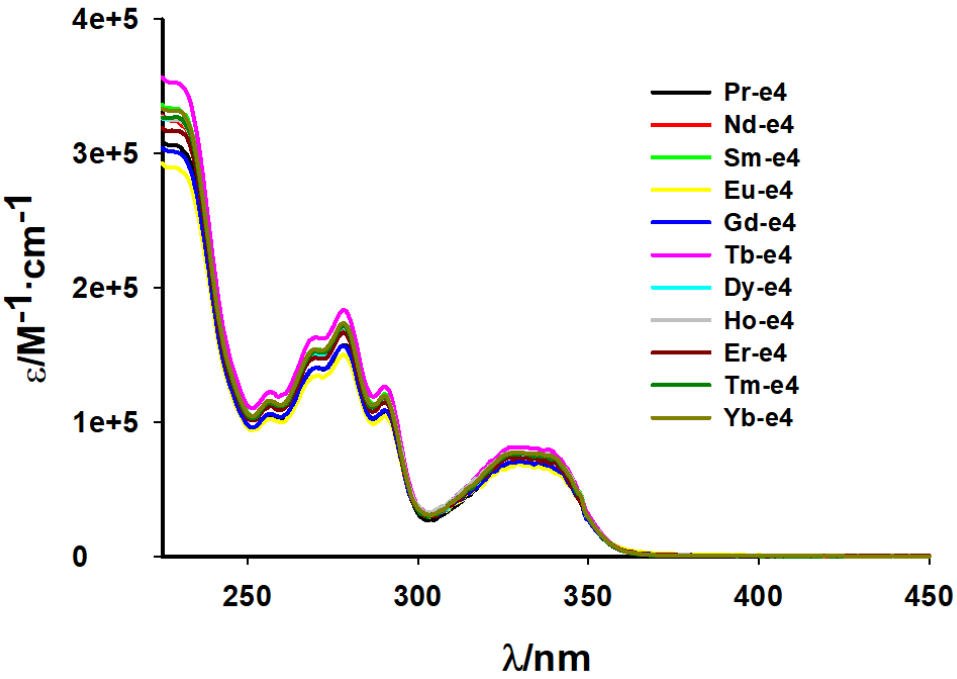

Figure 4.11. UV-Vis of absorbance **Ln-e8** MCs in MeOH at RT in 1-10 µM concentrations.

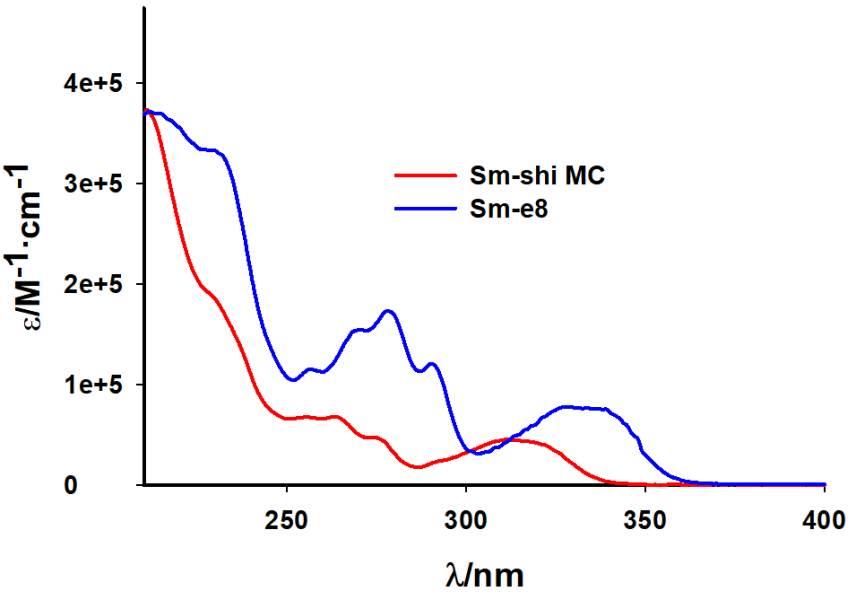

Figure 4.12. Comparison of UV-vis spectra of **Sm-e8** to the reported $\{Sm[12\text{-}MC_{Ga}{}^{III}{}_{N(shi)}\text{-}4]\}_2(iph)_4$ complex in methanol at RT.

Solid-State Photophysical Properties of Ethynyl Metallacrowns

The solid state photophysical properties of **Gd-e4**, **Tb-e4**, **Sm-e4**, and **Yb-e4** were measured and analyzed by Dr. Svetlana Eliseeva in CNRS-Orleans. The excitation spectra show ligand based excitation out to 380 nm for **Tb-e4**, **Sm-e4** and **Yb-e4** (Figure 4.13). When compared to the solution state excitation of $Ln[12\text{-}MC_{Ga}{}^{III}{}_{N(shi)}\text{-}4](OBz)_4$ there is a red shift in this excitation of about 30 nm. Saturation effects observed in the shi analogs prevents direct comparison to the **Ln-e4** series in the solid state. The emission spectra of **Ln-e4** show characteristic emissions for Sm^{3+}, in both the visible and NIR regions, as well as for Yb^{3+} emission in the NIR region (Figure 4.13). A Tb^{3+} emission was very weak and overlapped a ligand based emission. This is likely due to back transfer of energy from the Tb^{3+} to the antenna. Determination of the triplet energy of **Gd-e4** (Figure 4.14) confirms this hypothesis, since the T_1 energy was found at 484 nm (20,674 cm^{-1}), which is only 274 cm^{-1} higher in energy than the emissive level of Tb^{3+}.

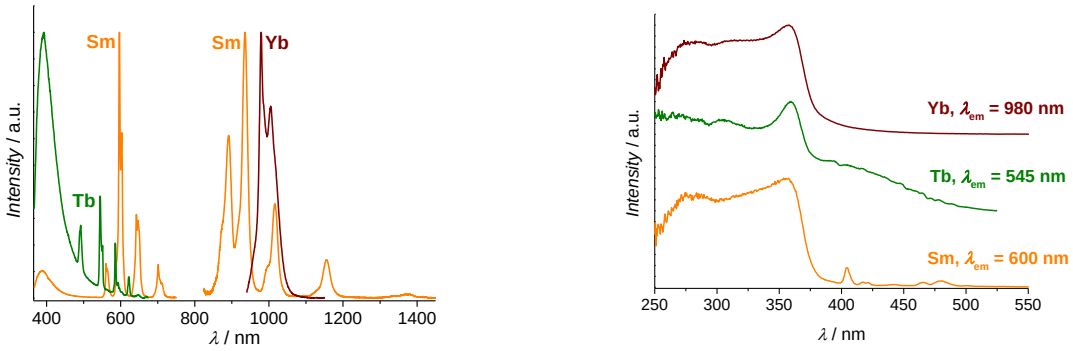

Figure 4.13. Solid state emission spectra (λ_{ex} = 350 nm, left) and excitation spectra (right) of **Ln-e4** Metallacrowns at RT.

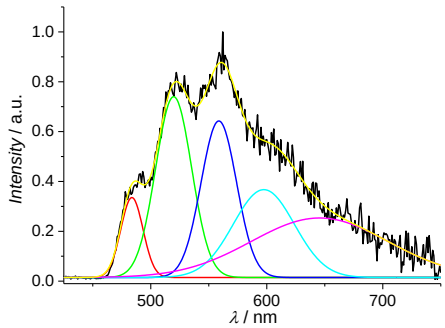

Figure 4.14. Emission spectrum of **Gd-e4** in the solid state under excitation at 320 nm at 77K upon applying a 100 µs delay after the excitation flash.

The solid state photophysical properties of the **Ln-e4** complexes are summarized in Table 4.7. When compared to the shi and benzoate metallacrown reported in 2016,[6] the quantum yields and life times are lower. The Tb^{3+} analog decreases in lifetime from 1080 µs to 3.2 µs and the quantum yield falls from 34.7% to 0.061%, which is a direct result of the shift in energy of the triplet state. The Sm^{3+} analog has a decrease in lifetime from 148 µs to an average lifetime of 85.6 µs. The quantum yield for both the visible and NIR emissions drop from 2.46 % (vis) and 0.45% (NIR) to 1.24% (vis) and 0.118% (NIR). Lastly, the Yb^{3+} analog's lifetime was reduced form 55.7 µs to 27.4 µs and the quantum yield dropped from 5.88% to 2.7%. It is unlikely that the red shift in T_1 energy is the cause for reduction the properties of Sm-e4 and Yb-e4. Both are outside of the 2,500 cm^{-1} benchmark for concern of significant energy back transfer where the emissive state of Sm^{3+} is 2,824 cm^{-1} lower than the T_1 and the emissive state of Yb^{3+} is 10,374 cm^{-1} lower than the T_1. Even though Sm^{3+} is approaching this limit, both analogs show an approximately 50% reduction in quantum yields and lifetimes. So, the reason for the drop should

be consistent between both analogs. Therefore, the most likely reason for this decrease in lifetime and quantum efficiency is due to the choice of bridging carboxylate, although other factors such as ligand to metal charge transfer effects may also play a role. Since PGSE-DOSY (Table 4.6) showed the best agreement in diffusion coefficients between hydroximate and carboxylate ligand protons for pivolate in the case of **Ln-e4**, the pivolate ligand was chosen to give the most likely stable MC. Yet, this carboxylate introduces more sp_3C-H oscillators in similar proximity to the Ln compared to the sp_2C-H oscillators in the reported shi^{3-}/OBz^- structure. These higher number of oscillators should quench the lanthanide-based luminescence more than the sp_2C-H oscillators in the previous stucture.

Table 4.7. Solid State Photophysical Properties of **Ln-e4** Metallacrowns.

Ln	**Lifetime / μs[a]**	**Quantum yield / %[b]**
Sm	86.6(6): 95(1) % 26.7(6): 5(1) % <τ> = 85.6	1.24(2) 0.118(4)
Tb	3.2(3)	0.061(3)
Yb	27.4(7)	2.7(2)

[a] λ_{ex} = 355 nm
[b] λ_{ex} = 350 nm

Solid state photophysical properties were also examined for the same analogs of **Ln-e8** metallacrowns by Dr. Svetlana Eliseeva. Much like the **Ln-e4** complexes, the excitation spectra of **Ln-e8** (Figure 4.15) show the operation of the antenna effect out to 380 nm for Sm^{3+}, Tb^{3+} and Yb^{3+}. This is a significant red shift in excitation range compared to the 350 nm limit of {Ln[12-$MC_{Ga(III)N(shi)}$-4](iph)4] complex (Figure 4.17) as well as the iodinated versions of this same scaffold. The emission spectra (Figure 4.15) of these with λ_{ex} of 350 nm show characteristic spectra for Sm^{3+} in both the visble and NIR regions as well as NIR emission of Yb^{3+}. For Tb^{3+}, the emission was again weak and accompanied by the emission of the hydroximate ligands, so there is likely back transfer of energy from the Tb^{3+} to the antenna. The triplet energy of **Gd-e8** has shifted from approximately 455 nm (21,980 cm^{-1}) for the analogous dimerized shi^{3-} complex

to 497 nm (20,100 cm^{-1}), which supports the hypothesis that Tb^{3+} experiences back transfer since the emissive level of Tb^{3+} (20 400 cm^{-1})[21] is actually slightly higher in energy than the triplet energy of the antenna (Figure 4.16). There is also a shift in about 500 cm-1 between **Gd-e4** to **Gd-e8**, which is likely due to the different contributions of pivolate versus isophthalate bridges in these complexes to the triplet energy overall. A similar observation is shown in Chapter two where the change from a shi^{3-}/OBz^{-} in the reported 12-MC-4 to the shi^{3-} exclusive Ln[3.3.1] also red shifts the T_1.

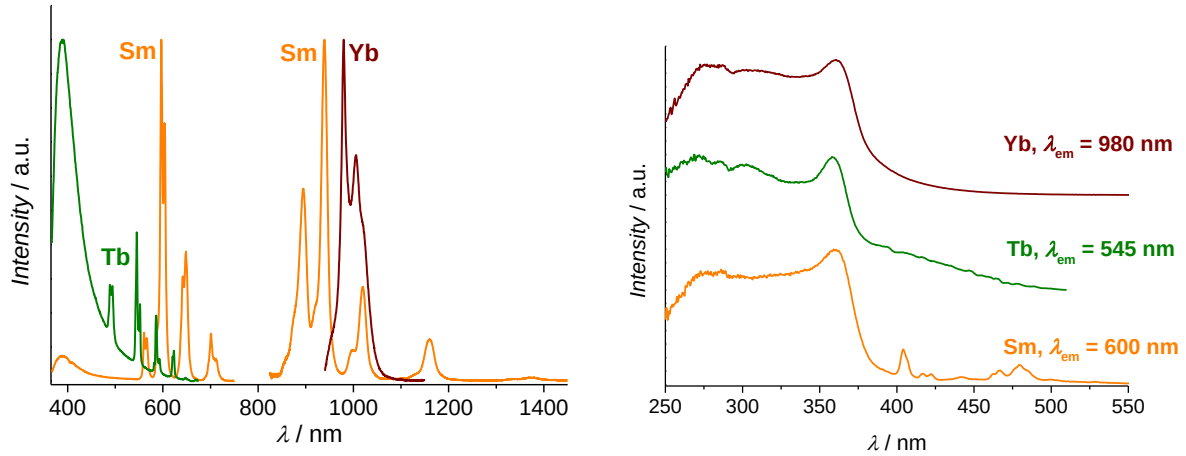

Figure 4.15. Solid state emission spectra (λ_{ex} = 350 nm) of **Ln-e8** (left) and excitation spectra (right) at RT.

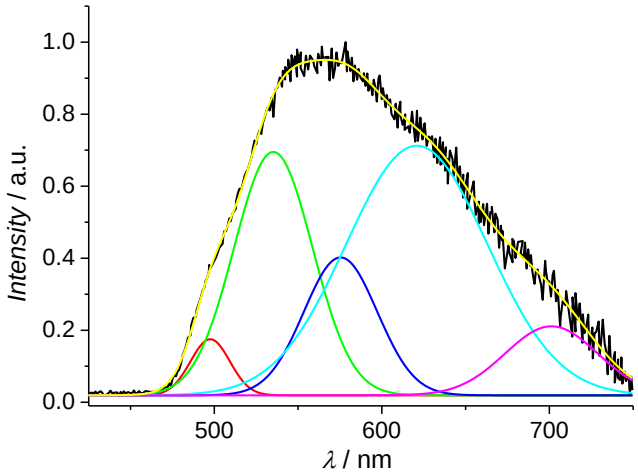

Figure 4.16. Emission spectrum of **Gd-e8** in the solid state under excitation at 320 nm at 77K upon applying a 500 µs delay after the excitation flash.

Examination of the photophysical properties of these complexes also suggest that this dimerized scaffold is not ideal for Tb^{3+}, yet is still excellent for Sm^{3+} and Yb^{3+} (Table 4.8). The lifetime for **Tb-e8** is 4.08 μs compared to 1,410 μs for the comparable {Ln[12-$MC_{Ga}{}^{III}{}_{N(shi)}$-4}$_2(iph)_4$ MC dimer complex[7] and the quantum yield for the Tb^{3+} emission is a mere 0.072% compared to the 31.2% for the shi complex. These **Tb-e8** values are similar to the **Tb-e4** complex (3.2 μs, and 0.061%). However, for **Sm-e8** and **Yb-e8**, the photophysics are on par or better when compared to the original dimerized shi scaffold, which separates these compounds from the **Ln-e4**. The average lifetime for the **Sm-e8** complex was 105 μs which is close to the 117 μs reported for the dimerized shi complex. Both the visible and NIR quantum yields were similar where **Sm-e8** has a visible QY of 2.03% and a NIR QY of 0.20 %, close to the respective shi values of 2.09% and 0.269 %. The **Yb-e8** complex shows an improved lifetime of 35.7 μs compared to 30.5 μs as well as an improved QY of 3.23% compared to 2.43%. These values are also an improvement from the **Ln-e4** photophysical properties, likely due to the return to an sp_2C-H oscillator. This is not the case for **Ln-e4** since there is a discrepancy between the number of C-H oscillators near the Ln. The superior solution state stability and photophysical properties of **Ln-e8** compared to **Ln-e4** places more weight on the selection of this scaffold for use in CuAAC coupling reactions.

Table 4.8. Photophysical Properties of **Ln-e8** metallacrowns.

Ln	**Lifetime / μs**[a]	**Quantum yield / %**[b]
Sm	105(2): 98.1(7) % 21.8(6): 1.9(7) % <τ> = 105	2.03(4) (540-750 nm) 0.20(1) (850-1450 nm)
Tb	4.08(8)	0.072(4)
Yb	35.7(7)	3.23(2)

[a] λ_{ex} = 355 nm
[b] λ_{ex} = 350 nm

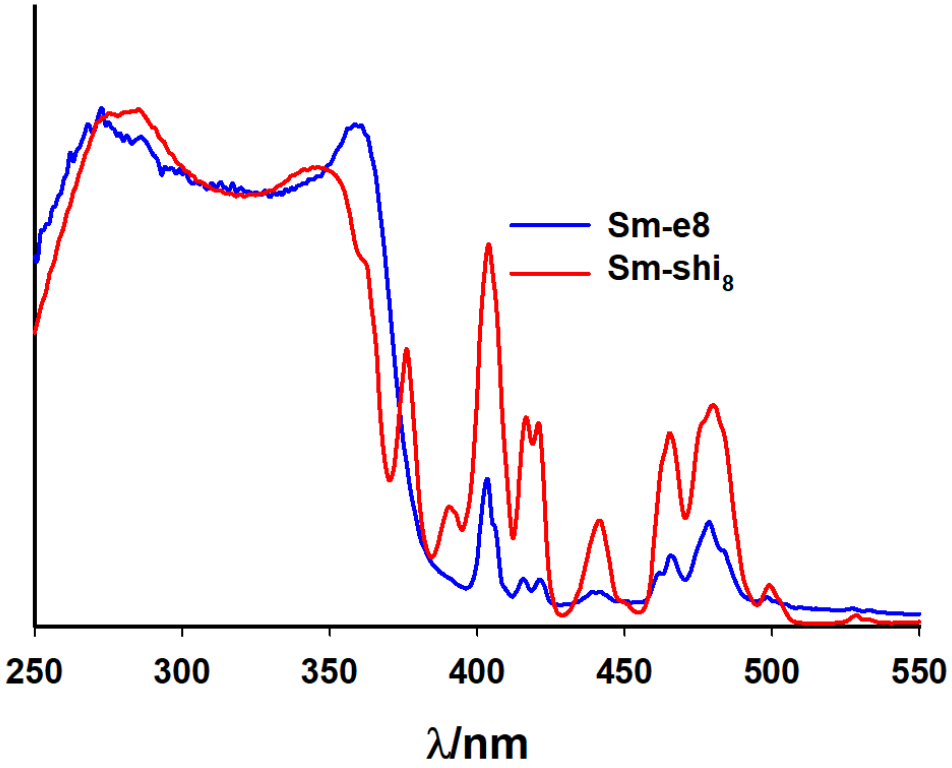

Figure 4.17. Overlay of normalized excitation spectra of **Sm-e8** (λ_{em} = 595 nm) to the reported complex with shi. Spectra were collected by Jacob Lutter with the assistance of Prof. Evan Trivedi at Oakland University.

CuAAC on Metallacrowns

In 2015 Rentschler and coworkers reported a method for appending azido compounds onto copper 12-MC-4s constructed using eshi^{3-}. Various coupling partners were employed using this method including adamantine as well as zinc or cobalt binding ligands. To see if this method of CuAAC is viable for a non-cupric metallacrown, an attempt was made to attach benzyl azide to **Sm-e8** following Scheme 4.2. The resulting solid collected by slow evaporation of the reaction solution and analyzed by ESI-MS (Figure 4.18). The results show that all eight eshi^{3-} ligands are coupled with a benzyl azide (peak at 1987.97 m/z), and that the gallium are not replaced by copper within the metallacrown. The other peaks match the mass of the clicked **Sm-e8** with copper adducts. A slurry with Chelex is likely the best option to remove these adducts, but this is not yet confirmed.

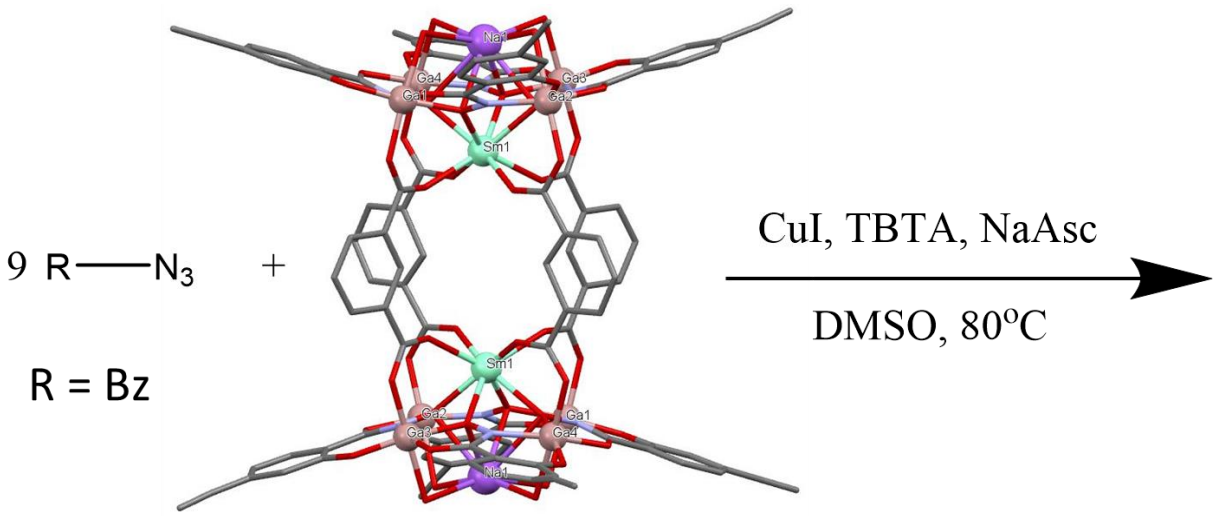

Scheme 4.2. CuAAC method to couple to all 8 eshi^{3-} ligands on **Sm-e8**. Modified from a known procedure to perform CuAAC on copper 12-MC-4s.[5]

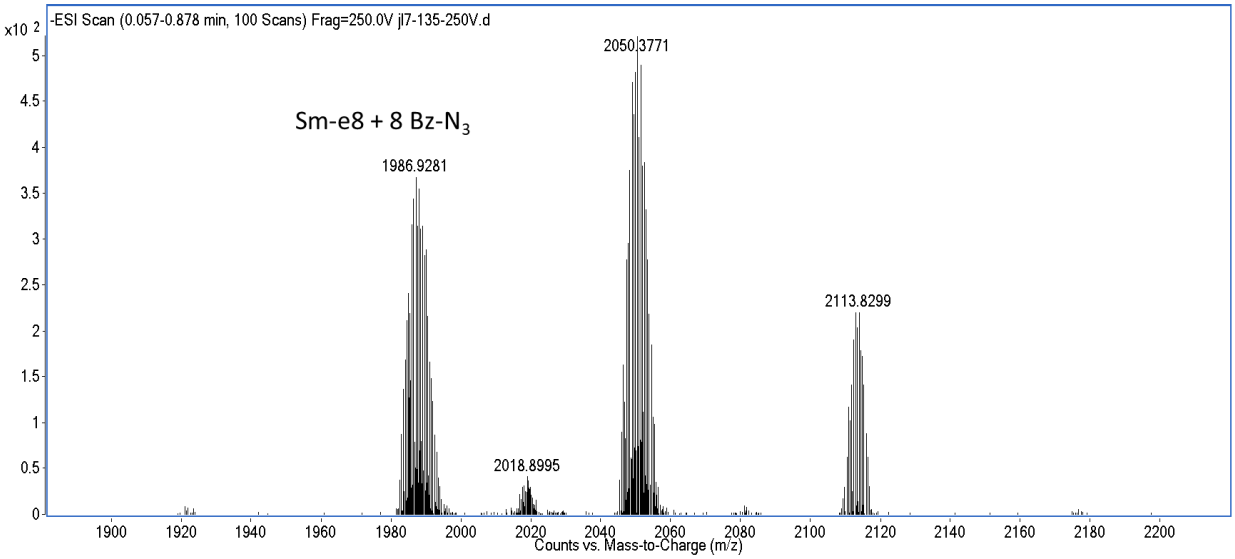

Figure 4.18. ESI-MS of the fully coupled **Sm-e8** with eight benzyl azides. The spectrum was collected in methanol in negative ion mode with a fragmentation voltage of 250V. The background spectrum was not subtracted.

These results are very interesting, however, in the case of coupling to expensive azide partners such as antibodies, it is desirable to only click one or two moieties to the metallacrown. Plus, one could take advantage of the excellent properties of eshi^{3-} as an antenna, such as red-shifted absorbance. These lower ratios may be achieved in two different ways. First, one could make the clicked hydroxamic acid then synthesize a metallacrown with a mixture of H_3eshi and the desired triazolyl ligand. Alternatively, CuAAC could be performed on the **Ln-e8** MC such that the

reaction does not go “to completion”. Towards method one, CuAAC was performed on the H_3eshi ligand as described in the synthetic section above. These couplings showed that both benzyl azide and **biotin-N_3** were able to couple to the H_3eshi hydroxamic acid. However, the synthesis of a metallacrown using these ligands has not yet shown positive results, likely due to issues related to solubility of the hydroximates and the desired metallacrowns. But, the second method has shown positive results via CuAAC on **Sm-e8** using either benzyl azide or **biotin-N_3**. The method, shown in Scheme 4.3, demonstrates how to attach a few azides onto the **Sm-e8** MC, but not a full conversion of all eight possible reaction sites. ESI-MS on the resulting solids shows a mixture of **Sm-e8** with up to one benzyl azide (Figure 4.19), and **Sm-e8** with up to two biotin moieties attached (Figure 4.20). The additional peak in Figure 4.15 is an unreacted **Sm-e8** with two copper adducts. These adducts should also be cleared using Chelex as described above. These results are very encouraging, since 1:1 or 1:2 ratios allows one to attach a limited number of the desired (and often costly) azide, while retaining the $eshi^{3-}$ to serve as an antenna for the lanthanide. Further steps still need to be optimized which includes isolation of the clicked metallacrowns from **Sm-e8**, which should be possible using HPLC.

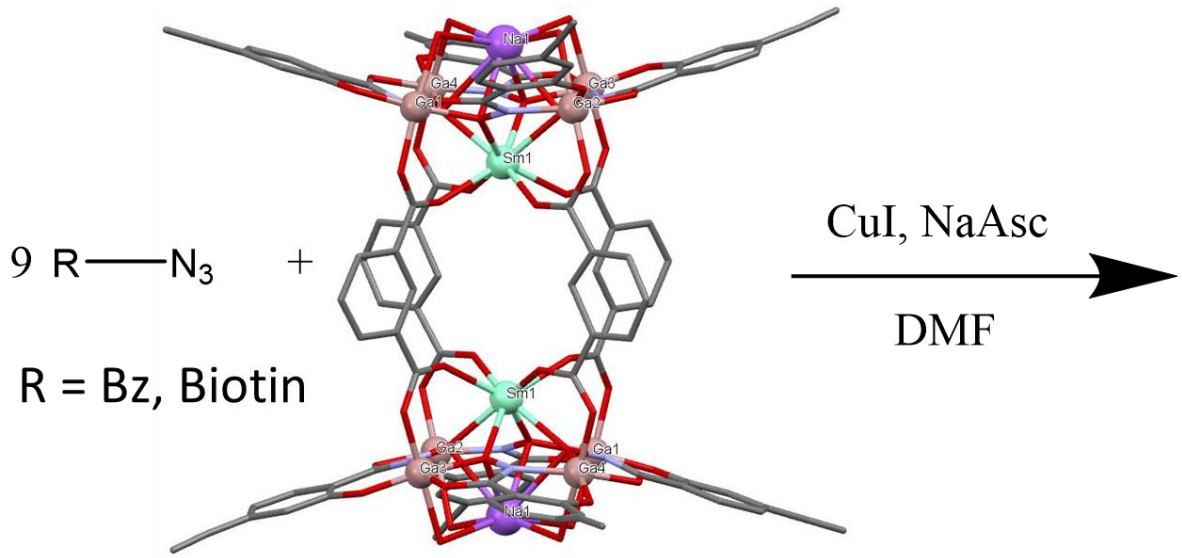

Scheme 4.3. CuAAC coupling on **Sm-e8** using benzyl azide or **Biotin-N_3**.

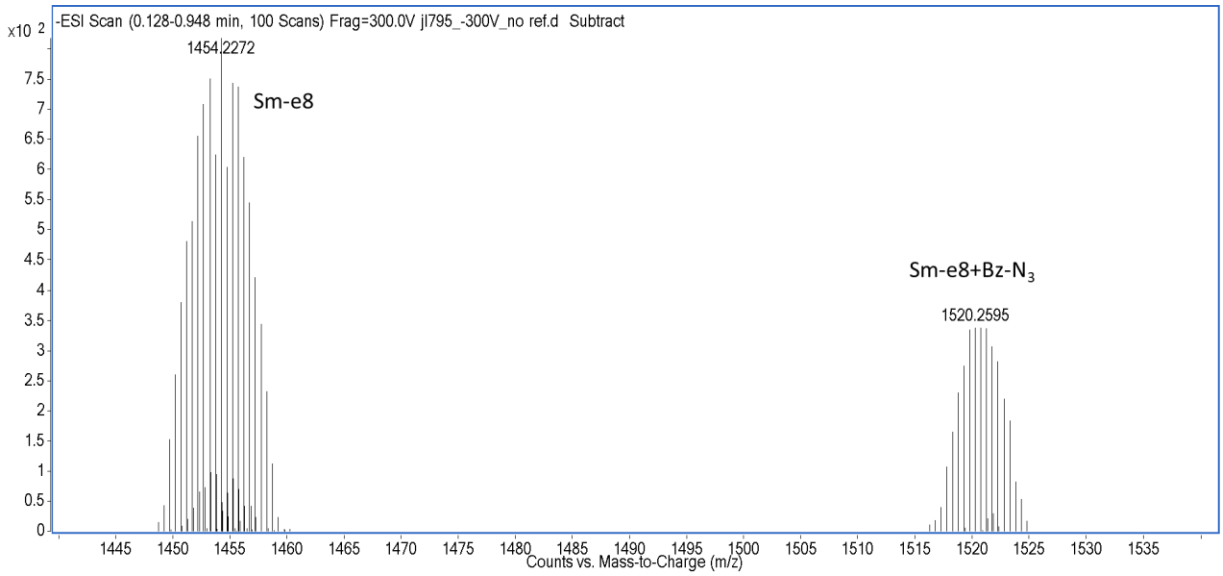

Figure 4.19. ESI-MS of the result of CuAAC on **Sm-e8** using benzyl azide. The spectrum was collected in methanol with a fragmentation voltage of 300V in negative ion mode. The background spectrum was subtracted once.

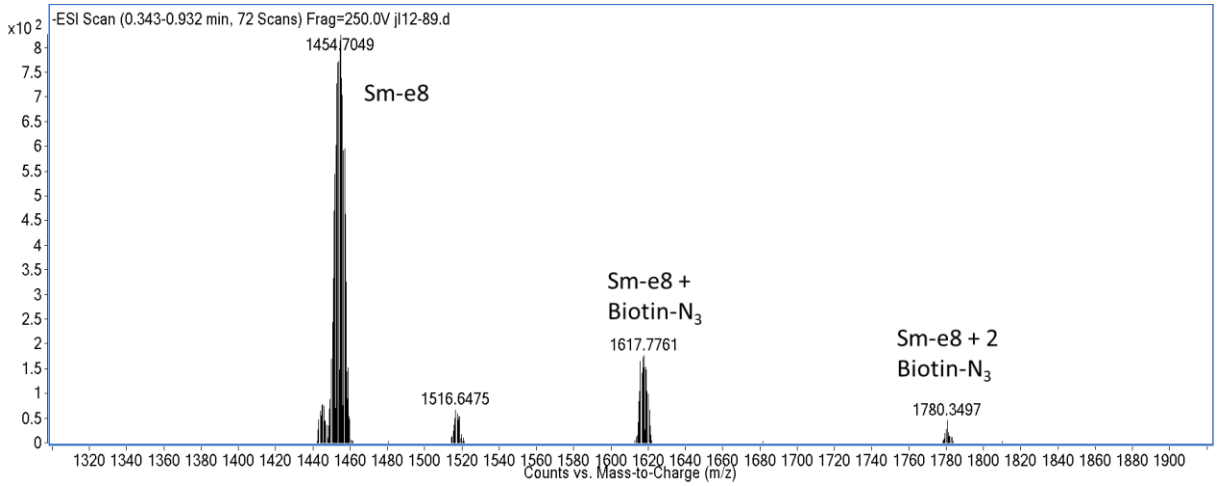

Figure 4.20. ESI-MS of the result of CuAAC on **Sm-e8** using **Biotin-N3**. The spectrum was collected in methanol in negative ion mode with a fragmentation voltage of 250V. The background spectrum was subtracted once.

Ethynyl Functionalization onto the $LnZn_{16}$ Scaffold

Given the recent demonstration of $Ln[12\text{-}MC_{Zn^{II}N(pyzHA)}\text{-}4]_2[24\text{-}MC_{Zn^{II}N(pyzHA)}\text{-}8](OTf)_3$ ($LnZn_{16}(pyzHA)_{16}$) as staining and fixation agents of human HeLa cells, the application of CuAAC technology on to this scaffold is highly desirable.[10,11] To achieve this objective, the H_2epic ligand was synthesized using Sonogashira coupling according to the method reported in the experimental section. However, to retain the solubility and effective use of the $pyzHA^{2-}$

antenna a mixed ligand species was synthesized according to Scheme 4.4, with a target of a 1:3 ratio between pyzHA and epic^{2-}. ESI-MS showed that it is possible to synthesize species of $LnZn_{16}(pyzHA)_{16-x}(epic)_x$ with x values ranging from one to five (Figure 4.22). It is important to note that the case of x equal to zero was not observed in the ESI-MS, which suggests that this metallacrown was able to be removed by virtue of solubility in water during the synthesis. Therefore, it is easy to separate a "clickable" metallacrown from an "unclickable" metallacrown using this method. UV-Vis spectroscopy of this mixture shows a slight change absorption compared to the picHA^{2-} and pyzHA^{2-} metallacrowns (Figure 4.21). Given that the extinction coefficient cannot be accurately determined at this time, this value was estimated based on what is known about the pyzHA^{2-} complex. Compared to the initial picHA^{2-} MC, the absorbance on the ILTC is redshifted to a maximum of 365 nm, which matches what is observed from pyzHA^{2-} MCs. There is a slight change in the 300 to 325 nm region of the spectra between the pyzHA MC and the new mixed MC, where there appears to be a slight increase in the absorbance of the π-π* band, which may be explained by the inclusion og the ethnylyl functionality. This mixture of pyzHA^{2-}/epic^{2-} MCs were used in CuAAC with **biotin-N$_3$** following Scheme 4.5. ESI-MS of the reaction solution after 48 hours shows distributions of [M]$^{3+}$ peaks consistent with the addition of one or two **biotin-N$_3$** to the mixed MCs (Figure 4.23). The other [M]$^{3+}$sets are copper ascorbate adducts. There are species between ~850 and 1080 mz are [M]$^{4+}$ peaks of the same products with a sodium-pyridine adduct. Again, these copper adducts could be cleared with Chelex and the MCs purified using HPLC. This result is an exciting first step towards functionalization using CuAAC in $LnZn_{16}L_{16}$ metallacrowns.

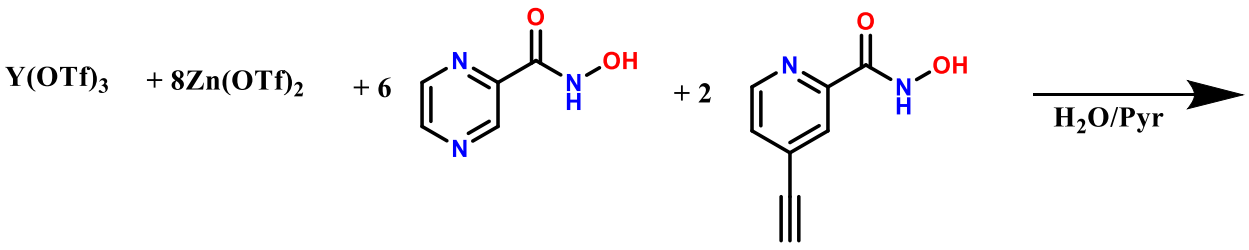

Scheme 4.4. Synthesis of the mixed $YZn_{16}(pyzHA)_{16-x}(epic)_x$ metallacrown.

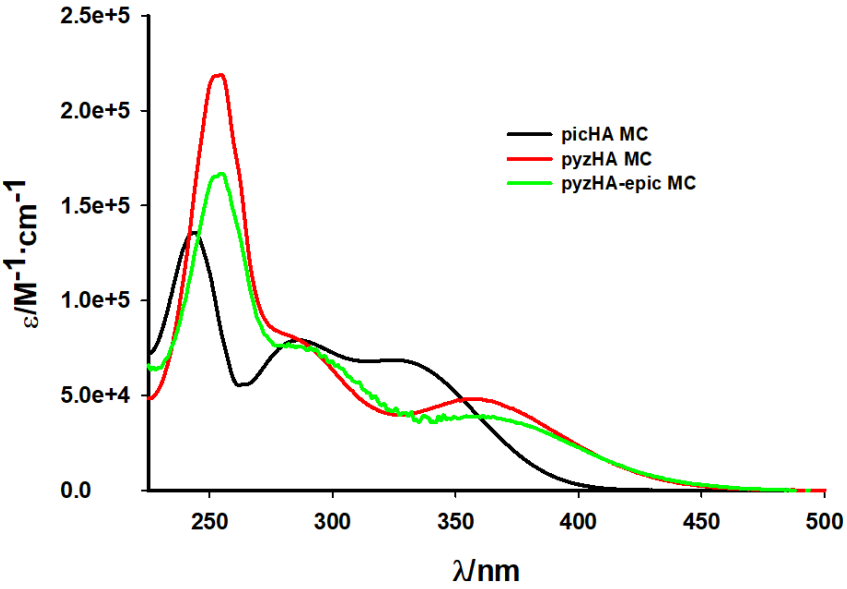

Figure 4.21. Comparison of UV-Vis spectrum of the picHA MC, the pyzHA MC and the pyzHA/epic MC, in methanol at RT.

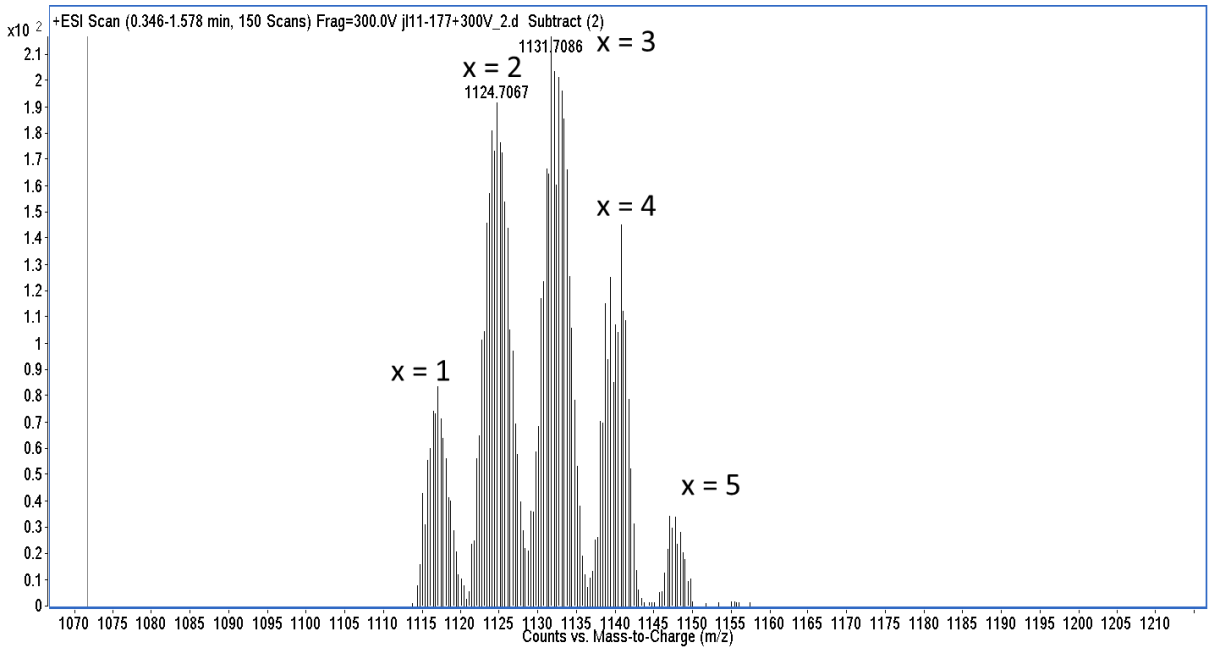

Figure 4.22. ESI-MS of the mixed $YZn_{16}(pyzHA)_{16-x}(epic)_x$ metallacrown in methanol with a fragmentation voltage of 300V.Background spectra were subtracted twice.

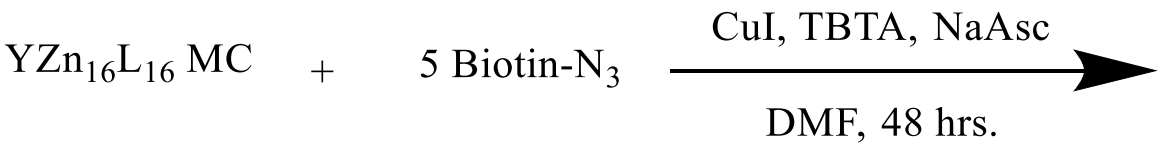

Scheme 4.5. CuAAC on $YZn_{16}(pyzHA)_{16-x}(epic)_x$ with **biotin-N_3**.

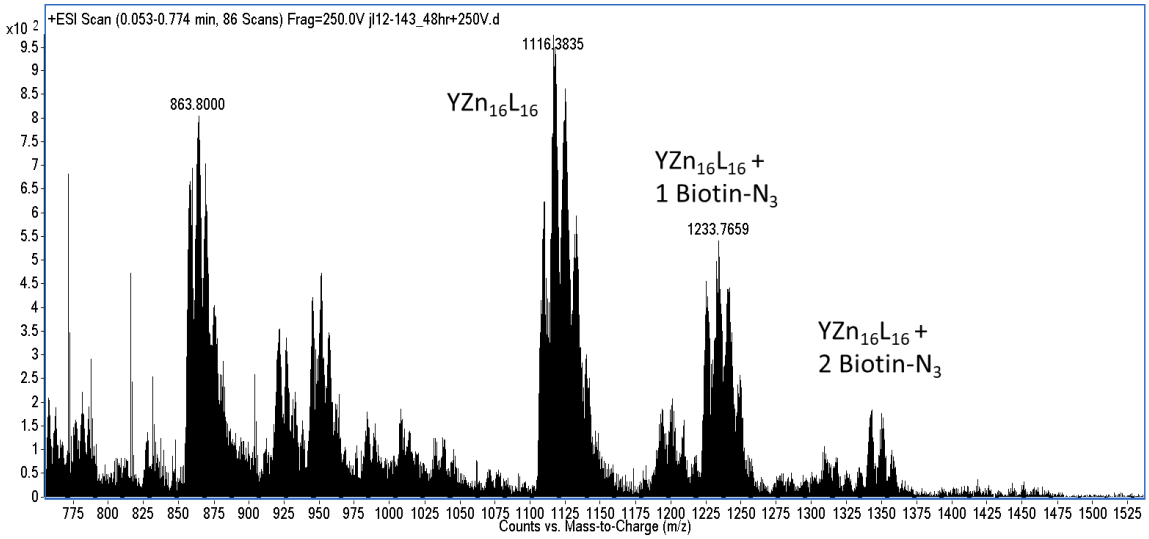

Figure 4.23. ESI-MS of CuAAC on $YZn_{16}(pyzHA)_{16-x}(epic)_x$ with **biotin-N_3** in methanol using a fragmentation voltage of 250V. Background spectra were not subtracted.

Further Functionalization of Hydroximate Antenna using Sonogashira Coupling.

Thus far this chapter has only explored the possibility of adding an ethynyl functionality onto metallacrowns. However, Sonogashira coupling is not limited to this derivatization. To explore possibilities in red shifting excitation and/or antenna with two photon absorbance, coupling of p-ethynyl anisole to 4-iodopicoline hydroximate (H_2maepic) and p-ethynyl-N,N-dimethylaniline to 5-iodosalicylhydroximate (H_3meanshi) was performed as described in the experimental section above. The rational of the design of these ligands is two-fold. First, by increasing the number of atoms in a conjugated system the absorbance should red shift. Second, by designing ligands with a dipole there is a chance for two photon absorbance which has been demonstrated by similar antenna.[22] The implications and design principles for two-photon absorbance will be discussed in more detail in the next chapter as future directions for this project. Comparison of UV-Vis spectra of H_2maepic to H_2picHA shows a significant red shift in the π-π^* band λ_{max} from 263 nm to 318 nm and a nearly sixfold increase in absorbance (Figure 4.25). However, when H_3shi and H_3meanshi are compared, there is not only a red shift in the π-

π* band λ_{max} from 300 nm to 317 nm with a similar sixfold increase in absorbance, but also the appearance of a weaker band with λ_{max} at 606 nm (Figure 4.25). This band is approximately half of the energy of the band with a λ_{max} of 317 nm, so it is possible that this could be used as a two photon absorbance. This transition is likely to be an intraligand charge transfer since this kind of charge transfer is known to occur with dimethylamino groups.[23] However, these dimethylamino charge transfer excitations are also associated with enhanced two-photon absorbance.[23] In any case this is still an amazing discovery in terms of antenna design for metallacrowns.

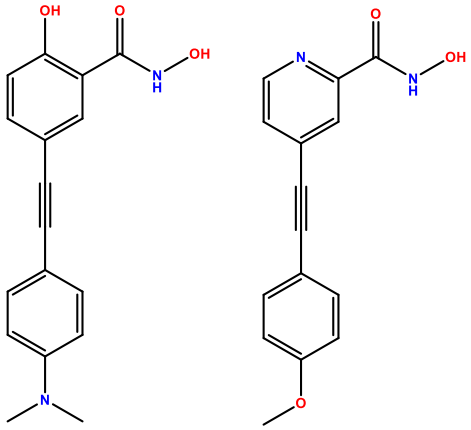

Figure 4.24. Structure of H_3meanshi (left) and H_2maepic (right) hydroxamic acid ligands.

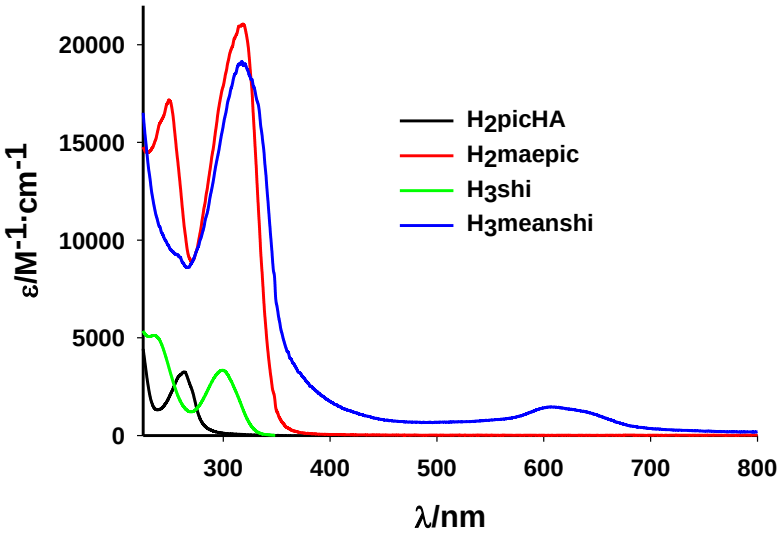

Figure 4.25. UV-Vis Absorbance of Arylethynyl Functionalized Hydroxamic Acids in Methanol at RT.

Conclusion

This chapter explored the potential for functionalization of the common metallacrown forming hydroximates shi^{3-} and $picHA^{2-}$. The H_3eshi ligand reported by Rentschler and coworkers was able to be incorporated into a gallium based metallacrown scaffold. Metallacrowns made from the H_3eshi ligand demonstrated a red shift in the π-π* absorbance band as well as a red shift in the excitation spectra when compared to metallacrowns made using H_3shi. The photophysics of both a monomeric 12-MC-4 (**Ln-e4**) and a dimeric 12-MC-4 complex (**Ln-e8**) were examined for the Tb^{3+}, Sm^{3+} and Yb^{3+} derivatives. The use of the pivolate bridging carboxylate, while conferring greater solution state stability of the complex shown by PGSE-DOSY studies, is likely a detriment to the lanthanide photophysical properties thanks to proximity of a higher energy oscillator. However, comparison of the same **Ln-e8** derivatives to the known structure using shi^{3-} showed either similar properties in the case of Sm^{3+} or an enhancement of Yb^{3+} photophysical properties. Tb^{3+} was poorly sensitized due to the similar energies of the Tb^{3+} emissive state and the triplet energy of the **Ln-e8** scaffold. CuAAC was performed on the **Sm-e8** complex using both benzyl azide and a more biologically relevant biotin azide as coupling partners. Two methods for coupling were demonstrated, where either one or two of the azido partners were coupled to **Sm-e8** or all eight sites on **Sm-e8** using benzyl azide. Both of these methods have merit, where the incomplete coupling of **Sm-e8** allows for use of the $eshi^{3-}$ antenna alongside the benefits of coupling an azide of interest, while the method for full conversion could be useful for magnetic studies, MOF synthesis, or the attachment of dendrons onto a metallacrown. The incorporation of an ethynyl functionalized ligand for use in the $LnZn_{16}$ system was shown by generating a mixed ligand species with $pyzHA^{2-}$. The $pyzHA^{2-}$ already has been shown to have fascinating photophysical properties, and metallacrowns using this ligand can fix and image necrotic HeLa cells. By including an ethyne in this scaffold, the metallacrown may now be labeled to target specific cells or have other antennae of interest placed onto the scaffold. Proof of concept was shown using **biotin-N_3** with the ethynyl functionalized metallacrown. Finally, the versatility of the Sonogashira coupling reaction was demonstrated by generating biaryl ligands based on shi^{3-} and $picHA^{2-}$. In both cases a significant red shift in absorbance was observed long with an increase in absorbance. In the case of H_3meanshi, there was also a smaller band observed at 606 nm. This band could be from either an intraligand charge transfer known to occur with dimethylamines or indicative of a strong possibility for two

photon absorbance. All of these achievements add to the concept of metallacrowns as molecular Legos, where the modularity of the hydroximate is emphasized.

References

(1) Kolb, H. C.; Finn, M. G.; Sharpless, K. B. *Angew. Chemie Int. Ed.* **2001**, *40* (11), 2004–2021.
(2) Huisgen, R. *Proc. Chem. Soc.* **1961**, 357–396.
(3) Meldal, M.; Tornøe, C. W. *Chem. Rev.* **2008**, *108* (8), 2952–3015.
(4) Wang, Q.; Chan, T. R.; Hilgraf, R.; Fokin, V. V.; Sharpless, K. B.; Finn, M. G. *J. Am. Chem. Soc.* **2003**, *125* (11), 3192–3193.
(5) Plenk, C.; Krause, J.; Beck, M.; Rentschler, E. *Chem. Commun.* **2015**, *51* (30), 6524–6527.
(6) Chow, C. Y.; Eliseeva, S. V; Trivedi, E. R.; Nguyen, T. N.; Kampf, J. W.; Petoud, S.; Pecoraro, V. L. *J. Am. Chem. Soc.* **2016**, *138* (15), 5100–5109.
(7) Nguyen, T. N.; Chow, C. Y.; Eliseeva, S. V.; Trivedi, E. R.; Kampf, J. W.; Martinić, I.; Petoud, S.; Pecoraro, V. L. *Chem. - A Eur. J.* **2018**, *24* (5), 1031–1035.
(8) Jankolovits, J.; Andolina, C. M.; Kampf, J. W.; Raymond, K. N.; Pecoraro, V. L. *Angew. Chemie Int. Ed.* **2011**, *50* (41), 9660–9664.
(9) Trivedi, E. R.; Eliseeva, S. V.; Jankolovits, J.; Olmstead, M. M.; Petoud, S.; Pecoraro, V. L. *J. Am. Chem. Soc.* **2014**, *136* (4), 1526–1534.
(10) Martinić, I.; Eliseeva, S. V; Nguyen, T. N.; Pecoraro, V. L.; Petoud, S. *J. Am. Chem. Soc.* **2017**, *139* (25), 8388–8391.
(11) Martinić, I.; Eliseeva, S. V.; Nguyen, T. N.; Foucher, F.; Gosset, D.; Westall, F.; Pecoraro, V. L.; Petoud, S. *Chem. Sci.* **2017**, *8* (9), 6042–6050.
(12) Sonogashira, K.; Tohda, Y.; Hagihara, N. *Tetrahedron Lett.* **1975**, *16* (50), 4467–4470.
(13) Chinchilla, R.; Najera, C. *Chem. Soc. Rev.* **2011**, *40* (10), 5084–5121.
(14) Meldal, M.; Tornøe, C. W. *Chem. Rev.* **2008**, *108* (8), 2952–3015.
(15) Barnard, A.; Long, K.; Martin, H. L.; Miles, J. A.; Edwards, T. A.; Tomlinson, D. C.; Macdonald, A.; Wilson, A. J. *Angew. Chemie Int. Ed.* **2015**, *54* (10), 2960–2965.
(16) Couturier, J.-P.; Sütterlin, M.; Laschewsky, A.; Hettrich, C.; Wischerhoff, E. *Angew. Chemie Int. Ed.* **2015**, *54* (22), 6641–6644.
(17) Fischer, E.; Speier, A. *Berichte der Dtsch. Chem. Gesellschaft* **1895**, *28* (3), 3252–3258.
(18) Addison, A. W.; Rao, T. N.; Reedijk, J.; van Rijn, J.; Verschoor, G. C. *J. Chem. Soc. Dalt. Trans.* **1984**, 1349–1356.
(19) Zuccaccia, D.; Macchioni, A. *Organometallics* **2005**, *24* (14), 3476–3486.
(20) Bünzli, J.-C. G.; Eliseeva, S. V. In *Lanthanide Luminescence: Photophysical, Analytical and Biological Aspects*; Hanninen, P., Harma, H., Eds.; Springer: Berlin, 2011; pp 1–45.
(21) Carnall, W. T.; Fields, P. R.; Rajnak, K. *J. Chem. Phys.* **1968**, *49* (10), 4447–4449.
(22) Picot, A.; Malvolti, F.; Le Guennic, B.; Baldeck, P. L.; Williams, J. A. G.; Andraud, C.; Maury, O. *Inorg. Chem.* **2007**, *46* (7), 2659–2665.
(23) Albota, M. *Science.* **1998**, *281* (5383), 1653–1656.

Chapter 5

Conclusions and Future Directions

Introduction

This dissertation discussed several routes for the improvement of lanthanide-based luminescence in metallacrowns. Chapter two described the synthesis and characterization of photophysical and magnetic properties of a gallium [3.3.1] metallacryptate. This is a new structure type, where the cryptand-like architecture follows the M-N-O motif of metallacrowns precisely. This complex was able to sensitize a wide range of lanthanide emissions similar to other shi^{3-} containing metallacrowns. While quantum yields and lifetimes were slightly inferior than reported gallium metallacrowns due to the proximity of N-H oscillators, the use of nine antennae per Ln(III) rather than four substantially increased the absorption of the metallacryptate compared to the metallacrown. The result is that the overall brightness of this new structure type approximates the very high values for other Ga/shi based MCs for most of the lanthanides. The [3.3.1] metallacryptate showed slow magnetic relaxation for the Dy^{3+}, Nd^{3+} and Yb^{3+} analogs. The Dy^{3+} was the only complex with a real barrier to relaxation (12 K). This dual emissive/magnetic behavior might be exploitable in smart materials that can monitor each phenomenon independently.

Chapter three described the synthesis and photophysical properties of iodinated gallium 12-MC-4s. While the monomeric 12-MC-4 complexes were shown by PGSE DOSY experiments to be unstable in solution by exchanging the bridging carboxylate groups, the dimeric metallacrowns were confirmed to be resilient in methanol and DMSO. This dimeric structure could systematically incorporate four, eight, or twelve iodines by including iodine on the isopthalate bridges, on the hydroximates, or on both ligands. Examination of the photophysics showed that as the number of iodines increases, the quantum yields and lifetimes decrease for most of the lanthanides. However, Sm^{3+} and Er^{3+} emission showed an increase in quantum yield. In addition, the capability of these iodinated metallacrowns as CT contrast agents were

examined. The results show that these compounds are excellent x-ray attenuators and could be employed as bimodal imaging agents using both the lanthanide luminescence and the CT contrast. Lastly, in chapter four the functionalization of gallium and zinc metallacrowns was described using Sonogashira coupling and CuAAC. The addition of an ethynyl group onto the shi^{3-} ligand demonstrated a slight increase in the lifetime and quantum yield of ytterbium, and little change for samarium. The Tb^{3+} could not be sensitized very well by the $eshi^{3-}$ ligand because the emissive state of Tb^{3+} is to close in energy to the T_1 of the MCs. CuAAc was performed on the H_3eshi ligand and the metallacrown, and both benzyl azide and biotin-N_3 could be coupled to the ligand and the metallacrown. For the $LnZn_{16}$ metallacrowns, a method for adding an ethynyl functionality onto $picHA^{2-}$ was developed, and a suite of mixed ligand species with $pyzHA^{2-}$ was synthesized, providing exclusivity for "clickable" metallacrowns. Finally, Sonogashira couplings of aryl ethynes were performed on shi^{3-} and $picHA^{2-}$ generating complexes that had a red shift in absorbance as well as an increase in extinction coefficient. The modified shi^{3-} ($meanshi^{3-}$) also showed a small absorbance at 606 nm. This body of work demonstrates how various ligand design strategies may be used to refine the lanthanide luminescence of a metallacrown. The metallacryptate demonstrated the power of using more antenna, even though it came with a cost of introducing an oscillator. The inclusion of iodine increased quantum yields and lifetimes of Sm^{3+} and Er^{3+} and allows for the use of the metallacrown as a CT contrast agent. The addition of an ethyne with subsequent CuAAC coupling demonstrates a powerful technology for metallacrowns as imaging agents. Plus these biaryl ligands further demonstrate the potential for functionalization of the hydroimate ligands. However, these results can lead to even more fascinating future projects, which are not restricted to lanthaninde luminescence.

Future Directions of the [3.3.1] Metallacryptate

For the metallacrypate, it may be possible to replace the two bridging $H_x$shi ligands with other ligands such as a carboxylate or solvent molecules. Depending on steric restrictions of these ligands the eighth and ninth coordination site of the lanthanide may be open to solvent, which could lead to fascinating MRI contrast properties for a gadolinium complex. Given that some copper metallacrowns are known to have interesting relaxivities by virtue of having multiple water binding sites,[1–3] the use of a gallium based construct could marry the fascinating

optical properties to these relaxivities. The Ln[3.3.1] could have up to five waters bound, where two are on the lanthanide, and the other three are bound to gallium ions. Combine this with what was observed for the iodinated mishi^{3-} and there is now enhanced CT contrast, so this metallacryptate could be an example of a trimodal imaging agent.

For the magnetic properties of the metallacryptate, a dicarboxylate ligand could be used to dimerize the **Ln[3.3.1]** as a "dumbbell" structure shown as a model in Figure 5.1. These structures could take advantage of Long's incorporation of a radical between lanthanides to increase the barrier to relaxation of a dimerized single ion magnet. Even without the radical, there could be weak Ln-Ln interactions which are important for the development of a qubit.[4] Lastly, it may be possible to substitute the gallium for iron in this cryptate. The motivation for this change would be to develop a possible magnetic refrigerant following the example shown by Pecoraro and coworkers using Fe^{3+}(carboxylate)$_3$[9-MC$_{Fe^{III}N(shi)}$-3] metallacrowns described in the introductory chapter.[5] By making the Gd^{3+} analog of the [3.3.1] metallacryptate using Fe^{3+}, there is a large amount of spin from isotropic paramagnetic ions in a highly asymmetric structure. This scaffold could have many low lying excited states as a result which can lead to desirable magnetic entropy values.

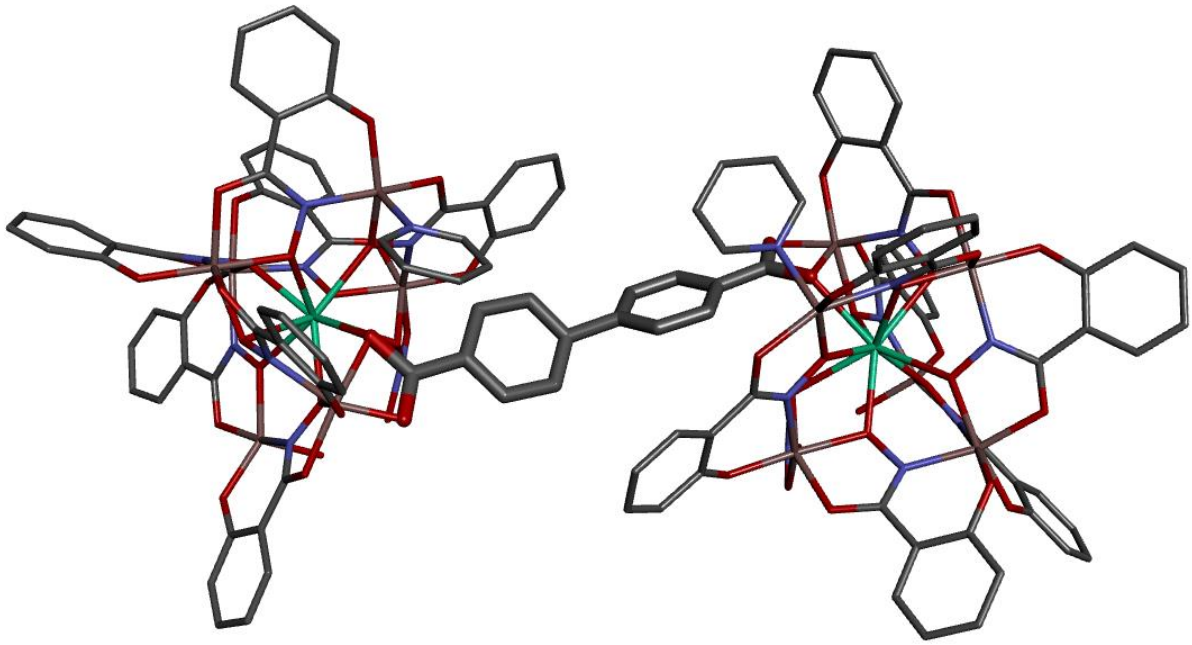

Figure 5.1. Model of a possible dimerized structure of **Tb[3.3.1]** using 4,4'-dibenzoate as a linker (shown in thicker bonds).

Future Directions for the use of Halogenated Metallacrowns

The studies in this thesis only investigated the incorporation of iodine onto gallium 12-MC-4 complexes. The initial luminescence results are consistent with, but do not prove that, a heavy ion effect is operative in these metallacrowns. Closer examination of the heavy atom effect within the sensitization process could give insight into why the photophysical properties of the metallacrowns were worse for most of the lanthanides as more iodine was introduced. One possible reason is that the heavy atom effect is in fact working as intended in the metallacrown, but the rate of ligand phosphorescence has accelerated so that it is much faster than the rate of energy transfer to the lanthanide. To understand this process, systematic measurements of ligand based fluorescence and phosphorescence photophysical properties should be performed. The quantum yields and lifetimes of **Gd-I$_0$**, **Gd-I$_4$**, **Gd-I$_8$**, and **Gd-I$_{12}$** fluorescence and phosphorescence can help understand how the ligand photophysics change with iodide content. These ligand scaffold studies could help explain another observation that the attachment of iodine to the bridging carboxylate enhances sensitization whereas covalent attachment of iodine to the shi ring red shifts excitation energy. By comparing **Gd-I$_4$** and **Gd-I$_8$** to **Gd-I$_0$**, and **Gd-I$_{12}$** to **Gd-I$_8$**, the effect of each ligand can be isolated. This suggests that further study is required to differentiate how these ligands participate in lanthanide sensitization. In addition, the extent of the heavy atom effect perturbations may be tuned by using chloro or bromo substituted ligands rather than iodo derivatives, which should be rather straightforward to accomplish following the synthetic strategies employed to synthesize the iodinated metallacrowns. These studies will show if there is a capability to tune the enhancement of ISC such that sensitization rate is faster than the rate of phosphorescence. Lastly, the position of the halogen on the shi^{3-} ring may be important. This thesis only discussed the 5-iodo derivative, but looking at the 4-iodo derivative may also give valuable information on how the iodide effects that photophysical properties of these lanthanide complexes.

One justification for the development of iodinated MCs was to enhance the photophysical properties (e.g., red-shift absorbance, enhance lifetimes and quantum yields); however, there is also the potential application of these iodinated metallacrowns as CT contrast agents. These initial results were completed in DMF and provided outstanding x-ray contrast. However, for these compounds to be useful in medical diagnostics, they must be modified to enhance water

solubility. One method for enhancing water solubility could be by increasing the charge of the metallacrown. If Ln-$I_{8,}$ was modified to include a sulfonate or a carboxylate in the 5 position (Figure 5.2) the net charge of this complex increases from MC^{2-} to MC^{6-}. This larger negative charge could help with solubility in addition to an entropic argument of dissolving seven ionic particles (6 Na^+ and one MC^{6-}) up from three (two Na^+ and one MC^{2-}), however, highly charged particles can result in patient discomfort. Alternatively these metallacrowns have been loaded into polystyrene beads by Dr. Ivana Martinic with the purpose of increasing biocompatibility and signal enhancement. These beads may also provide specific tissue targeting by including opportunity for functionalization of the iodinated systems via functionalizing the bead surface.

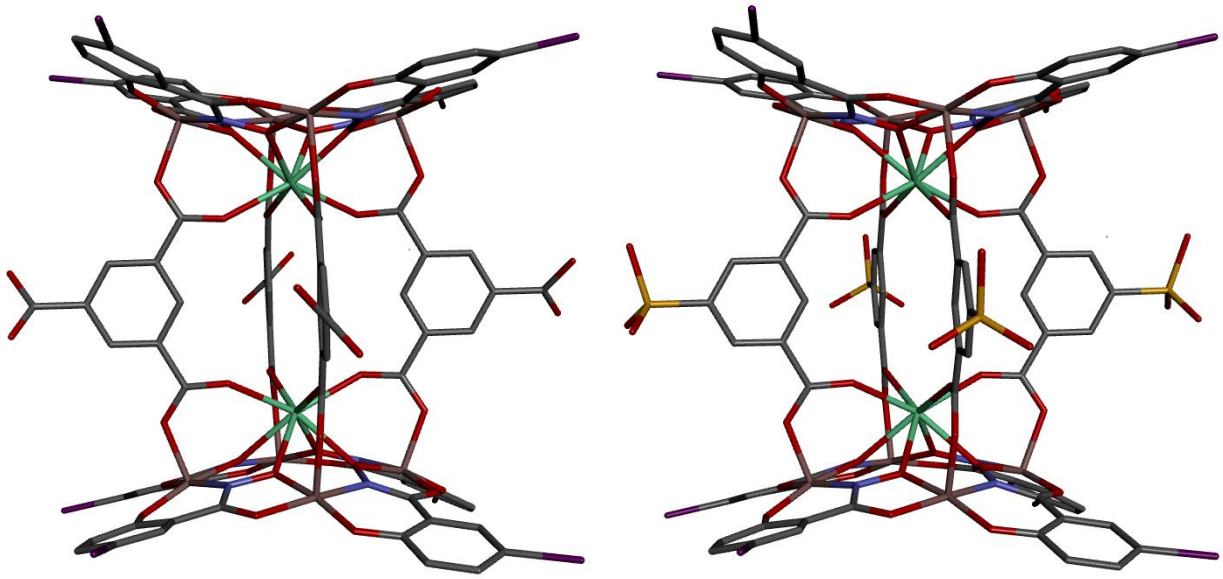

Figure 5.2. Models for potential carboxy (left) or sulfo (right) containing **Ln-I_8** metallacrowns.

Future Directions for Sonogashira and CuAAC Coupling with Metallacrowns.

Chapter 4 of this thesis demonstrated how to use CuAAC to couple an azide of interest to both the metallacrown precursor ligand or the metallacrown scaffold itself. Both of these design strategies are useful for the development of interesting ligands that can incorporate different types of coupling partners onto a metallacrown. Potential applications include tagging with antibodies to distinguish cancer cells selectively, appending additional antenna (e.g., anthraquinones) in order to shift the excitation wavelength of the molecule or linking long alkyl thiols for combination of metallacrowns to quantum dots or other nanoparticles. For example, the following scheme proposes a possible method for the generation of an azido Gd-DOTA complex

inspired by work from Luchinat, Mead and coworkers,[6] which may be coupled to a luminescent metallacrown to again achieve a bimodal imaging agent, which this time would combine an MRI contrast/Ln emissive agent.

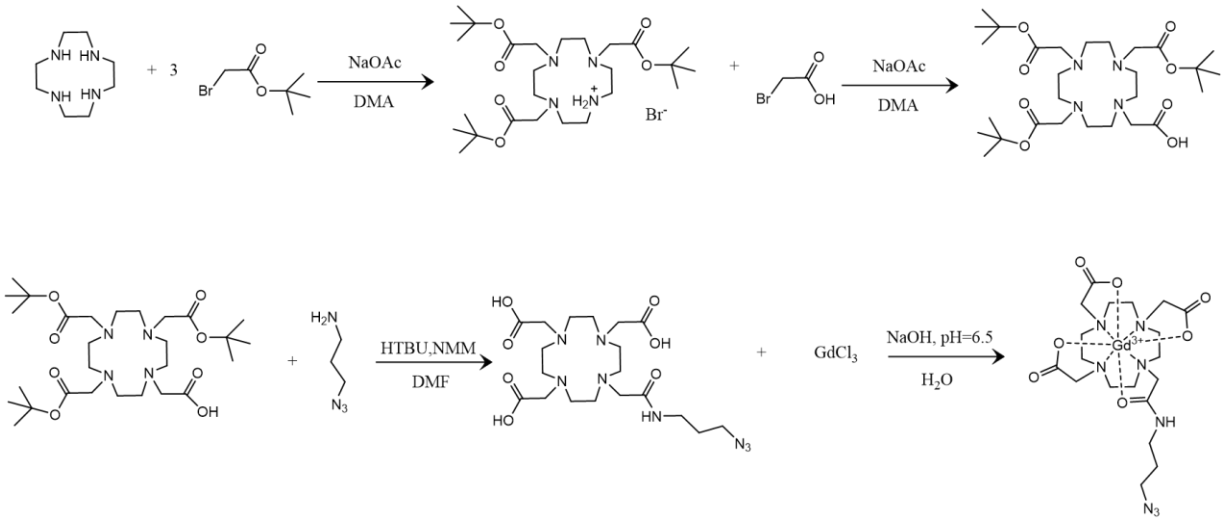

Scheme 5.1. Synthetic plan for making an azido Gd-DOTA derivative for clicking to an ethynyl metallacrown, modified from a known synthetic method.[6]

In addition, the construction of an azide onto a metallacrown should be possible either by direct addition of an azide or by addition of a linker as shown in scheme 5.2 below. The construction of azido metallacrowns not only allows for the study of linking metallacrowns to ethynes, but also opens the door to controlled coupling of metallacrowns with two separate lanthanides. Consider an ethynyl metallacrown which contains Yb^{3+} and an azido metallacrown which contains Er^{3+}. The controlled linkage of these two metallacrowns places these lanthanides in close proximity (Figure 5.3) and could allow for energy upconverson of NIR light to green light known to occur from this lanthanide pair.[7–12] In addition, it may be possible to generate a metallacrown coordination polymer with alternating lanthanides (Figure 5.4) for the same purpose. This controlled alternation combined with the work on Ce/Cu oxides from metallacrowns by Kremlev et al[13] could lead to new phases of Yb/Er/Ga oxides for upconversion.

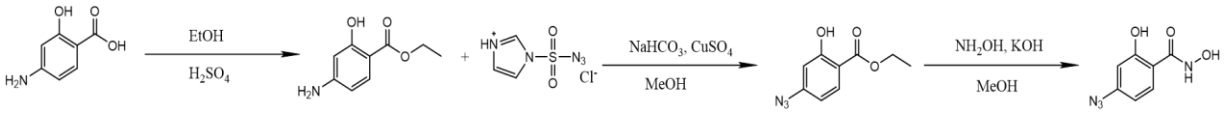

Scheme 5.2. Synthetic plan for an azido appended H_3shi derivative. The diaza transfer reagent shown in the second step may be synthesized according to literature procedures, and used according to another.[14,15]

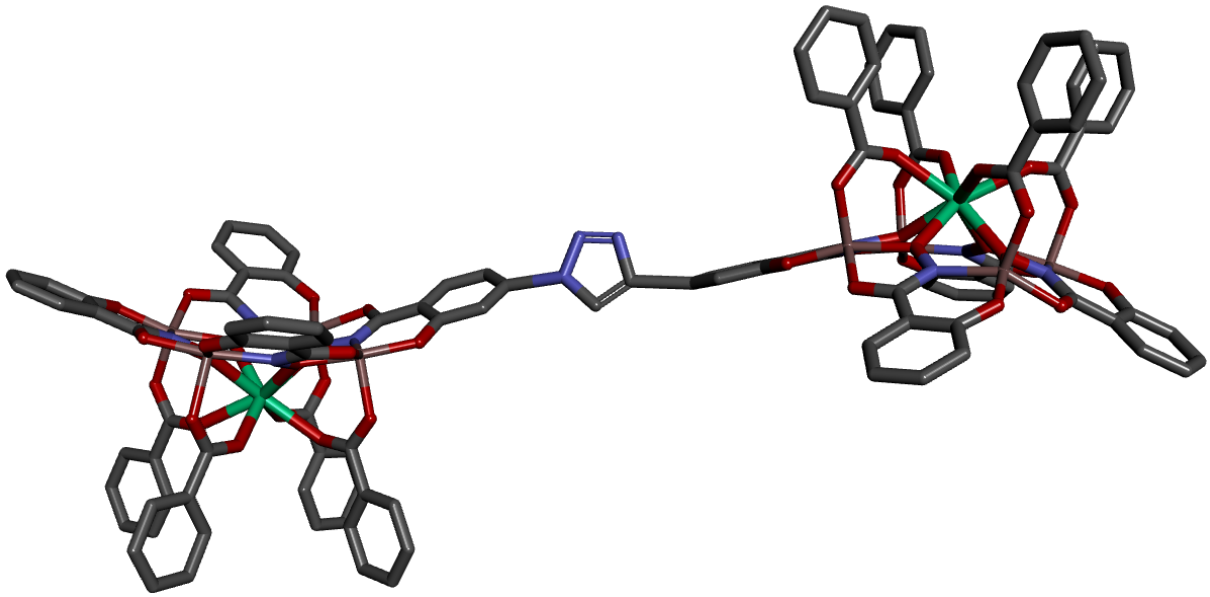

Figure 5.3. Model of a clicked dimer of metallacrowns for controlled Yb/Er interaction.

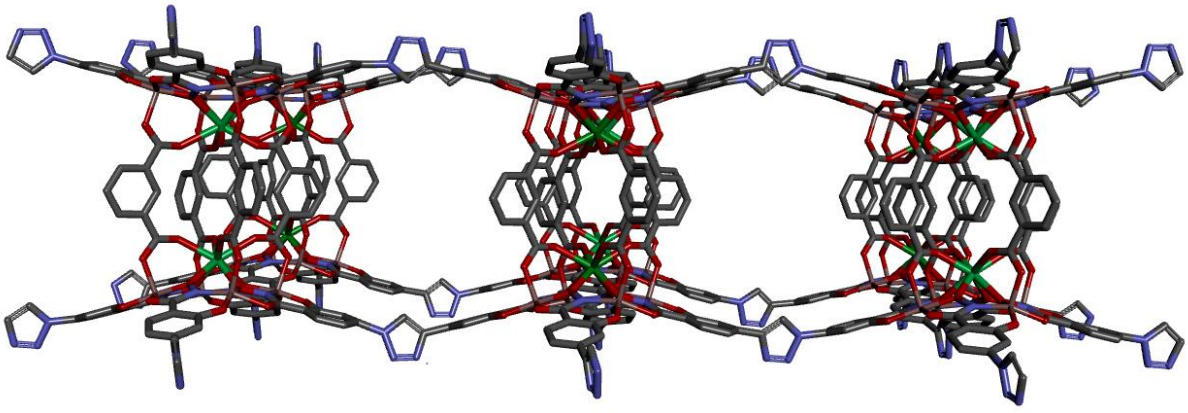

Figure 5.4. Model of a possible clicked 2D coordination polymer.

The use of Sonogashira coupling also has many possibilities for future work. This thesis only covered the coupling of the ethynyl functionality onto the hydroximate ligands, however,

the existence of H_2iiph means that it should be possible to synthesize H_2eiph (Scheme 5.3). This ligand on its own could be useful in $\{Ln[12\text{-}MCGaIIIN(L)\text{-}4]\}_2(L')_4$ dimeric MC structures, such as Ln-I_8 as another method to fuctionalized an iodinated metallacrown. But this ligand could also be combined with another H_2iiph to form a tetracarboxylate compound (Scheme 5.4). This tetracarboxylate could generate 2D or 3D coordination polymers shown in Figure 5.5.

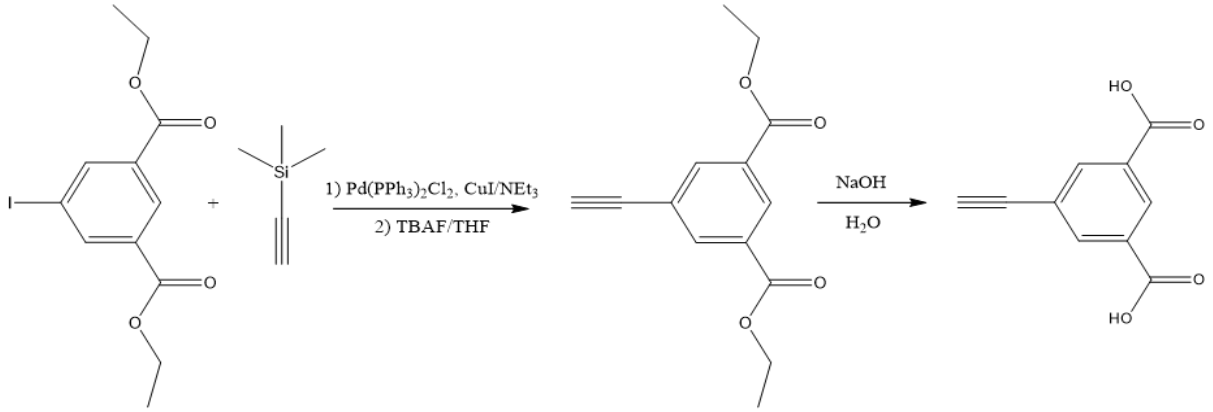

Scheme 5.3. Synthetic plan for 5-ethynyl isophthalic acid based on the known coupling to make H_3eshi.

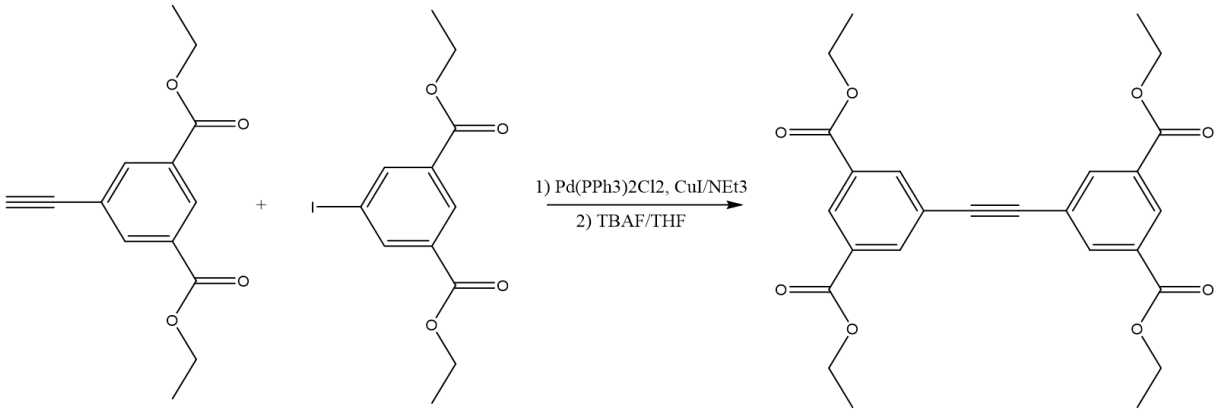

Scheme 5.4. Synthetic plan for 5-5'ethynyl diisophthalic acid. The ethyl ester may be converted to the carboxylic acid by base catalyzed hydrolysis.

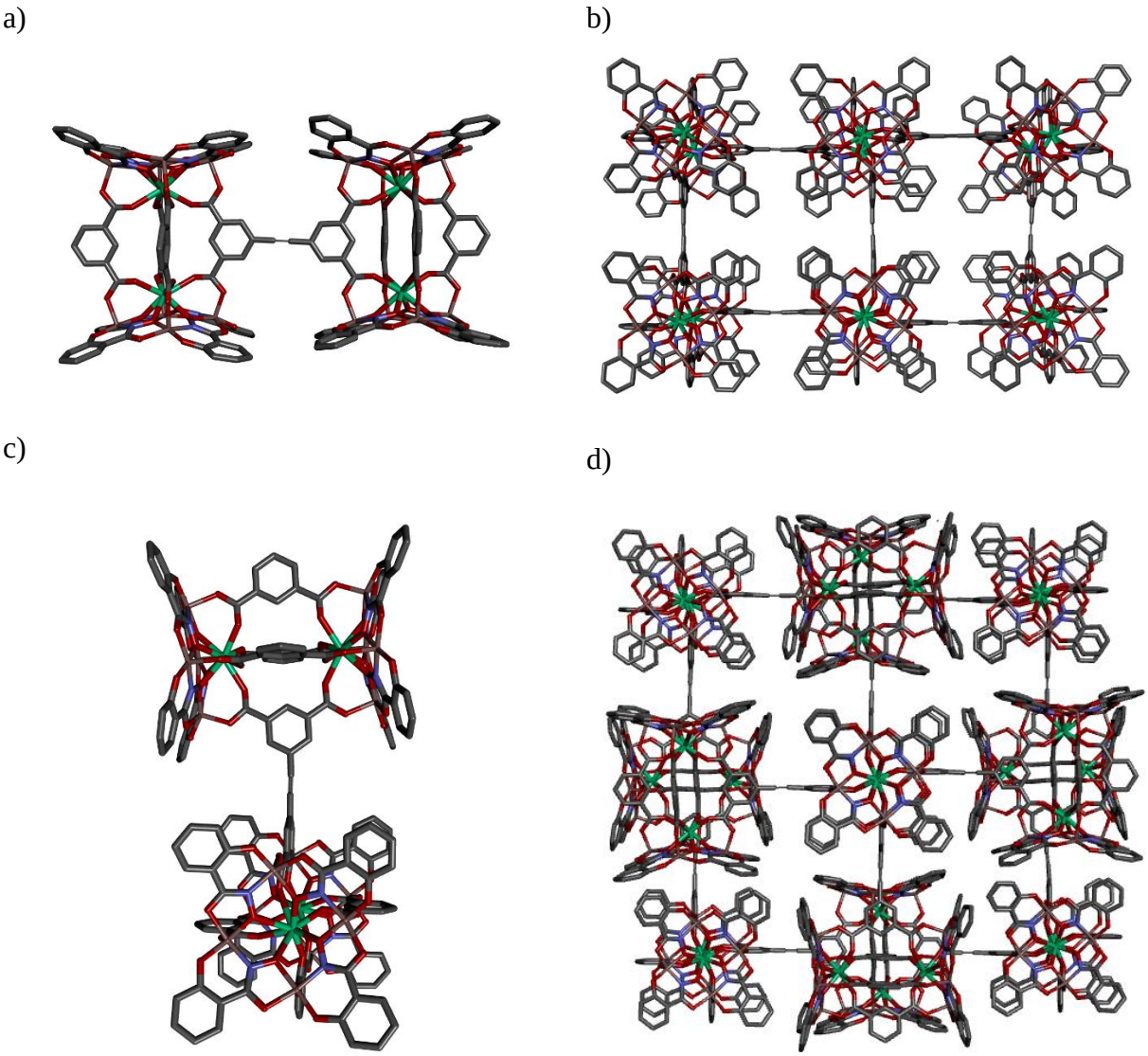

Figure 5.5. Models of potential 2D or 3D coordination polymers using the proposed tetracarbonyl. a) One possible binding confirmation where the MCs are parallel and b) the resulting 2D sheet. c) Another configuration where the metallacrowns are orthogonal to one another and d) the resulting 3D coordination polymer.

There is also the photophysical and synthetic implications of the biaryl hydroximates discussed in chapter four. The initial rationale for design of these ligands was to mimic known two photon excitation ligands or design principles shown for Eu^{3+} sensitization.[16,17] For the H_3meanshi ligand especially there is some evidence that this may be possible for metallacrowns given the appearance of a 606 nm absorption band for the ligand on its own. Initial attempts at

using this ligand in metallacrowns results in a loss of this blue color for the development of a yellow-brown color. The reason for this color change could be due to hydrolysis of the hydroxamic acid to a carboxylic acid since there was sodium hydroxide present in the solution. This color change is replicated by dissolving H_3meanshi in water/methanol with the pH adjusted to about 8 using sodium hydroxide, which supports this hypothesis. In the future this hydrolysis should be avoided by using a different base such as triethylamine. However, MCs with H_3meanshi could be fascinating, especially if there is potential for two photon absorbance.

The use of two photon absorption could lead to important advances in metallacrowns as optical imaging agents in tissues since red light ($\lambda < 600$ nm) has much deeper penetration than blue or green light.[18] However, an antenna with this highly red-shifted absorbance may not function as intended for lanthanide sensitization. Ideally, an energy gap of 5 000 cm^{-1} between the singlet and triplet energies would exist to facilitate intersystem crossing.[19] Also, another gap of 2 500 cm^{-1} is desired between the sensitizing excited state of the ligand (such as a triplet) and the emissive state of the lanthanide to inhibit back transfer.[19] So, a total gap of 7 500 cm^{-1} between the singlet energy and lanthanide emissive state is the ideal scenario. If one was to use H_3meanshi as is with a 606 nm absorbance (16 502 cm-1), then the lanthanide emissive state should be less than 9 000 cm-1. There is only one lanthanide that is less than 9 000 cm-1, which is Er^{3+} with an emissive state at 6 667 cm-1. To access more lanthanides such as Yb^{3+} a two photon excitation could be used. If two 606 nm photons are absorbed instead, then the emissive state maximum increases to 25 500 cm-1, which is inclusive of many more lanthanides. Perhaps there could even be as many as the original shi^{3-} ligand.

These modifications are also not restricted to H_3shi or H_2picHA modifications. There are examples of metallacrowns which contain a 3-hydroxy-2-naphthalene hydroximate (H_3nha) or quinaldic hydcroxamic acid (H_2quinHA).[20,21] It should be possible to append ethynyl functionalities onto these ligands as well which may induce an even larger red shift than the single ring alternatives (Scheme 5.5).

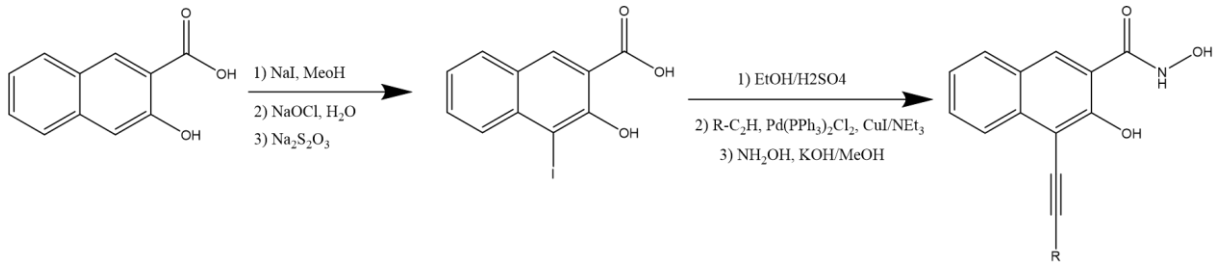

Scheme 5.5. Possible synthetic route for modification of H_3nha using Sonogashira Coupling. The iodination in the 4 position is a published procedure.[22]

It is also possible to perform CuAAC on alkynes which are not terminal which was demonstrated by Sharpless in his seminal "click" chemistry report.[23] In this case one can imaging creating controlled multifunctional hydroximates using Sonogashira coupling followed by CuAAC (Scheme 5.6).

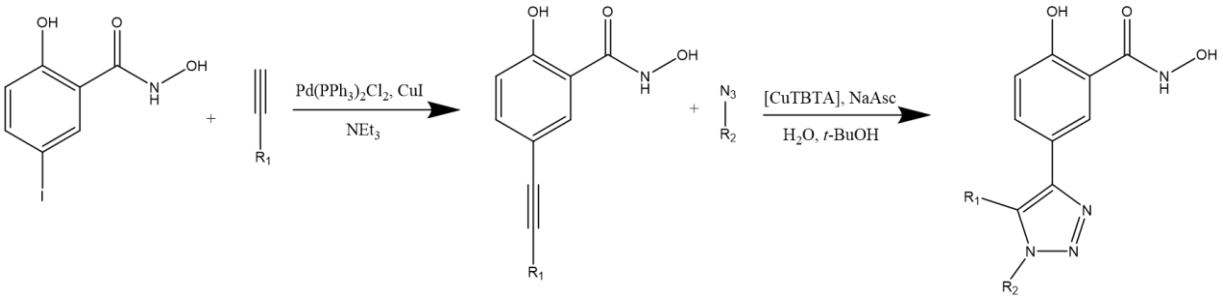

Scheme 5.6. Possible route for a bifunctionalized hydroximate ligand.

In essence, the use of Sonogashira or CuAAC coupling opens many doors for future ligand design in metallacrown complexes. Indeed, metallacrowns truly are a chemical equivalent to Legos, with many tunable parts across metal and ligand choices.

Future Directions of Metallacrowns

In total, this thesis described three separate ways to take advantage of the tunability of hydroximate ligands in metallacrown complexes. A new structure type was described and two new concepts of ligand design were introduced. These alterations were proposed for the purpose enhancing lanthanide based luminescence, but metallacrowns are capable of many other applications. The introduction of the new metallacryptate suggests that there are many other non-traditional metallacrown structures still to be discovered. Other non-traditional structures have been discovered in the past, one of which is currently the best example of a metallacrown single

molecule magnet from our group.[4] The addition of an interesting metallacryptate reinforces the need for vigilant and open-minded characterization for discovering something new. The other two chapters describe how ligand design may be taken advantage of in metallacrowns. This thesis has barely scratched the surface of possible designs for MCs using Sonogashira couplings or CuAAC. These ligand design tenets could be applied in other known metallacrowns as was shown by Rentschler and coworkers[24], or could be applied to the more non-traditional complexes such as the Dy/Mn 14-MC-5 complex reported by Pecoraro and coworkers.[25] This work in combination with other synthetically challenging ligand design such as H_3hinHA reported by Pecoraro, Tegoni and coworkers demonstrate the value in pursing hydroximates which are not commercially available, or straightforward to produce. Metallacrowns can thrive alongside creative design, and the future of MCs lies with the resolve to embrace these synthetic challenges.

References

(1) Muravyeva, M. S.; Zabrodina, G. S.; Samsonov, M. A.; Kluev, E. A.; Khrapichev, A. A.; Katkova, M. A.; Mukhina, I. V. *Polyhedron* **2016**, *114*, 165–171.

(2) Katkova, M. A.; Zabrodina, G. S.; Muravyeva, M. S.; Shavyrin, A. S.; Baranov, E. V.; Khrapichev, A. A.; Ketkov, S. Y. *Eur. J. Inorg. Chem.* **2015**, *2015* (31), 5202–5208.

(3) Katkova, M. A.; Zabrodina, G. S.; Muravyeva, M. S.; Khrapichev, A. A.; Samsonov, M. A.; Fukin, G. K.; Ketkov, S. Y. *Inorg. Chem. Commun.* **2015**, *52* (3), 31–33.

(4) Chow, C. Y.; Bolvin, H.; Campbell, V. E.; Guillot, R.; Kampf, J. W.; Wernsdorfer, W.; Gendron, F.; Autschbach, J.; Pecoraro, V. L.; Mallah, T. *Chem. Sci.* **2015**, *6* (7), 4148–4159.

(5) Chow, C. Y.; Guillot, R.; Rivière, E.; Kampf, J. W.; Mallah, T.; Pecoraro, V. L. *Inorg. Chem.* **2016**, *55* (20), 10238–10247.

(6) Mastarone, D. J.; Harrison, V. S. R.; Eckermann, A. L.; Parigi, G.; Luchinat, C.; Meade, T. J. *J. Am. Chem. Soc.* **2011**, *133*, 5329–5337.

(7) Binnemans, K. *Chem. Rev.* **2009**, *109*, 4283–4374.

(8) Biju, S.; Eom, Y. K.; Bunzli, J.-C. G.; Kim, H. K. *J. Mater. Chem. C* **2013**, *1* (21), 3454–3466.

(9) Sy, M.; Nonat, A.; Hildebrandt, N.; Charbonnière, L. J. *Chem. Commun. (Camb).* **2016**, *52* (29), 5080–5095.

(10) van der Ende, B. M.; Aarts, L.; Meijerink, A. *Phys. Chem. Chem. Phys.* **2009**, *11* (47), 11081–11095.

(11) Bünzli, J. C. G.; Eliseeva, S. V. *J. Rare Earths* **2010**, *28* (6), 824–842.

(12) Suffren, Y.; Zare, D.; Eliseeva, S. V.; Guénée, L.; Nozary, H.; Lathion, T.; Aboshyan-Sorgho, L.; Petoud, S.; Hauser, A.; Piguet, C. *J. Phys. Chem. C* **2013**, *117* (51), 26957–26963.

(13) Kremlev, K. V; Samsonov, M. A.; Zabrodina, G. S.; Arapova, A. V; Yunin, P. A.; Tatarsky, D. A.; Plyusnin, P. E.; Katkova, M. A.; Ketkov, S. Y. *Polyhedron* **2016**, *114*, 96–100.

(14) Ye, H.; Liu, R.; Li, D.; Liu, Y.; Yuan, H.; Guo, W.; Zhou, L.; Cao, X.; Tian, H.; Shen, J.; Wang, P. G. *Org. Lett.* **2013**, *15* (1), 18–21.

(15) Goddard-Borger, E. D.; Stick, R. V. *Org. Lett.* **2007**, *9* (19), 3797–3800.

(16) Picot, A.; Malvolti, F.; Le Guennic, B.; Baldeck, P. L.; Williams, J. A. G.; Andraud, C.; Maury, O. *Inorg. Chem.* **2007**, *46* (7), 2659–2665.

(17) Maury, O.; Daléo, A.; Picot, A.; Brasselet, S.; Baldeck, P. L.; Chaput, F.; Parola, S.; Andraud, C. In *Journal of Luminescence*; 2013; Vol. 133, pp 175–179.

(18) Trivedi, E. R.; Harney, A. S.; Olive, M. B.; Podgorski, I.; Moin, K.; Sloane, B. F.; Barrett, A. G. M.; Meade, T. J.; Hoffman, B. M. *Proc. Natl. Acad. Sci.* **2010**, *107* (4), 1284–1288.

(19) Bünzli, J.-C. G.; Eliseeva, S. V. In *Lanthanide Luminescence: Photophysical, Analytical and Biological Aspects*; Hanninen, P., Harma, H., Eds.; Springer: Berlin, 2011; pp 1–45.

(20) Gibney, B. R.; Stemmler, A. J.; Pilotek, S.; Kampf, J. W.; Pecoraro, V. L. *Inorg. Chem.* **1993**, *32* (26), 6008–6015.

(21) Trivedi, E. R.; Eliseeva, S. V.; Jankolovits, J.; Olmstead, M. M.; Petoud, S.; Pecoraro, V. L. *J. Am. Chem. Soc.* **2014**, *136* (4), 1526–1534.

(22) Albert, J. S.; Aharony, D.; Andisik, D.; Barthlow, H.; Bernstein, P. R.; Bialecki, R. A.; Dedinas, R.; Dembofsky, B. T.; Hill, D.; Kirkland, K.; Koether, G. M.; Kosmider, B. J.; Ohnmacht, C.; Palmer, W.; Potts, W.; Rumsey, W.; Shen, L.; Shenvi, A.; Sherwood, S.;

Warwick, P. J.; Russell, K. *J. Med. Chem.* **2002**, *45*, 3972–3983.
(23) Kolb, H. C.; Finn, M. G.; Sharpless, K. B. *Angew. Chemie Int. Ed.* **2001**, *40* (11), 2004–2021.
(24) Plenk, C.; Krause, J.; Beck, M.; Rentschler, E. *Chem. Commun.* **2015**, *51* (30), 6524–6527.
(25) Boron, T. T.; Kampf, J. W.; Pecoraro, V. L. *Inorg. Chem.* **2010**, *49* (20), 9104–9106.

Appendices

Appendix A. Supplemental Information for Chapter 2

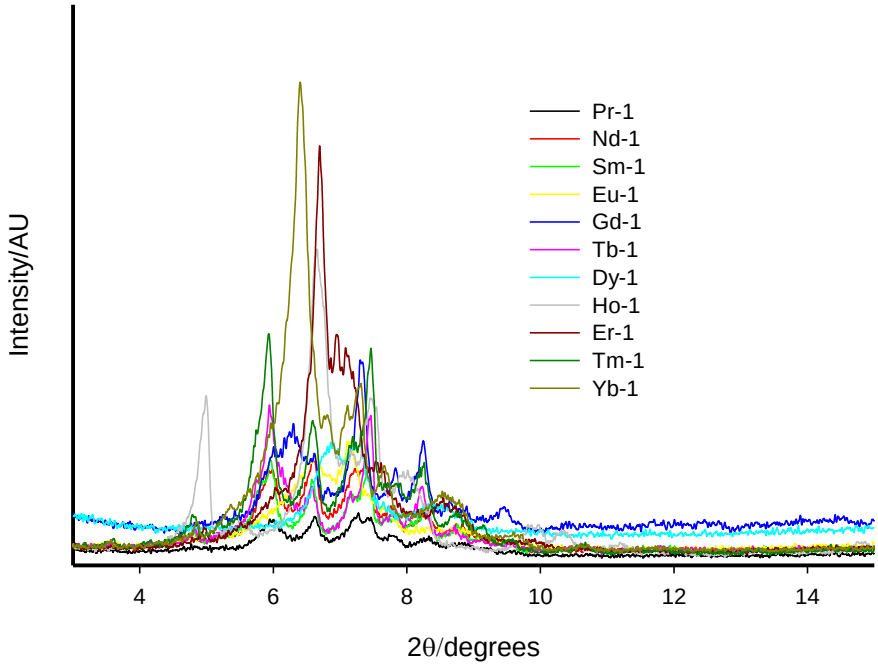

Figure A1. Powder X-ray diffraction of **Ln[3.3.1]** metallacryptates.

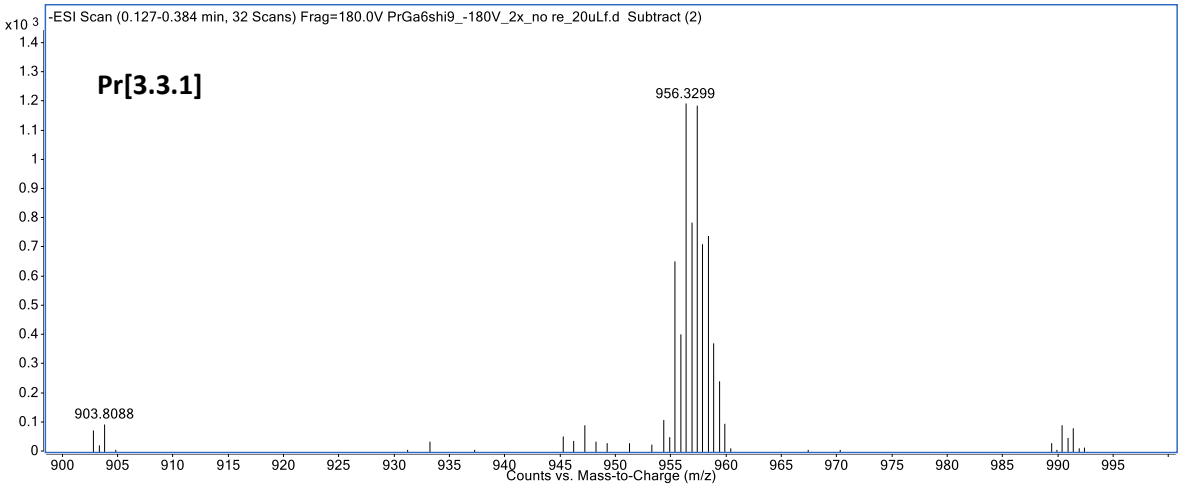

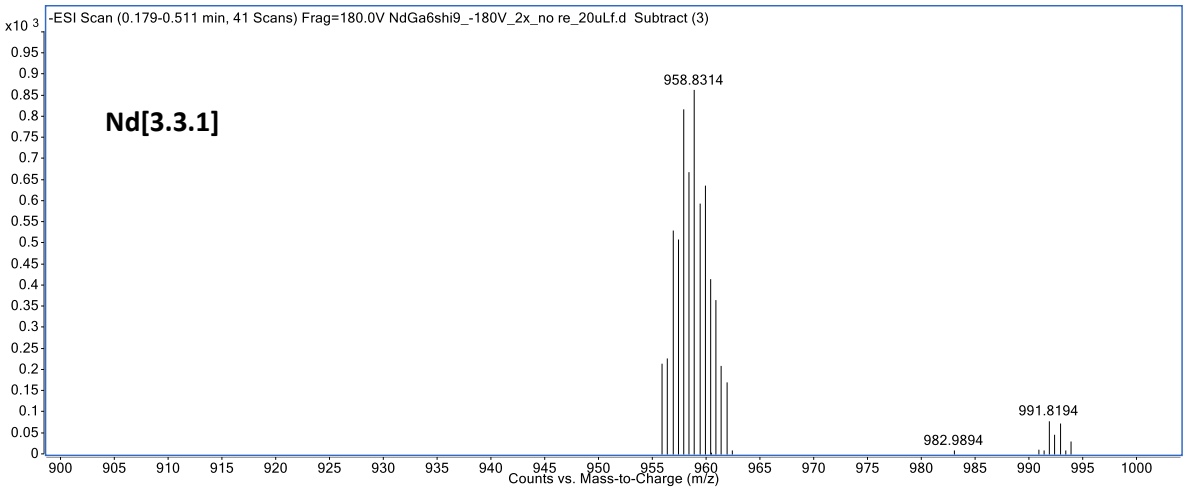
-ESI Scan (0.179-0.511 min, 41 Scans) Frag=180.0V NdGa6shi9_-180V_2x_no re_20uLf.d Subtract (3)
x10 3
Nd[3.3.1]
958.8314
991.8194
982.9894
Counts vs. Mass-to-Charge (m/z)

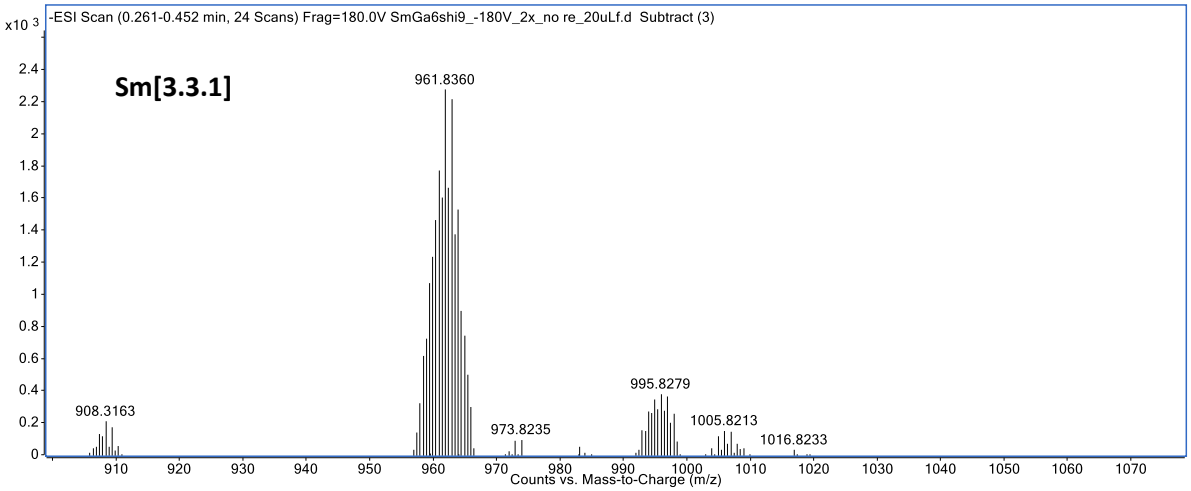
-ESI Scan (0.261-0.452 min, 24 Scans) Frag=180.0V SmGa6shi9_-180V_2x_no re_20uLf.d Subtract (3)
x10 3
Sm[3.3.1]
961.8360
995.8279
908.3163
973.8235
1005.8213
1016.8233
Counts vs. Mass-to-Charge (m/z)

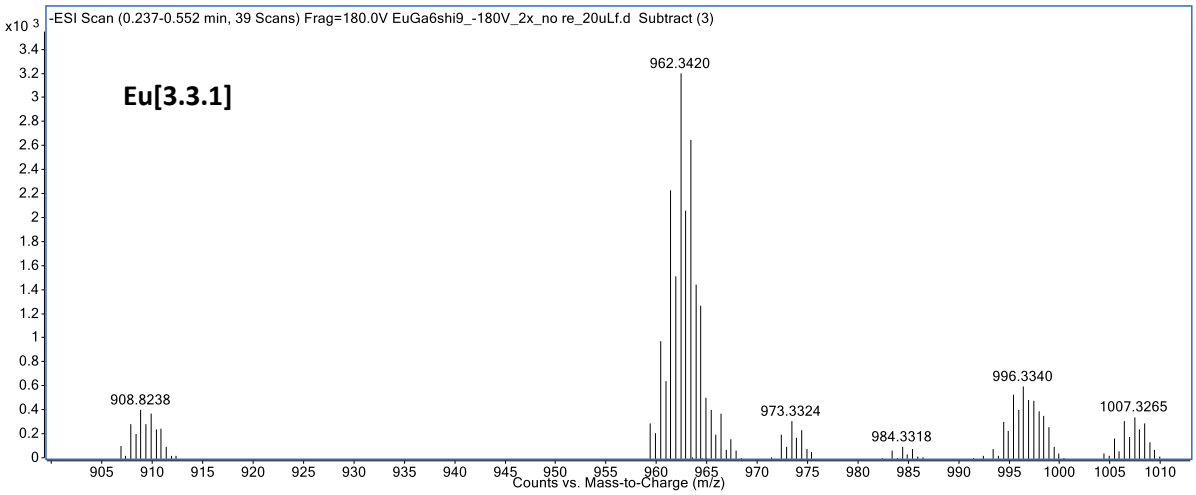
-ESI Scan (0.237-0.552 min, 39 Scans) Frag=180.0V EuGa6shi9_-180V_2x_no re_20uLf.d Subtract (3)
x10 3
Eu[3.3.1]
962.3420
908.8238
973.3324
984.3318
996.3340
1007.3265
Counts vs. Mass-to-Charge (m/z)

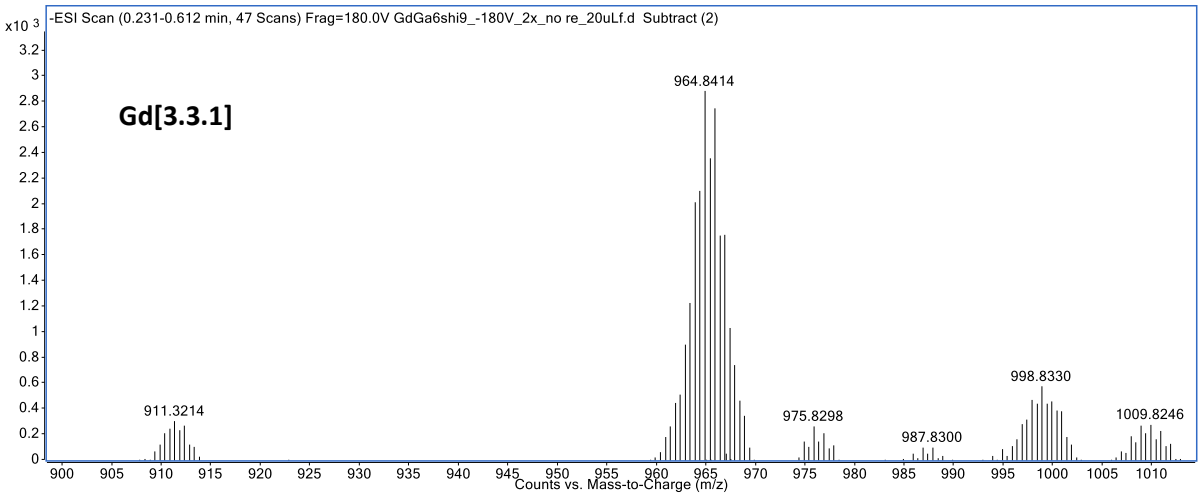
-ESI Scan (0.231-0.612 min, 47 Scans) Frag=180.0V GdGa6shi9_-180V_2x_no re_20uLf.d Subtract (2)
x10 3
Gd[3.3.1]
964.8414
911.3214
975.8298
987.8300
998.8330
1009.8246
Counts vs. Mass-to-Charge (m/z)

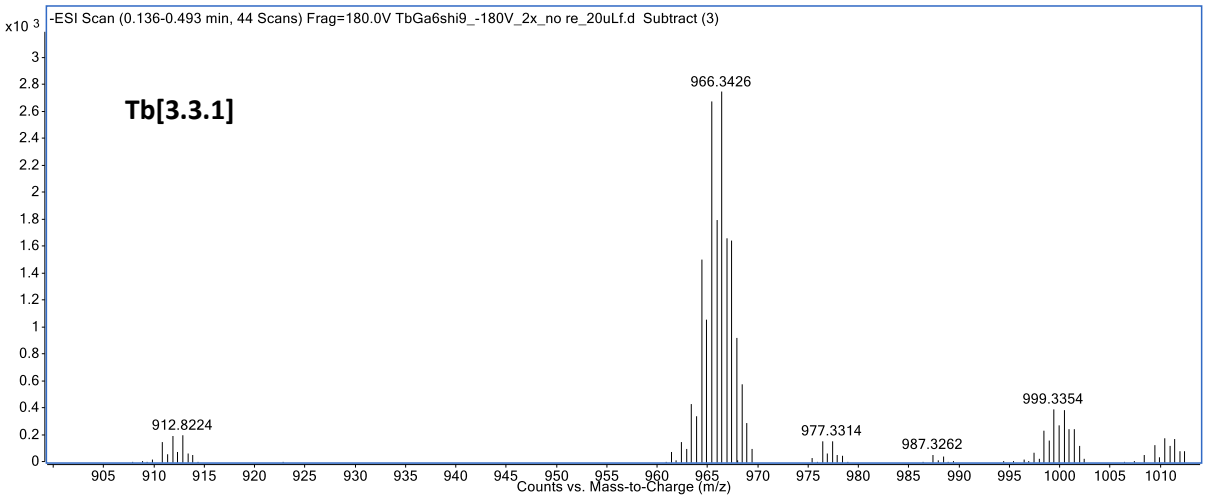
-ESI Scan (0.136-0.493 min, 44 Scans) Frag=180.0V TbGa6shi9_-180V_2x_no re_20uLf.d Subtract (3)
x10 3
Tb[3.3.1]
966.3426
912.8224
977.3314
987.3262
999.3354
Counts vs. Mass-to-Charge (m/z)

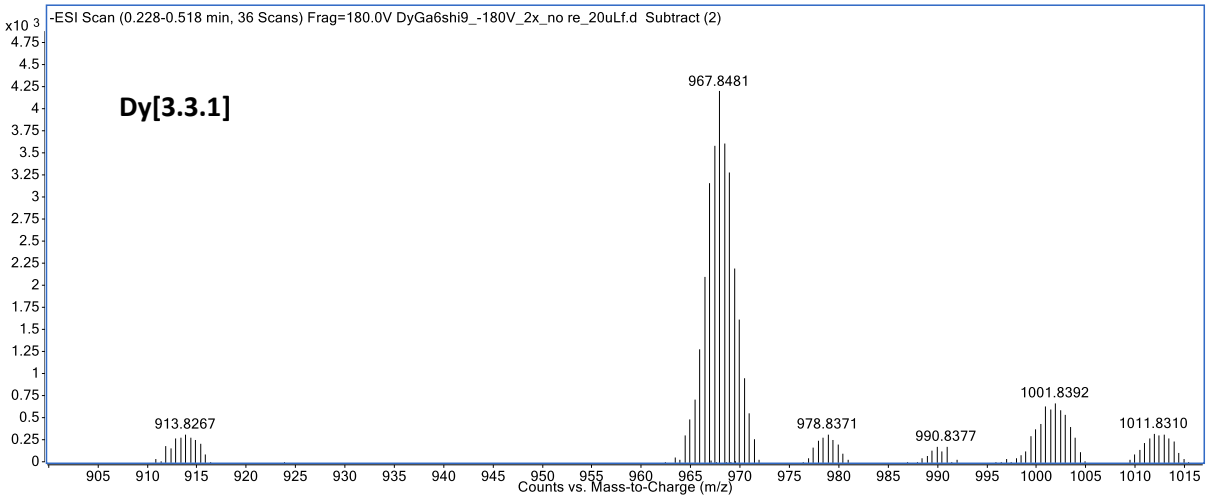
-ESI Scan (0.228-0.518 min, 36 Scans) Frag=180.0V DyGa6shi9_-180V_2x_no re_20uLf.d Subtract (2)
x10 3
Dy[3.3.1]
967.8481
913.8267
978.8371
990.8377
1001.8392
1011.8310
Counts vs. Mass-to-Charge (m/z)

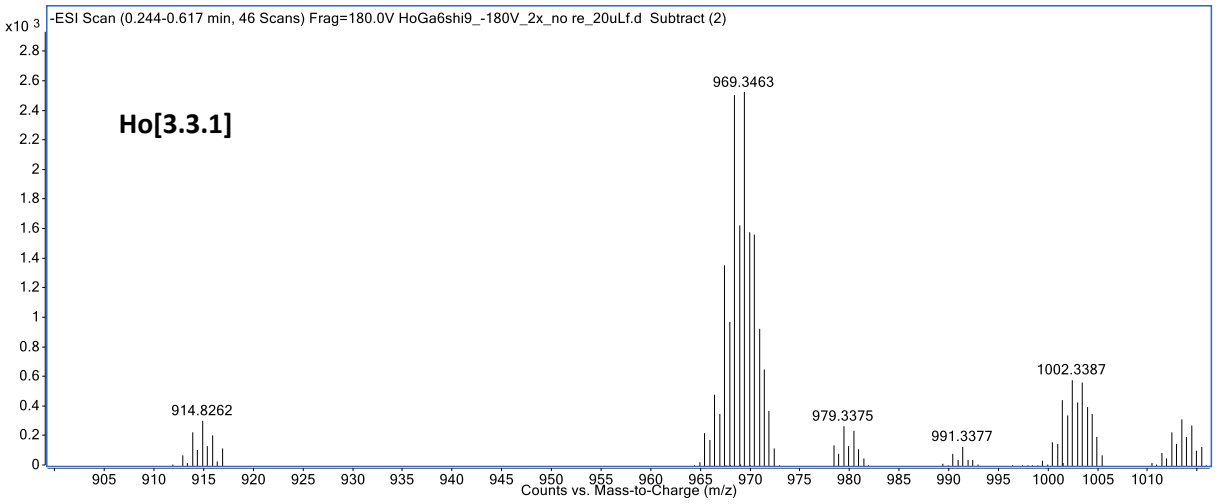
-ESI Scan (0.244-0.617 min, 46 Scans) Frag=180.0V HoGa6shi9_-180V_2x_no re_20uLf.d Subtract (2)
x10 3
Ho[3.3.1]
969.3463
914.8262
979.3375
991.3377
1002.3387
Counts vs. Mass-to-Charge (m/z)

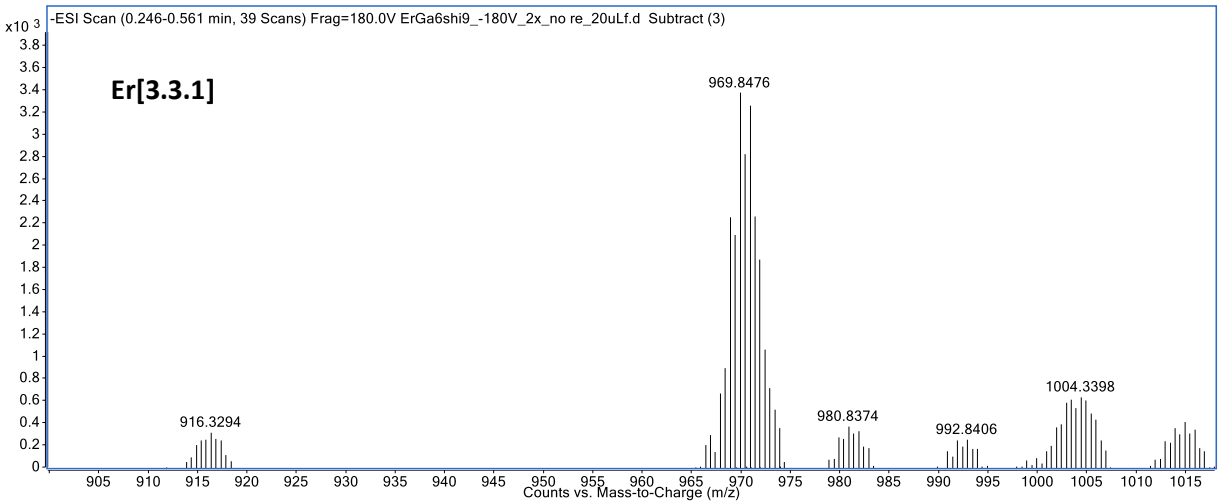
-ESI Scan (0.246-0.561 min, 39 Scans) Frag=180.0V ErGa6shi9_-180V_2x_no re_20uLf.d Subtract (3)
x10 3
Er[3.3.1]
969.8476
916.3294
980.8374
992.8406
1004.3398
Counts vs. Mass-to-Charge (m/z)

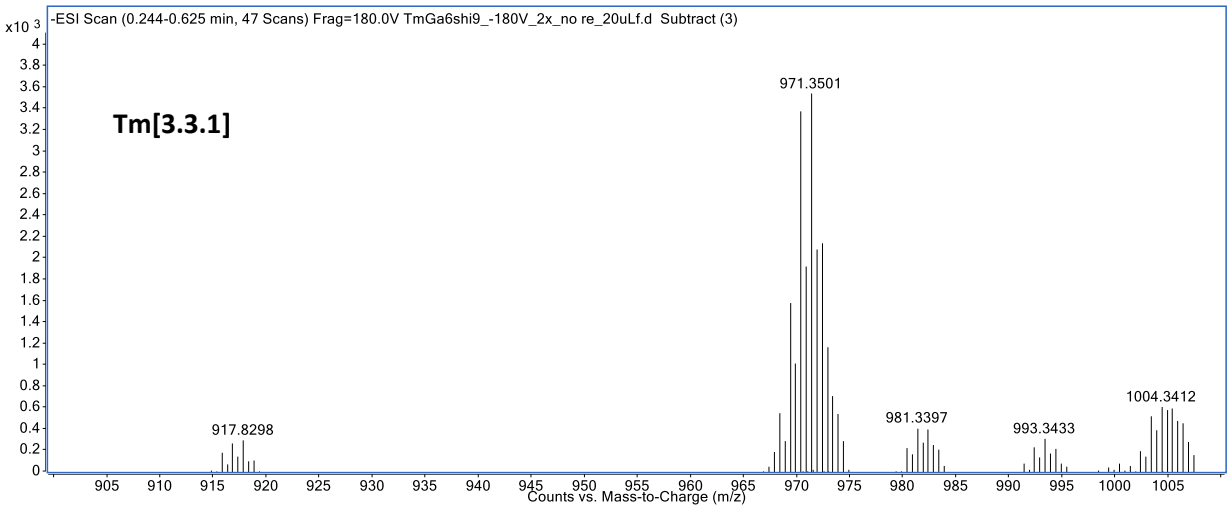
-ESI Scan (0.244-0.625 min, 47 Scans) Frag=180.0V TmGa6shi9_-180V_2x_no re_20uLf.d Subtract (3)
x10 3
Tm[3.3.1]
971.3501
917.8298
981.3397
993.3433
1004.3412
Counts vs. Mass-to-Charge (m/z)

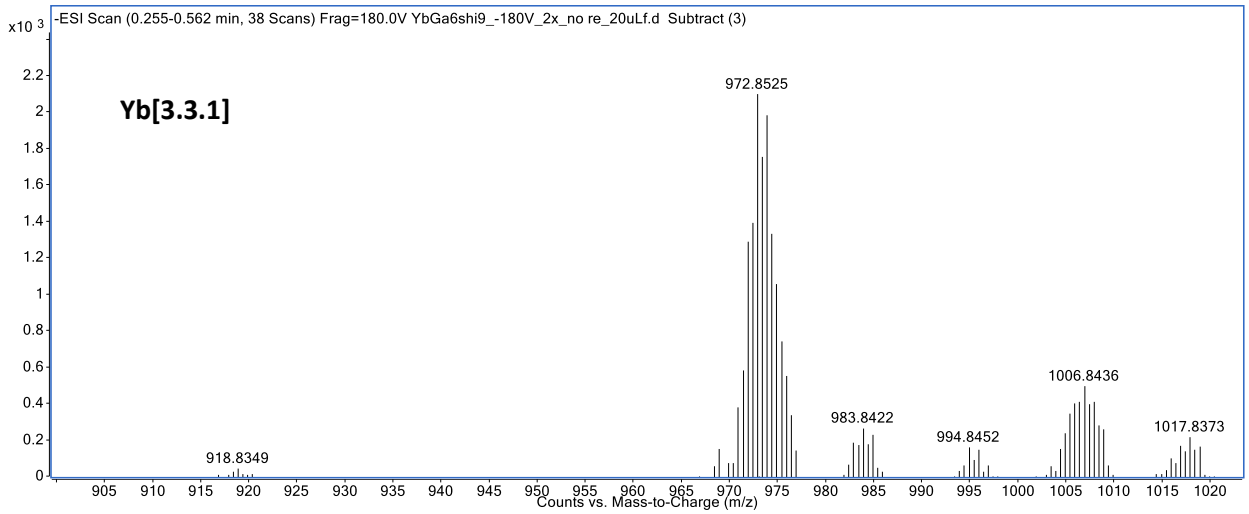

Figure A2. ESI-QTOF mass-spectra of **Ln[3.3.1]** complexes. Spectra were collected in negative ion mode with fragmentation voltage of 180 V in methanol. Background spectra were subtracted three times.

Appendix B. Supplemental Information for Chapter 3.

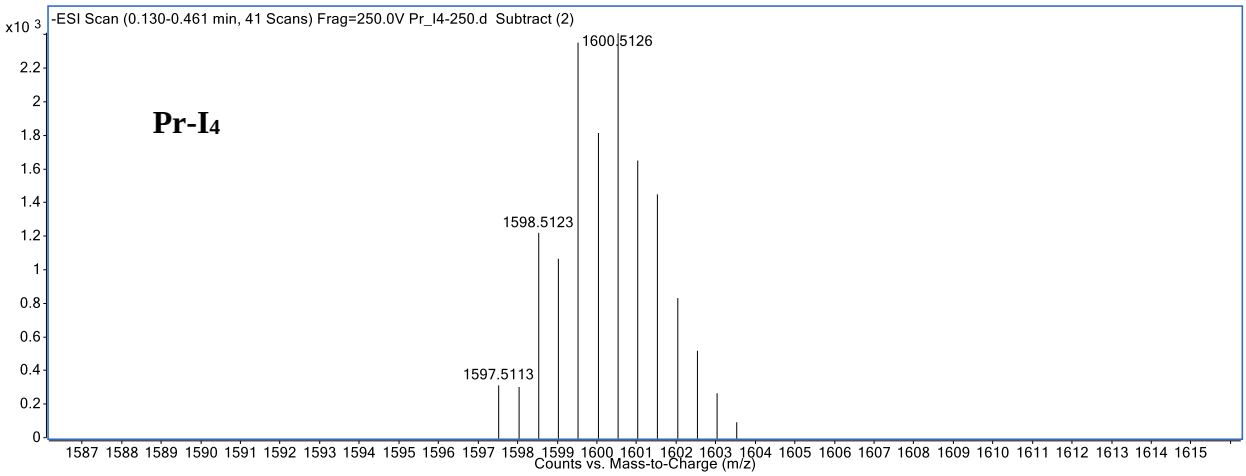

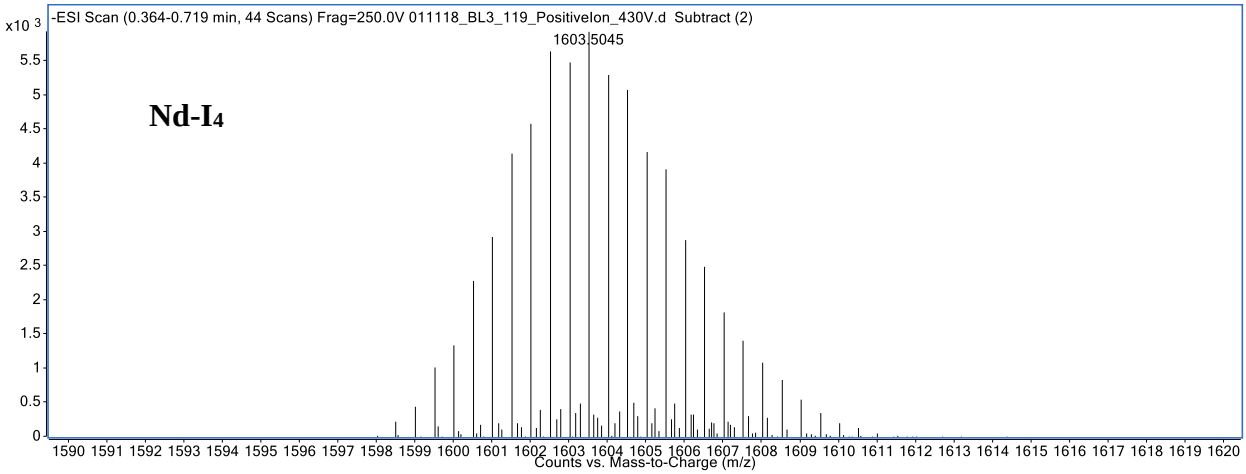

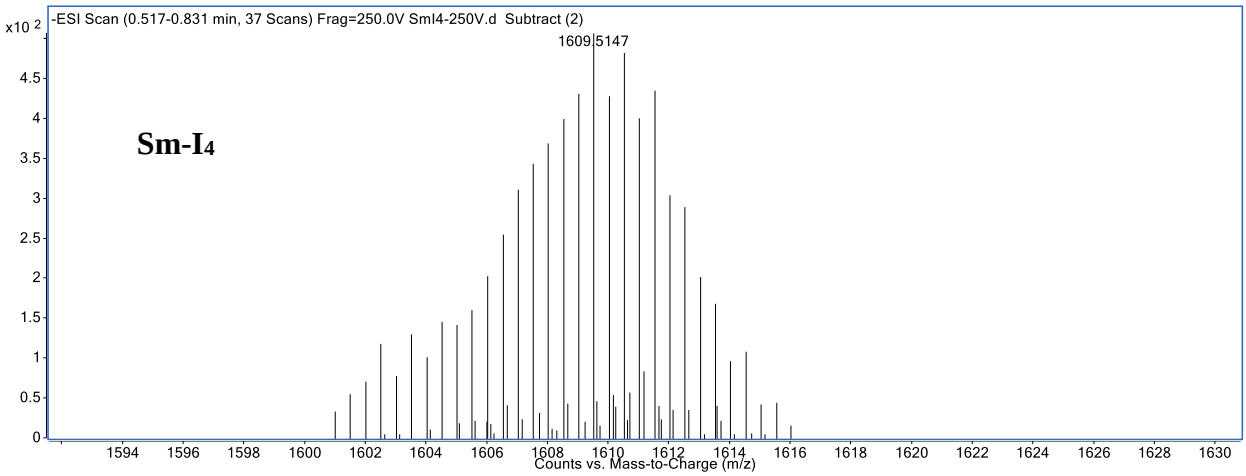

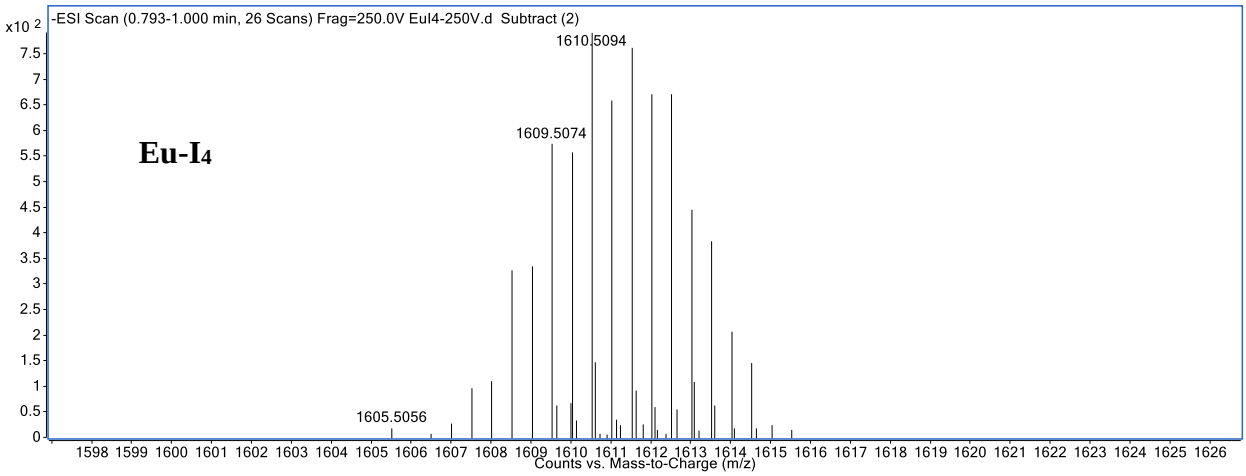
-ESI Scan (0.793-1.000 min, 26 Scans) Frag=250.0V EuI4-250V.d Subtract (2)
x10 2
Eu-I4
1610.5094
1609.5074
1605.5056
Counts vs. Mass-to-Charge (m/z)

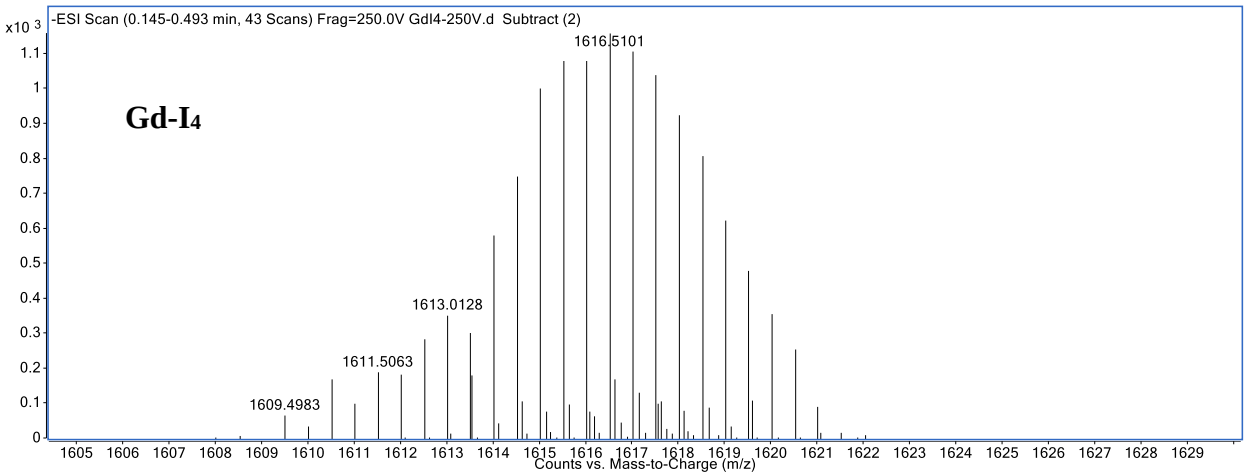
-ESI Scan (0.145-0.493 min, 43 Scans) Frag=250.0V GdI4-250V.d Subtract (2)
x10 3
Gd-I4
1616.5101
1613.0128
1611.5063
1609.4983
Counts vs. Mass-to-Charge (m/z)

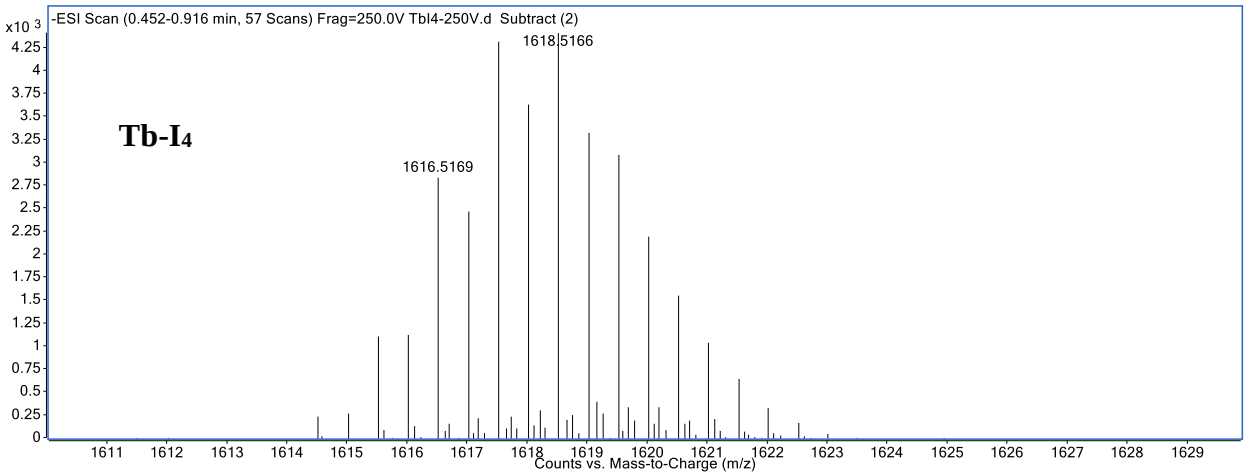
-ESI Scan (0.452-0.916 min, 57 Scans) Frag=250.0V TbI4-250V.d Subtract (2)
x10 3
Tb-I4
1618.5166
1616.5169
Counts vs. Mass-to-Charge (m/z)

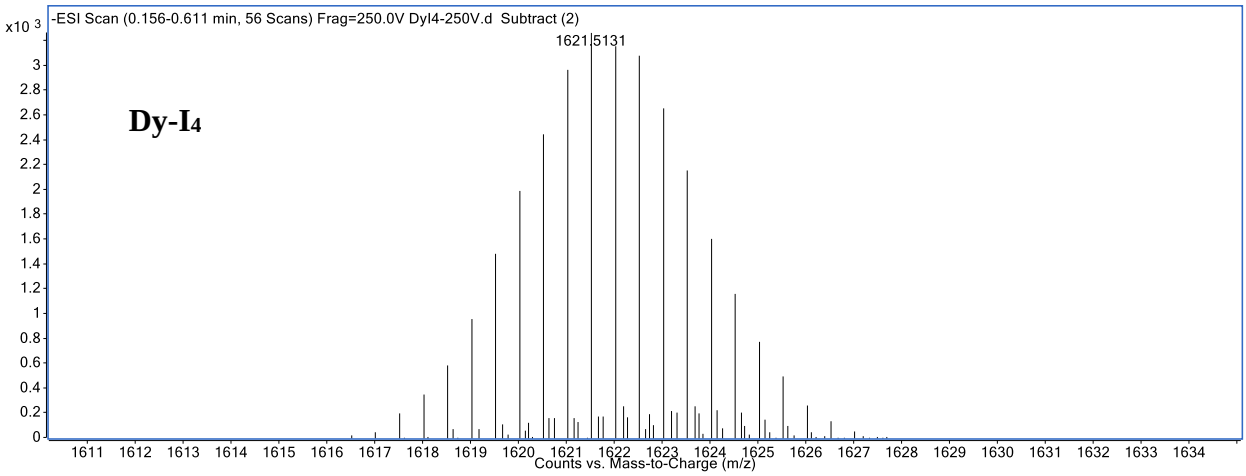
-ESI Scan (0.156-0.611 min, 56 Scans) Frag=250.0V DyI4-250V.d Subtract (2)
x10 3
1621.5131
Dy-I4
Counts vs. Mass-to-Charge (m/z)

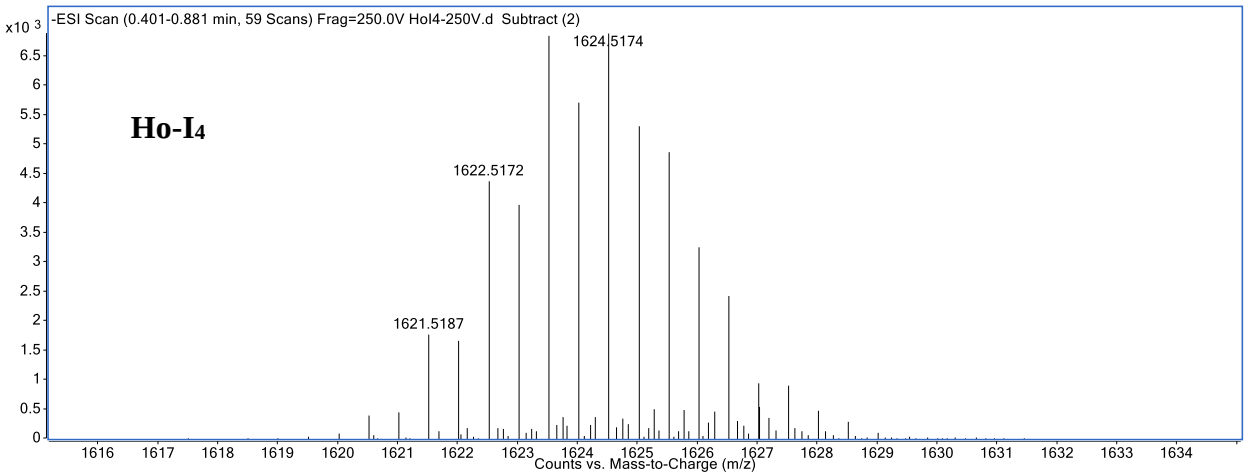
-ESI Scan (0.401-0.881 min, 59 Scans) Frag=250.0V HoI4-250V.d Subtract (2)
x10 3
1624.5174
Ho-I4
1622.5172
1621.5187
Counts vs. Mass-to-Charge (m/z)

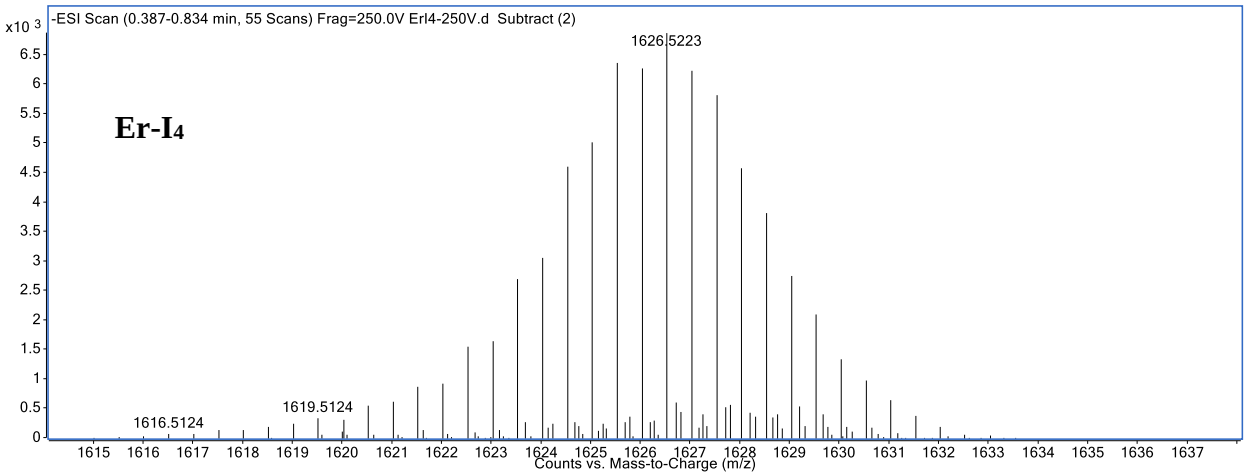
-ESI Scan (0.387-0.834 min, 55 Scans) Frag=250.0V ErI4-250V.d Subtract (2)
x10 3
1626.5223
Er-I4
1619.5124
1616.5124
Counts vs. Mass-to-Charge (m/z)

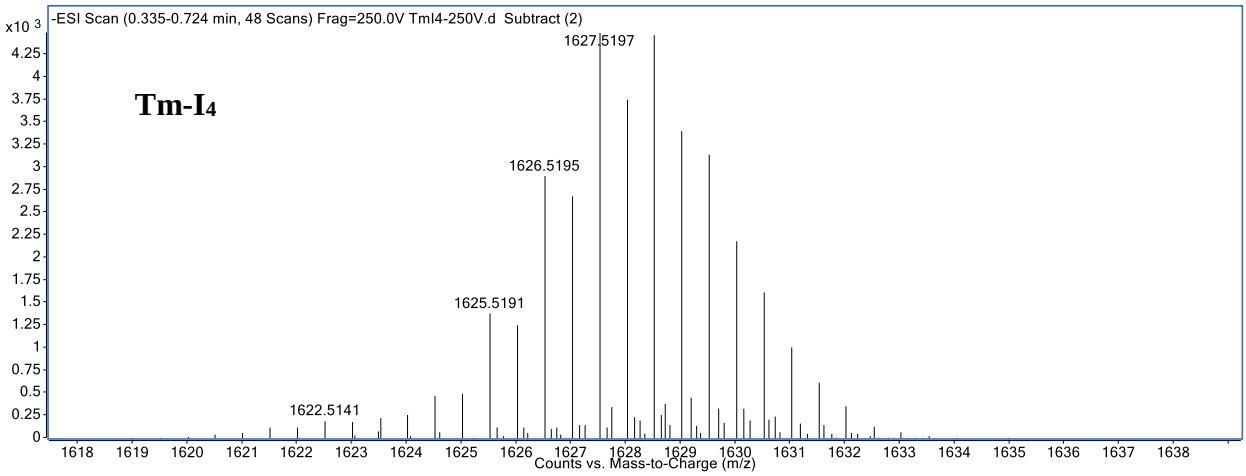
-ESI Scan (0.335-0.724 min, 48 Scans) Frag=250.0V TmI4-250V.d Subtract (2)
x10 3
Tm-I4
1627.5197
1626.5195
1625.5191
1622.5141
Counts vs. Mass-to-Charge (m/z)

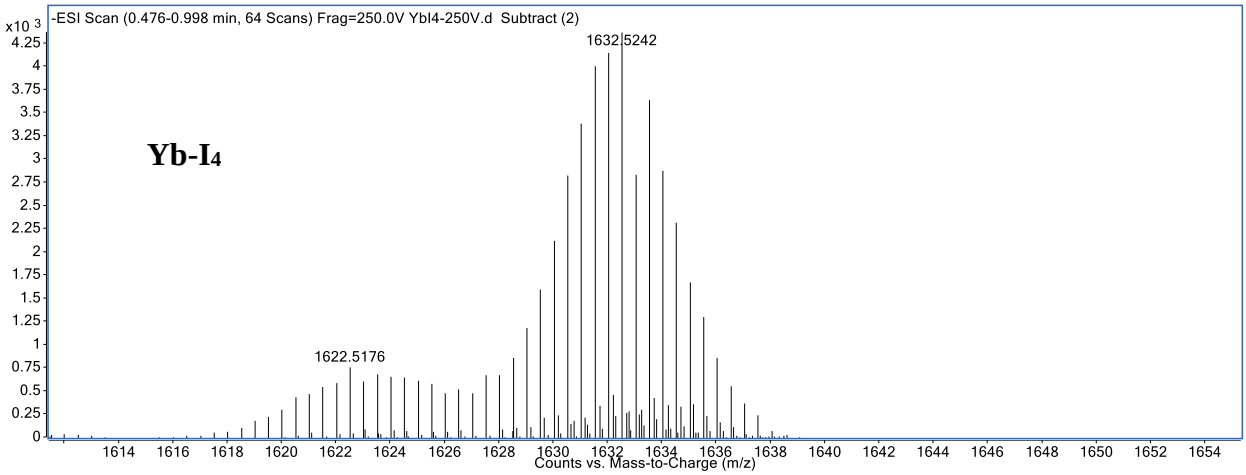
-ESI Scan (0.476-0.998 min, 64 Scans) Frag=250.0V YbI4-250V.d Subtract (2)
x10 3
Yb-I4
1632.5242
1622.5176
Counts vs. Mass-to-Charge (m/z)

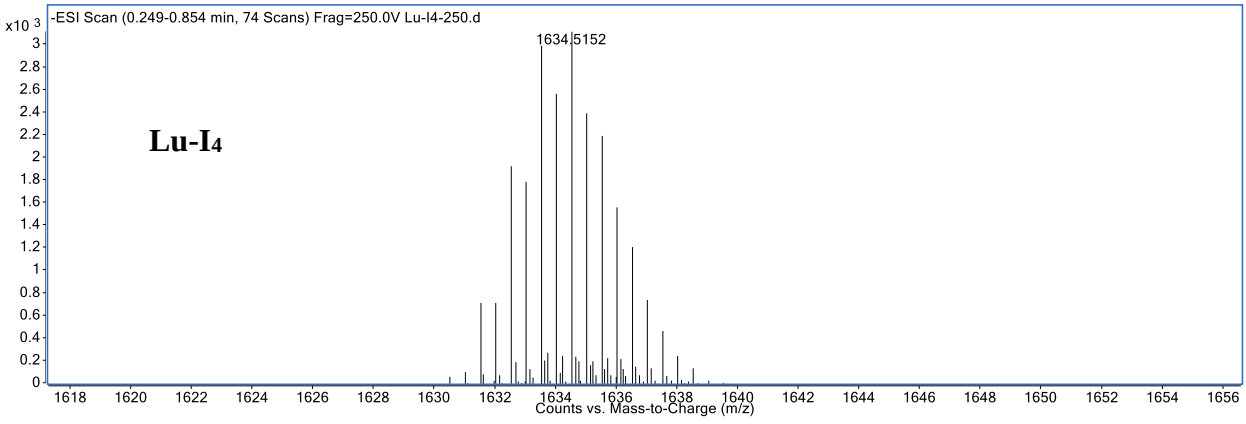
-ESI Scan (0.249-0.854 min, 74 Scans) Frag=250.0V Lu-I4-250.d
x10 3
Lu-I4
1634.5152
Counts vs. Mass-to-Charge (m/z)

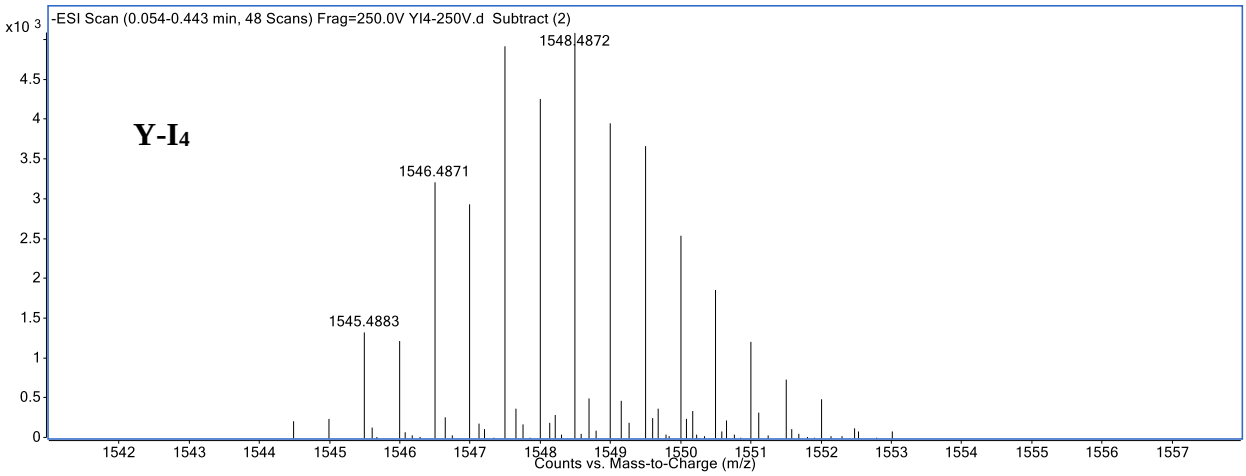

Figure B1. ESI-MS of **Ln-I4** complexes. Spectra were collected in negative ion mode with a fragmentation voltage of 250V in methanol. Background spectra were subtracted twice.

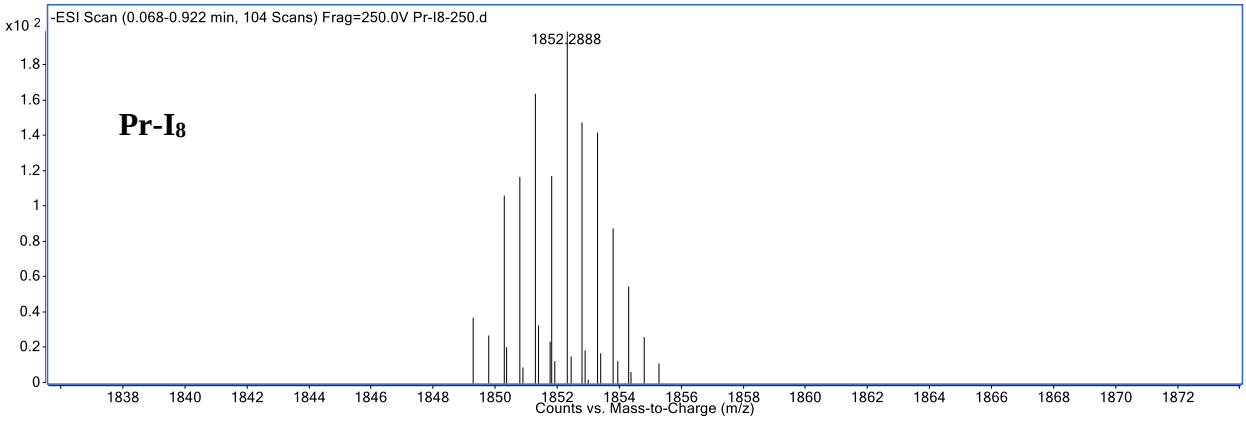

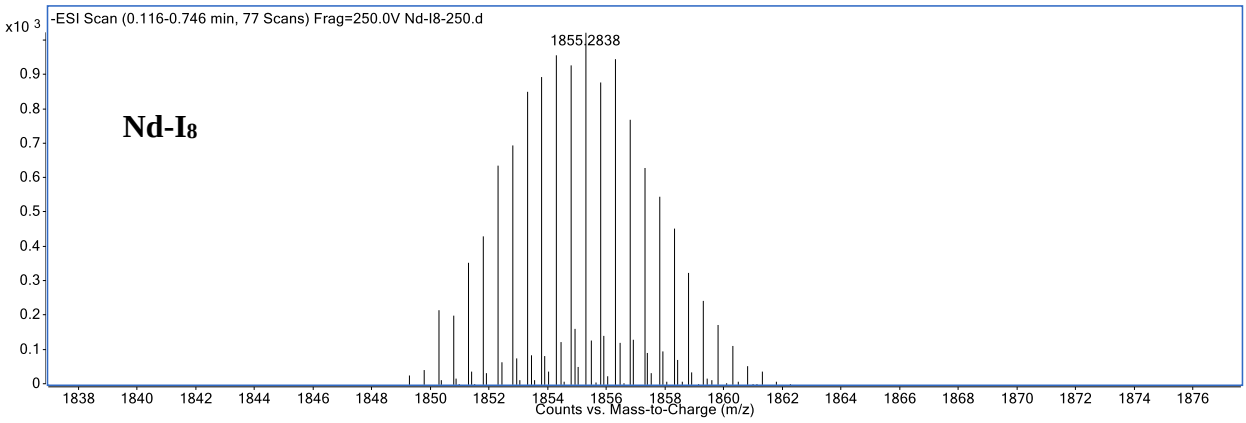

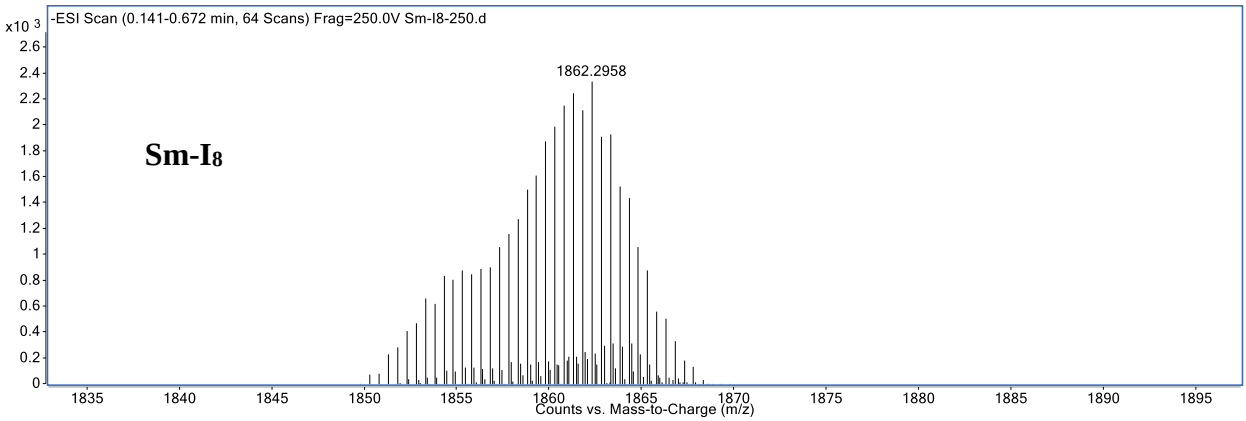
-ESI Scan (0.141-0.672 min, 64 Scans) Frag=250.0V Sm-I8-250.d
x10 3
1862.2958
Sm-I8
Counts vs. Mass-to-Charge (m/z)

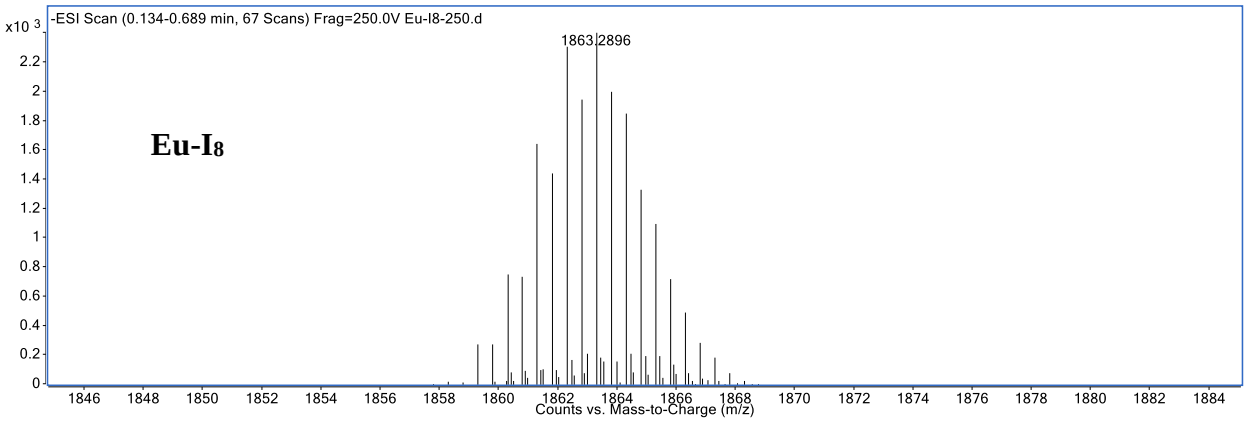
-ESI Scan (0.134-0.689 min, 67 Scans) Frag=250.0V Eu-I8-250.d
x10 3
1863.2896
Eu-I8
Counts vs. Mass-to-Charge (m/z)

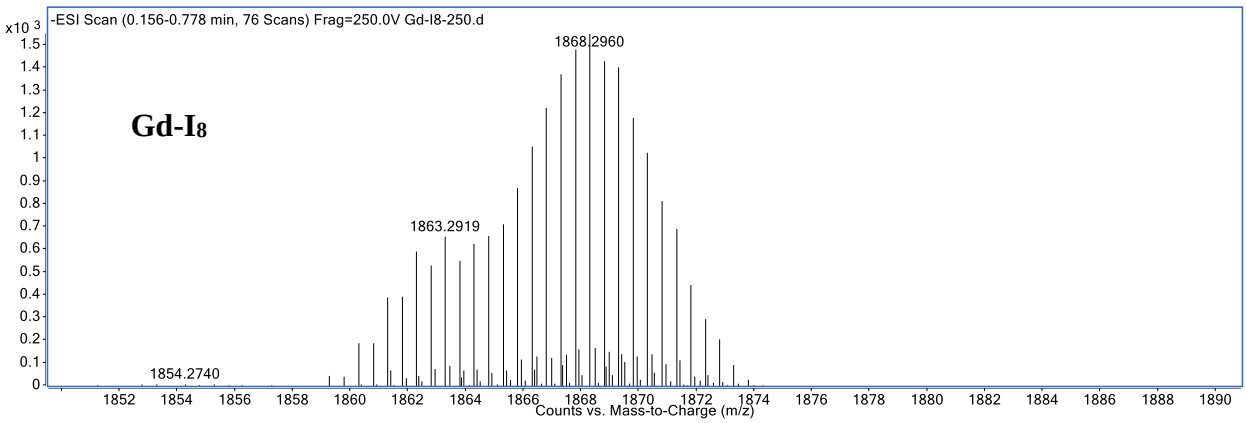
-ESI Scan (0.156-0.778 min, 76 Scans) Frag=250.0V Gd-I8-250.d
x10 3
1868.2960
Gd-I8
1863.2919
1854.2740
Counts vs. Mass-to-Charge (m/z)

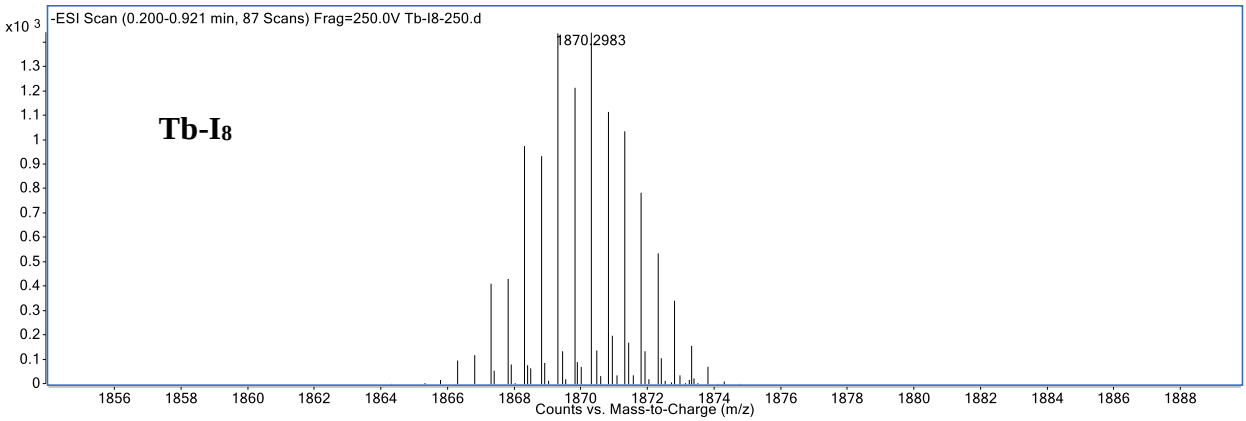
-ESI Scan (0.200-0.921 min, 87 Scans) Frag=250.0V Tb-I8-250.d
x10 3
1870.2983
Tb-I8
Counts vs. Mass-to-Charge (m/z)

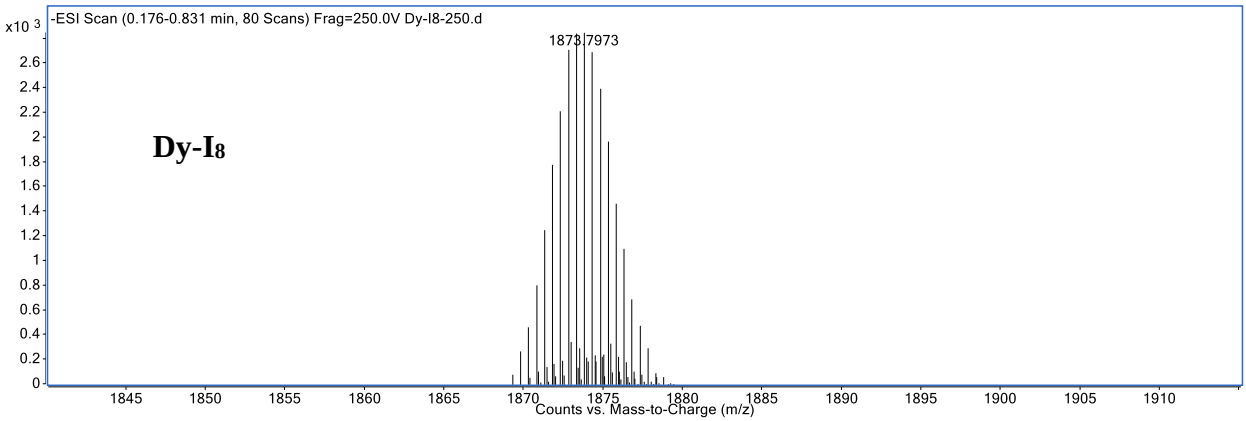
-ESI Scan (0.176-0.831 min, 80 Scans) Frag=250.0V Dy-I8-250.d
x10 3
1873.7973
Dy-I8
Counts vs. Mass-to-Charge (m/z)

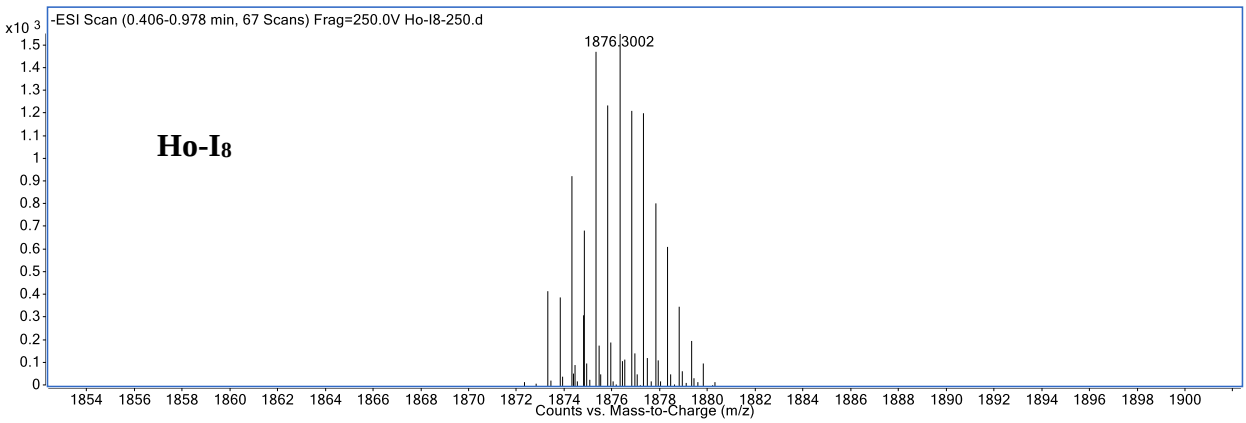
-ESI Scan (0.406-0.978 min, 67 Scans) Frag=250.0V Ho-I8-250.d
x10 3
1876.3002
Ho-I8
Counts vs. Mass-to-Charge (m/z)

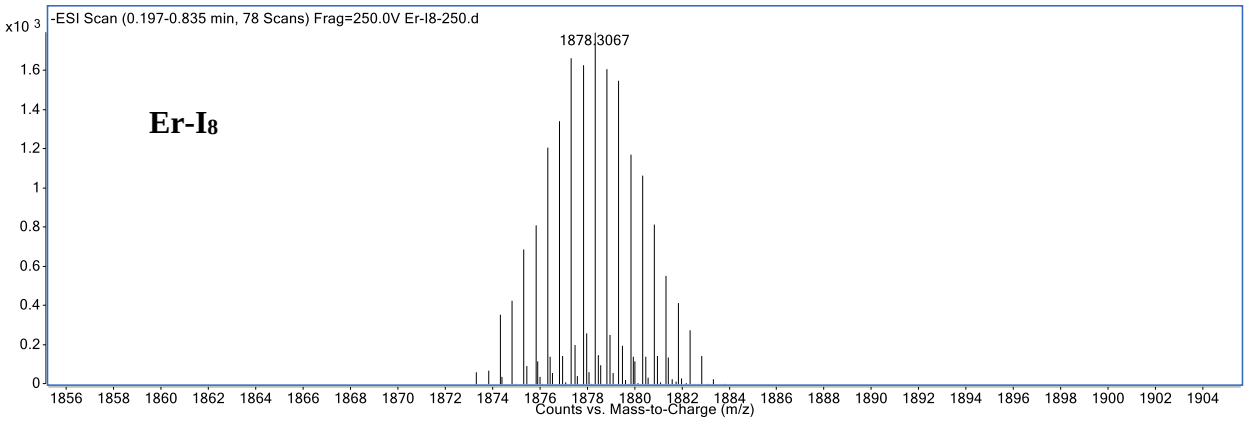
-ESI Scan (0.197-0.835 min, 78 Scans) Frag=250.0V Er-I8-250.d
x10 3
1878.3067
Er-I8
Counts vs. Mass-to-Charge (m/z)

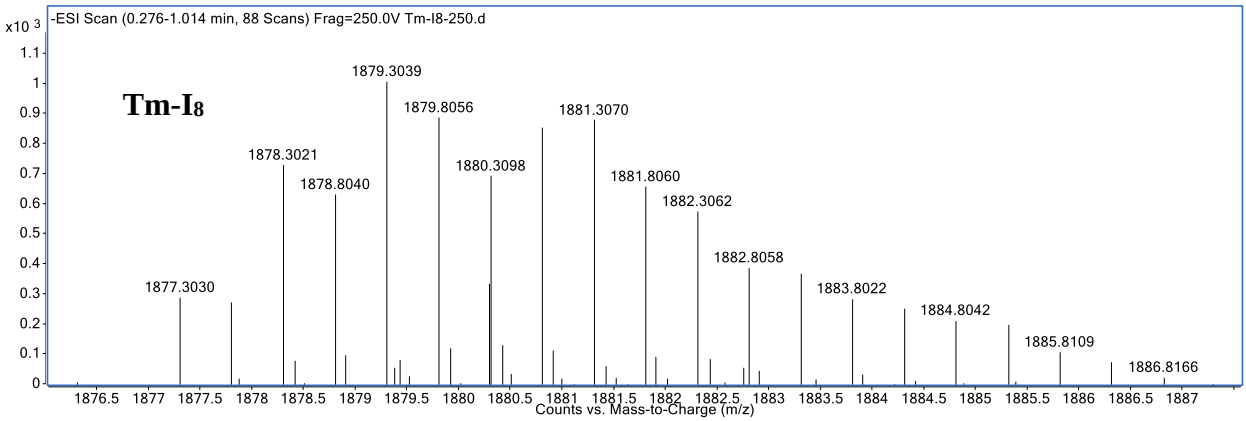
-ESI Scan (0.276-1.014 min, 88 Scans) Frag=250.0V Tm-I8-250.d
x10 3
Tm-I8
1879.3039
1879.8056
1881.3070
1878.3021
1880.3098
1878.8040
1881.8060
1882.3062
1882.8058
1877.3030
1883.8022
1884.8042
1885.8109
1886.8166
Counts vs. Mass-to-Charge (m/z)

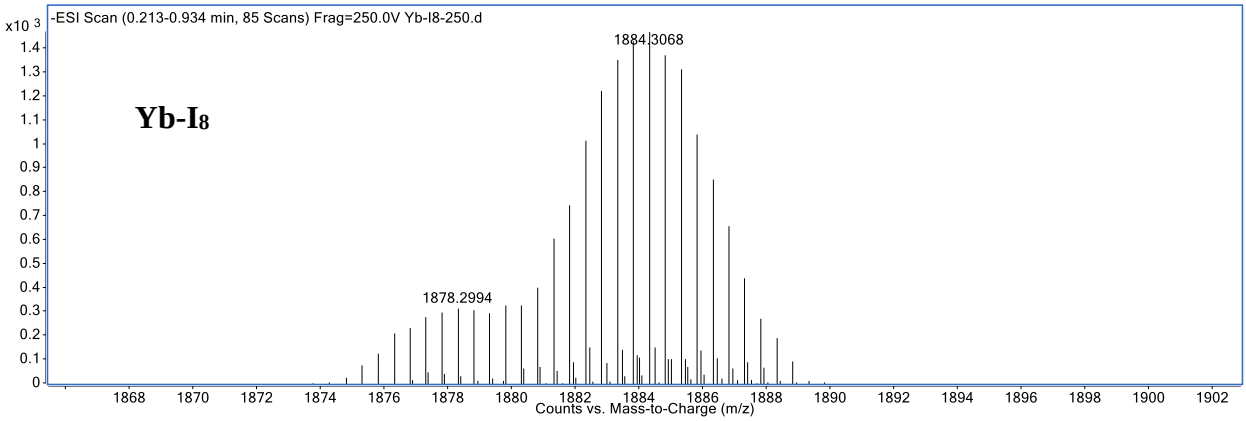
-ESI Scan (0.213-0.934 min, 85 Scans) Frag=250.0V Yb-I8-250.d
x10 3
1884.3068
Yb-I8
1878.2994
Counts vs. Mass-to-Charge (m/z)

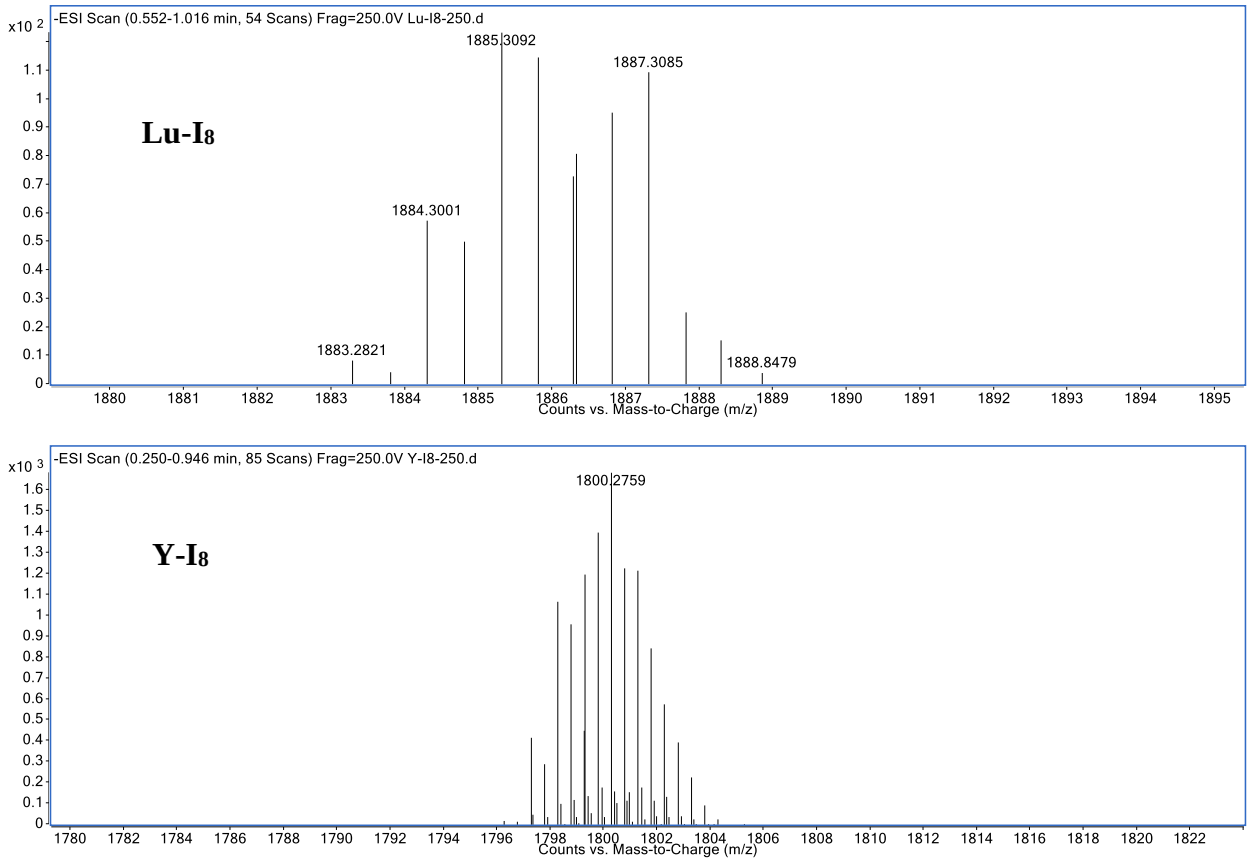

Figure B2. ESI-MS of **Ln-I$_8$** complexes. Spectra were collected in negative ion mode with a fragmentation voltage of 250V in methanol. Background spectra were subtracted twice.

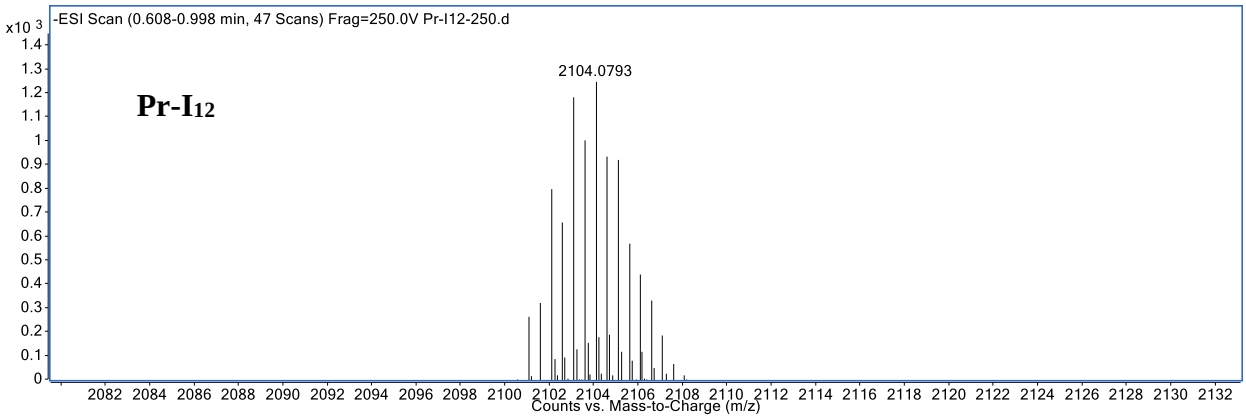
-ESI Scan (0.608-0.998 min, 47 Scans) Frag=250.0V Pr-I12-250.d
x10 3
Pr-I12
2104.0793
Counts vs. Mass-to-Charge (m/z)

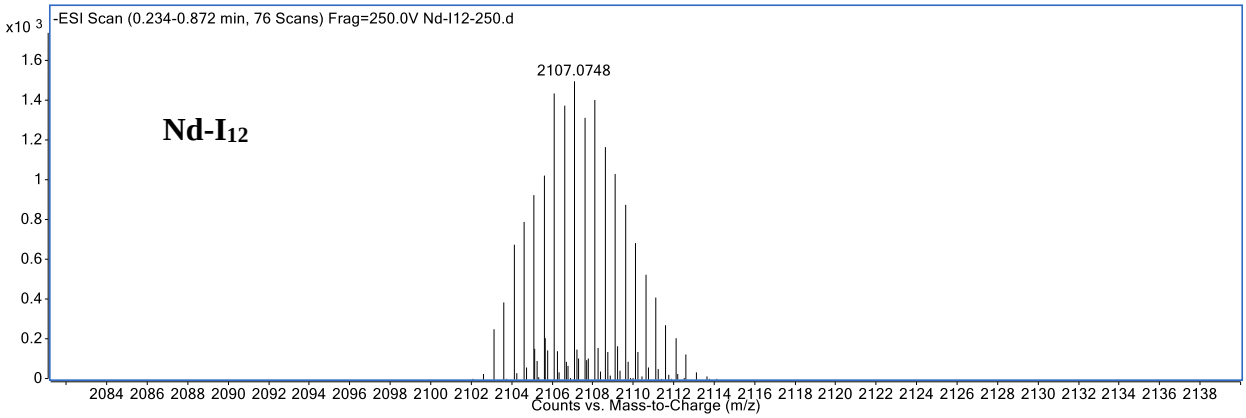
-ESI Scan (0.234-0.872 min, 76 Scans) Frag=250.0V Nd-I12-250.d
x10 3
Nd-I12
2107.0748
Counts vs. Mass-to-Charge (m/z)

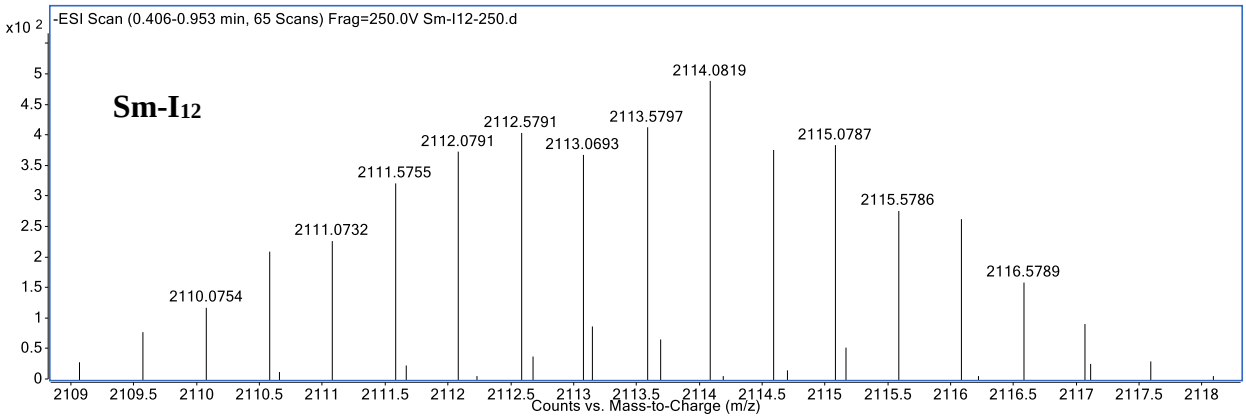
-ESI Scan (0.406-0.953 min, 65 Scans) Frag=250.0V Sm-I12-250.d
x10 2
Sm-I12
2114.0819
2112.5791
2113.5797
2112.0791
2113.0693
2115.0787
2111.5755
2115.5786
2111.0732
2116.5789
2110.0754
Counts vs. Mass-to-Charge (m/z)

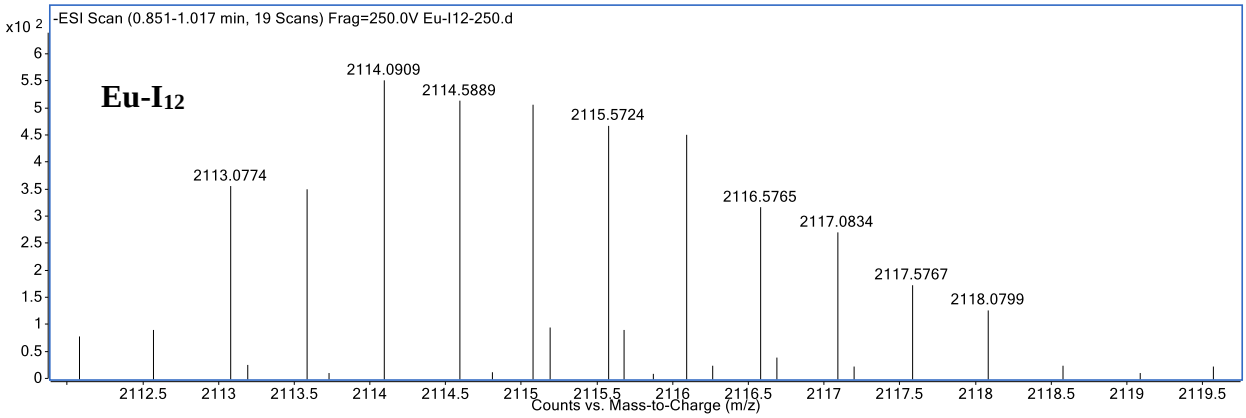
-ESI Scan (0.851-1.017 min, 19 Scans) Frag=250.0V Eu-I12-250.d
x10 2
Eu-I12
2114.0909
2114.5889
2115.5724
2113.0774
2116.5765
2117.0834
2117.5767
2118.0799
Counts vs. Mass-to-Charge (m/z)

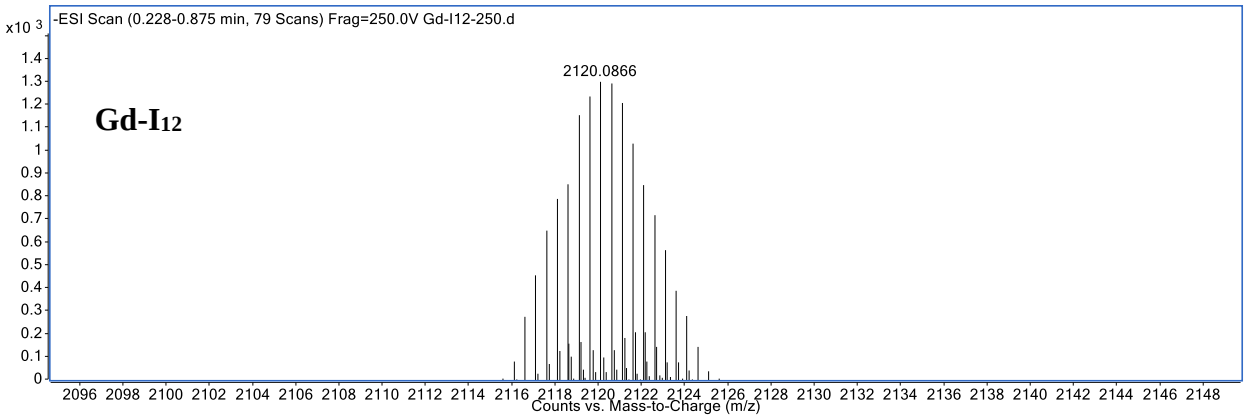
-ESI Scan (0.228-0.875 min, 79 Scans) Frag=250.0V Gd-I12-250.d
x10 3
2120.0866
Gd-I12
Counts vs. Mass-to-Charge (m/z)

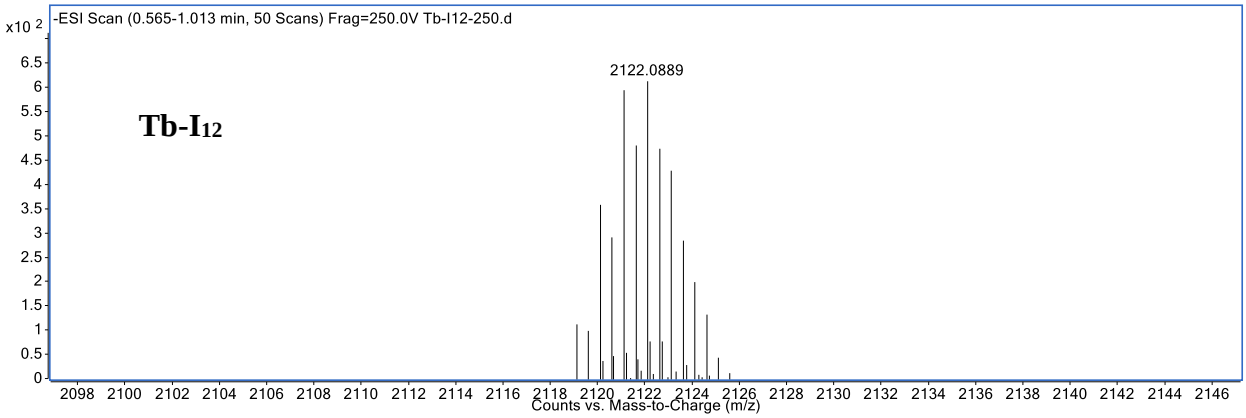
-ESI Scan (0.565-1.013 min, 50 Scans) Frag=250.0V Tb-I12-250.d
x10 2
2122.0889
Tb-I12
Counts vs. Mass-to-Charge (m/z)

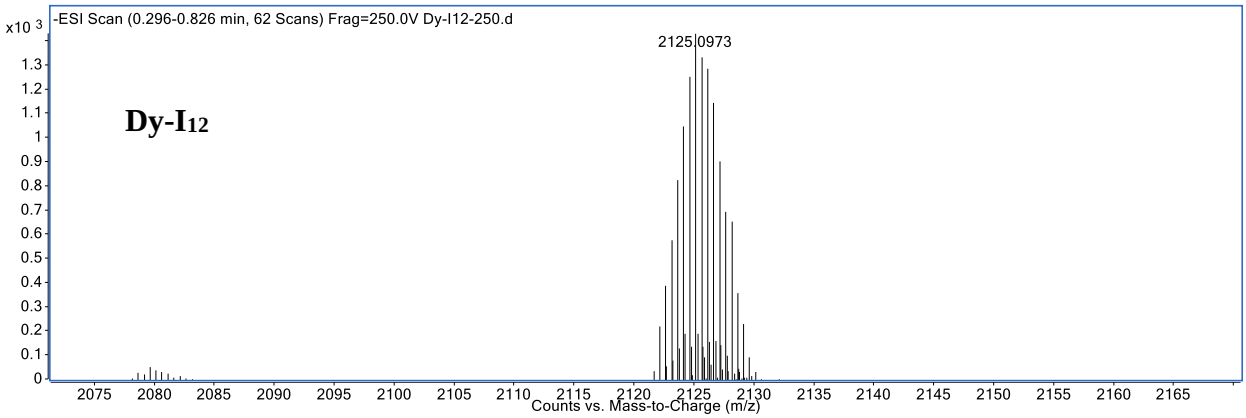
-ESI Scan (0.296-0.826 min, 62 Scans) Frag=250.0V Dy-I12-250.d
x10 3
2125.0973
Dy-I12
Counts vs. Mass-to-Charge (m/z)

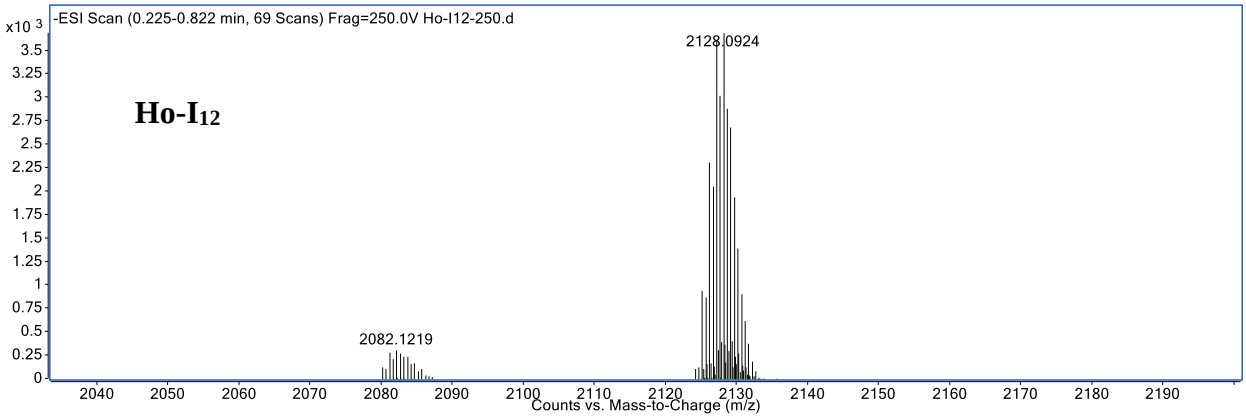
-ESI Scan (0.225-0.822 min, 69 Scans) Frag=250.0V Ho-I12-250.d
x10 3
2128.0924
2082.1219
Ho-I12
Counts vs. Mass-to-Charge (m/z)

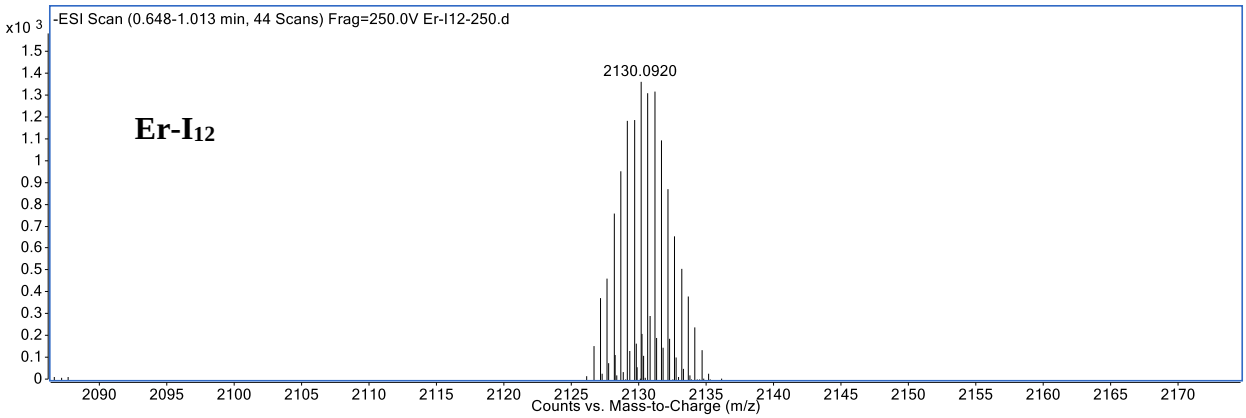
-ESI Scan (0.648-1.013 min, 44 Scans) Frag=250.0V Er-I12-250.d
x10 3
2130.0920
Er-I12
Counts vs. Mass-to-Charge (m/z)

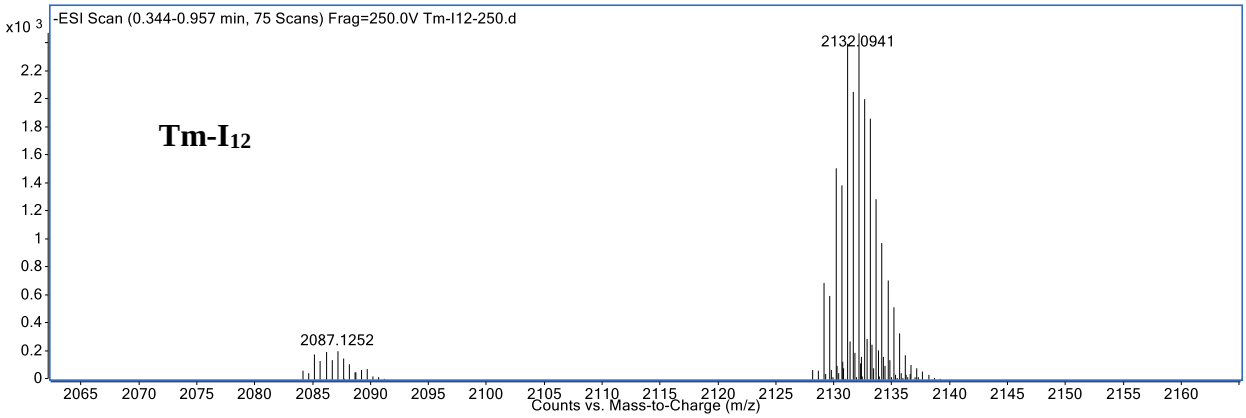
-ESI Scan (0.344-0.957 min, 75 Scans) Frag=250.0V Tm-I12-250.d
x10 3
2132.0941
Tm-I12
2087.1252
Counts vs. Mass-to-Charge (m/z)

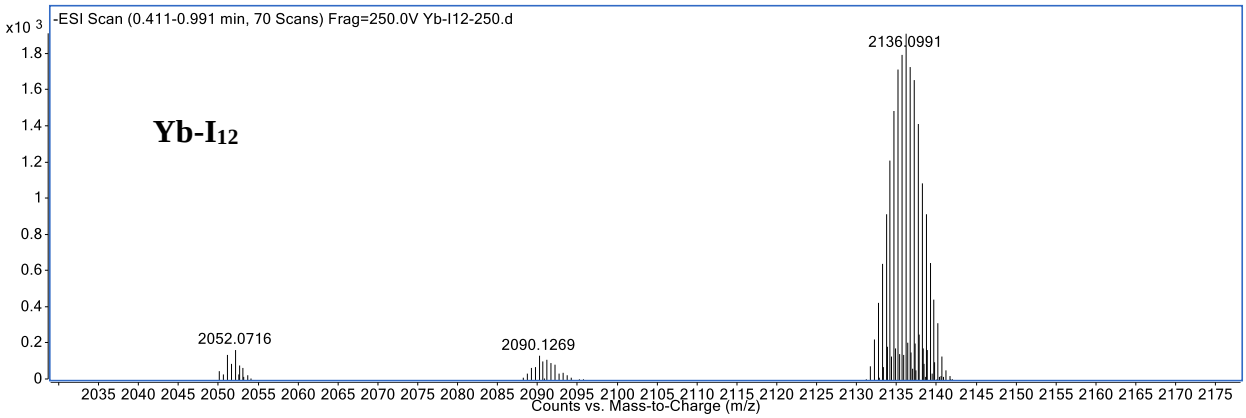
-ESI Scan (0.411-0.991 min, 70 Scans) Frag=250.0V Yb-I12-250.d
x10 3
2136.0991
Yb-I12
2052.0716
2090.1269
Counts vs. Mass-to-Charge (m/z)

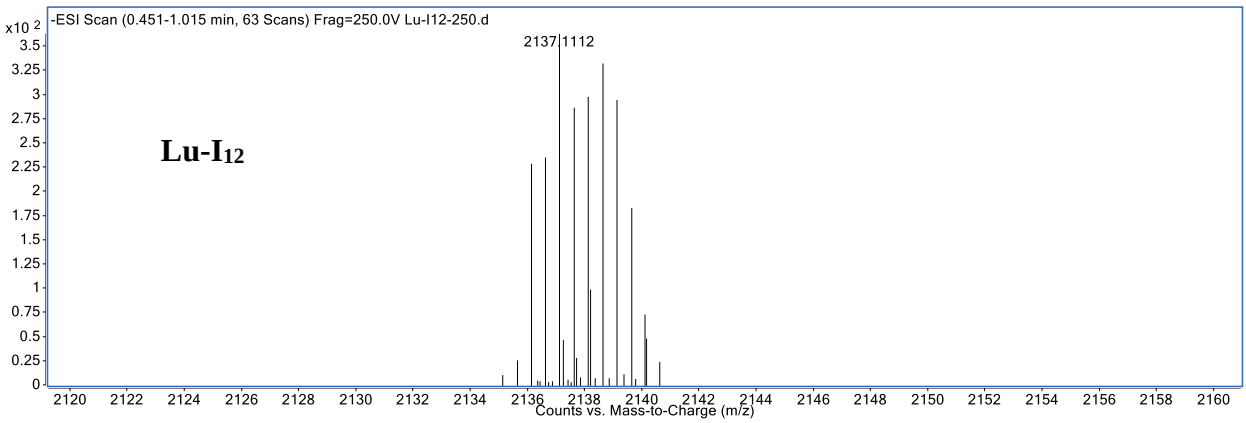
-ESI Scan (0.451-1.015 min, 63 Scans) Frag=250.0V Lu-I12-250.d
x10 2
2137.1112
Lu-I12
Counts vs. Mass-to-Charge (m/z)

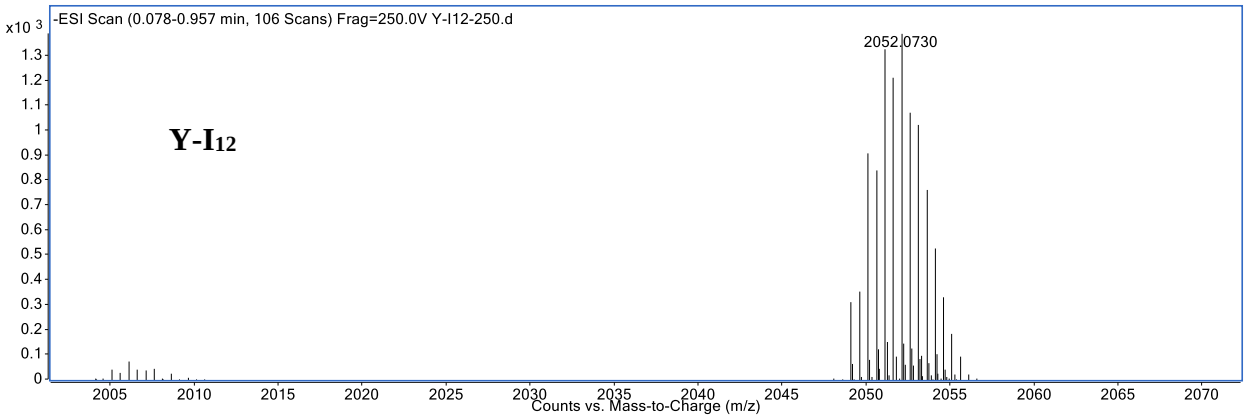

Figure B3. ESI-MS of **Ln-I$_{12}$** complexes. Spectra were collected in negative ion mode with a fragmentation voltage of 250V in methanol. Background spectra were subtracted twice.

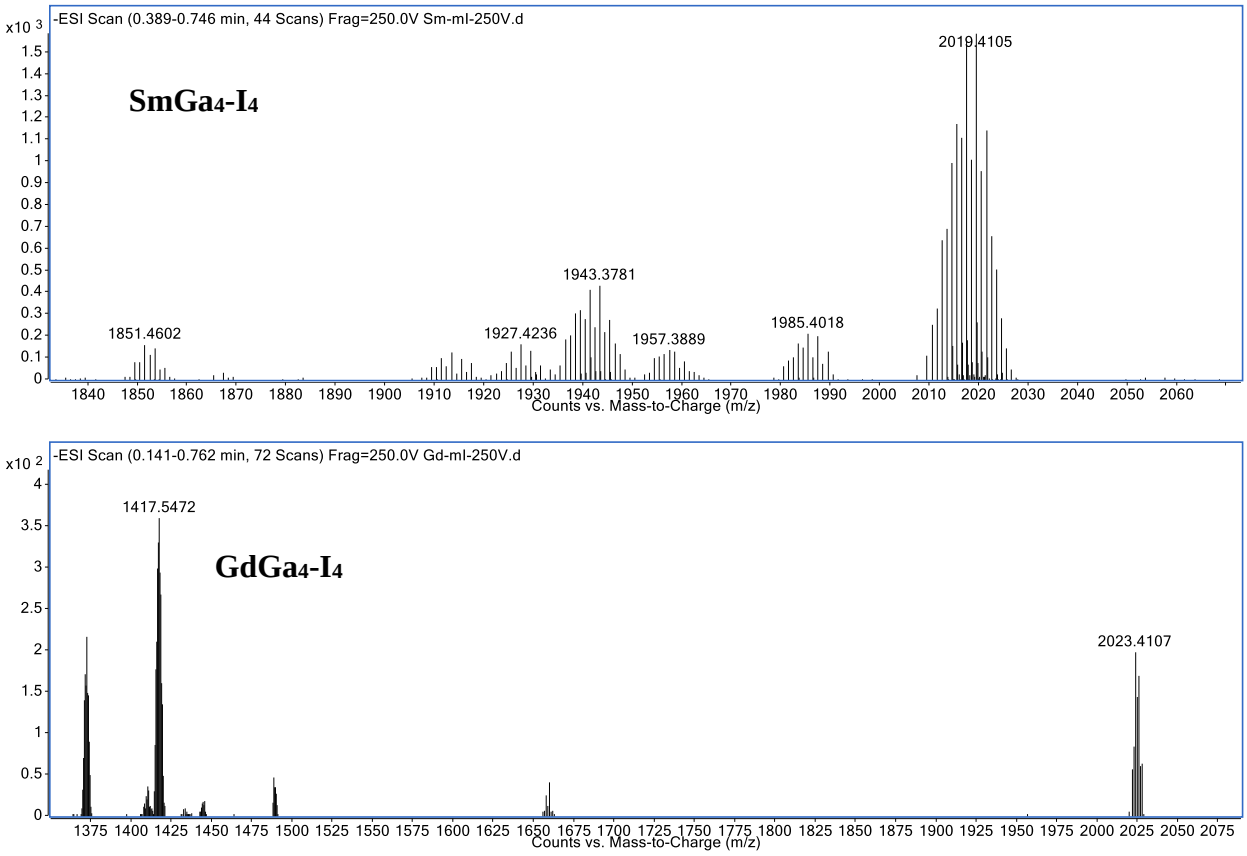

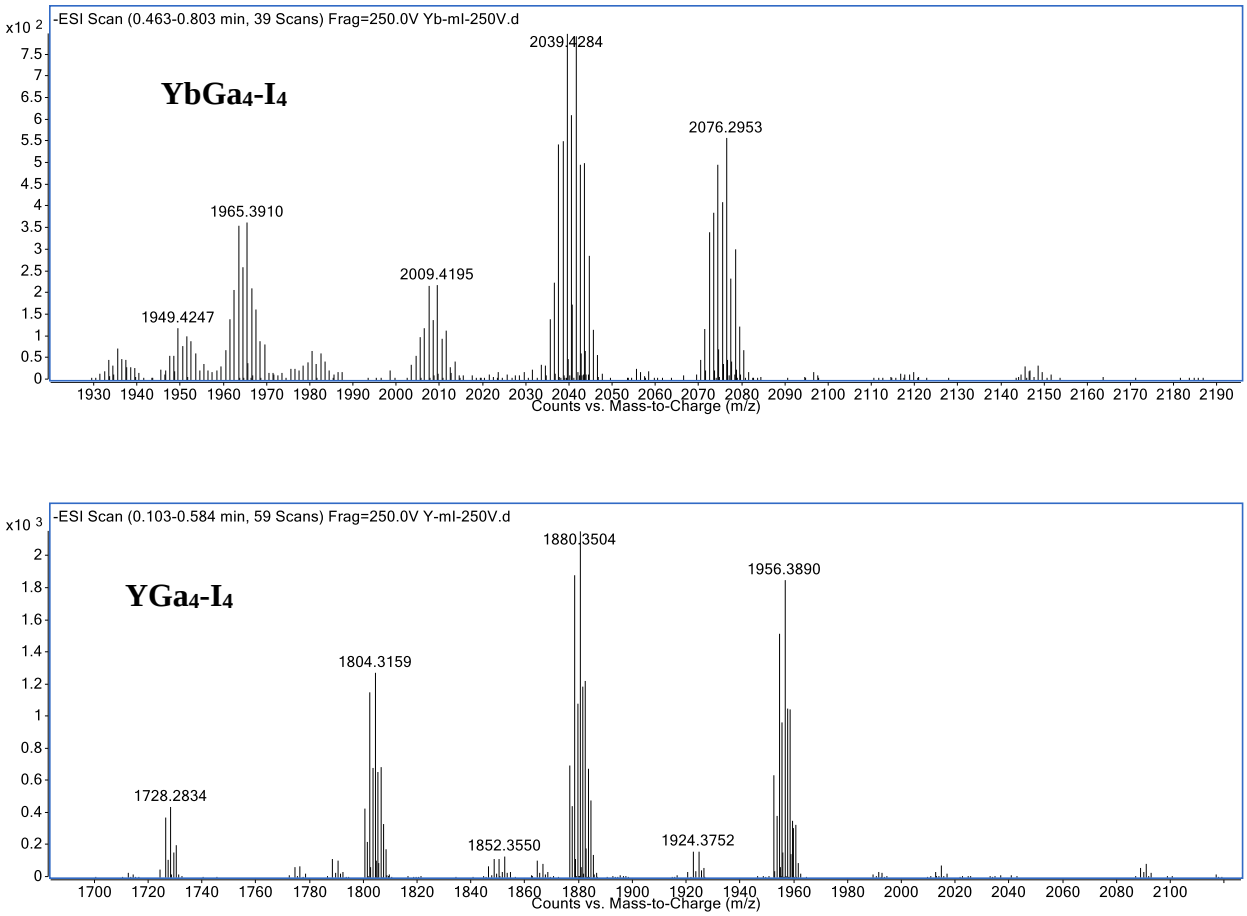

Figure B4. ESI-MS of **LnGa$_4$-I$_4$** complexes. Spectra were collected in negative ion mode with a fragmentation voltage of 250V in methanol. Background spectra were subtracted twice.

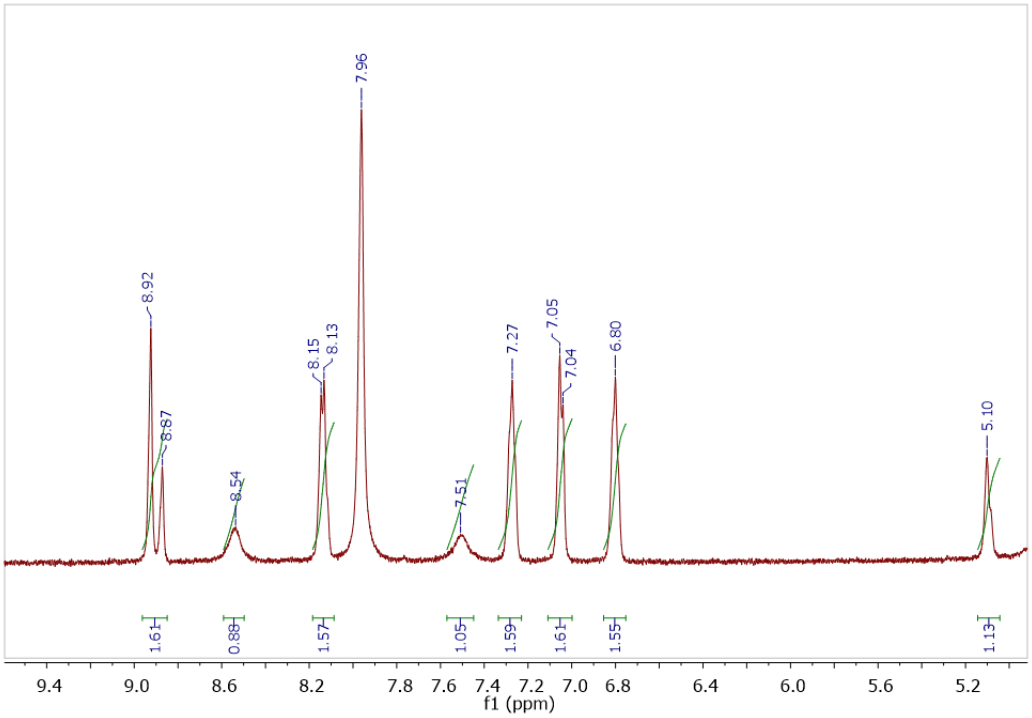

Figure B5. ^{1}H-NMR of **Sm-I$_4$** in *d$_4$*-MeOH at RT.

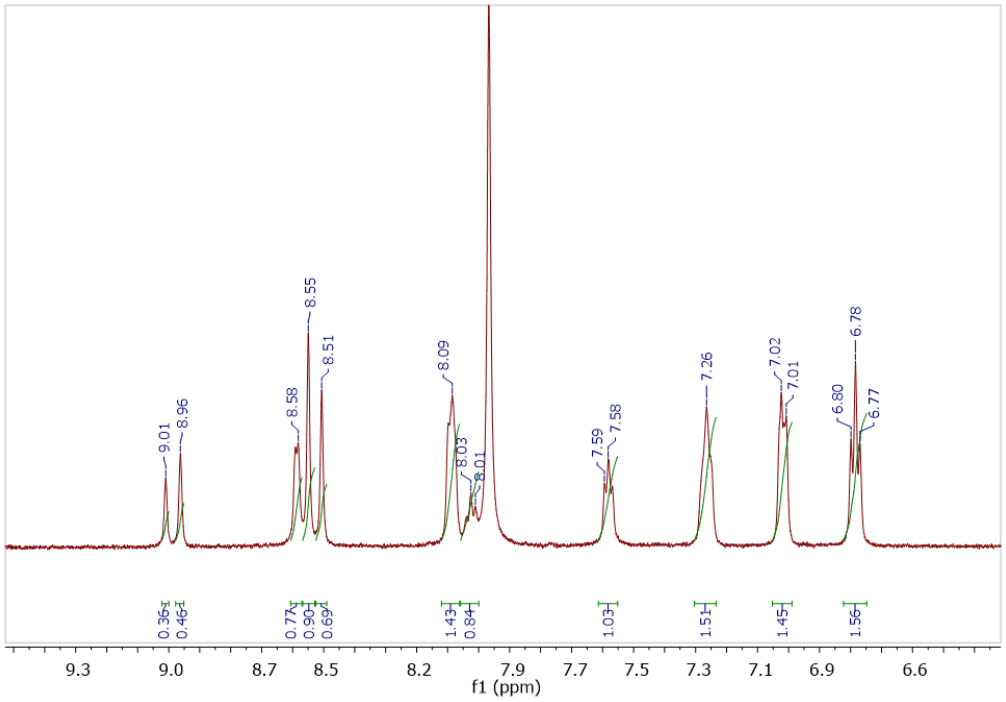

Figure B6. ^{1}H-NMR of **Y-I4** in *d$_4$*-MeOH at RT.

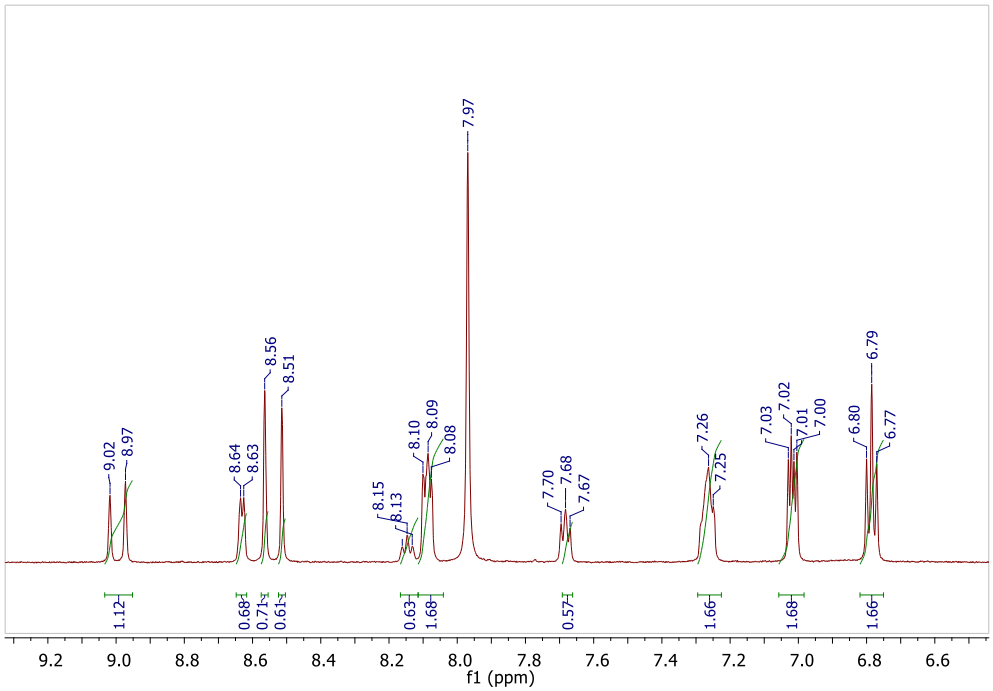

Figure B7. ^{1}H-NMR of **Lu-I$_4$** in *d*$_4$-MeOH at RT.

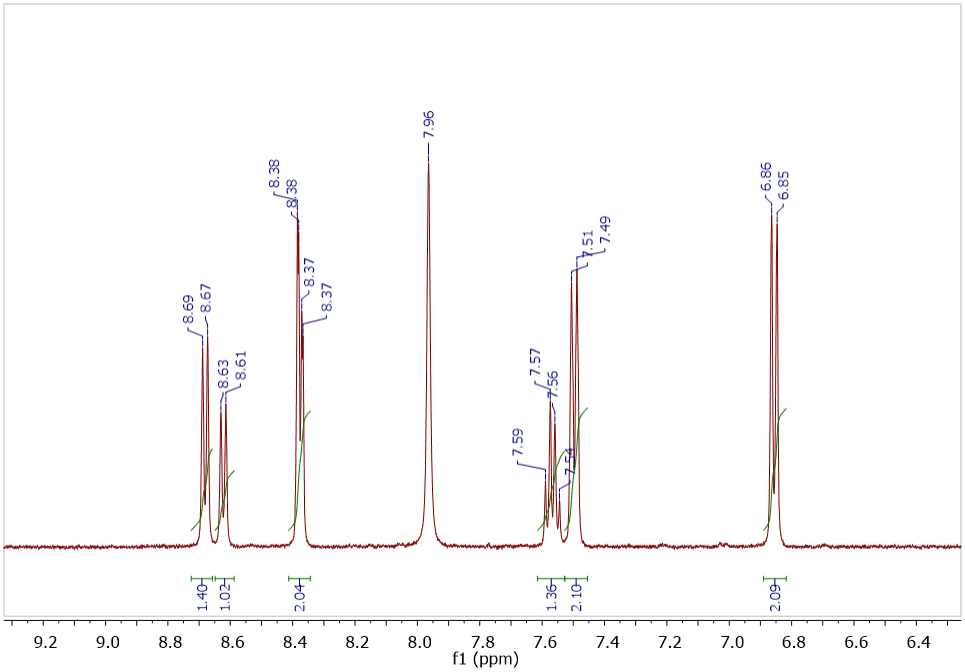

Figure B8. ^{1}H-NMR of **Sm-I$_8$** in *d*$_4$-MeOH at RT.

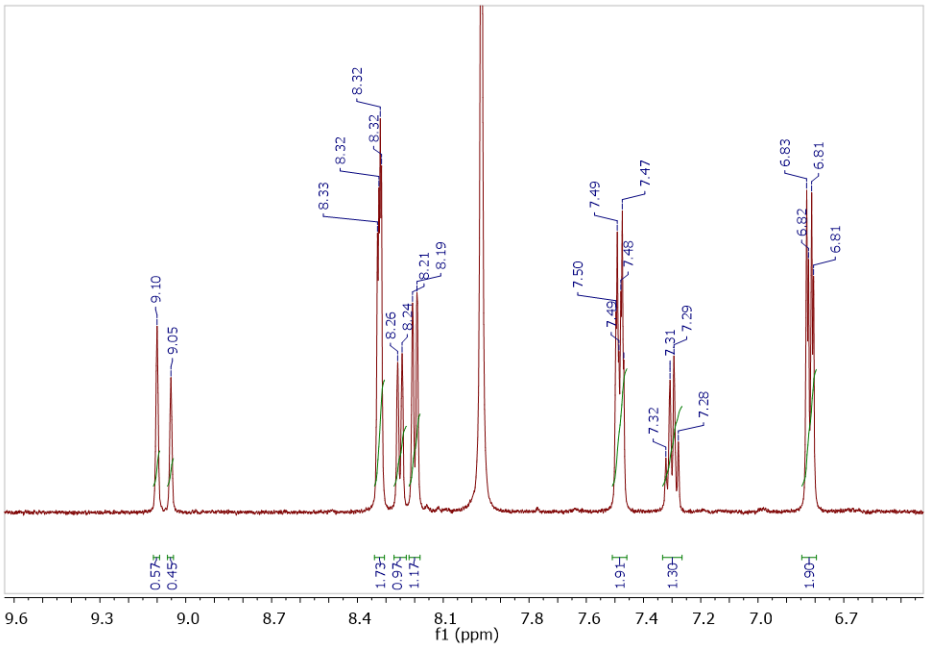

Figure B9. ^{1}H-NMR of **Y-I$_8$** in *d*$_4$-MeOH at RT.

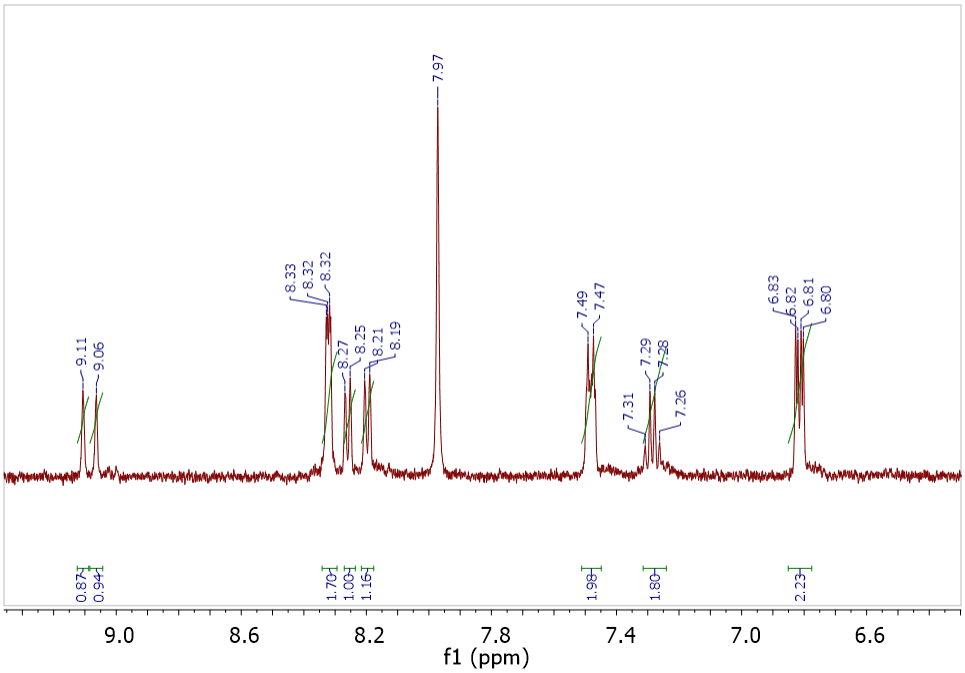

Figure B10. ^{1}H-NMR of **Lu-I$_8$** in *d*$_4$-MeOH at RT.

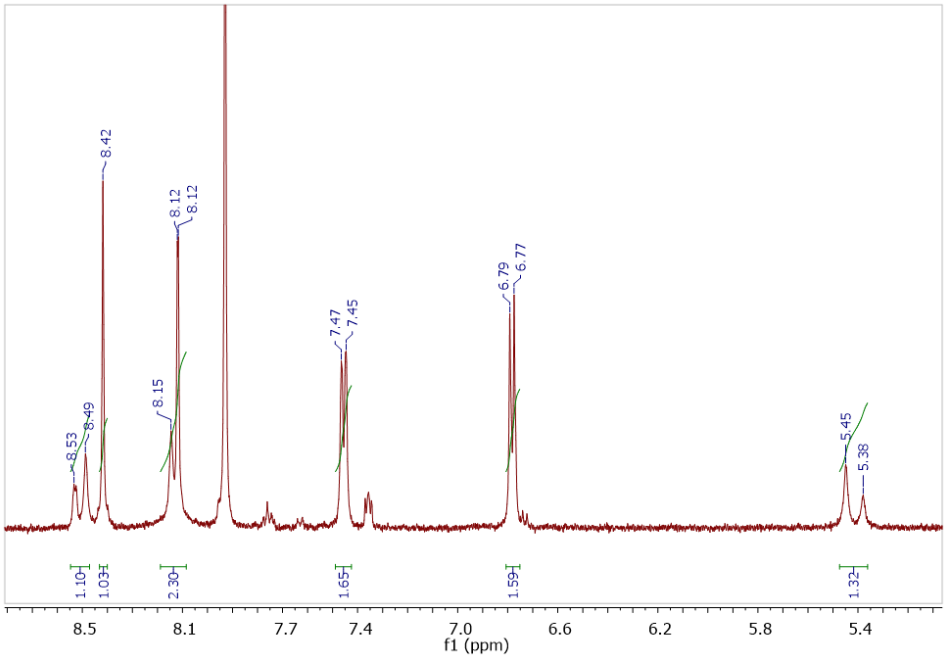

Figure B11. ^{1}H-NMR of **Sm-I$_{12}$** in d_6-DMSO at RT.

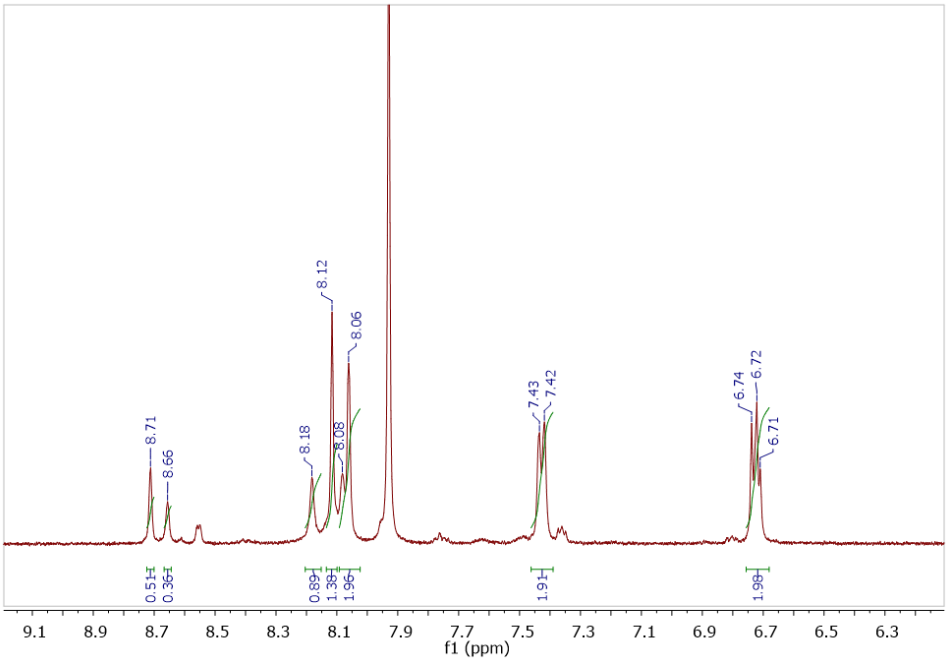

Figure B12. ^{1}H-NMR of **Y-I$_{12}$** in d_6-DMSO at RT.

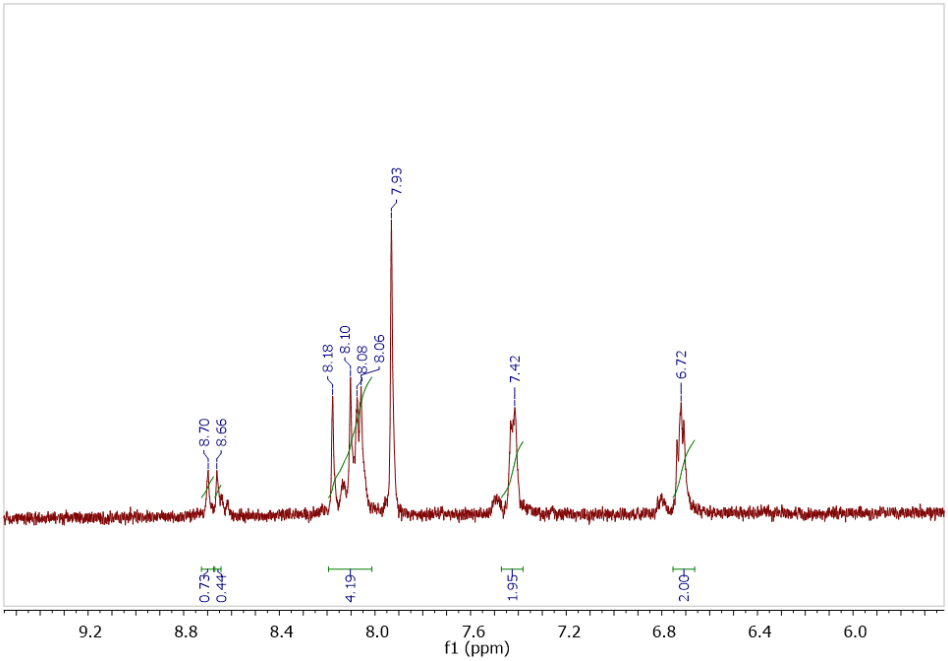

Figure B13. ^{1}H-NMR of **Lu-I$_{12}$** in *d*$_{6}$-DMSO at RT.

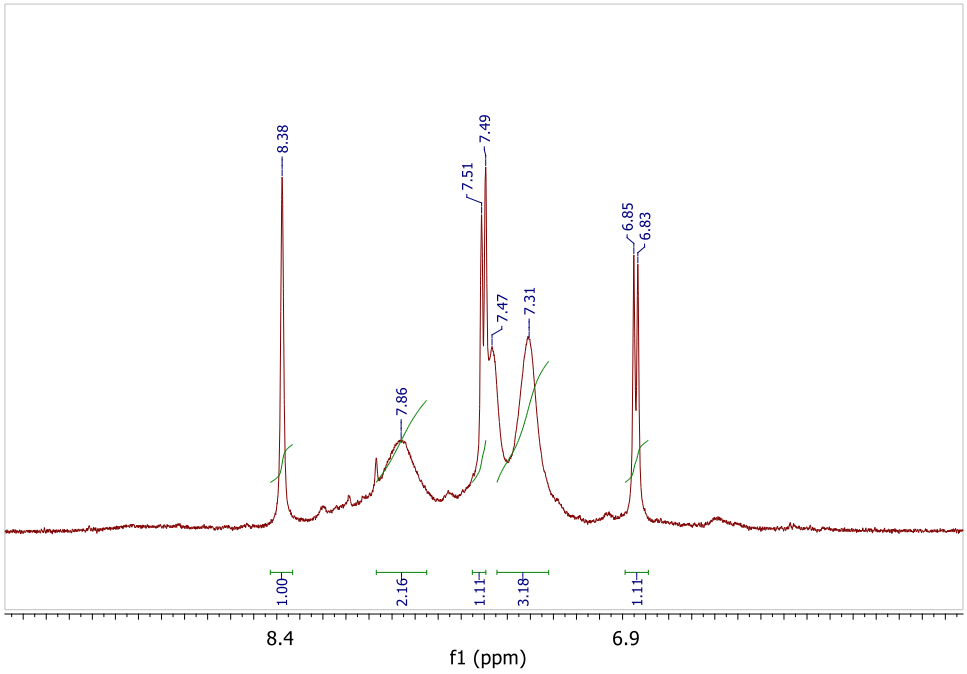

Figure B14. ^{1}H-NMR of **SmGa$_{4}$-I$_{4}$** in *d*$_{4}$-MeOH at RT.

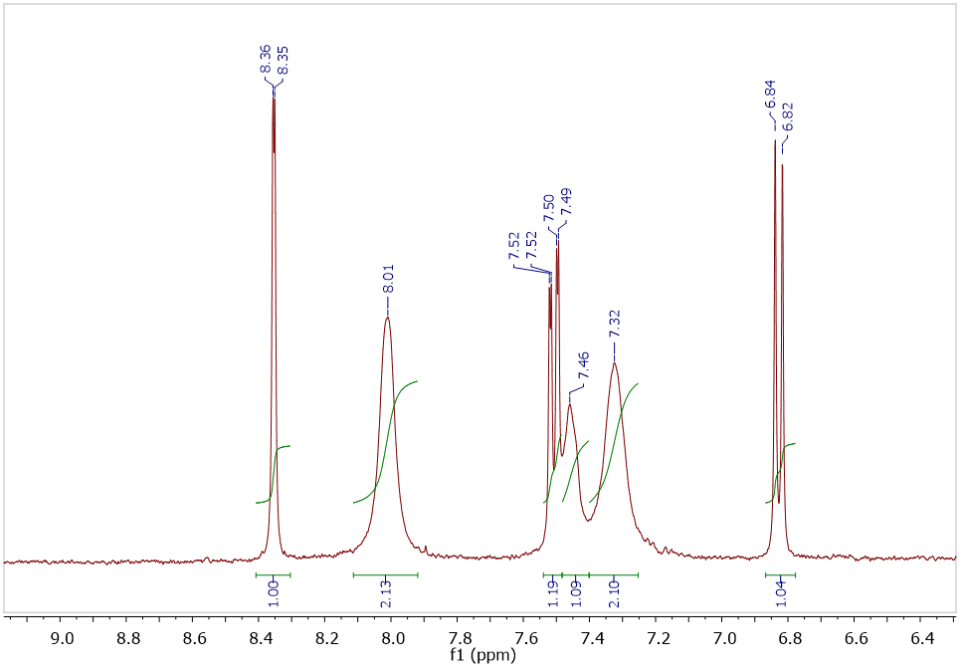

Figure B15. [1]H-NMR of **YGa$_4$-I$_4$** in *d$_4$*-MeOH at RT.

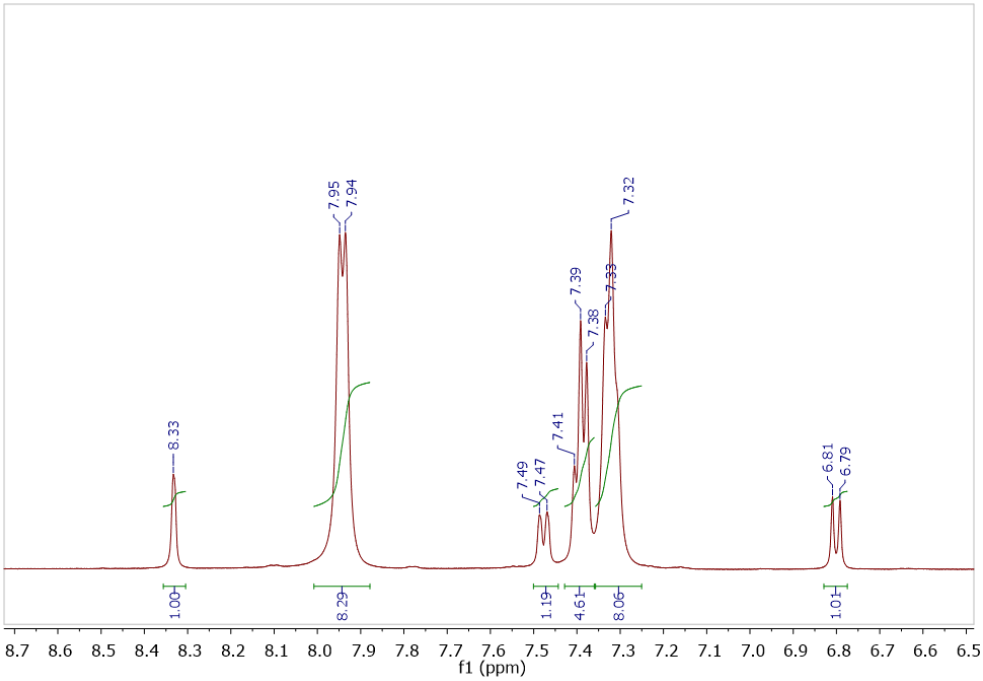

Figure B16. [1]H-NMR of **YGa$_4$-I$_4$** with excess NaOBz in *d$_4$*-MeOH at RT.

Appendix C. Supplemental Information for Chapter 4

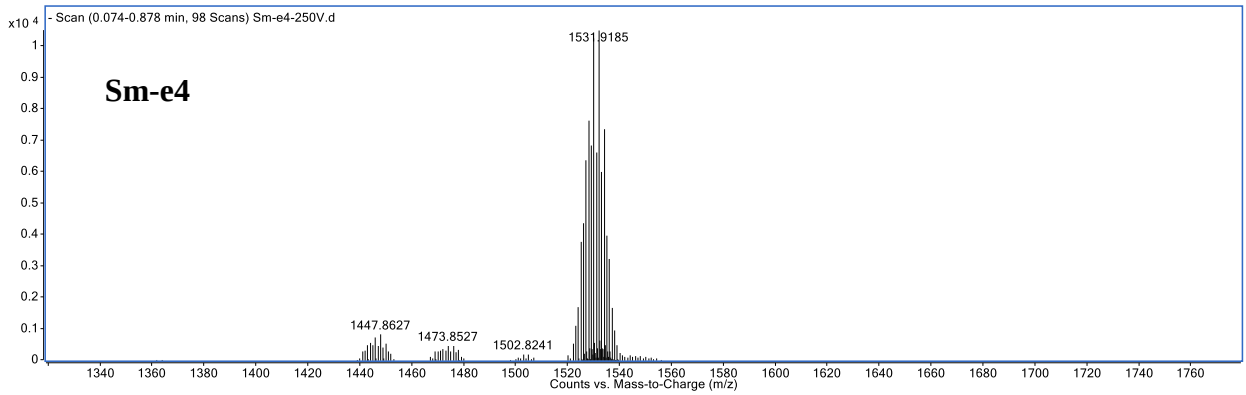

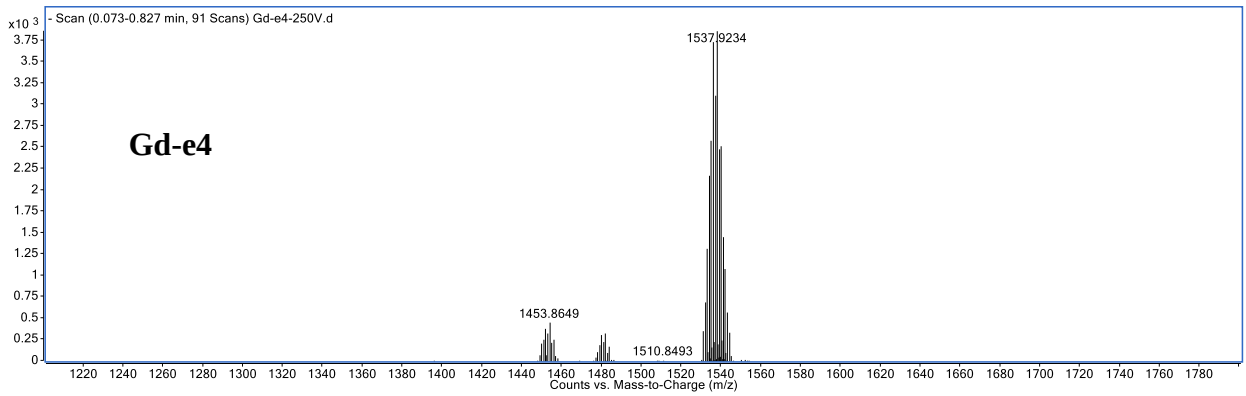

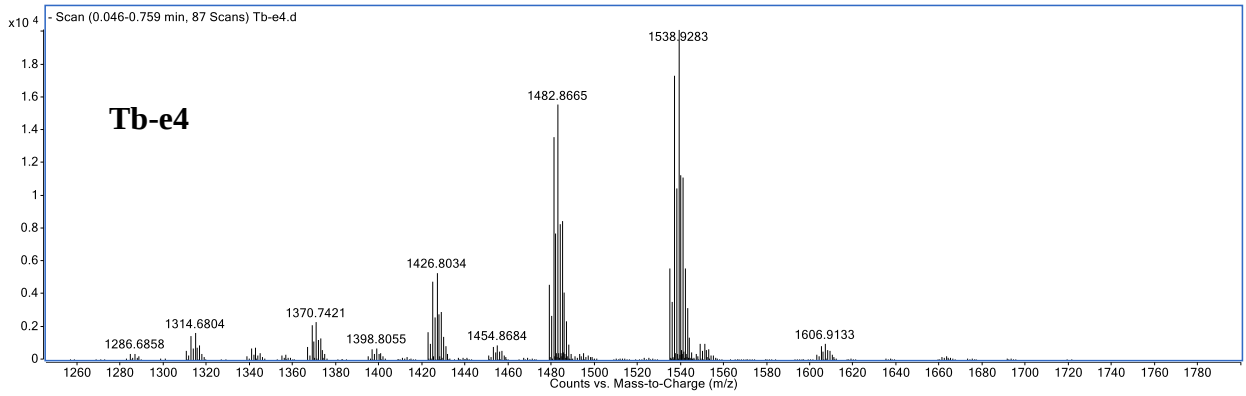

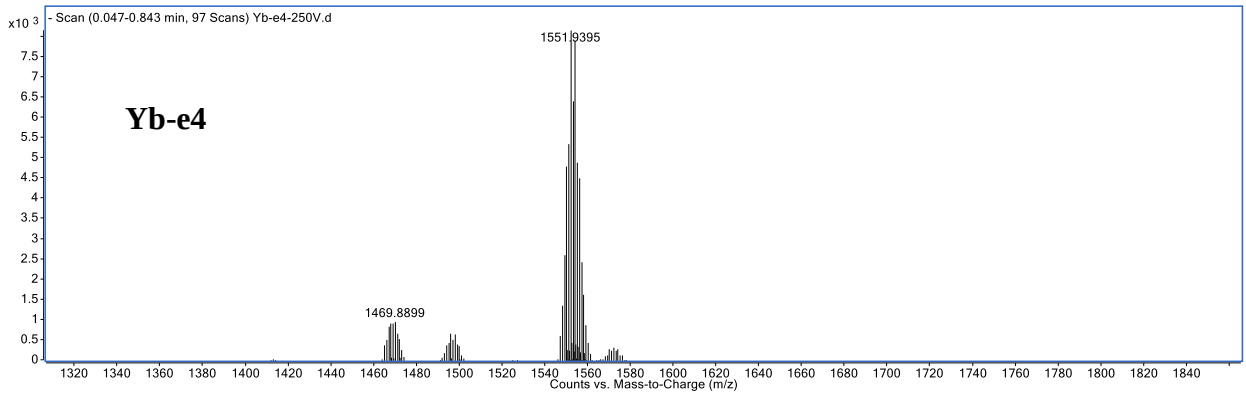

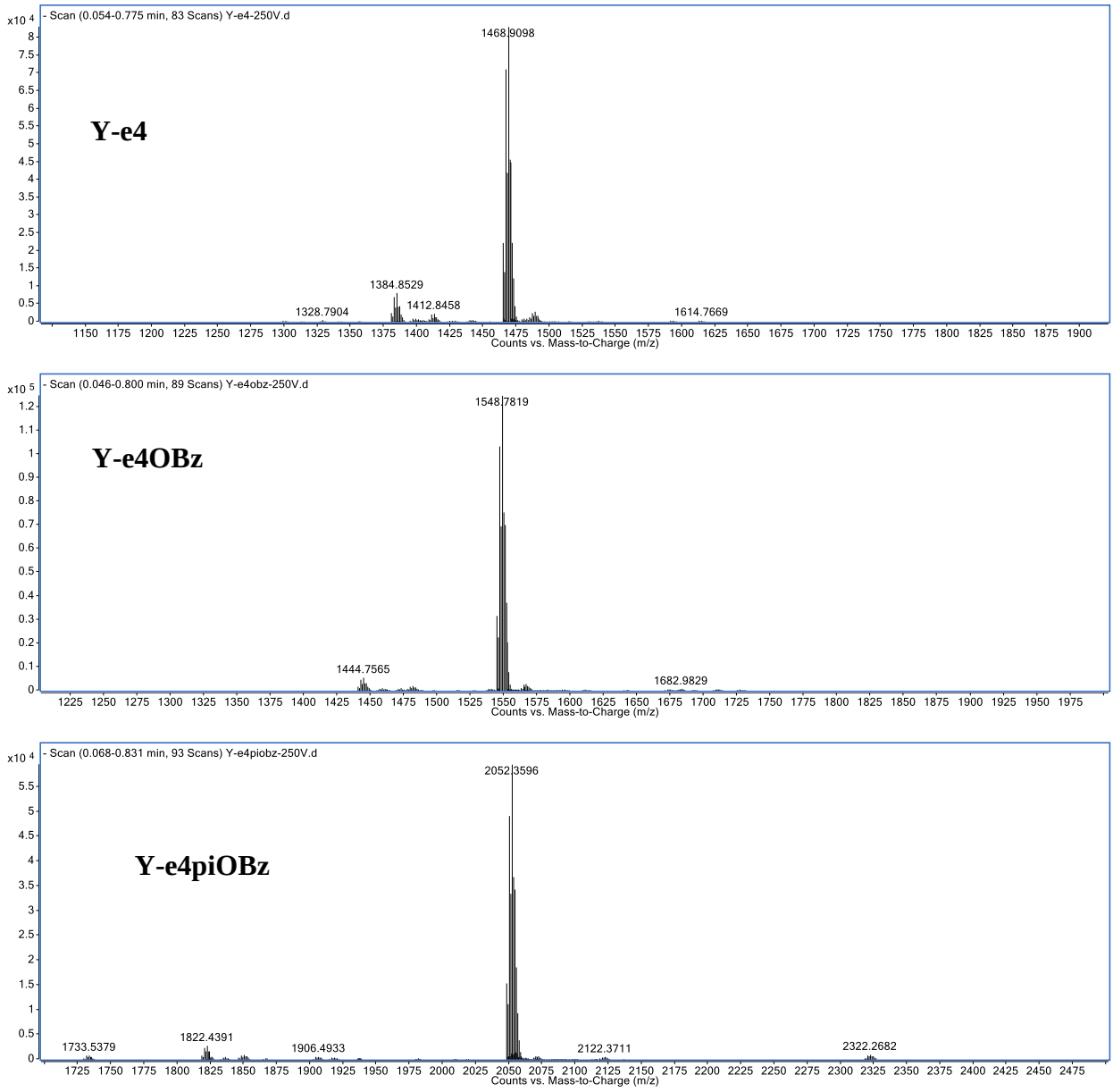

Figure C1. ESI-MS of **Ln-e4** complexes. Spectra were collected in negative ion mode with a fragmentation voltage of 250V in methanol. Background spectra were subtracted twice.

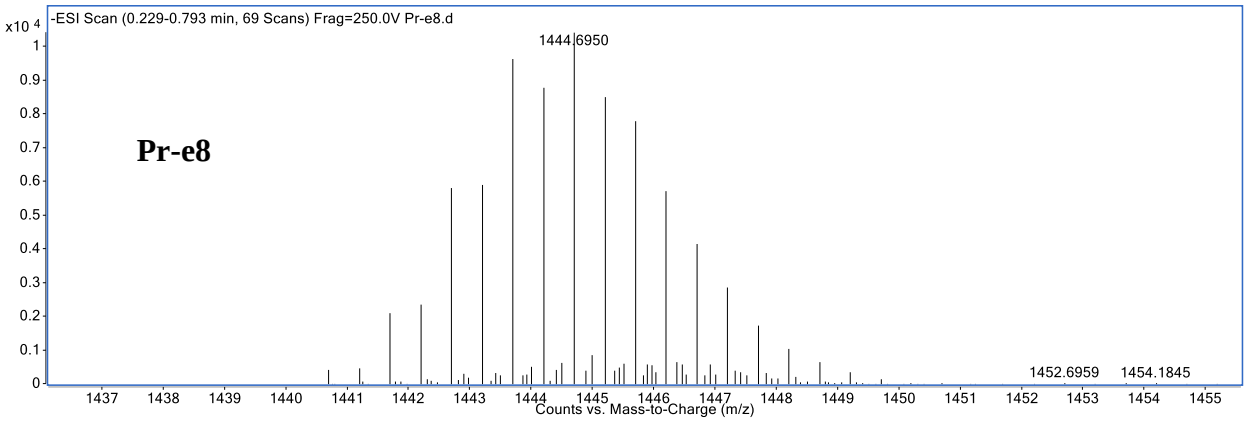
-ESI Scan (0.229-0.793 min, 69 Scans) Frag=250.0V Pr-e8.d
x10 4
1444.6950
Pr-e8
1452.6959
1454.1845
Counts vs. Mass-to-Charge (m/z)

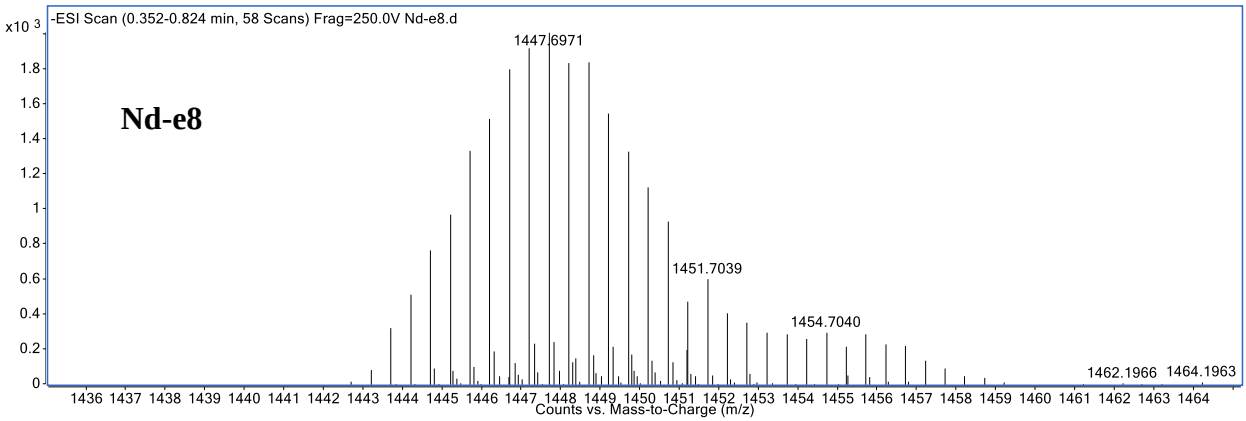
-ESI Scan (0.352-0.824 min, 58 Scans) Frag=250.0V Nd-e8.d
x10 3
1447.6971
Nd-e8
1451.7039
1454.7040
1462.1966
1464.1963
Counts vs. Mass-to-Charge (m/z)

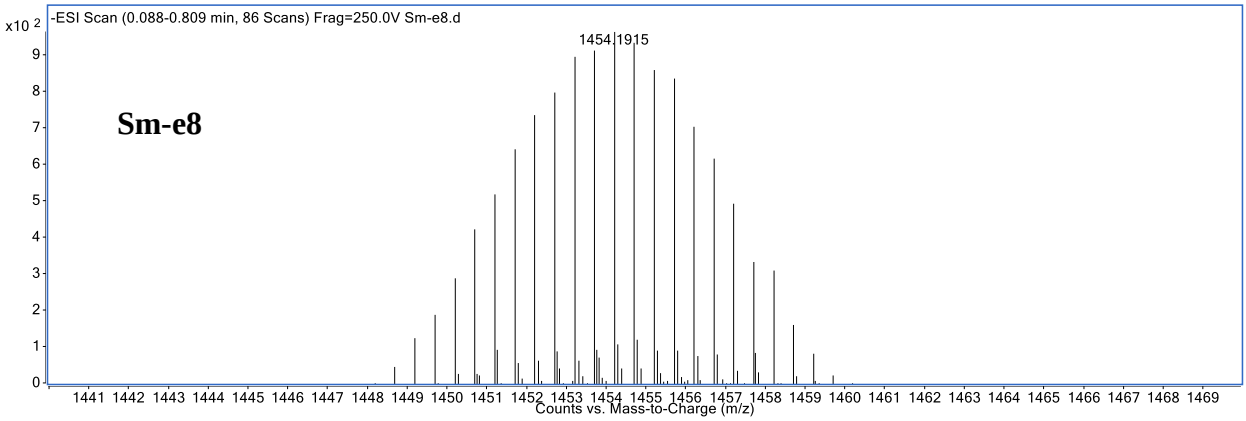
-ESI Scan (0.088-0.809 min, 86 Scans) Frag=250.0V Sm-e8.d
x10 2
1454.1915
Sm-e8
Counts vs. Mass-to-Charge (m/z)

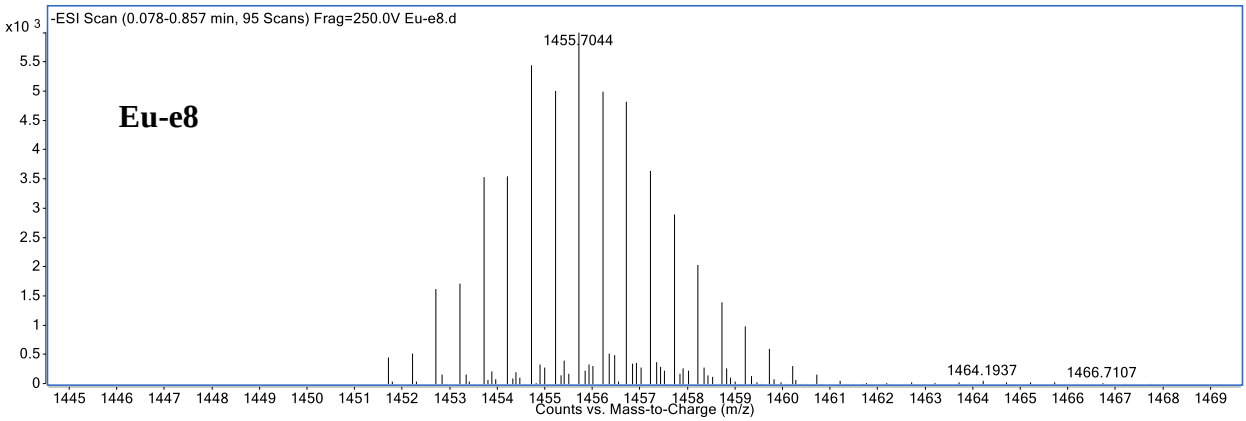
-ESI Scan (0.078-0.857 min, 95 Scans) Frag=250.0V Eu-e8.d
x10 3
Eu-e8
1455.7044
1464.1937
1466.7107
Counts vs. Mass-to-Charge (m/z)

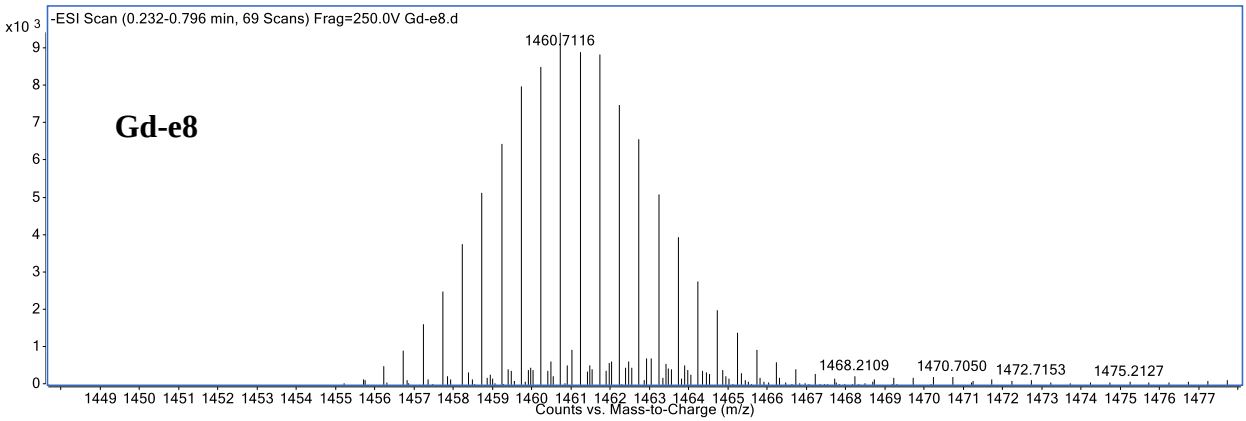
-ESI Scan (0.232-0.796 min, 69 Scans) Frag=250.0V Gd-e8.d
x10 3
Gd-e8
1460.7116
1468.2109
1470.7050
1472.7153
1475.2127
Counts vs. Mass-to-Charge (m/z)

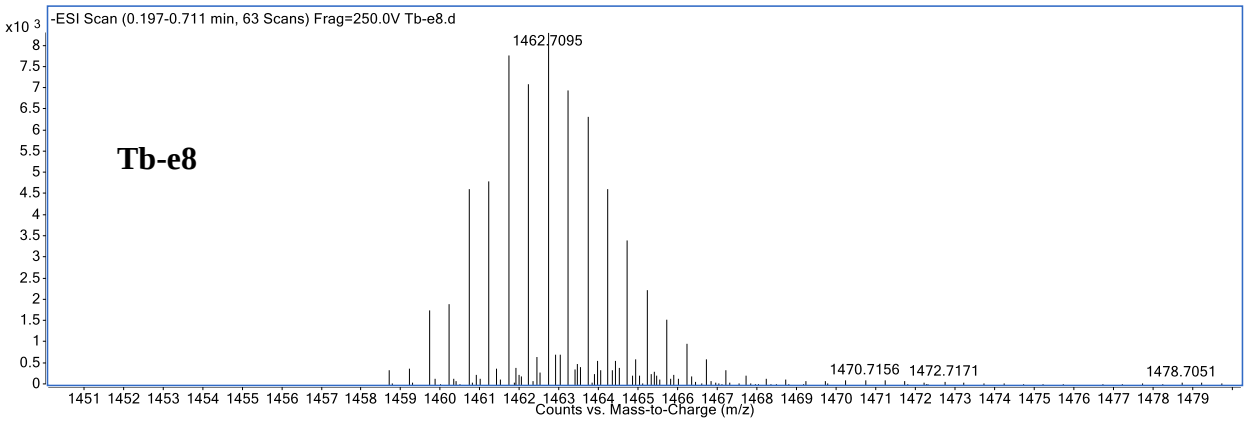
-ESI Scan (0.197-0.711 min, 63 Scans) Frag=250.0V Tb-e8.d
x10 3
Tb-e8
1462.7095
1470.7156
1472.7171
1478.7051
Counts vs. Mass-to-Charge (m/z)

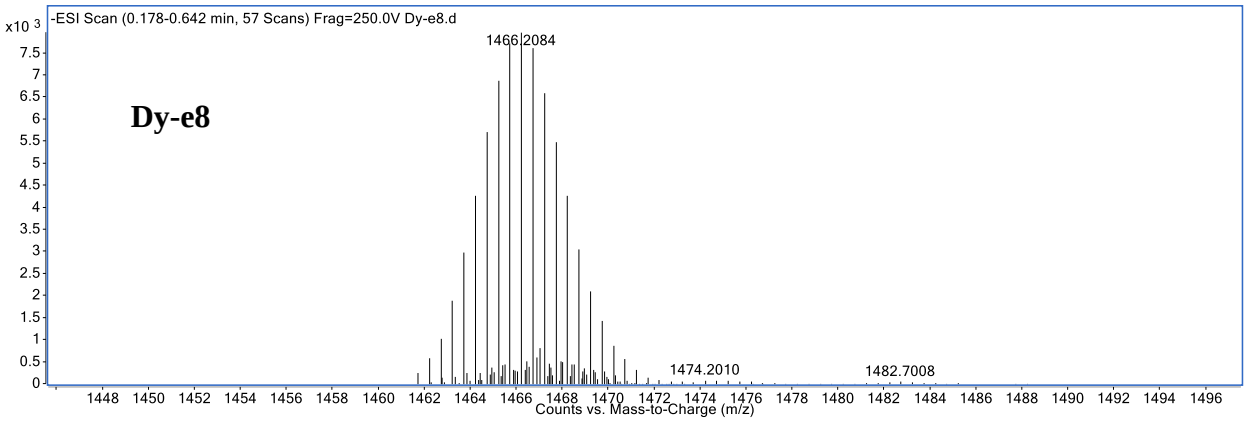
-ESI Scan (0.178-0.642 min, 57 Scans) Frag=250.0V Dy-e8.d
x10 3
Dy-e8
1466.2084
1474.2010
1482.7008
Counts vs. Mass-to-Charge (m/z)

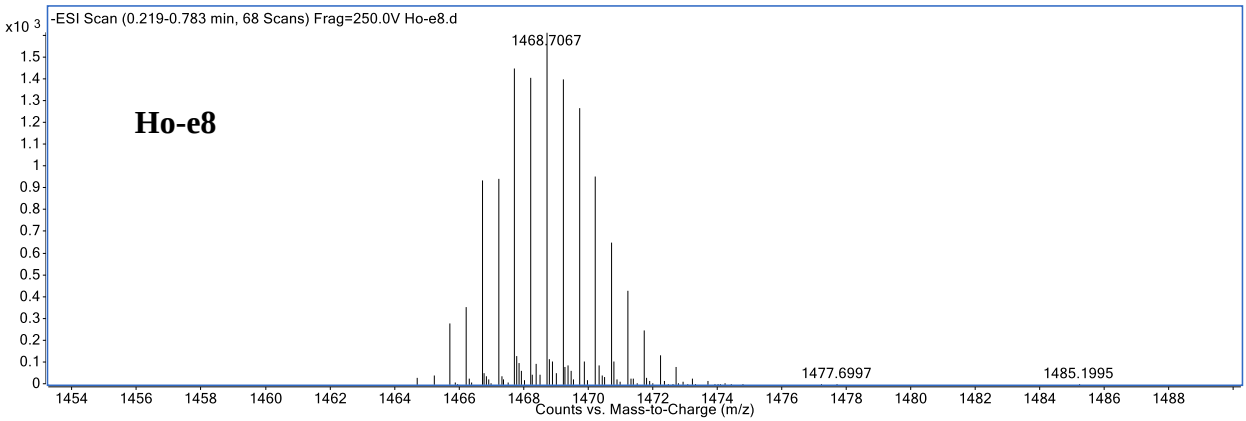
-ESI Scan (0.219-0.783 min, 68 Scans) Frag=250.0V Ho-e8.d
x10 3
Ho-e8
1468.7067
1477.6997
1485.1995
Counts vs. Mass-to-Charge (m/z)

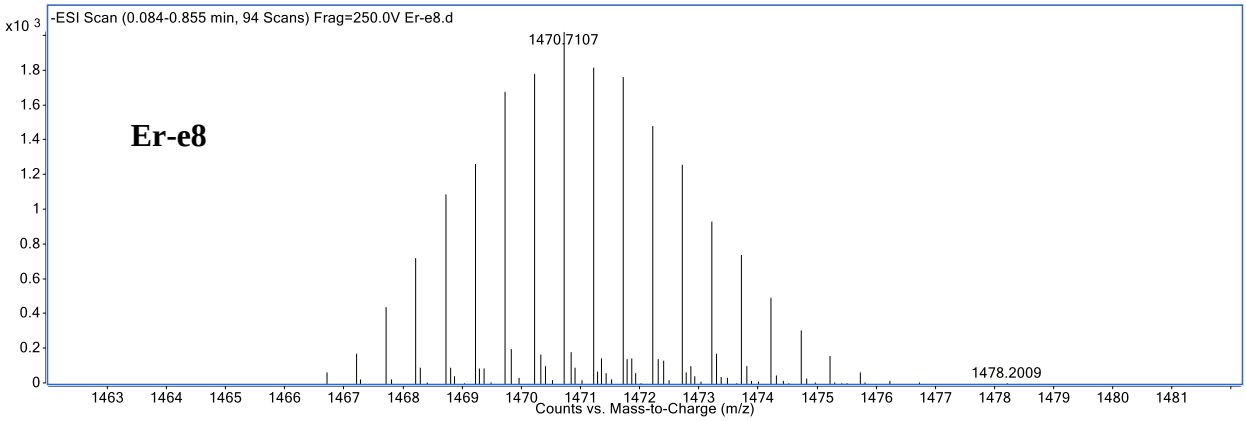
-ESI Scan (0.084-0.855 min, 94 Scans) Frag=250.0V Er-e8.d
x10 3
Er-e8
1470.7107
1478.2009
Counts vs. Mass-to-Charge (m/z)

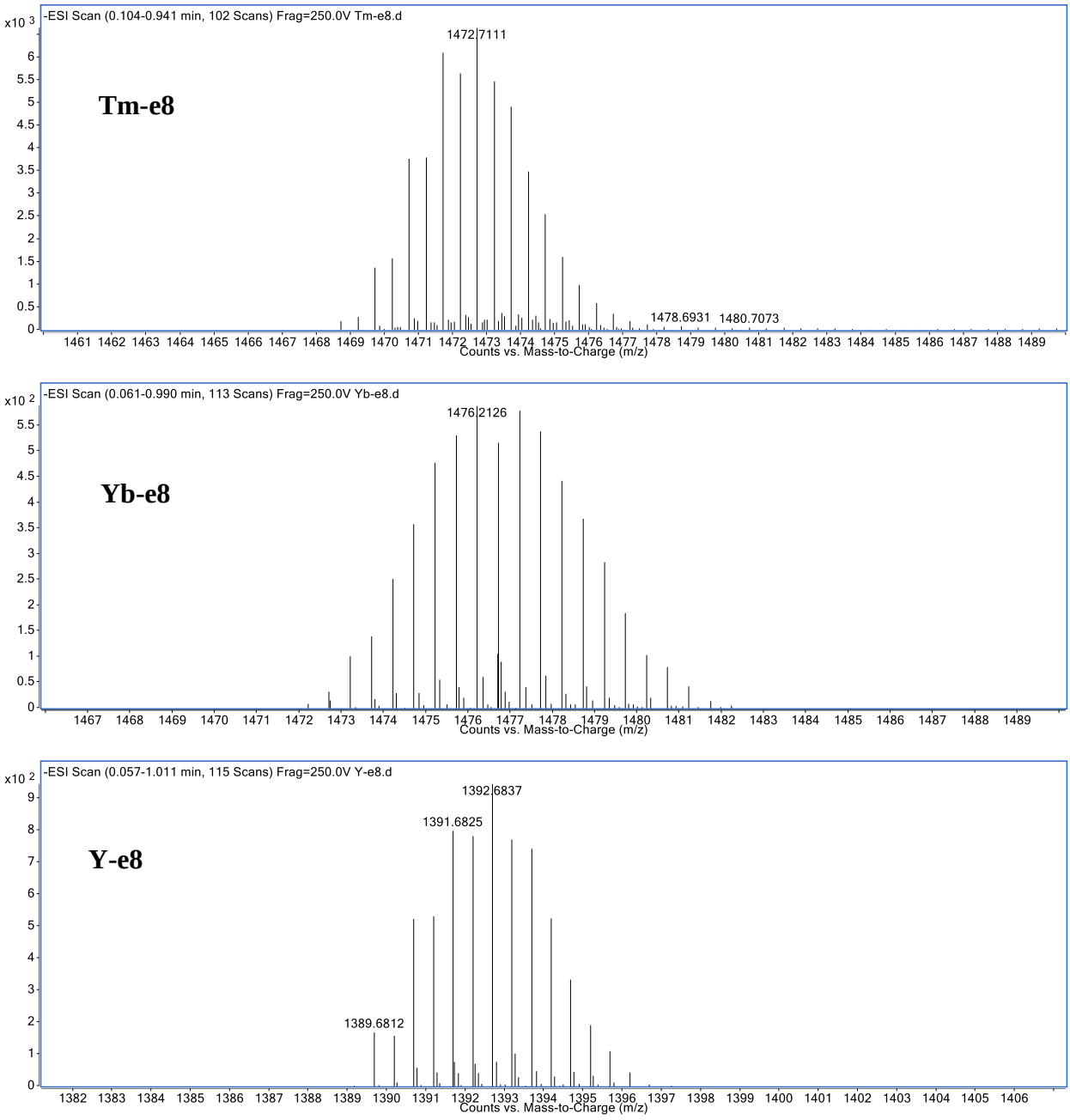

Figure C2. ESI-MS of **Ln-e8** complexes. Spectra were collected in negative ion mode with a fragmentation voltage of 250V in methanol. Background spectra were subtracted twice.

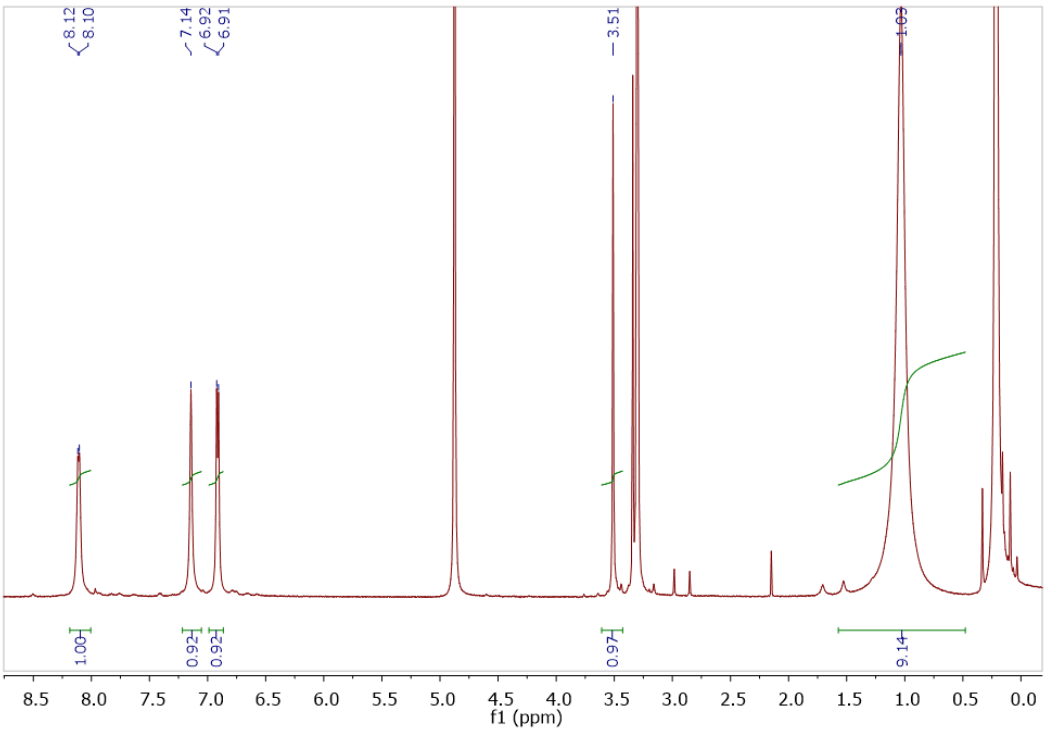

Figure C3. ^{1}H-NMR of **Sm-e4** in *d*$_4$-MeOH at RT.

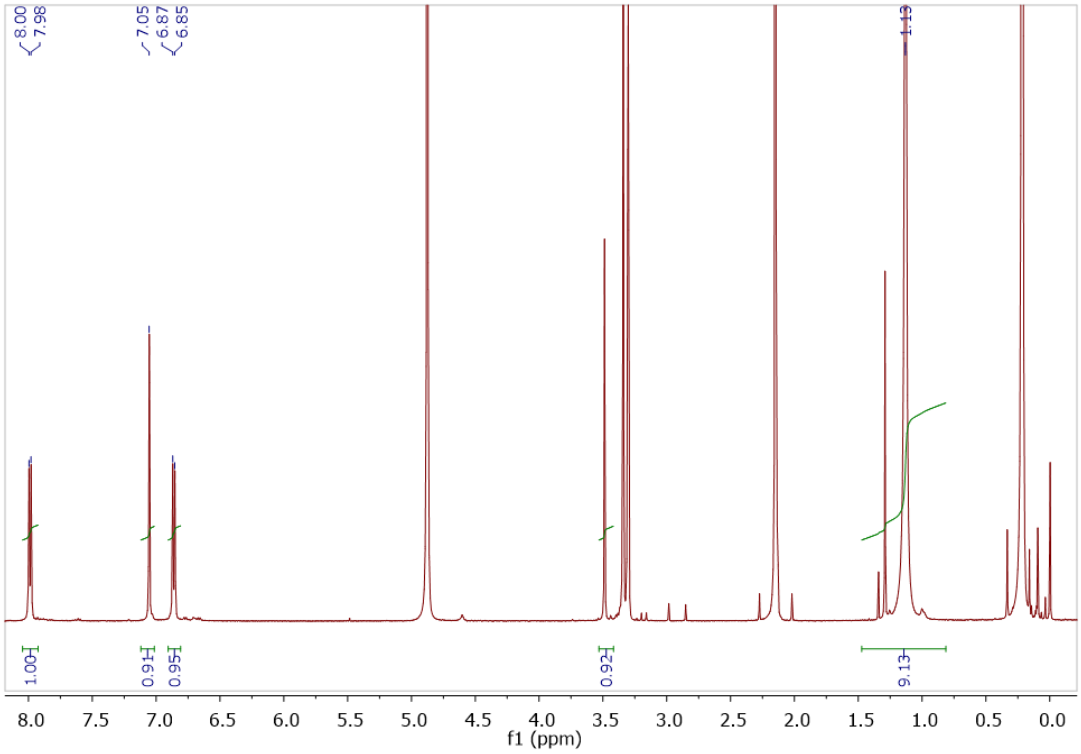

Figure C4. ^{1}H-NMR of **Y-e4** in *d*$_4$-MeOH at RT.

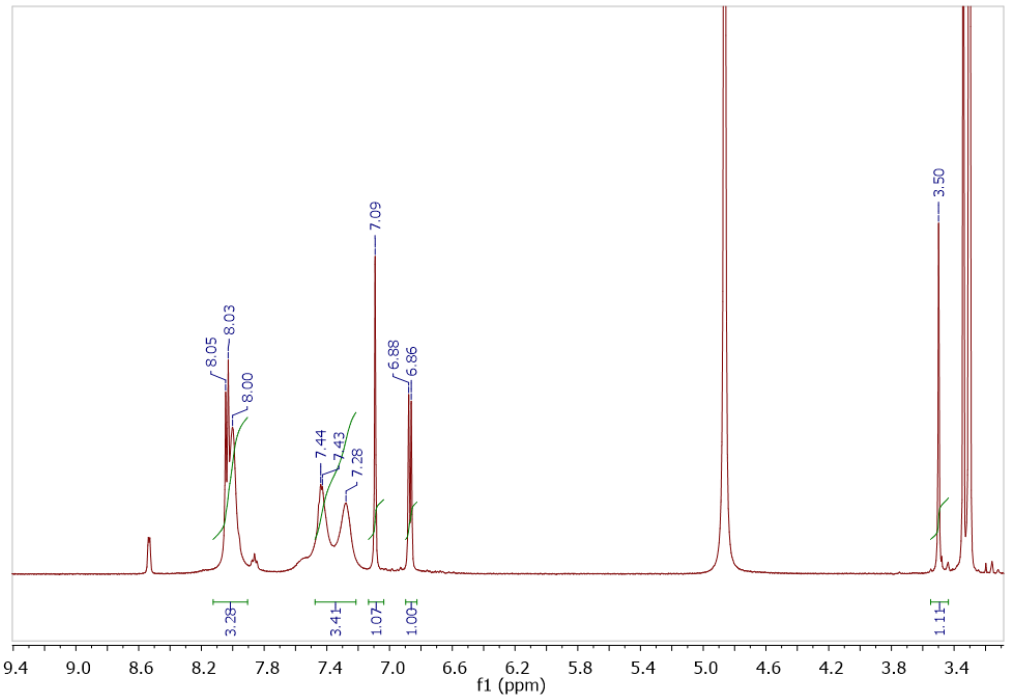

Figure C5. [1]H-NMR of **Y-e4OBz** in *d*$_4$-MeOH at RT.

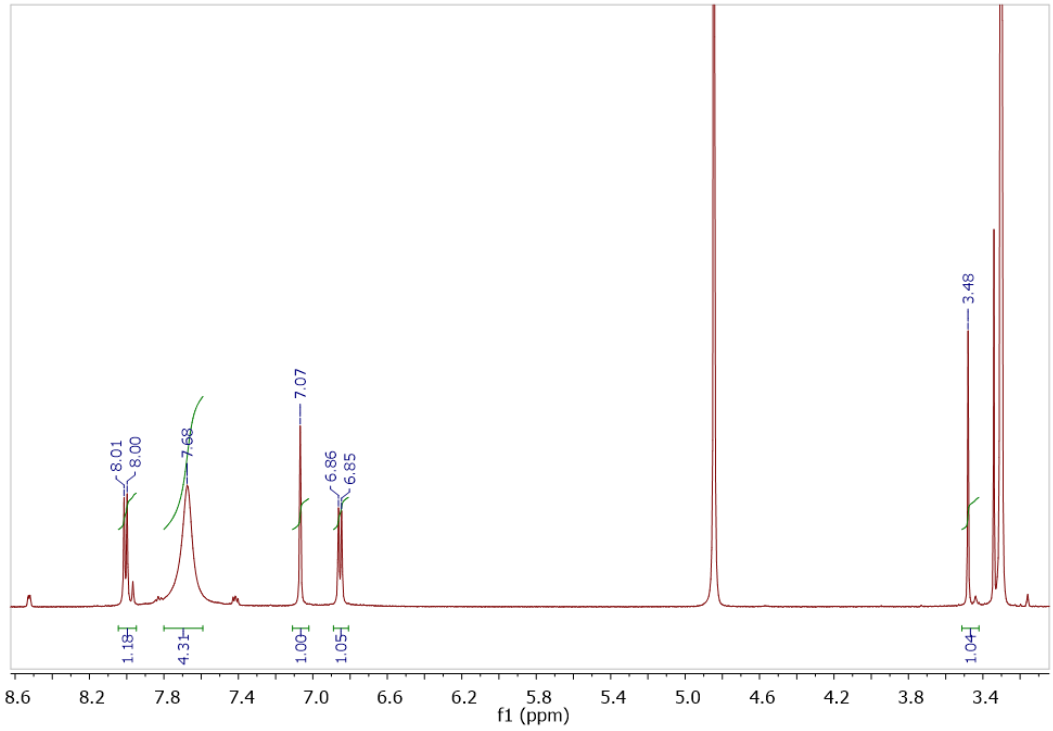

Figure C6. [1]H-NMR of **Y-e4piOBz** in *d*$_4$-MeOH at RT.

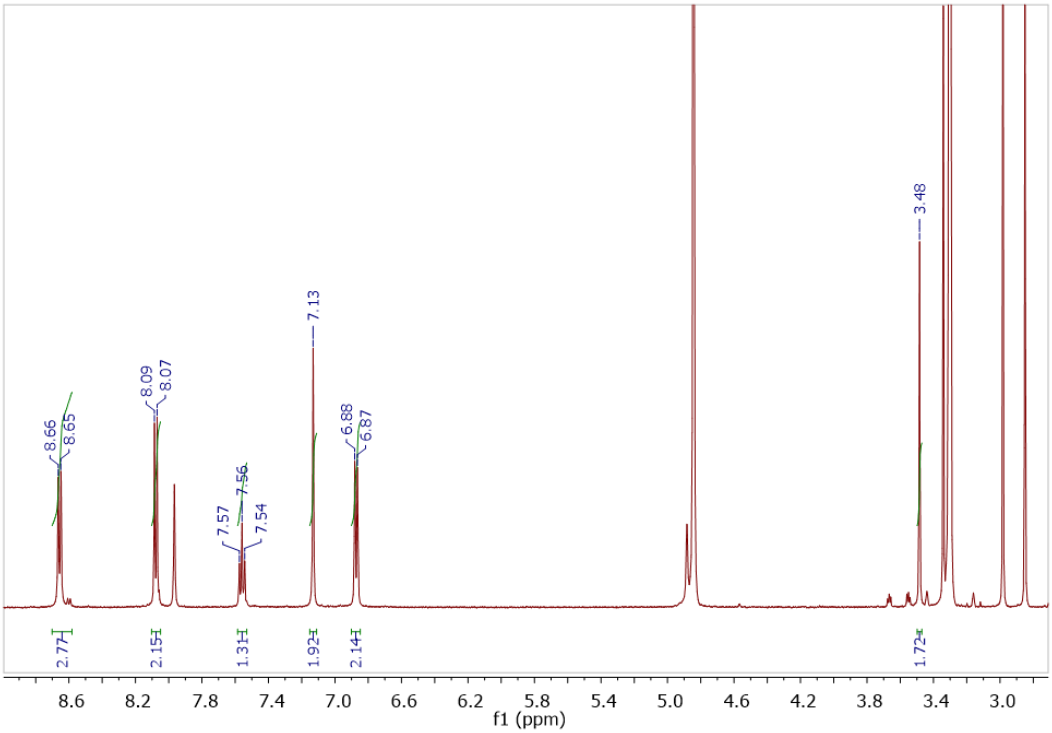

Figure C7. ^{1}H-NMR of **Sm-e8** in *d*$_4$-MeOH at RT.

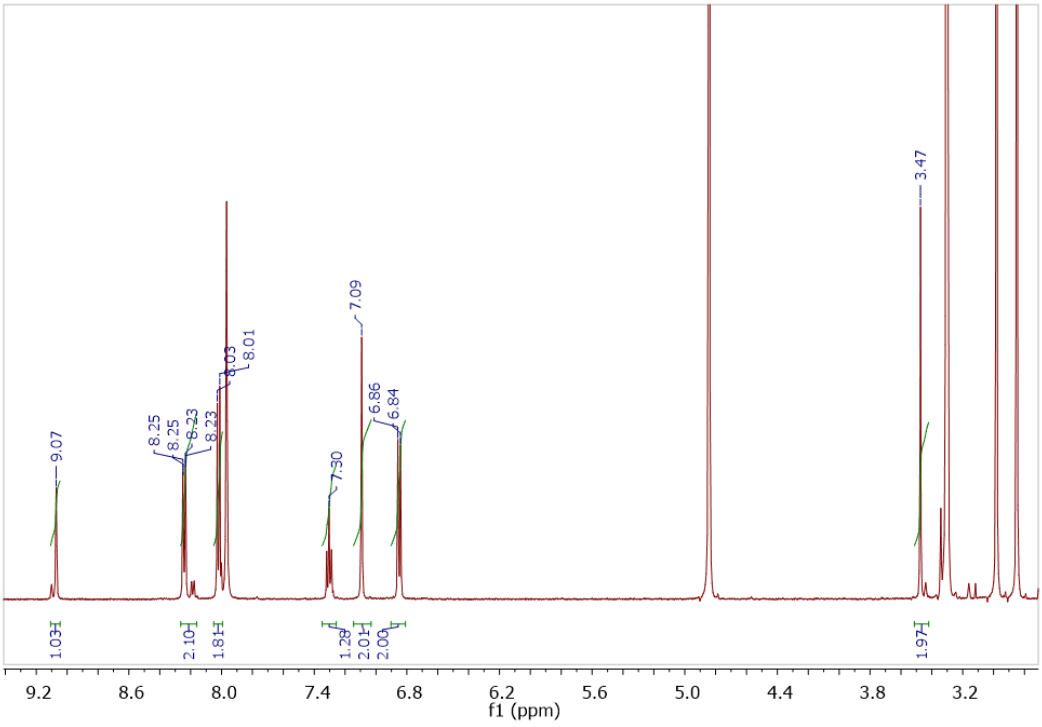

Figure C8. ^{1}H-NMR of **Y-e8** in *d*$_4$-MeOH at RT.

Appendix D. Calculating a Hydrodynamic Radius using the Stokes-Einstein Equation.[1]

First, the Stokes-Einstein Equation is defined as:

$$D = \frac{kT}{c\pi\eta r_H}$$

Where D is the diffusion coefficient, k is the Boltzman constant, T is the temperature, c is a numerical factor ranging from 4 to 6 related to "friction" of the molecule in solution, and η is the solution viscosity. To avoid approximating c, one may use a function derived via microfriction theory:

$$c = \frac{6}{1 + 0.695(\frac{r_{solv}}{r_H})^{2.234}}$$

Where r_{solv} is the hydrodynamic radius of the solvent. So by substituting for c the equation is now:

$$D = \frac{kT(1 + 0.695\left(\frac{r_{solv}}{r_H}\right)^{2.234})}{6\pi\eta r_H}$$

By using an internal standard (TMSS), the ratio of the molecule divided by the standard divides out many constants, leaving:

$$\frac{D}{D_{std}} = \frac{\frac{(1 + 0.695\left(\frac{r_{solv}}{r_H}\right)^{2.234})}{r_H}}{\frac{(1 + 0.695\left(\frac{r_{solv}}{r_{std}}\right)^{2.234})}{r_{std}}}$$

Since, the r_{solv} and r_{std} are known in the literature, only r_H remains. Finding r_H may be done by minimizing the difference between the calculated ratio to and the experimental ratio using Excel.

References

(1) Zuccaccia, D.; Macchioni, A. *Organometallics* **2005**, *24* (14), 3476–3486.